



**HAL**  
open science

# Femtosecond laser direct writing of circular optical properties in silica glass

Jing Tian

► **To cite this version:**

Jing Tian. Femtosecond laser direct writing of circular optical properties in silica glass. Material chemistry. Université Paris-Saclay, 2020. English. NNT : 2020UPASF038 . tel-03180913

**HAL Id: tel-03180913**

**<https://theses.hal.science/tel-03180913>**

Submitted on 25 Mar 2021

**HAL** is a multi-disciplinary open access archive for the deposit and dissemination of scientific research documents, whether they are published or not. The documents may come from teaching and research institutions in France or abroad, or from public or private research centers.

L'archive ouverte pluridisciplinaire **HAL**, est destinée au dépôt et à la diffusion de documents scientifiques de niveau recherche, publiés ou non, émanant des établissements d'enseignement et de recherche français ou étrangers, des laboratoires publics ou privés.

# Femtosecond laser direct writing of circular optical properties in silica glass

## Thèse de doctorat de l'université Paris-Saclay

École doctorale n°571 : 2MIB

(Sciences chimiques : molécules, matériaux, instrumentation et biosystèmes)

Spécialité de doctorat: Chimie

Unité de recherche : Université Paris-Saclay, CNRS, Institut de chimie moléculaire et des matériaux d'Orsay, 91405, Orsay, France.

Référent : Faculté des sciences d'Orsay

Thèse présentée et soutenue à Orsay, le 17 décembre  
2020, par

**Jing TIAN**

### Composition du Jury

**Fabian ZOMER**

Professeur des universités  
Université Paris Saclay

Président

**François COURVOISIER**

Directeur de recherche  
CNRS - Université de Franche-Comté

Rapporteur & Examineur

**Razvan STOIAN**

Directeur de recherche  
CNRS - Université Jean MONNET

Rapporteur & Examineur

**Enrique GARCIA-CAUREL**

Ingénieur de recherche  
Ecole polytechnique

Examineur

### Direction de la thèse

**Matthieu LANCRY**

Enseignant-Chercheur  
ICMMO, Université Paris-Saclay

Directeur de thèse



# OUTLINE

Acknowledgement .....	9
Introduction .....	11
Chapter1 State of the art of Femtosecond Laser Direct Writing in Glasses .....	20
1.1 Introduction.....	21
1.2 Silica Glass.....	21
1.3 Propagation of ultrashort laser pulses in a vitreous material .....	23
1.3.1 Basic principles .....	23
1.3.2 Self-focusing by Kerr effect.....	25
1.3.3 Filamentation.....	26
1.3.4 Self-phase modulation.....	26
1.3.5 Spectral dispersion and temporal broadening .....	26
1.4 Femtosecond laser interactions in glasses .....	28
1.4.1 Ionization and relaxation in intense field.....	28
1.4.2 Relaxation mechanisms .....	30
1.4.3 Material changes induced by femtosecond laser irradiation .....	31
1.4.4 Heat accumulation effects.....	32
1.5 Damage thresholds and different type of permanent modifications...34	
1.5.1 Isotropic index changes based modifications (Type I).....	36
1.5.2 Anisotropic refractive index changes based modifications (Type II).....	38
1.5.3 Voids (Type III) .....	40
1.6 Focus on Type II modifications and nanogratings formation.....	40
1.6.1 From LIPSS to self-organized nanogratings in silica.....	40
1.6.2 Physical and optical properties of nanogratings in silica glass.....	42
1.6.3 Tentative mechanisms for nanogratings formation.....	43
1.6.4 Nanogratings parameters dependence.....	48
1.7 Towards 3D imprinted optical chirality in inorganic glasses.....	54
1.8 Conclusions.....	57
1.9 References.....	59
Chapter2 Experimental details.....	71

2.1 Introduction.....	72
2.2 Femtosecond laser direct writing (FLDW) system.....	72
2.3 Fundamentals of polarization of light .....	76
2.3.1 Stokes vector and the Poincaré sphere .....	76
2.3.2 Mueller matrix formalism.....	78
2.4 Basic polarimetric properties.....	78
2.4.1 Dichroism and diattenuation.....	79
2.4.2 Retardation and linear birefringence.....	81
2.4.3 Depolarization.....	84
2.4.4 Polarizance .....	87
2.5 Extraction of polarimetric properties .....	88
2.5.1 Product decomposition .....	88
2.5.2 Sum decomposition.....	89
2.5.3 Logarithmic decomposition.....	90
2.6 Polarimetric instrumentation.....	93
2.6.1 “de Sénarmont” compensator.....	94
2.6.2 Circular Dichroism spectro-polarimeter - JASCO- J-810.....	97
2.6.3 Vis-Near IR (400-1000nm) Mueller Ellipsometry – MM-16.....	101
2.6.4 UV-Vis-Near-IR Mueller ellipsometry – MM-12.....	102
2.7 Conclusions.....	105
2.8 References.....	106

## Chapter3 Study of laser induced circular dichroism using a CD spectro-polarimeter..... 110

3.1 Introduction.....	112
3.2 Samples and Methodology.....	113
3.3 Preliminary experiments to identify the modifications thresholds of linear optical properties.....	116
3.3.1 Study of writing kinetics at various repetition rates .....	116
3.3.2 Study of writing kinetics according to the numerical aperture .....	118
3.3.3 Study of writing kinetics according to the laser polarization.....	119
3.3.4 Spectral measurements of the retardance and linear extinction difference ....	120
3.4 Study of femtosecond laser irradiated silica using a CD spectro-polarimeter.....	121

3.4.1 Preliminary observations.....	121
3.4.2 Study of circular diattenuation CD according to the pulse energy.....	122
3.4.3 Study of circular diattenuation CD according to the line-to-line spacing.....	123
3.4.4 Study of circular diattenuation according to the angle between polarization orientation and the laser scanning direction .....	126
3.4.5 Study of circular diattenuation according to the pulse-to-pulse overlapping rate and the laser repetition rate.....	129
3.4.6 Study of circular diattenuation according to the focusing depth.....	131
3.5 Analysis of CD measurements artifacts and asymmetric transmission of circularly polarized light.....	132
3.5.1 Study of CD artifacts due to the spectro-polarimeter.....	132
3.5.2 Investigations of Asymmetric transmission of circularly polarized light .....	135
3.6 Discussion on the origin of fs laser-induced chiral optical property. 137	
3.6.1 An introduction to chirality and chiral optical properties in molecules.....	137
3.6.2 Qualitative interpretation.....	138
3.7 Conclusions.....	140
3.8 References.....	144

Chapter4 Mueller matrix spectro-polarimetry in femtosecond irradiated silica glass .....	151
4.1 Introduction.....	152
4.2 Materials and methods .....	153
4.3 Typical results using MM-16 spectro-polarimetry .....	155
4.3.1 Raw Mueller matrix measurements.....	155
4.3.2 Extraction of polarimetric properties.....	157
4.3.3 Investigation of asymmetric transmission .....	160
4.4 Study of laser parameters dependence: pulse energy, pulse-to-pulse overlap and focusing depth .....	163
4.5 Influence of the laser writing configuration.....	172
4.5.1 Influence of the writing polarization direction for a fixed scanning direction and orientation i.e. along +X .....	175
4.5.2 Influence of the laser scanning direction with respect to the writing laser polarization.....	178

4.6 Dependence of the stress-induced birefringence with the laser writing polarization .....	180
4.7 Thermal stability of fs-induced anisotropic optical properties .....	184
4.8 Conclusions.....	193
4.9 References.....	196

Chapter5 Investigations of the UV-Vis-NIR spectral properties: comparison between nanogratings and stress-induced birefringence silica glass .....

5.1 Introduction.....	203
5.2 Spectral dependence of femtosecond laser induced circular optical properties in silica .....	204
5.3 A Comparison between Nanogratings-Based and Stress-Engineered Waveplates Written by Femtosecond Laser in Silica .....	205

Chapter6 Discussion on the origin of the anisotropic linear and circular optical properties created within Type II regime.....

6.1 Introduction.....	208
6.2 On the origin of the anisotropic linear optical properties within Type II regime in fs-irradiated silica glass .....	209
6.2.1 Form birefringence within Type II regime.....	209
6.2.2 Stress-induced birefringence within Type II regime .....	215
6.2.3 Point defects formation and annealing within Type II regime.....	219
6.2.4 Conclusion on anisotropic linear properties thermal stability .....	222
6.3 Modeling anisotropic circular optical properties using Mueller matrix formalism using a two linear retarders model .....	223
6.3.1 Short description of the modeling procedure .....	224
6.3.2 Modelling a single linear retarder .....	226
6.3.3 Modelling the formation of CB only using two linear retarders.....	227
6.3.4 Modeling the formation of CD with two linear retarders .....	231
6.3.5 Modeling the formation of both CB and CD using two linear retarders.....	234
6.4 Polarization dependent anisotropic optical properties: a comparison between modeling and experimental measurements.....	236

6.5 Interpretation of the polarization dependent anisotropic optical properties and the creation of circular optical properties.....	239
6.6 Conclusions.....	244
6.7 References.....	246
Conclusions and perspectives.....	252
Publications list.....	260
Résumé substantiel en Français .....	262





## Acknowledgement

I would like to express my gratitude to the numerous individuals whose help and support assisted my professional growth during my recent years and contributed to my work presented in this thesis.

Firstly, I want to thank to my PhD supervisor Matthieu LANCRY, who introduced me to the research in physics and optics and lead my doctoral project and creating good atmosphere in the laboratory.

I acknowledge all the help and support from our research group members Bertrand Poumellec, Rudy Desmarchelier, Yitao Wang, Maxime Cavillon, Ruyue Que, Benjamin Sapaly. Especially I want to thank to our collaborators Enric Garcia-Caurel, Sang Hyuk Yoo, Razvigor Ossikovski from Ecole Polytechnique and Michel Stchakovsky, Celine Eypert from HORIBA, as they helped me a lot to learn new field about Mueller matrix ellipsometry techniques.

I am grateful to my friends Miaobo Pan and Kuankuan Zheng who supported me a lot during my PhD.

And my final appreciation is to the China scholarship council (CSC) who gave the opportunity to study in the Université Paris-Saclay by supporting my PhD financially.



# Introduction

What is the common problem existing between the mastering of elaboration of all optical functions in a glass for integrated optics? It is the control of the final product structure (the atomic arrangement) and of its orientation resulting in a control of the imprinted optical properties. One current challenge is to achieve these goals “simply” by using laser light.

The photosensitivity of glass (e.g. in germanosilicates and Boron-doped silica glasses) to ultraviolet (UV) laser radiation (continuous wave or nanosecond pulsed lasers) was perceived in the 1990s as a tool for functionalizing materials. Chemistry quickly took its share within this field, as it was realized that photosensitivity was a function of glass chemical composition as well as its physico-chemical environment (including material thermal history and surrounding environmental conditions). Thus, the physical properties of the material, subsequent its laser irradiation, originated from photochemistry processes. The lasers used at that time, though relatively intense (usually continuous or nanosecond UV lasers) to induce substantial structural modifications of a material, were still in linear optical domain or nonlinear through two-photon absorption. The main strategy was to use point defects, absorbing in the material optical bandgap, as an initial step to couple energy into the glass network. Typically, homogeneous Gaussian laser beams, with an axisymmetric structure, were used to deposit optical energy inside the glass material mainly by linear absorption or sometimes through a two-photon process [1].

The development of femtosecond lasers, enabling the use of pulses having extremely high powers, completely transformed this vision. Using these lasers, the peak power density is such that the research community moved to nonlinear optics with the possibility of electrons excitation across the silica optical bandgap, using six photons or even eight photons at 800 nm or 1030 nm, respectively. In fact, the femtosecond pulses make it possible, by delivering the energy in a controlled volume, to easily reach very high power densities (typically  $10^{12-14}$ W/cm<sup>2</sup> after focusing). These multiphoton excitations lead to photo-induced physicochemical reactions and various structural modifications [2]: changes of the intrinsic material ordering (through a fictive temperature change), phase changes (re-crystallization, phase separation), chemical migrations. These modifications induce permanent changes of physical properties, including dielectric tensor, second order nonlinear optical properties (frequency doubling, electro-optical effects...). It is thus an attractive candidate for many applications since the photo-induced effects are by nature strongly localized in 3D in a “voxel” volume of a few cubic microns ( $\mu\text{m}^3$ ).

Since the early birth of femtosecond lasers in the 1990s, Femtosecond Laser Direct Writing (FLDW) has opened a new path allowing 3D micro/nano-structuring of the linear and non-linear optical properties of transparent materials with functionalities inaccessible by other processes. From a broader standpoint, it becomes possible to imprint optical components at low cost, and/or to shape any beam into any other one, characterized by a set of parameters  $\vec{k}(r)$ ,  $\vec{e}(r)$  and  $\vec{I}(r)$ , where  $r$  is a spatial position located in the beam cross-section,  $\vec{k}$  is the wave vector,  $\vec{e}$  is the polarization vector and  $I$  is the intensity). In this sense, the research community envisions to produce new structures and new 3D optical devices

such as Fresnel lenses, axicons, delay plates (e.g. for the compensation of aberrations), Bragg gratings in volume (e.g. pulse compression or stabilization of fiber lasers) but also birefringent elements such as micro-wave arrays for polarimetry, radial / azimuth polarization converters, polarizing waveguides [3-7]. These devices have enormous potential for micro-optics, communications, lasers, data storage systems or imaging. The impact at the industrial level is recognized and it is clear that this technology will generate employment activities. Thus, femtosecond laser direct writing is expected to become an ubiquitous tool of choice for the realization of micro optical devices in 3D. One objective of this thesis is to control the material transformations induced through it.

In this context, understanding interaction of matter with femtosecond laser pulses will enable the evaluation of the industrial potential this new direct writing method has to offer. Some aspects of the light-matter interaction are fundamentally new. The underlying physics is the behavior of electron plasma in the presence of an ionic support and of a light wave. Here, solid and plasma states coexist for a fraction of picosecond. In addition, both, matter and light are in interaction to produce a structured organization of the plasma density. The fundamental problems are to accurately describe the structuration of the plasma of free electrons produced at the end of multiphoton ionization (transition through the gap of the transparent insulator). Here the solid intervenes as a source of electrons. Its microstructure organizes the plasma in coherence with that of the light beam. Then, after the pulse, this electron density distribution is "imprinted" by trapping electrons in the solid, and, it can be used as a "source" by the next pulse thus ensuring a memory effect. In this operation, the solid is not destroyed; it remains below the vaporization threshold, it is restructured in the force field created by the laser. We can therefore imagine the orientation of the material, imprinted oriented nano/microstructures like directionally solidified eutectics. This is a new physics. But for chemistry too, there are new aspects because the processes involve highly excited states, which are largely off equilibrium. It is therefore necessary to question some previous ideas. For example, the knowledge on the effect of impurities, defects states, or easily ionized states, remains highly limited. In addition the use of ultrashort pulses has an original characteristic: a large spectral width ( $100 \text{ fs} \equiv 10 \text{ nm}$ ). The phasing of the spectral components is the laser manufacturer's goal to achieve maximum compression of the pulse (minimum duration of the pulse). But these components can be separated, modified and recombined to produce pulses of various shapes that have different effects in the transparent material. In particular, force fields and not energy fields are produced. Their control opens the door to a science of material modification by laser. This is the focus of the today work carried out by Bertrand Poumellec and Matthieu Lancry. In particular, three discoveries form the basis of this PhD thesis.

The first breakthrough is from our colleagues at Southampton and Kyoto Universities, namely Peter Kazansky and Y. Shimotsuma, who discovered self-organized nanogratings in  $\text{SiO}_2$  (200-400 nm periodicity persisting on mm range, including fringes as thin as 10-30 nm), which are in fact the smallest structures ever created by light [8]. From the authors, these nanogratings arise from modulation of the chemical composition (probably oxygen redistribution) and this would be related to stationary density waves in the plasma produced by the coupling between bulk plasmonic waves and light waves. In 2011, our group revealed

that nanogratings are in fact an assembly of nanoporous layers due to oxide decomposition [9, 10] likely through a tensile stress assisted nanocavitation process [11]. These structures, also called Type II modifications in the literature, are at the root of other experimental unusual phenomena like high linear birefringence response (up to  $-10^{-2}$ ), polarized luminescence, anisotropic light scattering, strong linear "dichroism", negative index changes and extraordinary good thermal stability (until a few 10's hours at 1000°C). These experimental observations left a number of opened questions that should be addressed to enable reliable applications. How to master such structures and the resulting properties, and consequently how to use them efficiently?

The second breakthrough is the discovery of a sensitive interaction with the direction of writing (***directional writing dependence***), which is original [12, 13]. Thus, we observed differences in the effect between scanning the sample (centrosymmetric) with the laser beam, for a given direction, in one direction and the other; a bit like we can see a difference between writing a line of characters from right to left or from left to right with the same pen holder! But this is also different according to the scanning orientation (***orientational writing dependence***). This asymmetrical behavior of the interaction is likely due to the interaction process between the laser and the material revealing some unusual behavior. It appears that the pulse is ultra-short, the latter being associated with a significant spectral width and that the beam at the focal point is probably not axisymmetric [14]. Moreover these asymmetric structures translate in an original way on several properties [15] such as the appearance of a strong linear birefringence, a linear dichroism, and the transition from nanogratings to bubbles formation...

The third breakthrough is our recent discovery of the creation of photo-induced ***chiral mechanical structures*** in silica glass by a femtosecond laser being linearly polarized [13, 16]. Let us recall that neither the laser beam (linearly polarized), nor the matter (glass is center-symmetric), show chirality. In addition, due to laser beam asymmetry, this interaction is also sensitive to the direction of writing. However, the inscription of orientable circular properties has not made a breakthrough until our recent publication [17]. This last point is a breakthrough because the creation of this circular di-attenuation has been done in an achiral glass (pure silica) with a beam that could have been considered achiral under an orthogonal geometry. This result and how it was obtained was thoroughly debated before being accepted because of the newly aspect. Such circular optical properties play a crucial role in optoelectronic devices, biological sensing, and analytical chemistry. The challenge of this PhD thesis was thus to pave the way of a new paradigm in the understanding of the interaction of femtosecond laser with mater, in order to control the overall anisotropic optical properties (sign, amplitude, orientation, at the microscale level) in transparent solid materials using a low cost, ideally environmentally friendly, and sustainable technology for optical applications. These experimental observations underpin a large number of questions to be answered. As a result, the heart of this thesis work aims to:

- Characterize and understand the laser-induced transformations in silica-based glasses, their types and their structuration. The principal interest it is to understand the mechanisms at the root of such spectacular changes in anisotropic optical properties and in particular circular optical properties.

- Master this type of photosensitivity that will allow us to correctly assess the potential of this new method and to fully exploit the strength of this interaction. This will open the door towards innovative applications based on these anisotropic linear and circular optical properties.

First of all, the first chapter provides a review of the basic knowledge necessary to fully understand this thesis. We will highlight the structure of silica glass, which is the principal material constituting our samples. We shall discuss ultrashort laser pulse propagation in glass as well. Therefore, we will summarize the different processes of interaction leading to structural changes, associated with the formation of permanent changes in the glass optical properties. Finally, the last part of this chapter will focus on the anisotropic optical properties (birefringence and dichroism) and nanogratings formation in silica glass. In particular these anisotropic optical properties will be measured and studies throughout this thesis.

The second chapter is dedicated to the experimental techniques necessary to carry out all of our studies in the next chapters. We describe the femtosecond laser direct writing (FLDW) bench available in our institute (ICMMO at University Paris Saclay) and the experimental conditions that I used to realize my thesis. The predominant nondestructive way of characterizing nanogratings is quantitative birefringence measurements and more generally anisotropic optical properties, which provide information on the dependence of induced modifications on the laser writing parameters. Thus, we will introduce fundamentals of polarization of light, Stokes formalism and the Mueller calculus formalism, which is a complete mathematical approach to describe the polarimetric light-matter interaction. Finally the overall spectro-polarimetric characterization methods will be described, since they provide the means to measure the key physical quantities of the femtosecond laser written structures with sufficient accuracy to draw meaningful conclusions from the experiments designed in each chapter.

Chapter 3 is dedicated the investigation of circular di-attenuation that might occur in the laser-matter interaction within a silica glass. The mechanism of interaction of the femtosecond laser light with dielectric materials is not fully understood. However, one recognized specificities due to the very small pulse duration is that the action of the light on electrons and ions is decoupled. Then, by choosing the correct configuration of the beam (e.g. pulse front tilt, polarization orientation and scanning direction) for controlling the ponderomotive force, we can imagine forcing the electrons to preferentially move to one side of the beam, creating inhomogeneous plasma densities. Therefore, the control of light intensity gradient and of the laser polarization according to the displacement should lead to the control of material local symmetry and its orientation. In addition, much literature have reported the following two phenomena when strongly focusing light inside an optical material: (1) self-focusing when the pulse energy exceeds the threshold and (2) spatial aberrations which increase with focus depth. Both phenomena should impact the creation of circular optical properties. In this chapter, we discuss the optical properties a series of samples prepared via different laser writing parameters to investigate the dependence of the writing laser polarization, pulse energy, focusing conditions, and the pulse-to-pulse overlapping rate on the photo-induced circular dichroism or circular diattenuation. All measurements have been made using a classical experimental technique, i.e., a circular

dichroism spectro-polarimeter based on photo-elastic modulator.

In chapter 4, we discuss the use of a quite recent method, called Mueller-matrix spectroscopic ellipsometry, as a powerful tool to examine structural and optical properties of materials that exhibit both linear and circular optical properties from a single measurement. The objective of this chapter is to widely investigate circular optical properties using differential matrix formalism on transmission Mueller matrices measured on femtosecond laser-induced modifications in silica within type II regime. This allows quantifying the effective or equivalent circular birefringence and dichroism in the presence of strong linear optical properties like linear birefringence. In particular, we will focus on photo-induced optical activity (or circular birefringence) in silica glass by laser irradiation. We will investigate the dependence of circular optical properties with pulse energy, the focusing depth, the repetition rate and the laser-writing configuration. In addition, it is known that compaction and rarefaction processes affecting the surrounding medium and lead to stress-induced birefringence that accompanies the formation of nanogratings. Accordingly we have imprinted Type II modifications following a specific design, in such a way we can create a confined stress-zone between laser-induced "stress bars". In particular we investigated the stress-induced birefringence (its amplitude and its slow axis orientation) according to the orientation of the writing laser polarization. Finally the thermal stability of the overall anisotropic optical properties within type II regime by step isochronal annealing is analyzed. The experimental results made possible the comparison between the thermal stability of anisotropic linear optical properties and circular optical properties, as well as the stress-induced birefringence. This work will tentatively bring additional insight on the origin of the imprinted chiral optical properties.

In chapter 5, the spectral dependence of both linear and circular optical properties are discussed on the basis of polarimetric and ellipsometric measurements in a wide spectral range, from the ultraviolet (250 nm) to the near infrared (1800 nm). Transmission Mueller-matrix spectroscopic ellipsometry will be applied to study femtosecond laser induced nanogratings in silica glass. The first part of the chapter follows a paper published in 2019, which discusses the use of the differential decomposition of Mueller matrices to quantify the circular birefringence of femtosecond laser irradiated SiO<sub>2</sub>. Then the second part is related to a paper published in 2020. Here we compared anisotropic linear optical properties (linear birefringence, linear dichroism, degree of polarization) and "performances" (absorption coefficient, thermal stability) of two types of birefringent waveplates fabricated in silica glass by femtosecond laser direct writing. The first type of waveplate is based on birefringence induced by self-organized nanogratings imprinted in the glass, whereas the second design is based on birefringence originating from the stress-field formed around the aforementioned nanogratings. In addition to the provided comparison, we report on the manufacturing of stress-engineered half waveplates in the UV-Visible range, and with mm-size clear aperture and negligible optical losses.

The characteristic feature of Type II modifications is the formation of nanogratings that can easily be detected through polarization dependent linear birefringence measurements but also simply with direct observation using scanning electron microscopy (SEM) techniques. However, the total birefringence, which comprises, both linear and circular



birefringence, arises from the addition of several contributions, including form birefringence, stress-induced birefringence but also the formation of point defects and Type I-densified zones (e.g. in between the porous nanolayers). The cumulative contribution from all these factors yields to refractive index and birefringence changes in the presence of nanogratings. In the light of new results, chapter 6 shortly reviews these different contributions, including their thermal stability since it provides a way to estimate the contribution of each mechanism and their potential link with the original chiral-optical properties we observed in the previous chapters. Then based on the overall results obtained in previous chapters, we investigate and discuss the mechanisms that could create anisotropic circular optical properties.

## References

1. Lancry, M. and B. Poumellec, *UV laser processing and multiphoton absorption processes in optical telecommunication fiber materials*. Physics Reports, 2013. **523**(4): p. 207-229.
2. Stoian, R., *Volume photoinscription of glasses: three-dimensional micro-and nanostructuring with ultrashort laser pulses*. Applied physics. A, Materials science & processing, 2020. **126**(6).
3. Cheng, G., et al., *Ultrafast laser photoinscription of polarization sensitive devices in bulk silica glass*. Optics Express, 2009. **17**(12): p. 9515-9525.
4. Fernandes, L.A., et al., *Femtosecond laser writing of waveguide retarders in fused silica for polarization control in optical circuits*. Optics Express, 2011. **19**(19): p. 18294-18301.
5. Beresna, M., M. Gecevičius, and P.G. Kazansky, *Polarization sensitive elements fabricated by femtosecond laser nanostructuring of glass [Invited]*. Optical Materials Express, 2011. **1**(4): p. 783-795.
6. Voigtländer, C., et al., *Inscription of high contrast volume Bragg gratings in fused silica with femtosecond laser pulses*. Applied Physics A, 2011. **102**(1): p. 35-38.
7. Zhang, B., X. Liu, and J. Qiu, *Single femtosecond laser beam induced nanogratings in transparent media-Mechanisms and applications*. J. of Materiomics, 2019. **5**(1): p. 1-14.
8. Shimotsuma, Y., et al., *Self-organized nanogratings in glass irradiated by ultrashort light pulses*. Physical review letters, 2003. **91**(24): p. 247405.
9. Canning, J., et al., *Anatomy of a femtosecond laser processed silica waveguide [Invited]*. Optical Materials Express, 2011. **1**(5): p. 998-1008.
10. Lancry, M., et al., *Ultrafast nanoporous silica formation driven by femtosecond laser irradiation*. Laser and Photonics Reviews, 2013. **7**: p. 953-962.
11. Rudenko, A., J.-P. Colombier, and T.E. Itina, *Nanopore-mediated ultrashort laser-induced formation and erasure of volume nanogratings in glass*. Physical Chemistry Chemical Physics, 2018. **20**(8): p. 5887-5899.
12. Kazansky, P.G., et al., *"Quill" writing with ultrashort light pulses in transparent materials*. Applied Physics Letters, 2007. **90**(15): p. 151120.
13. Poumellec, B., et al., *Femtosecond laser irradiation stress induced in pure silica*. Optics Express, 2003. **11**(9): p. 1070-1079.
14. Salter, P., R. Simmonds, and M. Booth. *Adaptive control of pulse front tilt, the quill effect, and directional ultrafast laser writing*. in *Frontiers in Ultrafast Optics: Biomedical, Scientific, and Industrial Applications XIII*. 2013.
15. Poumellec, B., et al., *Asymmetric Orientational Writing in glass with femtosecond laser irradiation*. Optical Materials Express, 2013. **3**(10): p. 1586-1599.
16. Poumellec, B., et al., *Non reciprocal writing and chirality in femtosecond laser irradiated silica*. Optics Express, 2008. **16**(22): p. 18354-18361.
17. Poumellec, B., et al., *Parity violation in chiral structure creation under femtosecond laser*

*irradiation in silica glass&quest.* Light: Science & Applications, 2016. **5**(11): p. e16178.



# Chapter1 State of the art of Femtosecond Laser Direct Writing in Glasses

---

---

## Content

1.1 Introduction.....	21
1.2 Silica Glass.....	21
1.3 Propagation of ultrashort laser pulses in a vitreous material.....	23
1.3.1 Basic principles.....	23
1.3.2 Self-focusing by Kerr effect.....	25
1.3.3 Filamentation.....	26
1.3.4 Self-phase modulation.....	26
1.3.5 Spectral dispersion and temporal broadening.....	26
1.4 Femtosecond laser interactions in glasses.....	28
1.4.1 Ionization and relaxation in intense field.....	28
1.4.2 Relaxation mechanisms.....	30
1.4.3 Material changes induced by femtosecond laser irradiation.....	31
1.4.4 Heat accumulation effects.....	32
1.5 Damage thresholds and different type of permanent modifications...34	
1.5.1 Isotropic index changes based modifications (Type I).....	36
1.5.2 Anisotropic refractive index changes based modifications (Type II).....	38
1.5.3 Voids (Type III).....	40
1.6 Focus on Type II modifications and nanogratings formation.....	40
1.6.1 From LIPSS to self-organized nanogratings in silica.....	40
1.6.2 Physical and optical properties of nanogratings in silica glass.....	42
1.6.3 Tentative mechanisms for nanogratings formation.....	43
1.6.4 Nanogratings parameters dependence.....	48
1.7 Towards 3D imprinted optical chirality in inorganic glasses.....	54
1.8 Conclusions.....	57
1.9 References.....	59

# 1.1 Introduction

First of all this chapter gives a reminder of the basic notions necessary for a full understanding of this thesis. We will see the structure of silica composing our samples and the ultrashort laser pulse propagation in these glasses. It will also be seen that during propagation, different processes of interaction leading to structural changes occur associated to the formation of permanent changes in the glass optical properties. Finally, the last part of this chapter presents of focus on the anisotropic optical properties (birefringence and dichroism) and nanogratings formation in silica glass. In particular these anisotropic linear and circular optical properties will be measured and studied throughout this thesis as part of the central point of our studies.

# 1.2 Silica Glass

Silica glasses have been studied a lot and especially since the discovery of their photosensitivity to Ultraviolet (UV) radiation at the end of the 70s [1]. Since the 1960s, the effects of electron bombardment on glasses have been studied with high-energy sources in the MeV range [2-4]. As early as the 1980s, some authors began using less energetic electron beams (of the order of keV) in order to study the induced changes in volume and induced optical modifications [5-7]. Irrespective of the type of irradiation, these changes are based on structural changes induced by irradiation. That is why we begin this first chapter with a short description of the structure and optical properties of silica glasses.

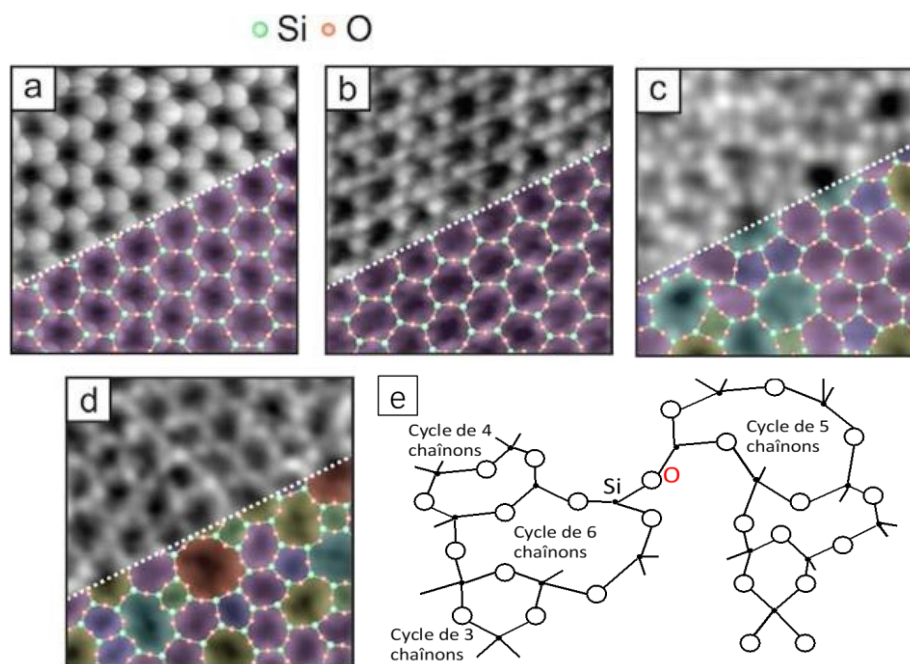


Figure 1.1: Atomic resolution STM images of silica bilayers: crystal structures of  $\alpha$ -quartz (a and b) and disordered  $\text{SiO}_2$  glass (c and d); scheme of the random network and silica rings (e). Adapted from [8].

Most commercial glasses are silicates and they contain many constituents included in a  $\text{SiO}_2$  based matrix. The glass with the simplest composition is pure silica glass, despite its difficulty to be technically developed with high purity. It is composed of an irregular 3D network consisting of disordered tetrahedral  $\text{SiO}_4$  units as shown in Figure 1.1 using atomic

resolution STM of silica bilayers [8]. In this PhD work we will mostly use Type III- silica glasses that are synthetic vitreous silica produced by hydrolysis of  $\text{SiCl}_4$  when spraying into an oxygen-hydrogen flame. This material is practically free from metallic impurities, but contains a high amount of OH, in the order of 1000 ppm, and because of the starting material, Cl, in quantities of the order of 100 ppm. Trade names are for example Suprasil (from Heraeus), Spectrosil or Corning 7940.

### **Silica glasses structure**

There are various possibilities of assembling  $\text{SiO}_4$  tetrahedra in 3D with each other. But the most stable configuration that is established is that for which the Si-Si distance will be longest, which is achieved in an assembly by the vertices. This mode of assembly is found in all forms of silica: quartz, tridymite, cristobalite and coesite. The intermediate bond of the Si-O-Si group gives an average angle of  $145^\circ$  [9], which admits a certain dispersion, corresponding to an Si-Si distance of approximately 3.12 Å. The distance Si-O varies between 1.62 Å and 1.77 Å and the distance O-O is between 2.50 Å and 2.65 Å [10]. The complete assembly of all the tetrahedra in silica glass thus forms a three-dimensional network presenting only a short-range order, but having no order at a long distance. This representation of the structure corresponds to the definition of the disordered or random network in the literature.

At a short distance, the order is governed by the coordination of silicon: a silicon atom is surrounded by 4 oxygen atoms forming a tetrahedron and, each oxygen is shared between 2 tetrahedra, to respect the  $\text{SiO}_2$  stoichiometry. Silica glass is a special case of disordered systems because it has a medium range order. The latter is due to molecular connectivity. There are always four tetrahedra surrounding a given tetrahedron. However, there is no Euclidean translational symmetry [11]. The correlation length is defined as the number of successive correctly ordered tetrahedra. The free space in the structure allows tetrahedra to rotate. In this case, the correlation length or the degree of polymerization of the glass may vary according to the method of preparation and especially the cooling rate and more generally the thermal history. The structure of a cooled glass is frozen from a so-called fictive temperature  $T_f$  as described in details in Ref. [12]. Silica has the same medium-range order as the crystalline form of tridymite and cristobalite. When silica is elaborated under high pressures [13], its specific volume is lower. It then adopts a denser structure, this new configuration approaching that of quartz or coesite. Silica subjected to a very high pressure can also adopt a rutile structure in the form of  $\text{SiO}_6$  octahedra, it is stishovite [14].

### **Point defects in silica glasses**

A glass can be subjected to a multitude of treatments such as heating, high pressure or laser irradiations and their combination. These treatments will locally modify the linkage sequence to form point defects. The definition of a defect in the glass is different from the definition given in a crystal. Indeed, in a crystal, any exception in translational symmetry is considered a defect. In a glass, this symmetry of translation does not exist and this definition cannot apply. The notion of defect is then based on the notion of chemical order. The

perfect network of silica glass can be presented as a sequence of SiO<sub>4</sub> tetrahedra interconnected by common oxygen atoms. Thus, each silicon atom is connected to four oxygen atoms and each oxygen atom must have two Si as nearest neighbors. Any exception in this sequence ≡Si-O-Si≡ can be considered as a defect. Each defect has a structure and properties (absorption, fluorescence, magnetism, etc ...) that are unique to it. In order to better understand and subsequently control the impact of point defects on the properties of silica, it is essential to know their atomic structure. This is usually determined by a combination of experimental results from spectroscopy and theoretical calculations of quantum chemistry. The experimental technique that quickly proved to be the most suitable for developing and confirming defect models was the RPE (Electronic Paramagnetic Resonance). Although the RPE is a priori only applicable to paramagnetic defects, the absence of RPE signal in the case of a diamagnetic defect can be important information in the search for models. Rigorously applied, the RPE can thus indicate the orbital composition of the spin functions of the single electron spins, as well as the chemical nature, the size and the steric environment of the atoms. Each defect thus has a signature RPE of its own. If we can thus demonstrate the correlation between the RPE signal and an optical absorption band, we can deduce the origin of this one. A certain number of absorption bands have thus been identified. Begun several decades ago, the study of point defects is far from over. The structure of many defects, the absorption bands associated with them, or the mechanisms that lead to their appearance or disappearance, are still the subject of many disagreements. For more details on the properties of point defects, we can refer to the works of Griscom [15, 16], Garapon [17], Skuja [18, 19] and Trukhin [20].

## 1.3 Propagation of ultrashort laser pulses in a vitreous material

This section lays the foundation for the propagation of laser pulses in a linear and nonlinear dielectric medium as well as the definition of the different notions relating to femtosecond laser pulses.

### 1.3.1 Basic principles

The equation of propagation of an electromagnetic wave in a dielectric medium is deduced from the Maxwell equations and is written in the following form [21]:

$$\nabla^2 \vec{E} - \frac{1}{c^2} \frac{\partial^2 \vec{E}}{\partial t^2} = \mu_0 \frac{\partial^2 \vec{P}}{\partial t^2} \quad \text{Equation 1.1}$$

where  $\vec{E}$  means the electric field;  $\mu_0$  is the magnetic permeability checking the relationship,  $\varepsilon_0 \mu_0 = \frac{1}{c^2}$  with  $c$  is the speed of light in the vacuum and  $\varepsilon_0$  is the electric permittivity;  $\vec{P}$  is the polarization. The polarization  $\vec{P}$  induced by electric dipoles is a non-linear function of the electric field  $\vec{E}$  and can be developed in increasing powers of the electric field [21] in the dipolar approximation as :

$$\vec{P} = \varepsilon_0 (\chi^{(1)} \vec{E} + \chi^{(2)} \vec{E}^2 + \chi^{(3)} \vec{E}^3 + \dots) \quad \text{Equation 1.2}$$



$$\vec{P} = \vec{P}^{(1)} + \vec{P}^{(2)} + \vec{P}^{(3)} + \dots \quad \text{Equation 1.3}$$

$$\vec{P} = \vec{P}_L + \vec{P}_{NL} \quad \text{Equation 1.4}$$

where  $\chi^{(i)}$  is the susceptibility and  $\vec{P}^{(i)}$  is the polarization of order I where according to the classical description of non-linear optics [22-24], the vector polarization is the sum of linear polarization  $\vec{P}_L = \vec{P}^{(1)}$  and non-linear polarization  $\vec{P}_{NL} = \vec{P}^{(2)} + \vec{P}^{(3)} + \dots$

In a centrosymmetric medium such as silica glass, the second order susceptibility tensor is identically zero because of the inversion center [21-23, 25]. We have thus:

$$\chi^{(2)} = 0 \quad \text{Equation 1.5}$$

By simplifying the expression of the polarization (Eq. 1.2) to the order 3, we obtain the expression in the case of an isotropic material:

$$\vec{P} = \varepsilon_0 \bar{\chi}^{(1)} \vec{E} + \varepsilon_0 \bar{\bar{\chi}}^{(3)} \vec{E} \cdot \vec{E} \cdot \vec{E} \quad \text{Equation 1.6}$$

$$\vec{P} = \varepsilon_0 (\bar{\chi}^{(1)} + \bar{\bar{\chi}}^{(3)} \vec{E} \cdot \vec{E}) \vec{E} \quad \text{Equation 1.7}$$

$$\vec{P} = \varepsilon_0 \left( n_0^2 - 1 + \frac{3}{4} \chi_{eff}^{(3)} |\vec{E}|^2 \right) \vec{E} \quad \text{Equation 1.8}$$

$$\vec{P} = \varepsilon_0 \left[ n_0^2 \left( 1 + \frac{3}{4} \frac{\chi_{eff}^{(3)}}{n_0^2} |\vec{E}|^2 \right) - 1 \right] \vec{E} \quad \text{Equation 1.9}$$

$$\vec{P} = \varepsilon_0 (n^2 - 1) \vec{E} \quad \text{Equation 1.10}$$

where  $n_0^2 = \chi_{eff}^{(1)} + 1$  is the linear refractive index of the medium and  $n = n_0 \left( 1 + \frac{3}{4} \frac{\chi_{eff}^{(3)}}{n_0^2} |\vec{E}|^2 \right)^{\frac{1}{2}}$  is the refractive index of the medium. By carrying out the limited development of  $(1 + x)^a$  at the first order, we get:

$$n \approx n_0 \left( 1 + \frac{3}{4} \frac{\chi_{eff}^{(3)}}{n_0^2} |\vec{E}|^2 \right)^{\frac{1}{2}} = n_0 + \frac{3}{8} \frac{\chi_{eff}^{(3)}}{n_0} |\vec{E}|^2 = n_0 + \frac{3}{8} \frac{\chi_{eff}^{(3)}}{\varepsilon_0 c n_0^2} I = n_0 + n_2 I \quad \text{Equation 1.11}$$

where  $I = \varepsilon_0 c n_0 |\vec{E}|^2$  is the laser intensity and  $n_2 = \frac{3}{8} \frac{\chi_{eff}^{(3)}}{\varepsilon_0 c n_0^2}$  is the non-linear refractive index that leads to the optical Kerr effect developed in the next section. The equation of evolution of the envelope of the electric field is given by the relation [26] :

$$T \frac{\partial E}{\partial z} = \frac{i}{2k_0} \Delta_T E - \frac{i k_0''}{2} \frac{\partial^2 E}{\partial \tau^2} + i \frac{k_0}{n_0} (n_2 I) E \quad \text{Equation 1.12}$$

where  $T = \left( 1 + \frac{i}{k_0 v_g} \frac{\partial}{\partial \tau} \right)$  is an operator;  $k_0 = \frac{\omega_0}{c} = \frac{2\pi}{\lambda_0}$  is the wave vector in the vacuum ;  $\omega_0$  is the central pulsation of the wave;  $\lambda_0$  is the central wavelength and  $c$  is the light speed

in the vacuum ;  $\Delta_T = \left( \frac{\partial^2}{\partial r^2} + \frac{1}{r} \frac{\partial}{\partial r} \right)$  is the transverse Laplacian of the envelope of the electric field in cylindrical coordinates;  $k_0'' = \left. \frac{d^2 k}{d\omega^2} \right|_{\omega_0}$  is the group speed dispersion (GVD) ;  $\tau = t - \frac{z}{v_g}$  represents the delayed time; with  $\frac{i}{2k_0} \Delta_T E$  is the diffraction term in a medium of index  $n_0$  in cylindrical coordinates ;  $\frac{ik_0''}{2} \frac{\partial^2 E}{\partial \tau^2}$  is the term of dispersion of the group velocity;  $i \frac{k_0}{n_0} (n_2 I) E$  is the term relating to the optical Kerr effect.

### 1.3.2 Self-focusing by Kerr effect

The self-focusing of light is a process in which the intensity of the beam changes the optical properties of the material, in particular the refractive index. Due to the intensity spatial distribution (Gaussian profile), the laser beam induces a variation of index such that the index at the center of the beam is larger than at its periphery. Thus, the material acts as a lens with a positive focal length gradient, called the Kerr lens, causing the beam to converge in its focus. This phenomenon occurs when the power of the laser beam is greater than or equal to the critical power defined by the relationship [21] :

$$P_{cr} = \frac{\pi(0,61\lambda_0)^2}{8n_0n_2} \quad \text{Equation 1.13}$$

where  $\lambda_0$  is the wavelength of the laser in vacuum. In the case of our silica sample irradiation experiments, we have:  $\lambda_0 = 1030nm$  ;  $n_2 = 3,2 \cdot 10^{-16} cm^2/W$  and  $n_0 = 1,45$  à  $1030nm$ . The critical power deduced is 3.3MW.

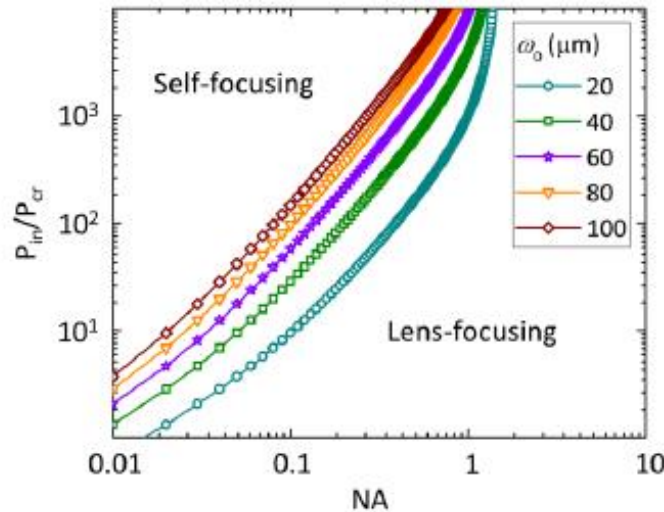


Figure 1.2: Self-focusing versus lens-focusing. Close to the boundary obtained for a given spot size ( $\omega_0$ ) of the beam at the plane of lens, both self-focusing and lens-focusing play a role. The calculations performed for fused silica at  $\lambda = 1030$  nm. Typically the critical power in silica is around 3,3 MW. Figure extracted from PhD thesis of Ausra Cerkauskeitė [27].

Self-focusing of a collimated Gaussian beam is observed if the radiation power is greater than the critical power. In such a situation the Kerr nonlinearity continuously dominates over the transverse diffraction. The situation may be different if the lens is used in the direct writing system as it is our case for laser writing. For tight focusing the lens-focusing is dominating and the Kerr nonlinearity could be neglected, and for loose focusing the self-

focusing is dominating. The boundary between these two regimes can be determined by [28, 29]:

$$\sqrt{\frac{P_{in}}{P_{cr}}} = 0.852 + \sqrt{0.0219 + 0.1347 \times \left( \frac{\left(\frac{k\omega_0}{2}\right)^2 - \left(\frac{n}{NA}\right)^2 + 1}{\left(\frac{n}{NA}\right)^2 - 1} \right)} \quad \text{Equation 1.14}$$

when near the boundary obtained for a given spot size of the collimated beam before the lens both self-focusing and lens-focusing play a role. For example, if numerical aperture of the focusing lens is less than 0.01, self-focusing is likely to occur at input powers close to critical ( $P_{in} \approx P_{cr}$ ). If the numerical aperture is higher than 0.1, in order to get self-focusing the input power has to be much higher than critical ( $P_{in} \approx 10P_{cr}$ ). However, the calculations do not account for plasma generation, and also loses its validity when the incident power is much larger than the critical power ( $P_{in} \approx 100P_{cr}$ ).

### 1.3.3 Filamentation

When there is a balance between the effect of self-focusing by Kerr effect, that of defocusing due to the formation of free electrons plasma excited the laser and the diffraction effect present during the entire propagation of the impulse even stronger that the size of the beam is small. The laser beam then propagates with a constant diameter: this is called filamentation (Figure 1.3).

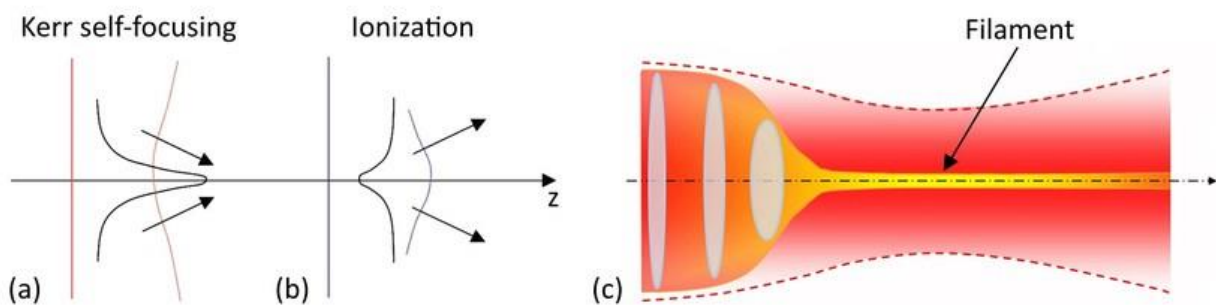


Figure 1.3: Representation of focusing cycles (due to the Kerr effect) / defocusing (due to plasma formation) giving rise to the phenomenon of Filamentation (c).

### 1.3.4 Self-phase modulation

As seen previously, the intensity of the beam propagating in a medium induces a variation of the refractive index. This variation leads to a phase shift in the pulse and therefore to a change in the frequency spectrum. This modification of the spectrum results in a spectral broadening of the pulses.

### 1.3.5 Spectral dispersion and temporal broadening

The relatively large spectral width associated with the femtosecond pulses makes it necessary to take into account the dispersion laws of the optical elements encountered by the pulse. Indeed these dispersive elements and in particular the microscope objective for focusing the pulses, can change the spectro-temporal characteristics. If we consider the

transparent materials in the visible and the IR like silica, their refractive index varies according to the wavelength, it is the chromatic dispersion. The analytical relationship between the refractive index and the wavelength is called the Sellmeier equation and is written in the following form:

$$n_0^2(\lambda) = 1 + \frac{B_1\lambda^2}{\lambda^2 - C_1} + \frac{B_2\lambda^2}{\lambda^2 - C_2} + \frac{B_3\lambda^2}{\lambda^2 - C_3} \quad \text{Equation 1.15}$$

where  $B_{1,2,3}$  et  $C_{1,2,3}$  are the Sellmeier coefficients specific to the material. Table 1.1 gives these coefficients for two variants of pure silica.

Table 1.1 Coefficients of Sellmeier for two silica materials: Infrasil and Suprasil families. Data from Heraeus technical datasheet.

Refraction index dispersion		
Dispersion constants (Sellmeier)		
	Suprasil®-family, Spectrosil®	Infrasil® / HOQ®
B1	4,73115591 · 10 <sup>-1</sup>	4,76523070 · 10 <sup>-1</sup>
B2	6,31038719 · 10 <sup>-1</sup>	6,27786368 · 10 <sup>-1</sup>
B3	9,06404498 · 10 <sup>-1</sup>	8,72274404 · 10 <sup>-1</sup>
C1	1,29957170 · 10 <sup>-2</sup>	2,84888095 · 10 <sup>-3</sup>
C2	4,12809220 · 10 <sup>-3</sup>	1,18369052 · 10 <sup>-2</sup>
C3	9,87685322 · 10 <sup>1</sup>	9,56856012 · 10 <sup>1</sup>

Consider the time domain of the electric field of an incident wave without coupling with the variable  $z$  denoted  $E_{in}(t)$  passing through a dispersive medium. The expression of the incident electric field is:

$$E_{in}(t) = \exp(-\Gamma_0 t^2) \exp(i\omega_0 t) \quad \text{Equation 1.16}$$

where  $\Gamma_0 = \frac{2 \ln 2}{\Delta t_0^2}$  with  $\Delta t_0$ , the half-width duration of the Gaussian laser pulse in the incoming time; or in the Fourier space:

$$\tilde{E}_{in}(\omega) = \exp\left[-\frac{(\omega - \omega_0)^2}{\Delta\omega^2}\right] \quad \text{Equation 1.17}$$

where  $\Delta\omega = 2\sqrt{\Gamma_0}$  is the spectral width of the pulse, or in the wavelength range  $\Delta\omega = 2\pi c \frac{\Delta\lambda}{\lambda^2}$ . After passing through the medium, the outgoing wave acquires a spectral phase  $\phi(\omega)$  corresponding to the time shift of the spectral components. This phase can develop into a Taylor series around the central pulsation  $\omega_0$  such as:

$$\phi(\omega) = \phi_0 + \left.\frac{d\phi}{d\omega}\right|_{\omega_0} (\omega - \omega_0) + \frac{1}{2} \left.\frac{d^2\phi}{d\omega^2}\right|_{\omega_0} (\omega - \omega_0)^2 + \dots \quad \text{Equation 1.18}$$

The outgoing wave can be written in the form:

$$\tilde{E}_{out}(\omega) = \exp\left[-\frac{(\omega - \omega_0)^2}{4\Gamma_0}\right] \exp[i\phi(\omega)] \quad \text{Equation 1.19}$$

or in the time space:

$$E_{out}(t) = \exp[-\Gamma(t - \phi'_0)^2] \exp[-i(\omega_0 t - \phi_0)] \quad \text{Equation 1.20}$$

- $\Gamma = \frac{2 \ln 2}{\Delta t^2}$  is defined by the relation  $\frac{1}{\Gamma} = \frac{1}{\Gamma_0} + i 2 \phi_0''$  which leads to defining the extension of the duration of the impulse  $\Delta t = \Delta t_0 \sqrt{1 + \left(4 \ln 2 \frac{\phi_0''}{\Delta t_0^2}\right)^2}$  in the case of a Gaussian pulse;
- $\phi_0$  is the constant phase term;
- $\phi'_0 = \left. \frac{d\phi}{d\omega} \right|_{\omega_0}$  is the delay representing the optical path time, therefore, it does not modify the beam characteristics;
- $\phi_0'' = \left. \frac{d^2\phi}{d\omega^2} \right|_{\omega_0}$  is called the quadratic phase and represents the group delay dispersion (GDD).

The GDD therefore introduces a variable propagation delay as a function of the frequency (or wavelength) of the laser propagating in a medium; this phenomenon is at the origin of the temporal chirp. This term is proportional to the dispersion of the group velocity (GVD) defined by  $k_0'' = \left. \frac{d^2k}{d\omega^2} \right|_{k_0}$  such as  $\phi_0'' = k_0'' z$ . GVD is also expressed as a function of the wavelength in the form:

$$k_0'' = \frac{\lambda^3}{2\pi c^2} \left( \frac{d^2n}{d\lambda^2} \right) \quad \text{Equation 1.21}$$

This term is specific to each material or optical system and is expressed in  $\text{fs}^2 \cdot \text{mm}^{-1}$ . For silica, it is equal to  $k_0'' = 36 \text{fs}^2 \cdot \text{mm}^{-1}$  at 800nm and  $k_0'' = 20 \text{fs}^2 \cdot \text{mm}^{-1}$  at 1030nm.

## 1.4 Femtosecond laser interactions in glasses

### 1.4.1 Ionization and relaxation in intense field

In order to introduce the interest of femtosecond lasers for the laser-matter interaction, this section briefly presents the mechanisms of interaction in glasses under the influence of an intense and ultra-brief electromagnetic field. Numerous fundamental studies on the physical processes involved have been conducted, allowing significant progress in understanding these mechanisms and leading to a fairly clear vision of the interaction processes shown in Figure 1.4.

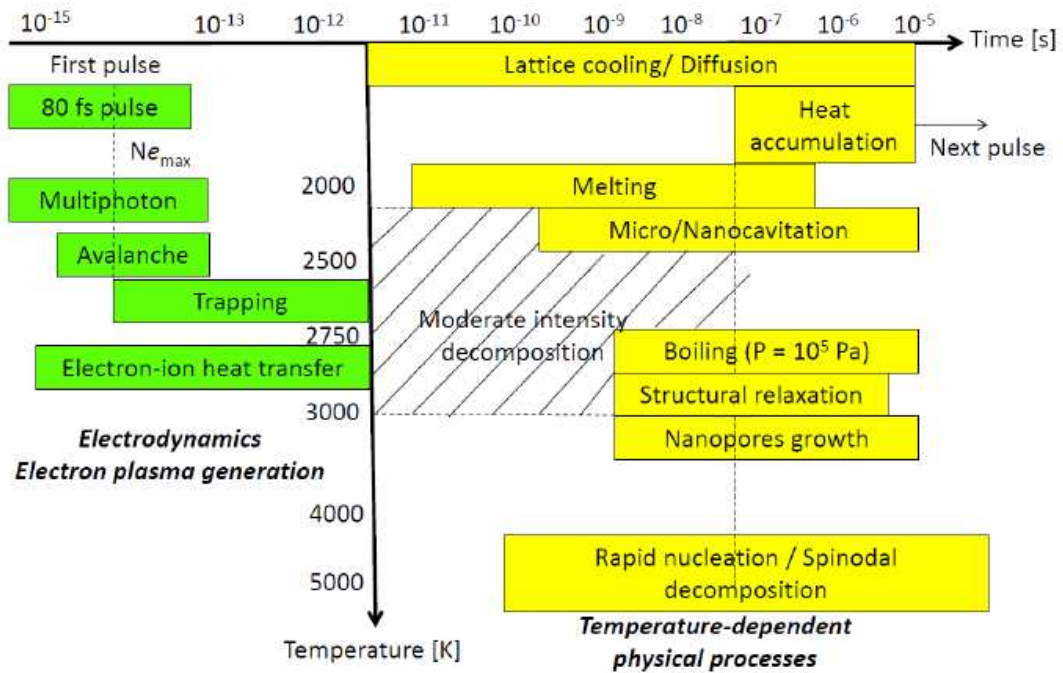


Figure 1.4: Schematics of main physical processes involved in the ultrashort laser processing of silica glass including temperature-dependent processes. Extracted from A. Rudenko et al. [30].

Figure 1.4 shows the time scale of the interaction mechanisms that can be summarized in three steps: the electronic excitation [31], the thermalization, the different relaxation mechanisms and the permanent modifications. Part of the laser energy absorbed by the electrons is transferred to the network (i.e. to the phonons) over a period of about ten picoseconds in the silica. After a few nanoseconds, a shock wave is emitted. On the time scale from nanosecond to microsecond, heat propagates around the focal zone. For rates that are low enough to prevent heat accumulation build-up [32, 33], the material returns to ambient temperature within a few microseconds in  $\text{SiO}_2$ . At sufficiently high energy, these processes can also cause non-thermal ionic motion and leave permanent structural changes such as inelastic deformation (densification or expansion depending on the irradiation conditions and the composition of the material), the appearance of an elastic response (stress) [34-38] in and around the irradiated area and the formation of point defects [39] that absorb in UV and VUV, etc ... These mechanisms are developed in the following references [40-44].

The solids we have studied in this thesis are essentially dielectric materials with wide bandgap, chosen either for their many applications in different fields that may be optics. We studied mostly silica glass ( $\text{SiO}_2$ ). In these materials, the conduction band is empty and the highest populated electronic states are those at the top of the valence band. Between the two, the forbidden band is of the order of 9 eV, and is therefore much higher than the energy of the incident photons (Eq. 1.5 eV for the Ti-Sa laser emitting radiation at the wavelength 800nm and 1.2 eV for 1030nm laser). Electronic excitation from the valence band to the conduction band can only occur by a non-linear process such as the simultaneous absorption of several photons. This multi-photon ionization process can only be observed for high laser field amplitude. It has been shown that at these high intensities, there is also a phenomenon of "electron heating" within the conduction band, which continue to absorb

a large number of photons after having crossed the forbidden band. Thus, by means of photoemission experiments, the measurement of the kinetic energy of the photoelectrons has made it possible to obtain the energy distribution of the electrons in the conduction band, which ranges between 10 and 40eV in the case of silica [45] and for irradiation conditions similar to the experiments we will performed within this PhD thesis.

Some results obtained by our group and published in collaboration with Stéphane Guizard (LSI, CEA Saclay) on this point shows that in our experimental conditions ( $NA = 0.5$  and  $I = 1-30\text{TW}/\text{cm}^2$ ), the main mechanism of ionization happens to be multiphoton ionization: 6 photons in silica and 5 photons in Germanium doped silica. It should be noted that under our experimental conditions, neither tunnel ionization nor the presence of avalanche ionization are detected for pulse durations below 200fs [46, 47]. More recently, it has been shown that in  $\text{SiO}_2$ , it is possible, under specific conditions, to observe an increase in carrier ionization impact [48]. All these results demonstrate that the avalanche process, which is often invoked in the laser breakdown literature, does not play a dominant role in optical breakdown induced by short pulses. The relative importance of this phenomenon is always subject to intense discussion. It is now widely accepted that this relative importance depends largely on the experimental parameters [49-53]. In particular, it seems to depend on the pulse duration as well as its illumination or the width of the bandgap of the material.

## 1.4.2 Relaxation mechanisms

After this phase of electronic excitation, which takes place during the excitatory pulse, the photo-excited charge carriers are "out of equilibrium" and will thermalize with the solid by different mechanisms according to their kinetic energy. If the energy of the electrons is greater than the forbidden band, the inelastic collisions between electrons of the conduction band and the valence band, or the impact ionization, can occur at the attosecond scale (Figure 1.5 step1). In this case, the electron loses a significant energy, at least equal to the forbidden band and we end up with two electrons of lower energy at the bottom of the conduction band. For time scales from femtosecond to picosecond (Figure 1.5 step 2), lower energy electrons transfer their energy mainly via collisions with the lattice, by acoustic or optical phonon emission leading to heat effects leading permanents change like phase transition, photochemistry... In some materials, the electron-hole or exciton pairs induces local polarization and lattice deformation (Figure 1.5 step 3). At this deformation or atomic displacement, defined in the following part, corresponds to the appearance of electronic levels in the forbidden band, on which the charge carriers will be able to locate (Figure 1.5 step 4). We talk about trapped excitons (or self-trapped excitons noted STE) but also STH (self-trapped holes). This mechanism has a very short lifetime and occurs for a small percentage of charge carriers. STE has been studied in all alkali halides [54]. It has been demonstrated much more recently in silica and doped silica, and constitutes the intermediate step between electronic excitation and the formation of point defects, also known as "colored centers". Finally, non-trapped electrons will recombine with a hole in the valence band (Figure 1.5 step 5).

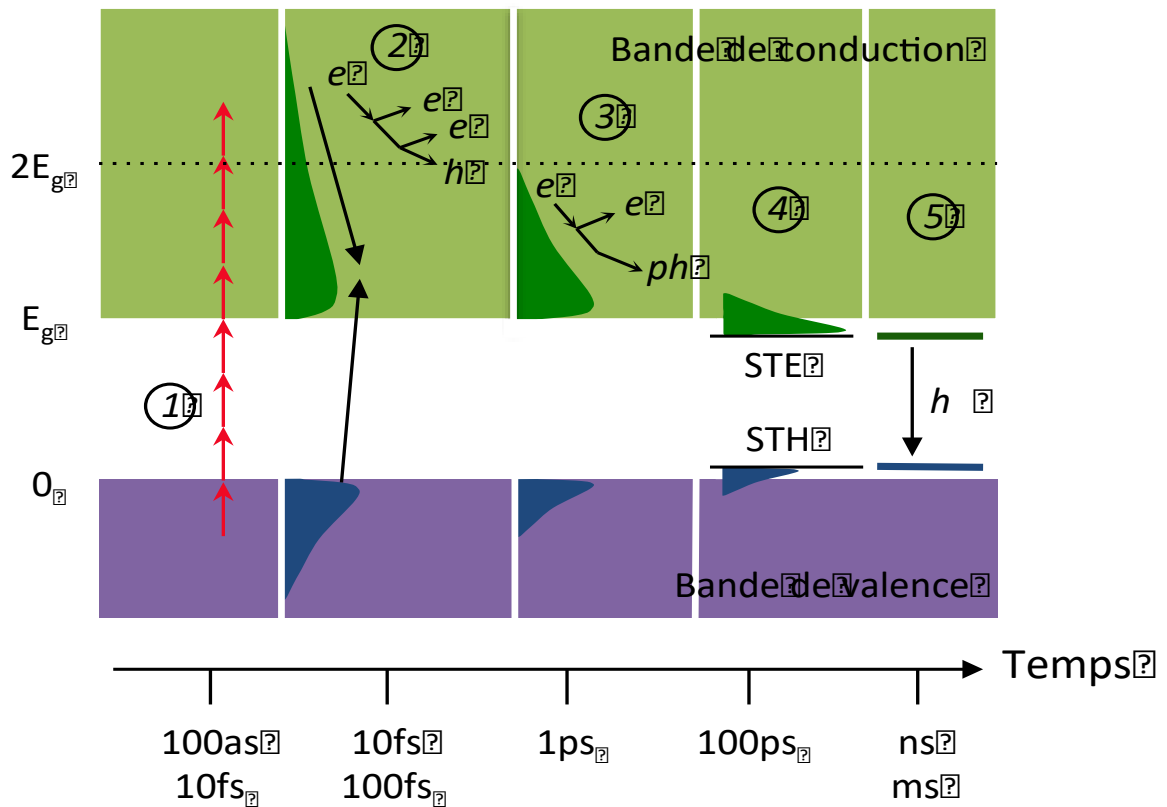


Figure 1.5: Diagram showing the different elementary mechanisms involved during and after the interaction between a short pulse and a dielectric sample. 1: electronic excitation: either multiphoton ( $h\nu < E_g$ ) or one photon ( $h\nu > E_g$ ); 2: electronic relaxation: process of inelastic electron-electron collisions or impact ionization; 3: electronic relaxation, continued: thermalization via collisions with the network; 4: trapping and location of charges (self-trapped excitons); 5: radiative recombination of excitons [extracted from HDR of S. Guizard, CEA/LSI/ Ecole polytechnique].

### 1.4.3 Material changes induced by femtosecond laser irradiation

The structural modifications of the glass are, of course, dependent on the efficiency of transfer of light energy to the material. As we have said before, in the case of an ultrashort light pulse and sufficiently powerful, interband transitions by multiphoton absorption are possible. They lead to the creation of quasi-free electron plasma, which is followed by electronic relaxations (STE, point defects, network heating). In silica, three structural transformation regimes are observed and correspond to different kind of modifications as shown in Figure 1.6: an isotropic modification of the refractive index of the medium [55], anisotropic modification of the refractive index mainly due to form birefringence according to the literature [56-58], and micro-explosions leading to nano/micro-voids formation [59]. These modification regimes depend not only on the laser parameters: energy, pulse duration, laser repetition rate, wavelength, polarization (state and orientation), numerical aperture, depth of focus, writing speed, etc [60] but also properties of the material: band gap, viscosity, density, heat capacity, thermal conductivity and their dependence with temperature [61-64].



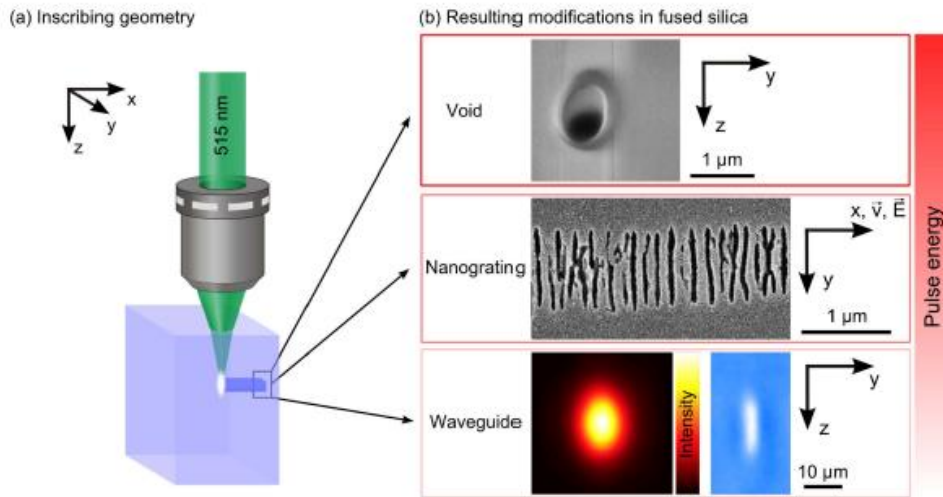


Figure 1.6 (a) Typical writing geometry for Femtosecond Laser Direct Writing (FLDW) and (b) Description of the three main kind of permanent modifications photo-induced in silica glass as review in Refs [44, 60, 65].

### 1.4.4 Heat accumulation effects

The time required for the dissipation of the deposited energy out of the focal volume (diffusion time  $t_D$ ) is given by  $t_D = \omega_0^2 / 2D$ , with  $\omega_0$  the focal radius and  $D$  the diffusivity of the material [66]. The diffusivity is defined as:

$$D = \kappa / \rho \cdot C_p \quad \text{Equation 1.22}$$

with  $\kappa$  the thermal conductivity,  $C_p$  the specific heat and  $\rho$  the density of the material. For a focusing with a NA of about 0.5, the width of a single pulse modification in fused silica is about 1  $\mu\text{m}$ , resulting in a diffusion time of about 1  $\mu\text{s}$ . If the time between two successive pulses is shorter than this heat diffusion time, the temperature inside the focal volume will increase stepwise by each pulse. This process is called heat accumulation [32, 43, 67]. Figure 1.7 shows the calculated temperature rise for different repetition rates at fixed pulse energy of 200 nJ in fused silica in a distance of 2  $\mu\text{m}$  from the focal center (pulse duration 450 fs, NA of 0.5). The model used to calculate the temperatures is based on Fourier equation with a Gaussian heat source along the radial axis and a Lorentzian distribution along the beam propagation.

In irradiation regime with a large number of pulses at a low repetition rate (for example <200 kHz in silica), the material cools to room temperature between two successive pulses. Indeed the energy deposited by a pulse in the focal volume is "removed" by thermal diffusion in the mass of the material in about a microsecond in  $\text{SiO}_2$ . No thermal accumulation mechanism is expected a priori, the modification of the material being carried out independently by each pulse. However, it is possible to observe incubation effects due to the large number of pulses. During strong focusing (NA = 1.4), Schäffer et al. [68] do not observe any incubation effects: the size of the modified zone increases with energy but not with the number of pulses whereas the  $\Delta n$  increases with the number of pulses. On the other hand, at low focusing (typ. NA = 0.25), the incubation is responsible for the reduction of the damage threshold, as observed during surface experiments [69, 70]. In the latter case, it has

been demonstrated in experiments [71] that the effect of the incubation is twofold: i) it modifies the absorption by accumulation of point defects ii) it introduces new possibilities of energy deposition in the network, in addition to the electron-phonon coupling. These possibilities are based on a coupling of electrons trapped in the network. The increase in the concentration of the defects is proportional to the initial concentration of defects, to the increment of the number of pulses, and also depends on the number of atomic sites likely to be affected during the accumulation process. Still in this low repetition rate regime (<200 kHz), Streltsov and Borelli [72] have shown in silica that the refractive index increase as a function of the laser energy seems to follow the temperature increase caused by a single pulse. On the other hand, since a high temperature (2500 °C) limits the refractive index increase, the effect of the temperature is not clearly established.

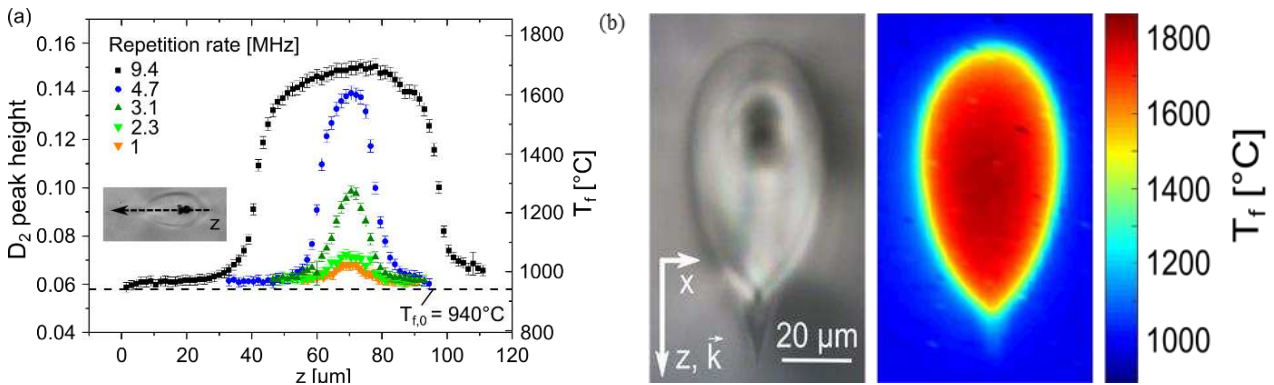


Figure 1.7: Results of the Raman measurements from our group's previous work [73]. (a)  $D_2$  peak height (left axis) and corresponding fictive temperature (right axis) as function of the longitudinal cross section (inset shows an optical micrograph with indication of the measurement trace). (b) Microscopic optical image and corresponding map of the fictive temperature for a laser-induced modification inscribed with 9.4 MHz, 150 nJ and 1000 pulses per laser spot. The arrow indicates the propagation direction of the laser pulses.

Recently Yoshino et al. have [74] measured the temperature inside glass during femtosecond laser microprocessing by time-resolved micro-Raman microscopy. They successfully obtained the time evolution of heat and its dependence on pulse energy, which were found to be different for fused silica and Borofloat33. The maximum temperature was found to be as high as 5000 K in silica for 2 J whereas the temperature remains limited below 1500 K in Borofloat33, whereas their thermal properties are of the same magnitude. However the melting temperature and the viscosities are quite different since the viscosity of Borofloat33 is several orders of magnitude lower than  $\text{SiO}_2$ . This indicates that the maximum temperature is relaxation time dependent and it seems limited by phase transformation like in Borofloat33.

In the high repetition rate regime (> 0.5 MHz in  $\text{SiO}_2$ ), the period between two consecutive pulses is shorter than the thermal diffusion time out of the focal volume. The pulse train then gradually heats the material, this thermal accumulation leads to the permanent modification of a volume that is much greater than the focal volume [32]. In addition, the thermal diffusion is isotropic and the volume of the heated-affected zone increases with the number of pulses. The main mechanism is based on a local melting, in agreement with the corresponding simulations [32]. When the irradiation is stopped, the

material resolidifies with possible densification mechanisms for the silica (due to the existence of an "anomaly" between the density and the fictive temperature: the silica becomes denser at high fictive temperature unlike other vitreous materials). A study of the thermal contribution to the increase of the refractive index as a function of the laser rate is proposed by Eaton et al. [33], following the increase of the size of the modified zone with the repetition rate [75]. A thermal accumulation effect was demonstrated from 200 kHz in a borosilicate glass with a weak bandgap of 3.9 eV, in agreement with the experiments of Schäffer et al. [32]. In both cases, the diameter of the modified zone corresponds to the diameter calculated to be melted, when taking into account the thermal characteristics of the corresponding glass. Osellame et al. [76] show that thermal accumulation effects for the production of high-speed waveguides depend closely on the type of glass used. Recently we report on the processing of silica-based glasses by ultrashort laser pulses at high repetition rates. Heat accumulation leads to strong local heating of the glass and the subsequent quenching results in a fictive temperature rise that scales with the repetition rate as shown in Figure 1.7. For all heat affected zones a significant increase of fictive temperature in contrast to the value for pristine glass of  $T_{f,0} = (940 \pm 20) \text{ }^\circ\text{C}$  is measured. Interestingly,  $T_f$  scales with the laser repetition rate and reaches values up to 1700 °C at 9.4 MHz for 150 nJ and 1000 pulses per laser spot [73].

## 1.5 Damage thresholds and different type of permanent modifications

Refractive index changes induced by femtosecond laser irradiation in silica have been reported in several papers. Authors investigated the magnitude, the kinetics, the stability, the anisotropy according to the laser pulse energy, pulse duration, numerical aperture and writing velocity etc... From these results, it is possible to identify 4 regimes with 3 "damage" thresholds in SiO<sub>2</sub> glass as we reviewed according maser parameters (NA, pulse duration, ..) in [60] :

- Below the first threshold, T1, (e.g.  $0.085 \pm 0.015 \text{ } \mu\text{J/pulse}$  in pure silica, 800nm, 160fs, 0.5 NA, 100 kHz, 100 m/s), the increase of the index relaxes following third order kinetics. The writing process is two-photon dependent when an absorption band exists at the relevant final energy. The index change decays within a few seconds.
- Between the two damage thresholds, the index change is permanent and nearly isotropic, the thermal stability is increased when compared to UV-induced changes but moderate. The maximum index change is  $3\text{-}6 \times 10^{-3}$  in fused silica [77]. This is very large compared to UV laser-induced one which is limited to  $3 \cdot 10^{-4}$  using 157nm or 193nm excimer laser writing [78].
- Above the second damage threshold, T2, (e.g.  $0.31 \pm 0.05 \text{ } \mu\text{J/pulse}$  in pure silica, 800nm, 160fs, 0.5 NA, 100 kHz), the characteristics are quite different. The index change magnitude can be as large as  $\sim 10^{-2}$  and resists to decay during at least two hours at 1000°C [79, 80]. The index change is highly anisotropic [56, 81, 82] and this is the most striking feature. The principal axes are determined by the laser polarization [81]. This is attributed to the formation of self-organized nanogratings [57] made of nanoporous silica [83] as extensively described

in the next section.

- Above the third damage threshold, T3 (e.g. 4  $\mu\text{J}/\text{pulse}$  in pure silica, 800nm, 160fs, 0.5 NA, 100 kHz), we can observe voids [80, 84].

These three regimes can be clearly distinguished employing laser pulses shorter than 200 fs [53, 58, 85] (Figure 1.8). But at longer pulses, the region II narrows a lot which make it difficult to realize Type I modifications in multipulses regime.

As shown in Figure 1.8, another important parameter for femtosecond laser direct writing is focusing conditions, which roughly can be arranged into three groups depending on the numerical aperture. The low NA regime is related to lenses with  $\text{NA} < 0.1$ , this gives a spot size of more than 10  $\mu\text{m}$ . The femtosecond laser beam weakly focused into the bulk of transparent material turns into filament below damage threshold preventing single-shot permanent structural modification [86, 87]. As a result, low NA lenses are typically used for surface modification, where self-focusing is not playing a crucial role. The lenses with numerical aperture from 0.1 to 0.6 can already induce a confined permanent modification inside of transparent material. At these numerical apertures spherical aberration can strongly affect the laser beam propagation. The refractive index of fused silica is higher than air's by roughly 0.45. The light is therefore non-uniformly refracted at the interface between the air and the material. As a result the adjacent part of the beam is focused deeper than the central, the waist is shifted and the focal spot is elongated in the propagation direction whereas the lateral spot size remains the same [88]. The strength of this effect is increasing with numerical aperture. The refractive index mismatch can be compensated by using objectives with spherical aberration correction, immersion optics or adaptive optics methods [89, 90]. Even larger numerical apertures ( $\text{NA} > 0.9$ ) can be achieved with immersion oil lenses. The immersion optics not only tightly focuses the laser beam but also compensates refractive index mismatch at the surface of the sample. As a result, tightly focused femtosecond laser beam can modify material even at nanojoule energy level [91, 92], i.e. ultrashort pulse oscillator energy is sufficient to induce the permanent modifications. The characteristics of these different regimes and modifications are detailed below.

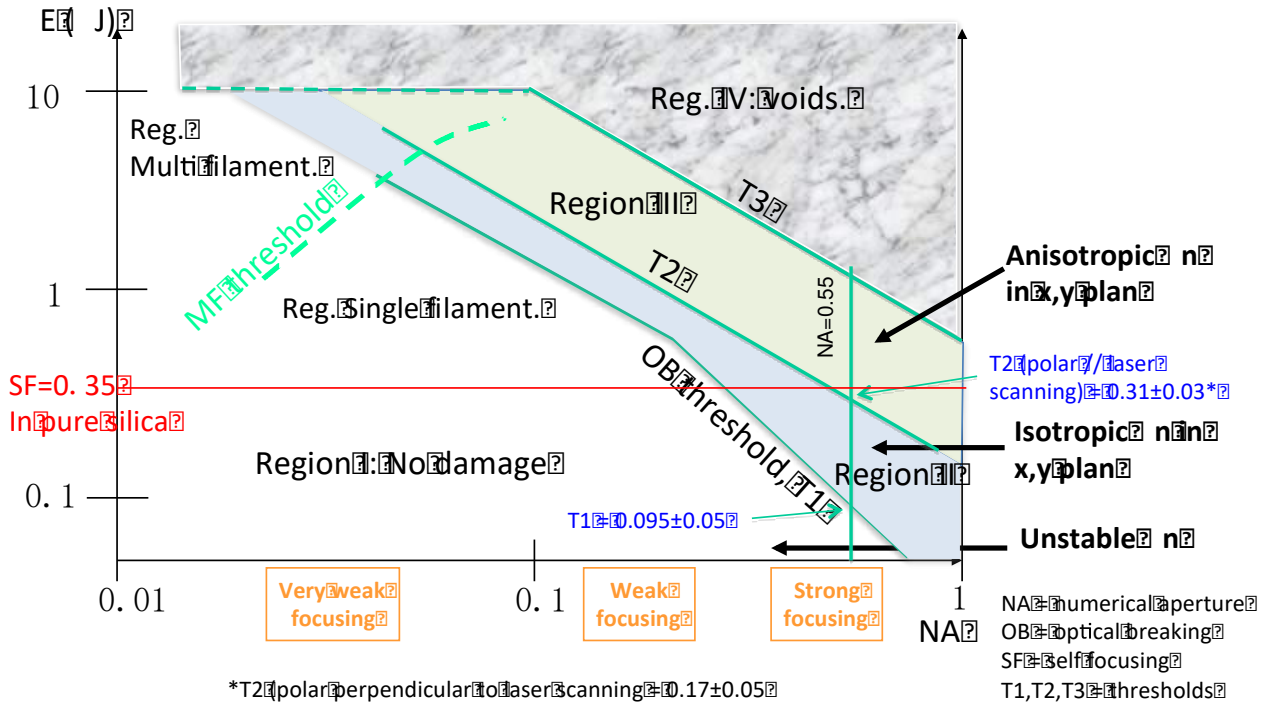


Figure 1.8 Diagram of the different types of damage according to the energy of the laser pulses and the numerical aperture (NA) of the focusing. MF: multi-filamentation; AF: Self-focusing; T1, T2 and T3: thresholds of the different types of damage; \* T2 (polarization perpendicular to the direction of laser writing) =  $0.17 \pm 0.05$  J. Laser writing parameters: 800nm; 160fs; 100kHz; 100m / s; parallel configuration; SiO<sub>2</sub>. Adapted from Ref. [60].

### 1.5.1 Isotropic index changes based modifications (Type I)

The first observation of a threshold that we can report under a sufficiently intense irradiation is the reduction of the optical transmission. It is observed over a wide range of wavelengths from infrared to blue [26, 91] This indicates that the glass is modified in its structure. The corresponding threshold energy has been tentatively defined by Schaffer et al. [43] taking into account the beam propagation effect. For diffraction-limited focusing and taking into account the presence of weak self-focusing, the energy required to reach the breakdown intensity is related to the NA by using the relation:

$$E_{th} = \frac{I_{th}\Delta t\lambda^2}{\pi(NA)^2 + I_{th}\frac{\lambda^2}{P_{cr}}} \quad \text{Equation 1.23}$$

where  $I_{th}$  is the intensity;  $\Delta t$  is the pulse duration;  $\lambda$  is the wavelength; NA is the numerical aperture of the focusing lens and  $P_{cr}$  is the critical power defined in the relationship Equation 1.23

At low energy, an increase (from  $10^{-4}$  up to  $5 \cdot 10^{-3}$ ) of the refractive index is observed in the silica which is one order magnitude higher than with UV ns laser (193nm or 157nm) [78]. It is attributed to a permanent densification due to a rapid cooling of the initially very hot focal volume [94, 95]. In addition, the focusing of the femtosecond laser pulses gives rise to a constraint that plays a role in this densification under certain conditions [96]. Defects centers (also called color centers) induced by femtosecond laser irradiation may be responsible for a portion of the refractive index change through the Kramers-Kronig

relationship (a change in absorption leads to a refractive index change since these two quantities are conjugate complexes of the dielectric constant) [97]. Although color centers induced in femtosecond laser irradiated glasses have been observed [72, 98], there has been no experimental evidence so far of a strong link between their formation and induced index change. Waveguides formed in silica with an infrared femtosecond laser [99] showed photo-induced absorption peaks at 213nm and 260nm corresponding to the respective center defects E' and NBOHC. However, the two defects were completely erased after annealing at 400°C, although it retained its guiding properties up to 900°C. As a result, color centers are unlikely to have played a strong role in the refractive index change [99]. Other results lead to the conclusion that the thermal stability of the colored centers produced in borosilicate and silica glasses is not compatible with that of the change in refractive index [72]. It has recently been shown, in pure silica glasses for the realization of waveguides, that colored centers contribute to the refractive index changes for only 20% [77] whereas the major part has been attributed to defects-assisted densification by the authors.

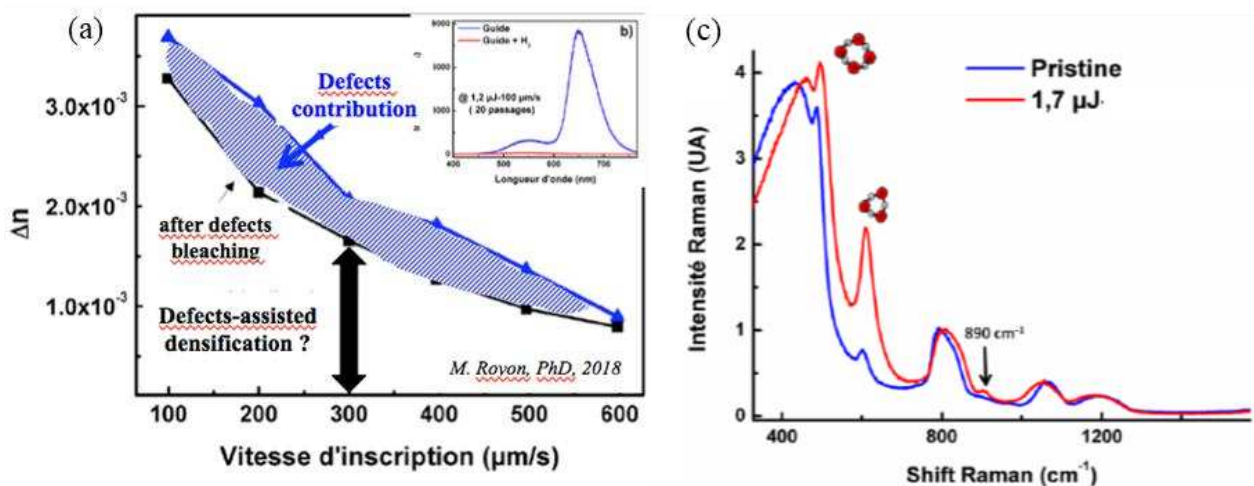


Figure 1.9 (a) Measurements of  $\Delta n$  waveguides in a Corning 7980 fused silica, adapted from Royon et al. [77]. The blue curve represents the change in index after femtosecond irradiation while the black curve shows the index change following hydrogen loading and complete desorption. (b) NBOHC PL emission that is bleached after  $H_2$ -loading. (c) Raman spectra of the pristine sample and of a waveguide ( $\Delta n = 3.10^{-3}$ , Type I regime) photo-inscribed with the following conditions: 1.7  $\mu J$  (slit shaping conditions)- 100  $\mu m/s$  with 8 passes [100].

In an extremely simplistic view of the free electron plasma relaxation created by laser irradiation, it can be said that the transfer of energy from free electrons to the glass network leads to very high local temperature. The temperature can reach several thousand degrees [33] at the focal point limited by thermal conduction [101] (and likely high pressures), up to the local melting of the glass, inducing densification (or expansion as a function of the relationship between the density and the cooling rate i.e. glass fictive temperature) after the fast cooling of the glass [102]. This results, for example, in a lower average Si-O-Si angle and thus some changes in some infrared bands (for example, the antisymmetric elongation vibration centered at 1120  $cm^{-1}$ ) and a change in the  $D_1$  and  $D_2$  bands observed in Raman spectroscopy [102, 103],  $D_1$  and  $D_2$  being respectively associated with the vibrations of cycles with 4 and 3 tetrahedra. In silica, these structural modifications are correlated with an increase in the refractive index, of the order of a few  $10^{-3}$  in writing conditions close to ours. The hypothesis of local densification of glass as a contribution to the increase of the

refractive index was already advanced during the first publications on this subject [55, 72, 97, 104-108] following atomic force microscopic or phase shift interferometer observation of the depression of the surface (i.e. a valley) by a few tens of nanometers at the level of the irradiated zone.

Our team recently published a model of an original physico-chemical mechanism to explain these observations for Type I modifications. We proposed that the first threshold, named T1, is based on the modification of the fictive temperature  $T_f$  of the glass when the duration of the heat pulse corresponding to the light energy is greater than the glass relaxation time  $\eta(T)/G(T)$ . This one depends on the viscosity  $\eta$  and the shear modulus  $G$  of the material, the lower the viscosity, the smaller the relaxation time and globally the larger the  $T$ , the smaller the relaxation time. If the increase of the temperature is long enough to transform the glass, this defines the first threshold noted T1. For that we have solved the Fourier equation and taken into account the variations of heat capacity, of thermal diffusion, of modulus of shear and viscosity with doping and temperature. The results show that the glass fictive temperature increases (several hundred degrees higher than the original temperature) and then does not change significantly. We have also described the dependence of photosensitivity on the chemical composition of glass in the germanium, phosphorus, F-doped silica family [101].

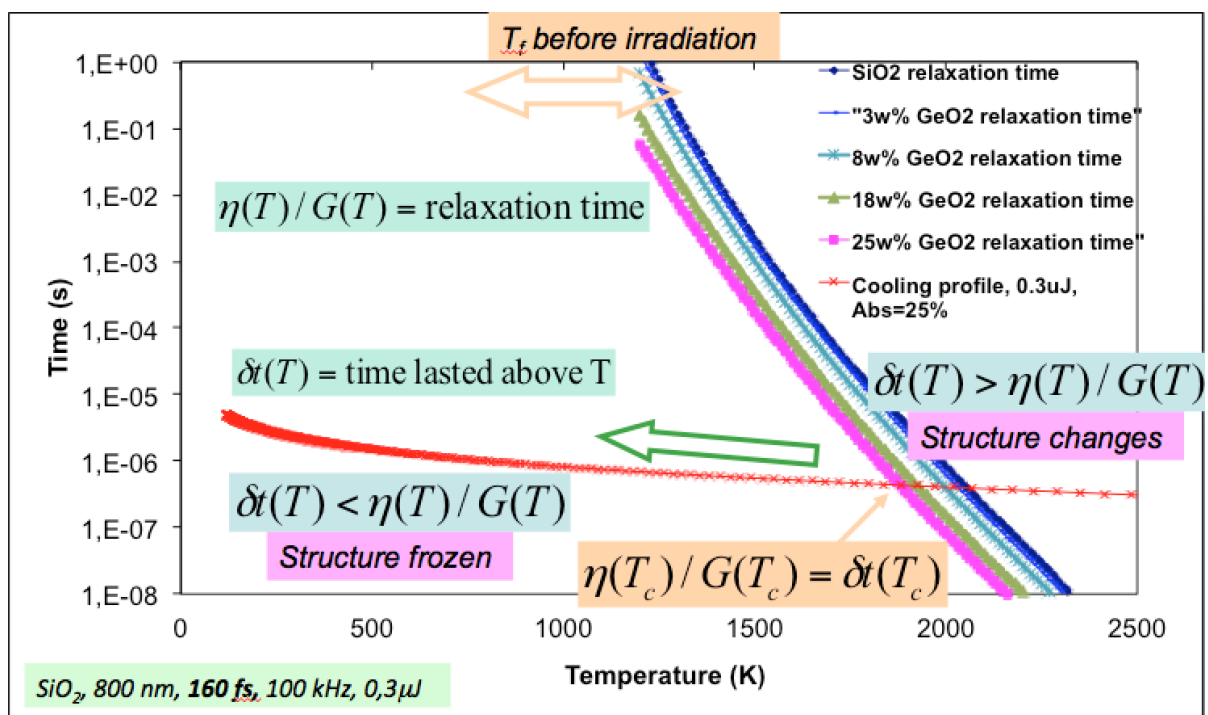


Figure 1.10 This graph compares the glass relaxation time and the cooling profile after single pulse femto-second laser irradiation for pure and GeO<sub>2</sub>-doped silica. The heat cooling profile is for pure silica only. Graph adapted from our group work in Ref. [101].

## 1.5.2 Anisotropic refractive index changes based modifications (Type II)

For higher energy pulses, a second threshold is observed which is based on the

appearance of nanostructures (see Figure 1.11) caused for example by the interference between the laser field and the electron plasma wave (a bulk plasmon) according to the first model that was proposed in 2003 [57].

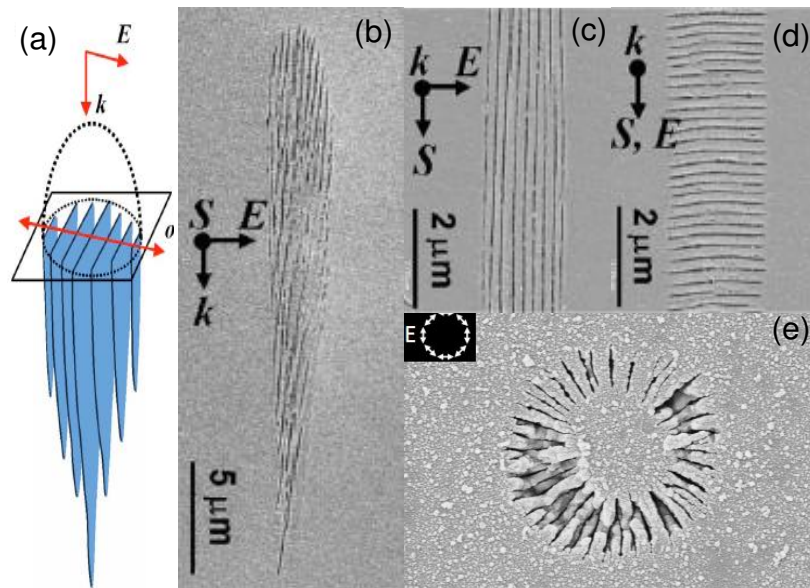


Figure 1.11 Nanogratings scheme within a laser track cross-section (a). Scanning electron microscopy (SEM) image of the nanogratings inscribed at 65 nm from the surface with a linear polarization perpendicular (b, c) and parallel (d) to the writing direction and azimuthal polarization (e). Laser parameters: 125fs, 0,65 NA, 0,3 J, 100kHz, 30 m/s. Images extracted from Ref. [109].

Y. Shimotsuma and P. Kazansky made this discovery in 2003. It remained to determine the nature of these nanoplanes. Some saw fractures, others oxygen depletions [57]. In 2011 we finally revealed that nanogratings are formed by a decomposition of silica (nanoporous silica formation [110]) as confirmed in 2013 [83] and shortly described in Figure 1.12 Nonlinear picture of the plasma density wave. At the nanoscale the free-electron density (or electronic temperature) modulation is imprinted in the matter by decomposition of SiO<sub>2</sub>, revealing a high plasma temperature  $T_e$  (or density) that is higher than a "decomposition" limit. Graph extracted from Lancry et al. [83]. This decomposition of silica into nanoporous layers can be done, contrary to the fictive temperature modification, only by a pulse-to-pulse accumulation. As the material cooled down completely between pulses, we initially proposed an accumulation of point defects. We then explain the variations with doping by production of defects that vary greatly. This production is favored by the addition of germanium or conversely, it can be inhibited to observe only isotropic index change by adding fluorine in silica, which provide interesting results depending on the type of application envisaged [101].



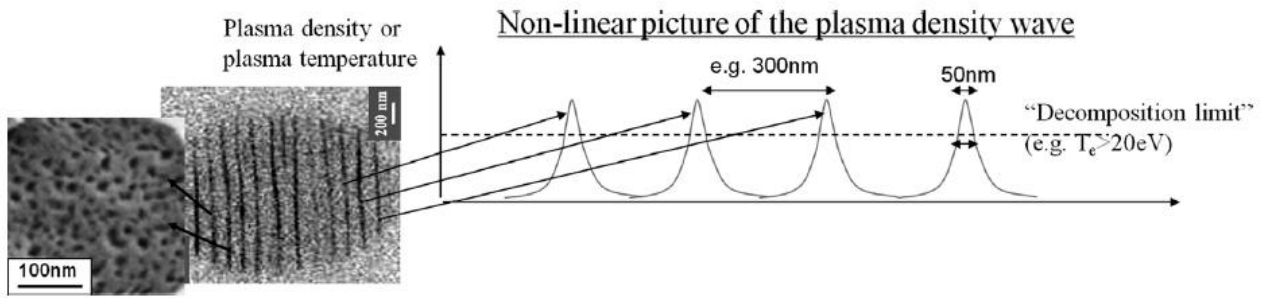


Figure 1.12 Nonlinear picture of the plasma density wave. At the nanoscale the free-electron density (or electronic temperature) modulation is imprinted in the matter by decomposition of  $\text{SiO}_2$ , revealing a high plasma temperature  $T_e$  (or density) that is higher than a "decomposition" limit. Graph extracted from Lancry et al. [83].

### 1.5.3 Voids (Type III)

For even higher energy pulses giving rise to peak intensities greater than  $10^{14} \text{ W/cm}^2$ , holes in volume (so-called voids) are achievable by femtosecond laser irradiation. They are at the origin of a mechanism called the micro-explosion. A first model was proposed by Fleischer's team [111] and also reported later by Schaffer [112]. The mechanism at the base of void formation was initially suggested to be a Coulombian explosion i.e. when the density of excitations at a point in the material is very large, the Coulombian force between ions can overcome their binding energy. In this case, ions are also moved to interstitial positions around the starting point. However this is unlikely to happen in the mentioned irradiation conditions so the mechanism was then revisited as follows: the energy is absorbed in a small volume producing a pressure which subsequently drives a shock wave and stress exceeding the Young modulus of the material. The strong spherical shock wave starts to propagate outside the centre of symmetry of the absorbed energy region compressing the material [113-117]. At the same time, a rarefaction wave propagates to the centre of symmetry decreasing the density in the area of the energy deposition. The shock wave stops when the pressure behind the shock front becomes comparable with the Young modulus. The corresponding threshold is noted  $T_3$  in our threshold diagram in Figure 1.8. Such voids can be exploited for 3D storage of information [118].

## 1.6 Focus on Type II modifications and nanogratings formation

### 1.6.1 From LIPSS to self-organized nanogratings in silica

Laser induced periodic surface structures (LIPSS) are a universal phenomenon and can be generated on virtually any type of media including metals, semiconductors and dielectrics upon irradiation with linearly polarized light [119-122]. The ripples can be formed with wavelengths ranging from the mid-infrared to the blue end of the visible spectrum and at pulse durations from continuous wave operation to femtosecond laser systems [123, 124]. For normal incidence, the period of surface structures was known to be close to the

wavelength of the light and oriented perpendicular to the laser beam polarization [125]. For oblique incidence and  $TM$  polarization (electric field is oriented parallel to the plane of incidence) the ripples occur with one of two possible periods [121]:

$$\Lambda = \frac{\lambda}{1 \pm \sin \theta'} \quad \text{Equation 1.24}$$

where  $\theta$  is the angle of the incident of laser beam, and the negative or positive signs correspond to the forward and backward scattering, respectively. One interesting prospect from applications point of view is that when laser beam is moved with respect to the sample, the ripples can coherently extend over the scanned area.

Lately, ultrashort laser pulses were observed to induce two types of periodic surface structures depending on the period of the structure [126]: above single pulse damage threshold – ripples with a period close to the wavelength ( $\sim\lambda$ ), and below single pulse damage threshold – subwavelength ripples with periods down to 30 nm ( $\lambda/10$ ) [120, 127]. Here, the period was found to be dependent on the number of pulses and the subsequent carrier density [120, 128, 129], where the final subwavelength structure is formed only after tens or even thousands of pulses.

In general, the understanding of formation of LIPSS is a challenging task as this involves a complex sequence of inter- and intra-pulse physical processes as review in [130, 131]. It is generally accepted that low-spatial frequency LIPSS (LSFL), are generated by the interference of the incident laser beam with an electromagnetic wave scattered at the rough structure and may involve the excitation of surface plasmon-polaritons (SPPs), particularly important when irradiating with femtosecond laser pulses [124, 129, 132, 133]. The surface wave driven periodic modulation of the electromagnetic field along the laser polarization gives anisotropy in the following modification processes. It is assumed that the further steps are governed by the fast (non-thermal) and slow (thermal) phase transitions [134]. Interestingly, the early stage ripples upon a subsequent pulse irradiation modulates the light-matter interaction and reduces the periodicity of the pattern.

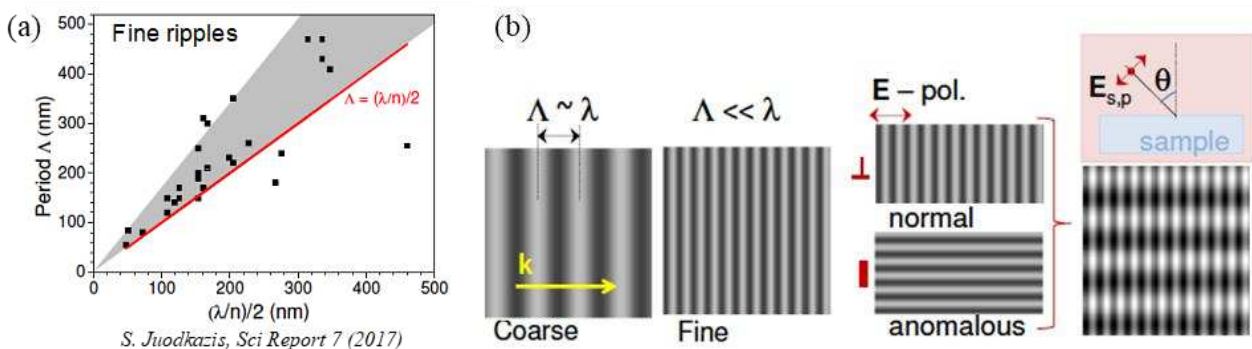


Figure 1.13: (a) Fine ripple period  $\Lambda$  dependence on the laser wavelength  $\lambda$  and refractive index of materials,  $n$ . The gray-shaded region marks an expected  $(0.5 - 0.85)\lambda$  span of  $\Lambda$  values for the absorbing (plasma) surfaces according to the SPP surface plasma wave mechanism. (b) Ripples of period  $\Lambda$  on surfaces irradiated with wavelength  $\lambda$  laser pulses at an incidence angle  $\theta = 0^\circ$  (normal incidence): coarse, fine, normal ( $\perp$ ), anomalous and mixture, which occurs at  $\theta > 0^\circ$ . Graphs extracted from Ref. [131]

In contrast, the high-spatial frequency LIPSS (HSFL) exhibit several features: (i) are

formed at fluencies very close to the damage threshold of the irradiated material; (ii) have spatial periods significantly smaller than the irradiation wavelength; (iii) are usually observed for irradiation with ultrashort laser pulses (iv) mostly for excitation of transparent materials with a photon energy below the bandgap and (v) hundreds to thousands of laser pulses per irradiation spot. Within the interpretations proposed in previous studies, the early stage laser induced unstable nanostructures, during the relaxation of a highly non-equilibrium surface, tend to self-organize into HSFL patterns. However, the origin of the HSFL is still under debate [130, 131].

## 1.6.2 Physical and optical properties of nanogratings in silica glass

In 2003, a new type of self-organization was observed inside SiO<sub>2</sub> glass after irradiation with an ultrafast laser [57], which was found to be responsible for femtosecond pulse induced anisotropy [56, 81, 82] and the propeller shape of light scattering reported earlier in 1999 [135]. Under certain irradiation conditions, the interaction of femtosecond pulses with silica is known to induce highly ordered sub-wavelength structures with lamellae-like nanoporous regions oriented perpendicular to the incident beam polarization [83], as sketched in Figure 1.14. At that early time, linear birefringence and related original structures such as self-organized nanogratings and chiral mechanical structures [38, 136] are spectacular but they appear to be only in specific materials (namely fused silica and Ge-doped silica). For instance, in BK7, no such structure is detected, although strong damage occurs [137]. In 84SiO<sub>2</sub>-16SnO<sub>2</sub> no birefringence is detected and, in addition, the index change is positive in contrast to pure silica [137].

Among the first discovered properties, Bricchi et al. [81] demonstrated that such nanostructures due to the sub-wavelength periodicity behave as a uniaxial linear birefringent material where the optical axis is parallel to the orientation of the laser polarization and the slow axis is perpendicular to the writing laser polarization. The effect of form birefringence, unlike intrinsic birefringence, which is due to the anisotropy of oriented molecules, manifests itself due to the alignment of submicroscopic rodlets or platelets. The light polarized parallel to the interfaces experiences a larger refractive index and as a result a phase difference for two perpendicular polarizations is acquired. The strength of the form birefringence can be controlled by periodicity and material composition of the microstructure. Under a linear approximation, refractive indices of nanogratings for ordinary  $n_o$  and extraordinary  $n_e$  waves are [81, 138, 139]:

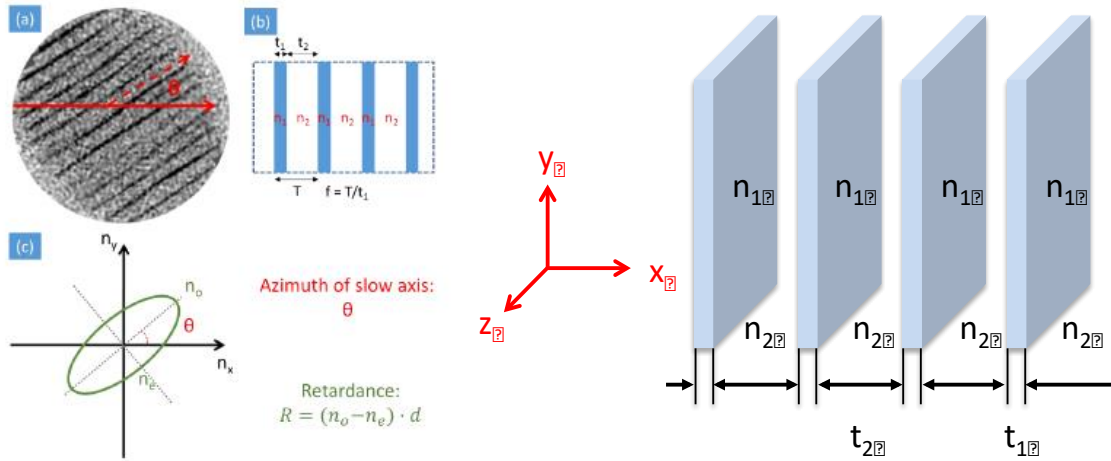


Figure 1.14 Periodic assembly of parallel thin strips of index  $n_1$  and thickness  $t_1$  spaced by a distance  $t_2$  in a medium of index  $n_2$ . Schemes are adapted from Refs. [140, 141].

Let's determine the theoretical linear birefringence. We consider a wave of the form:

$$\vec{E} = \begin{bmatrix} E_{O,x} \cos(\omega t - k_z z - \phi_x) \\ E_{O,y} \cos(\omega t - k_z z - \phi_y) \end{bmatrix} \quad \text{Equation 1.25}$$

where  $\phi_{x,y} = \frac{2\pi}{\lambda} n_{x,y} l$  is the phase shift along the axis considered  $x$  or  $y$ . Bricchi [141] theoretically shows that the refractive indices are of the form:

$$n_x^2 = \frac{n_1^2 n_2^2}{\tau n_2^2 + (1-\tau) n_1^2} = n_e^2 \quad \text{Equation 1.26}$$

$$n_y^2 = \tau n_1^2 + (1-\tau) n_2^2 = n_o^2 \quad \text{Equation 1.27}$$

where  $\tau = \frac{t_1}{t_1 + t_2}$  est the fraction of the total volume occupied by the thin sections. We deduce the linear birefringence of the assembly shown in Figure 1.14:

$$\Delta n = n_x - n_y = n_e - n_o \leq 0 \quad \text{Equation 1.28}$$

Here the negative birefringence of  $\Delta n \approx -5 \cdot 10^{-3}$  up to  $-10^{-2}$ , and of the order comparable to the natural birefringence of uniaxial crystals such as quartz (uniaxial positive  $8 \cdot 10^{-3}$ ), ruby and sapphire, was reported.

### 1.6.3 Tentative mechanisms for nanogratings formation

The formation of the periodic nanostructures in transparent dielectrics remains under debate. However, most of the studies agree that the seeding processes governed by some kind of randomly distributed inhomogeneity are taking place [142-148] but this is still not clear if whether these are point defects, glass free volume, nano-agregates already present or initiate by the first pulse like nanovoids for example in some recent suggestions. For example, the single isolated nanoplane was achieved in porous silica prepared from the phase-separated alkali-borosilicate glass [149-151]; and combining the experimental results with the concept of the surface plasma wave excitation, the significance of the seed structure was proposed. In addition, the constructive interference of scattered light was considered to

explain the extreme reduction down to sub-100 nm of the nanogratings period, which breaks the limits of some models like  $\lambda/n$  or  $\lambda/2n$ . This correlates very well with the formation of surface ripple, when experimentally is proven that the period depends on the number of pulses [120].

One of the first models for nanogratings formation was proposed by P. Kazansky and based on the interference of the bulk electron plasma longitudinal wave propagating in the plane of light polarization with the incident light [142]. The early stage coupling is triggered by inhomogeneities induced along with the motion of free carriers. The periodic structure results due to the interference, enhances the coupling and generates a periodic modulation of the plasma concentration ( $N_e \sim 10^{21} \text{ cm}^{-3}$ ). As a result, this modulation is further frozen into a material structural change. Conversely, the model does not work in the case of subcritical plasma concentrations. Further, this model was adjusted by assuming a two-plasmons decay [152]. The two-plasmons decay is the parametric process in which the incident photon is separated into two plasmons, i.e. two electron plasma waves. The interference between two plasmons of the same frequency propagating in opposite directions produces periodic sub-wavelength modulations (Cherenkov mechanism of momentum conservation). The characteristic generation of the 3/2 harmonic may be observed due to the decay process. Although the model is valid for plasma concentrations ( $\sim 10^{20} \text{ cm}^{-3}$ ) lower than the critical density  $N_{cr}$ , this was never confirmed experimentally by independent research groups.

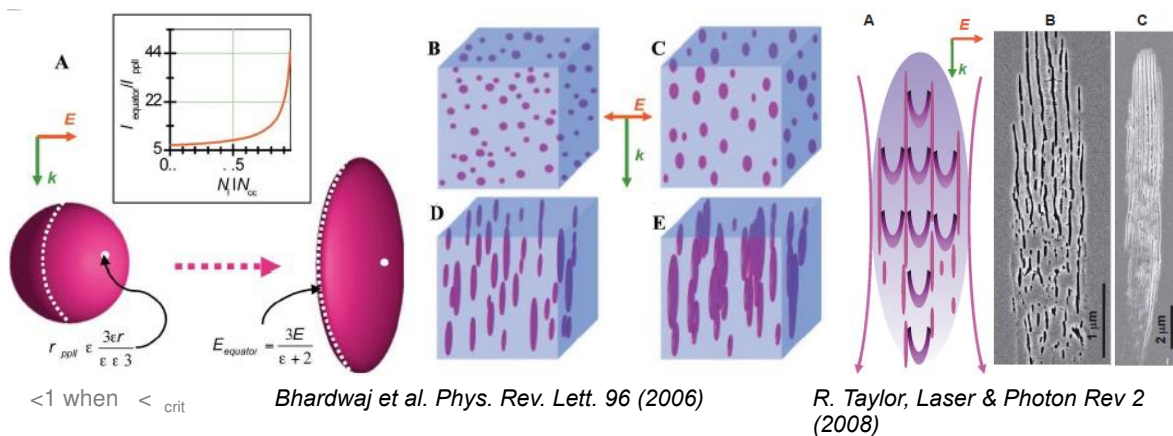


Figure 1.15 (a) Asymmetric field enhancement at two locations on a nanoplasma under the influence of the laser electric field  $E$  [144]. (b to e) Evolution of nanoplasmas into nanoplanes. Randomly distributed underdense nanoplasma droplets (typ. a few nm- 10's nm) grow asymmetrically in the presence of the laser field over hundreds of laser pulses to become ellipsoidal and finally flatten and merge to become micrometer-sized nanoplanes. (Right side, [153, 154]) Panel A: schematic diagram of periodic  $\lambda/2n$ -spaced planar structures. When irradiated they form plasma planes ( $N_e > N_{cr}$ ) that guide light to reinforce the growth of planes in the bottom portion of the carrot structure. Panels B and C: cross-sectional SEM images of plane formation. Panel B: 100 fs, 350 nJ and 1 mm/s scanning speed. Panel C: 150 fs, 300 nJ and scanning speed of 30  $\mu\text{m/s}$ .

The model based on attractive interaction and self-trapping of exciton-polaritons was suggested to explain the periodicity of nanogratings in the direction of light propagation [146]. The two dispersion branches of exciton-polaritons are excited simultaneously by multi-photon absorption. As a result, the interference of propagating exciton-polaritons results in the polarization grating. After the relaxation process ( $\sim \text{ps}$ ) to indirect states decoupled from light, the excitons can be trapped freezing the grating pattern formed by

the exciton-polariton interaction with light [155]. The process is followed by the generation of molecular oxygen [83, 156] and nanoporous structure [83, 157] that originate the formation of nanogratings.

The most accepted model for nanogratings formation is thus based on a nanoplasmonic process [144, 153, 154] as described in 错误!未找到引用源。 . More specifically, the generation of "defects" (still to be identified) inside silica matrix is followed by the formation of inhomogeneous plasma. Under the multipulse regime, the plasma hotspots evolve into spherically shaped nanoplasma. But due to the local field enhancement at the boundaries, the polarization sensitive growth of initially spherical nanoplasma will occur. When the electron concentration is below the critical density, the electric field is enhanced at the equator leading to nanoplanes formation in a multipulses process. The final pattern leads to the period of  $\lambda/2n$ . However, if the plasma density is too high, the dominant enhancement at poles would be initiated, and nanogratings would not be produced. Recently, the nanoplasmonic model has been improved by introducing randomly distributed inhomogeneities to seed the process in fused silica [147]. When increasing the seed concentration, two types of nanoplanes oriented perpendicular to the polarization were identified. For low concentration of nanospheres, the low spatial frequency nanoplanes with the period of  $\lambda/n$  are formed, and attributed to the interference between the incident wave and the inhomogeneity scattered light waves (see Figure 1.16a, b, c). For high concentrations of nanospheres, the mechanism changes as the mutual enhancement induced by the multiple scattering from nanoplasmas becomes dominant. The nanoplasmas develop from random inhomogeneities into the highly ordered high spatial frequency pattern, with the characteristic period around  $\lambda/2n$ . In fact, as described in Figure 1.16b the periodicity may decrease drastically with the further increase of inhomogeneities concentration until the nanoplanes merge i.e. generation of uniformly distributed plasma over the irradiated region. Interestingly this model could be adapted explaining both volume nanogratings and surface ripples.

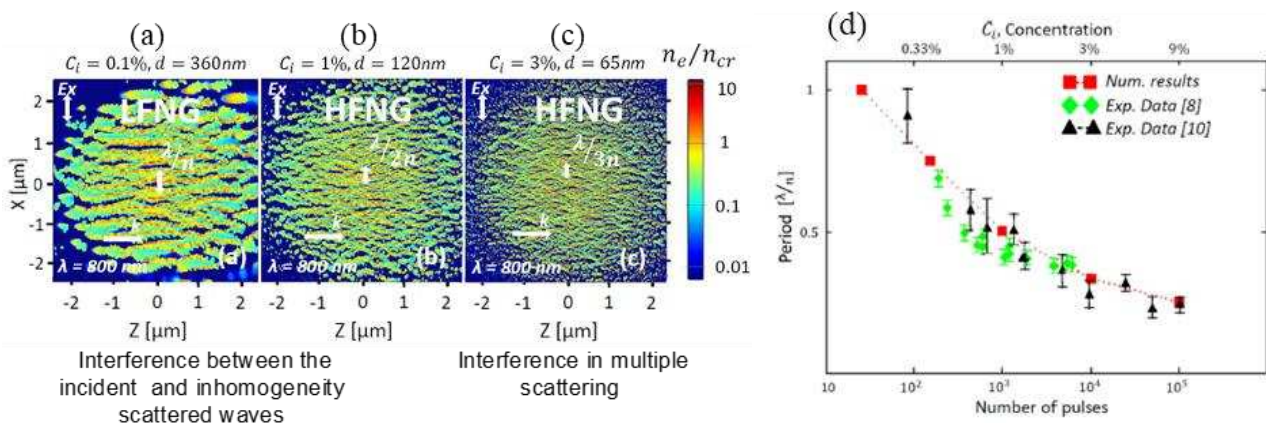


Figure 1.16 Electron density snapshots are calculated by coupled 2D-FDTD at the end of the pulse duration  $\theta = 240$  fs (FWHM) for different initial concentration of randomly distributed (a)  $C_i = 0.1\%$ , (b)  $C_i = 1\%$ , and (c)  $C_i = 3\%$ . The pulse energy is fixed to  $E = 500$  nJ. The irradiation wavelength is 800 nm. (d) Period dependence on the number of pulses from experimental data comparing with the dependence on the concentration of inhomogeneities from numerical modeling. Extracted from Ref. [147].

It remained to determine the nature of these nanoplanes. Some saw fractures, others

oxygen depletions [57]. Our recent studies using both SEM and TEM (never published) indicate that nanogratings are formed by the alternation of “uniform” and porous glass layers [83, 110, 157] (see Figure 1.17 below). The interior of the nanogratings was examined by cleaving the sample after laser irradiation. If the nanograting planes were parallel to the cleavage the interior structure could be observed with field emission electron microscope, which could reveal small features otherwise covered by conductive coating. The areas appearing white are areas that, although having been irradiated, have remained dense, while the parts that are nanoporous are the nanoplanes that have been cleaved in their plane. The formation of nanopores was attributed to  $\text{SiO}_2$  decomposition into  $\text{SiO}_{2(1-x)} + x.\text{O}_2$  due to an electronic heating leading to an expulsion of ionized oxygen atoms [83] with a tensile stress mechanism [158] that was recently revisited as a nanocavitation process [30]. The oxygen atoms are thus found in the interstitial position and recombine to form oxygen bubbles as confirmed by Raman spectroscopy. The typical diameter of nanopores ranges from 10 to 30 nm. Small angle X-ray scattering measurements further confirmed nanoporous structure of the nanogratings interior [157, 159, 160].

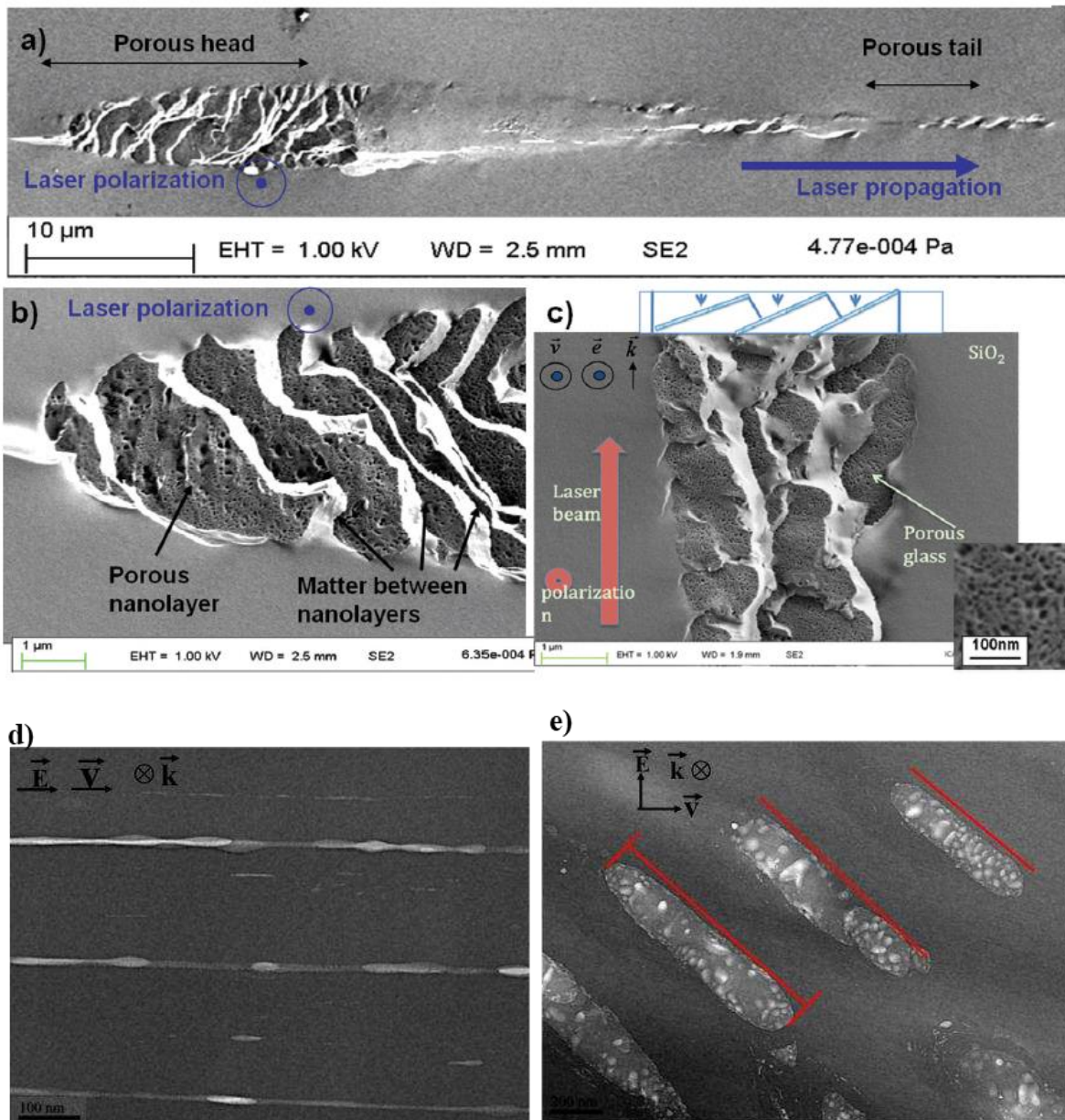


Figure 1.17 SEM images of laser tracks cross-section. With the laser polarization parallel (a) to the scanning direction. (b) and (c) show close-ups of the nanoporous regions. Images extracted from Lancry et al. [83]. TEM images (not published) for (d) perpendicular polarization and (e) parallel polarization to the scanning direction. Laser parameters were: 1030 nm, 250 fs, 200 kHz, 200  $\mu\text{m/s}$ , 0,6 NA and 0.5  $\mu\text{J/pulse}$ .



## 1.6.4 Nanogratings parameters dependence

The ultimate goal is to produce a 3D printable anisotropic material, combining the benefits of durability and polarization sensitivity. In this section, the range of different parameters was discussed in order to gain the basic understanding how to control the ultrafast laser engineered birefringent structure. The main processing parameters are roughly summarized in Figure 1.18.

### **Chemical composition**

Up to now the influence of the glass physical properties (melting temperature, thermal diffusivity, absorption) on the nanogratings formation process have been quite widely investigated indirectly but there are no rationalization yet. This analysis would enable the tailoring of the chemical composition and structure of glasses including nanoporous silica to define the best laser conditions for a targeted application e.g. reduce the required number of pulses for optical data storage or increasing the writing speed for writing birefringent optics. As part of the task, different dopants of silica glass have been analyzed in the context of nanogratings formation namely germanium, phosphorus, fluorine or Chlorine [60, 158, 159, 161]. After more than a decade, nanostructures inside material were found for handful materials: fused silica, GeO<sub>2</sub> [162-164], sapphire [165], tellurium oxide [166], quartz [167], ULE glass [168, 169] and even in some variety of alumino-borosilicate glasses [160, 162, 168, 169] but this is still growing. From this list, fused silica is the most common material for inducing nanogratings. Nanogratings were also found in porous silica prepared from phase-separated alkali-borosilicate glass by removing the borate phase in the hot acid solution [151]. Even twin or single isolated nanoplane could be induced by controlling laser pulse energy [170], which could be used for writing nanofluidic channels [149-151]. The most widely used material is fused silica and it provides relatively large processing window in contrast to most others materials. However, the highest retardance was obtained in porous silica glass with a porosity size in the range of 2.5 to 5 nm, also providing Type II modifications with less stress [27, 171]. It is also expected to enhance nanogratings formation by inducing oxygen deficiency centers in the glass matrix, which could act as a precursor for the nanostructure formation.

### **Laser parameters (pulse duration, pulse energy, etc...).**

Experimental observations suggest that the stationary printing and scanned modification require different parameters to obtain uniform nanostructures towards practical applications. If the target is high retardance, the pulse energy and pulse duration have to be increased, reducing the quality of the structure. If the target is uniform modification in scanning regime, sufficient pulse energy and repetition rate have to be chosen. Therefore, the best trade-off between all the parameters and the nanostructure should be achieved. A summary of the main experimental results and typical trends related to retardance formation within Type II regime in silica glasses is shown in Figure 1.18. This summary was extracted from the PhD thesis of Ausra Cerkauskeitė [27].

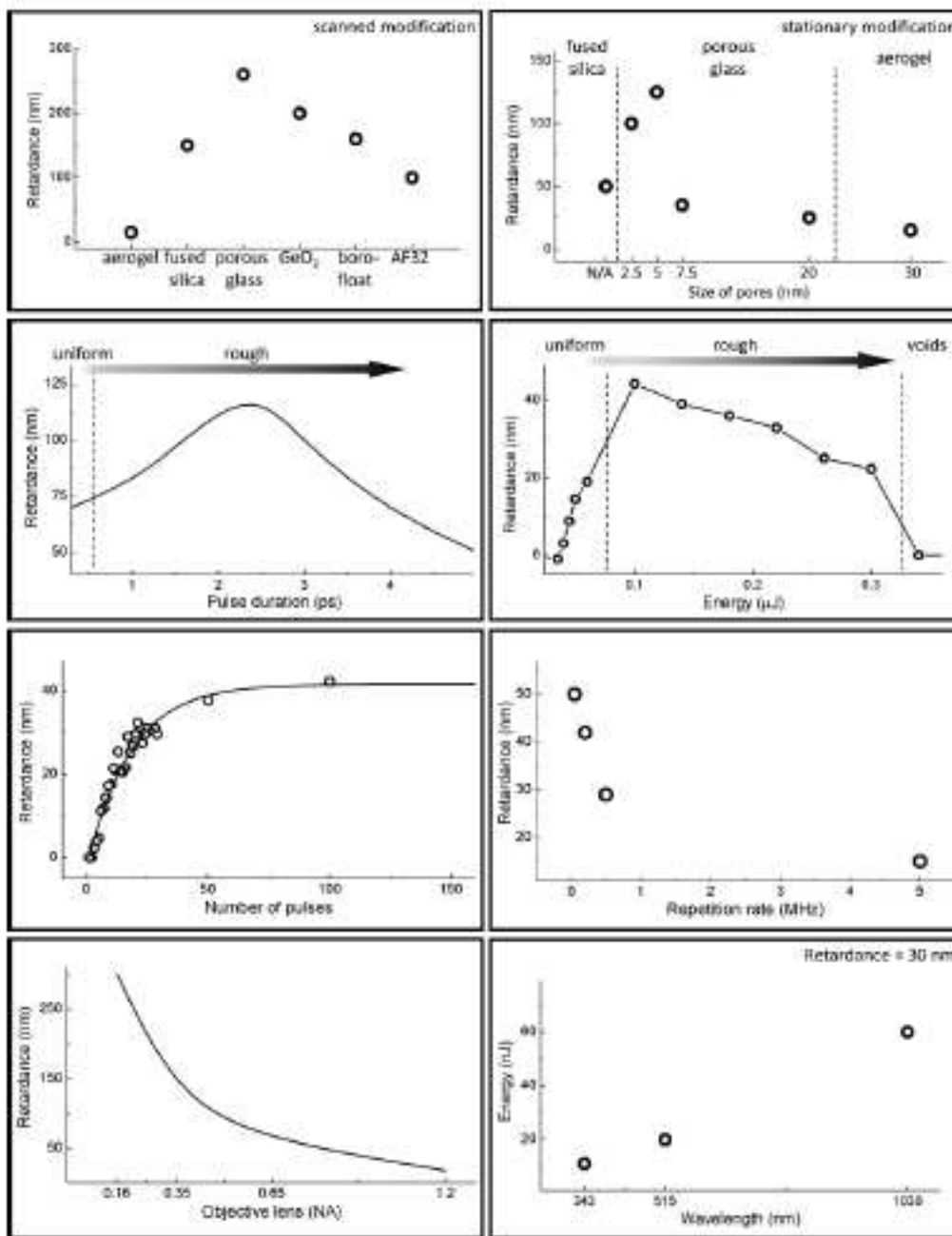


Figure 1.18 Summary of the main experimental results and typical trends related to retardance formation within Type II regime in silica glasses. Extracted from PhD thesis of Ausra Cerkauskeitė [27]

- **Wavelength:** Decrease in wavelength leads to lower pulse energy required to obtain the modifications with the same level of retardance and a short period (see Figure 1.19a). It has been also demonstrated that shorter wavelength provides lower modification threshold but at the expense of higher losses in the UV-Vis range [172]. This is promising in terms of high density printing for 3D geometric phase optics but also optical data storage (energy reduction). However, the systematic investigation of the quality of the structure and processing parameters should be done in order to optimize the writing system.

- **Pulse number:** Currently a few pulses are required to induce self-organized nanostructure i.e. to create orientable linear birefringence. Retardance tends to saturate within at least tens of pulses delivered to the same spot. Period is decreasing with increasing pulses (see

Figure 1.19a).

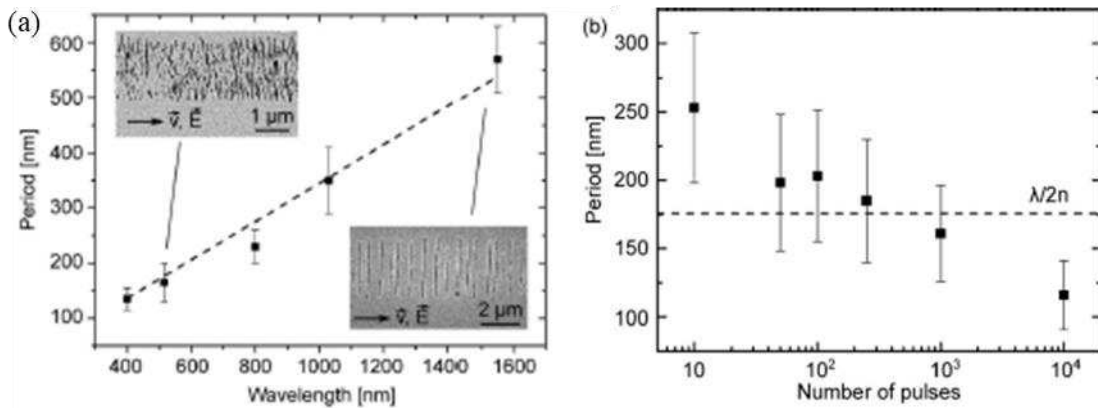


Figure 1.19: (a) Nanogratings period dependence on the laser wavelength. Dash line is for the  $\lambda/2n$  theoretical limit predicted by the nanoplasmonic model and considering material dispersion. (b) Nanogratings period dependence with the number of pulses. Laser parameters: 515 nm, 450 fs, 500 kHz, 190 nJ/pulse. Data extracted from Ref. [173].

- Pulse duration: As it can be seen in see Figure 1.20, with the increase of pulse duration and pulse energy, the increase of retardance is observed leading to more rough structure [58, 60, 84, 174]. This suggests working close to the modification threshold, as in general smooth modification produces less scattering and allows recording information with the distance of the modification spot leading to high-density data storage. Strongest retardance is observed in the 500-2000 fs range.

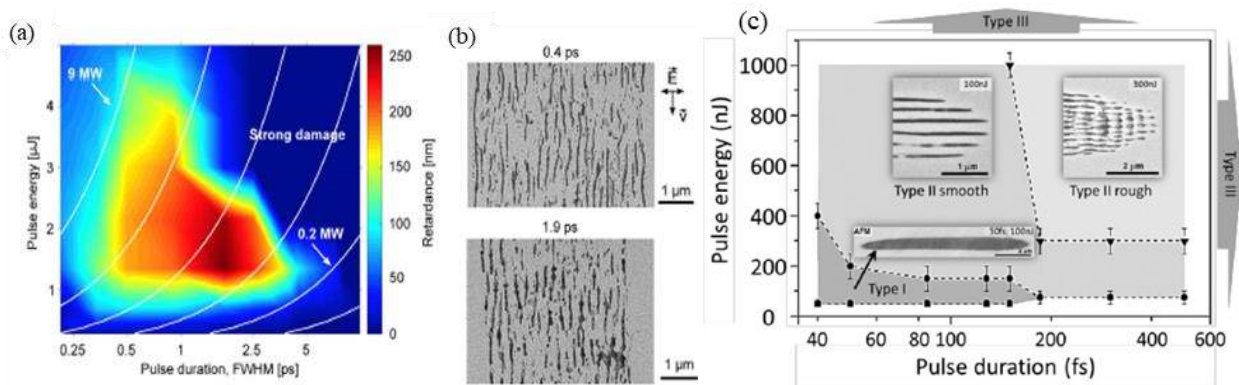


Figure 1.20: (a) False-color map of the optical retardance within Type II regime (nanogratings) in dependence of pulse energy and pulse duration, extracted from Ref. [156]. (b) Typical SEM images are shown for 0,4 ps and 1,9 ps pulse durations (1030 nm, 0,55 NA, 1,5 J/pulse). (c) Threshold pulse energies for the different regimes in silica glass according to the laser pulse duration, from Ref. [58].

- Repetition rate: The nanogratings formation is very sensitive to the laser processing conditions and usually is affected by other effects such as heat accumulation and further local temperature increase. Although the periodic structure is formed within hundreds of picosecond after the irradiation, under high local temperatures the self-organized nanostructure can relax to its initial state before the resolidification takes place leading to the erasure of nanogratings [30, 73, 169]. So with the increase of repetition rate up to the tested region of 10 MHz, retardance decreases [173] as shown in Figure 1.21a. However, the nanogratings induced with 5 MHz still could be exploited for fast data printing, high-speed writing of space variant birefringent optics, 5D optical data storage [27] or polarization

maintaining waveguides.

- Focusing conditions: Using tight focusing, the shorter structure is induced providing the lower value of retardance [60, 85, 175, 176] as illustrated in Figure 1.21b. Nonetheless, the use of nanogratings for multidimensional data storage lies behind relative high and low levels of retardance, and not behind absolute values. Thus, even with high numerical aperture objective the additional dimension can be explored. Apart from that, using tight focusing, it is expected to have smaller structure leading to higher spatial density of “printed data”.

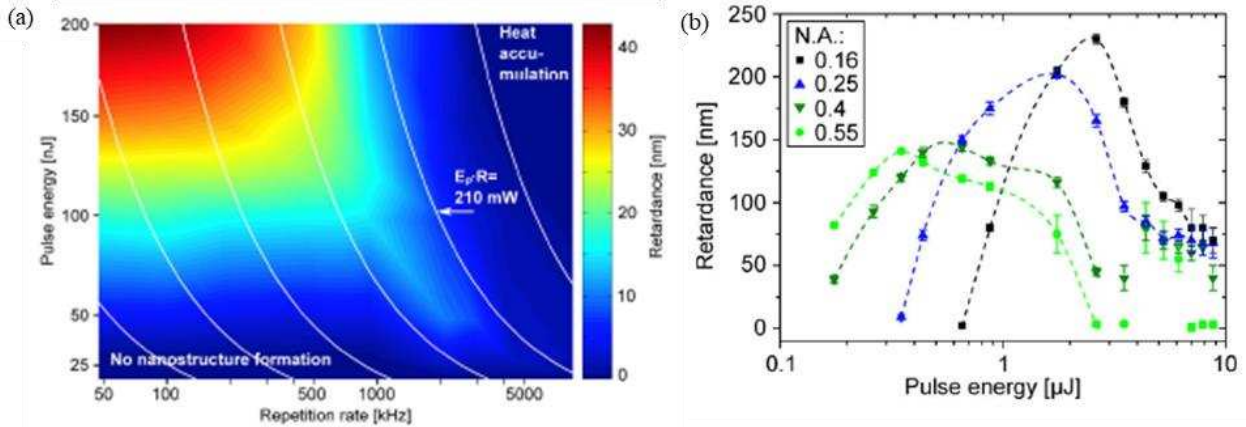


Figure 1.21 (a) Fast color map of the retardance as function of repetition rate and pulse energy. White lines correspond to constant average power in Watts. Laser parameters: 515 nm, 450 fs, 0,55 NA and the pulse number was kept fixed at  $10^3$  per micron by adjusting the scanning speed. (b) Optical retardance in Type II regime for different objectives NA and according to the laser pulse energy. Dashed lines represent a guide-to-the eye. Laser parameters: 1030 nm, 450 fs, 200 kHz,  $10^3$  pulses per micron. Graphs are extracted from Ref. [156].

- Formation timescales. The ultrashort pump pulses will be used to seed electrons and defects to facilitate nanogratings formation [173, 177, 178]. The ability to control self-assembly processes by ultrashort laser pulses (seeding and efficient energy deposition) will allow to induce nanostructures with several pulses (burst of pulses) increasing writing speed by multiple orders of magnitude. For example when the number of pulses within a pulse is between 2 and 4, a much higher retardance is measured (See Figure 1.22a). The short time (typ. 100ns) between pulses within a burst promotes a more efficient absorption due to laser-induced transient defects from previous pulse. In particular the relaxation of excited electrons involves the formation of STE [47, 179], which decays at least several hundred ps into point defects. Thus it seems that transient defects facilitates the formation of nanostructures [146, 177] as shown in Figure 1.22b.

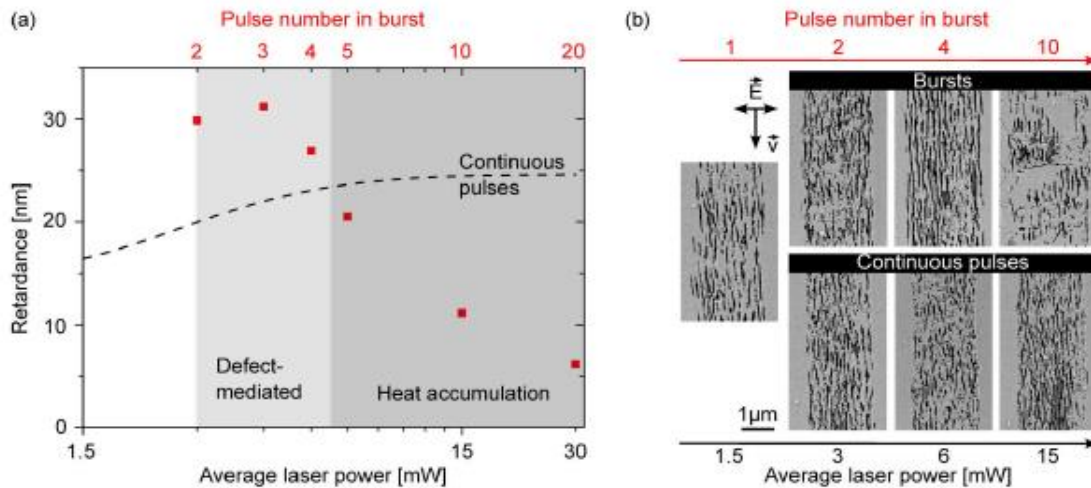


Figure 1.22: (a) Retardance within Type II regime for laser tracks written with bursts of different pulse numbers within each burst and with continuous pulses (dash line). (b) SEM images for nanogratings written with continuous pulses and burst mode. Laser parameters: 515nm, 450 fs, 1 MHz, 0,55 NA and 0,15 J/pulse. Extracted from PhD thesis of F. Zimmermann [156].

- Structure quality. Optical scattering is one of the key factors limiting the technology for multiple layer printing. Because of imperfections of induced nanostructures, like stress, cracks, melting, typically as much as 10-50% of the incident light is scattered in visible spectral range [172]. Also, for most optical components the slow-axis and retardance uniformity have to be achieved. As it was shown in [27], the uniformity of nanogratings can be realized working close to modification threshold but also using nanoporous silica materials [171].

- Future work. It is technologically attractive to use the ultrafast laser direct writing, which offers manufacturability and rapid prototyping of optical elements at reduced costs. However, the mechanisms, which lead to the induced modification in the bulk material, are still not well understood. It is known that the process is strongly compromised by plasma scattering and self-focusing, which clamps laser intensity. The lack of control over these processes leads to slow writing speed and uneven nanostructures resulting in excessive scattering in the fabricated optical elements. Therefore, the key challenges towards the practical use of the technology have to be considered and explored in the future work including this PhD thesis.

**As an intermediate conclusion,** the observation of femtosecond laser-induced nanogratings structures in transparent medium has opened an avenue to a new research topic in the field of laser-matter interaction. The self-assembly periodic structures of nanogratings not only imply new mechanisms of the ultrafast laser-matter interaction process under extreme physical conditions but also exhibit favorable properties that are promising in developing micro optical elements and new micromachining technologies. Therefore, it will continue to be a hot research topic in future time. Through years of study, the details of the nanogratings formation process have been constantly revealed, leading to new theories and improvement in previous models. However, there are still plenty of contradictory results between physical models and experimental results, since none of the existing theories can completely explain all the formation mechanisms of nanogratings induced in different mediums. And even the existence of a universal theory still remains

controversial. Much more fundamental research is needed in the future to fully understand the whole process. Concerning practical application, great progress has been gained in recent years and some research groups have demonstrated several impressive integrated optical elements in labs. Despite all of these achievements, the regularity of nanogratings prepared by existing process is yet far from commercialization and the available materials for practical nanogratings fabrication are still very limited. This is because that the mechanism of nanogratings formation in many materials is not very clear yet. Namely, the exact relationship between processing conditions and final dimension of nanogratings in different materials has not been fully established. Besides, due to the limit of the size of tightly focused light spot, the efficiency of inducing nanogratings is also not high enough for large-scale fabrication. Hence, further investigation is necessary in expanding available materials, refining quality and improving efficiency. In recent years, we witnessed a quick development of various advanced ultrafast laser related techniques such as time-resolved femtosecond laser technique, real-time femtosecond imaging, femtosecond pulse shaping, multi-beam interference and phase control of ultrafast light field, etc. We believe these technological advances will definitely contribute a lot to help researchers to understand the dynamics of ultrafast laser-matter interaction and will lead to a much more precise control of optical properties of the nanogratings.

## 1.7 Towards 3D imprinted optical chirality in inorganic glasses

In the past decade, several new and innovative observations have been discovered: nanogratings for high birefringence application with polarization direction dependence [56], “quill” writing [180] with dependence of modification with the direction of writing, silica decomposition [181], shear stress induced field [38, 136] and an efficient creation of oriented anisotropic defects [182]. All these findings show that asymmetric printing in center-symmetric medium could be controlled [183]. This idea of symmetry breaking (the Pierre Curie principle stipulates that the symmetry of the effects is always higher than the symmetry of the causes [184]) from nonlinear interaction of IR light appeared with the development of nonlinear optics and optical fibers. A famous example is the spontaneous appearance of second harmonic generation under IR irradiation [185] which is normally forbidden in the center-symmetric media. On the other hand, it is conceivable that chiral light action in an achiral material can produce chiral modification. However, the efficiency is usually low or undetectable if an amplification process is not used [186].

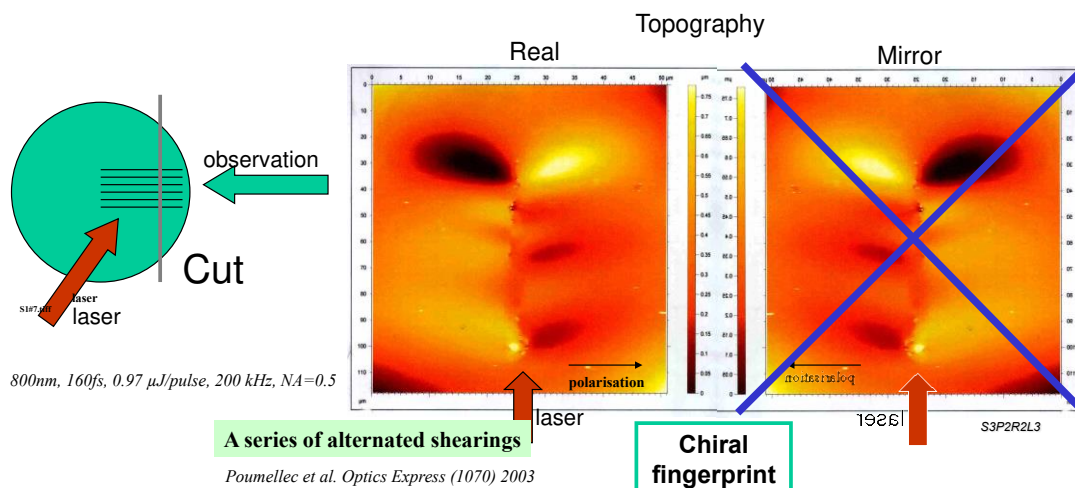


Figure 1.23 2D image of the surface topography obtained by Phase Shift Interferometry with x40 objective in the laser track cross-section [38, 136]. Cross section of a single laser track is shown together with its mirror image. The femtosecond laser propagation axis is from bottom to top. The laser polarization was parallel to the scanning direction. Laser conditions: 800 nm, 160 fs, 1.1  $\mu\text{J}/\text{pulse}$ , 200 kHz, 0.5 NA, 500 $\mu\text{m}/\text{s}$ .

In 2003 and later confirmed in 2008, our group proved that femtosecond laser interaction can shear matter in a manner similar to a scissor cutting material, moving matter on one side in one direction and matter on other side in the opposite direction, depending on the laser scanning direction and on the femtosecond light polarization [38, 136]. It was surprising to discover that an achiral beam (axially symmetric distribution of intensity, linearly polarized) penetrating into an achiral material (namely pure silica glass) in an achiral geometry (orthogonal incidence) can give rise to a chiral strain if we take into account the light propagation axis. As shown in Figure 1.23, this observation was performed in the domain of the strain field (especially regarding shearing) and this strain does not give rise to optical circular properties by itself like the torsion can do in matter.

In 2008, Taylor et al. [187] revealed that circularly polarized (CP) femtosecond laser light

focused into fused silica produces a permanent recording of optical helicity as shown in Figure 1.24. Material modification is in the form of highly ordered sub-micrometer chiral structures (surrounded by disordered modification) whose handedness follows the handedness of the CP light. These chiral structures emerge out of chaos through a complex multipulse ordering process. The process requires a delicate balance between initially having good localized CP to form a dominant central modification and, with continued irradiation, having just the right amount of depolarization to initiate curled strands. However no circular optical properties were observed in these conditions.

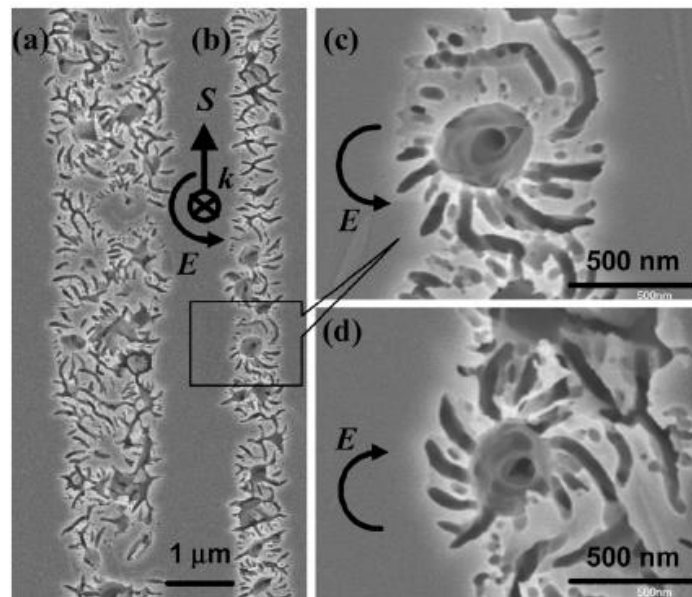


Figure 1.24 SEM images obtained in the horizontal observation plane (a) 4  $\mu\text{m}$  below the top of the modified region using  $E_p = 350 \text{ nJ}$  and (b) 2  $\mu\text{m}$  below the top of the modified region but with  $E_p = 200 \text{ nJ}$ . (c) Enlarged image of one of the chiral units shown in (b) produced with right-handed CP light. (d) Chiral unit produced using left-handed CP with the same pulse energy and scan rate that was used in (c). (a)–(d) Structures produced at a speed of 30  $\mu\text{m/s}$  (i.e. 3300 pulses/ $\mu\text{m}$  of scan). Extracted from [187].

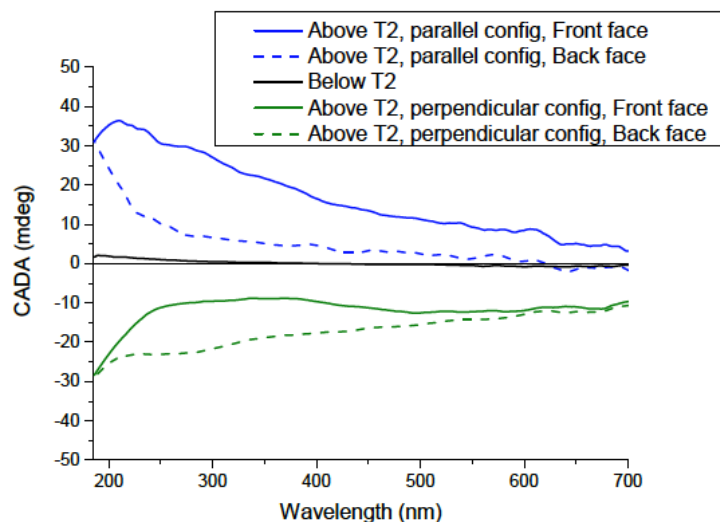


Figure 1.25 Ellipticity or Circular polarization degree of attenuation (CADA) according to the probe wavelength, measured below and above the porous nanoplanes energy threshold T2. Laser writing conditions: wavelength: 800 nm, pulse duration: 160fs, repetition rate: 250 kHz, numerical aperture NA: 0.55, writing speed: 500  $\mu\text{m/s}$ , focal depth: 200  $\mu\text{m}$ , energy: 0.07  $\mu\text{J}$  (below T2) and 1.3  $\mu\text{J}$  (above T2). Extracted from Ref. [188].



In 2015, Poumellec et al. showed that the fs irradiation of silica glass with a linear polarized Gaussian beam can imprint chiral optical properties [188] namely circular diattenuation as illustrated in Figure 1.25. A 160fs pulse duration laser has been used because this pulse duration allows a clear splitting between T1 and T2 thresholds [60]. Here the pulse energy must overcome the energy threshold T2 related to the production of nanogratings giving rise to form birefringence accompanied with a significant ellipticity. The sign of the ellipticity seems reversible with laser polarization i.e. positive when the polarization is parallel to the scanning direction and negative when the polarization is perpendicular to the scanning direction but it is not generally true, as linear properties can modify this sign. This result is surprising because pure quartz exhibits no circular dichroism in the UV-Vis range. The CD reaches a magnitude that is quite high compared to some organic molecules [109]. In most samples irradiated in various laser conditions,  $\theta$  can reach a few tens of mdeg in the blue or UV range. This should be compared to the linear birefringence (LB) that reaches around  $130^\circ$  (i.e. a retardance of 200nm) in the same sample whereas linear dichroism (LD) can reach about 0,1 OD (OD stands for Optical Density) at 550nm (corresponding to 6-7° in phase difference) [172]. Notice that chiral assemblies of metal nanoparticles devices are actually based on a few mdeg circular dichroism [189].

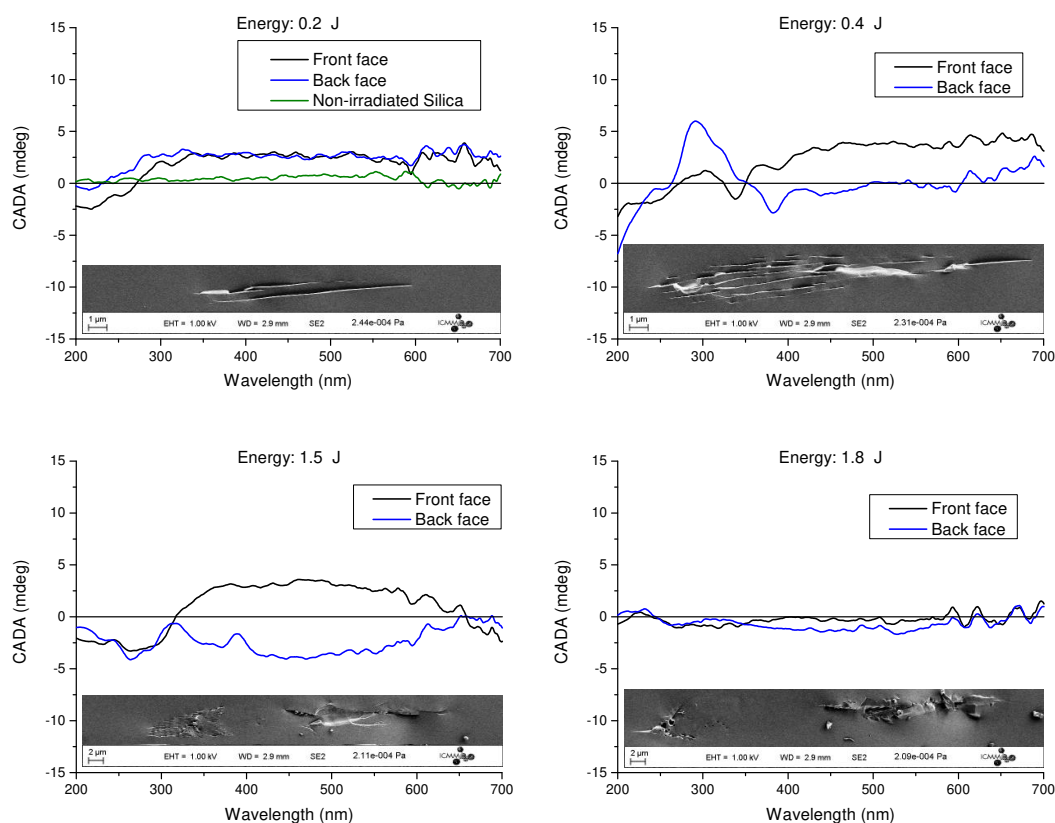


Figure 1.26 Ellipticity (or circular diattenuation noted CADA) spectra and FEG-SEM secondary electrons images of laser tracks cross-section according to pulse energy. 1030nm, 250fs, 500kHz, 0.6nA, 500 $\mu$ m/s, configuration is Xy. N.B. The laser propagation direction was from left to the right side of the picture.

Figure 1.26 shows that ellipticity depends on the laser pulse energy as well. At low energy around 0.2  $\mu$ J, it does not depend on the sample face order through which the measurement is performed. This means that linear birefringence is too weak to play a role here if the two properties are not intricated in depth or linear and circular properties are

intricated in depth. CADA or ellipticity disappears above  $1.8 \mu\text{J}$ , for the laser conditions used. The SEM images show that nanoplanes form clearly at  $0.3 \pm 0.1 \mu\text{J}$  and disappears at  $1.8 \mu\text{J}$  together with strong damages formation. This indicates that circular properties are likely appearing in the same conditions as for nanoplanes formation i.e. Type II regime.

Figures 1.25 and 1.26 also reveal a parity violation (the reciprocity of the light propagation in the glass is broken) by efficient chiral structure creation. Moreover, Poumellec et al. [188] propose that the breaking of symmetry arises from the chirality of the set, including the DC (static) electric field (defined by the pulse front tilt and the laser polarization), the direction of light propagation, and the direction of scanning introducing a chiral force (similar to the creation of torque) with a tightly focused femtosecond laser light in transparent solid material via the combination of non-linear effects.

## 1.8 Conclusions

The short-term vision of femtosecond laser direct writing (FLDW) is to make the ultrafast photonics manufacturing available within the next years to many fields of application, part of which being already known (e.g. integrated optics, microfluidics) and a majority being new applications (e.g. fully integrated nonlinear devices, optical components with specifically tailored properties in a wide range of transparent materials, micro-reactor for asymmetric synthesis, local piezoelectricity, multiferroic domain orientation). One important aspect will include the development of real 3D solutions such as 3D integrated optical devices and stacked micro-optics. As recognized in Photonics community, lithography and laser material micro-processing are complementary at the mid/long term. The advantages of the fs laser manufacturing are tightly linked to the unique properties of the photon:

- Due to small photon energy ( $\approx 1\text{eV}$ ) when compared to the bandgap energy ( $\approx 9\text{eV}$  in silica) and ultrashort pulse duration (minimized heat diffusion, delivering a finite quantity of energy in very short time, multiphoton ionization/absorption), the **dose can be tailored precisely** to the process resulting in very **high 3D precision**.
  - Contact-less processing is possible opening up the way to completely novel processes.
  - The ability to precisely alter the material properties in the volume of a transparent medium uniquely enables the generation of photonic devices in the bulk. **Furthermore, the generation of linear and potentially circular anisotropic optical properties in amorphous media**, but also 2nd order non-linear susceptibility opens up new exciting possibilities.
  - Variable parameters such as wavelength, power, polarization and especially their **spatio-temporal distribution** along the beam propagation and in the beam cross-section, make it a very flexible tool, which can be controlled very precisely and automated to a large extend.

In this chapter, we have reviewed the progress in the field of FLDW, which has rapidly developed from the initial scientific studies to commercially viable technology. Over two decades this field has grown enormously. We did not attempt to include everything in the scope of this review; we mainly concentrated on modification of transparent silica glass and did not touch on such topics as processing of metals, semiconductors, polymers, or non-

oxide glasses, which are vast and active areas of femtosecond laser processing. The flexibility of this technique in terms of materials and ability to implement 3D geometries with sub-wavelength precision turned it into an ideal low-cost platform for rapid prototyping, which was explored in the fields of microfluidics, quantum optics, etc...

We first briefly introduce basic characteristics and relevant phenomena mostly related to the formation of nanogratings structures within the so-called Type II regime. Then, several important hypotheses and models that explain the mechanism of nanogratings formation are summarized. Important controlling parameters and the processes involved in the nanogratings formation are then discussed. Considering the fast development of nanogratings based applications, some representative demonstrations for potential applications were reported by many research groups around the world as described in the following references [176, 190-200]. The last section points out one major challenge and a potential future direction in this field i.e. imprinting optical chirality in inorganic glasses. Femtosecond laser direct writing potentially thus offers a new advantage: it allows restructuring of our most important optical material to enable circular dichroism and potentially circular birefringence (and thus "passive" optical rotation).

## 1.9 References

1. Hill, K.O., et al., *Photosensitivity in optical fiber waveguides: Application to reflection filter fabrication*. Applied Physics Letters, 1978. **32**(10): p. 647-649.
2. Arnold, G.W. and W.D. Compton, *Radiation effects in silica at low temperatures*. Phys. Rev., 1959. **116**(4): p. 802-811.
3. Primak, W. and R. Kampwirth, *The radiation compaction of vitreous silica*. Journal of Applied Physics, 1968. **39**(12): p. 5651-5658.
4. Rajaram, M., T.-E. Tsai, and E.J. Friebele, *Radiation-Induced Surface Deformation in Low-Thermal-Expansion Glasses and Glass-Ceramics*. Advanced Ceramic Materials, 1988. **3**(6): p. 598-600.
5. Barbier, D., M. Green, and S.J. Madden, *Waveguide fabrication for integrated optics by electron beam irradiation of silica*. Journal of Lightwave Technology, 1991. **9**(6): p. 715-720.
6. Dellin, T.A., D.A. Tichenor, and E.H. Barsis, *Volume, index-of-refraction, and stress changes in electron-irradiation vitreous silica*. Applied Physics, 1977. **48**(3): p. 1131.
7. Syms, R.R.A., T.J. Tate, and M.F. Grant, *Reduction of propagation loss in silica-on-silicon channel waveguides formed by electron beam irradiation*. Electronics Letters, 1994. **30**(18): p. 1480-1481.
8. Lichtenstein, L., M. Heyde, and H.-J. Freund, *Atomic arrangement in two-dimensional silica: from crystalline to vitreous structures*. The Journal of Physical Chemistry C, 2012. **116**(38): p. 20426-20432.
9. Warren, B.E., *Summary of work on atomic arrangement in glass*. American Ceramic Society, 1941. **24**(8): p. 256-261.
10. Liebau, F., *Structural chemistry of silicates*. 1985.
11. Wright, A.C., *The structure of vitreous silica: what have we learned from 60 years of diffraction studies?* Journal of Non-Crystalline Solids, 1994. **179**: p. 84-115.
12. Lancry, M., E. Régnier, and B. Pommellec, *Fictive temperature in silica-based glasses and its application to optical fiber manufacturing*. Progress in Materials Science, 2012. **57**(1): p. 63-94.
13. Arndt, J., *Physics and Chemistry of Glasses*, 1983. **24**: p. 104-10.
14. Stishov, S.M. and S.V. Popova, *New dense polymorphic modification of silica*. Geokhimiya, 1961. **10**: p. 837-839.
15. Griscom, D.L., *The natures of point defects in amorphous silicon dioxide*, in *Defects in SiO<sub>2</sub> and Related Dielectrics: Science and Technology*, L.S.a.D.L.G. G. Pacchioni, Editor. 2000. p. 117-159.
16. Griscom, D.L., *Optical Properties and Structure of Defects in Silica Glass: Optical Materials*. Journal of the Ceramic Society of Japan, 1 October 1991. **99**(1154): p. 923-942.
17. Garapon, J., *Etude théorique des défauts déficitaires en oxygène dans la silice pure ou dopée*, 2001, Université de Paris Sud.
18. Skuja, L.N., *Optically active oxygen-deficiency-related centers in amorphous silicon dioxide*. Journal of Non-Crystalline Solids, 1998. **239**(Section 1. Defect studies in vitreous silica and related materials): p. 16-48.

19. Skuja, L., *Optical properties of defects in silica*. Pacchioni, G., Skuja, L., Griscom, D. ed. Defect in SiO<sub>2</sub> and related dielectrics : Science and Technology, ed. P.a.C. Mathematics. 2000, Dordrecht, Netherlands: Kluwer Academic.
20. Trukhin, A.N., et al., *Cathodoluminescence and IR absorption of oxygen deficient silica - influence of hydrogen treatment*. Radiation effects and defects in solids., 1999. **149**: p. 61-68.
21. Boyd, R.W., *Nonlinear optics*. 1992: Academic Press, 3 edition (April 11, 2008).
22. Shen, Y.R., *The principles of nonlinear optics*. 1984: Wiley.
23. Agrawal, G.P., ed. *Non-linear effects in optical fibers*. 1989, Academic Press, San Diego.
24. Shen, Y.R., *Recent Advances in nonlinear optics*. Review of modern physics, 1976. **48**: p. 1-32.
25. Toulouse, J., *Optical nonlinearities in fibers: review, recent examples, and systems applications*. Lightwave Technology, Journal of, 2005. **23**(11): p. 3625-3641.
26. Sudrie, L., *Propagation non-linéaire des impulsions laser femtosecondes dans la silice.*, 2002, Université de Paris Sud XI Orsay.
27. Čerkauskaitė, A., *Ultrafast laser nanostructuring for photonics and information technology*, 2018, UNIVERSITY OF SOUTHAMPTON. p. 206.
28. Couairon, A. and A. Mysyrowicz, *Femtosecond filamentation in transparent media*. Physics reports, 2007. **441**(2-4): p. 47-189.
29. Shen, Y., *The principles of nonlinear optics Wiley 85*, 1984, Sons, New York.
30. Rudenko, A., J.-P. Colombier, and T.E. Itina, *Nanopore-mediated ultrashort laser-induced formation and erasure of volume nanogratings in glass*. Physical Chemistry Chemical Physics, 2018. **20**(8): p. 5887-5899.
31. Mao, S., et al., *Dynamics of femtosecond laser interactions with dielectrics*. Applied Physics A, 2004. **79**(7): p. 1695-1709.
32. Schaffer, C., J. García, and E. Mazur, *Bulk heating of transparent materials using a high-repetition-rate femtosecond laser*. Applied Physics A: Materials Science & Processing, 2003. **76**(3): p. 351-354.
33. Eaton, S.M., et al., *Heat accumulation effects in femtosecond laser-written waveguides with variable repetition rate*. Optics Express, 2005. **13**(12): p. 4708-4716.
34. Bellouard, Y., et al., *Stress-state manipulation in fused silica via femtosecond laser irradiation*. Optica, 2016. **3**(12): p. 1285-1293.
35. Champion, A., et al., *Stress distribution around femtosecond laser affected zones: effect of nanogratings orientation*. Optics Express, 2013. **21**(21): p. 24942-24951.
36. Dürr, F., et al., *Tomographic measurement of femtosecond-laser induced stress changes in optical fibers*. Applied Physics Letters, 2004. **84**(24): p. 4983-4985.
37. Bhardwaj, V., et al., *Stress in femtosecond-laser-written waveguides in fused silica*. Optics Letters, 2004. **29**(12): p. 1312-1314.
38. Poumellec, B., et al., *Femtosecond laser irradiation stress induced in pure silica*. Optics Express, 2003. **11**(9): p. 1070-1079.
39. Guizard, S., et al., *Time-resolved study of laser-induced colour centres in*. Journal of Physics: Condensed Matter, 1996. **8**(9): p. 1281.
40. Mishchik, K., et al., *Ultrafast laser induced electronic and structural modifications in bulk fused silica*. Journal of Applied Physics, 2013. **114**(13): p. 133502.

41. Mishchik, K., *Ultrafast laser-induced modification of optical glasses: a spectroscopy insight into the microscopic mechanisms*, 2012.
42. Itoh, K., et al., *Ultrafast processes for bulk modification of transparent materials*. MRS Bulletin, 2006. **31**: p. 620-625.
43. Schaffer, C.B., A. Brodeur, and M. E., *Laser-induced breakdown and damage in bulk transparent materials induced by tightly focused femtosecond laser pulses*. Measurement Science Technology, 2001. **12**: p. 1784-1794.
44. Stoian, R., *Volume photoinscription of glasses: three-dimensional micro- and nanostructuring with ultrashort laser pulses*. Applied physics. A, Materials science & processing, 2020. **126**(6).
45. Quéré, F., S. Guizard, and P. Martin, *Time-resolved study of laser-induced breakdown in dielectrics*. EPL (Europhysics Letters), 2001. **56**(1): p. 138.
46. Mao, S.S., et al., *Dynamics of femtosecond laser interactions with dielectrics*. Applied Physics a-Materials Science & Processing, 2004. **79**(7): p. 1695-1709.
47. Lancry, M., et al., *Time-resolved plasma measurements in Ge-doped silica exposed to infrared femtosecond laser*. Physical Review B, 2011. **84**(24): p. 245103.
48. Mouskeftaras, A., et al., *Mechanisms of femtosecond laser ablation of dielectrics revealed by double pump-probe experiment*. Applied Physics A, 2013. **110**(3): p. 709-715.
49. Lenzner, M., et al., *Femtosecond optical breakdown in dielectrics*. Physical review letters, 1998. **80**(18): p. 4076.
50. Stuart, B.C., et al., *Nanosecond-to-femtosecond laser-induced breakdown in dielectrics*. Physical review B, 1996. **53**(4): p. 1749.
51. Itina, T.E. and N. Shcheblanov, *Electronic excitation in femtosecond laser interactions with wide-band-gap materials*. Applied Physics A, 2010. **98**(4): p. 769-775.
52. Schaffer, C.B., A. Brodeur, and E. Mazur, *Laser-induced breakdown and damage in bulk transparent materials induced by tightly focused femtosecond laser pulses*. Measurement Science and Technology, 2001. **12**(11): p. 1784.
53. Rajeev, P., et al., *Field dependent avalanche ionization rates in dielectrics*. Physical Review Letters, 2009. **102**(8): p. 83001.
54. Wasiela, A., G. Ascarelli, and Y. Merle d'Aubigné, *Détection optique de la résonance électronique de l'exciton autopiégé dans les halogénures alcalins ; observation d'un croisement de niveaux*. J. Phys. France, 1974. **35**(5): p. 466.
55. Miura, K., et al., *Photowritten optical waveguides in various glasses with ultrashort pulse laser*. Applied Physics Letters, 1997. **71**(23): p. 3329-3331.
56. Sudrie, L., et al., *Writing of permanent birefringent microlayers in bulk fused silica with femtosecond laser pulses*. Optics Communications, 1999. **171**(4-6): p. 279-284.
57. Shimotsuma, Y., et al., *Self-organized nanogratings in glass irradiated by ultrashort light pulses*. Physical Review Letters, 2003. **91**(24): p. 247405.
58. Hnatovsky, C., et al., *Pulse duration dependence of femtosecond-laser fabricated nanogratings in fused silica*. Applied Physics Letters, 2005. **87**: p. 14104-1/3.
59. Juodkazis, S., et al., *Laser-induced microexplosion confined in the bulk of a sapphire crystal: evidence of multimegabar pressures*. Phys Rev Lett, 2006. **96**(16): p. 166101-166101.

60. Poumellec, B., et al., *Modification thresholds in femtosecond laser processing of pure silica: review of dependencies on laser parameters [Invited]*. Optical Materials Express, 2011. **1**(4): p. 766-782.
61. Chan, J.W., et al., *Waveguide fabrication in phosphate glasses using femtosecond laser pulses*. Applied Physics Letters, 2003. **82**(15): p. 2371-2373.
62. Siegel, J., et al., *Waveguide structures in heavy metal oxide glass written with femtosecond laser pulses above the critical self-focusing threshold*. Applied Physics Letters, 2005. **86**: p. 121109.
63. Vega, F., et al., *Mechanisms of refractive index modification during femtosecond laser writing of waveguides in alkaline lead-oxide silicate glass*. Applied Physics Letters, 2005. **87**(2): p. 021109.
64. Zoubir, A., et al., *Femtosecond laser fabrication of tubular waveguides in poly(methyl methacrylate)*. Opt. Lett., 2004. **29**(16): p. 1840-1842.
65. Itoh, K., et al., *Ultrafast processes for bulk modification of transparent materials*. MRS Bulletin, 2006. **31**: p. 620-625.
66. Carslaw, H.S. and J.C. Jaeger, *Conduction of heat in solids*. 1992: Clarendon press.
67. Eaton, S., et al., *Heat accumulation effects in femtosecond laser-written waveguides with variable repetition rate*. Optics Express, 2005. **13**(12): p. 4708-4716.
68. Schäffer, C.B., *Interaction of femtosecond laser pulses with transparent materials*, 2001, Harvard.
69. Lenzner, M., et al., *Incubation of laser ablation in fused silica with 5-fs pulses*. Applied Physics A, 1999. **69**(4): p. 465-466.
70. Ashkenasi, D., et al., *Surface damage threshold and structuring of dielectrics using femtosecond laser pulses: the role of incubation*. Applied Surface Science, 1999. **150**(1-4): p. 101-106.
71. Stoian, R., *Investigations of the dynamics of material removal in ultrashort pulsed laser ablation of dielectrics*. 2000.
72. Streltsov, A.M. and N.F. Borrelli, *Study of femtosecond-laser-written waveguides in glasses*. J. Opt. Soc. Am. B, 2002. **19**(10): p. 2496-2504.
73. Zimmermann, F., et al., *Ultrashort Pulse Laser Processing of Silica at High Repetition Rates—from Network Change to Residual Strain*. International Journal of Applied Glass Science, 2016.
74. Yoshino, T., et al., *In situ micro-Raman investigation of spatio-temporal evolution of heat in ultrafast laser microprocessing of glass*. Japanese Journal of Applied Physics, 2012. **51**(10R): p. 102403.
75. Shah, L., et al., *Waveguide writing in fused silica with a femtosecond fiber laser at 522 nm and 1 MHz repetition rate*. Optics Express, 2005. **13**(6): p. 1999-2006.
76. Osellame, R., et al., *Optical properties of waveguides written by a 26 MHz stretched cavity Ti:sapphire femtosecond oscillator*. Opt. Express, 2005. **13**(2): p. 612-620.
77. Lancry, M. and B. Poumellec, *UV laser processing and multiphoton absorption processes in optical telecommunication fiber materials*. Physics Reports, 2013. **523**(4): p. 207-229.
78. Bricchi, E. and P.G. Kazansky, *Extraordinary stability of anisotropic femtosecond direct-written structures embedded in silica glass*. Applied Physics Letters, 2006. **88**(11): p. 2-

- 4.
79. Grobncic, D., et al., *Long-term thermal stability tests at 1000°C of silica fibre Bragg gratings made with ultrafast laser radiation*. Measurement Science and Technology, 2006. **17**(5): p. 1009.
  80. Bricchi, E., B.G. Klappauf, and P.G. Kazansky, *Form birefringence and negative index change created by femtosecond direct writing in transparent materials*. Optics Letters, 2004. **29**(1): p. 119-121.
  81. Bricchi, E., et al., *Birefringent Fresnel zone plates in silica fabricated by femtosecond laser machining*. Opt. Lett., 2002. **27**(24): p. 2200-2202.
  82. Lancry, M., et al., *Ultrafast nanoporous silica formation driven by femtosecond laser irradiation*. Laser and Photonics Reviews, 2013. **7**: p. 953-962.
  83. Glezer, E.N., et al., *3-D Optical Storage Inside Transparent Materials*. Optics Letters, 1996. **21**: p. 2023-2026.
  84. Onda, S., et al., *Study of filamentary damage in synthesized silica induced by chirped femtosecond laser pulses*. JOSA B, 2005. **22**(11): p. 2437-2443.
  85. Ashcom, J.B., et al., *Numerical aperture dependence of damage and supercontinuum generation from femtosecond laser pulses in bulk fused silica*. Journal of Optical Society of America B, 2006. **23**(11): p. 2317-2322.
  86. Von der Linde, D. and H. Schüler, *Breakdown threshold and plasma formation in femtosecond laser–solid interaction*. JOSA B, 1996. **13**(1): p. 216-222.
  87. Nemoto, S., *Waist shift of a Gaussian beam by plane dielectric interfaces*. Applied optics, 1988. **27**(9): p. 1833-1839.
  88. Marcinkevičius, A., et al., *Effect of refractive index-mismatch on laser microfabrication in silica glass*. Applied Physics A, 2003. **76**(2): p. 257-260.
  89. Simmonds, R.D., et al., *Three dimensional laser microfabrication in diamond using a dual adaptive optics system*. Optics express, 2011. **19**(24): p. 24122-24128.
  90. Streltsov, A.M. and N.F. Borelli, *Fabrication and analysis of a directional coupler written in glass by nanojoule femtosecond laser pulses*. Optics Letters, 2001. **26**(1): p. 42-43.
  91. Schaffer, C. and E. Mazur, *Micromachining using ultrashort pulses from a laser oscillator*. Optics & Photonics News, 2001. **12**(4): p. 20-23.
  92. Couairon, A., et al., *Filamentation and damage in fused silica induced by tightly focused femtosecond laser pulses*. Physical Review B, 2005. **71**(12): p. 125435.
  93. Chan, J.W., et al., *Modification of the fused silica glass network associated with waveguide fabrication using femtosecond laser pulses*. Applied Physics a-Materials Science & Processing, 2003. **76**(3): p. 367-372.
  94. Brückner, R., *Properties and structure of vitreous silica. I*. Journal of Non-Crystalline Solids, 1970. **5**(2): p. 123-175.
  95. Sakakura, M., et al., *Temperature distribution and modification mechanism inside glass with heat accumulation during 250kHz irradiation of femtosecond laser pulses*. Applied Physics Letters, 2008. **93**(23): p. 231112-231112-3.
  96. Hirao, K. and K. Miura, *Writing waveguides and gratings in silica and related materials by a femtosecond laser*. Journal of Non-Crystalline Solids, 1998. **239**(1): p. 91-95.
  97. Chan, J.W., et al., *Modification of the fused silica glass network associated with waveguide fabrication using femtosecond laser pulses*. Applied Physics A, 2003. **76**(3):



- p. 367-372.
98. Saliminia, A., R. Vallée, and S.L. Chin, *Waveguide writing in silica glass with femtosecond pulses from an optical parametric amplifier at 1.5 $\mu$ m*. Optics Communications, 2005. **256**(4-6): p. 422-427.
  99. Royon, M., et al., *X-ray preconditioning for enhancing refractive index contrast in femtosecond laser photoinscription of embedded waveguides in pure silica*. Optical Materials Express, 2019. **9**(1): p. 65-74.
  100. Royon, M., *Ingénierie de verres de silice: influence de pré-traitements sur la variation d'indice de réfraction de guides d'ondes photo-inscrits par laser femtoseconde*. 2018.
  101. Lancry, M., et al., *Dependence of the femtosecond laser refractive index change thresholds on the chemical composition of doped-silica glasses*. Optical Materials Express, 2011. **1**(4): p. 711-723.
  102. Bressel, L., et al., *Femtosecond laser induced density changes in GeO<sub>2</sub> and SiO<sub>2</sub> glasses: fictive temperature effect*.
  103. Chan, J.W., et al., *Structural changes in fused silica after exposure to focused femtosecond laser pulses*. Opt. Lett., 2001. **26**(21): p. 1726-1728.
  104. Davis, K.M., et al., *Writing waveguides in glass with a femtosecond laser*. Optics Letters, 1996. **21**(21): p. 1729-1731.
  105. Bernasconi, M., *Ab-initio molecular dynamics simulation of amorphous silica surface*, in *Defects in SiO<sub>2</sub> and related dielectrics: Science and Technology*, L.S.a.D.L.G. G. Pacchioni, Editor. 2000, Kluwer: Dordrecht.
  106. Nolte, S., et al., *Waveguides produced by ultrashort laser pulses inside glasses and crystals*. 2002: p. 188-196.
  107. Efimov, O., et al., *Waveguide writing in chalcogenide glasses by a train of femtosecond laser pulses*. Optical Materials, 2001. **17**(3): p. 379-386.
  108. Petite, G., et al., *Ultrafast processes in laser irradiated wide bandgap insulators*. Applied Surface Science, 1997. **109-110**(0): p. 36-42.
  109. Hnatovsky, C., et al., *Fabrication of microchannels in glass using focused femtosecond laser radiation and selective chemical etching*. Applied Physics A, 2006. **84**(1-2): p. 47-61.
  110. Canning, J., et al., *Anatomy of a femtosecond laser processed silica waveguide [Invited]*. Optical Materials Express, 2011. **1**(5): p. 998-1008.
  111. Fleischer, R., P. Price, and R. Walker, *Solid-state track detectors: Applications to nuclear science and geophysics*. Annual Review of Nuclear Science, 1965. **15**(1): p. 1-28.
  112. Schaffer, C., et al., *Laser-induced microexplosions in transparent materials: microstructuring with nanojoules*. Proceedings of SPIE, 1999. **3616**: p. 143.
  113. Stoian, R., et al., *Investigation and control of ultrafast laser-induced isotropic and anisotropic nanoscale-modulated index patterns in bulk fused silica*. Optical Materials Express, 2013. **3**(10): p. 1755-1768.
  114. Glezer, E.N. and E. Mazur, *Ultrafast-laser driven micro-explosions in transparent materials*. Applied physics letters, 1997. **71**(7): p. 882-884.
  115. Juodkazis, S., et al., *Laser-induced microexplosion confined in a bulk of silica: Formation of nanovoids*. Applied Physics Letters, 2006. **88**(20): p. 201909.

116. Mermillod-Blondin, A., et al., *Dynamics of femtosecond laser induced voidlike structures in fused silica*. Applied Physics Letters, 2009. **94**(4): p. 041911.
117. Juodkasis, S., et al., *Laser-induced microexplosion confined in the bulk of a sapphire crystal: evidence of multimegabar pressures*. Physical review letters, 2006. **96**(16): p. 166101.
118. Glezer, E.N., et al., *Three-dimensional optical storage inside transparent materials*. Optics Letters, 1996. **21**(24): p. 2023-2025.
119. Birnbaum, M., *Semiconductor surface damage produced by ruby lasers*. Journal of Applied Physics, 1965. **36**: p. 3688.
120. Bonse, J., et al., *Femtosecond laser-induced periodic surface structures*. Journal of Laser Applications, 2012. **24**(4): p. 042006.
121. Guosheng, Z., P. Fauchet, and A. Siegman, *Growth of spontaneous periodic surface structures on solids during laser illumination*. Physical Review B, 1982. **26**(10): p. 5366.
122. Van Driel, H., J. Sipe, and J.F. Young, *Laser-induced periodic surface structure on solids: a universal phenomenon*. Physical Review Letters, 1982. **49**(26): p. 1955.
123. Nemanich, R., D. Biegelsen, and W. Hawkins, *Aligned, coexisting liquid and solid regions in laser-annealed Si*. Physical Review B, 1983. **27**(12): p. 7817.
124. Bonse, J., et al., *Femtosecond laser ablation of silicon—modification thresholds and morphology*. Applied Physics A, 2002. **74**(1): p. 19-25.
125. Siegman, A. and P. Fauchet, *Stimulated Wood's anomalies on laser-illuminated surfaces*. IEEE journal of quantum electronics, 1986. **22**(8): p. 1384-1403.
126. Borowiec, A. and H. Haugen, *Subwavelength ripple formation on the surfaces of compound semiconductors irradiated with femtosecond laser pulses*. Applied Physics Letters, 2003. **82**(25): p. 4462-4464.
127. Yasumaru, N., K. Miyazaki, and J. Kiuchi, *Femtosecond-laser-induced nanostructure formed on hard thin films of TiN and DLC*. Applied Physics A, 2003. **76**(6): p. 983-985.
128. Gaković, B., et al., *Surface modification of titanium nitride film by a picosecond Nd: YAG laser*. Journal of Optics A: Pure and Applied Optics, 2007. **9**(6): p. S76.
129. Bonse, J., A. Rosenfeld, and J. Krüger, *On the role of surface plasmon polaritons in the formation of laser-induced periodic surface structures upon irradiation of silicon by femtosecond-laser pulses*. Journal of Applied Physics, 2009. **106**(10): p. 104910.
130. Bonse, J., et al., *Laser-induced periodic surface structures—A scientific evergreen*. IEEE Journal of selected topics in quantum electronics, 2016. **23**(3).
131. Buividas, R., M. Mikutis, and S. Juodkasis, *Surface and bulk structuring of materials by ripples with long and short laser pulses: Recent advances*. Progress in Quantum Electronics, 2014. **38**(3): p. 119-156.
132. Bonse, J., M. Munz, and H. Sturm, *Structure formation on the surface of indium phosphide irradiated by femtosecond laser pulses*. Journal of Applied Physics, 2005. **97**(1): p. 013538.
133. Bonse, J. and J. Krüger, *Pulse number dependence of laser-induced periodic surface structures for femtosecond laser irradiation of silicon*. Journal of Applied Physics, 2010. **108**(3): p. 034903.
134. Sundaram, S. and E. Mazur, *Inducing and probing non-thermal transitions in semiconductors using femtosecond laser pulses*. Nature materials, 2002. **1**(4): p. 217-

- 224.
135. Kazansky, P.G., et al., *Anomalous anisotropic light scattering in Ge-doped silica glass*. Physical Review Letters, 1999. **82**(10): p. 2199-2202.
  136. Poumellec, B., et al., *Non reciprocal writing and chirality in femtosecond laser irradiated silica*. Optics Express, 2008. **16**(22): p. 18354-18361.
  137. Paleari, A., et al., *SnO<sub>2</sub> nanoparticles in silica: nanosized tools for femtosecond-laser*. Applied Physics Letters, 2006. **88**: p. 131912-1/3.
  138. Born, M. and E. Wolf, *Principles of optics: electromagnetic theory of propagation, interference and diffraction of light*. 1999: CUP Archive.
  139. Shimotsuma, Y., et al., *Ultrafast Manipulation of Self-Assembled Form Birefringence in Glass*. Advanced Materials, 2010. **22**(36): p. 4039-4043.
  140. Gecevičius, M., *Polarization sensitive optical elements by ultrafast laser nanostructuring of glass*, 2015, University of Southampton.
  141. Bricchi, E., *Femtosecond laser micro-machining and consequent self-assembled nano-structures in transparent materials*. 2005.
  142. Shimotsuma, Y., et al., *Self-organized nanogratings in glass irradiated by ultrashort light pulses*. Physical review letters, 2003. **91**(24): p. 247405.
  143. Gu, C. and P. Yeh, *Form birefringence dispersion in periodic layered media*. Optics letters, 1996. **21**(7): p. 504-506.
  144. Bhardwaj, V., et al., *Optically produced arrays of planar nanostructures inside fused silica*. Physical review letters, 2006. **96**(5): p. 57404.
  145. Liang, F., R. Vallée, and S.L. Chin, *Mechanism of nanograting formation on the surface of fused silica*. Optics express, 2012. **20**(4): p. 4389-4396.
  146. Beresna, M., et al., *Exciton mediated self-organization in glass driven by ultrashort light pulses*. Applied Physics Letters, 2012. **101**(5): p. 053120.
  147. Rudenko, A., J.-P. Colombier, and T.E. Itina, *From random inhomogeneities to periodic nanostructures induced in bulk silica by ultrashort laser*. Physical Review B, 2016. **93**(7): p. 075427.
  148. Zimmermann, F., et al., *The onset of ultrashort pulse - induced nanogratings*. Laser & Photonics Reviews, 2016. **10**(2): p. 327-334.
  149. Liao, Y., et al., *Formation of in-volume nanogratings with sub-100-nm periods in glass by femtosecond laser irradiation*. Optics Letters, 2015. **40**(15): p. 3623-3626.
  150. Liao, Y., et al., *High-fidelity visualization of formation of volume nanogratings in porous glass by femtosecond laser irradiation*. Optica, 2015. **2**(4): p. 329-334.
  151. Liao, Y., et al., *Femtosecond laser nanostructuring in porous glass with sub-50 nm feature sizes*. Optics letters, 2013. **38**(2): p. 187-189.
  152. Kazansky, P.G., et al. *Self-assembled nanostructures and two-plasmon decay in femtosecond processing of transparent materials*. in *2007 Conference on Lasers and Electro-Optics (CLEO)*. 2007. IEEE.
  153. Taylor, R., C. Hnatovsky, and E. Simova, *Applications of femtosecond laser induced self - organized planar nanocracks inside fused silica glass*. Laser & Photonics Reviews, 2008. **2**(1 - 2): p. 26-46.
  154. Rajeev, P., et al., *Transient nanoplasmonics inside dielectrics*. Journal of Physics B: Atomic, Molecular and Optical Physics, 2007. **40**: p. S273.

155. Martin, P., et al., *Subpicosecond study of carrier trapping dynamics in wide-band-gap crystals*. Physical Review B, 1997. **55**(9): p. 5799-5810.
156. Zimmermann, F., *Ultrashort pulse induced nanostructures in transparent materials*, 2017.
157. Richter, S., et al., *On the fundamental structure of femtosecond laser-induced nanogratings*. Laser & Photonics Reviews, 2012. **6**(6): p. 787-792.
158. Lancry, M., et al., *Nanoscale femtosecond laser milling and control of nanoporosity in the normal and anomalous regimes of GeO<sub>2</sub>-SiO<sub>2</sub> glasses*. Optical Materials Express, 2016. **6**(2): p. 321-330.
159. Zimmermann, F., et al., *Femtosecond laser written nanostructures in Ge-doped glasses*. Optics letters, 2016. **41**(6): p. 1161-1164.
160. Zimmermann, F., et al., *Ultrashort laser pulse induced nanogratings in borosilicate glass*. Applied Physics Letters, 2014. **104**(21): p. 211107.
161. Shimotsuma, Y., et al., *Tunability of form birefringence induced by femtosecond laser irradiation in anion - doped silica glass*. Journal of the American Ceramic Society, 2017. **100**(9): p. 3912-3919.
162. Asai, T., et al., *Systematic Control of Structural Changes in GeO<sub>2</sub> Glass Induced by Femtosecond Laser Direct Writing*. Journal of the American Ceramic Society, 2015. **98**(5): p. 1471-1477.
163. Zhang, F., et al., *Microengineering of optical properties of GeO<sub>2</sub> glass by ultrafast laser nanostructuring*. Advanced Optical Materials, 2017. **5**(23): p. 1700342.
164. Zhang, F., et al., *Embedded nanogratings in germanium dioxide glass induced by femtosecond laser direct writing*. JOSA B, 2014. **31**(4): p. 860-864.
165. Wortmann, D., et al., *Micro- and nanostructures inside sapphire by fs-laser irradiation and selective etching*. Optics Express, 2008. **16**(3): p. 1517-1522.
166. Shimotsuma, Y., et al., *Nanofabrication in transparent materials with a femtosecond pulse laser*. Journal of Non-Crystalline Solids, 2006. **352**(6-7): p. 646-656.
167. Zhang, F., et al., *Self-assembled three-dimensional periodic micro-nano structures in bulk quartz crystal induced by femtosecond laser pulses*. Optics express, 2019. **27**(5): p. 6442-6450.
168. Richter, S., et al., *Laser induced nanogratings beyond fused silica-periodic nanostructures in borosilicate glasses and ULE™*. Optical Materials Express, 2013. **3**(8): p. 1161-1166.
169. Lancry, M., et al., *Nanogratings formation in multicomponent silicate glasses*. Applied Physics B, 2016. **122**(3): p. 66.
170. Desmarchelier, R., et al., *In the Heart of Femtosecond Laser Induced Nanogratings: From Porous Nanoplanes to Form Birefringence*. World Journal of Nano Science and Engineering, 2015. **5**(04): p. 115.
171. Cerkauskaite, A., et al., *Ultrafast laser-induced birefringence in various porosity silica glasses: from fused silica to aerogel*. Optics Express, 2017. **25**(7): p. 8011-8021.
172. Beresna, M., et al., *Broadband anisotropy of femtosecond laser induced nanogratings in fused silica*. Applied Physics Letters, 2013. **103**(13): p. 131903.
173. Richter, S., et al., *Nanogratings in fused silica: Formation, control, and applications*. Journal of Laser Applications, 2012. **24**: p. 042008(1)-042008(8).

174. Guo, H.C., et al., *The pulse duration dependence of femtosecond laser induced refractive index modulation in fused silica*. Journal of Optics a-Pure and Applied Optics, 2004. **6**(8): p. 787-790.
175. Lancry, M., et al., *Compact Birefringent Waveplates Photo-Induced in Silica by Femtosecond Laser*. Micromachines, 2014. **5**(4): p. 825-838.
176. Beresna, M., *Polarization engineering with ultrafast laser writing in transparent media*, 2012, Southampton.
177. Richter, S., et al., *The role of self-trapped excitons and defects in the formation of nanogratings in fused silica*. Optics letters, 2012. **37**(4): p. 482-484.
178. Shimotsuma, Y., K. Miura, and H. Kazuyuki, *Nanomodification of Glass Using fs Laser*. International Journal of Applied Glass Science, 2013. **4**(3): p. 182-191.
179. Lancry, M. and B. Poumellec, *Femtosecond Laser Direct Writing in P, Ge Doped Silica Glasses: Time Resolved Plasma Measurements*. Femtosecond Laser Microfabrication, 2009.
180. Kazansky, P.G., et al., *"Quill" writing with ultrashort light pulses in transparent materials*. Applied physics letters, 2007. **90**(15): p. 151120.
181. Lancry, M., et al., *Ultrafast nanoporous silica formation driven by femtosecond laser irradiation*. Laser & Photonics Reviews, 2013. **7**(6): p. 953-962.
182. Lancry, M., et al., *Oriented creation of anisotropic defects by IR femtosecond laser scanning in silica*. Optical Materials Express, 2012. **2**(12): p. 1809-1821.
183. Poumellec, B., et al., *Asymmetric Orientational Writing in glass with femtosecond laser irradiation*. Optical Materials Express, 2013. **3**(10): p. 1586-1599.
184. Curie, P. *Sur la symétrie dans les phénomènes physiques, symétrie d'un champ électrique et d'un champ magnétique*. in *Annales de la Fondation Louis de Broglie*. 1994. Fondation Louis de Broglie.
185. Österberg, U. and W. Margulis, *Dye laser pumped by Nd: YAG laser pulses frequency doubled in a glass optical fiber*. Optics letters, 1986. **11**(8): p. 516-518.
186. Noorduyn, W.L., et al., *Complete chiral symmetry breaking of an amino acid derivative directed by circularly polarized light*. Nat Chem, 2009. **1**(9): p. 729-732.
187. Taylor, R., E. Simova, and C. Hnatovsky, *Creation of chiral structures inside fused silica glass*. Optics Letters, 2008. **33**(12): p. 1312-1314.
188. Poumellec, B., et al., *Parity violation in chiral structure creation under femtosecond laser irradiation in silica glass*. Light: Science & Applications, 2016. **5**(11): p. e16178.
189. Schreiber, R., et al., *Chiral plasmonic DNA nanostructures with switchable circular dichroism*. Nature communications, 2013. **4**.
190. Della Valle, G., R. Osellame, and P. Laporta, *Micromachining of photonic devices by femtosecond laser pulses*. Journal of Optics A: Pure and Applied Optics, 2008. **11**(1): p. 013001.
191. Cheng, G., et al., *Ultrafast laser photoinscription of polarization sensitive devices in bulk silica glass*. Optics Express, 2009. **17**(12): p. 9515-9525.
192. Osellame, R., G. Cerullo, and R. Ramponi, *Femtosecond Laser Micromachining: Photonic and Microfluidic Devices in Transparent Materials*. Vol. 123. 2012: Springer Science & Business Media.

193. Yuan, L., et al., *Stress-induced birefringence and fabrication of in-fiber polarization devices by controlled femtosecond laser irradiations*. Optics Express, 2016. **24**(2): p. 1062-1071.
194. Mihailov, S.J., et al., *Extreme Environment Sensing Using Femtosecond Laser-Inscribed Fiber Bragg Gratings*. Sensors, 2017. **17**.
195. Beresna, M., M. Gecevičius, and P.G. Kazansky, *Polarization sensitive elements fabricated by femtosecond laser nanostructuring of glass [Invited]*. Optical Materials Express, 2011. **1**(4): p. 783-795.
196. Zhang, J., et al., *Seemingly unlimited lifetime data storage in nanostructured glass*. Physical Review Letters, 2014. **112**(3): p. 033901.
197. Beresna, M., M. Gecevičius, and P.G. Kazansky, *Harnessing Ultrafast Laser Induced Nanostructures in Transparent Materials*, in *Progress in Nonlinear Nano-Optics*. 2015, Springer. p. 31-46.
198. Desmarchelier, R., et al., *Achromatic polarization rotator imprinted by ultrafast laser nanostructuring in glass*. Applied Physics Letters, 2015. **107**(18): p. 181111.
199. Drevinskas, R., et al., *Ultrafast laser - induced metasurfaces for geometric phase manipulation*. Advanced Optical Materials, 2017. **5**(1): p. 1600575.
200. Sun, Q., et al. *Control of Laser Induced Stress for Diffractive Optics in Transparent Media*. in *The European Conference on Lasers and Electro-Optics*. 2019. Optical Society of America.



## Chapter2 Experimental details

---

### Content

2.1 Introduction.....	72
2.2 Femtosecond laser direct writing (FLDW) system.....	72
2.3 Fundamentals of polarization of light .....	76
2.3.1 Stokes vector and the Poincaré sphere .....	76
2.3.2 Mueller matrix formalism.....	78
2.4 Basic polarimetric properties.....	78
2.4.1 Dichroism and diattenuation.....	79
2.4.2 Retardation and linear birefringence.....	81
2.4.3 Depolarization.....	84
2.4.4 Polarizance .....	87
2.5 Extraction of polarimetric properties .....	88
2.5.1 Product decomposition .....	88
2.5.2 Sum decomposition.....	89
2.5.3 Logarithmic decomposition.....	90
2.6 Polarimetric instrumentation.....	93
2.6.1 “de Sénarmont” compensator.....	94
2.6.2 Circular Dichroism spectro-polarimeter - JASCO- J-810.....	97
2.6.3 Vis-Near IR (400-1000nm) Mueller Ellipsometry – MM-16 .....	101
2.6.4 UV-Vis-Near-IR Mueller ellipsometry – MM-12 .....	102
2.7 Conclusions.....	105
2.8 References.....	106



## 2.1 Introduction

This chapter describes the methods used for the fabrication and characterization of the 2D or 3D microstructures (lines, squares, spirals) produced using femtosecond laser exposure. Most of the contents of this thesis rely on these experimental procedures specifically applied to planar fused silica glass substrates. The femtosecond laser described in Section 2.1 has characteristics, like pulse duration and energy per pulse, ideal to produce nonlinear absorption in glasses and therefore to produce the required permanent changes in the substrate. Additional components in the laser delivery system, also described in Section 2.1, further allow for the manipulation of the femtosecond laser beam to facilitate the fabrication of segmented lines and to obtain the desired 2D and 3D structures.

The predominant way of characterizing nanogratings is the analysis of the structure under a scanning electron microscope. Despite its straightforwardness, the method restricts characterization of the femtosecond laser induced anisotropy to the measurements of the nanogratings period and the porosity-filling factor. The alternative, nondestructive way of characterizing the anisotropic structure is quantitative birefringence measurements and more generally anisotropic optical properties, which provide information on the dependence of induced modification on writing parameters such as fluence, repetition rate, numerical aperture, etc... Thus, it is necessary to introduce fundamentals of polarization of light in section 2.2. The concept of polarization of light together with the basic polarimetric properties; dichroism, birefringence, and depolarization are introduced in section 2.3. We also discuss the Stokes formalism and the Mueller calculus formalism, which is a complete mathematical approach to describe the polarimetric light-matter interaction. In section 2.4, we illustrate how the basic polarimetric properties are extracted through a post treatment method called decomposition based on linear algebra properties of Mueller matrices. We introduce different types of decomposition methods depending on the sample structure, yielding a different mathematical description. A special emphasis is put to describe the logarithmic (also called by some authors differential) decomposition, since this latter will be extensively used to treat the simulated and experimental data discussed in the forthcoming chapters of the manuscript. The overall characterization methods described in Section 2.5 provide the means to measure the key physical quantities of the femtosecond laser written structures with sufficient accuracy to draw meaningful conclusions from the experiments designed in each chapter.

## 2.2 Femtosecond laser direct writing (FLDW) system

For the work described in this thesis, we mostly used a femtosecond fiber laser writing system. The femtosecond fiber laser system used for fabrication of our samples in bulk fused silica consists of a directly diode-pumped Ytterbium fiber laser (Satsuma HP from Amplitude Systèmes), with a center wavelength of 1030 nm and variable repetition rates from 200 kHz to 2 MHz. The key characteristics of this system are summarized in Figure 2.1. It is equipped with a pulse picker (acousto-optic modulator), which allows to reduce the repetition rate down to a single pulse if need. The average power is fixed to 10 W that allows reaching up

to 25  $\mu\text{J}/\text{pulse}$  at 400 kHz or 10  $\mu\text{J}/\text{pulse}$  at 1 MHz.

IR	Laser Parameters		Unit	Target		Measurement	
				400 kHz	2000 kHz	400 kHz	2000 kHz
	Energy per pulse		$\mu\text{J}$	$\geq 25$	$\geq 5$	26.5	27
Average power		$\text{W}$	$\geq 10$	$\geq 10$	11.1	11.3	
Center wavelength		nm	1030 +/- 5		1032.1	1032.2	
Bandwidth FWHM			$\leq 10$		8.6	8.9	
Pulse duration		fs	$< 500$		220	240	
Pulse energy over 12h		Average	$\mu\text{J}$	$> 25$	$> 5$	27.8	-
		RMS	%	$< 2$		0.08	
Polarization ratio		-	$> 100:1$		625:1		
$M^2$		$M^2_x$	-	$< 1.30$		1.10	
		$M^2_y$	-	$< 1.30$		1.07	
Beam diameter		$W_{0x}$	mm	$2 \pm 0.5$		1.53	
		$W_{0y}$		$2 \pm 0.5$		1.50	
Beam ellipticity		%	$< 13\%$		1.9		
Astigmatism			$< 50\%$		27.8		
Waist ellipticity			$< 13\%$		0.1		

Figure 2.1: Certificate of Conformance (CoC) of the Satsuma HP Laser used in this PhD work.

After amplification and compression, the pulse width is typ. 250 fs full width at half maximum (FWHM). Note that the intra-cavity distance between the chirped gratings is adjustable using a motorized translation stage in order to optimize the compression of the pulses according to the repetition rate provided by the laser. An example of an autocorrelation function measurement performed on typical 1030nm output pulses is shown in Figure 2.2, where the experimental data was fitted to a Lorentzian function in order to determine an autocorrelation FWHM value of 341 fs. This value corresponds to a real pulse width of 221 fs in optimal conditions and before the focusing lens. The spatial chirp (wavelength vs. position) was measured around 0,54nm/mm along x-axis and 0,02 nm/mm along y-axis.

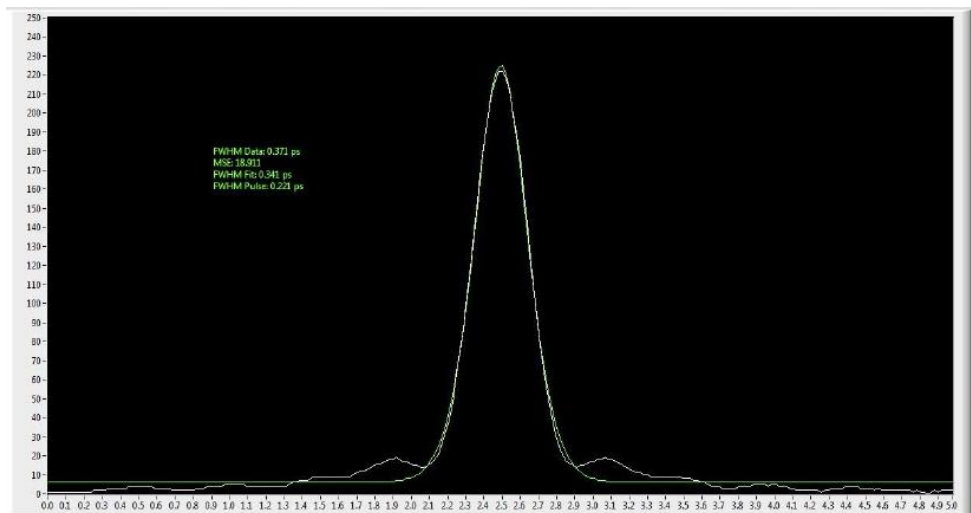


Figure 2.2: Measurements of the laser temporal pulse profile using an optical autocorrelator (x axis is expressed in ps, y axis is a power in arbitrary units).

The laser is linearly polarized horizontally (parallel to the optical table) and perpendicular to the z-axis (as defined in Figure 2.3). The computer controlled half waveplate (Newport SR50CC rotation stage) and the Glan-Laser polarizer provides a way of tuning the beam power while guaranteeing the linear polarization of the laser, which is fixed horizontal

at this point (along x-axis, and thus parallel the ideal plane of the laser compressor). The laser path can then be selected between two alternatives, the acousto-optic modulator (AOM) path and non-AOM path.

The AOM is also computer controlled by a digital RF driver signal, and is optimized to create one first order diffraction beam with an adjustable diffraction efficiency from 0 up to 100% of the total power of the input beam. In some cases this configuration serves as a fast on/off switch for the laser beam and can reliably operate at frequencies up to 2 MHz with the current setup. For example the ability to modulate the laser beam with the AOM allows the direct fabrication of Bragg grating waveguides (BGWs) [1-3], by creating a waveguide composed of periodic segments, or volumetric pixels (voxels), of refractive index higher than that of the background refractive index of fused silica. At this point in the fabrication setup of Figure 2.3, the laser wavelength is 1030 nm and the pulse width is typ. 250 fs with a variable repetition rate ranging from 400 kHz to 2 MHz and the possibility of AOM modulation (typ. 100 kHz and down to single pulse) and an additional shutter for synchronization.

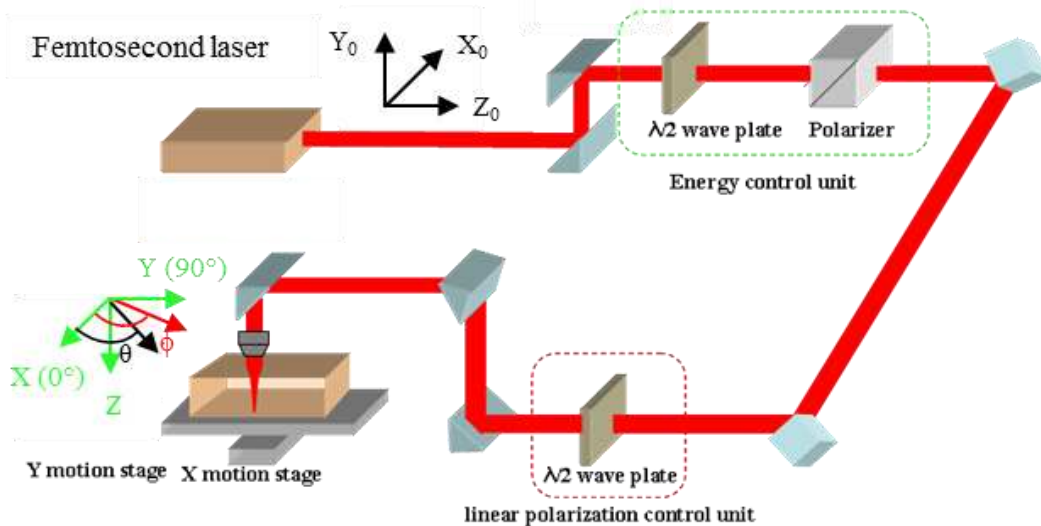


Figure 2.3: Schematic diagram of the femtosecond laser direct writing (FLDW) setup used at ICMMO laboratory.

The laser beam is then aligned inside the target delivery system described in Figure 2.4 and focused into the silica glass sample that is mounted in the computer controlled motion XY-stages (one-XY200HA from Newport) having a minimum resolution of 50 nm, a bi-directional repeatability of 90 nm and a speed up to 200mm/s. The computer controlled Z-stage (Newport UTS100CC) positions the laser spot typically at 300  $\mu\text{m}$  below the surface of the glass substrate. Aspheric lenses with numerical apertures (NAs) ranging from 0.16 NA to 0.65 NA were used to create spot sizes with diameters ranging from 4,5  $\mu\text{m}$  to 1,1  $\mu\text{m}$  (e.g. 1,3  $\mu\text{m}$  for 0.55 NA). The diameter is calculated at  $1/e^2$  of the maximum intensity with Equation 2.1, where  $\omega_0$  is the spot radius for the infrared 1030 nm wavelength, considering a typical beam quality of  $M^2 < 1.1$ , and assuming a Gaussian distribution.

$$\omega_0 = \frac{M^2 \lambda}{\pi \text{NA}} \quad \text{Equation 2.1}$$

The additional motorized half-waveplate pictured in the diagram of Figure 2.4 further permits the control of the laser beam polarization state to be linear along the y-axis, linear along the x-axis or any linear polarization state in between at the sample position. This waveplate is mounted on a fast belt driven rotation stage (Newport URB100CC) with a typical speed of 720°/s. Using this freedom to control the laser polarization, the laser power together with the XYZ motion control, it is possible to have the polarization of the laser beam oriented parallel or perpendicular, or, even oriented at an arbitrary azimuth with respect to the laser scanning direction in the glass sample.

Figure 2.4 illustrates the laser being focused into a fused silica sample and a laser written line (like a waveguide for example in Ref. [4]) being formed by scanning the sample through the laser spot. The geometry shown in Figure 2.4 also illustrates the orientation of the birefringence proper polarization axis of the waveguide modes, or polarization eigenmodes, which are formed by the orthogonal directions: Vertical, V, and Horizontal, H, defined with respect to the optical table.

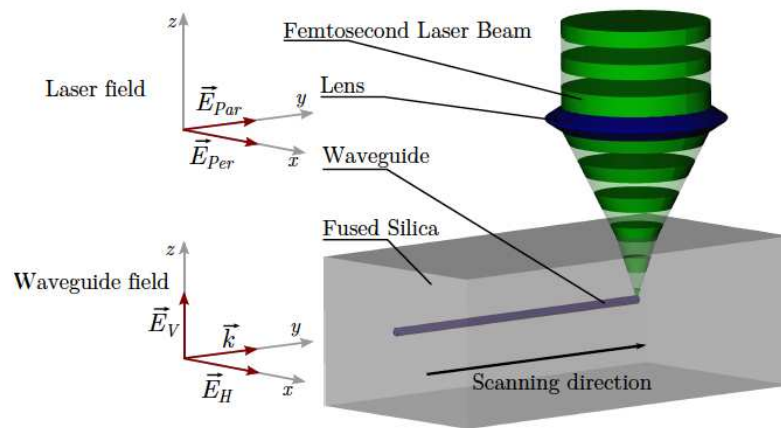


Figure 2.4: Schematic diagram of the laser lines (waveguide like) fabrication where E<sub>par</sub> and E<sub>per</sub> represent the parallel and perpendicular polarizations of the writing laser. The scanning direction was fixed along Y-axis. For E<sub>par</sub> (Yy writing configuration), we have the nanogratings form birefringence optical fast axis along y whereas slow axis is along x. For E<sub>per</sub> case (Yx writing configuration), we have optical fast axis along x whereas slow axis is along y. Graph adapted from Ref. [5].

All motorized components are connected to a computer via an XPS - 8-axis controller from Newport. The control interface is made from the GOL3D software whose schematic description is shown in Figure 2.5. This software is designed to centralize the control of the elements of the assembly, but also to control the translation plates where the sample is positioned. This makes it possible to perform complex writing paths at a constant speed such as a spiral or sets of objects in 3D. The write speed is an important parameter to take into account because it influences the pulse accumulation on the laser trace. It is therefore necessary that it remains identical throughout the trajectory by optimization of the writing algorithm and the writing synchronization with the shutter.

Throughout this work, the substrates used were Heraeus SuprasilCG fused silica: a Type III silica variety that contains 400-1000pm OH and with a glass annealing temperature T<sub>a</sub>

around 1000°C. The typical dimensions are 75 mm or length, 25 mm width, and 1 mm thickness, with double side optically polished. The length chosen in each case depended on the minimum length required for each particular experimental device.

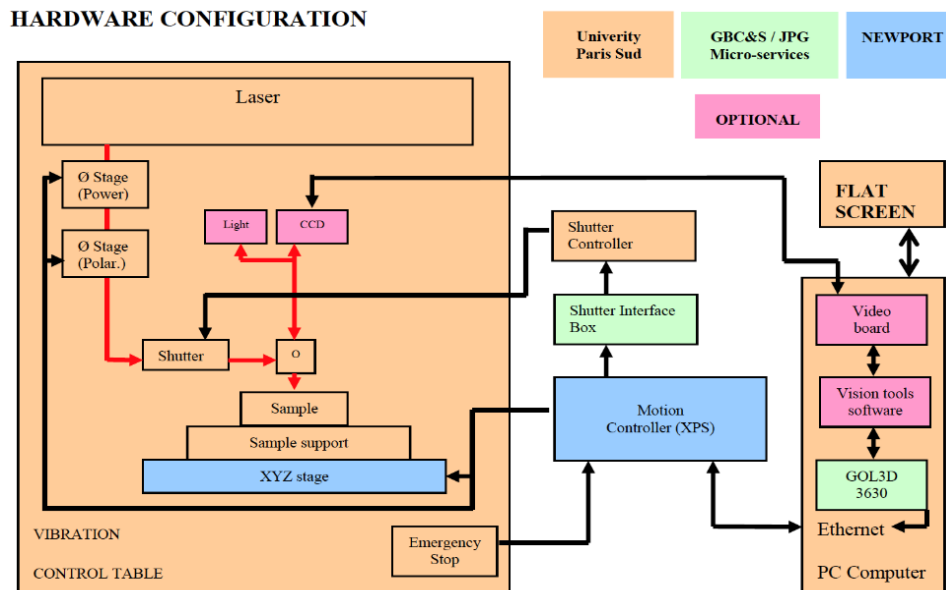


Figure 2.5: Schematic diagram of the hardware configuration related to our direct writing software "GOL3D".

## 2.3 Fundamentals of polarization of light

The state of a fully polarized light beam can be described using the Jones formalism, which was discovered by R. C. Jones in 1941 [6]. Jones approach is the simplest way to treat polarized light and it is based on a complex bi-dimensional vector to describe a given state of polarization. The corresponding 2 by 2-complex Jones matrix represents the transformation of a sample or an optical element on the polarization state of an illuminating beam. Although the Jones formalism is an intuitive method to treat the light polarization and samples anisotropic properties, it can be only applied with fully polarized light.

Mueller calculus, which was already completed in 1943 by Hans Mueller [7] is a generalization of the Jones formalism and can be used to represent any state of polarization including partially polarized light and unpolarized light. The Mueller calculus is general and can always be applied but is mandatory when partially polarized light has to be treated.

### 2.3.1 Stokes vector and the Poincaré sphere

In the Mueller calculus, the polarization states of light can be represented with a four-dimensional vector, which is called the Stokes vector. Stokes parameters, which are components of the Stokes vector, describe the polarization states of the electromagnetic wave. George Gabriel Stokes defined them in 1852 [8, 9] before the Mueller matrices were introduced. The Stokes vector,  $\mathbf{S}$ , is composed of four Stokes components usually referred

as,  $S_0$ ,  $S_1$ ,  $S_2$ , and  $S_3$ , or as  $I$ ,  $Q$ ,  $U$ , and  $V$  respectively. The different representations of the Stokes vector are specified in the following expression:

$$\mathbf{S} = \begin{pmatrix} S_0 \\ S_1 \\ S_2 \\ S_3 \end{pmatrix} = \begin{pmatrix} I \\ \rho I \cos 2\alpha \cos 2\chi \\ \rho I \sin 2\alpha \cos 2\chi \\ \rho I \sin 2\chi \end{pmatrix} = \begin{pmatrix} I \\ Q \\ U \\ V \end{pmatrix} = \begin{pmatrix} I_x + I_y \\ I_x - I_y \\ I_{45^\circ} - I_{-45^\circ} \\ I_L - I_R \end{pmatrix}$$

$$= \begin{pmatrix} \langle E_x E_x^* + E_y E_y^* \rangle \\ \langle E_x E_x^* - E_y E_y^* \rangle \\ \langle E_x E_y^* + E_y E_x^* \rangle \\ i \langle E_x E_y^* - E_y E_x^* \rangle \end{pmatrix} \quad \text{Equation 2.2}$$

where  $\rho$ ,  $I$ ,  $2\alpha$  and  $2\chi$  are the spherical coordinates of the three-dimensional vector of Cartesian coordinates ( $S_1$ ,  $S_2$ ,  $S_3$ ).  $I$  is the total intensity of the beam.  $I_x$  and  $I_y$  are the intensities of the light linearly polarized along  $x$  and  $y$  directions.  $I_{45^\circ}$  and  $I_{-45^\circ}$  are for the light linearly polarized at  $45^\circ$  and  $-45^\circ$  degrees to the  $x$ -axis.  $I_L$  is the circularly polarized light in counter-clockwise, while  $I_R$  is for the clockwise circularly polarized light. The factor two in front of  $\alpha$  means that any polarization ellipse is indistinguishable from one rotated by  $180^\circ$ . Another factor of two in front of  $\chi$  shows that an ellipse is indistinguishable from one with the semi-axis lengths swapped accompanied by a  $90^\circ$  rotation. Finally  $\rho$  is the so-called degree of polarization (DOP) and can be represented using the Stokes parameters as,

$$\rho = \frac{\sqrt{Q^2 + U^2 + V^2}}{I} \quad \text{Equation 2.3}$$

The Stokes vectors can be graphically shown, in a tridimensional space, they are comprised in the volume of a sphere called the Poincaré sphere, which is shown in Figure 2.6. The points on the sphere (or inside the sphere) show the polarization states of light. The points on the surface of sphere, for instance, correspond to perfectly polarized light which has the  $\rho = 1$ . Conversely, the points inside the sphere are for the partially polarized light with  $0 < \rho < 1$ .

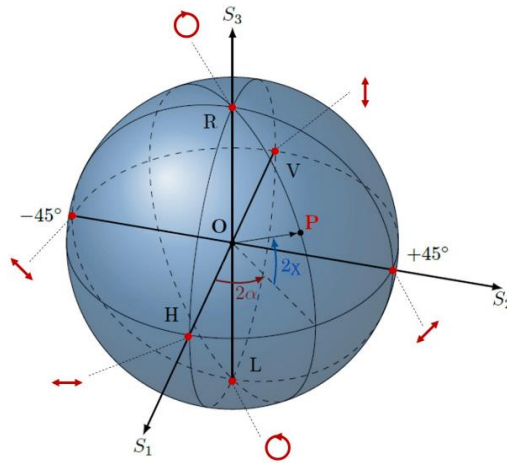


Figure 2.6: The Poincaré sphere is a graphical tool for visualizing different types of polarized light using Stokes vector on the three-dimensional coordinates. Extracted from Ref. [10].

### 2.3.2 Mueller matrix formalism

The Stokes vectors are accompanied by a four-dimensional matrix, called the Mueller matrix,  $\mathbf{M}$ , which represents the polarimetric interaction of polarized light with a given sample. The incident beam as illustrated with Stokes vector  $\mathbf{S}_{in}$  passes through an optical element  $\mathbf{M}$  and comes out with  $\mathbf{S}_{out}$  as written below:

$$\mathbf{S}_{out} = \mathbf{M} \cdot \mathbf{S}_{in} \quad \text{Equation 2.4}$$

This can be also represented using each component of Mueller matrix as below,

$$\begin{pmatrix} I \\ Q \\ U \\ V \end{pmatrix}^{out} = \begin{pmatrix} M_{11} & M_{12} & M_{13} & M_{14} \\ M_{21} & M_{22} & M_{23} & M_{24} \\ M_{31} & M_{32} & M_{33} & M_{34} \\ M_{41} & M_{42} & M_{43} & M_{44} \end{pmatrix} \cdot \begin{pmatrix} I \\ Q \\ U \\ V \end{pmatrix}^{in} \quad \text{Equation 2.5}$$

## 2.4 Basic polarimetric properties

Generally speaking, the polarimetric response of a given sample describes how the incident light polarization is changed due to the interaction with the sample. In spite of its apparent complexity, this response can be rationalized in terms of three fundamental properties, namely the sample diattenuation, retardation, and depolarization. In many cases of practical interest, among which the usual ellipsometric characterization of anisotropic materials or thin films, all these properties can be unambiguously defined from the measured data. Pure diattenuators, pure retarders and depolarizers give the fundamental polarimetric properties used as "building blocks" to characterize more complex systems. To understand these properties, it is useful to use the concept of pairs of fully polarized orthogonal eigenstates. Each eigenstate is characterized by its length and ellipticity. An ellipticity equal to zero corresponds to linearly polarized light, an ellipticity equal to  $\pm 1$  corresponds to right (+) or left (-) circularly polarized light, while other values of ellipticity correspond to

elliptically polarized light. The sign of the ellipticity states the difference between clockwise or counterclockwise rotation.

## 2.4.1 Dichroism and diattenuation

### Dichroism

A material has a property of dichroism if it reveals a difference in absorption of the intensity of the incident wave according to its polarization. This property is usually found in isotropic liquids and solutions because of the structure of molecules and provides information on the structure of the molecules that compose it. As for birefringence, linear and circular dichroisms are differentiated according to the state of polarization of the incident wave passing through the medium. Subsequently, we develop the case of circular dichroism and we will make the analogy with linear dichroism.

Let a circular electric field of initial amplitude  $E_0$  pass through a medium of length  $l$ . According to the definition of a circular dichroic medium and the Beer-Lambert law, following the state of the left or right circular polarization, the expression of the outgoing fields  $E_{-,+}$  is written:

$$E_{-,+} = E_0 \exp\left(-\frac{1}{2} \alpha'_{-,+} \cdot l\right) \quad \text{Equation 2.6}$$

where  $\alpha'_{-,+} = \frac{4\pi\kappa_{-,+}}{\lambda}$  is the absorption coefficient in  $\text{cm}^{-1}$  defined in the intensity and  $\kappa_{-,+}$  is the linear extinction coefficient. We can then define a circular dichroism expressed in  $\text{cm}^{-1}$  as the difference of the respective absorption coefficients at left and right circular polarizations:

$$\Delta\alpha'_c = \alpha'_{left} - \alpha'_{right} = \alpha'_- - \alpha'_+ \quad \text{Equation 2.7}$$

As with circular dichroism, we can also define the linear dichroism (x-y) by the relation:

$$\Delta\alpha'_l = \alpha'_x - \alpha'_y \quad \text{Equation 2.8}$$

Chemists often use the notion of absorbance  $A = \log\left(\frac{I_0}{I}\right) = \epsilon \cdot c \cdot l$ , where  $\epsilon$  is the molar extinction coefficient,  $c$  is the concentration and  $l$  is the dichroic medium length while others use:

$I = I_0 \exp(-\alpha' \cdot l)$ , which can be written  $I = I_0 \exp(-A \cdot \ln(10))$ , where  $\alpha' = \frac{1}{l} A \cdot \ln(10)$ .

So we have the following expressions of the optical phase difference expressed in radians units:



$$\begin{aligned} \text{Circular dichroism } CD &= \frac{\ln(10) (A_- - A_+)}{2} = \frac{(\alpha'_- - \alpha'_+).l}{2} \\ &= \frac{1}{2} \frac{4\pi(\kappa_- - \kappa_+).l}{\lambda} = \frac{2\pi(\kappa_- - \kappa_+).l}{\lambda} \end{aligned} \quad \text{Equation 2.9}$$

$$\begin{aligned} (x - y) \text{ Linear dichroism } LD &= \frac{\ln(10) (A_x - A_y)}{2} = \frac{(\alpha'_x - \alpha'_y).l}{2} \\ &= \frac{1}{2} \frac{4\pi(\kappa_x - \kappa_y).l}{\lambda} = \frac{2\pi(\kappa_x - \kappa_y).l}{\lambda} \end{aligned} \quad \begin{array}{l} \text{Equation} \\ 2.10 \end{array}$$

$$\begin{aligned} 45^\circ \text{ Linear dichroism } LD &= \frac{\ln(10) (A_{45} - A_{135})}{2} \\ &= \frac{1}{2} \frac{4\pi(\kappa_{45} - \kappa_{135}).l}{\lambda} = \frac{2\pi(\kappa_{45} - \kappa_{135}).l}{\lambda} \end{aligned} \quad \begin{array}{l} \text{Equation} \\ 2.11 \end{array}$$

## Diattenuation

According to this picture, elliptical diattenuators, which can be seen as partial elliptical polarizers, transmit (or reflect) each of their elliptical eigenstates without altering neither their ellipticity nor their azimuth, but may change their intensities as shown in Figure 2.7.

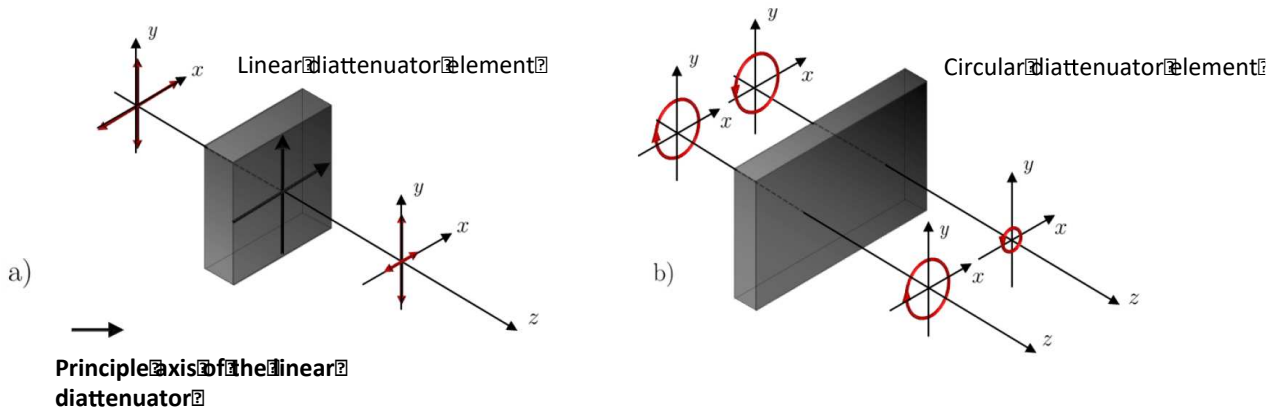


Figure 2.7: A change of the eigenstates by a linear diattenuator (a)  $M_D$  or a circular diattenuator (b) when the light propagates in the  $z$  direction. Extracted from Ref. [10].

Diattenuation, the polarimetric property of the general elliptical diattenuators, is defined in practice by a scalar, called  $D$ , characterizing the maximum variation of transmitted (or reflected) light intensity with as a function of the incident polarization state. Diattenuation is defined as follows:

$$D = \frac{I_{\max} - I_{\min}}{I_{\max} + I_{\min}} \quad \text{Equation 2.12}$$

where  $I_{\max}$  and  $I_{\min}$  accord with the intensities of the two transmitted or reflected eigenstates. This features the maximum variation of transmitted or reflected light intensity, corresponding to the incident polarization state. The amplitude ratio in ellipsometry,  $\psi$ , can

be deduced from this definition.  $\tan 2\psi$  can be defined as  $I_{\max}/I_{\min}$ . Since the parameters can be decided,  $D$  for intensities and  $\psi$  for amplitudes of the electromagnetic field, the square is taken as below,

$$D = \frac{1 - \tan^2 \psi}{1 + \tan^2 \psi} = \cos 2\psi \quad \text{Equation 2.13}$$

In case of the ideal dichroic linear polarizers, the  $I_{\min}$  is almost 0 and the  $D$  is close to 1 and  $\psi$  is close to  $0^\circ$  or  $90^\circ$ . A vector  $\mathbf{D}$  can define the diattenuation. This provides the orientational information of the eigenstates from diattenuators as below,

$$\mathbf{D} = D \begin{pmatrix} d_1 \\ d_2 \\ d_3 \end{pmatrix} = \begin{pmatrix} D_{\text{horizontal}} \\ D_{45^\circ} \\ D_{\text{circular}} \end{pmatrix} \quad \text{Equation 2.14}$$

where  $d_1^2 + d_2^2 + d_3^2 = 1$  and the polarization eigenstates of the Stokes vectors are given by,

$$\mathbf{S}_{\max}^T = (1, d_1, d_2, d_3), \mathbf{S}_{\min}^T = (1, -d_1, -d_2, -d_3) \quad \text{Equation 2.15}$$

The components of the vector  $\mathbf{D}$  describe the horizontal, the  $45^\circ$ , and the circular diattenuation, respectively. In the Mueller matrix, the  $\mathbf{D}$  of any sample can be represented as a simple function of the first row of Mueller matrix as below,

$$\mathbf{D} = \frac{1}{M_{11}} \begin{pmatrix} M_{12} \\ M_{13} \\ M_{14} \end{pmatrix} \quad \text{Equation 2.16}$$

The Mueller matrix of an ideal diattenuator  $\mathbf{M}_D$  can be defined with the scalar diattenuation  $D$  and the diattenuation vector  $\mathbf{D}$  as below,

$$\mathbf{M}_D = \tau \begin{pmatrix} 1 & \mathbf{D}^T \\ \mathbf{D} & \mathbf{m}_d \end{pmatrix}, \text{ and } \mathbf{m}_d = \sqrt{1 - D^2} \mathbf{I}_3 + (1 - \sqrt{1 - D^2}) \mathbf{D} \mathbf{D}^T \quad \text{Equation 2.17}$$

where the first-row element and the first-column element are illustrated by the  $\mathbf{D}$ . The  $\mathbf{m}_d$  is a three-dimensional symmetric sub-matrix which is composed of the  $3 \times 3$  identity matrix  $\mathbf{I}_3$ , the  $\mathbf{D}$ , and the  $D$ . The  $\tau$  shows the entire transmittance or reflectivity of the sample when the incident light is perfectly depolarized.

## 2.4.2 Retardation and linear birefringence

Elliptical retarders (also called waveplate) pass their eigenstates conserving their ellipticity,  $\varepsilon$ , and an azimuth,  $\alpha$ . and the intensities but modifying only their phases as shown in Figure 2.8.

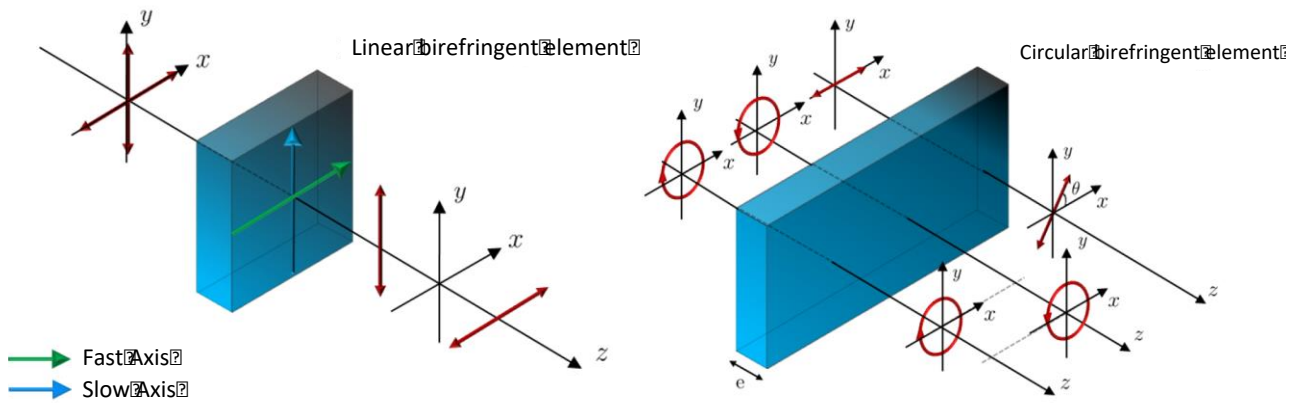


Figure 2.8: A change of the eigenstates by a linear or a circular retarder  $\mathbf{M}_R$  when the light propagates in the  $z$  direction. Extracted from Ref. [10].

When light travels from one medium to another, the speed but also the wavelength change since the electric field of the light interacts with the electrons in the medium. The refractive index can also be stated in terms of wavelength dependency. The refractive index exhibits different values depending on the type of material and the light frequency (namely spectral dispersion). In Figure 2.9 a, the black circles represent the motion of electrons, which move to the opposite direction of the electric field in a medium when the light travels. So, the light that interacts with a bunch of electrons of atoms can be affected depending on the configuration of crystals in the medium. The spring means the amplitude of the relative force of the electric field, which interacts with the electrons of the medium.

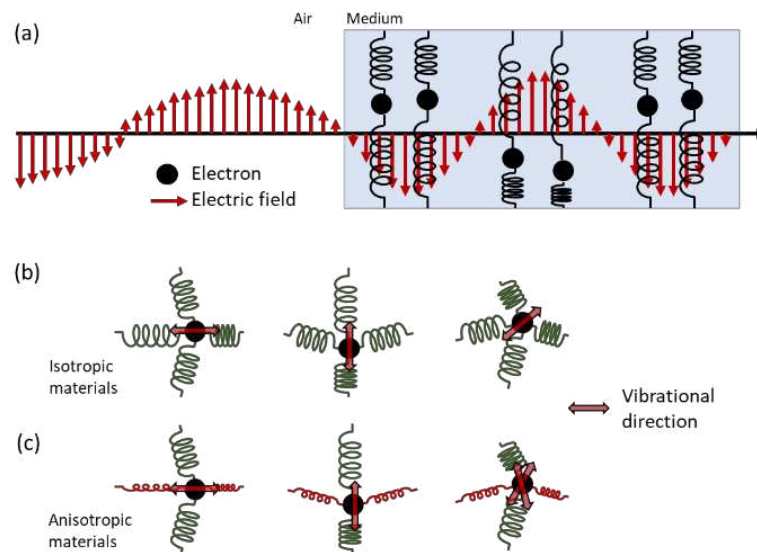


Figure 2.9: (a) The motion of electrons when light travels from one medium to another, (b) the motion of electrons in the isotropic materials, and (c) the motion of electrons in the anisotropic materials. The spring represents the amplitude of the relative force of the electric field that interacts with the electrons of the medium. From Ref. [11].

Figure 2.9 (b) and (c) show the motion of electrons in either isotropic or anisotropic materials, respectively. When a crystal has no specific directional property, the crystal structure is called isotropic material such as a cubic structure (ex. NaCl). On the other hand, when a crystal has a specific directional property, the electrical properties depend on the

direction of the structure and that is called anisotropic material such as a trigonal structure (ex. Calcite or -Quartz). In the isotropic material, the electric field oscillates in all direction. However, the oscillation of electric field that defines the speed and wavelength of the light depends on the incident light direction in anisotropic materials. The oscillation of electrons decides the motion of electric field and the light trajectory and therefore anisotropic materials have different refractive indices depending on the incident beam "status" such as its polarization state. This is called birefringence (also called birefractive materials).

Birefringence is an optical phenomenon that split of the incident light beam when the material exhibits different refractive indices depending on the polarization direction of light. We can thus say that the material is optically anisotropic or birefringent. In Uniaxial materials, this birefringence can be expressed mathematically as:

$$\Delta n = n_e - n_o \quad \text{Equation 2.18}$$

where  $n_o$  is the refractive index for an ordinary ray whose oscillation direction of the electric field (or a polarization direction) is perpendicular to the optical axis,  $n_e$  is the refractive index for an extraordinary ray parallel to the optical axis. The material which having a negative  $\Delta n$  shows negative birefringence and the material having a positive  $\Delta n$  shows a positive birefringence. For a negative uniaxial birefringent sample, the ordinary axis is called slow axis through which the light propagates slower than in other axes. And the extraordinary axis is called fast axis through which the light propagates faster than in other axes. The retardance or retardation  $R = \Delta n l$  is the optical pathway difference (usually expressed in nm) between the two different polarization states, where  $l$  is for the thickness of the birefringent layer. Note that the retardance  $R$  can be rewritten as the difference in phase shift  $\delta$  (expressed in radians) between the two polarization states:

$$\delta = \frac{2\pi\Delta n l}{\lambda} = \frac{2\pi R}{\lambda} \quad \text{Equation 2.19}$$

In case of a half-waveplate, the orientation of the fast axis is what determines the orientation of the linearly polarized light emitting from the retarder. As a result, if a half-waveplate is rotated at  $45^\circ$  with respect to the incoming linear polarized light, the transmitted light will be rotated at  $90^\circ$  (i.e. twice the initial angle) with respect to the polarization direction of the incident light.

As the diattenuation was defined in the previous section, the time delay between two eigenstates after they propagate through an ideal waveplate can be described by the scalar retardance,  $R$ , using a vector representation,  $\mathbf{R}$  as below,

$$\mathbf{R} = R \begin{pmatrix} r_1 \\ r_2 \\ r_3 \end{pmatrix} = \begin{pmatrix} R_{\text{horizontal}} \\ R_{45^\circ} \\ R_{\text{circular}} \end{pmatrix} \quad \text{Equation 2.20}$$

where  $r_1^2 + r_2^2 + r_3^2 = 1$ . The components of  $\mathbf{R}$  show the horizontal, the  $45^\circ$ , and the

circular retardance, respectively.

The Stokes vectors of the fast and the slow eigenstates  $\mathbf{S}_f$  and  $\mathbf{S}_s$  are respectively defined by,

$$\mathbf{S}_f^T = (1, r_1, r_2, r_3), \mathbf{S}_s^T = (1, -r_1, -r_2, -r_3) \quad \text{Equation 2.21}$$

An ideal retarder is illustrated geometrically as the rotation in the space of Stokes vectors. The Mueller matrix of an ideal retarder  $\mathbf{M}_R$  can be expressed as,

$$\mathbf{M}_R = \begin{pmatrix} 1 & \mathbf{0}^T \\ \mathbf{0} & \mathbf{m}_R \end{pmatrix}, \text{ and } (\mathbf{m}_R)_{ij} = \delta_{ij} \cos R + r_i r_j (1 - \cos R) \sum_{k=1}^3 \varepsilon_{ijk} r_k \sin R \quad \text{Equation 2.22}$$

where the three-dimensional sub-matrix  $\mathbf{m}_R$  is an orthogonal rotation matrix with a unit determinant,  $\det(\mathbf{m}_R) = 1$ . The vector  $\mathbf{0}$  is the null vector. The  $\varepsilon_{ijk}$  is the Levi-Civita permutation sign and the  $\delta_{ij}$  represents the Kronecker delta which are expressed as,

$$\delta_{ij} = \begin{cases} 0 & \text{if } i \neq j \\ 1 & \text{if } i = j \end{cases}, \quad \varepsilon_{ijk} = \begin{cases} +1 & \text{if } (i, j, k) \text{ is } (1, 2, 3), (2, 3, 1) \text{ or } (3, 1, 2) \\ -1 & \text{if } (i, j, k) \text{ is } (3, 2, 1), (1, 3, 2) \text{ or } (2, 1, 3) \\ 0 & \text{otherwise: } i = j \text{ or } j = k \text{ or } k = i \end{cases} \quad \text{Equation 2.23}$$

Scalar retardance and vector retardance can be defined from the experimental Mueller matrices as below,

$$R = \cos^{-1} \left( \frac{\text{trace}(\mathbf{M}_R)}{2} - 1 \right), \quad r_i = \frac{1}{2 \sin R} \sum_{j,k=1}^3 \varepsilon_{ijk} (\mathbf{m}_R)_{jk} \quad \text{Equation 2.24}$$

where the 'trace' is a sum of the diagonal elements.

### 2.4.3 Depolarization

Depolarization is a property related to the transformation of polarized light into completely unpolarized light or partially polarized light. The pure depolarizers do not leave any polarization state invariant. They make perfectly depolarized states that can be described by the decrease of the DOP defined in (Eq. 2.3). For totally polarized states, DOP becomes 1 whereas DOP becomes 0 for totally unpolarized light. Therefore, the DOP is between 0 and 1 for partially polarized light. Thus, the depolarizers change the eigenstates of the perfectly polarized states into those of partially polarized states. After passing a depolarizer with a well-defined polarization ellipse, the motion of the electric field is no more a perfect ellipse as shown in Figure 2.10.

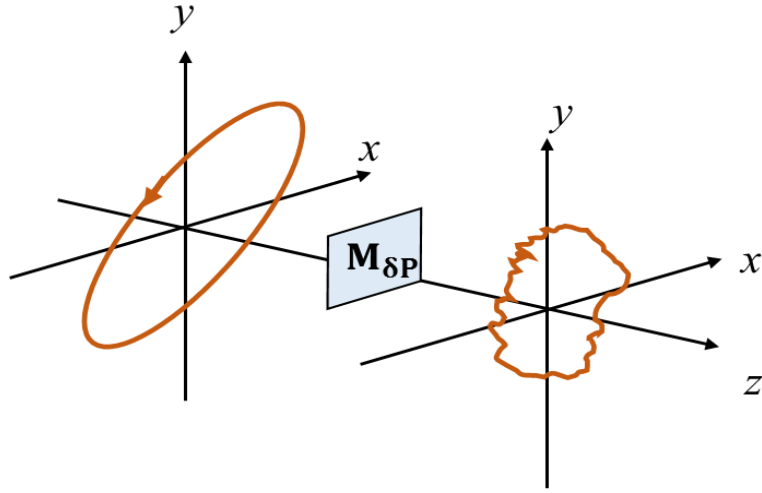


Figure 2.10: A change of the eigenstates by the depolarizer  $\mathbf{M}_{\delta P}$  when the light propagates in the  $z$  direction [11].

When the depolarization is detected, the polarization is determined at any instant but varies considerably over time scale, which is much shorter than the detector's integration time. Consequently, the detector considers the temporal averages of the intensities, sequentially generated by different perfectly polarized states. The perfectly depolarized light needs that the detected signal is the sum of intensities related to various polarized contributions with different polarization states. As a result, this summation would be done temporally, spatially or spectrally. That is, the depolarization depends not only on the sample, but also on the characteristics of the illumination source and the detector. Note that a multiple scattering leads to some depolarization of the incident polarized light.

The Mueller matrix of an ideal depolarizer  $\mathbf{M}_{\delta P}$  can be defined as below,

$$\mathbf{M}_{\delta P} = \begin{pmatrix} 1 & \mathbf{0}^T \\ \mathbf{0} & \mathbf{m}_{\delta} \end{pmatrix} \quad \text{Equation 2.25}$$

where the  $\mathbf{m}_{\delta}$  is a  $3 \times 3$  symmetric matrix and it would be simplified to a diagonal form in a suitable orthonormal basis defined by three eigenvectors  $\mathbf{v}_i$ . Consequently, in a basis represented by the four Stokes vectors as (Eq. 2.23), the Mueller matrix  $\mathbf{M}_{\delta P}$  becomes diagonal as expressed below,

$$\mathbf{S}_0^T = (1,0,0,0), \text{ and } \mathbf{S}_i^T = (1, \mathbf{v}_i^T), \quad (1 \leq i \leq 3) \quad \text{Equation 2.26}$$

$$\mathbf{M}_{\delta P} = \begin{pmatrix} 1 & 0 & 0 & 0 \\ 0 & a & 0 & 0 \\ 0 & 0 & b & 0 \\ 0 & 0 & 0 & c \end{pmatrix} \quad \text{Equation 2.27}$$

where the eigenvalues of  $\mathbf{m}_{\delta}$  ( $a$ ,  $b$ , and  $c$ ) are real numbers from  $-1$  to  $1$ . These three eigenvalues of  $\mathbf{M}_{\delta P}$  corresponds to the horizontal, the  $45^\circ$ , and the circular depolarization respectively.  $\mathbf{M}_{\delta P}$  shows that the DOP decreases by a factor equal to the corresponding eigenvalue  $a$ ,  $b$  or  $c$ , while the perfectly depolarized state remains unchanged. Namely, a

general depolarizer has only one eigen-polarization, concerning the perfectly depolarized state.

Since  $\mathbf{m}_\delta$  is symmetric, the Mueller matrices of the ideal depolarizers  $\mathbf{M}_{\delta P}$  explicitly depend on six parameters. Due to this dependence on six parameters, depolarizers are more mathematically complex than retarders or diattenuators, which involve only three parameters each. However, the symmetry properties of the sample can considerably reduce the number of independent parameters. For example when observing in forward or backward scattering geometries, a suspension of spherical (or statistically isotropic) "scatterers" acts as an ideal depolarizer with different depolarization powers for linearly and circularly polarized incident states. Furthermore, for the specific case of a suspension of spheres, the depolarization power for linear states is independent of the orientation of the polarization of incident light. These properties can be mathematically represented as,

$$a = b \neq c, \text{ and } \mathbf{v}_1^T = (\cos \alpha, \sin \alpha, 0), \mathbf{v}_2^T = (-\sin \alpha, \cos \alpha, 0),$$

$$\mathbf{v}_3^T = (0, 0, 1)$$

Equation 2.28

where  $\alpha$  can be chosen arbitrarily.

It is convenient for practical reasons to define a single numerical function defining the entire depolarization power to characterize the depolarizing properties of a depolarizer. The depolarizing power varies from 0 to 1. If the value is 0, it means that the matrix is non-depolarizing. If the value is 1, it means the matrix behaves as a total depolarizer. The first example of such function is the quadratic depolarization index,  $P_q$ , for the general Mueller matrix and the pure depolarizers expressed as below,

$$P_q = \sqrt{\frac{\sum_{ij} M_{ij}^2 - M_{11}^2}{3M_{11}^2}} = \sqrt{\frac{\text{trace}(\mathbf{M}^T \mathbf{M}) - M_{11}^2}{3M_{11}^2}}$$

Equation 2.29

A physical Mueller matrix is non-depolarizing, if any fully polarized input Stokes vector is converted into a fully polarized output Stokes vector without decreasing its DOP. Conversely, the DOP of output Stokes vector is smaller than that of input Stokes vector for depolarizing Mueller matrices. For any resulting Mueller matrix, the decrease of the DOP depends on the input state. For example, a given sample can be more depolarizing for input circular states (c coefficient) than for input linear ones (a and b coefficients), or vice versa. It is unfeasible to specifically represent the depolarization power of a generic Mueller matrix  $\mathbf{M}$ . The depolarization index,  $P_q$ , to illustrate the depolarization power of a sample represented by the  $\mathbf{M}$  has a range between 1 (for a total depolarizer) and 0 (for non-depolarizing matrices). Another way to define this depolarization power has been studied specifically for depolarizers by Lu and Chipman [12] as the expression below,

$$\Delta = 1 - \frac{1}{3}(|a| + |b| + |c|), \quad 0 \leq \Delta \leq 1$$

Equation 2.30

where  $\Delta$  is the average of the principal depolarization factors and indicates the averaged depolarization capability of the depolarizer. Thus, it can be also called the depolarization power [12]. There have been many possible propositions on the definition of this depolarization [13, 14] and another way to define the depolarization using the logarithmic decomposition will be introduced in the following section.

## 2.4.4 Polarizance

Polarizance is the ability to transform unpolarized light into polarized light. In other words, the polarizance increases the DOP of an incident unpolarized or partially polarized light beam. When the incident unpolarized light travels through the sample, the resulting Stokes vector of the light is expressed as below,

$$\mathbf{S}_{\text{out}} = \mathbf{M} \begin{pmatrix} 1 \\ 0 \\ 0 \\ 0 \end{pmatrix} = \begin{pmatrix} M_{11} \\ M_{21} \\ M_{31} \\ M_{41} \end{pmatrix} \quad \text{Equation 2.31}$$

The scalar polarizance,  $P$ , can be described with the DOP of the output Stokes vector as below,

$$P = \frac{\sqrt{M_{21}^2 + M_{31}^2 + M_{41}^2}}{M_{11}} \quad \text{Equation 2.32}$$

Then the polarizance vector,  $\mathbf{P}$ , can be expressed as below,

$$\mathbf{P} = \frac{1}{M_{11}} \begin{pmatrix} M_{21} \\ M_{31} \\ M_{41} \end{pmatrix} \quad \text{Equation 2.33}$$

In general, the diattenuation vector,  $\mathbf{D}$ , and the polarizance vector,  $\mathbf{P}$ , are equal when the system is homogenous. However, when the system is inhomogeneous, the  $\mathbf{D}$  and  $\mathbf{P}$  are not equal as shown in Figure 2.11.



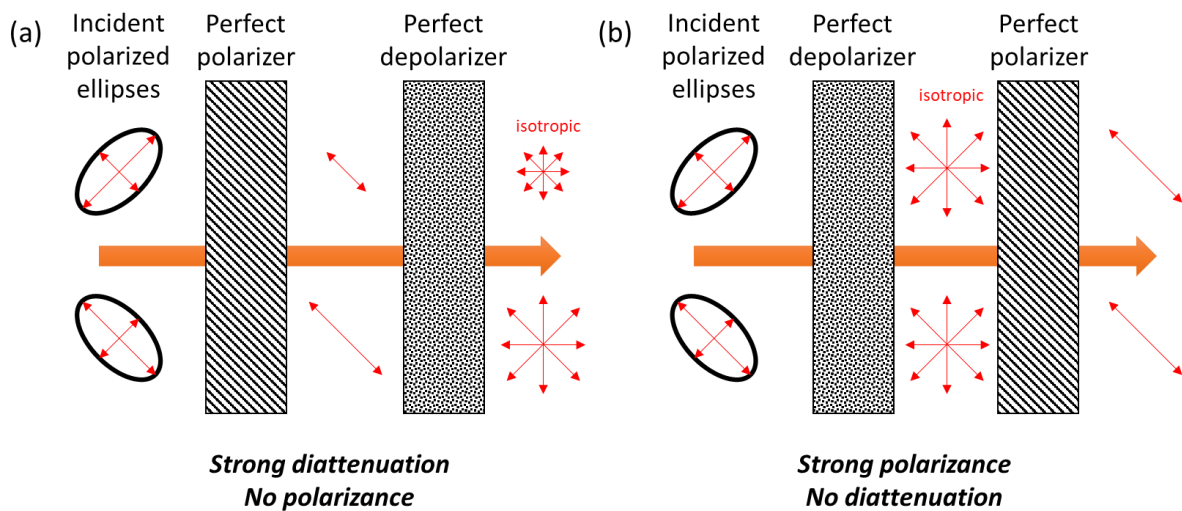


Figure 2.11: The concepts of the diattenuation (a) and polarizance (b) in the different order of the perfect depolarizer and the polarizer illuminating two different polarization ellipses. The red arrows represent the polarization direction and their length shows the intensity of the light. Extracted from Ref. [10].

When a perfect polarizer is in front of a perfect depolarizer (Figure 2.11 a), the system shows diattenuation since the final intensity depends on the orientation of the incident polarization state showing no polarizance. Therefore, such a system is considered as a strong diattenuator not a polarizer. However, when the perfect depolarizer is in front of the perfect polarizer (Figure 2.11.b), any incident polarized state is converted by the depolarizer into a perfectly depolarized state whose intensity is not defined by the initial polarization state. As a result, this system shows no diattenuation but a strong polarizance ( $P = 1$  for an ideal output polarizer) called a strong polarizer and not a diattenuator.

## 2.5 Extraction of polarimetric properties

The Mueller matrix itself is too complex to illustrate the polarimetric properties at a glance. Thus various approaches have been proposed to extract the polarimetric properties from the Mueller matrix, called Mueller matrix decomposition. The decompositions methods have been classified and needs to be considered properly depending on the type of studied samples. In other words, the choice of a given decomposition is mainly determined by the spatial structure of the sample [15, 16]. In this section, three different types of the Mueller matrix decompositions will be discussed. These different types of decomposition method can be applied depending on different type of sample structures to compare the extracted properties and errors.

### 2.5.1 Product decomposition

Product decompositions need to be selected when the layers of different polarimetric properties are separated in the plane parallel to the plane of incidence. The most widely-used product decomposition was proposed by Lu and Chipman [12]. In the product decompositions, the light interacts sequentially with different parts of the sample, each of

which being characterized by a well-defined fundamental polarization property showing a random and complex Mueller matrix as a product of elementary Mueller matrices, which are diattenuators, retarders, and depolarizers. For example one way of ordering them is represented as below,

$$\mathbf{M} = \mathbf{M}_{\delta P} \mathbf{M}_R \mathbf{M}_D \quad \text{Equation 2.34}$$

where  $\mathbf{M}_{\delta P}$  is a Mueller matrix for a depolarizer, the  $\mathbf{M}_R$  is a Mueller matrix for a retarder, and the  $\mathbf{M}_D$  is a Mueller matrix for a diattenuator. Note here that in a more complex approach  $\mathbf{M}_R$  can be further decomposed into a linear retarder and a circular retarder that could be distributed differently. Following the same view,  $\mathbf{M}_D$  can be decomposed into circular diattenuator and a linear diattenuator.

When the diattenuator and the retarder are in the ideal forms, then the depolarizer cannot be an ideal form since the Mueller matrix,  $\mathbf{M}$ , should not show the polarizance as shown in Figure 2.11.a. Consequently, the depolarizer has a non-zero polarizance and its Mueller matrix can be illustrated by:

$$\mathbf{M}_{\delta P} = \begin{pmatrix} 1 & \mathbf{0}^T \\ \mathbf{P} & \mathbf{m}_\delta \end{pmatrix} \quad \text{Equation 2.35}$$

Following these assumptions, the procedure would be numerically stable, and it would always provide physically possible elementary matrices  $\mathbf{M}_{\delta P}$ ,  $\mathbf{M}_R$  and  $\mathbf{M}_D$ . If the order of the elementary components is changed, a simple calculation illustrates that the above results are simply generalized to the other two cases,

$$\mathbf{M}' = \mathbf{M}'_R \mathbf{M}'_{\delta P} \mathbf{M}'_D \quad \text{or} \quad \mathbf{M}'' = \mathbf{M}''_{\delta P} \mathbf{M}''_D \mathbf{M}''_R \quad \text{Equation 2.36}$$

Strictly speaking, the matrices of depolarizers conserve the form in (Eq. 2.32) and  $\mathbf{M}'$  and  $\mathbf{M}''$  matrices are derived from those provided by the standard decomposition of (Eq. 2.31) by the unitary transformations. This simple generalization, however, is no longer valid when the depolarizer is located before the diattenuator as shown in Figure 2.11.b. J. Morio and F. Goudail introduced a reverse decomposition for these three cases with the same definition of the depolarizer [17]. However, this procedure could show unstable or unphysical results when there is strong depolarization. This issue has been solved by R. Ossikovski et al. assuming that the depolarizer is after the diattenuator [18]. Then the standard reverse product decomposition is shown as below,

$$\mathbf{M} = \mathbf{M}_D \mathbf{M}_R \mathbf{M}_{\delta P}, \quad \text{where} \quad \mathbf{M}_{\delta P} = \begin{pmatrix} 1 & \mathbf{D}'^T \\ \mathbf{0} & \mathbf{m}_\delta \end{pmatrix} \quad \text{Equation 2.37}$$

## 2.5.2 Sum decomposition

Sum decompositions or parallel decompositions should be considered when the beam comprises different polarimetric properties that is, the discrete polarimetric properties are in

the plane vertical to the plane of incidence. The sum decompositions, a Cloude decomposition [19] and a Le Roy-Brehonnet decomposition [20], utilize the depolarizing Mueller matrix,  $\mathbf{M}$ , as an incoherent addition of non-depolarizing matrices,  $\mathbf{M}_k$ , as shown in the equation below and Figure 2.12.

$$\mathbf{M} = \lambda_1 \mathbf{M}_1 + \lambda_2 \mathbf{M}_2 + \lambda_3 \mathbf{M}_3 + \lambda_4 \mathbf{M}_4, \text{ where } \lambda_k > 0 \quad \text{Equation 2.38}$$

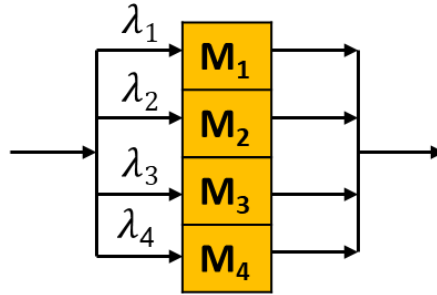


Figure 2.12: In the sum (or parallel) decompositions, any depolarizing Mueller matrix,  $\mathbf{M}$ , can be represented as a parallel combination of non-depolarizing components  $\mathbf{M}_k$ .

The sum decompositions can be widely utilized since they describe physical situations frequently encountered in ellipsometry. The incoherent superposition of differently polarized contributions may be caused by the sample or by the measurement system itself. Therefore, the sum decompositions are well adapted for the multiple reflections with the spatially inhomogeneous samples and the tightly focused beams [21], which do not correspond to the cases we met in this thesis.

### 2.5.3 Logarithmic decomposition

A logarithmic or differential decomposition is suitable to describe uniform samples in which polarization and depolarization properties appear together and are well distributed across the sample in transmission configuration. The first logarithmic decomposition formalism was suggested for linear optically anisotropic media (non-depolarizing) by P. Soleillet [22] in 1929, then reformulated by R. M. A. Azzam [23] for fully polarized light and it has been completed for depolarizing media by R. Ossikovski [24] who is our collaborator from X/PICM in Palaiseau. An interesting historical revision of the development of the concept leading to the modern full formulation of the logarithmic decomposition has been recently done by O. Arteaga [25]. The logarithmic decomposition is for the samples, which are not discrete systems, but rather continuous and homogeneous media as expressed in the following equation and in Figure 2.13.

$$\frac{d\mathbf{M}(z)}{dz} = \mathbf{m} \cdot \mathbf{M}(z) \quad \text{Equation 2.39}$$

where  $\mathbf{m}$  is a differential Mueller matrix,  $\mathbf{M}(z)$  is the Mueller matrix of the anisotropic sample,  $d\mathbf{M}(z)/dz$  is a gradient of  $\mathbf{M}$  along the direction of light propagation,  $z$ .

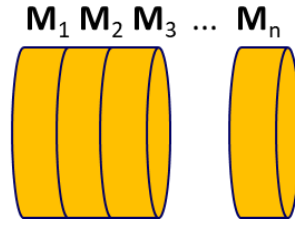


Figure 2.13: The logarithmic decomposition is for samples, which are not discrete systems, but rather continuous and homogeneous media.

The Mueller matrix,  $\mathbf{M}(z)$ , can be represented with the exponential function as below,

$$\mathbf{M}(z) = \exp(\mathbf{m} \cdot z) \quad \text{Equation 2.40}$$

and can be rewritten to define the logarithm of the Mueller matrix,  $\mathbf{L}$ , as below,

$$\mathbf{m} \cdot z = \ln \mathbf{M}(z) = \mathbf{L} \quad \text{Equation 2.41}$$

The differential Mueller matrix,  $\mathbf{m}$ , contains the elementary polarimetric properties of the sample per unit of distance; linear dichroism along the  $x$ - $y$  coordinate axes  $0^\circ - 90^\circ$  (LD), linear dichroism along the  $x$ - $y$  coordinate axes  $45^\circ - 135^\circ$  (LD'), circular dichroism (CD), linear birefringence along the  $x$ - $y$  coordinate axes  $0^\circ - 90^\circ$  (LB), linear birefringence along the bisectors of the  $x$ - $y$  coordinate axes  $45^\circ - 135^\circ$  (LB'), circular birefringence (CB) and isotropic absorption ( $\alpha$ ).

For depolarizing media, the values of the differential Mueller matrix can be assumed to randomly fluctuate around an average value,  $\langle \mathbf{m} \rangle$ . The brackets stand for a statistical averaging of the matrices, necessary to consider the multiple realizations, or paths that a photon can follow across the sample. The fluctuations can be interpreted as the statistic variances of the elementary polarimetric properties,  $\Delta \mathbf{m}$ , of the sample as below,

$$\mathbf{m}_f = \langle \mathbf{m} \rangle + \Delta \mathbf{m} \quad \text{Equation 2.42}$$

Assuming the fluctuations to be sufficiently small, a first-order approximation relating the Mueller matrix to the exponential of the matrix  $\mathbf{m}$  times the thickness,  $z$ , leads to the following expression relating the polarization and the depolarization properties with the matrices and  $\langle \Delta \mathbf{m} \rangle$ , respectively,

$$\mathbf{L}(z) = \mathbf{L}_m(z) + \mathbf{L}_u(z) = \langle \mathbf{m} \rangle z + \frac{1}{2} \langle \Delta \mathbf{m}^2 \rangle z^2 \quad \text{Equation 2.43}$$

The matrices  $\mathbf{L}_m$  and  $\mathbf{L}_u$  are the G-antisymmetric and G-symmetric parts of  $\mathbf{L}$  according to,

$$\mathbf{L}_m = \frac{1}{2}(\mathbf{L} - \mathbf{G}\mathbf{L}^T\mathbf{G}) \quad \text{and} \quad \mathbf{L}_u = \frac{1}{2}(\mathbf{L} + \mathbf{G}\mathbf{L}^T\mathbf{G}) \quad \text{Equation 2.44}$$

in which  $\mathbf{G} = \text{diag}(1, -1, -1, -1)$  is the Minkowski metric matrix.

If the sample is non-depolarizing,  $\langle \Delta \mathbf{m}^2 \rangle = 0$  so that the  $\mathbf{L}_u = 0$  leaving  $\mathbf{L}(z) = \mathbf{L}_m$ . The matrix  $\mathbf{L}_m$  contains the elementary polarization properties of the sample; LD, LD', CD, LB, LB' and CB, evolving linearly along  $z$  axis as shown below:

$$\mathbf{L}_m = \begin{pmatrix} 0 & \text{LD} & \text{LD}' & \text{CD} \\ \text{LD} & 0 & \text{CB} & -\text{LB}' \\ \text{LD}' & -\text{CB} & 0 & \text{LB} \\ \text{CD} & \text{LB}' & -\text{LB} & 0 \end{pmatrix} \quad \text{Equation 2.45}$$

However, if the sample is depolarizing,  $\langle \Delta \mathbf{m}^2 \rangle \neq 0$  and the diagonal elements of  $\mathbf{L}_u$  show the depolarization coefficients,  $\text{diag}(\mathbf{L}_u) = (0, \alpha_1, \alpha_2, \alpha_3)$ , which depend quadratically on the propagation distance along  $z$ .

effect	symbol	definition <sup>a</sup>	Jones matrix
isotropic phase retardation	$\eta$	$\frac{2\pi}{\lambda}(n_x + n_y)l$	$\begin{bmatrix} e^{-i\eta} & 0 \\ 0 & e^{-i\eta} \end{bmatrix}$
isotropic amplitude absorption	$\kappa$	$\frac{2\pi}{\lambda}(k_x + k_y)l$	$\begin{bmatrix} e^{-\kappa} & 0 \\ 0 & e^{-\kappa} \end{bmatrix}$
horizontal linear dichroism projection	LD	$\frac{2\pi}{\lambda}(k_x - k_y)l$	$\begin{bmatrix} e^{-\text{LD}/2} & 0 \\ 0 & e^{\text{LD}/2} \end{bmatrix}$
horizontal linear birefringence projection	LB	$\frac{2\pi}{\lambda}(n_x - n_y)l$	$\begin{bmatrix} e^{-i\text{LB}/2} & 0 \\ 0 & e^{i\text{LB}/2} \end{bmatrix}$
45° linear dichroism projection	LD'	$\frac{2\pi}{\lambda}(k_{45} - k_{135})l$	$\begin{bmatrix} \cosh \text{LD}'/2 & -\sinh \text{LD}'/2 \\ -\sinh \text{LD}'/2 & \cosh \text{LD}'/2 \end{bmatrix}$
45° linear birefringence projection	LB'	$\frac{2\pi}{\lambda}(n_{45} - n_{135})l$	$\begin{bmatrix} \cos \text{LB}'/2 & -i \sin \text{LB}'/2 \\ -i \sin \text{LB}'/2 & \cos \text{LB}'/2 \end{bmatrix}$
circular dichroism	CD	$\frac{2\pi}{\lambda}(k_- - k_+)l$	$\begin{bmatrix} \cosh \text{CD}/2 & i \sinh \text{CD}/2 \\ -i \sinh \text{CD}/2 & \cosh \text{CD}/2 \end{bmatrix}$
circular birefringence	CB	$\frac{2\pi}{\lambda}(n_- - n_+)l$	$\begin{bmatrix} \cos \text{CB}/2 & \sin \text{CB}/2 \\ -\sin \text{CB}/2 & \cos \text{CB}/2 \end{bmatrix}$

<sup>a</sup>  $n$  stands for refractive index,  $k$  for the extinction coefficient,  $l$  for path length through the medium, and  $\lambda$  for the vacuum wavelength of light. Subscripts specify the polarization of light as,  $x$ ,  $y$ , 45° to the  $x$  axis, 135° to the  $x$  axis, circular right +, or left -.

Figure 2.14: Symbols and definitions of the polarimetric optical properties together with their respective Jones Matrix. Definitions are the phase shift expressed in radians. Note, this phase shift CB (expressed in radians) corresponds to twice the angle  $\theta$  that the vector of the electric field of a linearly polarized wave would have turned around the axis of propagation after passing through the sample e.g. the specific optical rotation  $\theta = \text{CB}/2$ . Adapted from Ref. [26]

## 2.6 Polarimetric instrumentation

Different types of polarimeter have been developed and they can be categorized depending on their applications and measurement techniques [27, 28]. The most basic concept of polarimeter is a Stokes polarimeter. Generally speaking, Stokes polarimeters consist of a single optical arm, which is equipped with a polarization state analyzer (PSA) and a detector to measure the Stokes vector components (I, Q, U, and V). In the most general configuration, the PSA is made of a succession of retarders, used to get access to the different types of retardation (linear and circular) as well as their orientation, followed by a linear polarizer, used to determine the diattenuation properties of the beam as well as its orientation. Since the Stokes polarimeters do not have an illumination arm to control the incident polarization states, they are applicable in areas such as astronomy, remote sensing, or characterization of light sources [29-31]. The first type of polarimeters is usually referred as Stokesmeters or Stokes polarimeters.

In the second type of polarimeter, the polarization of both, the illumination and the analysis part can be controlled. In general, these polarimeters are made of two arms and the sample to be studied is placed between them. Each arm is equipped with optical elements to control the polarization of the light. In the first arm, polarization states are generated, and in the second arm, polarization states are analyzed. In normal operation, the sample is sequentially illuminated with a set of well-defined polarization states. Then, each state, after being modified by the sample, is analyzed thanks to the optical elements in the second arm. As a result, measurements are retrieved, which allows characterizing the sample optical response. In general, the set of measurements are arranged to form a matrix. Depending on the physical properties of the sample, and the instrumentation used to build the polarimeter, the formalism used to write the matrices can be different.

If the interaction with the sample modifies the polarization state of the incoming light but preserves the polarization purity (polarization degree) then by convention, there is a tendency to refer to the instrument used to do the measurements as an ellipsometer, and the technique, whose goal is to characterize the optical properties is called ellipsometry. Thanks to their fast, accurate, and precise properties, the spectroscopic ellipsometers have achieved great success in semiconductor industries or other in-situ real-time characterization in the process of glass fabrication. However, they remain as an incomplete characterization technique since the Jones vectors are defined only for fully polarized states, so they cannot be conveniently used to explore situations in which the interaction of the light beam with the sample and the instrument itself modifies its degree of polarization.

A Mueller polarimeter, in contrast to an ellipsometer, is an instrument that is able to measure partially polarized light. Since a Mueller polarimeter can be also used as an ellipsometer to measure fully polarized light, a Mueller polarimeter can be understood as the most general and complete form of an ellipsometer. When working with partially polarized light, it is common to use a mathematical formalism representing polarization as a four-

dimensional vector, the Stokes vector, and consequently the optical properties of the sample in the form of a 4 by 4 matrix, called the Mueller matrix.

Regarding Mueller polarimeters, they can be sub-divided into two categories: spectroscopic polarimeters or imaging polarimeters. The spectroscopic polarimeters give a multi-wavelength characterization of the sample. The polarimetric imagers measure the spatial information of the sample. The spatial information can be a real surface when the system measures the real plane of the imaging lens. Another capability of the polarimetric imager is that it measures a spatial distribution of the scattered, transmitted, or reflected light when it focuses on Fourier plane of the imaging lens. The measurement in Fourier plane corresponds to the angle resolved measurement or the conoscopic measurement.

### 2.6.1 "de Sénarmont" compensator

The "de Sénarmont" compensator couples a highly precise quarter wave birefringent quartz or mica crystalline plate with a 180-degree rotating analyzer to provide retardation measurements having an accuracy that approaches one thousandth of a wavelength or less. The device is utilized for retardation measurements over an optical path difference range of approximately 550 nanometers (one wavelength in the green region) for the quantitative analysis of crystals, fibers, and birefringence in living organisms, as well as investigations of optical strain. In addition, "de Sénarmont" compensators are useful for emphasizing contrast in weakly birefringent specimens that ordinarily are difficult to examine under crossed polarized illumination.

As described by the Olympus resource centers, the principle behind the "de Sénarmont" compensation technique rests on the fact that the elliptically (or circularly) polarized light electric vector emerging from the specimen is superimposed upon the circular polarization vector introduced by the quarter waveplate to yield plane (linearly) polarized light having a vibration azimuth different from that of the polarizer (see Figure 2.15). The effect occurs because the quarter waveplate produces linearly polarized light from elliptically or circular polarized light that is incident on the crystal surface. The azimuth of the linear polarized light emerging from the compensator is a direct function of the optical path difference induced by the specimen. By rotating the analyzer until the specimen is extinct (dark), the azimuth of the vibration produced by the compensator can be ascertained along with the optical path difference introduced by the specimen.

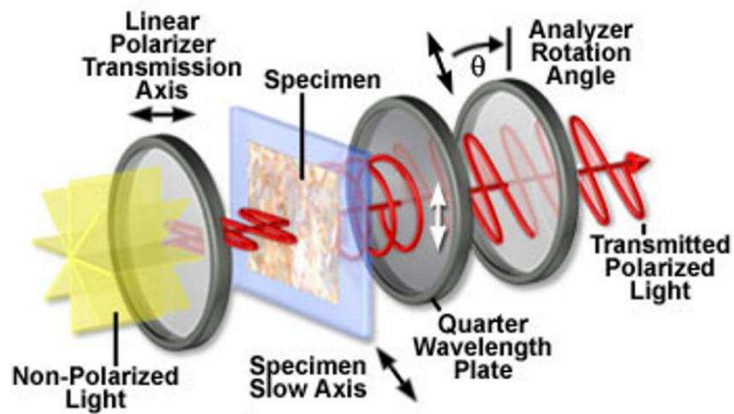


Figure 2.15: Diagram of the “de Sénarmont” compensator configuration with the OXY benchmarks related to the assembly reference and Oxy linked to the reference frame of the irradiated sample [source: <http://www.olympusmicro.com/>]

In order to obtain a measurement of specimen birefringence (and the related optical path difference), the “de Sénarmont” compensator is placed into the microscope optical train after the sign of birefringence and orientation of the specimen slow axis has been established with a first-order retardation plate. Without prior knowledge of the birefringent characteristics (positive or negative sign) of a specimen, it may be difficult to ascertain the correct extinction angle for the analyzer during “de Sénarmont” compensation measurements. For example, in some cases the same rotation angle of the analyzer can produce extinction for a positively birefringent specimen that retards the wavefronts and a negatively birefringent specimen that advances the wavefronts.

The rotation angle  $\theta$  of the analyzer at extinction is equal to one-half of the full phase shift ( $\theta = \frac{\phi_1}{2}$ ) between the orthogonal (ordinary and extraordinary) wavefronts passing through the specimen. Therefore, the relative retardation  $R$  (in nanometers) is described by the following equation:

$$R = \Delta n l = \theta \frac{\lambda}{\pi} \quad \text{or} \quad R = \Delta n l = \theta \frac{\lambda}{180} \quad \text{if } \theta \text{ is in degree} \quad \text{Equation 2.46}$$

In the case of the femtosecond laser written lines illustrated in Figure 2.16, the green interference filter has a narrow bandpass centered at 546 nm (i.e. around 3 nm per degree), and the analyzer rotation angle was 78,7 degrees. Therefore, the measured retardation value  $R$  for these lines is approximately 239 nm for a 546 nm probe. For highly accurate measurements of relative retardation, several trials should be conducted. In addition, the specimen can be rotated by 90-degrees and the analyzer rotated to the opposite side of the crossed position to obtain extinction for additional measurements (and better accuracy).



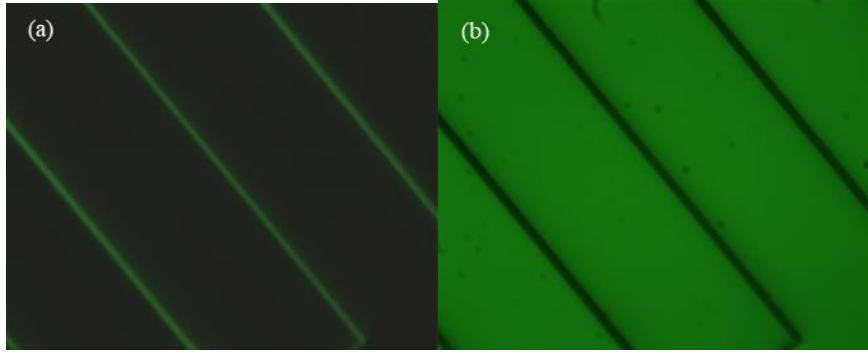


Figure 2.16: Image through the microscope eyepiece in the “de Senarmont” compensator configuration of laser irradiation traces (parallel fine lines) in a silica slide. (a): for a positioning of the crossed analyzer to the polarizer ( $\theta = 0^\circ$ ), the isotropic bottom appears black; (b): for a positioning of the analyzer minimizing the transmission of light through the irradiated areas.

**Determining the impact of errors:** The error on the determination of the delay  $\delta R$  is defined by the following equation, which has been deduced from the theoretical relation of the delay:

$$\delta R^2 = \left(\frac{\partial R}{\partial \theta}\right)^2 \delta \theta^2 + \left(\frac{\partial R}{\partial \lambda}\right)^2 \delta \lambda^2 = \left(\frac{\lambda}{\pi}\right)^2 \delta \theta^2 + \left(\frac{\theta}{\pi}\right)^2 \delta \lambda^2 \quad \text{Equation 2.47}$$

where  $\delta \theta$  is the error on the analyzer defined by the angle measured experimentally  $\theta_{\text{exp}}$  to regain the extinction of transmitted light subtracts from the initial angle  $\theta_0$  crossed with the polarizer. So we can deduce  $\delta \theta^2 = \left(\frac{\partial \theta}{\partial \theta_{\text{exp}}}\right)^2 \delta \theta_{\text{exp}}^2 + \left(\frac{\partial \theta}{\partial \theta_0}\right)^2 \delta \theta_0^2 = \delta \theta_{\text{exp}}^2 + \delta \theta_0^2$ ;  $\delta \lambda$  is the error on the wavelength defined by the interference filter. For a filter at 546nm, we determine a  $\theta_{\text{exp}}$  error of  $1,52^\circ$  over 40 measurements,  $\delta \theta_0 = 0,1^\circ$  and considering  $\theta_{\text{exp}} = 80^\circ$ , we get an error on the delay of  $\delta R = \sqrt{\left(\frac{\lambda}{\pi}\right)^2 \delta \theta^2 + \left(\frac{\theta}{\pi}\right)^2 \delta \lambda^2} = 4,9 \text{ nm}$ .

**Polarizer error:** a polarizer positioning error does not change the extinction angle of the transmitted intensity but only the amplitude of the transmitted intensity.

**Sample orientation error:** In the case of a sample positioning angular error  $\gamma$ , it has been modeled in the thesis of R. Desmarchelier [32] that this error relates to the measurement of  $\theta$ . So for an error:

- $\gamma = 5^\circ$ ,  $\theta_\gamma = 44,1^\circ$  (instead of  $45^\circ$ ) corresponding to an error of 4,1 nm on the retardance.
- $\gamma = 1^\circ$ ,  $\theta_\gamma = 44,9^\circ$  corresponding to an error of 3,1 nm on the retardance.

**Conclusion:** After developing the measurement of birefringence by the “de Sénarmont” method, we have seen how to measure  $\Delta n$  through the angle of the analyzer for which a minimum of transmitted intensity is observed. But when the sample has several anisotropic optical properties (linear or circular), we observe changes in the intensity transmitted but also a variation in the measured angle of the birefringence, especially when the sample has

circular dichroism or circular birefringence. In the simulations of R. Desmarchelier [32] related the linear birefringence measurement, he has shown that when circular properties are small ( $CB = \pi/160$  and  $CD = \pi/320$ ), the errors on the retardance are then less than 4 nm which is relatively low.

## 2.6.2 Circular Dichroism spectro-polarimeter - JASCO- J-810

The principle of measuring a circular dichroism spectrum is the measurement of the difference in intensity of an alternately polarized right and left circular light after passing through the sample to be analyzed [33]. This polarization modulation is obtained using a photo-elastic modulator (PEM) operating at the frequency of 50 kHz. The meter is called the spectropolarimeter or dichrograph (Figure 2.17). The spectrum given by the apparatus is the value of the ellipticity in millidegrees of the polarization of the beam at the output of the medium. JASCO J810 dichrograph measures this angle  $\theta$  rather than phase shift  $\phi_1 = 2\theta$ , while sometimes calling it optical activity, which can lead to confusion if one does not formalize the nature of the thing actually measured.

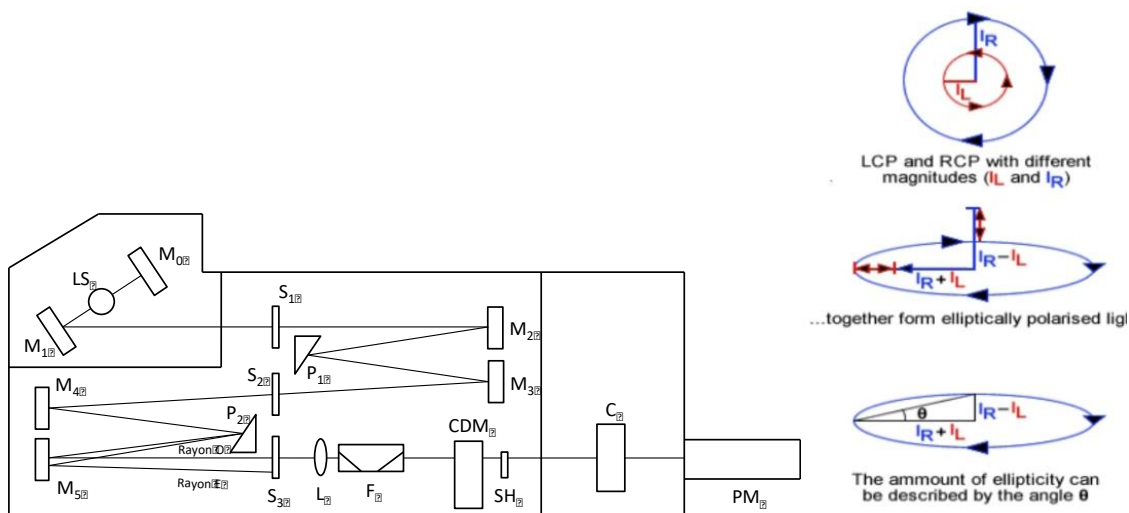


Figure 2.17: Diagram of JASCO J-810 spectropolarimeter (LS: mercury xenon lamp (163 to 900 nm); M<sub>0</sub> ... M<sub>5</sub>: mirrors; S<sub>1</sub> ... S<sub>3</sub>: slots; P<sub>1</sub> ... P<sub>3</sub>: prisms; L: lens; F: polarization filter; CDM: photo-elastic modulator; SH: shutter; C: analysis cell; PM: photomultiplier). Extracted from JASCO J-810 datsheet.

The most direct data is  $\Delta A = A_- - A_+$  (delta Absorbance) is the difference between absorbance of left circularly polarized (LCP) and right circularly polarized (RCP) light (this is what is usually measured).  $\Delta A$  is a function of wavelength  $\lambda$ , so for a measurement to be meaningful the wavelength at which it was performed must be known. This value is often reported in milliabsorbance units (mA), which are a thousandth of an absorbance unit. This is the same for  $\Delta\alpha'_c = \alpha'_- - \alpha'_+$  where  $\alpha'_{-,+}$  is the absorption coefficient usually expressed in  $\text{cm}^{-1}$ .

Although  $\Delta A$  is usually measured, for historical reasons most measurements are reported as a phase difference in the polarimetric community whereas in chemistry it is often reported as an angle in degrees (or millidegrees noted mdeg) of ellipticity  $\theta$  related to

electric field by the following relation:

$$\tan \theta = \frac{E_- - E_+}{E_- + E_+} = \frac{\sqrt{I_-} - \sqrt{I_+}}{\sqrt{I_-} + \sqrt{I_+}} \quad \text{Equation 2.48}$$

Generally, the circular dichroism effect is very small (typ.  $\theta < 1^\circ$ ), so  $\tan \theta$  is small and can be approximated as  $\theta$  in radians. Since the intensity or irradiance  $I$  is proportional to the square of the electric-field vector, the ellipticity becomes:  $\theta = \frac{\sqrt{I_-} - \sqrt{I_+}}{\sqrt{I_-} + \sqrt{I_+}}$ . Then by substituting for  $I$  using Beer's law in natural logarithm form:

$$I = I_0 \exp(-\alpha \cdot l) = I_0 \exp(-A \cdot \ln(10)) \quad \text{Equation 2.49}$$

The ellipticity can now be written as:

$$\theta(\text{radians}) = \frac{(e^{-\frac{A_R}{2} \ln 10} - e^{-\frac{A_L}{2} \ln 10})}{(e^{-\frac{A_R}{2} \ln 10} + e^{-\frac{A_L}{2} \ln 10})} = \frac{e^{\Delta A \frac{\ln 10}{2}} - 1}{e^{\Delta A \frac{\ln 10}{2}} + 1} \quad \text{Equation 2.50}$$

Since  $\Delta A \ll 1$ , this expression can be approximated by expanding the exponentials in a Taylor series to first-order and then discarding terms of  $\Delta A$  in comparison with unity and converting from radians to degrees:

$$\theta \text{ in degree} \approx \frac{\ln(10)}{4} \frac{180}{\pi} \Delta A_c = 32,98 \cdot \Delta A_c = \frac{32,98}{\ln(10)} \Delta \alpha'_c \cdot l \quad \text{Equation 2.51}$$

$$\theta \text{ in degree cm}^{-1} \approx \frac{\ln(10)}{4} \frac{180}{\pi} \frac{1}{l} \Delta A_c = 32,98 \cdot \frac{1}{l} \cdot \Delta A_c = \frac{32,98}{\ln(10)} \Delta \alpha'_c \quad \text{Equation 2.52}$$

These various ways to express the circular dichroism are summarized in Table 2.1. Note, this phase shift noted CD corresponds to twice the angle  $\theta$  that the vector of the electric field of a linearly polarized wave would have turned around the axis of propagation after passing through the sample i.e.

$$\theta = CD/2 \quad \text{Equation 2.53}$$

Table 2.1 Typical ways to express the circular dichroism or diattenuation in the literature: absorbance, molar extinction coefficient, molar ellipticity, angle in degrees or millidegrees.

From ↓ To →	Absorbance <sup>1</sup>	Milliabsorbance <sup>2</sup>	Molar Extinction <sup>3</sup>	Degrees <sup>4</sup>	Millidegrees <sup>5</sup>	Molar Ellipticity <sup>6</sup>
(A)	A	A*1000	A*M/(C*L)	A*32.98	A*32980	A*M*3298/(L*C)
(mA)	mA/1000	mA	A*M/(C*L*1000)	mA*0.03298	mA*32.98	mA*M*3.298/(L*C)
(ε)	ε*C*L/M	ε*C*L*1000/M	ε	ε*C*L*32.98/M	ε*C*L*32980/M	ε*3298
(°)	°/32.98	°/0.03298	°*M/(C*L*32.98)	°	°*1000	°*M*100/(L*C)
(m°)	m°/32980	m°/32.98	m°*M/(C*L*32980)	m°/1000	m°	m°*M/(10*L*C)
[Θ]	[Θ]*C*L/(3298*M)	[Θ]*C*L/(3.298*M)	[Θ]/3298	[Θ]*C*L/(100*M)	[Θ]*C*L*10/M	[Θ]

<sup>1</sup>Units are Absorbance (Abs)  
<sup>2</sup>Units are milliabsorbance (mAbs)  
<sup>3</sup>Units are A\*L/mol\*cm  
<sup>4</sup>Units are degrees (°)  
<sup>5</sup>Units are millidegrees (m°)  
<sup>6</sup>Units are deg\*cm<sup>2</sup>/dmol

C is concentration in g/L  
M is average molecular weight (g/mol)  
L is path length of cell (cm)

**Towards experimental data:** using Beer's law, the circular dichroism  $\Delta A_c$  is define by the expression:

$$\Delta A_c = A_- - A_+ = \log_{10} \left( \frac{I_0}{I_-} \right) - \log_{10} \left( \frac{I_0}{I_+} \right) = \log_{10} \left( \frac{I_+}{I_-} \right) \quad \text{Equation 2.54}$$

where  $I_{-,+}$  is the intensity transmitted to the photomultiplier (PM) after passing through the sample. By referring 2.6.2 in 2.6.1, we obtain the ellipticity measured by the device:

$$\theta \approx 32,98 \log_{10} \left( \frac{I_+}{I_-} \right) \quad \text{Equation 2.55}$$

Theoretically, the linear ellipticity can be defined by the ratio of the intensities transmitted according to their circular polarizations  $I_+/I_-$ . However, the determination of  $[\psi]$  with high precision is difficult using the Equation 2.55 because the value  $I_+/I_-$  is close to 1. To overcome this difficulty, we substitute the following quantities:

$$I_A = \frac{1}{2} (I_+ + I_-) \quad \text{Equation 2.56}$$

$$I_S = I_+ - I_- \quad \text{Equation 2.57}$$

The ratio  $I_S/I_A$  can be determined with sufficiently high precision in the case of experimental measurements. In practice, the dichrograph determines the quantities  $V_S$  and  $V_A$ , which are the output voltages of the multiplier tube (PM) corresponding to the light intensities  $I_S$  and  $I_A$ . The measurement of the intensities transmitted through the sample thus makes it possible to calculate the linear ellipticity (Eq. 2.55). This ellipticity is then connected to circular dichroism by a relation of proportionality as indicated below:

$$\begin{aligned}\theta \text{ in degree} &\approx 32,98 \cdot \Delta A_c = 32,98 \log_{10} \left( \frac{I_+}{I_-} \right) = \frac{32,98}{\ln(10)} \Delta \alpha'_c \cdot l \\ &= -\frac{32,98}{\ln(10)} 2 \frac{I_- - I_+}{I_+ + I_-}\end{aligned}\quad \text{Equation 2.58}$$

**Measurement errors:** According to the calculations developed in the thesis of Rudy Desmarchelier [32], we note that only the measurement error related to the dichrograph takes place for a sample having circular dichroism alone. Indeed the measurements are independent of the azimuth of the sample for example. Typical errors according to the range of measurements are as follows:

- 0.0005mdeg (at  $\pm 10$ mdeg on full scale)
- 0.01mdeg (at  $\pm 200$ mdeg on full scale)
- 0.1mdeg (at  $\pm 2000$ mdeg on full scale)

**Conclusion:** The propagation of light in a material is a continuous process, and cannot be presented as a "one-shot" interaction. As light propagates in the medium, the polarization of the wave progressively changes or even disappears due to effects such as linear retardation, diattenuation or depolarization. A beam of light, initially circularly polarized, changes its polarization as it propagates and, globally, it is refracted or absorbed with an index that is not  $n_+$  or  $n_-$ . Only in an isotropic optically active media the circular polarization is a Eigen-mode of propagation, which means that the circular polarization is preserved everywhere in the path-length. This is the only case where the method outlined above to measure circular dichroism works easily.

However we know that our samples written by femtosecond laser exhibit other anisotropic properties such as linear birefringence due to nanogratings formation and stress field. It was therefore interesting to model the influence of these other optical parameters on circular dichroism measurements in the case of a "perfect" dichrograph (e.g., with no residual constraints in the various elements making up the apparatus). In this framework our group [32] has shown that the measurement of circular dichroism (or more generally circular diattenuation) is strongly influenced for a sample having a mixture of multiple anisotropic optical properties if they have different distributions in depth. By extension, if there are some significant residual linear birefringence or linear dichroism within the experimental setup (like in the PM window), this could create some CD artifacts. These points will be discussed in chapter 3 in the light of our measurements. Alternatively it is advisable to use polarimetric solutions based on the determination of the Mueller matrix as described below and presented in chapters 4 and 5.

### 2.6.3 Vis-Near IR (400-1000nm) Mueller Ellipsometry – MM-16

The MM-16 is a spectroscopic Mueller matrix polarimeter based on liquid crystal devices. Owing to this unique technology the MM-16 has the ability to provide full Mueller Matrix measurements in addition to the capabilities of a classical ellipsometer for characterizing film thicknesses and optical constants with exceptionally high accuracy. The design of the instrument has been optimized in order to minimize the errors in the final result for a given magnitude of the errors in the raw measurements [34]. The design uses only fixed elements, with no moving parts during signal acquisition.

#### **Description of the optical setup used by the MM-16**

The light source is a combination of a tungsten-halogen lamp and a blue-LED to provide stable illumination across the visible spectra range from 400-1000 nm. The input head and the output head are identical and comprise of a polarizer, two ferroelectric liquid crystals and a fixed retardation plate. The light is analyzed by a spectrograph using a CCD detector and is able to deliver the complete 16-element Mueller matrix in 2 seconds with high accuracy and precision.

Any Mueller matrix polarimeter comprises [28] a polarization state generator (PSG), which generates at least four linearly independent polarization states  $\mathbf{S}_{in}$  forming the modulation matrix  $\mathbf{W}$ , and a polarization state analyzer (PSA), which analyzes  $\mathbf{S}_{out}$  by measuring its projections over at least another four linearly independent basis states to define the analysis matrix  $\mathbf{A}$ . With these notations, a set of 16 measurements of a sample characterized by a Mueller matrix  $\mathbf{M}$  can be written in matrix form  $\mathbf{B}=\mathbf{AMW}$ . The matrix  $\mathbf{M}$  can be extracted from  $\mathbf{B}$  if  $\mathbf{A}$  and  $\mathbf{W}$  are known and this information is provided by calibration of the system.

#### **Calibration and Setup**

Calibration of the instrument is rapid and straightforward. It is based on the Eigenvalue Calibration Method [35], which requires only a linear polarizer and retardation plate as reference samples. The plate retardation used as the reference is not critical and this method does not need a detailed description of the PSG and the PSA. The calibration is user-friendly and is performed automatically. The need of any optical or electrical fine adjustment is identified, and the quality of the instrument is evaluated during the calibration.

#### **Advantages and Limitations**

- **Undepolarized isotropic sample:** With an isotropic sample the Mueller data are redundant. Only two parameters are needed to describe the sample (usually  $\Psi$  and  $\rho$  or a complex number  $\rho$ ). However, measuring the complete Muller matrix allows us to increase the measurement accuracy and can be used for checking the consistency of the measurements. Two parameters are required to describe the sample for this case, but because we do not have direct access to these elements, the measurement of several parameters are needed

to achieve an optimized accuracy for the measured sample. The MM-16 measures  $\cos(2\Psi)$ ,  $\sin(2\Psi)\sin(\delta)$  and  $\sin(2\Psi)\cos(\delta)$  in one measurement without moving any optical elements, and this allows us to obtain quite easily the optimum accuracy for all values of  $\Psi$  and  $\delta$  for any sample

- **Undepolarized anisotropic sample:** For the case of anisotropic sample, six parameters are needed to describe the sample [36] (for example three complex numbers  $\rho$ ,  $\rho_s$  and  $\rho_p$ ). As with the isotropic case measuring the whole Muller Matrix allows us to improve the accuracy and precision of the measurements. As we do not have direct access to these three complex numbers the measurement of several parameters are required to achieve optimum accuracy. Classical ellipsometers are able to measure only a part of the Mueller Matrix and can only make this determination if many hardware configurations are used. These systems provide incomplete information regarding the polarization properties of a sample as they may only measure a maximum of 12 elements, and therefore may not be able to characterize all sample types. On the other hand the MM-16 provides the complete 16-elements Mueller Matrix in one measurement cycle.

- **Depolarization sample:** The MM-16 measures two different parameters: the classical degree of polarization  $P$  which can be measured using a phase modulated ellipsometry (PME [37]) and rotating compensator ellipsometry (RCE) if several configurations are defined but the general degree of polarization can only be measured with a Mueller Matrix polarimeter defined as shown above:

$$P_q = \sqrt{\frac{\sum_{ij} M_{ij}^2 - M_{11}^2}{3M_{11}^2}} \quad \text{Equation 2.59}$$

**Conclusion:** This innovative system extends the range of application of ellipsometry to cover all classes of samples ranging from isotropic to non-isotropic materials simply and accurately. Indeed by having the ability to measure the complete Mueller Matrix the MM-16 simplifies the characterization of unknown samples. Most anisotropic phenomena may be detected and classified, and the user receives information on the degree of anisotropy and its orientation to model complex sample types quickly and efficiency.

## 2.6.4 UV-Vis-Near-IR Mueller ellipsometry – MM-12

The UVISEL spectroscopic ellipsometer of HORIBA Jobin-Yvon use photoelastic modulators to perform polarization modulation at a high frequency (50 kHz) without any mechanical movement. Owing to this technology these systems have the advantage of being very fast, having no moving parts and providing high accuracy measurements over a wide spectral range without the need for extra optical elements. Phase modulation allows the achievement of higher sensitivity for the characterization of thin film thickness and optical constants when compared with conventional ellipsometers.

## Description of the optical setup used by the MM-12

The light source is a Xenon lamp that covers a large spectral range from 190 to 2100 nm. After passing through the first polarizer, which establishes a linear polarization, the light reflects at oblique angle (generally  $70^\circ$ ) from the sample under study. The output head comprises a photoelastic modulator and an analyzing polarizer that resolves the polarization state of the reflected beam. However the setup can also operate in transmission mode as we made in this thesis.

Both polarizers are held fixed during the measurement while the photoelastic modulator is used to induce a modulated phase shift of the reflected beam. The photoelastic modulator is a fused silica bar exhibiting isotropic behavior when no stress is applied. The photoelastic modulator is an optical element that can be described as a birefringence modulator. If a mechanical strain is applied to the quartz bar (e.g. by a piezoelectric transducer attached to the end of the bar), the modulator becomes birefringent ( $n_o \neq n_e$ ). This means that light travels along one axis faster than the other when passing through it, which produces a different phase velocity for each, and a modulated phase shift is induced to the light beam.

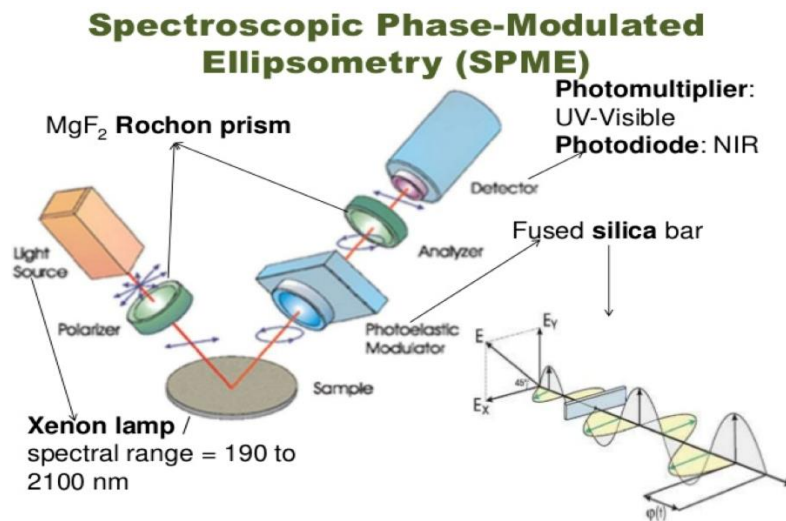


Figure 2.18: Optical setup of the UVISEL and Schematic of the photoelastic modulator working. Scheme from Horiba Jobin Yvon UVISEL datasheet.

The light is analyzed by a monochromator that directs sequentially the light for each individual wavelength onto the detector. Two types of detectors are available: photomultipliers for UV-VIS applications, and InGaAs photodiodes for NIR applications. Scanning monochromator systems have the advantage of controllable bandwidth providing very accurate experimental spectra, high resolution that is useful for thick layer applications and excellent repeatability of the measurements. The configuration of the UVISEL phase modulated ellipsometer is shown in 错误!未找到引用源。 . Finally by measuring  $I_s$ ,  $I_c$  and  $I_{c'}$ , UVISEL allows the calculation of  $\Psi$  and  $\Delta$  as follows:



$$I_s = \sin 2\Psi \sin \Delta$$

$$I_c = \sin 2\Psi \cos \Delta$$



Provides an accurate measurement of the  $\Delta$  parameter over the full range [0 – 360°].

and

$$I_s = \sin 2\Psi \sin \Delta$$

$$I_{c'} = \cos 2\Psi$$



Provides an accurate measurement of the  $\Psi$  parameter over the full range [0 – 90°].

## Advantages and Limitations

- **Wide spectral range coverage:** A major advantage is that a wide spectral range from the UV to the Near-IR is covered without the need for several hardware configurations, and without moving any optical elements, the UVISEL provides a continuous and accurate measurement over the wide spectral range from 190 to 2100 nm.

- **Large acceptance angle:** The photoelastic modulator optical element has a large tolerance of the incident angle allowing more simple alignment of the system. As the light beam need not follow the principal axis of a rotating element this is a great advantage when performing measurements in liquid cells, on deposition / etch reactors in-situ.

- **Microspot capability:** The UVISEL integrates mirror based optical coupling to the sample providing a microspot capability up to 50  $\mu\text{m}$  over the whole spectral range. Measurements with microspot are useful for the characterization of patterned materials found in semiconductor wafers, display materials, and biosensors. It provides as well several advantages for the analysis of rough layers and devices with transparent substrates.

- **High accuracy measurements for all values of Psi and Delta:** The phase modulated ellipsometer delivers optimum accuracy for all values of  $\Psi$  and  $\Delta$  for any sample by measuring the parameters. Straight-through ellipsometric measurements of air performed on UVISEL in the range 1.5 – 5 eV with a fixed 2000 ms integration time leads to  $\Psi = 45^\circ \pm 0,01^\circ$  and  $\Delta = 0^\circ \pm 0,02^\circ$ .

- **High sensitivity:** The sensitivity of an ellipsometer is determined by all the different components used. When a PEM is used as the key component, its 50 kHz modulation frequency provides a wide dynamic range without noise. When combined with powerful digital signal averaging the UVISEL phase modulated ellipsometer features an excellent signal to noise ratio from the UV to Near-IR.

- **Fast data acquisition speed:** With a modulation frequency of 50 kHz the phase modulated ellipsometer can work with response times as short as 1ms/point, and with good signal : noise ratio. This makes the instrument the ideal system for real-time process control, and to follow dynamic studies and liquid-surface measurements in real-time.

- **Advanced measurement capability / Depolarization effects:** Depolarization can occur in case of incoherent reflection, roughness, scattering, inadequate spectral resolution, inhomogeneity. By measuring  $I_s$ ,  $I_c$  and  $I_{c'}$  the UVISEL software allows the calculation of the

degree of polarization DOP as defined as:

$$P = (I_s)^2 + (I_c)^2 + (I_c)^2 \quad \text{Equation 2.60}$$

• **Advanced measurement capability / Mueller Matrix:** up to 12 elements of the Mueller matrix can be measured by the UVISEL - Phase Modulated Ellipsometer. Mueller matrix measurements are useful when the sample is both depolarizing and anisotropic. Determination of the Mueller matrix elements was performed using 8 different configurations. The relations for the intensities  $I_o$ ,  $I_s$ , and  $I_c$  of a phase-modulated ellipsometer in the configuration ASMP (analyzer - sample - modulator - polarizer) with a sample represented by the corresponding Mueller-Matrix  $M$  are described in technical documentation of the UVISEL.

## 2.7 Conclusions

In this chapter, after describing the femtosecond laser direct writing experiments, we introduced the fundamentals of polarization of light and in particular a linear algebra called Mueller formalism. The three main polarimetric properties are introduced: the dichroism (or diattenuation), the birefringence (or retardation) and the depolarization. For the depolarizing power, which shows the capability to decrease the DOP, there have been many studies to define it. In this thesis, we mostly focused on the parameters from the logarithmic decomposition such as the polarization properties (LD, LD', CD, LB, LB' and CB) and the depolarization coefficients. Indeed the configurations of the Spectro-polarimeters used in this thesis are in transmission and the studied samples are transparent without discrete layers that show separated polarimetric responses but this will be discussed later in chapter 4.

## 2.8 References

1. Marshall, G.D., M. Ams, and M.J. Withford, *Direct laser written waveguide-Bragg gratings in bulk fused silica*. Optics Letters, 2006. **31**(18): p. 2690-2691.
2. Zhang, H., et al., *Type II high-strength Bragg grating waveguides photowritten with ultrashort laser pulses*. Optics Express, 2007. **15**(7): p. 4182-4191.
3. Zhang, H., S.M. Eaton, and P.R. Herman, *Single-step writing of Bragg grating waveguides in fused silica with an externally modulated femtosecond fiber laser*. Optics letters, 2007. **32**(17): p. 2559-2561.
4. Nemoto, S., *Waist shift of a Gaussian beam by plane dielectric interfaces*. Applied optics, 1988. **27**(9): p. 1833-1839.
5. Fernandes, L.A., et al., *Femtosecond laser writing of waveguide retarders in fused silica for polarization control in optical circuits*. Optics Express, 2011. **19**(19): p. 18294-18301.
6. Jones, R.C., *A new calculus for the treatment of optical systemsiii. the sohncke theory of optical activity*. Josa, 1941. **31**(7): p. 500-503.
7. Jarrendahl, K. and B. Kahr, *Hans Mueller (1900-1965)*. Woollam Journal, 2011.
8. Stokes, G.G., *XXX. On the change of refrangibility of light*. Philosophical transactions of the Royal Society of London, 1852(142): p. 463-562.
9. Stokes, G.G., *Memoir and Scientific Correspondence of the Late Sir George Gabriel Stokes, Bart.: Selected and Arranged by Joseph Larmor*. Vol. 2. 2010: Cambridge University Press.
10. Vizet, J., *Conception d'un dispositif de caractérisation polarimétrique de Mueller à travers une fibre optique endoscopique, destiné à l'imagerie biomédicale avancée*, 2016, Université de Limoges.
11. Yoo, T.S.H., *Application of a Multimodal Polarimetric Imager to Study the Polarimetric Response of Scattering Media and Microstructures*, 2018, Univseristy Paris Saclay.
12. Lu, S.-Y. and R.A. Chipman, *Interpretation of Mueller matrices based on polar decomposition*. JOSA A, 1996. **13**(5): p. 1106-1113.
13. Espinosa-Luna, R., et al., *Dealing depolarization of light in Mueller matrices with scalar metrics*. Optik, 2010. **121**(12): p. 1058-1068.
14. Ossikovski, R., *Alternative depolarization criteria for Mueller matrices*. JOSA A, 2010. **27**(4): p. 808-814.
15. Perez, J.J.G. and R. Ossikovski, *Polarized Light and the Mueller Matrix Approach*. 2016: CRC Press.
16. Ossikovski, R., *Differential and product Mueller matrix decompositions: a formal comparison*. Optics letters, 2012. **37**(2): p. 220-222.

17. Morio, J. and F. Goudail, *Influence of the order of diattenuator, retarder, and polarizer in polar decomposition of Mueller matrices*. Optics letters, 2004. **29**(19): p. 2234-2236.
18. Ossikovski, R., A. De Martino, and S. Guyot, *Forward and reverse product decompositions of depolarizing Mueller matrices*. Optics letters, 2007. **32**(6): p. 689-691.
19. Cloude, S.R., *Group theory and polarisation algebra*. Optik (Stuttgart), 1986. **75**(1): p. 26-36.
20. Le Roy-Brehonnet, F. and B. Le Jeune, *Utilization of Mueller matrix formalism to obtain optical targets depolarization and polarization properties*. Progress in Quantum Electronics, 1997. **21**(2): p. 109-151.
21. Garcia-Caurel, E., et al., *Ellipsometry at the Nanoscale*. Ellipsometry at the Nanoscale, chapter Advanced M, 2013: p. 225-256.
22. Soleillet, P., *Sur les paramètres caractérisant la polarisation partielle de la lumière dans les phénomènes de fluorescence*. AnPh, 1929. **10**(12): p. 23-97.
23. Azzam, R., *Propagation of partially polarized light through anisotropic media with or without depolarization: a differential 4x 4 matrix calculus*. JOSA, 1978. **68**(12): p. 1756-1767.
24. Ossikovski, R., *Differential matrix formalism for depolarizing anisotropic media*. Optics letters, 2011. **36**(12): p. 2330-2332.
25. Arteaga, O., *Historical revision of the differential Stokes–Mueller formalism: discussion*. JOSA A, 2017. **34**(3): p. 410-414.
26. Arteaga, O. and A. Canillas, *Analytic inversion of the Mueller-Jones polarization matrices for homogeneous media*. Optics letters, 2010. **35**(4): p. 559-561.
27. Goldstein, D., *Polarized Light, Second*. Mercel Dekker, New York, 2010.
28. Chipman, R.A., *Handbook of Optics: Ch. 22 Polarimetry*, 2010, McGraw-Hill.
29. Kemp, J.C., et al., *The optical polarization of the Sun measured at a sensitivity of parts in ten million*. Nature, 1987. **326**(6110): p. 270-273.
30. Povel, H., C. Keller, and I.-A. Yedigargolu, *Two-dimensional polarimeter with a charge-coupled-device image sensor and a piezoelastic modulator*. Applied Optics, 1994. **33**(19): p. 4254-4260.
31. Stenflo, J.O., *Stokes polarimetry of the Zeeman and Hanle effects*, in *Observing Photons in Space*. 2013, Springer. p. 583-598.
32. Desmarchelier, R., *Analyses des forces photo-induites par le laser femtoseconde dans les verres à base de silice*, 2014, Paris 11.
33. Johnson, W.C., *Circular dichroism instrumentation*, in *Circular Dichroism and the Conformational Analysis of Biomolecules*. 1996, Springer. p. 635-652.
34. De Martino, A., et al., *General methods for optimized design and calibration of Mueller polarimeters*. Thin Solid Films, 2004. **455**: p. 112-119.

35. Compain, E., S. Poirier, and B. Drevillon, *General and self-consistent method for the calibration of polarization modulators, polarimeters, and Mueller-matrix ellipsometers*. Applied optics, 1999. **38**(16): p. 3490-3502.
36. Jellison Jr, G.E., *Data analysis for spectroscopic ellipsometry*. Handbook of Ellipsometry, 2005.
37. Ossikovski, R., et al., *Anisotropic incoherent reflection model for spectroscopic ellipsometry of a thick semitransparent anisotropic substrate*. Applied Optics, 2000. **39**(13): p. 2071-2077.



# Chapter3 Study of laser induced circular dichroism using a CD spectro-polarimeter

---

## Content

3.1 Introduction.....	112
3.2 Samples and Methodology.....	113
3.3 Preliminary experiments to identify the modifications thresholds of linear optical properties.....	116
3.3.1 Study of writing kinetics at various repetition rates.....	116
3.3.2 Study of writing kinetics according to the numerical aperture.....	118
3.3.3 Study of writing kinetics according to the laser polarization.....	119
3.3.4 Spectral measurements of the retardance and linear extinction difference.....	120
3.4 Study of femtosecond laser irradiated silica using a CD spectro-polarimeter.....	121
3.4.1 Preliminary observations.....	121
3.4.2 Study of circular diattenuation CD according to the pulse energy.....	122
3.4.3 Study of circular diattenuation CD according to the line-to-line spacing.....	123
3.4.4 Study of circular diattenuation CD according to the angle between polarization orientation and the laser scanning direction.....	126
3.4.5 Study of circular diattenuation according to the pulse-to-pulse overlapping rate and the laser repetition rate.....	129
3.4.6 Study of circular diattenuation according to the focusing depth....	131
3.5 Analysis of CD measurements artifacts and asymmetric transmission of circularly polarized light.....	132
3.5.1 Study of CD artifacts due to the spectro-polarimeter.....	132
3.5.2 Investigations of Asymmetric transmission of circularly polarized light.....	135
3.6 Discussion on the origin of fs laser-induced chiral optical property..	137

3.6.1 An introduction to chirality and chiral optical properties in molecules	137
3.6.2 Qualitative interpretation of our key results	138
3.7 Conclusions	140
3.8 References	144



## 3.1 Introduction

Femtosecond laser pulses focusing in silica are absorbed through nonlinear photoionization mechanisms, which induce various modifications in the glass volume depending on the laser parameters such as refractive index changes [1], the formation of 3D nanostructuring [2], or voids [3]. Applications are numerous in a large number of domains for health [4], electronics, optical data storage [5-7], optofluidics [8, 9]) and optical components like 3D optical waveguides [1, 10] or polarizing optical devices [11-14]. Research efforts are considerable in the optical materials as it is possible to achieve strong refractive index increase (a few  $\pm 10^{-3}$  to more than  $\pm 10^{-2}$  in a large range of transparent glasses) localized in the bulk (due to strong non-linear effect) and because the spatial resolution coincides with the requirement for waveguide elaboration (a few  $\mu\text{m}$ ). It is thus necessary to know how to control the interaction of femtosecond laser light with optical materials and in particular with optical glasses, the most important of them being silica. If one proves to be able to control the forces involved in these processes, one could exceed the current applications of the lasers and open new possibilities in materials sciences.

In the past decade, several new and innovative observations have been discovered: nanogratings for high birefringence application with polarization direction dependence [15], "quill" writing [16] with dependence of modification with the direction of writing, silica decomposition [17], shear stress induced field [18] and an efficient creation of oriented anisotropic defects [19]. Taylor reported highly ordered « chiral-like » nanostructures using circular polarized laser light [20] but no circular optical properties. All these findings show that asymmetric printing in-centrosymmetric medium could be controlled [21].

In 2008, Poumellec et al. [22] ascertain by measuring the surface topography of a cleaved sample (yz plane) in which damage lines have been written in volume by scanning along the +x and -x axis with a femtosecond laser, that matter shearing occur along the laser track with alternating sign. This creates up/down, down/up surface topography that evolves along the laser track cross-section (scissor or chiral effect). Note that the shearing in the head of the laser tracks changes its sign with the change in scanning direction (pen effect or non reciprocal writing). We also show that nanostructures in the head are nano-shearing, with all the same sign whatever the direction of writing may be. So our group suggests that symmetries revealed by the shearing mimic the laser induced electron plasma density structures and inform on their unusual symmetries induced by the laser beam structures. It was quite surprising to see that a linearly polarized Gaussian beam can create such chiral mechanical structures. However, recently we demonstrated that another phenomenon occurring in the laser-matter interaction can lead to imprint chiral optical properties within a glass material. This might reveal a kind of transmission asymmetry (the reciprocity of the light propagation in the glass is broken) by efficient chiral optical structure creation. This could involve the creation of chiral forces like the creation of torque with a tightly focused femtosecond laser in transparent glass by combination of non-linear effects as suggested by Poumellec et al. [23].

This opens the door towards the creation and the control of circular properties namely rotating power and circular dichroism. Nowadays, it is not possible to obtain similar optical properties in solids with the exception of the creation of specific single crystals. Optical activity plays a crucial role in analytical chemistry, biological sensing, and optoelectronic devices. It is thus of great importance to create, analyze and control circular optical properties that might occur in the laser–matter interaction including within a glass material. The mechanism of interaction of the femtosecond laser light with dielectric materials is not fully understood but one recognized specificity due to the very small pulse duration is that the action of the light on electrons and ions is decoupled. Then, by choosing the correct configuration of the beam (e.g. pulse front tilt, polarization orientation and scanning direction) for controlling the ponderomotive force, we can imagine forcing the electrons to move towards one particular side of the beam, creating inhomogeneous plasma. Therefore the control of light intensity gradient and of the laser polarization according to the displacement should lead to the control of local symmetry and its orientation. In addition, an extensive amount of literature have reported the following two phenomena when strongly focusing inside an optical material: (1) self-focusing when the pulse energy exceeds the threshold (0.35  $\mu\text{J}/\text{pulse}$  in silica), and (2) spatial aberrations which increase with focus depth. Both phenomena should impact the creation of circular optical properties. In this chapter, we discuss the results based on the set of samples prepared via different laser writing parameters to investigate the dependence of the writing laser polarization, pulse energy, focusing conditions, and the pulse-to-pulse overlapping rate on the photo-induced circular dichroism.

## 3.2 Samples and Methodology

### *Femtosecond laser writing*

The laser radiation, in a Gaussian mode, was produced by a femtosecond laser system (Satsuma, Amplitude Systèmes Ltd.) operating at 1030nm and delivering pulses of 250fs at a repetition rate of 100 kHz. Considering that the propagation vector  $\vec{k}$  is along  $\vec{z}$  direction, the beam was focused from 100  $\mu\text{m}$  above to few 100's  $\mu\text{m}$  below the entry surface of 1-mm-thick silica plates (SuprasilCG from Heraeus) using a 0.6 NA (or 0,16 NA) aspheric lens. The writing configurations defined by writing and polarization directions are shown in Figure 3.1.

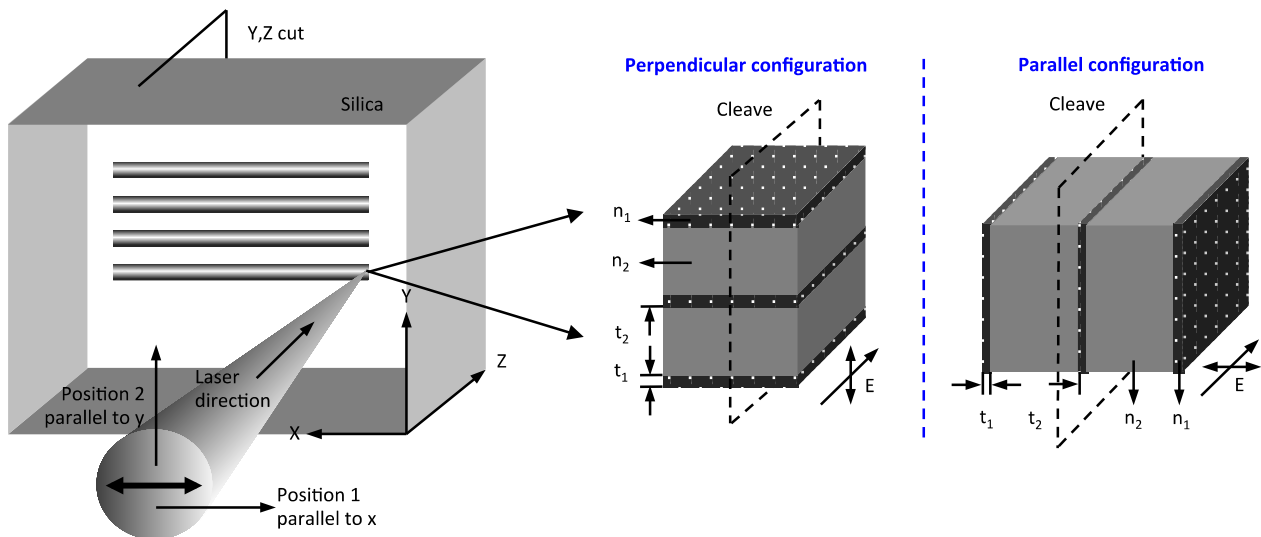


Figure 3.1 Experimental setup scheme writing and schematic of sub-wavelength periodic structure formed in cross-section of the irradiated region.  $n_1$  et  $n_2$  : local refractive indices of the nanoplates;  $t_1$  and  $t_2$ , are their respective thicknesses.

Therefore, when the laser was moving along X (or Y) and the polarization was lying along x, it is defined as “Xx writing” (or “Yx writing”). Then moving the sample along X or Y-axis with scanning speed in the range from 10 up to 1000  $\mu\text{m/s}$ , we wrote either single lines, or, a few mm squares made of group of lines. The lines or the squares were all photo-induced in silica plates with various pulse energies ranging within a few fractions of  $\mu\text{J}$  per pulse and also with the polarization direction either along the X, or, the Y-axis. The lines were written paying attention to their direction (referenced to the laboratory) and orientation (e.g. left to right and right to left). In the usual cases the irradiated squares were written following a linear scanning trajectory with a 1  $\mu\text{m}$  pitch to achieve uniformly scanned region and eliminate any diffraction effects. Then, some single laser lines were observed in transmission using a polarized optical microscope for detecting neutral axes, determining slow axis orientation, optical rotation power and for measuring the linear birefringence by using the Sénarmont method. Squares samples were used to perform the circular dichroism measurements using a JASCO J-810 spectro-polarimeter equipped with a 50kHz photoelastic modulator. Measurements were performed in the 185-700nm range with a 1nm spectral resolution and with a 2s integration time resulting in an error of less than 1mdeg.

Here are the series of sample list for study the writing laser parameter dependence.

Table 3.1 list of the main samples used in chapter 3 together with the different laser writing parameters.

Writing config.	Line gap ( $\mu\text{m}$ )	Pulse energy ( $\mu\text{J}$ )	Focusing depth ( $\mu\text{m}$ )	NA	Repetition rate (kHz)	Scanning speed ( $\mu\text{m/s}$ )	Overlapping rate (pulse/ $\mu\text{m}$ )
Xy	1	1.5	300	0.6	100	1000	100
	2						
	3						
	5						
	10						
Xy	1	1.5	300	0.6	100	1000	
Xx							

X45							
X-45							
X45	1	0.15	300	0.6	100	1000	
		0.5					
		1.0		0.16			
		1.0					
		1.5		0.6			
		2					
		4					
		6					
X45	1	1.5	100	0.6	100	1000	
			200				
			300				
			400				
			600				
			800				
X45	1	1.5	300	0.6	10	1000	10
					50		50
					100		100
					200		200
					500		500
					100		100
					1000		1000
X0-360°	1	1.5	300	0.6	100	1000	100

Measurement of circular dichroism CD in the presence of heterogeneous linear dichroism in depth but transversally (xy plan) homogeneous. Usually CD is measured in homogeneous and centrosymmetric substances but no circular symmetry like a liquid. It is measured by recording the light attenuation through the sample alternating left and right circular polarization using a photo-elastic modulator. The attenuation difference normalized by the sum is called the ellipticity  $\theta$  expressed in mdeg. The relation with the circular dichroism is  $\theta = (\alpha_L - \alpha_R)e/2$ , where  $\alpha$  is the absorption coefficient and  $e$  is the circular property thickness. However, this is true only for a sample that exhibits neither linear birefringence nor linear dichroism.

In the case of a sample mixing uniformly linear and circular properties in depth, the isotropy is broken and we can suspect a dependence on the azimuthal position of the sample. The calculation shows that it is not the case and the angular position of the neutral axes of the sample can be ignored [25].

In the case of a sample exhibiting non-uniform distribution of linear and circular properties, any series of rotator and a linear phase shifter matrices can be reduced to a simple combination of one rotator ( $R$ ) and one linear phase shifter ( $D$ ) matrices in arbitrarily

order containing equivalent rotation angle, equivalent slow axis angle, and equivalent dephasing angle. In addition, in the case of linear properties much larger than the circular one, equivalent orientation of the slow axis of the equivalent linear phase shift can be ignored and set to zero. It is thus possible to simulate the sample action as  $R(\varphi)D(\phi)$  through one face and  $D(\phi)R(\varphi)$  through the other face, arbitrarily.  $\varphi$  is the complex circular angle containing the circular birefringence ( $Im(\varphi)$ , imaginary part) and dichroism ( $Re(\varphi)$ , Real part).  $\phi$  is the same for linear properties. In this case, the ellipticity  $\theta$  is deduced from  $\tanh(\theta) = \tanh(2Im(\varphi))$  when incident on one face and  $\tanh(\theta) = \tanh[2Im(\varphi)] \cos[Re(\phi)] / \cosh[Im(\phi)]$  when incident on the other sample face. This shows that the ellipticity difference between faces arises from the linear optical properties and that a non-zero ellipticity indicates the presence of circular dichroism under these hypotheses as we discuss in Ref. [26].

From practical point of view, this shows that the light propagation is likely to be non-reciprocal (or more accurately called asymmetric transmission in the literature) in our samples and thus ellipticity measurements have to be made from both sides of the sample. Thus in this chapter all experiments were repeated by turning the backside of the irradiated sample toward the light source, thus effectively changing the sign of the wave vector. The turn over was done by rotating the sample  $180^\circ$  around the y-axis of the instrument system of reference. In the first pass, light was incident on the sample front face (forward configuration) i.e. the face through which femtosecond laser was focused and in the second pass; light entered the sample through the glass substrate back face (backward configuration).

### 3.3 Preliminary experiments to identify the modifications thresholds of linear optical properties

#### 3.3.1 Study of writing kinetics at various repetition rates

In previous PhDs or on the literature, it was already demonstrated that with increase of laser power (pulse energy), retardance increases until certain value and then saturates. However the laser pulse energy has also other influence on modification such as smoothness and nature of the involved modifications (e.g. Type I, Type II, Type III). For all samples, we wrote series of straight lines with various femtosecond laser pulse energies ranging from  $E \sim 0.05$  to  $E \sim 4$  J/pulse. For each series, 6 lines were produced with a linear polarization oriented along the y-axis (perpendicular configuration). Identical sets of lines were fabricated at four different repetition rates: 100kHz, 250kHz, 500kHz and 1MHz (Figure 3.2). Laser beam was focused below the entry surface of 1-mm-thick silica plates (SuprasilCG) with 0.6 NA aspheric lens. In order to induce nanogratings, pulse densities of few tens to few hundred pulses are required (this number varies for different pulse energies) [27-29]. However recently the polarization sensitive structuring in porous glass by two pulses of ultrafast laser irradiation has been demonstrated [30].

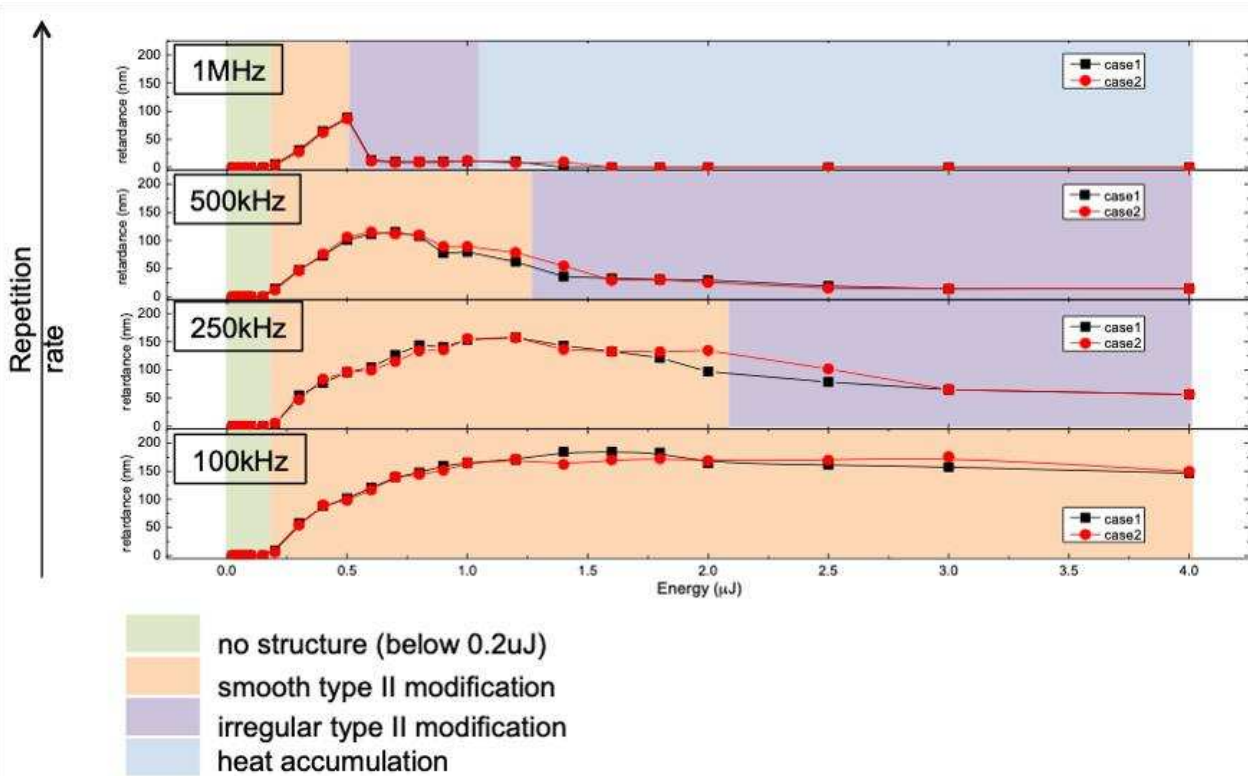


Figure 3.2: Growth kinetics of the fs laser-induced retardance  $R$  (in nm) according to the pulse energy. The pulse-to-pulse repetition rate was varied from 100 kHz up to 1 MHz to investigate the Type II processing windows. Measurements were repeated for both faces so called “case1” for the front face and “case2” for the back face. Laser writing conditions: 1030 nm, 250 fs, 0.6 NA, 300  $\mu\text{m}$  focusing depth, 1 mm/s scanning speed, SuprasilCG.

Then the retardance  $R$  (proportional to the linear birefringence  $B$ ) was measured using the Sénarmont compensator technique. Depending on the laser power we can see three distinctive phases of modification. At lowest laser power, we have birefringent and very uniform modification exhibiting refractive index decrease (Type II modification) which is visible using optical transmission imaging in crossed polarizers. Retardance value increases with increase of laser power until it reaches maximum. Depending on other laser parameters (focusing conditions, pulse duration, writing speed), the required pulse energy to induce such modification can vary. For example if fabrication speed would be lower, even at lowest power (just above threshold) nanogratings would be induced. And if we have shorter pulse duration (typ. below 200fs) and lower NA focusing lens, even at high pulse energy Type I modification is induced as it can be seen in the literature [31]. With higher pulse energy smooth strong irregularities in the structure and retardance decrease. Further increase in the laser pulse energy results in the formation of void-like structure especially at high repetition rate i.e. 1MHz. *Note that all retardance measurements (Figure 3.2) reveal very small difference (within error bars) between the two measurements configurations (front face and back face) whatever the energy and the repetition rate.*

With repetition rates below 500 kHz, quarter-wave retardance value (128.75 nm) at 515 nm can be achieved. Therefore we can conclude that in order to fabricate quarter-wave plate (or any optical element based on micro quarter-wave plates) following parameters can be used: 250-300 fs pulse duration, 100-500 kHz laser repetition rate, 0.6 NA objective to

focus the laser beam, 1 mm/s fabrication speed, 0,8-1 J/pulse. However, we cannot achieve retardance as high as half-wave value (257.5 nm) at 515 nm. Even though decreasing the repetition rate to avoid heat accumulation effects, it still saturates at around 200 nm. Reducing writing speed down to 0,1 mm/s will allow reaching half-wave retardance, but that would increase time required for fabricating optical elements with a practical size.

### 3.3.2 Study of writing kinetics according to the numerical aperture

Another way to increase retardance value is to focus laser beam with lower NA objective or lens. It can be explained by the fact that beam focused with lower NA lens will produce longer structure. Retardance value depends not just on birefringence ( $n_o - n_e$ ) but also on the length of the structure:

$$R = (n_o - n_e) \times d \quad \text{Equation 3.1}$$

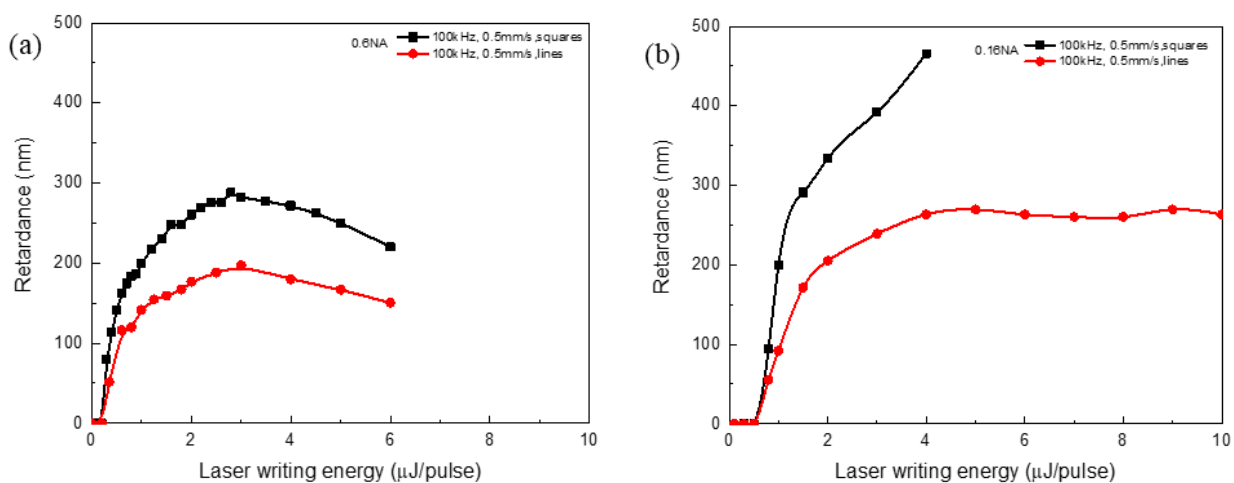


Figure 3.3: Retardance (in nm) according to laser writing energy for single lines versus square samples. Samples were written in Xy configuration (i.e. scanning direction along X and laser polarization along Y axis). Laser writing conditions: 1030 nm, 250 fs, 100 kHz, 300 μm focusing depth, 1mm/s scanning speed, SuprasilCG. (a) 0,6 NA laser writing; (b) 0.16 NA laser writing.

The 0,6 NA focusing lens was changed with low NA aspheric lens (NA = 0.16), structures were written again and retardance measured (Figure 3.3). In addition it should be highlight that waveplates or micro-waveplates are usually written by assembling a set of lines to create some homogeneous area with a size ranging from a few 10's μm up to cm. We have thus compared in the following figure: since lines and 0,1mm squares made of lines with a pitch of 1 μm. Firstly we can see that with lower NA, the threshold for inducing nanogratings increased, but it became possible to reach higher retardance value. Also the objects design strongly impacts the amplitude resulting a much higher retardance for squares when compares to single lines. For 0,6 NA squares results in 280nm retardance at the plateau in comparison to 200nm for a single line. For 0,16 NA, the retardance can be as high as 700nm for the squares whereas it saturates around 300nm for single lines. From these results the conclusion can be made on set of laser fabrication parameters required for polarization elements (converters, micro-waveplate array, etc...) based on half-wave plate: 250-300 fs pulse duration, 100 kHz laser repetition rate, 0.16 NA lens to focus laser beam, 1 mm/s fabrication speed, 3 J/pulse for a single line and 1,5-2 J/pulse for a 0,1mm square.

In most experiments reported in this PhD we will thus fixed the following parameters to have high enough pulse density for high writing speed (typ. 1 mm/s) i.e. a laser repetition rate of 100 kHz was used, 0,6 NA and a typical pulse energy of 1,5 J/pulse so the retardance remains below 200nm (i.e. a half waveplate at 400nm).

### 3.3.3 Study of writing kinetics according to the laser polarization

Two parameters of the birefringent modification, retardance and the azimuth of the slow axis, can be controlled during the writing process as the slow axis is defined by the polarization and the retardance as a function of the laser fluence. Retardance depends also on the laser wavelength, the pulse duration and the number of pulses transmitted through the modified region [32-34]. However, the retardance also is affected by the orientation of the polarization plane with respect to the writing direction. As the direction of the slow axis is varied during the writing process, the angle between the laser polarization and the writing direction is changing accordingly, which couples the induced retardance with the polarization direction. The difference in modification for 0° and 90° angles of polarization with respect to the writing direction is known for metals [35]. Recently, a similar effect was reported for laser processing of dielectrics [36]. However, it is important to keep the retardance value independent on the light polarization for the fabrication of variant polarization optical elements, for applications such as polarization beam converters, polarization sensitive camera and 5D optical memory [37-39]. In the simplest view, such polarization dependence is explained by the boundary conditions. The absorption is stronger for light polarized perpendicular to the interface, as described by the Fresnel coefficients.

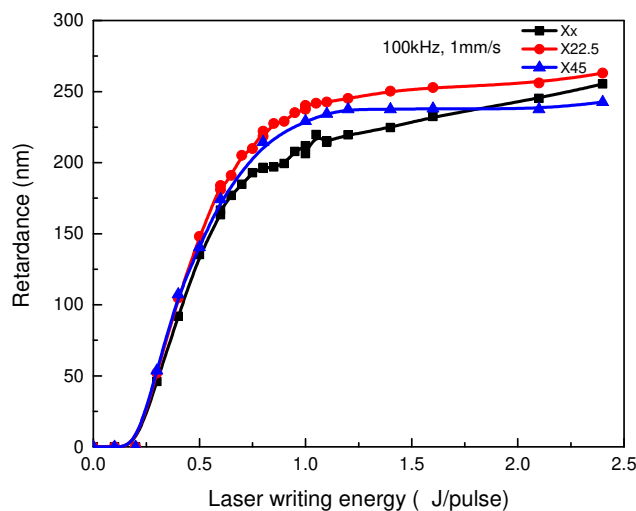


Figure 3.4: The dependence of retardance on pulse energy for different polarization orientation of the laser. Laser writing conditions: 1030 nm, 250 fs, 100 kHz, 1 mm/s, 0,6 NA, SuprasilCG.

Structures with different laser pulse energy and linear polarization orientation were fabricated with laser setup described in chapter 2. Laser power was from 0,1 J/pulse to 2,5 J/pulse and structures were written with three different laser polarizations (0°, 22,5° and 45°). Typical results are shown in Figure 3.4. The retardance was measured the Sénarmont compensator setup. With this birefringence measurement system it was possible to measure high retardance values (typ. up to ~550 nm) and even more using an additional calibration



sample or using the Michel Levy color chart. However, the disadvantage is that birefringence slow axis of the sample has to be known before the measurement and in this setup the distribution of the retardance could not be measured accurately. Note that if the user needs to achieve high retardance, structure with two or more layers can also be fabricated. The thickness of one layer is roughly around 50 nm (under the focusing conditions described above).

### 3.3.4 Spectral measurements of the retardance and linear extinction difference

Here we have decided to measure the spectral dependence of both the retardance and the linear extinction difference (proportional to the linear dichroism) in a large spectral range from UV to visible range and up to the near-IR. Again all measurements were repeated by turning the backside of the samples toward the light source. If circular properties are negligible in front of linear ones by about 2 or 3 orders of magnitude then they do not perturbate the measurement of linear properties. It is quite the opposite when measuring the circular optical properties.

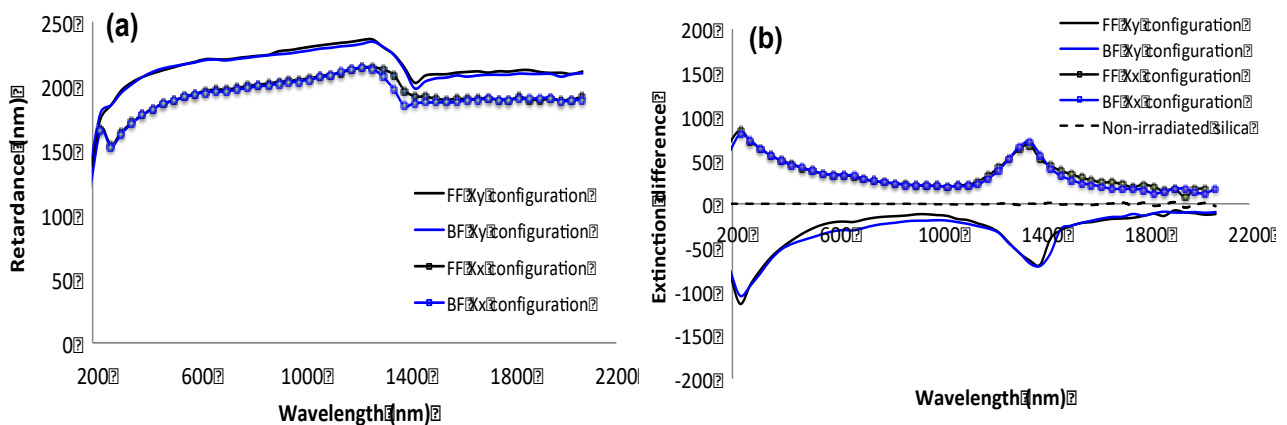


Figure 3.5: (a) UV-Vis-NIR spectra of retardance  $R$  and (b) the linear extinction difference  $\Delta I$  for the irradiated silica with Xx and Xy writing configurations. FF is for the front face and BF for the back face. Laser writing conditions: 1030 nm, 250 fs, 100 kHz, 0.6 NA, 1 mm/s, 1.5  $\mu$ J/pulse, SuprasilCG.

At first, we positioned the slow axis ( $\pm 1^\circ$ ) of the irradiated sample according to the  $O_x$  reference of the ellipsometer. For the Xx configuration, Figure 3.5a shows that the retardance increases from 200 nm up to 600 nm and then saturates at about 250 nm. In addition, we detect a slight “oscillation” around 1370 nm that is likely due to linear dichroism shown in Figure 3.5b. Notice that for both faces (namely FF for the front-face and BF for the back-face), we observe similar curves, revealing the reversibility of our measurements. Figure 3.5b reveals a strong positive linear extinction difference in the UV range up to  $\Delta I = 80 \text{ nm}$  at 250 nm. Then  $\Delta I$  decreases exponentially towards the visible and the near-IR range. Moreover, there is a significant dichroic band around 1370 nm that might be ascribed to the presence of oriented Si-OH species as discussed later in the first section of chapter 5. Then as shown in Figure 3.5a, for the Xy configuration, the spectral dependence of the retardance is very similar to that for the Xx configuration. Here again, we observe a reversibility of all our measurements according to the probed sample face. However,  $\Delta I$  in Figure 3.5b has

reversed its sign when compared to the Xx writing configuration; that is, we measured a negative  $\Delta n$ . This indicates that  $\Delta n$  is related to the nanogratings, with the higher attenuation being for light polarization parallel to the porous nanolayers.

## 3.4 Study of femtosecond laser irradiated silica using a CD spectro-polarimeter

### 3.4.1 Preliminary observations

#### *Rotated neutral axes*

For this specific observation, single lines of glass modifications, separated from each other typically by 100  $\mu\text{m}$  at least, were written in silica glass plates as it is described in section 3.1. They were then placed under a polarized optical microscope for examination in transmission and birefringence quantitative measurements. Samples exhibited strong linear birefringence on the order of 250nm for a thickness of 40 $\mu\text{m}$ , which implies a linear birefringence of  $6 \cdot 10^{-3}$ . From the symmetry of the writing process and when the polarization is aligned or perpendicular to the written line direction, it is expected one neutral axis aligned with the written line direction or perpendicular to it [33] respectively. However, it was surprising to observe that the complete optical extinction was not possible between crossed polarizers. It was necessary to slightly uncross the analyzer that means the neutral axis was turned by a few degrees around the laser propagation axis. This departure angle depends on the writing sense in such a way that it is possible to vary the contrast of the line written in one sense over the others written in the other sense just by rotating the sample between crossed polarizers. This leads us to consider the existence of an optical rotating power.

#### *Optical rotation*

One of the samples shown in Table 3.1 was used for measuring optical rotation. Maximal extinction between crossed polarizers was searched and the analyzer was then uncrossed for tentatively improving the optical extinction. We found an uncrossing angle of  $0.5^\circ$  for a 40 $\mu\text{m}$  (or less) active thickness corresponding to an optical rotation of  $12,5^\circ/\text{mm}$  at 632nm that is big enough for practical applications. For this silica sample the irradiation parameters were: 1030nm, 250fs, 100kHz, 0.6NA, 1.5 $\mu\text{J}$ . It is worth noticing that rotating power for quartz is around  $21.73^\circ/\text{mm}$  at 589nm [40]. The sign is not defined as it is determined by the crystal arrangement that can be levogyre or dextrogyre. No rotating power was found for pulse energies below the porous nanoplanes formation [41]. **This is a preliminary proof that the femtosecond laser can render a glass chiral at the macroscopic level.** The irradiated glass is thus linearly and circularly birefringent. In that case, some additional circular dichroism can be expected. Note that in solids, optical chirality can originate from chirality at the molecular level and/or from a chiral arrangement of achiral motif like for the quartz itself (that is, by the way, a crystalline phase of silica) [41].

### 3.4.2 Study of circular diattenuation CD according to the pulse energy

Here, due to the size of the beam (typ. 1mm), series of close lines (1 $\mu$ m pitch) were written like a Piano function for filling a square of 3x3 mm<sup>2</sup>. Remind that the quantitative circular dichroism in a solid sample that is linearly and circularly birefringent at the same time is not directly measurable. The quantity actually measured by the instrument is the ellipticity of the electromagnetic field (mdeg) that is defined as follows:

$$\theta = 2 \tanh^{-1} \left( \frac{I_L - I_R}{I_L + I_R} \right) = \frac{(\alpha_L - \alpha_R)e}{2} \quad \text{Equation 3.2}$$

It is proportional to circular dichroism  $\alpha_R - \alpha_L$ , where  $\alpha$  is the lineic absorption and  $e$  is the thickness of the circular dichroic layer, only when the sample is isotropic i.e. in samples that exhibit neither linear birefringence nor linear dichroism. Otherwise, it is preferable to call it ellipticity (or circular diattenuation) as it will be done in this chapter.

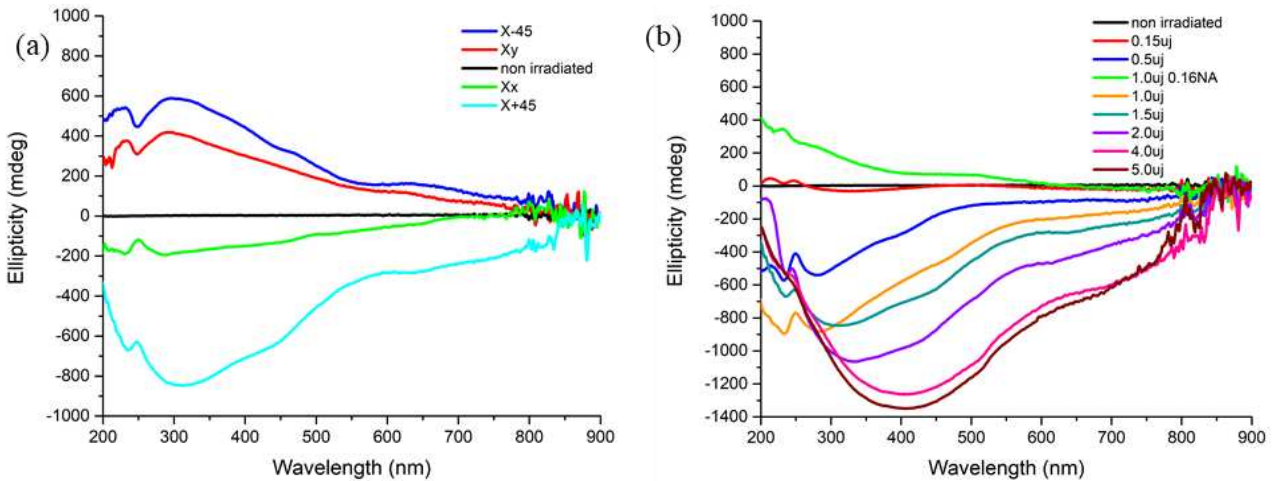


Figure 3.6: (a) Ellipticity spectra according to the wavelength for Xx, Xy, X+45° and X-45° writing configurations for 1.5 J. (b) Influence of the pulse energy of the spectral ellipticity for a fixed focusing depth of 300  $\mu$ m. For sake of comparison we add a SiO<sub>2</sub> sample written a 1 $\mu$ m with 0,16 NA. The others laser parameters are as follows: 1030 nm, 250 fs, 100 kHz, 0,6 NA, 1mm/s, polarization at 45° off the scanning direction (X+45° configuration), SuprasilCG.

In order to find the most suitable writing configuration to create some significant ellipticity, we have first analyzed samples written in four different writing configurations noted Xx and Xy (namely parallel and perpendicular polarization to writing direction), X+45° and X-45°. At first we should remind that our spectral ellipticity measurements are invariant by sample rotation in the spectrometer. For the front face measurements shown in Figure 3.6a, we observe a positive ellipticity in the whole spectral range for the Xy configuration. Rotating the laser polarization by 90 can reverse the apparent sign of the ellipticity° i.e. it is negative when the polarization is parallel to the scanning direction (Xx configuration). Specifically for X-45° configuration, we observe a strong positive ellipticity in the whole spectral range whereas X+45° reveal a strong negative ellipticity. So, the ellipticity strongly varies with the direction of the polarization. In most samples the ellipticity can reach at least 200mdeg in the blue or UV range. However as shown in Figure 3.6a, using a polarization oriented at +45° off the scanning direction, the ellipticity can be as high as -800mdeg at 300nm for a pulse energy

of 1,5 $\mu$ J and 300 $\mu$ m focusing depth. This observation could be compared to the linear dichroism, which reaches the range of 20–30° in the same samples. The phase angle associated with circular properties is thus much smaller than that associated with the anisotropic linear properties. This explains why the circular optical properties perturbing the linear measurements are not usually detected [42].

Then in order to correlate the circular diattenuation to the existence of porous nanogratings, we have analyzed samples written with different pulse energies as reported in Figure 3.6b. The laser polarization was fixed at 45° of the writing direction in order to maximize the ellipticity amplitude (see Figure 3.6a). In agreement with [43], below the energy threshold for the appearance of porous nanoplanes, there is no linear birefringence and negligible ellipticity. On the contrary, for pulse energies above nanogratings formation (typ. >0,15 J in our conditions: 1030nm, 250fs, 0,6NA, 100kHz, 1mm/s), a significant ellipticity appears. Firstly, there is a trend towards increasing the spectral width and the absolute amplitude of the ellipticity as the pulse energy increases from 0.5 to 4 J. At low energy, we observe two main bands located around 240nm and 280nm accompanied with a tail extending up to 500nm. The spectral position of the second band is shifting towards higher wavelength, from 280 to 400nm, when increasing the pulse energy. Within the 300-700nm spectral range, the absolute ellipticity follows a monotonous increase with the energy up to 5 J. Then, above 5 J, there is a slight decrease of the ellipticity, especially in the UV range. Note that ellipticity can reach more than -1500 mdeg around 300-400nm corresponding to an equivalent value of -30deg/mm if we take into account that laser tracks length is around 50  $\mu$ m in our conditions.

### 3.4.3 Study of circular diattenuation CD according to the line-to-line spacing

Gecevičius et al. [44] reported the line gap dependence on linear birefringence (they measured the retardance): as the polarization dependence of the writing kinetics is related to a previously written track, this effect should disappear with increasing the separation between consecutive lines or tracks. In their work, the dependence of retardance on the light polarization disappeared at the laser track separation of 3  $\mu$ m.

Here we prepared a set of 3x3 mm<sup>2</sup> samples with increasing line gap from 1  $\mu$ m to 10  $\mu$ m. With a line spacing of 1  $\mu$ m we have a uniform scanned region that avoids diffraction effects whereas diffraction starts to appear for higher spacing. In Figure 3.7 we reported samples irradiated in the following conditions: 1030nm, 250fs, 100kHz, 1mm/s, 0.6NA, 300  $\mu$ m focusing depth. The pulse energy was fixed to 1,5 J/pulse to ensure at least that we will cross Type II threshold. The sample was moving along X (horizontal direction on the laser compressor) and the linear polarization was oriented +90° from the writing direction defined as: Xy writing configuration.

Figure 3.7 gives the circular “dichroism” expressed in ellipticity (mdeg). In this Figure, the ellipticity decreases and nearly disappears at the track separation of 3  $\mu$ m. Taking into

account that the estimated laser spot diameter was about less than  $1,5 \mu\text{m}$ , we can assume that consecutive lines do not overlap when line gap is above  $3 \mu\text{m}$  where there is nearly no ellipticity. Our results are thus consistent with Gecevičius et al. [44]. In their work, they suggest an explanation based on the stress produced by the neighboring track, which impact the glass photosensitivity.

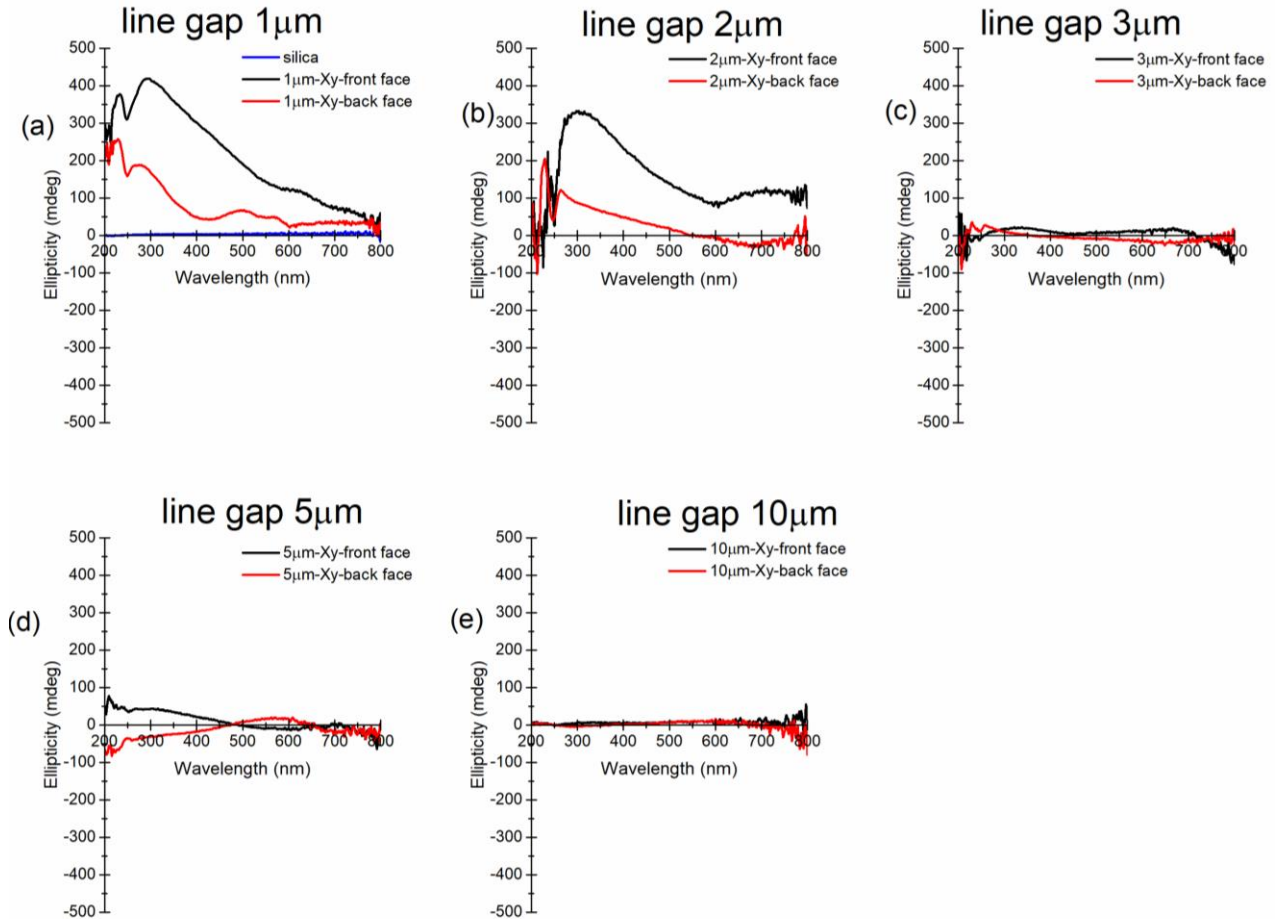


Figure 3.7: Ellipticity (proportional to circular diattenuation) according to line-to-line gap of square samples written in Xy writing (scanning direction along X axis, writing laser polarization along y axis). Laser conditions: 1030 nm, 250 fs, 100 kHz, 0.6 NA, 300  $\mu\text{m}$  depth, 1 mm/s, 1.5 J/pulse, SuprasilCG.

So, a few things can be highlighted about this result are the following:

- The first point is that the ellipticity decreases much faster than surface area covered by the laser irradiation e.g. with a  $3 \mu\text{m}$  gap, the ellipticity is close to zero whereas the irradiated area still covers 80% of the probed area.
- The second point is an additional effect related to our design. Indeed, due to the increasing line gap, the probe beam exhibits some significant diffraction effects when passing through our sample and especially for  $5 \mu\text{m}$  and  $10 \mu\text{m}$  line gap. So this effect might contribute to the above-mentioned observation.
- The last point is related to the neighbouring lines effect. These results suggest that stress effects might be involved in the process of creation of the circular optical properties. In this view, provided that the next line is written close enough from the preceding one, it is in turn affected by the stress field generated mostly inside or also

around the first line and so on... Therefore, laser writing with 5  $\mu\text{m}$  or 10  $\mu\text{m}$  line gap corresponds to nearly independent lines, which are less affected by the stress field of previously written lines.

As a result in the next set of experiments we are going to reproduce the same measurements by playing on the sample-detector distance in such a way we can meet the following two cases:

- *Close to the detector* (less than 1 cm), most of the light is collected i.e. both the direct transmitted beam and the diffracted ones and a part of the forward light scattering as well.
- *Away from the detector* (typ. 30 cm away) we collect mostly the direct transmitted probe beam and neither the diffracted ones (especially for line gap larger than 3  $\mu\text{m}$ ) nor the light scattering.

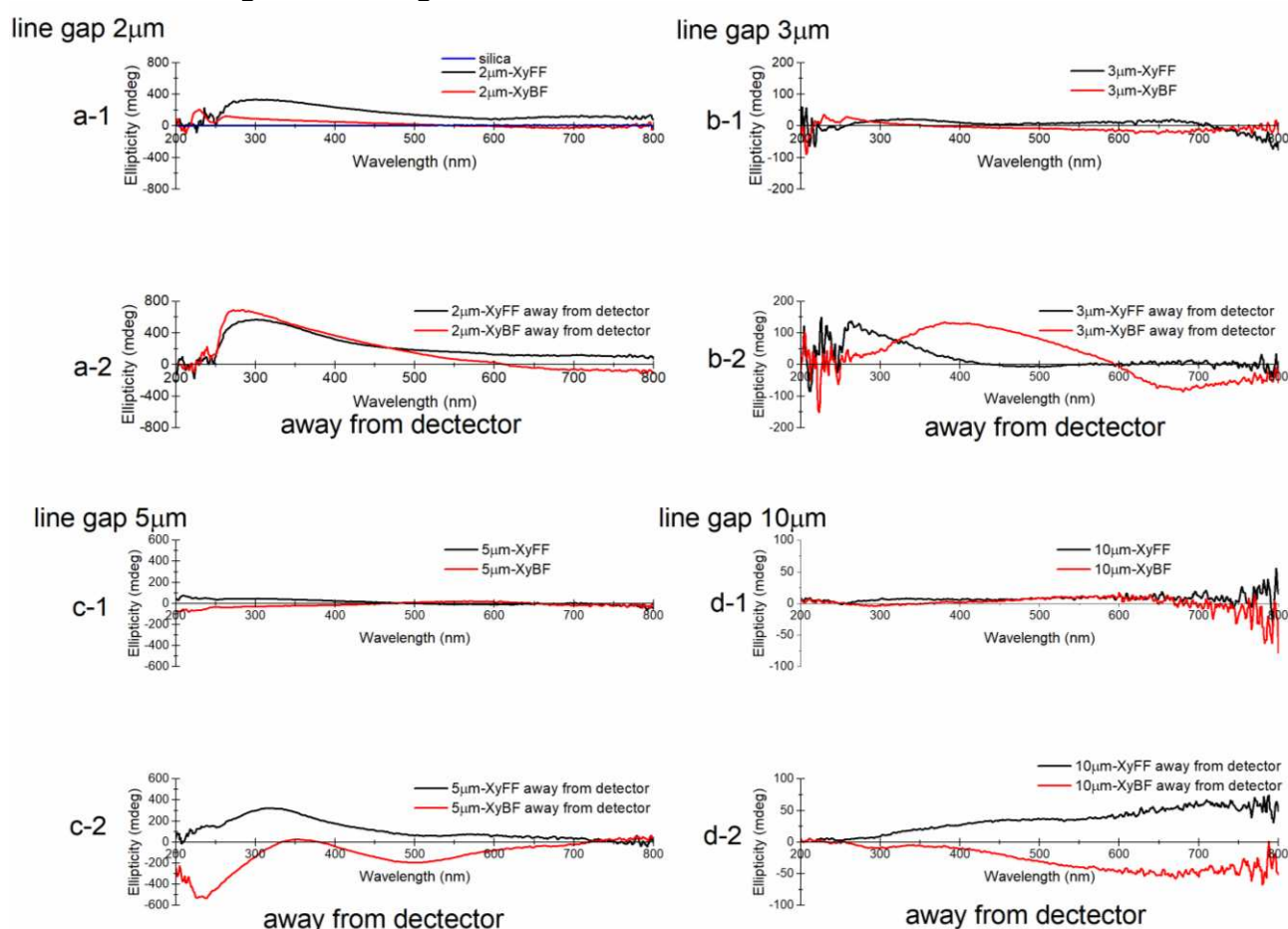


Figure 3.8: Ellipticity (or circular diattenuation) spectra according to line-to-line gap and distance between sample-detector. Laser writing conditions: 1030 nm, 250 fs, 100 kHz, 0.6 NA, 300  $\mu\text{m}$  depth, 1 mm/s, 1.5 J/pulse, Xy configuration, SuprasilCG.

Figure 3.8 expresses the CD signal of sample in Figure 3.7 with difference distances from the sample to the detector. When sample is "away from the detector", the CD signal declines obviously along the whole spectra range. However when the sample is "close to the detector", the ellipticity decreases with increasing line gap but more slowly when compared to previous measurements? Even for the larger line gap of 10  $\mu\text{m}$ , a significant ellipticity can still be

recorded. So from Figure 3.8 this reveals that the light diffraction and/or light scattering impact our measurements since the recorded ellipticity is much higher when these are collected on the detector. About diffraction let's discuss qualitatively two cases:

- If the diffraction efficiency (noted  $\eta_{\text{left}}$  or  $\eta_{\text{right}}$ ) depends on the sign (left or right) of the circular polarization, there will be a higher related ellipticity when the sample is away from the detector since the diffracted beams ( $\eta_{\text{left}} I_0$  or  $\eta_{\text{right}} I_0$ ) will be not collected but only the direct beam  $(1 - \eta_{\text{left}}) I_0$  or  $(1 - \eta_{\text{right}}) I_0$  (at least for 5 and 10  $\mu\text{m}$  line gap). In contrast, when the sample is close to the detector the overall transmitted light will be collected  $(1 - \eta_{\text{left}}) I_0 + \eta_{\text{left}} I_0$  for left circular polarization and  $(1 - \eta_{\text{right}}) I_0 + \eta_{\text{right}} I_0$  for right circular polarization so there should be no difference here i.e. "no additional" ellipticity is observed. So this situation does not correspond to our measurements.
- If the diffraction efficiency (noted  $\eta$ ) does not depend on the sign, the distance between sample and detector will have no impact on the ellipticity measurements. This is not the situation observed here.

Finally it appears that diffraction effects cannot explain our observations: a higher ellipticity when the sample is close to the detector. In addition we have the same result with a 1  $\mu\text{m}$  line gap whereas there are no diffraction effects observed in such sample. In these conditions, our main hypothesis is related to occurrence of strong light scattering effects, which are light polarization dependent. Indeed it is well known that nanogratings are made of porous nanolayers, which exhibit strong light scattering as reported in [46, 47]. This leads to a strong linear dichroism, which reversed its sign when comparing  $X_x$  and  $X_y$  writing configuration. This is in agreement with a negative linear dichroism related to the nanogratings, with the higher attenuation being for light polarization parallel to the porous nanolayers. Note again this is more correct to say it is linear diattenuation (and not a dichroism) since this is likely due to light scattering and not absorption.

### 3.4.4 Study of circular diattenuation according to the angle between polarization orientation and the laser scanning direction

As suggested in the introduction of this chapter, the control of the laser polarization according to the displacement should lead to the control of local symmetry and its orientation. Following this view and in order to investigate the most suitable writing configuration to create some significant ellipticity, we have analyzed a wide set of samples written with 16 different writing configurations noted  $X_x$  and  $X_y$  (namely parallel and perpendicular polarization to writing direction, which is fixed along  $X$ ), or  $X+45^\circ$  and  $X-45^\circ$  (for a linear polarization oriented at  $\pm 45^\circ$  off the scanning direction). In Figure 3.9 we reported samples irradiated at 1,5  $\mu\text{J}/\text{pulse}$  ensuring we fall within Type II modifications regime. This is likely a key experiment of this PhD chapter. So we should remind that our spectral ellipticity measurements are invariant by sample rotation in the spectrometer chamber. Again since previous investigations have revealed that the ellipticity measurements

are “non-reversible” (so called asymmetric transmission) i.e. front face is different from back face, we will measure all samples in both geometries i.e. from the front face (FF) and back face (BF).

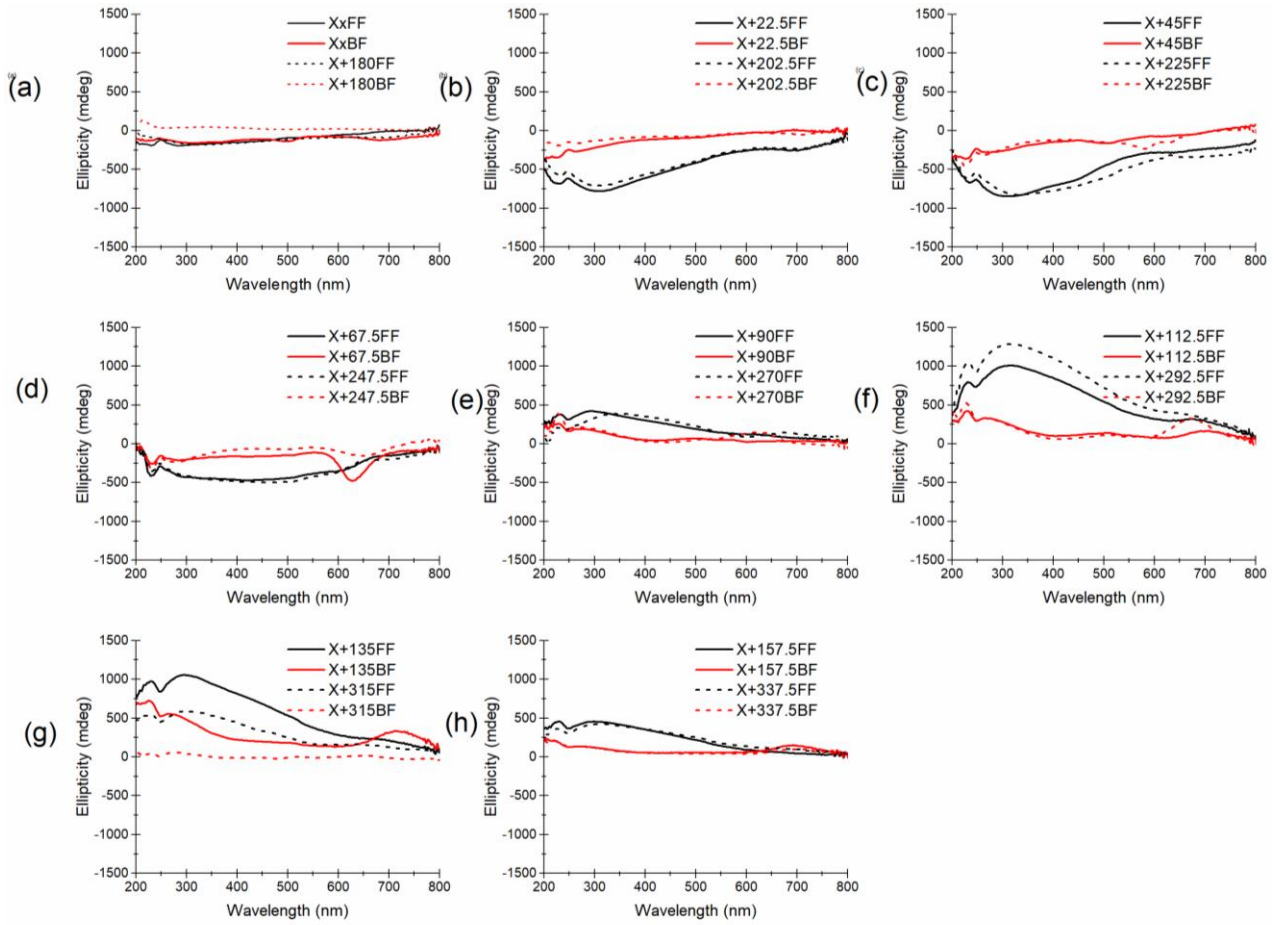


Figure 3.9: Ellipticity (or circular diattenuation) spectra for 16 different writing configurations. All samples were written along X scanning direction. Laser writing conditions: 1030 nm, 250 fs, 100 kHz, 0.6 NA, 300  $\mu$ m focusing depth, 1 mm/s and 1.5 J/pulse.

For the front face measurements shown in Figure 3.9, we observe a positive ellipticity over the whole spectral range for the X90° configuration. Rotating the laser polarization by 90° can reverse the apparent sign of the ellipticity i.e. it is negative when the polarization is parallel to the scanning direction (Xx configuration). Specifically, for X45° (or X225°) configuration, we observe a strong negative ellipticity in the whole spectral range whereas X135° (or X315°) reveal a strong positive ellipticity. So, the ellipticity strongly varies with the direction of the laser polarization (being always linear) with respect to the scanning direction. In most samples the ellipticity can reach at least 200 mdeg in the blue or UV range. However as shown in Figure 3.9, using a polarization oriented at +45° off the scanning direction, the ellipticity can be as high as -800 mdeg at 300 nm for an energy of 1,5 J/pulse and 300  $\mu$ m focusing depth.

To summarize the results in a different way, we have thus drawn the ellipticity measured in the visible range, at 550 nm, according to the orientation of the writing laser polarization (which remains linear). In Figure 3.10 we can thus observe the ellipticity measured from the



front face (FF) and the back face (BF). As it can be seen the ellipticity is positive in the 0-90° range and negative for polarization between 90° and 180°. *The maximum ellipticity corresponds roughly to +/- 45° orientation of the polarization or more correctly we should say when the angle between the scanning direction and the laser polarization is +/- 45°.*

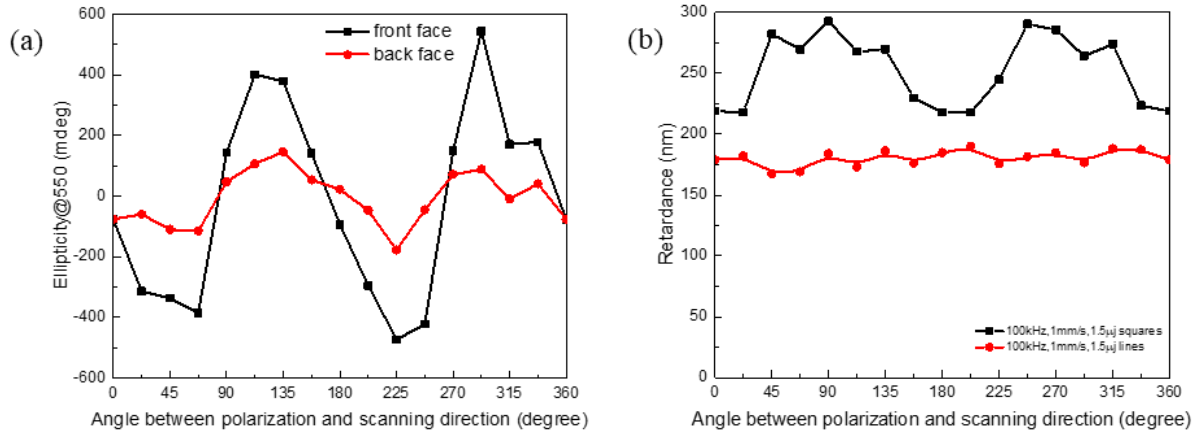


Figure 3.10: (a) Ellipticity (or circular diattenuation) at 550nm; (b) Retardance (proportional to the linear birefringence) at 550nm according to the i.e. angle between the scanning direction and the laser polarization. Full lines are a guide for eye. Laser writing conditions: 1030 nm, 250 fs, 100 kHz, 0,6 NA, 300 µm depth, 1 mm/s, 1,5 J/pulse, SuprasilCG.

In addition it should be noted that we can observe a quite strong asymmetric transmission based on the ellipticity measurements (see Figure 3.10a) whereas we did not observe such effects on the retardance (linear birefringence) as we measured in Figure 3.2 for example. This observation should be compared to the linear birefringence and linear dichroism amplitudes observed in the same or similar writing conditions. The retardance (proportional to the linear birefringence) is thus shown in Figure 3.10b for single lines and squares (a set of lines separated by 1 mm) for the same samples. It can be seen that the retardance of single lines is around 180nm and remains independent on the angle between the polarization orientation and the scanning direction (along X). In contrast the effects of neighboring lines (likely due to stress effects [44]) leads to some significant modulation of the retardance which increase around 90 and -90° (also called 270°). By rewriting the retardance  $R$  as the difference in phase shift  $\delta$  (in radians) between the two polarization states  $\delta = \frac{2\pi\Delta n l}{\lambda} = \frac{2\pi R}{\lambda}$ , we obtain a phase shift  $\delta$  of 2,1 rad or 118°. Based on publications the linear dichroism reaches around 0,1 OD at 550nm in similar samples [46] which can be converted in rad using the following expression:  $(x - y)$  Linear dichroism LD =  $\frac{\ln(10)(A_x - A_y)}{2}$  (see chapter 2 for definition) so 0,115 rad and 6-7°. The phase angle associated with circular properties is thus much smaller than that associated with the anisotropic linear properties. This explains why the circular optical properties perturbing the linear measurements are not usually detected while it is commonly expected. However we observed some significant asymmetric transmission in all investigated samples as shown in Figure 3.7, Figure 3.8 and Figure 3.9. As explained in a few words in the beginning of this chapter, it is shown in the literature [48] that asymmetric transmission appears when linear and circular anisotropic optical properties have not the same depth distribution.

### 3.4.5 Study of circular diattenuation according to the pulse-to-pulse overlapping rate and the laser repetition rate

In order to correlate the circular dichroism to the existence of porous nanogratings (i.e. Type II modifications), we have analyzed samples written with different repetition and their corresponding pulse-to-pulse overlap. The laser radiation was produced by a femtosecond laser system operating at 1030 nm and delivering pulses of 250 fs at a repetition rate  $f$  of 10-500 kHz. The beam was focused within 300  $\mu\text{m}$  below the front face of 1-mm-thick silica glass plates (SuprasilCG) using a 0.6 NA aspheric lens. Based on preliminary investigations made with the circular dichroism spectro-polarimeter, we have chosen to investigate here a specific writing configuration in terms of polarization orientation. The laser was moving along X (horizontal direction on the laser) and the linear polarization was oriented  $+45^\circ$  from the writing direction defined as "X+45°" writing configuration, which leads to a high ellipticity as described in details in next section of this PhD chapter. Then, by moving the sample along +X axis with at a scanning speed  $v$  of 1 mm/s, we created several squares ( $3 \times 3 \text{ mm}^2$ ) made of a set of lines with a line spacing of 1  $\mu\text{m}$  to have a uniform scanned region and to avoid diffraction effects. The pulse energy was fixed to 1,5  $\mu\text{J}/\text{pulse}$  which ensure at least that we will cross Type II threshold. The pulse-to-pulse overlapping rate (roughly defined as  $v/f$ ) was varied from 10 up to 500 pulses/ $\mu\text{m}$  since the pulse repetition rate was varied from 10 kHz up to 500kHz. In addition, we have written an additional sample at 0,1 mm/s and 100 kHz corresponding to 1000 pulses/ $\mu\text{m}$  without heat accumulation effects.

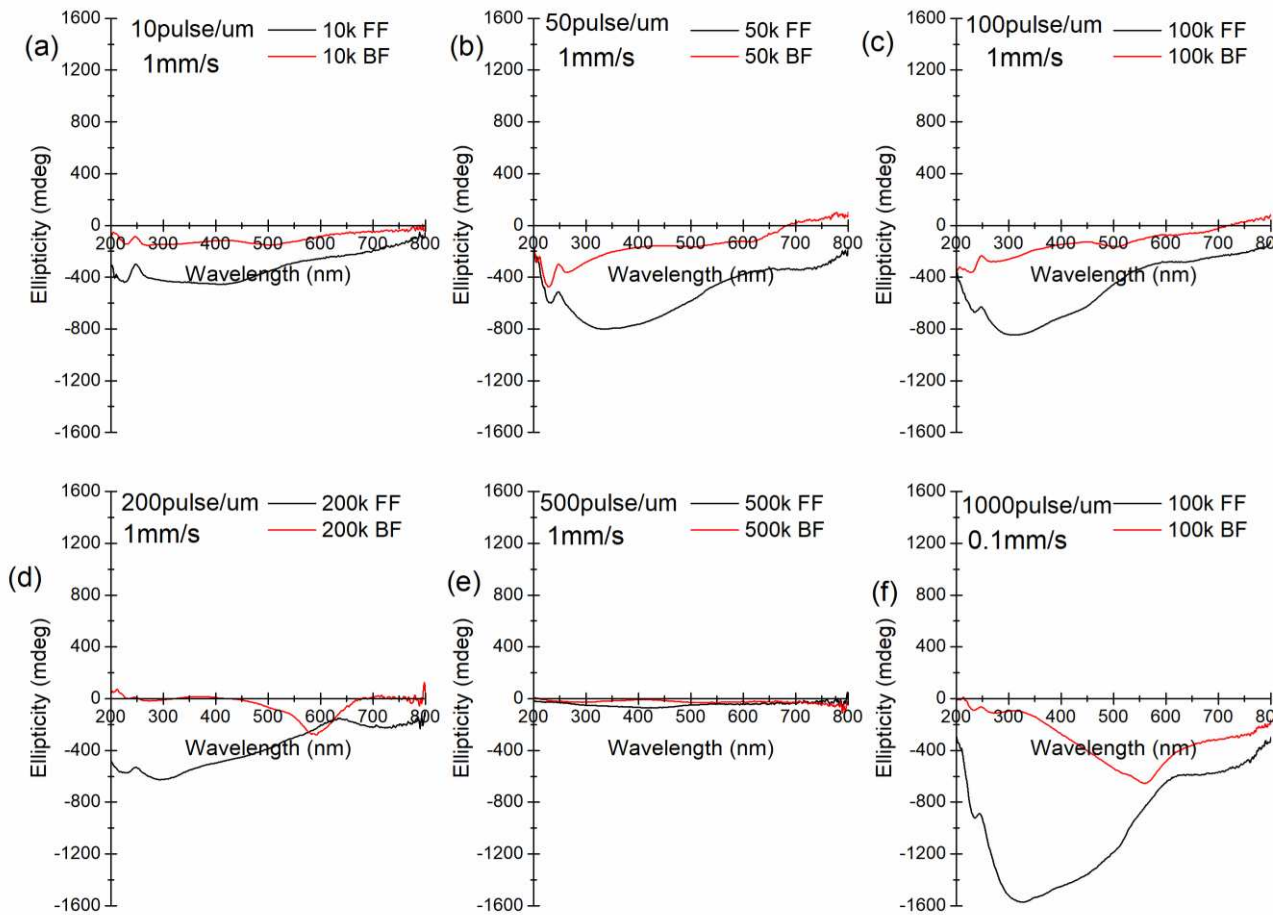


Figure 3.11: Ellipticity (or circular diattenuation) according to the laser repetition rate from 10 kHz up to 500 kHz. The laser parameters are as follows: 1030 nm, 250 fs, 0,6 NA, 300  $\mu\text{m}$  depth, 1 mm/s, 1.5  $\mu\text{J}/\text{pulse}$  and X+45° writing configuration.

The spectral dependence of photo-induced ellipticity is shown in Figure 3.11 as a function of the overlapping rate (defined as  $v/\lambda$ ) for different repetition rates. There are two regions shown in this Figure. Below 100 kHz, the ellipticity amplitude is increasing together with the overlapping rate from 10 up to 1000 pulses/  $\text{m}$  (insets a, b, c and f). With the chosen writing configuration at 100 kHz, the sample shows a maximum ellipticity of -1,6 deg at 300nm. When increasing the repetition rate above 200 kHz at 1,5  $\text{J}/\text{pulse}$ , the amplitude of the ellipticity declines sharply even with the increasing overlapping rate 200 pulses/  $\text{m}$  (at 200 kHz) or 500 pulses/  $\text{m}$  (at 500 kHz). At the same time birefringence imaging experiments reveal that heat accumulation occurs in these conditions and destroy partly the nanostructures and the related retardance as well. Again it seems that the formation of circular diattenuation is strongly related to the occurrence of nanogratings and related anisotropic linear optical properties.

Figure 3.12a displays the measured retardance (proportional to the linear birefringence) as a function of the repetition rate for different glass samples as we reported in [49]:  $\text{SiO}_2$  (SuprasilCG),  $7\text{TiO}_2:93\text{SiO}_2$  (Corning ULE),  $\text{GeO}_2$  glass and an alumino-borosilicate glass (Borofloat33 from Schott). As it was reported in a preliminary study [50], the retardance is constant at low repetition rates (typ. below 10 kHz) and then decreases at higher repetition rates. The upper limit of the repetition rate, when no retardance is observed anymore,

depends on the glass chemical composition. For the pulse energy of 1  $\mu\text{J}/\text{pulse}$ , a significant retardance can still be obtained in  $\text{SiO}_2$  up to 1 MHz but the optimal value is around 100 kHz. Figure 3.12b exemplifies the maximum glass temperature after 1000 laser pulses at 2  $\mu\text{m}$  from the center of absorption (radial distance,  $z = 0$ ) for different repetition rates. More details about this thermal accumulation modeling and related conclusions can be found in the related paper we have published in 2017 [49]. As expected heat accumulation takes place as the repetition rate increases. When the repetition rate is low enough (typ. below 100kHz), due to the temporal separation of the adjacent pulses of  $>10 \mu\text{s}$ , the temperature drops below the melting point of the glass between individual pulses and the average temperature remains below the glass melting temperature. In comparison to that, at higher repetition rates the temperature for 1000 pulses exceeds the melting point  $T_m$  of Borofloat33 for 100kHz. In contrast, fused silica and  $\text{GeO}_2$  are in the conditions to melt for repetition rates larger than 500 kHz resulting in the destruction of nanogratings and related anisotropic linear properties but also circular optical properties in  $\text{SiO}_2$  (see Figure 3.11a).

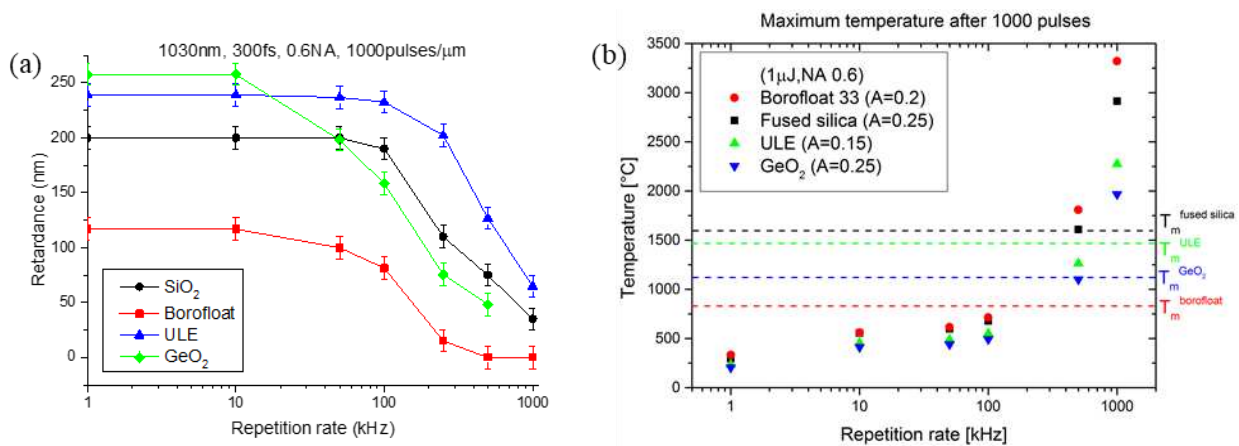


Figure 3.12: (a) Retardance according to the laser repetition rate. The laser parameters were 1030 nm, 250 fs, 0.6 NA and 1  $\mu\text{J}/\text{pulse}$ . The writing speed was varied to keep a fixed overlapping rate of 1000 pulses/ $\mu\text{m}$ . (b) Calculated maximum temperature for different laser repetition rates (for 1000 pulses/ $\mu\text{m}$ ).  $T_m$  denotes the melting temperature.

### 3.4.6 Study of circular diattenuation according to the focusing depth

The focusing depth dependence of the ellipticity was studied using a 0.6 NA microscope objective. In the following experiments the geometrical focus was moved from the surface down to 800  $\mu\text{m}$  into the bulk of the 1 mm thick silica sample. The laser-writing configuration was X+45°. The ellipticity spectra were then recorded according to the focusing depth for a fixed energy of 1,5  $\mu\text{J}/\text{pulse}$  as shown in Figure 3.13a. The data were also drawn according to the pulse energy in Figure 3.13b for a better comparison. For shallow focusing below 200  $\mu\text{m}$ , the absolute ellipticity decreases linearly for deeper focusing penetration down to a minimum value at 200  $\mu\text{m}$  corresponding to the positive spherical aberration compensated depth of the microscope objective. From 200 up to 500  $\mu\text{m}$ , the absolute ellipticity amplitude increases monotonously with the focusing depth in the whole spectral range. This indicates the strong influence of spherical aberration on the laser-induced ellipticity at this relatively high numerical aperture. Above 200  $\mu\text{m}$ , the deeper the geometrical focus is moved into the bulk of the sample, the stronger the beam is distorted and elongated due to the negative

spatial aberration. The ellipticity of the written structure is a product of the effective circular dichroism multiplied by the length of the structure.

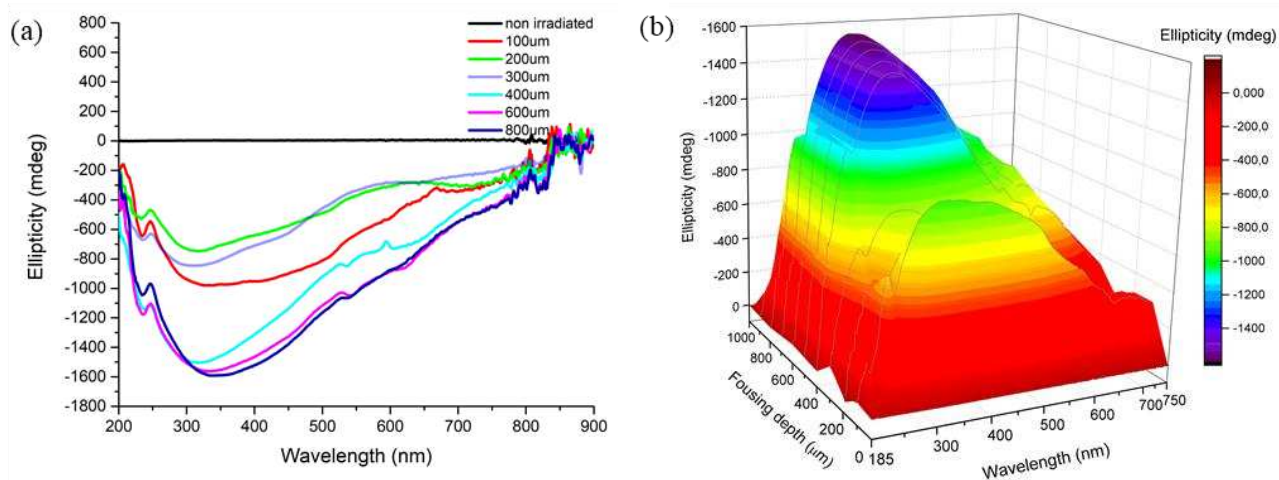


Figure 3.13: (a) Influence of the focusing depth on the spectral ellipticity using 0,6 NA. (b) 3D representation of the ellipticity spectra according to the focusing depth. The laser parameters are as follows: 1030 nm, 250 fs, 100 kHz, 1mm/s, 1.5  $\mu$ J/pulse and polarization at 45° off the scanning direction (X+45° configuration).

As a result, one way to increase the induced ellipticity is the introduction of strong spherical aberration provided that the energy is high enough to photo-induce the chiral optical properties. For deeper focusing depths, the measurements demonstrated that we managed to keep a nearly constant ellipticity from 500  $\mu$ m up to 800  $\mu$ m. This is likely due to a balance between the occurrence of self-focusing effects and spherical aberration even when the focus goes very deep [51]. For sake of comparison additional measurements were done using a 0,16 NA objective. An example of ellipticity spectrum is shown in Figure 3.6b for 1 J/pulse but the same trend was observed at high energies. With such a medium NA, it can be seen that absolute ellipticity is lower (especially in the visible range) than with 0,6 NA but we can also notice that the spectral shape and even the sign are different. This indicates that the linear beam elongation (due to low NA focusing) is not sufficient to create a high ellipticity but we rather need to increase the circular dichroism itself, which appears to be higher for strong focusing conditions and deep focusing.

## 3.5 Analysis of CD measurements artifacts and asymmetric transmission of circularly polarized light

### 3.5.1 Study of CD artifacts due to the spectro-polarimeter

As we told shortly in the first section of chapter 3, circular dichroism measurements are usually performed in homogeneous substances like true liquids that are isotropic and without circular symmetry. It is measured by recording the light attenuation through the sample alternating left and right circular polarization using a photo-elastic modulator. The attenuation difference normalized by the sum is called the ellipticity  $\theta$  and expressed in mdeg. The relation with the measured ellipticity  $\theta$  and circular dichroism is  $\theta = (\alpha_L - \alpha_R)e/2$ , where  $\alpha$  is the absorption and  $e$  is the circular property thickness. However, this is true only

for a sample that exhibits neither linear birefringence LB nor linear dichroism LD. In the literature the presence of measurements artefacts [24] have been tentatively quantified using a linear birefringent or dichroic quartz etalons that reveal minor ellipticity (<1 mdeg above 250nm; <5 mdeg below 250nm). In addition, our ellipticity measurements are invariant by sample rotation, which indicate that these artefacts do not impact significantly the ellipticity results.

Y. Shindo et al. [24] studied the artifacts of CD machine, as a CD spectrophotometer is a polarization–modulation instrument and remind that CD spectra are necessarily accompanied by artifacts due to linear anisotropies namely LB and LD coming either from the sample but also from residual birefringence in the spectrometer setup itself. From the Stokes vector and the Mueller matrices formalisms, Kuroda *et al.* reported that CD signal measured by a conventional CD spectrometer, such as the Jasco CD polarimeter we used, could be approximated as [52, 53]:

$$\begin{aligned}
 CD \text{ signal} = G_1(P_y^2 + P_x^2) & \left[ CD + \frac{1}{2}(LD'LB - LDLB') \right. \\
 & + (LD \cos 2\theta - LD' \sin 2\theta) \sin \alpha] \\
 & + G_1(P_y^2 - P_x^2) \sin 2\alpha (LB \cos 2\theta - LB' \sin 2\theta) \\
 & + G_1(P_y^2 - P_x^2) \cos 2\alpha (LB \sin 2\theta - LB' \cos 2\theta)
 \end{aligned}
 \tag{Equation 3.}$$

where  $P_x$  and  $P_y$  are the transmittance of the photomultiplier window along the x and y directions and " $\alpha$ " is the azimuthal angle of its optical axis with respect to the y axis,  $\theta$  is the rotation angle of the analyzed sample,  $LD$  is the residual static birefringence of the photoelastic modulator (PEM) and  $G_1$  is the apparatus constant related to the sensitivity of the spectrometer at 50 kHz. In our work the presences of such measurements artifacts have been quantified using linear birefringent, linear dichroic and circular birefringent quartz etalons.

- At first, because the CD spectrometer was already calibrated, we postulated  $G_1(P_y^2 + P_x^2) = 1$ . Figure 3.14a expresses the ellipticity of a pure CD liquid (i.e. without optical rotation) with three different concentrations. With 1cm path high concentration the signal reaches the limit of CD machine i.e. around 2000mdeg.
- Then we tested if CB could eventually create some artifact on the measured CD signal since this was not including in the equation above. The result is given in Figure 3.14b, obviously CB alone does no create any artifacts.
- Figure 3.14c shows the circular diattenuation spectra of a linear birefringent sample oriented along x-axis (a quarter waveplate at 550nm so corresponding to  $LB = \pi/2$  rad and  $LB'=0$ ). Here we can observe little artifact with an apparent CD up to 8 mdeg so we can determine that  $G_1(P_y^2 - P_x^2) * \sin(2\theta)$  remains smaller than  $5 \cdot 10^{-3}$ .
- We investigated the impact of LD using dichroic sheet polarizer. These polarizers are constructed by laminating a thin, stretched, and dyed polymer film. From Figure 3.14d we can see the LD has a big effect on the apparent CD with amplitude of -90

mdeg at 400 nm. In addition, by changing the orientation of LD sample, the apparent circular diattenuation changes a lot and a minimum appears when LD is oriented at 32 degree off the spectrometer horizontal axis. Taking into account that our LD polarizer owns an extinction ratio of 500, we get  $LD = \ln(500)/2 = 3.11$  radians. So we can estimated the maximum value of  $\sin(\ )$  at 400 nm that is around  $-2,9 \cdot 10^{-2}$  corresponding to residual birefringence of  $2-3 \cdot 10^{-6}$  within the photo-elastic modulator.

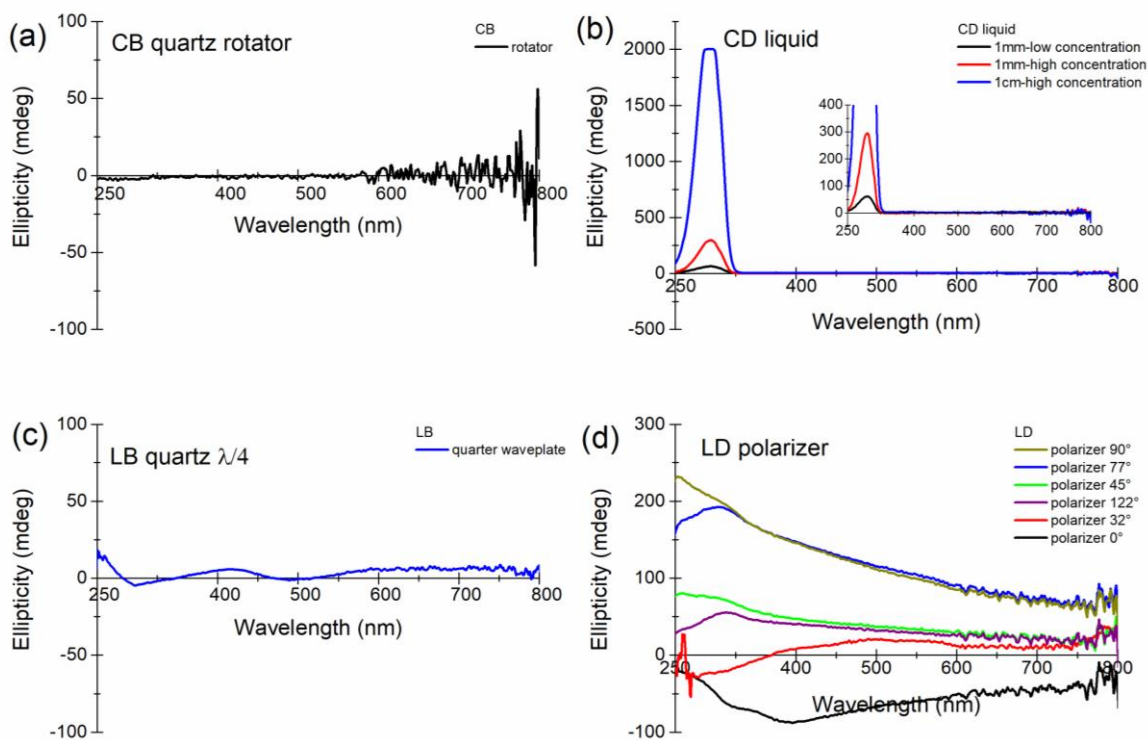


Figure 3.14: Investigations of potential CD artifacts creating an apparent ellipticity using CD spectro-polarimeter. Samples were single anisotropic optical property etalons: a) a CB quartz rotator, b) a pure CD liquid, c) a pure LB quartz quarter waveplate and d) a pure LD polarizer made of linear dichroic stretched polymer.

So assuming the following cases: a) presence of LD only, b) presence of LD only or c) presence of LB and LD with parallel or perpendicular slow/fast axis. We can estimate that CD spectro-polarimeter artifacts related to both PEM residual birefringence and polarization dependence of photomultiplier transmittance remain quite low. Indeed by considering some typical values of LB and LD reported in the nanogratings regime i.e. a LD of a few degree [46] and a LB on the order of  $\lambda/2$ , we can estimate their related CD artifacts to respectively  $<3$  mdeg and  $<8$ mdeg at 400nm. In addition, our ellipticity measurements are invariant by sample rotation, which indicate that these artefacts do not impact significantly the ellipticity results. However in the case d) where LB and LD have non parallel, non perpendicular orientation with respect to each others, the  $(LD' \cdot LB - LD \cdot LB')$  term become significant and can create an apparent CD signal up to a few hundreds mdeg and this even if the sample has no CD itself.

### 3.5.2 Investigations of Asymmetric transmission of circularly polarized light

The Lorentz reciprocity theorem is a key point of the electromagnetic theory of non-magnetic media. This may be formulated as follows: if two incident beams of equal intensity with the same polarization state but that exhibit opposite direction emerge from a medium, the same polarization components must have equal intensities. However our femtosecond-irradiated samples within Type II regime appear to violate the Lorentz reciprocity theorem because of their non-reciprocal (or asymmetric) transmission of left and right circularly polarized light. In addition this observation is quite distinct from materials that exhibit a natural optical activity like circular birefringence CB or circular dichroism CD because natural optical activity does not depend on the orientation of the wave vector [54, 55].

In the literature, asymmetric transmission is consequence of the "sample matrix  $M$ " being non-reciprocal. Non-reciprocal  $M$  are quite usual in optical systems made of sequences of optical elements, because the matrix product in general is no commutative. A classic example of such non-reciprocal response is an optical system composed of a polarizer followed by a retarder that is not equivalent to its reciprocal, a retarder followed by polarizer. Here, we might have a more subtle manifestation of non-reciprocity in the specific case of circular polarized light, originating in a single medium i.e. an achiral material (silica glass) modified by an achiral laser beam. However the easiest way to explain this asymmetric transmission of circularly polarized light is to consider a train of different optical elements namely a rotator followed by a linear phase shifter or the reverse as explained in the following paper [26] that we have inserted in this chapter. So it is worth to remind that, although our fs-irradiated samples are showing rather large non-reciprocal "effects", such type of optical response is not a consequence of any new optical phenomena and it is a quite ubiquitous in the polarimetric literature.



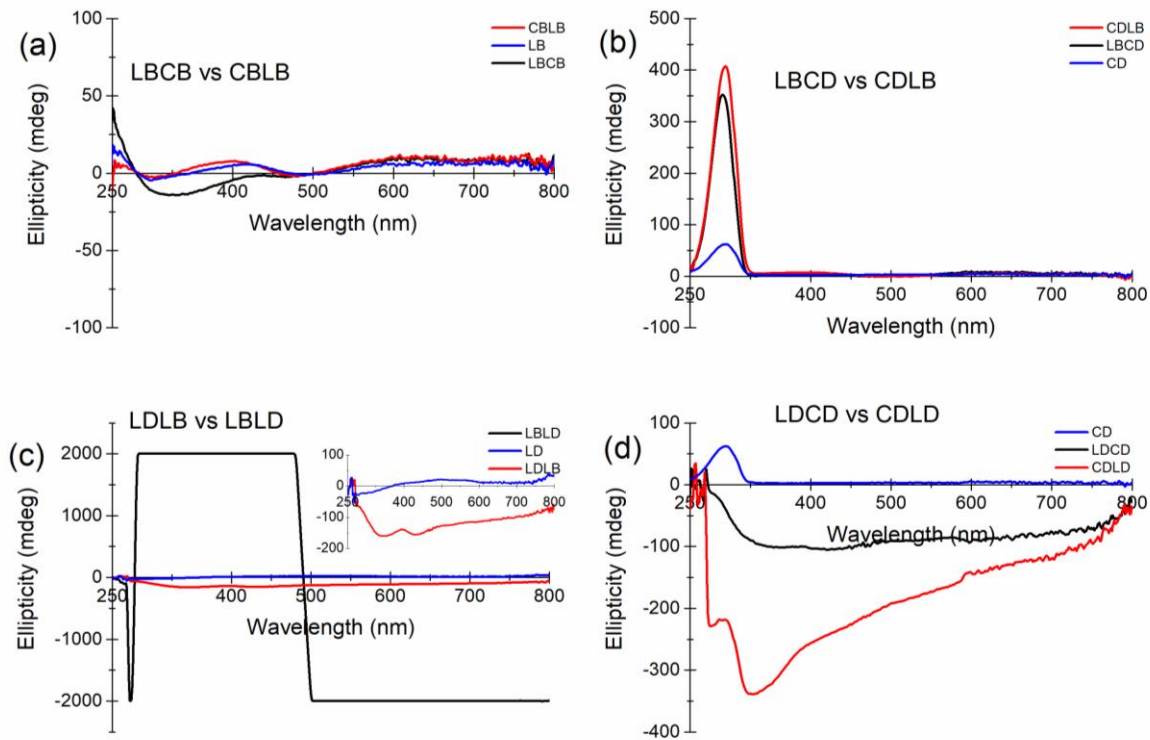


Figure 3.15: Investigations of potential CD artifacts creating an apparent ellipticity using CD spectro-polarimeter. Samples were the combination of two single property etalons. In addition we the asymmetric transmission of the couple of etalons was investigated. a) LB – CB combination, b) LB – CD combination, c) LB – LD combination and d) LD – CD combination.

On the one hand, we know that the non-reversibility (asymmetric transmission) of circular diattenuation could be due to the coexistence of linear and circular properties with different distribution in depth, which can be deduced from [48] as discussed in R. Desmarchelier PhD thesis from our group [51]. On the other hand, we have studied the artifacts of the CD spectrophotometer in the previous section and we have revealed that CD spectra are necessarily accompanied by artifacts due to macroscopic anisotropies such as linear birefringence (LB) and linear dichroism (LD), which are unique in the solid state. Thus in order to investigate more deeply both asymmetric transmission of circular polarized light and the creation of an apparent CD, we have decided to perform another set of experiments based on combination of two optical elements. For these experiments we used the following etalons:

- *CB etalon*: a quartz rotator cut in such a way there is neither LB nor LD. CB is on the order of  $45^\circ$  at 250nm.
- *CD etalon*: (+)-camphor in liquid solution with an ellipticity of few 10's mdeg in the UV range
- *LB etalon*: a quartz quarter waveplate at 550nm i.e. a LB of  $\pi/2$  at 550nm
- *LD etalon*: a dichroic sheet polarizer with an extinction ratio of 500 so  $LD = \ln(500)/2 = 3.11$  radians

All experiments were repeated by turning the backside of the set of etalons toward the light source, thus effectively changing the sign of the wave vector. The turn over was done

by rotating the combination of two etalons  $180^\circ$  around the y-axis of the spectro-polarimeter. As an example of case in Figure 3.15a the first pass, light was incident on the CB layer and then LB layer (forward configuration) and in the second pass; light entered the sample through the LB layer and then CB layer (backward configuration). All results are shown in Figure 3.15 and results can be summarized as follows:

- Case a), LB.CB vs CB.LB: Here the CD artifacts remain smaller than 20 mdeg in the whole spectral range and the measurements are nearly identical so have a symmetric light transmission.
- Case b), LB.CD vs CD.LB: Here the presence of LB in addition to a CD liquid sample leads to an enhancement by nearly one order of magnitude of the apparent CD that is accompanied by an asymmetric transmission in the 200-300nm spectral range where we have a non-zero CD.
- Case c), LD.LB vs LB.LD: Here we have first chosen the right orientation of LB in such a way we have nearly no apparent CD in the spectro-polarimeter due to the  $\sin(\ )$  term. Then we have inserted the LB etalon and we observe a significant apparent CD signal (up to 200 mdeg) for the forward configuration (LD.LB) and a huge one ( $>2$  deg) for the backward configuration (LD.LB). This confirms that a set of non-parallel, non-orthogonal anisotropic linear objects, namely here LB and LD, can create a strong effective CD.
- Case d), LD.CD vs CD.LD: First we have measure the CD etalon alone, which exhibits a CD only within the 200-300nm spectral range. Then when inserting the LD etalon in forward configuration (LD.CD), there is an apparent CD signal that has the same amplitude and spectral dependence observed for the LD etalon alone (see Figure 3.14d). Whereas for the backward configuration (CD.LD), we observe a higher apparent CD which reveals again an asymmetric transmission of circularly polarized light.

## 3.6 Discussion on the origin of fs laser-induced chiral optical property

The measured results above open to the following question: it seems that linearly polarized femtosecond laser beam entering an isotropic sample, a glass, under an axially symmetric geometry is able to break the chiral symmetry of the glass but what is the origin of this observation? Indeed we discover here a phenomenon, which is predicted to be achiral in the state of the knowledge and it actually gives rise to a chiral optical property like optical rotation and circular dichroism (or at least circular diattenuation).

### 3.6.1 An introduction to chirality and chiral optical properties in molecules

The optical definitions for circular dichroism (CD) and circular birefringence (CB) have been given in the chapter 2. A molecule is chiral when the mirror image of the molecular

structure cannot be "brought" to coincide with itself. Here "brought" refers to translations and rotations. A chiral molecule is said to be optical active (or possess optical activity) if it exhibits CD and CB. The structure of chiral molecules belong to symmetry point groups that lack the symmetry elements of a mirror plane, a center of inversion, or a rotation-reflection axis  $n > 2$ . Other symmetry elements like axis of rotation are allowed. Image and mirror image of a chiral molecule are called enantiomers. As a consequence of the lack of mirror symmetry the enantiomers are "non-superposable". In chemistry, the word racemic is used for compounds or mixtures of chiral molecules that have equal amounts of left- and right-handed enantiomers of a chiral molecule. Therefore, a racemic compound despite of containing chiral molecules is optically inactive, i.e. shows no CD or CB, because the contributions of both enantiomers, that are present in equal amounts, cancel each other.

A substance can, however, also be optically active due to an asymmetrical arrangement of molecules. In these cases, the molecules themselves need not necessarily to be chiral. For instance, the arrangement of achiral molecules on a helix results in an optically active molecule because a helix and its mirror image cannot be superposed (since reflection reverses the screw sense). Chirality excludes improper symmetry elements i.e. centers of inversion, reflection planes and rotation-reflection axes. A chiral molecule is not necessarily asymmetric as it can have, for example, rotational symmetry.

These spatial symmetry restrictions that impose chirality are not only applicable to molecules, but also to crystals and they are mathematically studied with the point group classification and constitute a very important subject in stereochemistry (that studies molecular geometry) and in crystallography. The origin of the optical activity in crystals can be of two types. The origin of optically active crystal can be attributed due optically active molecules (molecular origin) but it can also result from the crystal structure itself (i.e. crystalline origin). In the second case the crystal is usually characterized by the presence of a helix structure, i.e. the atoms or molecules lie on the helices the axes that are parallel to the optical axis of the crystal. The best-known optically active crystals are those of the space groups of symmetry  $D_{4d}$  and  $D_{6d}$  the elementary cell of which consist of three atoms or molecules. Typical examples of these crystals are quartz, tellurium, selenium, benzil or cinnabar. The majority of them are optically active due to the crystalline structure, which means that, for example, if they are melted they lose the optical activity. However, in a certain number of crystals (e.g. camphor and benzyl), the optical activity has both contributions: molecular and crystalline. *So the next question is how to explain the creation of circular optical properties (here a circular diattenuation) in a glass.*

### 3.6.2 Qualitative interpretation

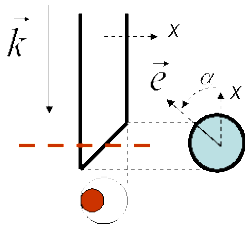
In this chapter we have decided to investigate the recent discovery of circular dichroism according to laser parameters namely polarization orientation, the energy per pulse and the focusing conditions. First we reveal that the creation of ellipticity (proportional to circular dichroism) is strongly correlated with formation of Type II modifications (nanogratings) in  $\text{SiO}_2$ . Then, we reveal that polarization can control the amplitude and the sign of the

imprinted circular dichroism. It is shown that by choosing a polarization oriented at 45° off the scanning direction and by optimizing the energy and the focusing conditions (NA, focusing depth), we can create a quite high ellipticity of -30 deg/mm in the UV range. This reveals the creation of a large circular diattenuation in a useful range for potential applications. In addition we have shown that spatial aberrations in strong focusing conditions are closely related to the creation of circular dichroism. In this case the deeper the geometrical focus penetrates into the bulk of the sample, the stronger the beam is distorted and elongated and the stronger is the observed circular dichroism. Mostly, this effect is usually undesired as it strongly distorts the intensity distribution in the focus, and this will likely affect the photo-induced optical properties written at different depths. It has been shown firstly by E. Mazur group in [56] that effect in matter is dependent on the focusing strength. Intensity at the focus in strong focusing conditions may reach TeraWatt/cm<sup>2</sup>. The beam is focused through the surface of the transparent material (here silica glass) and thus only at the focus; the intensity is large enough to be absorbed. In an usual case, the focal volume is something like an ellipsoid elongated [57, 58] not depending of the time-dependent phase relation between the electromagnetic field at different points. The fundamental quantities of the electromagnetic field at each point of this volume are polarization, intensity and phase. For Gaussian beams produced by the laser, the polarization is uniform in the cross section. In the best case, the phase surface is a plane perpendicular to the direction of propagation at the center along the direction of propagation of the ellipsoid if there is no aberration (geometrical, chromatical...) but this is never the case if some correcting optics are not used [59]. In addition, due to dispersion properties of the condensed phase, the phase differences between the different Fourier components of the pulse are modified and the pulse shape is therefore also modified. If perfect, the intensity is Gaussian in the cross section of the ellipsoid and also almost Gaussian in the propagation direction i.e. it is axi-symmetric but this is usually not the case, and there exist a spatial chirp and a related Pulse Front Tilt (PFT) from compression system in the laser. Then by choosing the correct configuration of the beam (e.g. a polarization non parallel to the PFT direction), we can force the electrons to move in the beam and create a inhomogeneous plasma in tailoring the amplitude and the direction of the ponderomotive force exerted on the electrons [60]. Just before my PhD, our group suggests [23] a non-linear mechanism summarized here : at the end of the pulse, this electron density distribution is trapped in the matter and a DC electric field is built in. Then, it may couple (during the tail of the first pulse or with a close next pulse) with the stress field  $(\vec{P} = \epsilon_0 \chi^0 \vec{E}_{DC} + \epsilon_0 \overline{\overline{\chi}} \vec{E}_{DC})$  and generate component, not parallel to  $\vec{E}$ . So this misalignment between  $\vec{E}_{DC}$  and the material polarization  $\vec{P}$  generates a volumic torque  $\vec{P} \wedge \vec{E}_{DC}$ , whose orientation and sign are controllable, and may twist the matter and create chiral atomic arrangements or chiral nanogratings distribution in 3D. At this step we assume that the polarization dependence of the photo-induced circular dichroism can be tentatively explained following this qualitative model as sketched in Figure 3.16.

### 1. Ponderomotive force $\vec{f}_e$ + PFT

$$I(x, z, t) \propto f(t + ax)$$

$$N_e \propto I^2$$



$$\omega_p^2 = \frac{N_e e^2}{m_e \epsilon_0}$$

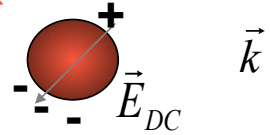
$$\epsilon = \epsilon_0 - \omega_p^2 / \omega^2$$

$$\vec{J} = \xi \vec{E}^* (\nabla \vec{E}) = -\xi \vec{E}^* (\vec{E} \frac{\nabla \epsilon}{\epsilon})$$

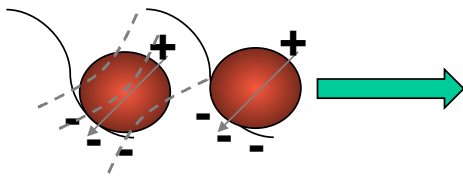
Kazansky et al. 2010

### 2. Trapping of the asymmetric electron density

Creation of a space charge and a DC electric field



### 3. DC-induced stress field is stored that is not center-symmetric



### 4. Combined action of the EDC and stress field giving rise to a volume torque

$$\vec{P} = \epsilon_0 \vec{E}_{DC} + \epsilon_0 \vec{E}_{DC}$$

$$\vec{P} = \epsilon_0 \vec{E}_{DC} + \epsilon_0 \text{Tr}(\overline{\overline{\epsilon}}) \vec{E}_{DC} + 2 \epsilon_0 \overline{\overline{\epsilon}}_{12} \vec{E}_{DC}$$

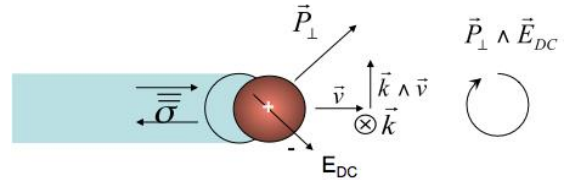


Figure 3.16: Scheme showing the combined action of the  $E_{DC}$  and stress field giving rise to a volume torque at the end of the written line.  $\vec{P}_\perp$  is the component of  $\vec{P}$  perpendicular to  $\vec{E}_{DC}$ . Scheme extracted from Poumellec et al. [23].

Previous studies have shown that symmetry breaking and anisotropic photosensitivity with respect to writing direction [61-64] are due to the presence of spatial chirp and/or Pulse Front Tilt (PFT). The occurrence of spatial chirp (wavelength vs. position) was thus measured in our system before the objective lens by scanning a fiber spectrometer across the laser spot. The spatial chirp was measured to be around 0,54nm/mm along X-axis and 0,02nm/mm along Y-axis. Then the combination of PFT (due to spatial chirp and the presence of dispersive optics) and strong focusing conditions (depth, high NA) can lead to a "light house effect" [65] and a Wave Front Rotation [66] conditioning the effects in the materials like anisotropic photosensitivity, asymmetric orientational writing [61-64] and the imprinting of circular optical properties. For example, it has been reported that after the objective lens (NA=0,65), the PFT increases from 13,5 fs/mm to 44 fs/mm [67] due to the GDD induced by the glass lens. So we expect a higher PFT when focusing deeper and especially at high NA whereas this effect is much less pronounced using a low NA, which agree qualitatively with our observations related to the amplitude of imprinted circular dichroism.

## 3.7 Conclusions

To summarize the key observations of this chapter:

- In agreement with previous investigations [23], an apparent CD (circular diattenuation) accompanied with an asymmetric transmission of circularly polarized light was observed in silica glass irradiated by femtosecond laser in various experimental conditions. In contrast we did not observe any asymmetric transmission of linearly polarized light based on the measurements of the anisotropic linear properties namely LB( ) and LD( ).
- To explain this asymmetric transmission, we modeled the ellipticity measurements using Jones formalism and we revealed that this effect arises from linear anisotropy as summarized in Ref. [26] and in the supplementary information's provided at the end of this chapter. In particular asymmetric transmission appears when linear and circular anisotropic optical properties have not the same depth distribution.
- Based on energy and pulse overlap dependence it appears that CD formation appears to be correlated with the formation of Type II modifications in silica (i.e. nanogratings formation) whereas no CD is observed in Type I regime.
- The positive LD for Xx configuration (and negative for Xy writing configuration) that we observed in [26] implies that higher losses were measured for polarization oriented perpendicular to the nanolayers in agreement with [46]. It is known that a layered medium made of alternating layers of two different isotropic materials with complex refractive indices, exhibits a linear dichroism [68]. However the linear dichroism observed in the UV-Vis range should be rather called linear diattenuation since it can be mostly attributed to polarization dependent scattering [46] due to the intrinsic nanoporous nature of the nanogratings. Following the same view, investigations of the line-to-line interval and of the distance between the sample and the detector (in the CD spectrometer) indicate that there is likely a contribution of anisotropic light scattering to the measured CD in relationship with the nanogratings formation.
- The control of polarization orientation and spatial aberrations under strong focusing conditions offer a way for creating strong circular diattenuation that could be further controlled including its sign.
- Estimates of equivalent circular dichroism for X+45° writing show values close to -30 deg/mm in the UV range and -20 deg/mm at 550 nm that is sufficient to think about optical devices.

### *About mechanisms*

The results confirm that a linearly polarized femtosecond laser beam entering an isotropic sample—a glass—under an axially symmetric geometry is able to break the chiral symmetry of the glass. Here, the material (silica glass) is predicted to be achiral, but femtosecond laser irradiation actually gives rise to a chiral property, i.e., circular dichroism (or more carefully said circular diattenuation because it is likely due to anisotropic light scattering) after fs irradiation.

As a first model Poumellec et al. [23] suggest that the breaking of symmetry arises from a volume torque due to the combined action of the stress field and a DC electric field (defined by the pulse front tilt, the focusing conditions and the laser polarization). The

misalignment between  $\vec{E}_{DC}$  and the material polarization  $\vec{P}$  generates a volumic torque  $\vec{P} \wedge \vec{E}_{DC}$ , whose orientation and sign are controllable, and may twist the matter and create chiral atomic arrangements.

At this step we do not know yet if the observed circular diattenuation originates from a fs pulse induced molecular optical activity. Another plausible explanation would be that CD band originates from several internal linear dichroism and birefringence contributions with non-parallel, non-perpendicular neutral axes. Following this view, the amplitude of the observed CD band will not only be related to the LD or LB optical phase shift of each contribution but also to the misalignment between their respective neutral axes.

#### *Next step – Mueller matrix spectro-polarimetry*

We confirm that laser–matter interaction can imprint circular optical properties beside linear ones with such efficiency that the reciprocity of light propagation in the glass is broken or more accurately asymmetric transmission is revealed [69]. After theoretical analysis of circular dichroism measurements using Jones formalism, we reveal that asymmetric transmission of circularly polarized light can be attributed to the coexistence of linear and circular properties with different distribution in depth.

However, in Type II regime there is some significant light scattering especially in the UV-Visible range due to the porous nanogratings, which likely leads to a significant light depolarization that could also be at the origin of the observed asymmetric transmission. Although the Jones formalism is an intuitive method to treat the light polarization and samples anisotropic properties, it can be only applied with totally polarized light. In contrast Mueller calculus is a generalization of the Jones formalism and can be used to represent any state of polarization including partially polarized light and unpolarized light. The Mueller calculus is general and can always be applied but is mandatory when partially polarized light has to be treated.

Although CD and CB are two effects that are interrelated, they are usually treated separately. CD is nonzero only in the spectral regions in which the molecule under study has optical transitions. However, CB is a dispersive measurement, and for an accurate study requires a scan over a wide spectrum. With CD it is easier to measure isolated transitions whereas CB measurements usually combine information about many electronic and vibrational transitions but CB (amplitude and spectral dispersion) is also of interest for optical applications.

In conclusion, in order to tentatively solve these problems or limitations, we need to use Mueller matrix spectro-polarimetry. This will allow us to investigate more deeply our samples and to tentatively extract all anisotropic optical properties, namely (LB, LB', LD, LD', CB, CD and the depolarization rates), but also their spectral dependence from the UV to the near-IR range.





### 3.8 References

1. Davis, K., et al., *Writing waveguides in glass with a femtosecond laser*. Opt. Lett, 1996. **21**(21): p. 1729-1731.
2. Shimotsuma, Y., et al., *Self-organized nanogratings in glass irradiated by ultrashort light pulses*. Physical Review Letters, 2003. **91**(24): p. 247405.
3. Schaffer, C., et al., *Laser-induced microexplosions in transparent materials: microstructuring with nanojoules*. Proceedings of SPIE, 1999. **3616**: p. 143.
4. He, L., K. Sheehy, and W. Culbertson, *Femtosecond laser-assisted cataract surgery*. Current opinion in ophthalmology, 2011. **22**(1): p. 43-52.
5. Glezer, E.N., et al., *Three-dimensional optical storage inside transparent materials*. Optics Letters, 1996. **21**(24): p. 2023-2025.
6. Podlipensky, A., et al., *Femtosecond laser assisted production of dichroitic 3D structures in composite glass containing Ag nanoparticles*. Applied Physics a-Materials Science & Processing, 2005. **80**(8): p. 1647-1652.
7. Watanabe, M., et al., *Three-dimensional optical data storage in vitreous silica*. Japanese journal of applied physics, 1998. **37**(12B): p. L1527.
8. Monat, C., P. Domachuk, and B. Eggleton, *Integrated optofluidics: A new river of light*. Nature photonics, 2007. **1**(2): p. 106-114.
9. Bellouard, Y., et al., *Fabrication of high-aspect ratio, micro-fluidic channels and tunnels using femtosecond laser pulses and chemical etching*. Optics express, 2004. **12**(10): p. 2120-2129.
10. Corrielli, G., et al., *Rotated waveplates in integrated waveguide optics*. Nature communications, 2014. **5**.
11. Beresna, M., M. Gecevičius, and P.G. Kazansky, *Polarization sensitive elements fabricated by femtosecond laser nanostructuring of glass [Invited]*. Optical Materials Express, 2011. **1**(4): p. 783-795.
12. Fernandes, L.A., et al., *Stress induced birefringence tuning in femtosecond laser fabricated waveguides in fused silica*. Optics Express, 2012. **20**(22): p. 24103-24114.
13. Heilmann, R., et al., *Arbitrary photonic wave plate operations on chip: Realizing Hadamard, Pauli-X, and rotation gates for polarisation qubits*. Scientific reports, 2014. **4**.
14. Desmarchelier, R., et al., *Achromatic polarization rotator imprinted by ultrafast laser nanostructuring in glass*. Applied Physics Letters, 2015. **107**(18): p. 181111.
15. Sudrie, L., et al., *Writing of permanent birefringent microlayers in bulk fused silica with femtosecond laser pulses*. Optics Communications, 1999. **171**(4-6): p. 279-284.
16. Kazansky, P.G., et al., *"Quill" writing with ultrashort light pulses in transparent materials*. Applied physics letters, 2007. **90**(15): p. 151120.

17. Lancry, M., et al., *Ultrafast nanoporous silica formation driven by femtosecond laser irradiation*. Laser & Photonics Reviews, 2013. **7**(6): p. 953-962.
18. Poumellec, B., et al., *Femtosecond laser irradiation stress induced in pure silica*. Optics Express, 2003. **11**(9): p. 1070-1079.
19. Lancry, M., et al., *Oriented creation of anisotropic defects by IR femtosecond laser scanning in silica*. Optical Materials Express, 2012. **2**(12): p. 1809-1821.
20. Taylor, R., E. Simova, and C. Hnatovsky, *Creation of chiral structures inside fused silica glass*. Optics Letters, 2008. **33**(12): p. 1312-1314.
21. Poumellec, B., et al., *Asymmetric Orientational Writing in glass with femtosecond laser irradiation*. Optical Materials Express, 2013. **3**(10): p. 1586-1599.
22. Poumellec, B., et al., *Non reciprocal writing and chirality in femtosecond laser irradiated silica*. Optics Express, 2008. **16**(22): p. 18354-18361.
23. Poumellec, B., et al., *Parity violation in chiral structure creation under femtosecond laser irradiation in silica glass*. Light: Science & Applications, 2016. **5**(11): p. e16178.
24. Shindo, Y., M. Nakagawa, and Y. Ohmi, *On the problems of CD spectropolarimeters. II: artifacts in CD spectrometers*. Applied spectroscopy, 1985. **39**(5): p. 860-868.
25. Salimnia, A., R. Vallée, and S.L. Chin, *Waveguide writing in silica glass with femtosecond pulses from an optical parametric amplifier at 1.5 $\mu$ m*. Optics Communications, 2005. **256**(4-6): p. 422-427.
26. Desmarchelier, R., et al., *Chiroptical properties photo-induced by femtosecond laser irradiation in silica glass*. Applied Physics Letters, 2017. **110**(2): p. 021112.
27. Zimmermann, F., et al., *The onset of ultrashort pulse - induced nanogratings*. Laser & Photonics Reviews, 2016. **10**(2): p. 327-334.
28. Taylor, R., C. Hnatovsky, and E. Simova, *Applications of femtosecond laser induced self - organized planar nanocracks inside fused silica glass*. Laser & Photonics Reviews, 2008. **2**(1 - 2): p. 26-46.
29. Taylor, R., et al., *Femtosecond laser erasing and rewriting of self-organized planar nanocracks in fused silica glass*. Optics Letters, 2007. **32**(19): p. 2888-2890.
30. Cerkauskaite, A., et al., *Ultrafast laser-induced birefringence in various porosity silica glasses: from fused silica to aerogel*. Optics Express, 2017. **25**(7): p. 8011-8021.
31. Poumellec, B., et al., *Modification thresholds in femtosecond laser processing of pure silica: review of dependencies on laser parameters [Invited]*. Optical Materials Express, 2011. **1**: p. 766.
32. Hnatovsky, C., et al., *Pulse duration dependence of femtosecond-laser fabricated nanogratings in fused silica*. Applied Physics Letters, 2005. **87**: p. 14104-1/3.
33. Bricchi, E., B.G. Klappauf, and P.G. Kazansky, *Form birefringence and negative index change created by femtosecond direct writing in transparent materials*. Optics Letters,

2004. **29**(1): p. 119-121.
34. Ramirez, L.P.R., et al., *Tuning the structural properties of femtosecond-laser-induced nanogratings*. Applied Physics A, 2010. **100**(1): p. 1-6.
  35. Venkatakrishnan, K., et al., *The effect of polarization on ultrashort pulsed laser ablation of thin metal films*. Journal of Applied Physics, 2002. **92**(3): p. 1604-1607.
  36. Corbari, C., et al., *Femtosecond versus picosecond laser machining of nano-gratings and micro-channels in silica glass*. Optics Express, 2013. **21**(4): p. 3946-3958.
  37. Zhang, J., et al., *Seemingly unlimited lifetime data storage in nanostructured glass*. Physical Review Letters, 2014. **112**(3): p. 033901.
  38. Beresna, M., et al., *Radially polarized optical vortex converter created by femtosecond laser nanostructuring of glass*. Applied Physics Letters, 2011. **98**(20): p. 201101.
  39. Gecevičius, M., M. Beresna, and P.G. Kazansky, *Polarization sensitive camera by femtosecond laser nanostructuring*. Optics letters, 2013. **38**(20): p. 4096-4099.
  40. Chandrasekhar, S., *The optical rotatory power of Quartz and its variation with temperature*. The proceedings of the indian academy of sciences 1952. **35**(3): p. 103-113.
  41. Kleinman, D.A. and W.G. Spitzer, *Theory of the Optical Properties of Quartz in the Infrared*. Phys. Rev., 1962. **125**: p. 16-30.
  42. Shimotsuma, Y., K. Miura, and H. Kazuyuki, *Nanomodification of Glass Using fs Laser*. International Journal of Applied Glass Science, 2013. **4**(3): p. 182-191.
  43. Poumellec, B., et al., *Parity violation in chiral structure creation under femtosecond laser irradiation in silica glass? Light: Science & Application, 2016. **5**, doi:10.1038/lssa.2016.178.*
  44. Gecevičius, M., et al., *Extraordinary anisotropy of ultrafast laser writing in glass*. Optics Express, 2013. **21**(4): p. 3959-3968.
  45. Gecevičius, M., *Polarization sensitive optical elements by ultrafast laser nanostructuring of glass*. 2015, University of Southampton.
  46. Beresna, M., et al., *Broadband anisotropy of femtosecond laser induced nanogratings in fused silica*. Applied Physics Letters, 2013. **103**(13): p. 131903.
  47. Kazansky, P.G., et al., *Anomalous anisotropic light scattering in Ge-doped silica glass*. Physical Review Letters, 1999. **82**(10): p. 2199-2202.
  48. Huard, S., *Polarization of light*. Polarization of Light, by Serge Huard, pp. 348. ISBN 0-471-96536-7. Wiley-VCH, January 1997., 1997. **1**.
  49. Lancry, M., et al., *Nanogratings formation in multicomponent silicate glasses*. Applied Physics B, 2016. **122**(3): p. 66.
  50. Lancry, M., et al. *Porous nanogratings and related form birefringence in silicate and germanate glasses*. in *Bragg Gratings, Photosensitivity, and Poling in Glass Waveguides*.

2014. Optical Society of America.

51. Lancry, M., et al., *Compact Birefringent Waveplates Photo-Induced in Silica by Femtosecond Laser*. *Micromachines*, 2014. **5**(4): p. 825-838.
52. Shindo, Y., M. Nishio, and S. Maeda, *Problems of CD spectrometers (V): Can we measure CD and LD simultaneously? Comments on differential polarization microscopy (CD and linear dichroism)*. *Biopolymers: Original Research on Biomolecules*, 1990. **30**(3 - 4): p. 405-413.
53. Kuroda, R., T. Harada, and Y. Shindo, *A solid-state dedicated circular dichroism spectrophotometer: Development and application*. *Review of Scientific Instruments*, 2001. **72**(10): p. 3802-3810.
54. Kaminsky, W., *Experimental and phenomenological aspects of circular birefringence and related properties in transparent crystals*. *Reports on Progress in Physics*, 2000. **63**(10): p. 1575.
55. Berova, N., et al., *Comprehensive chiroptical spectroscopy: applications in stereochemical analysis of synthetic compounds, natural products, and biomolecules*. Vol. 2. 2012: John Wiley & Sons.
56. Schaffer, C.B., A. Brodeur, and M. E., *Laser-induced breakdown and damage in bulk transparent materials induced by tightly focused femtosecond laser pulses*. *Measurement Science Technology*, 2001. **12**: p. 1784-1794.
57. Corkum, P.B., *Plasma perspective on strong field multiphoton ionization*. *Physical Review Letters*, 1993. **71**(13): p. 1994.
58. Couairon, A. and A. Mysyrowicz, *Femtosecond filamentation in transparent media*. *Physics Reports*, 2007. **441**(2): p. 47-189.
59. Cerullo, G., et al., *Femtosecond micromachining of symmetric waveguides at 1.5 mm by astigmatic beam focusing*. *Opt. Lett.*, 2002. **27**: p. 1938-1940.
60. Bethune, D., *Optical second-harmonic generation in atomic vapors with focused beams*. *Physical Review A*, 1981. **23**: p. 3139-3151.
61. Kazansky, P.G., et al., *Photosensitivity control of an isotropic medium through polarization of light pulses with tilted intensity front*. *Optics express*, 2011. **19**(21): p. 20657-20664.
62. Poumellec, B., et al., *Asymmetric Orientational Writing in glass with femtosecond laser irradiation*. *Optical Materials Express*, 2013. **3**(10): p. 1586-1599.
63. Vitek, D.N., et al., *Spatio-temporally focused femtosecond laser pulses for nonreciprocal writing in optically transparent materials*. *Optics Express*, 2010. **18**(24): p. 24673-24678.
64. Yang, W., P. Kazansky, and Y. Svirko, *Non-reciprocal ultrafast laser writing*. *Nature Photonics*, 2007. **2**: p. 99-104.
65. Quéré, F., et al., *Applications of ultrafast wavefront rotation in highly nonlinear optics*.

- Journal of Physics B: Atomic, Molecular and Optical Physics, 2014. **47**(12): p. 124004.
66. Akturk, S., et al., *Spatio-temporal couplings in ultrashort laser pulses*. Journal of Optics, 2010. **12**(9): p. 093001.
  67. Patel, A., M. Beresna, and P. Kazansky. *Harnessing polarization spatio-temporal coupling: a new degree of freedom in ultrafast laser material processing*. in *CLEO: Science and Innovations*. 2015. Optical Society of America.
  68. Yeh, P., *A new optical model for wire grid polarizers*. Optics Communications, 1978. **26**(3): p. 289-292.
  69. Arteaga, O., et al., *Complete polarimetry on the asymmetric transmission through subwavelength hole arrays*. Optics Express, 2014. **22**(11): p. 13719-13732.

## Supplementary material

### Appendix

$\varphi$  represents equivalent circular optical properties  $\varphi = \frac{\pi}{\lambda}(n_{Right} - n_{Left}) + \frac{1}{4}i(\alpha_{Right} - \alpha_{Left})$

$\phi$  represents equivalent linear optical properties  $\phi = \frac{\pi}{\lambda}(n_Y - n_X) + \frac{1}{4}i(\alpha_Y - \alpha_X)$

**Case 12 (noted  $\psi_{12}$  in the paper) ,  $M_{DR} = DR$**

$$|M_{DR}v|^2 = |DRv|^2 = DRv\overline{DRv}$$

$$DRv\overline{DRv} = 2 \cosh(Im\phi) [\cosh(2Im\phi) + m \sinh(2Im\phi)]$$

$$|M_{DR}v|^2 = 2 \cosh(Im\phi) [\cosh(2Im\phi) + m \sinh(2Im\phi)]$$

$$\psi_{12} = \psi_{DR} = \frac{|M_{DR}v_L|^2 - |M_{DR}v_R|^2}{|M_{DR}v_L|^2 + |M_{DR}v_R|^2}$$

$$= \frac{2 \cosh(Im\phi) [\cosh(2Im\phi) + \sinh(2Im\phi)] - 2 \cosh(Im\phi) [\cosh(2Im\phi) - \sinh(2Im\phi)]}{2 \cosh(Im\phi) [\cosh(2Im\phi) + \sinh(2Im\phi)] + 2 \cosh(Im\phi) [\cosh(2Im\phi) - \sinh(2Im\phi)]}$$

$$\psi_{12} = \frac{\sinh(2Im\phi)}{\cosh(2Im\phi)} = \tanh(2Im\phi)$$

**Case 21 (noted  $\psi_{21}$  in the paper):  $M_{RD} = RD$**

$$|M_{RD}v|^2 = |RDv|^2$$

$$= |RDv|[\overline{RDv}]$$

$$= 2 \cosh(Im\phi) \cosh(2Im\phi) - 2m \cos(Re\phi) \sinh(2Im\phi)$$

$$\psi_{21} = \psi_{RD} = \frac{|M_{RD}v_L|^2 - |M_{RD}v_R|^2}{|M_{RD}v_L|^2 + |M_{RD}v_R|^2}$$

$$\psi_{21} = \frac{\cos(Re\phi) \sinh(2Im\phi)}{\cosh(Im\phi) \cosh(2Im\phi)} = \tanh(2Im\phi) \frac{\cos(Re\phi)}{\cosh(Im\phi)}$$

To model the ellipticity  $\psi_{12}$ , for a beam going from face 1 to face 2, we can choose that  $M_{12} = D(\theta, \phi)R(\varphi)$ , where the probe beam passes through a rotator and then an optical phase shifter. When the sample is reversed, the matrices have to be permuted;  $\phi$  and  $\varphi$  are kept the same but  $\theta$  changes its sign. The ellipticity can be read as follows for both face orders of measurement:

$$\psi_{12} = \tanh[2 \operatorname{Im}(\varphi)] \quad \psi_{21} = \tanh[2 \operatorname{Im}(\phi)] \frac{\cos[\operatorname{Re}(\varphi)]}{\cosh[\operatorname{Im}(\varphi)]} = \tanh[2 \operatorname{Im}(\phi)] \frac{\cos[\frac{2\pi}{\lambda} \Delta n_L l_t]}{\cosh[\frac{1}{2} \Delta \alpha_L l_t]}$$

The ellipticity is a combination of linear and circular properties, whereas due to their magnitude, the equivalent linear properties coincide with the real ones. Thus we can see that the non-reciprocity of the ellipticity measurements arises from the different distribution in depth of circular and linear properties.



# Chapter4 Mueller matrix spectro-polarimetry in femtosecond irradiated silica glass

---

## Content

4.1 Introduction.....	152
4.2 Materials and methods .....	153
4.3 Typical results using MM-16 spectro-polarimetry .....	155
4.3.1 Raw Mueller matrix measurements.....	155
4.3.2 Extraction of polarimetric properties.....	157
4.3.3 Investigation of asymmetric transmission .....	160
4.4 Study of laser parameters dependence: pulse energy, pulse-to-pulse overlap and focusing depth .....	163
4.5 Influence of the laser writing configuration.....	172
4.5.1 Influence of the writing polarization direction for a fixed scanning direction and orientation i.e. along +X .....	175
4.5.2 Influence of the laser scanning direction with respect to the writing laser polarization.....	178
4.6 Dependence of the stress-induced birefringence with the laser writing polarization .....	180
4.7 Thermal stability of fs-induced anisotropic optical properties .....	184
4.8 Conclusions.....	193
4.9 References.....	196



## 4.1 Introduction

The predominant way of characterizing directly nanogratings is the analysis of the structure under a scanning electron microscope. Despite its straightforwardness, the method restricts characterization of the femtosecond laser induced anisotropy to the measurements of the nanogratings period and the porosity-filling factor. The alternative, nondestructive way of characterizing the anisotropic structure is conventional quantitative birefringence measurements (e.g. a quarter waveplate based technique like Sénarmont compensator or the Abrio commercial setup), which provide information on the dependence of induced modification on writing parameters such as pulse energy, repetition rate, numerical aperture, linear polarization orientation etc... However these methods are limited to linear birefringence measurements and suffer from strong errors when others anisotropic properties are also co-existing in the same sample. The three main polarimetric properties are the dichroism (or diattenuation), the birefringence (or retardation) and the depolarization.

This problem was recently investigated in the PhD thesis of Rudy Desmarchelier (2013-2016) using Jones matrix formalism. Indeed the state of light of a fully polarized beam can be described using the Jones formalism, which was discovered by R. C. Jones in 1941 [1]. Jones approach is the simplest way to treat polarized light using a complex bi-dimensional vector to describe a given state of polarization, and the corresponding 2 by 2 complex Jones matrix representing the transformation action of an optical element on the polarization state of an illuminating beam. Although the Jones formalism is an intuitive method to treat the light polarization and samples with anisotropic properties, it can be only applied with totally polarized light. Mueller calculus, which was already completed in 1943 by Hans Mueller is a generalization of the Jones formalism and can be used to represent any state of polarization including partially polarized light and unpolarized light. The Mueller calculus is general and can always be applied but is mandatory when partially polarized light has to be treated but the phase is lost. Thus, in this chapter we will use the Mueller calculus formalism as we deal with only one beam, which is a complete mathematical approach to describe the polarimetric light-matter interaction as described in chapter 2. This method should provide us the means to measure the key physical quantities of the femtosecond laser written structures with sufficient accuracy to draw meaningful conclusions from the experiments designed in this chapter.

In the previous chapter we discovered the creation of UV-Vis circular diattenuation [2], measuring it using a circular dichroism spectrometer and we reveal that the beam asymmetry and laser polarization determine the amplitude and the sign of circular attenuation [3]. Here, we use a quite recent method, Mueller-matrix spectroscopic ellipsometry, as a powerful tool to examine structural and optical properties of surfaces, thin films, and multilayered materials that exhibit both linear and circular optical properties from a single measurement [4, 5]. A few years ago, Mueller matrix ellipsometry was tentatively used in femtosecond laser irradiated silica but the authors reveal only well-known linear

birefringence related to the nanogratings for polarization parallel or perpendicular to the scanning direction [6]. The objective of this chapter is to investigate in depth widely circular optical properties, mostly in the visible range, using differential matrix formalism [7] on transmission Mueller matrices measured on femtosecond laser-induced modifications in silica within Type II regime. This allows quantifying the effective or equivalent circular birefringence and dichroism in the presence of strong linear optical properties. In particular, we will focus on optical activity (or circular birefringence) photo-induced in silica glass by laser irradiation. We will investigate circular optical properties dependence according to the pulse energy, the focusing depth, the repetition rate and the writing configuration (scanning direction vs linear polarization direction). We also consider compaction and rarefaction processes since it is known that they can create some mechanical stress during the formation of the nanogratings. Mechanical stress can create birefringence due to the non-negligible photoelastic tensor of glass. In this view we have imprinted Type II modifications following a specific design in such a way we can create a confined stress-zone between laser-induced "stress bars". In particular we will investigate the stress-induced birefringence (its amplitude and its slow axis orientation) according to the orientation of the writing laser polarization. Finally the thermal stability of the overall anisotropic optical properties within Type II regime by step isochronal annealing is analyzed. The experimental results allow comparing the thermal stability anisotropic linear optical properties and circular optical properties but also to the stress-induced birefringence to tentatively bring additional insight on the origin of the imprinted chiral optical properties.

## 4.2 Materials and methods

### *Femtosecond laser writing*

The laser radiation was produced by a femtosecond laser system operating at 1030 nm and delivering pulses of 250 fs at a repetition rate  $f$  of 10-500 kHz. The beam was focused within 300  $\mu$ m below the front face of 1-mm-thick silica glass plates (SuprasilCG from Heraeus) using a numerical aperture (NA) of 0.6 aspheric lens. Based on preliminary investigations that we made with a circular dichroism spectro-polarimeter, we chose to investigate here a specific writing configuration in terms of polarization orientation. When the laser was moving along +X (horizontal direction on the laser) and the linear polarization was oriented +45° from the writing direction, we define it as "X+45°" configuration of writing. Then, by moving the sample along +X axis with at a scanning speed  $v$  of 1 mm/s, we created several squares (3x3 mm<sup>2</sup>) made of a set of lines with a line spacing of 1  $\mu$ m to have a uniform scanned region and to avoid diffraction effects. The pulse energy was varied from 0.1 up to 6  $\mu$ J and the pulse density ( $v/f$ ) from 10 up to 1000 pulses/ $\mu$ m. Studies have shown that symmetry breaking and variable photosensitivity with respect to writing (or scanning) direction [8, 9] are based around spatial chirp and related pulse front tilt (PFT). The spatial chirp (wavelength vs. perpendicular position) was thus measured before the objective lens by scanning a spectrometer across the laser spot. The spatial chirp was found around 0,54nm/mm along x-axis and 0,02nm/mm along y-axis. Note that in order to avoid blurring

such asymmetric orientational writing effects (e.g. a difference between forward and backward scanning), all samples were written using a single scanning orientation e.g. +X and not using a forward/backward scanning trajectory.

### *Measurement of Mueller Matrix using MM-16 method*

Spectral normalized Mueller matrices were recorded with a spectroscopic Mueller ellipsometer Smart SE, JY HORIBA) in transmission at normal incidence. Owing to this unique technology the MM-16 has the ability to provide full Mueller Matrix measurements in addition to the capabilities of a classical ellipsometer. The design of the instrument has been optimized in order to minimize the errors in the final result for a given magnitude of the errors in the raw measurements as referenced in the experimental chapter. We have seen in our preliminary experiments that our samples show asymmetric transmission when measuring ellipticity using a circular dichroism spectrometer based on photo-elastic modulation [2, 3]. Later this asymmetric transmission appeared to be ascribed to the co-existence of linear and circular optical properties with different spatial distribution [3] as discussed in chapter 3. So, we decided to perform most of this study from both sides of the sample i.e. the front face (FF) and the back face (BF), with the FF being the one, which received the direct fs irradiation.

### *Extraction of polarimetric properties using the Log decomposition approach*

According to [10], the polarimetric optical response of a medium which has its optical path-length,  $l$ , can be defined as a superposition of the following basic polarimetric properties as defined in chapter 2: linear birefringence  $LB = \frac{2\pi}{\lambda}(n_X - n_Y)l$ ,  $45^\circ$  linear birefringence  $LB' = \frac{2\pi}{\lambda}(n_{45} - n_{135})l$ , linear dichroism  $LD = \frac{2\pi}{\lambda}(\kappa_X - \kappa_Y)l$ ,  $45^\circ$  linear dichroism  $LD' = \frac{2\pi}{\lambda}(\kappa_{45} - \kappa_{135})l$ , circular birefringence  $CB = \frac{2\pi}{\lambda}(n_L - n_R)l$  and circular dichroism  $CD = \frac{2\pi}{\lambda}(\kappa_L - \kappa_R)l$ . Note, this phase shift corresponds to twice the angle  $\theta_{ii}$  that the vector of the electric field of a linearly polarized wave would have turned around the axis of propagation after passing through the sample e.g. the specific optical rotation  $\theta_{CB} = CB/2$ .

By using the differential decomposition described extensively in [10] and detailed in chapter 2, it is possible to extract all the above-mentioned polarimetric properties of a sample if these are homogeneous along the direction of light propagation. Indeed a logarithmic or differential decomposition is suitable to describe continuous samples in which polarization and depolarization properties appear together and are well distributed across the sample in transmission configuration. In short, the logarithmic decomposition is well adapted for samples, which are not discrete systems, but rather continuous and homogeneous media as expressed in the following equation.

$$\frac{d\mathbf{M}(z)}{dz} = \mathbf{m} \cdot \mathbf{M}(z) \quad \text{Equation.1}$$

where  $\mathbf{m}$  is a differential Mueller matrix that does not depend on  $z$ ,  $\mathbf{M}(z)$  is the Mueller matrix of the anisotropic sample,  $d\mathbf{M}(z)/dz$  is a gradient of  $\mathbf{M}$  along the direction of light propagation,  $z$ . The Mueller matrix,  $\mathbf{M}(z)$ , can be represented with the exponential function as below,

$$\mathbf{M}(z) = \exp(\mathbf{m} \cdot z) \quad \text{Equation 4.2}$$

and can be rewritten to define the logarithmic of Mueller matrix,  $\mathbf{L}$ , as below,

$$\mathbf{m} \cdot z = \ln\mathbf{M}(z) = \mathbf{L} \quad \text{Equation 4.3}$$

The differential Mueller matrix,  $\mathbf{m}$ , contains the elementary polarimetric properties of the sample per unit of distance. The connection between the basic polarimetric properties and the elements of the matrix  $\mathbf{m}$  is discussed in [10, 11] and specified for clarity in the upper-left inset of most figures showing the matrix after decomposition.

### *Nanogratings direct imaging using SEM*

For a deeper investigation the influence of laser parameters or annealing on the change of nanogratings, the samples were cleaved using a diamond pen. The laser tracks have been observed using a Field-Emission Gun Scanning Electron Microscope (FEG-SEM, ZEISS SUPRA 55 VP). This allows to examine uncoated dielectric specimens using low accelerating voltage (typ. in the range of 1 kV) and very low current (a few pA) because they can keep an image resolution good enough even in these extreme conditions) and thus the original characteristics of the samples may be preserved for further testing or manipulation (no conductive coating and no etching in particular). So we can observe the intimate structure of the nanogratings namely either the internal structure of the porous nanolayers or the nanogratings distribution. As a reminder, the parallel condition (Xx or X0°) enable to observe pores inside of the laser-induced nanoplanes, while the orthogonal condition (Xy or X90°) permits sideways visualization of several nanolayers.

## **4.3 Typical results using MM-16 spectro-polarimetry**

### 4.3.1 Raw Mueller matrix measurements

Figure 4.1 and Figure 4.2 show the Mueller matrix,  $\mathbf{M}$ , of three samples written at 1.5 J/pulse and measured from the front face FF with the direction of writing parallel to the reference x-axis of the system (this is called azimuth  $=0^\circ$ ). These three samples were written with different writing configurations namely Xx, Xy and X+45°. All samples show low linear and circular dichroism because the elements  $m_{12}$ ,  $m_{21}$ ,  $m_{13}$  and  $m_{31}$  are either null or very small. In contrast, the elements  $m_{34}$  and  $m_{43}$ , being close to +1 and -1 respectively highlight a significant high linear birefringence. The Mueller matrix of the Xx and Xy samples have been found to be approximated by  $M_{\Psi\Delta}$  whereas X+45° sample corresponds to  $\mathbf{M} = \mathbf{R}(-45^\circ)$

$M_{\Psi\Delta}R(45^\circ)$ , where  $R(\ )$  is the rotation matrix and  $M_{\Psi\Delta}$  is the standard block-diagonal Mueller matrix of a non-depolarizing linear retarder, with the following non-null elements  $M_{11}=M_{22}=1$ ,  $M_{12}=M_{21}=\cos(2\Psi)$ ,  $M_{33}=M_{44}=\sin(2\Psi)\cos(\Delta)$  and  $M_{34}=-M_{43}=\sin(2\Psi)\cos(\Delta)$ . The parameter  $\Psi$  is related to the total linear dichroism  $=\cos(2\Psi)$  and  $\Delta$  corresponds to the total linear retardance  $\Delta = \sqrt{(LB^2 + LB'^2)}$ .

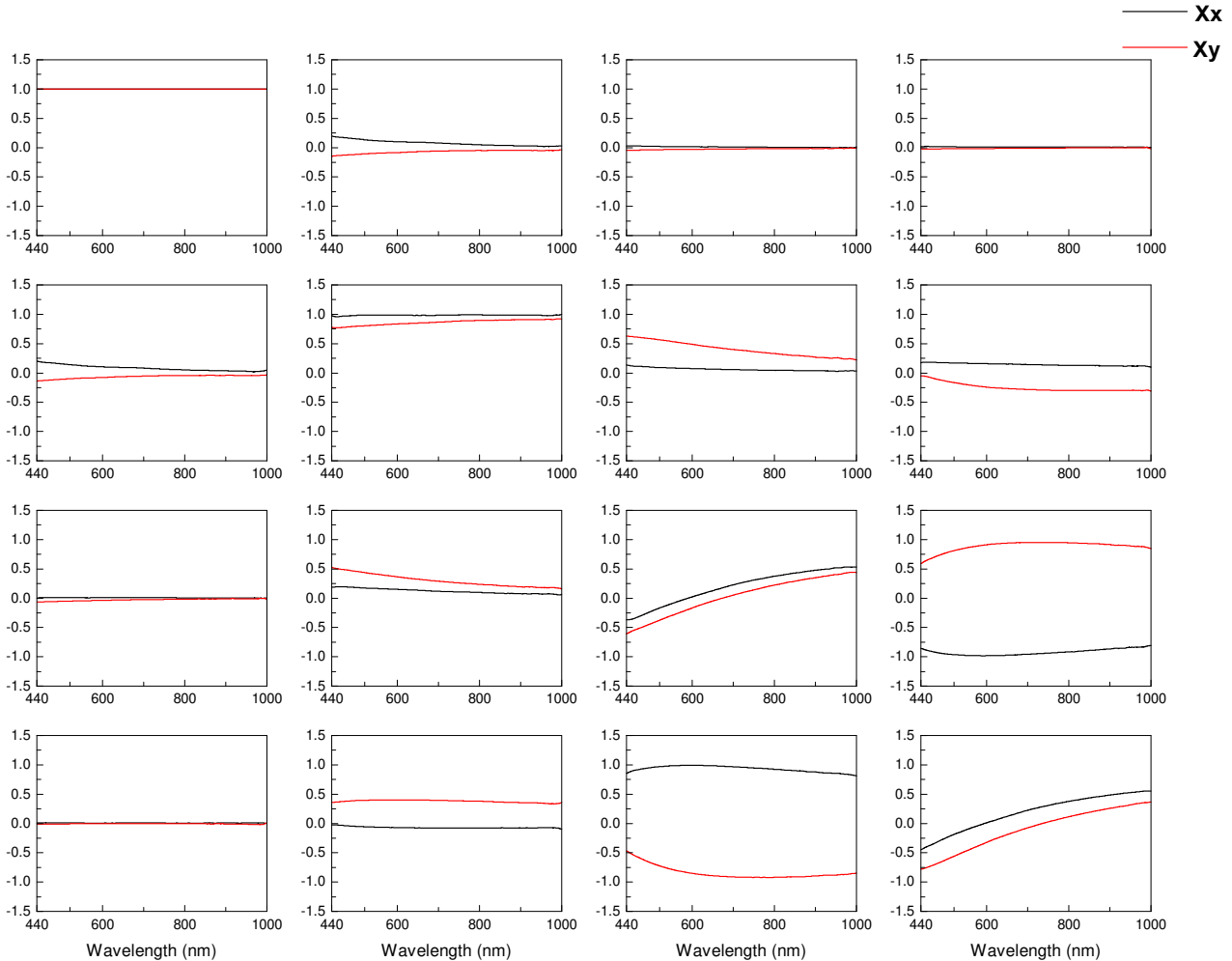


Figure 4.1: Spectroscopic Mueller matrix (normalized intensity) corresponding to samples written according to the (left) Xx and (right) Xy configurations. Measurements are shown for the sample measured from the front face. The sign changes observed for off-diagonal elements are mostly related to the rotation of the neutral axis of the anisotropic linear optical properties. Laser parameters: 1030 nm, 250 fs, 0.6 NA, 1,5 J/pulse.

This corresponds to say that the slow axis direction of the linear birefringence coincides with the chosen writing polarization orientation that is rotated from the direction of writing i.e.  $90^\circ$  for Xx,  $0^\circ$  for Xy and  $= -45^\circ$  for X+45° sample. This is in agreement with the fact that these samples exhibit mostly a strong form birefringence (uniaxial negative) due to the presence of nanogratings [12]. Therefore the previous results seem to suggest that the orientation of the neutral axes (i.e. the orientation of the linear birefringence) is determined by the direction of the linear polarization of the writing laser. Moreover when comparing the latter to the results from the scanning electron microscopy images, it can be said that the slow axis of the linear retardance, aligns with orientation of the nanolayers, which is in turn perpendicular to the orientation of the linear polarization of the writing laser.

According to an ideal model based on the above interpretation the Mueller matrix element  $M_{33}$  should be equal to one for the configurations Xx and Xy. However, the fact that the measured values of  $M_{22}$  appear to be slightly smaller (0.95–0.99) than one, especially in the violet-blue spectral regions, seem to indicate that a small amount of depolarization is induced by the sample. In summary, high linear retardation, low linear diattenuation, and small depolarization effects characterize our samples in the 450–1000 nm spectral range.

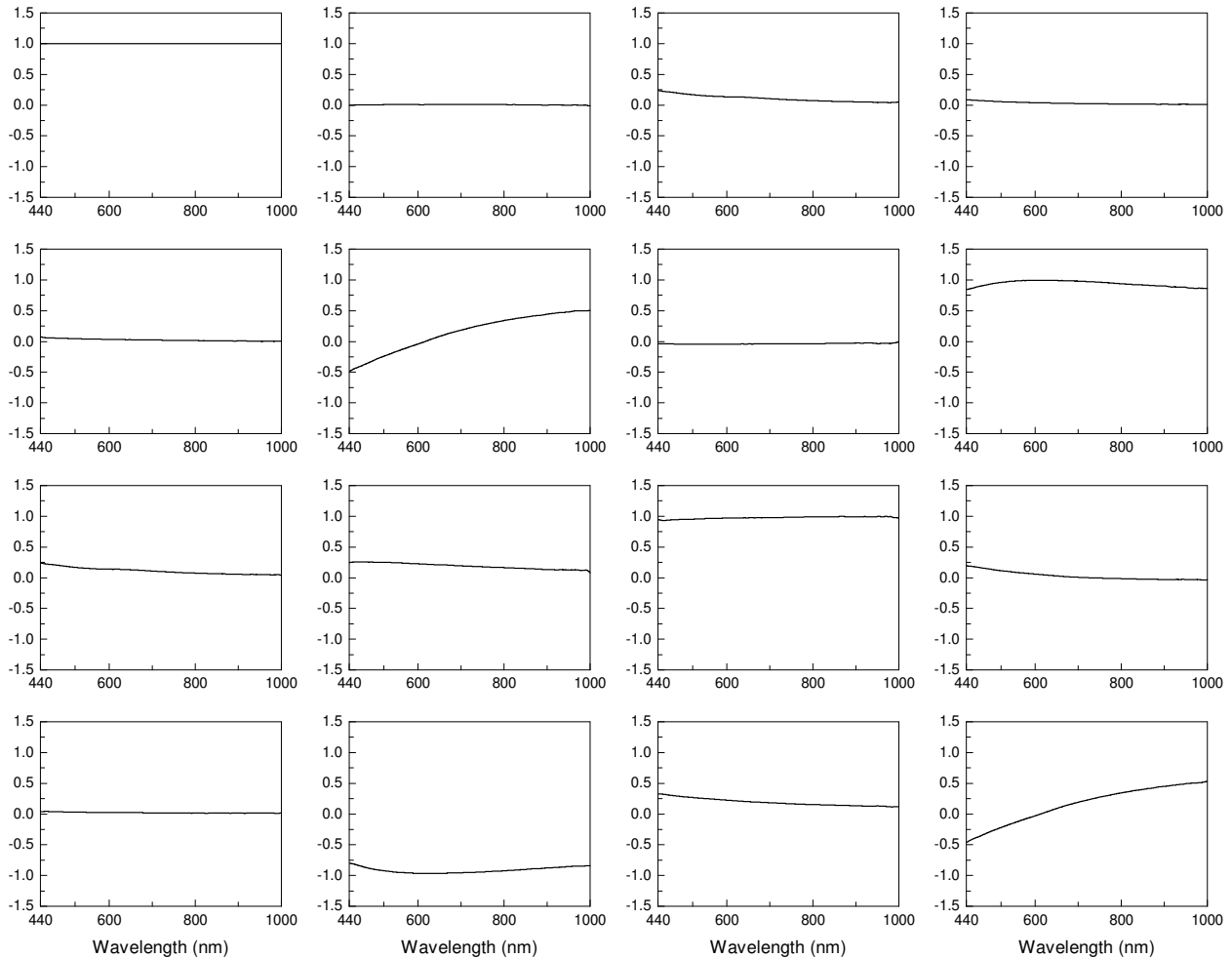
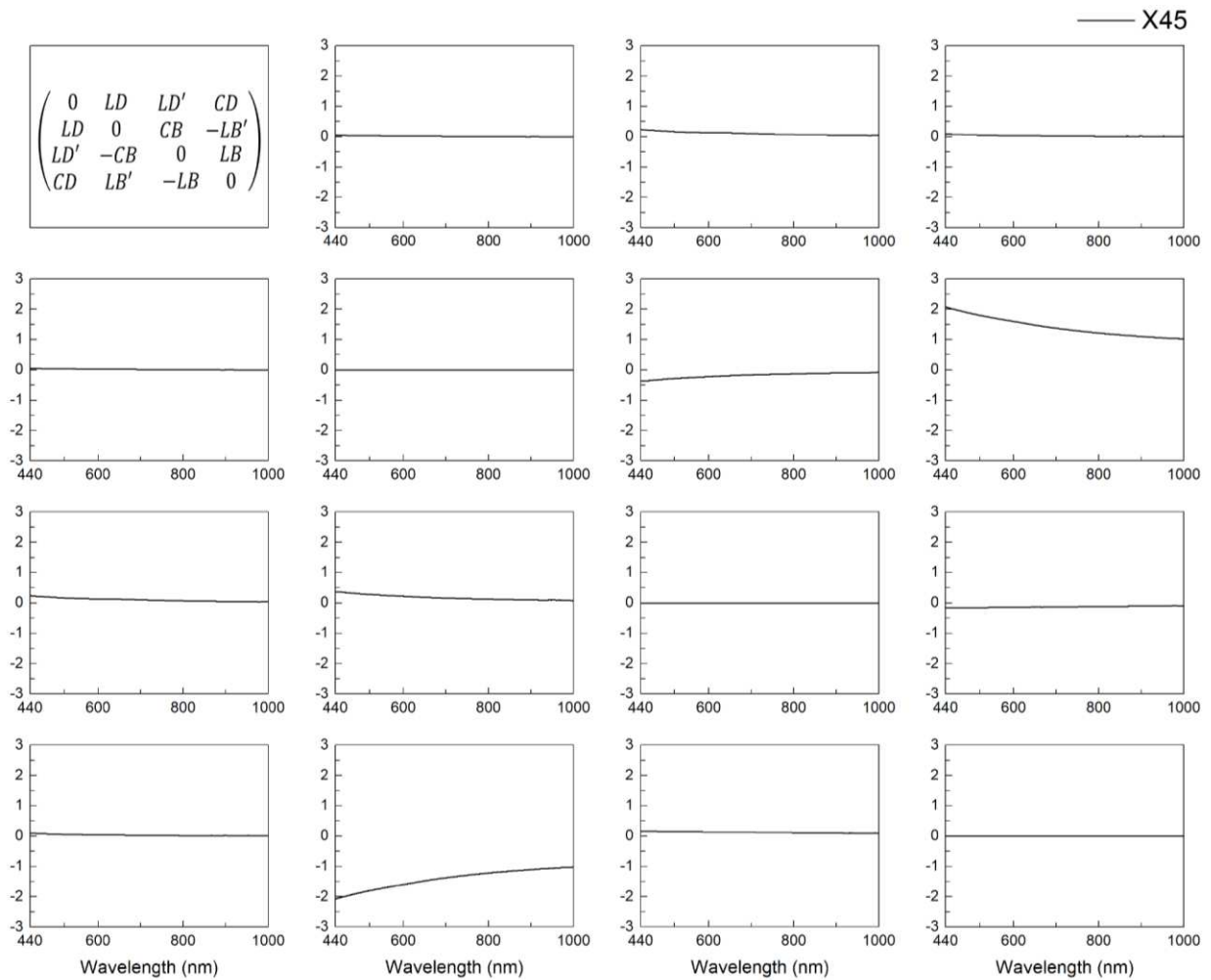


Figure 4.2: Spectroscopic Mueller matrix (normalized intensity) corresponding to a sample written according to X+45° configuration. Measurements are shown for the sample measured from the front face. The sign changes observed for off-diagonal elements are mostly related to the rotation of the neutral axis of the anisotropic linear optical properties which are mostly related to the nanogratings orientation as described schematically on the right side. Laser parameters: 1030 nm, 250 fs, 0.6 NA, 1,5 J/pulse.

### 4.3.2 Extraction of polarimetric properties

In the following we will apply differential decomposition formalism to a X+45° sample written at various fs pulse energy ranging from 0.1 up to 6 J/pulse. An example of differential decomposition of  $M$  is shown in Figure 4.3. For a non-depolarizing medium, the differential matrix  $L$  is Minkowski antisymmetric and contains the six elementary optical properties fully characterizing the medium: linear dichroism (LD) and birefringence (LB), 45° linear dichroism (LD') and birefringence (LB'), and circular dichroism (CD) and birefringence

(CB) [13]. If the medium is depolarizing as it is slightly the case for the violet-blue range (up to 10 % of depolarization at 450 nm) [14], the depolarization can be interpreted as resulting from the fluctuations of the optical properties i.e. linear birefringence (nanogratings and stress distributions) and extinction coefficient, which influence the elementary polarization properties of the irradiated silica glass [10, 11]. Note the depolarization rate is slightly higher for linearly polarized light than for circularly polarized light.



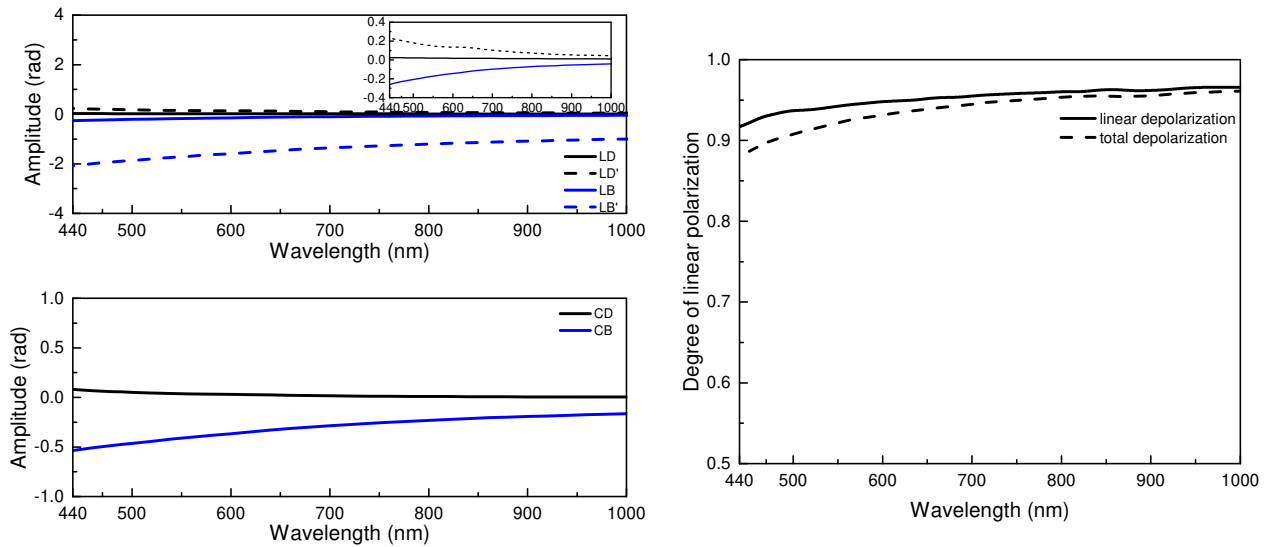


Figure 4.3: Experimental differential matrix corresponding to a sample written according to the X+45° configuration. The correspondence between the polarimetric properties and the matrix elements is shown in the upper-left inset. The values of the polarimetric properties are given in radians. Extractions of the anisotropic optical properties together with the degree of depolarization are shown below. Laser parameters: 1030 nm, 250 fs, 0.6 NA, 1,5 J/pulse.

For  $\lambda > 750$  nm all depolarization effects remain smaller than 5 % and monotonically decrease. Therefore, we suggest that the observed depolarization is likely due to light scattering effects related to the nanoporosity [15] that are intrinsic of nanogratings [16–19] generated in Type II regime. The spectral variation of the six parameters CB, CD, LB, LD, LB', and LD' in the differential Mueller matrix is shown in the bottom part of Figure 4.3. It is seen that the couple of x-y linear effects (LB and LD) is small, while the couple of crossed linear properties (LB' and LD') is quite important. This is because the polarization of the sample (X+45°) written by laser was oriented at  $\pm 45^\circ$  to the reference axis. If the polarization had been oriented parallel or perpendicular to the X direction (Xx or Xy), the couple of LB and LD would have been maximal and the couple of LD' and LB' would have been minimized due to related nanogratings orientation and the associated form birefringence. That's why we will also use the notion of total LB and total LD since these two properties are independent of the sample orientation in the x-y plan. For the circular effects, we notice a monotonous increase of CD for shorter wavelengths. Above 800 nm, CD is close to zero. The corresponding Kramers–Kronig consistent feature in CB also tends to zero for longer wavelengths whereas it approaches toward negative values for shorter wavelengths, i.e.  $-0.365$  rad ( $20.9^\circ$ ) at 450nm.

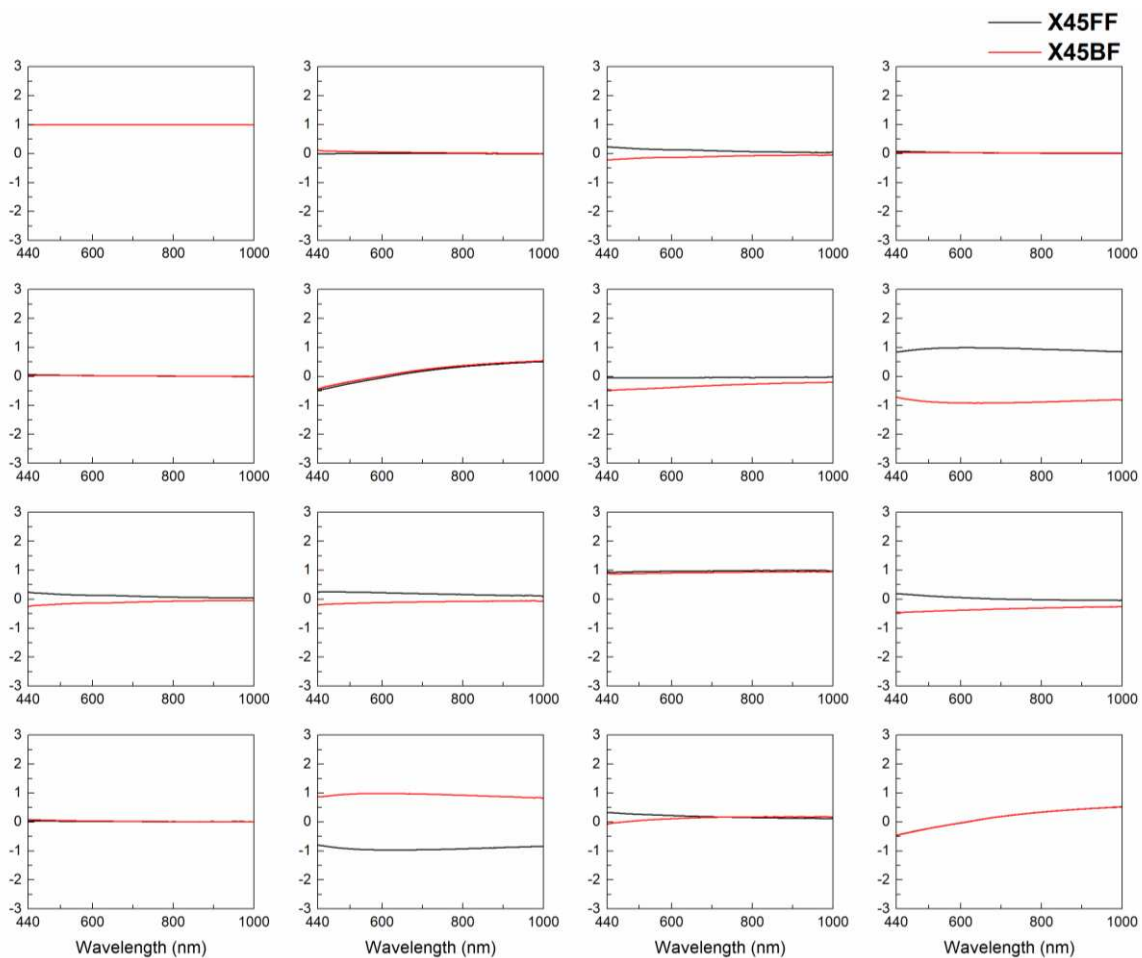
The results establish that a linearly polarized femtosecond laser beam focus in a glass under an axially symmetric geometry is able to break the chiral symmetry. Here the material (silica glass) is achiral but femtosecond laser irradiation actually gives rise to a chiral property i.e. a significant optical rotation ( $\theta = CB/2$ ) that is reported for the first time. However based on preliminary investigations [2, 3], we know that fs irradiation modifies the physical structure of the material along the pulse path across the sample like the creation of nanogratings, permanent volume changes and the formation of a stress field. *In*



consequence, it is expected here that the measured birefringence or dichroism parameters do not correspond to intrinsic material properties but to effective or equivalent structural parameters induced by fs laser pulse.

### 4.3.3 Investigation of asymmetric transmission

Figure 4.4 shows the Mueller matrix,  $M$ , of a  $X+45^\circ$  sample written at 1.5 J/pulse and measured from the front face FF (black line). The sample was oriented in such a way that its direction of writing is parallel to the reference x-axis of the system (this is called azimuth  $0^\circ$ ). Also shown is  $M_{rev}$ , i.e., the Mueller matrix measured in the reverse direction i.e. from the back face BF (red line). The differences between the two matrices are that  $m_{13}$ ,  $m_{31}$ ,  $m_{24}$ , and  $m_{42}$  change their respective signs whereas all other elements remain invariant. This symmetry implies that  $M$  fulfills the principle of reciprocity. The difference between the elements of predicted  $M_{rev}$  from a measured Mueller matrix,  $M$ , and the elements of the measured  $M_{rev}$  is typically  $<0.1$  which is attributed to slight misalignment of the sample  $\pm 2^\circ$  with respect to the azimuth. This can be further confirmed after the differential decomposition where the total LB and total LD are identical within 0,01 rad. This indicates that the anisotropic optical properties are quite similarly distributed along the propagation direction [3].



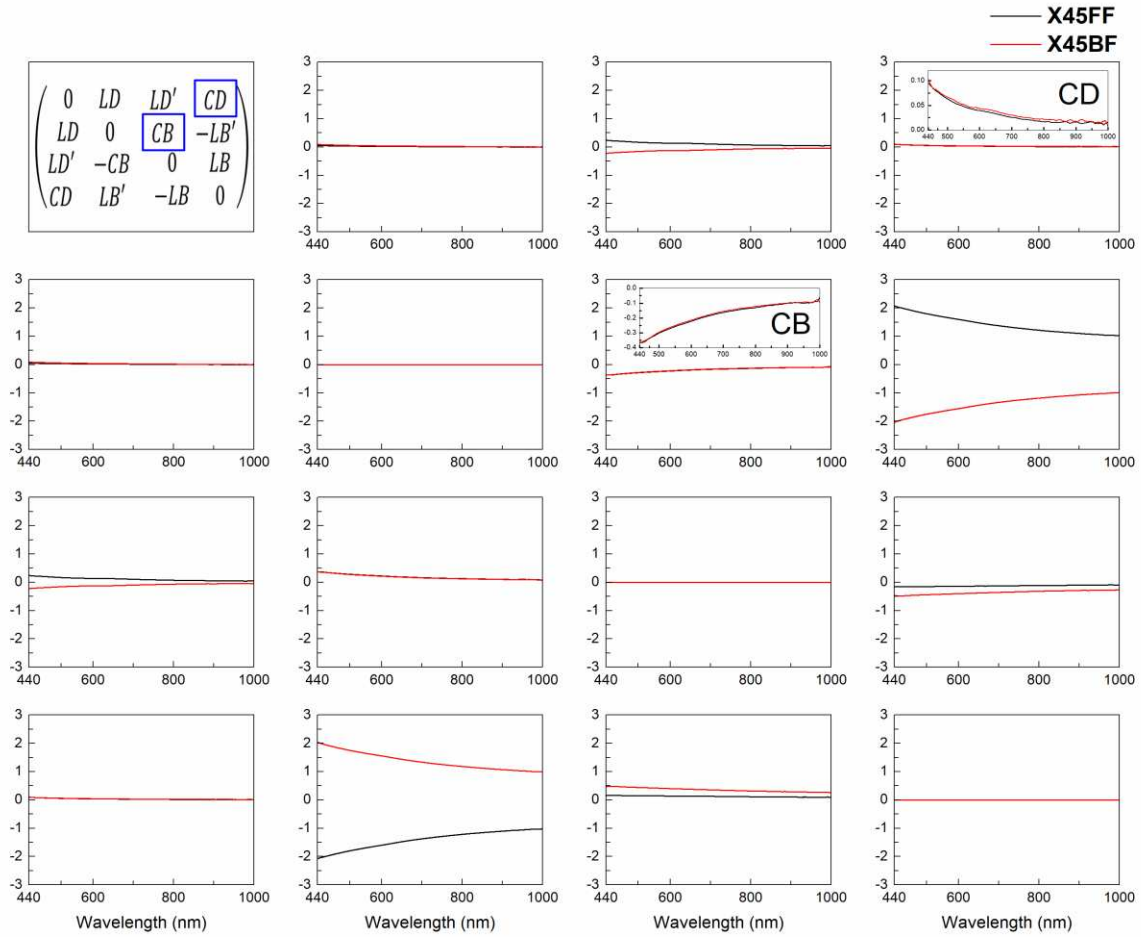


Figure 4.4: Spectroscopic Mueller raw matrix (Left) and its log decomposition (Right) for a sample written according to the X+45° configuration. Measurements are shown for the sample measured from the front face (black lines) and from the back face (red lines). The off-diagonal elements of the matrix for FF have opposite sign respect to those of the matrix at BF, whereas the rest of elements have equal sign. Laser parameters: 1030 nm, 250 fs, 0.6 NA, 1,5 J/pulse

Li demonstrated [20] that the off-diagonal elements of the Jones matrix are anti-symmetric for symmetric structures as a result of the electromagnetic reciprocity theorem. For a pure linear anisotropic sample, this gives a Mueller matrix which satisfies the following symmetry  $M_{12} = M_{21}$ ;  $M_{14} = M_{41}$ ;  $M_{24} = M_{42}$  and anti-symmetry conditions:  $M_{13} = -M_{31}$ ;  $M_{23} = -M_{32}$ ;  $M_{34} = -M_{43}$ . However this does not fully match with our experiments (we have  $M_{24} = -M_{42}$ ) since our way to investigate light reciprocity consists in a sample rotation of 180° as described in the case a/ in Figure 4.5. When a perfect linear retarder sample is rotated azimuthally of 180° (case a) the resulting geometry is equivalent to the original non-rotated one, except that the s component of the electric field of the light have changed its sign. In other words, "p( $\phi$ )" = "p( $\phi \pm 180^\circ$ )" and "s( $\phi$ )" = "-s( $\phi \pm 180^\circ$ )". This transformation makes the signs of all the off-diagonal elements of a rotated Mueller matrix to change respect to the elements of the non-rotated matrix. In particular for a symmetric linear retarder the following relations are always satisfied:

$$M_{13}(\varphi) = -M_{13}(\varphi \pm 180^\circ) = -M_{31}(\varphi) = M_{31}(\varphi \pm 180^\circ)$$

$$M_{14}(\varphi) = -M_{14}(\varphi \pm 180^\circ) = M_{41}(\varphi) = -M_{41}(\varphi \pm 180^\circ)$$

Equation 4.4

$$M_{23}(\varphi) = -M_{23}(\varphi \pm 180^\circ) = -M_{32}(\varphi) = M_{32}(\varphi \pm 180^\circ)$$

$$M_{24}(\varphi) = -M_{24}(\varphi \pm 180^\circ) = M_{42}(\varphi) = -M_{42}(\varphi \pm 180^\circ)$$

$$M_{34}(\varphi) = -M_{34}(\varphi \pm 180^\circ) = -M_{43}(\varphi) = M_{43}(\varphi \pm 180^\circ)$$

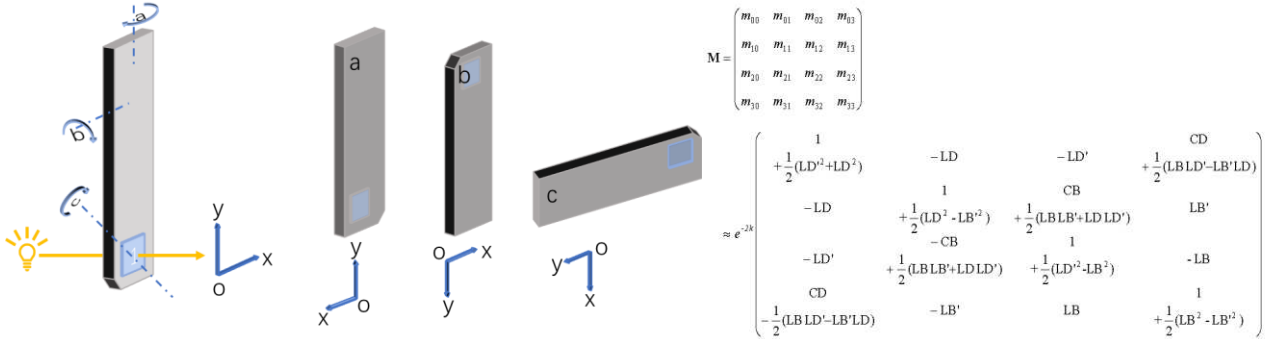


Figure 4.5: Scheme of samples possible rotations that we investigated. Reduced Mueller matrix for a thin specimen with mixed anisotropies and assuming that CD and CB are smaller than LD and LB (as it is the case in practice) so second-order terms in the chiral anisotropies as well as quadratic terms were neglected.

Note that different sample rotations were investigated as described by the three different cases in Figure 4.5. Figure 4.6a shows the Mueller matrix,  $M$ , of a  $X-22^\circ$  sample written at  $1.5 \text{ } \mu\text{m}$  and measured from the front face FF. As it can be seen *cases a and b* are leading to the same results after the differential decomposition. In contrast for the *case c*, a  $90^\circ$  rotation, the off-diagonal elements related to the linear properties have opposite sign respect to *cases a and b*, whereas the rest of elements have equal sign. However calculating the total LB and the total LD, as shown in Figure 4.6b, leads to identical spectral dependence for all investigated samples as expected.

These symmetry relations under rotation are not fulfilled if the sample is not a perfect linear retarder as shown in Figure 4.5. The lack of symmetry can be due the presence of asymmetry or imperfection induced by the laser writing process like the creation of circular optical properties [21-23] or the presence of depolarization effects. For example elements  $m_{14}$  and  $m_{41}$  are formed by a superposition of effects due to both circular and linear parts, with the linear contribution intervening with opposite signs in  $m_{14}$  and  $m_{41}$  respectively. Therefore since linear properties are non-zero, one expects that before decomposition  $m_{14}$  be different than  $m_{41}$ .

In many practical situations, the asymmetric effects due to circular optical properties are small because these are at least 1 or 2 orders of magnitude lower than the linear ones, and may be comparable in magnitude to the measurement errors of standard ellipsometric systems. In our case, the fact of being able to measure a full Mueller matrix allows to profit the redundancies of all elements of the Mueller matrix to achieve an optimal discrimination between asymmetric effects and experimental measurement errors. Therefore, when only partial Mueller matrices are available, an extra-care must be taken in order to not mix-up

both effects. In the following we will always measure the full Mueller matrices and we will investigate asymmetric transmission for all our samples.

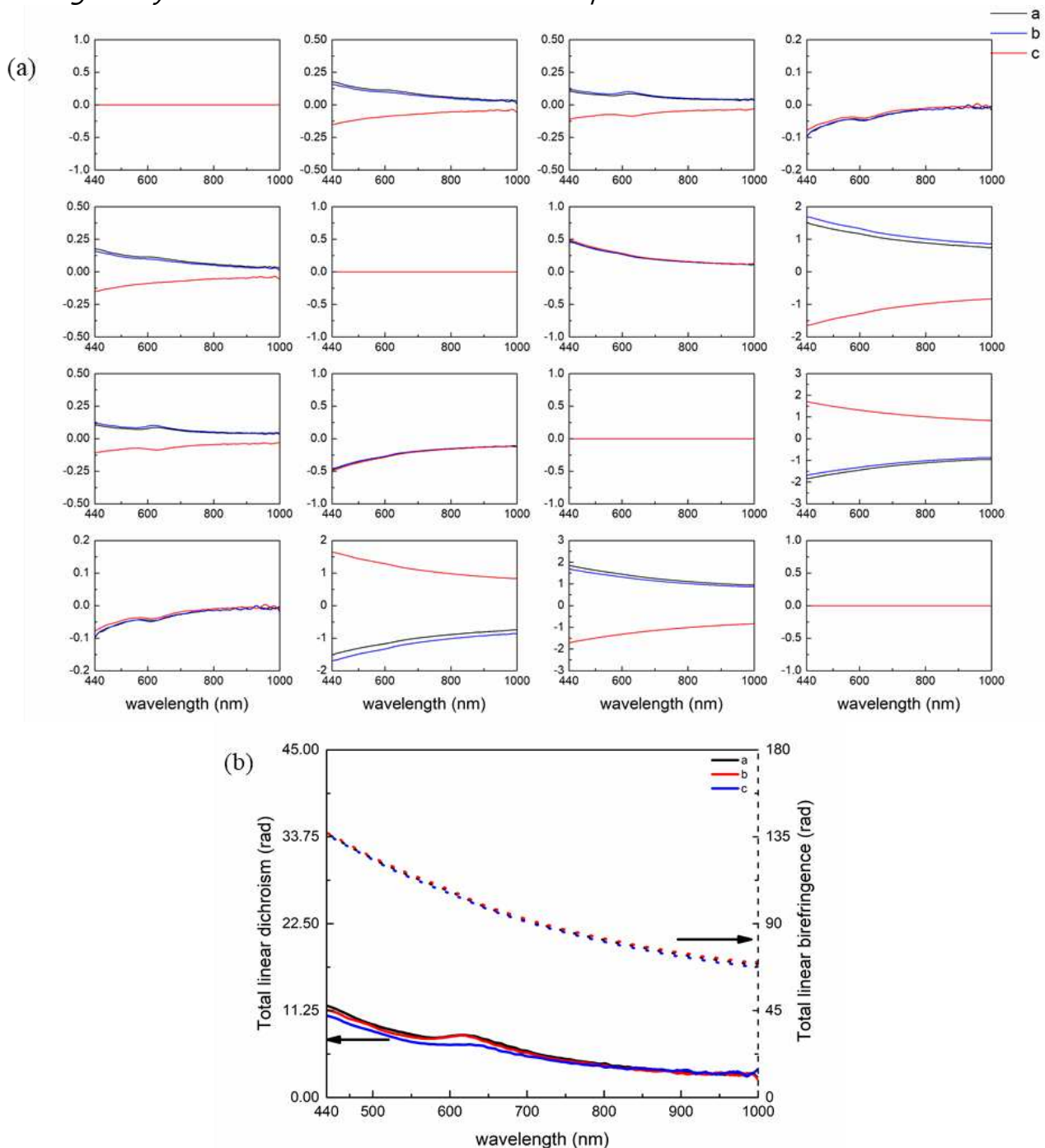


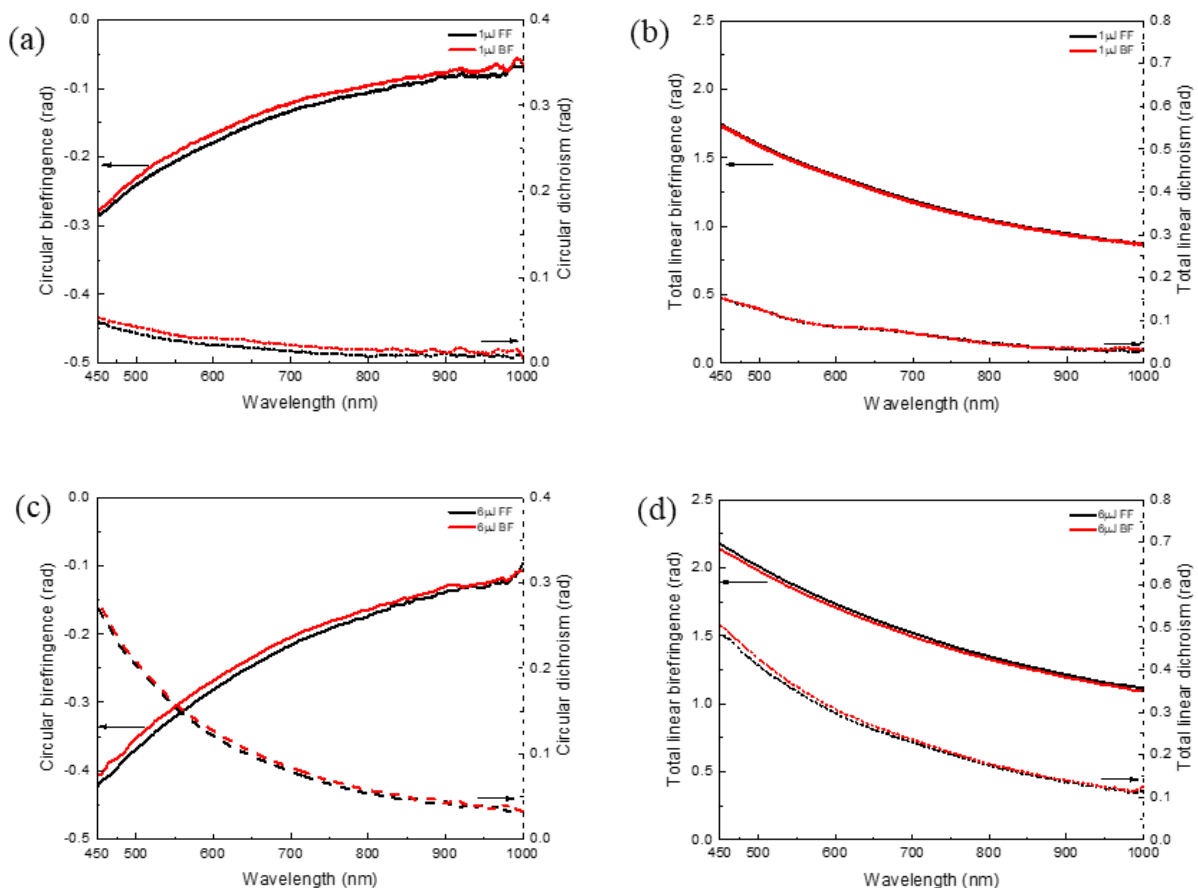
Figure 4.6: Spectroscopic Mueller matrix after decomposition (Left); total LB and total LD (Right) for a sample written according to the X-22° configuration. The off-diagonal elements of the *c* matrix (90° rotation) have opposite sign in respect to others whereas the rest of elements have equal sign. Laser parameters: 1030 nm, 250 fs, 0.6 NA, 1,5 J/pulse.

## 4.4 Study of laser parameters dependence: pulse energy, pulse-to-pulse overlap and focusing depth

In the previous chapter it was already demonstrated, that when increasing the pulse

energy, linear retardance increases until certain value and then saturates. In addition laser pulse energy has also other influence on modification such as smoothness and associated light scattering. Finally further increasing the laser pulse energy, leads to a decrease of the retardance and the formation of voids like structure (at high energy) or bubbles formation if a significant heat accumulation occurs (at high repetition rate). So to correlate the formation of linear and circular optical properties we have investigated samples in a wide range of experimental conditions. Squares (3x3 mm) with different laser energies 0,1 up to 6 J/pulse were fabricated with a 0.6 NA objective (300 μm focusing depth) and a laser emitting at 1030nm with pulse duration fixed to 250 fs. For these samples "high writing speed" of 1 mm/s and a laser repetition rate of 100 kHz were used.

In order to induce nanogratings, pulse density of few ten's to few hundred's pulses is required. So we have also investigated samples written with different speed (0,01 to 1 mm/s) and repetition rates in order to play on the pulse density. The focusing depth dependence of anisotropic optical properties was also studied using a 0.6 NA aspheric lens and the geometrical focus was moved from 100 down to 800 μm into the bulk of the 1mm thick silica sample (SuprasilCG). Finally the fabricated structures were measured with MM-16 Mueller spectro-polarimetric method.



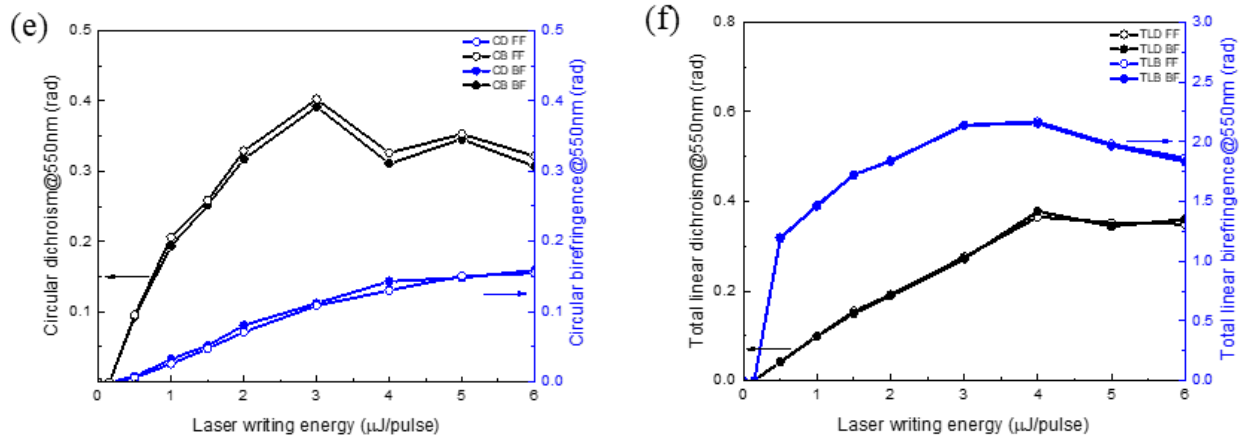


Figure 4.7: (a) circular birefringence, CB, and circular dichroism, CD spectra for 1 J/pulse; (b) TLB and TLD spectra for for 1 J/pulse; (c) CB and CD spectra for 6 J/pulse; (d) TLB and TLD spectra for 6 J/pulse; (e) Experimental values of effective CB and CD, at 550 nm as a function of fs pulse energy. Note there is no CB or CD in Type I regime. (f) TLB and TLD recorded at 550 nm. All data are shown for both, back and front faces. Laser parameters: 1030 nm, 250 fs, 100 kHz, 0.6 NA, 1 mm/s, X45° configuration.

### *Influence of laser pulse energy and anisotropic optical properties*

In order to correlate the creation of circular optical properties (namely both CD and CB) to the existence of porous nanogratings and related anisotropic optical properties (namely LB, LD), we have first analyzed samples written with different pulse energies. The chosen writing configuration was X+45° in order to create some significant CB, CD as point out in section 4.2. In agreement with [24], below the energy threshold T2 for the appearance of nanogratings [25], there are negligible linear optical properties and no circular ones. On the contrary, for pulse energies above nanogratings formation (typ. >0,15 J in our conditions: 1030 nm, 250 fs, 0,6 NA, 300 μm focusing depth, 100 kHz, 1 mm/s), significant circular optical properties, both CB and CD, appear together with the linear ones. Some typical CB and CD spectra are shown in Figure 4.7a to Figure 4.7d, whereas Figure 4.7e highlights the variations of laser-induced CD and CB measured at 550nm according to fs laser pulse energy.

- Firstly, there is a trend towards increasing all properties (CB, CD, LB, LD) at short wavelengths and the absolute amplitude of all properties increases from 0.5 to 3 J/pulse.
- Secondly, depending on laser pulse energy we can see three distinctive phases of modification for LB and CB. At lowest laser pulse energy, we have no modification. With a pulse energy higher than 0,5 J, we have the creation of CB and LB. From Figure 4.7e and Figure 4.7f we can observe that total linear birefringence TLB and CB values increase monotonously with increase of laser pulse energy until it reaches maximum around 3-4 J/pulse. Further increase in the pulse energy results in a decrease of both CB and TLB, which appear thus correlated to each other. Note that CB can reach -0,4 rad at 550nm.
- Third, concerning the dichroism, we do not observe any decrease in the investigated energy range. We observe a monotonous growth of both CD and LD as a function of

the energy and there is a trend to saturation in the 4 to 6 J/pulse energy range. CD can reach 0,15 rad at 550nm

For all measurements we made here in X+45° configuration, we observed that all samples exhibit a symmetric transmission. In addition the apparent sign of the *ellipticity* is positive but it can be reversed by rotating the polarization axis of the laser by 90° as we revealed in [3] and further discussion will be provided in the next section of this chapter.

#### *Influence of laser pulse energy on nanogratings formation*

In order to correlate the birefringence to the existence of porous nanogratings, we have analyzed the laser tracks cross-sections written in X+45° configuration using SEM images. In addition for better investigation, we have studied two parameters dependence: the pulse energy and the focusing depth. The FEG-SEM secondary electrons images shown in Figure 4.8 highlight the modifications morphology occurring above T2 threshold for different pulse energy. The laser polarization was at 45° off the writing direction in order to reveal both the nanoplanes but also their intrinsic nanoporosity. At low energy, we observe only a few nanoplanes in the laser propagation direction for the studied overlapping rate  $v/f$  that has been fixed at  $10^2$  pulses/micron. Then, there is a trend towards increasing widths and lengths of the modified regions as the pulse energy increases from 0.5 to 4 J/pulse. In particular, we can observe that the number of nanoplanes is increasing along the width of the laser tracks. In all our samples, we observed that nanopores always occur along with nanoplane formation for pulse energies higher than 0.5 J/pulse as it can be seen on the right side images. In Figure 4.8, a bifurcation forms in the "head part" of microstructure when the laser pulse energy is higher than 3 J/pulse. The head part demonstrated an energy-dependent evolution on the "bifurcation formation" [26]. When the laser energy was small ( $< 0.5 \mu\text{J}$ ), the bifurcation was not visible in experiments (nor simulations). With increasing pulse energy, the intensity bifurcation emerges and becomes increasingly pronounced. Such shapes should be attributed to the optical intensity distribution as a high-energy fs pulse converges into the focal point [27-29].

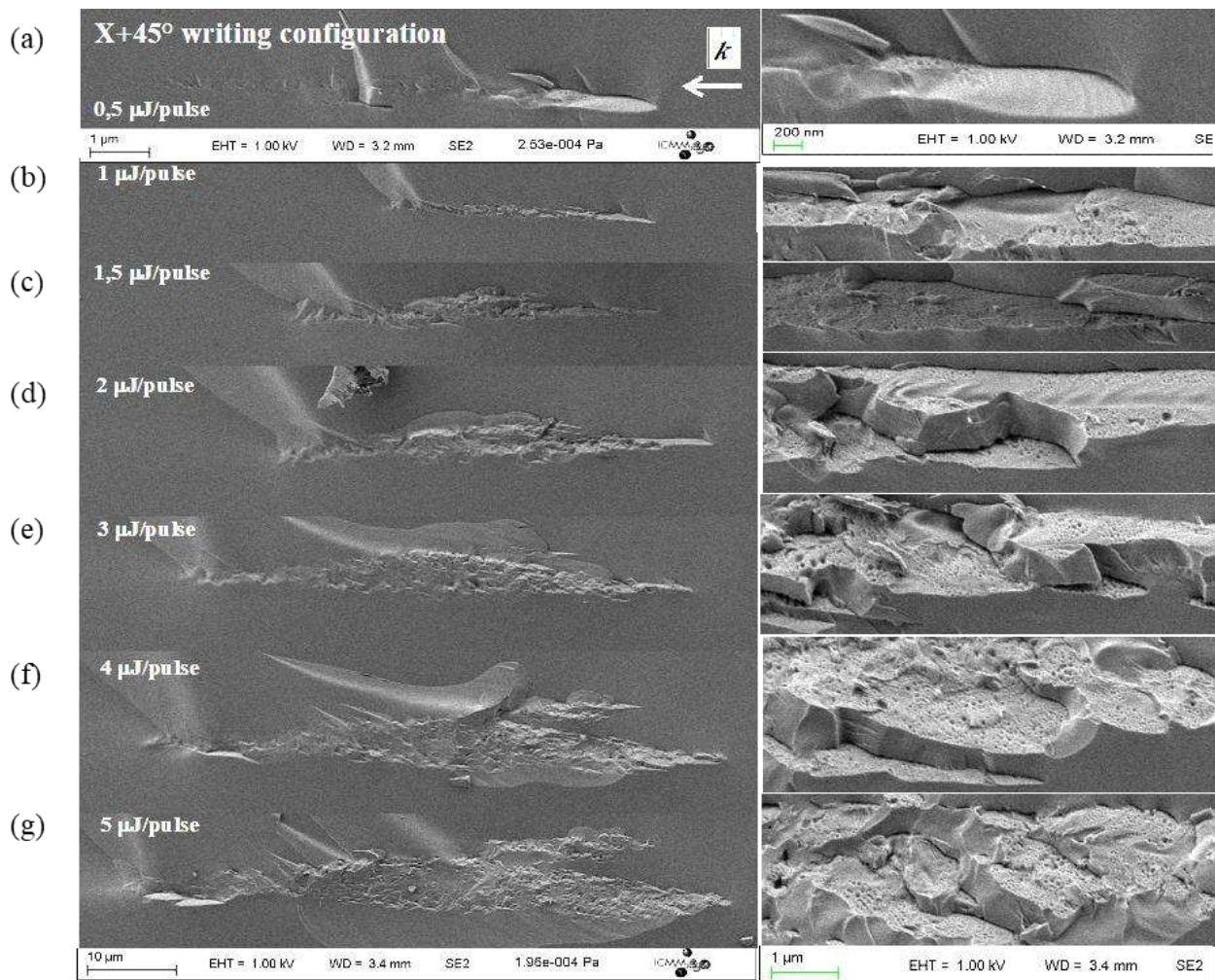


Figure 4.8: FEG-SEM, Secondary electrons images of laser tracks cross-section written with different pulse energy (from 0,5 up to 5  $\mu\text{J}/\text{pulse}$ ). The laser parameters were: 1030 nm, 250 fs, 0.6 NA, 300  $\mu\text{m}$ , 100 kHz, 1 mm/s, X+45° configuration.

The evolution of the particle size and distribution is investigated through the variation of the laser pulse energy, everything else being set constant. The results are reported in Figure 4.9 Increasing the pulse energy is associated with an increase in the pore size diameter, which exhibits an almost linear rate, within the investigated interval, of  $\sim 8\text{-}9$  nm diameter increase per  $\mu\text{J}$ . The evolution of the standard deviation is found more or less constant with respect to the pulse energy increase (typ. around 5 nm from 0.2  $\mu\text{J}$  up to 1.0  $\mu\text{J}$ , respectively). In addition, the increase in the pulse energy is associated with an increase of the filling factor, and this is in agreement with a higher retardance or TLB values. Note this also contributes to much higher polarization dependent light scattering (due to porous nanolayers) and thus increasing the apparent TLD.



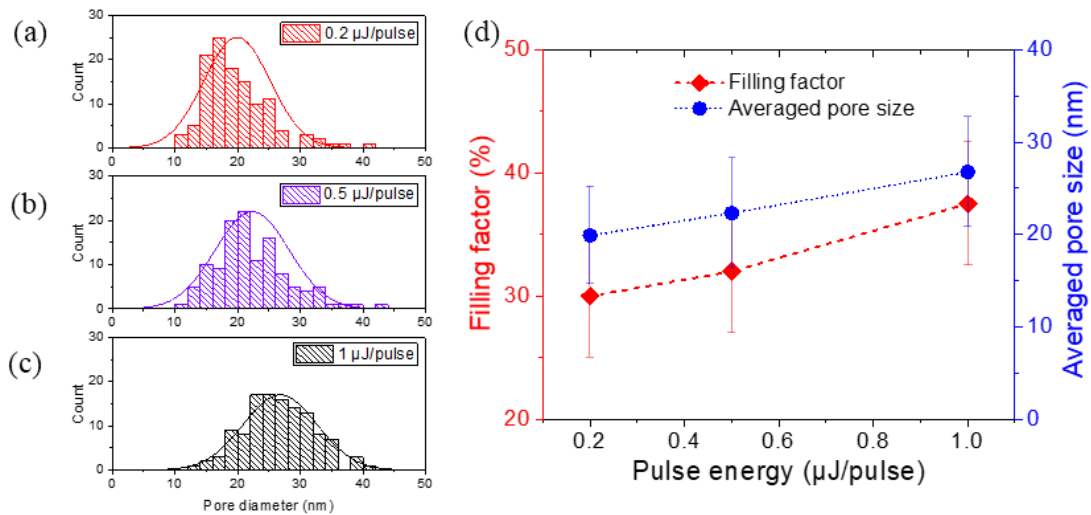


Figure 4.9: (a, b, c) Pore size diameter distribution with respect to pulse energy; (d) Evolution of the filling factor and the average pore size diameter as a function of pulse energy. The laser parameters were: 1030 nm, 250 fs, 0.6 NA, 300  $\mu\text{m}$ , 100 kHz, 1 mm/s, X+45° configuration.

#### *Influence of pulse density and repetition rate*

The dependence of CD and CB at 550nm is shown in Figure 4.10(a, b) as a function of the pulse density (roughly defined here as  $f/v$ ) for different repetition rates (100, 200 and 500 kHz). There are two regions shown in Figure 4.10. For a fixed repetition rate of 100 kHz, the amplitudes of both circular and linear anisotropic properties are increasing with the increase of the pulse density from 10 up to 1000 pulse/ $\mu\text{m}$ . With the chosen writing configuration at 100 kHz, the sample shows a maximum CB of 0.8 rad at 450nm. When increasing the repetition rate above 200 kHz at 1,5  $\mu\text{J}/\text{pulse}$ , the amplitude of circular properties declines sharply even with an increasing overlapping rate 200 or 500 pulse/ $\mu\text{m}$ . At the same time, optical microscope-imaging experiments reveal that heat accumulation occurs in these conditions and destroy partly the nanostructures as it can be confirmed by the evolution of anisotropic linear optical properties i.e. LB and LD in Figure 4.10(c, d) and in agreement with the literature [30].

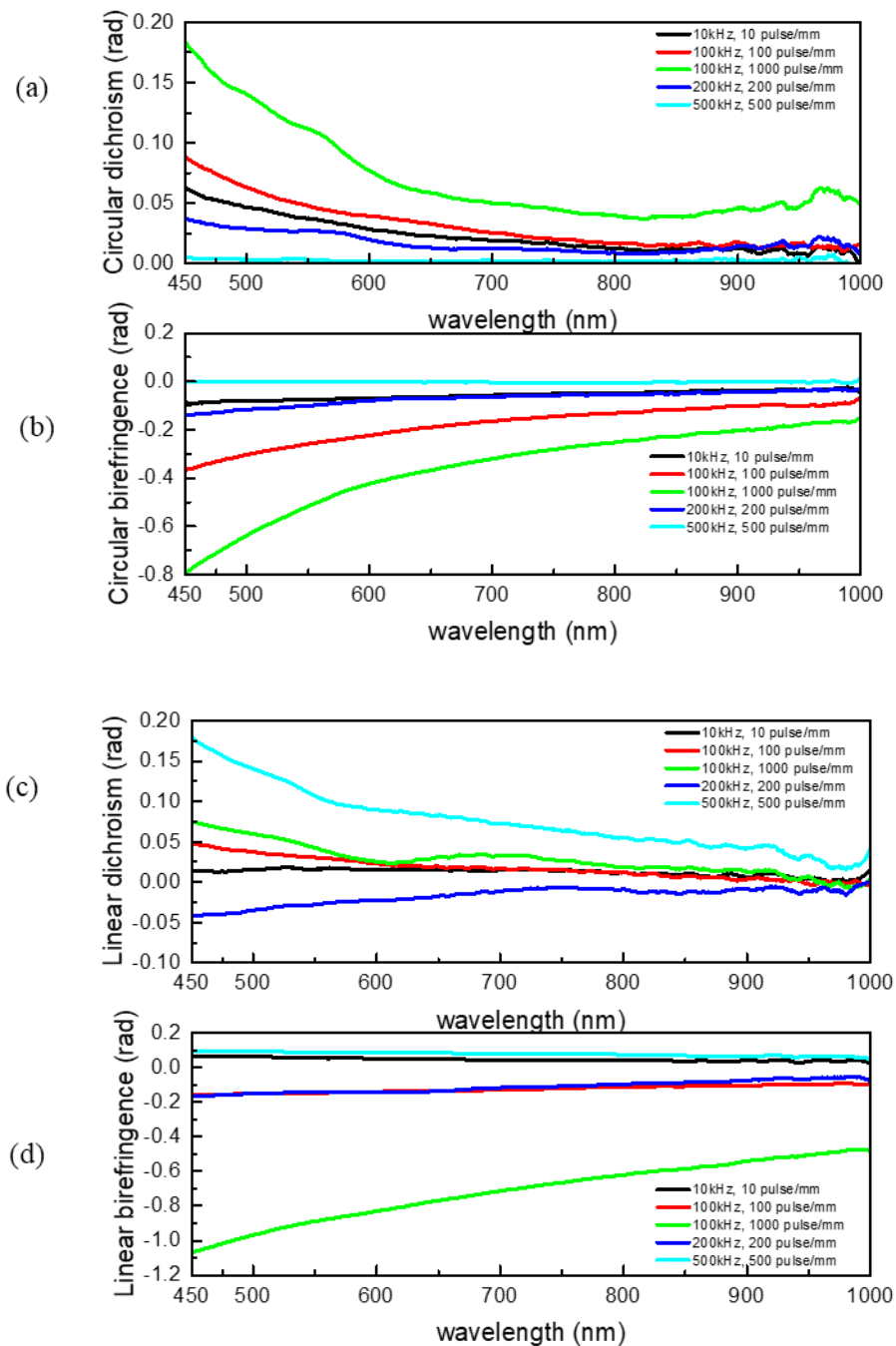


Figure 4.10: (a, b) Effective circular dichroism (CD) and circular birefringence (CB) corresponding to sample written according to the X+45° configuration with various overlapping rate  $v/f$  (proportional to the pulse numbers). (c, d) LB and LD spectra recorded in the same conditions. Laser parameters: 1030 nm, 250 fs, 0.6 NA, 1.5 J, 1mm/s X+45° configuration.

The impact of the writing speed in the nanopores distribution is depicted in Figure 4.11, where SEM micrographs, pore size distribution, filling factor and averaged pore size diameter as a function of writing speed, are displayed. The filling factor (FF) corresponds to the surface taken by the pores per unit area of nanoporous region, and is expressed in percent (%). FF is directly related to magnitude of the measured retardance as expressed in [18]. We observed that the average pore diameter increases when writing speed increases (from 53 nm to 77 nm from 0.01 mm/s to 10 mm/s, respectively, corresponding to a ~ 45% increase).

As the writing speed increases, the spread of the pore diameter distribution become also larger e.g. standard deviation is increased from 13 nm to 34 nm between 0.01 mm/s and 10 mm/s). While the average pore size is increased when speed is increased, the filling factor comparatively decreases. The evolution of the FF observed in Figure 4.11 is qualitatively in agreement with retardance values reported in [31]. However, it is worth pointing out that other contributions factor into the measured retardance value, such as laser track length, nanoporous layer thickness or periodicity.

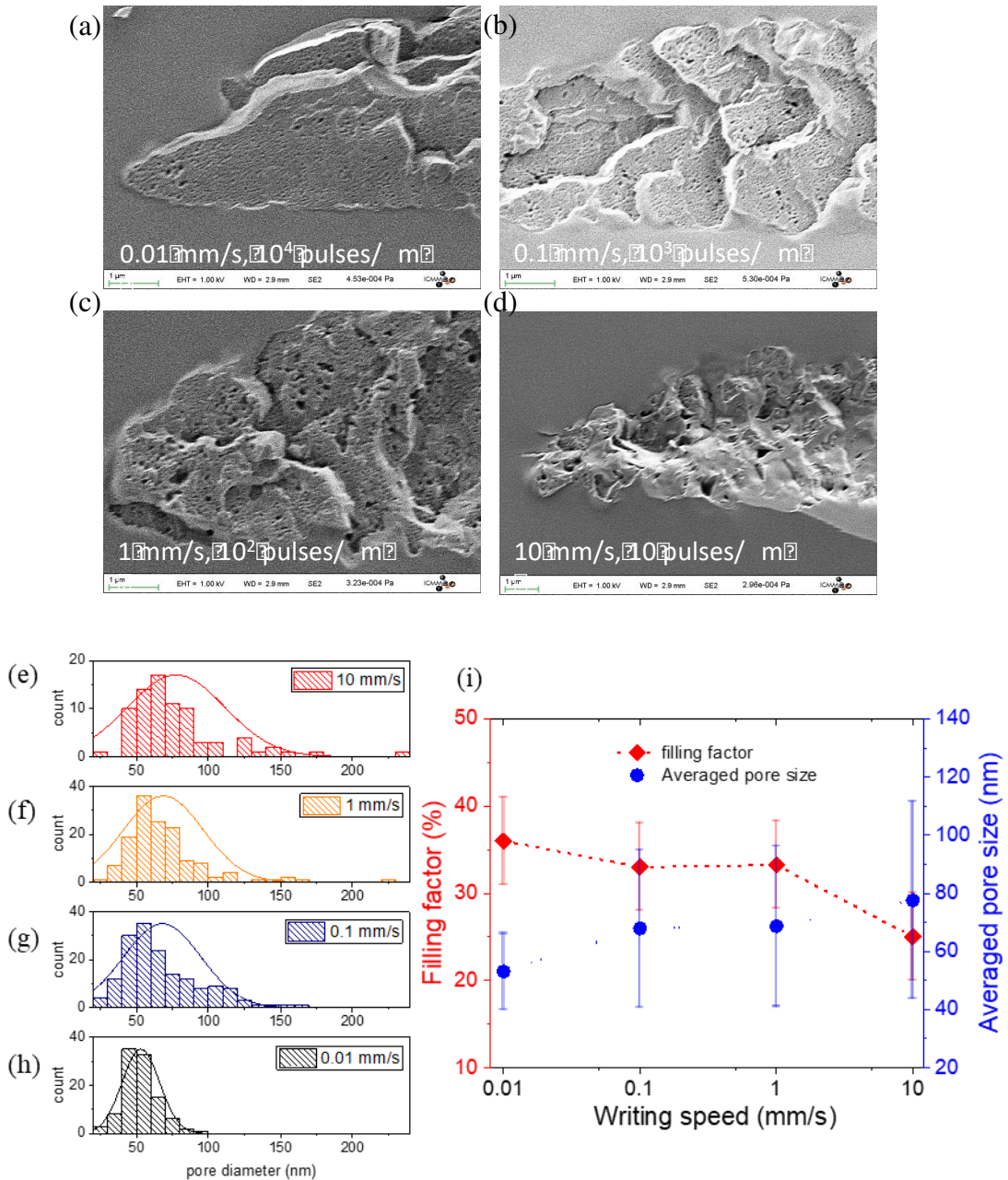


Figure 4.11: (up, a-d) Scanning electron micrograph of the nanoporous regions for different writing speeds (from 0,01 mm/s up to 10 mm/s); (down left, e-h) Pore size diameter distribution with respect to the writing speed; (down right) Evolution of the porosity filling factor and the average pore size diameter as a function of writing speed. The laser parameters were: 1030 nm, 250 fs, 1,5 J/pulse, 0.6 NA, 100 kHz, 1 mm/s, X+45° configuration.

### *Influence of the focusing depth*

The focusing depth dependence of anisotropic optical properties was studied using a 0.6 NA microscope objective. In the following experiments the geometrical focus was moved from the surface down to 800  $\mu\text{m}$  into the bulk of the 1mm thick silica sample (SuprasilCG). The laser-writing configuration was again fixed to  $X+45^\circ$ . The CB, CD spectra were then recorded and their amplitudes at 550nm are shown in Figure 4.12a according to the focusing depth for a fixed energy of 1,5  $\mu\text{J}/\text{pulse}$ . The linear optical properties, TLB and TLD, were also drawn according to the pulse energy in Figure 4.12b for a better comparison. For "shallow" focusing below 200  $\mu\text{m}$ , the absolute CD and CB decrease for deeper focusing penetration down to a minimum value at 200  $\mu\text{m}$  corresponding to the positive spherical aberration compensated depth of the microscope objective. From 200 up to 500  $\mu\text{m}$ , the absolute CB, CD amplitudes increase monotonously with the focusing depth (and this in the whole spectral range, not shown here). As a result, one way to increase the induced circular optical properties is the introduction of strong spherical aberration provided that the energy is high enough to photo-induce such chiral optical properties. For deeper focusing depths, the measurements demonstrated that we managed to keep a nearly constant CB, CD from 600  $\mu\text{m}$  up to 800  $\mu\text{m}$ . This is likely due to a balance between the occurrence of self-focusing effects and spherical aberration even when the focus goes very deep [18].

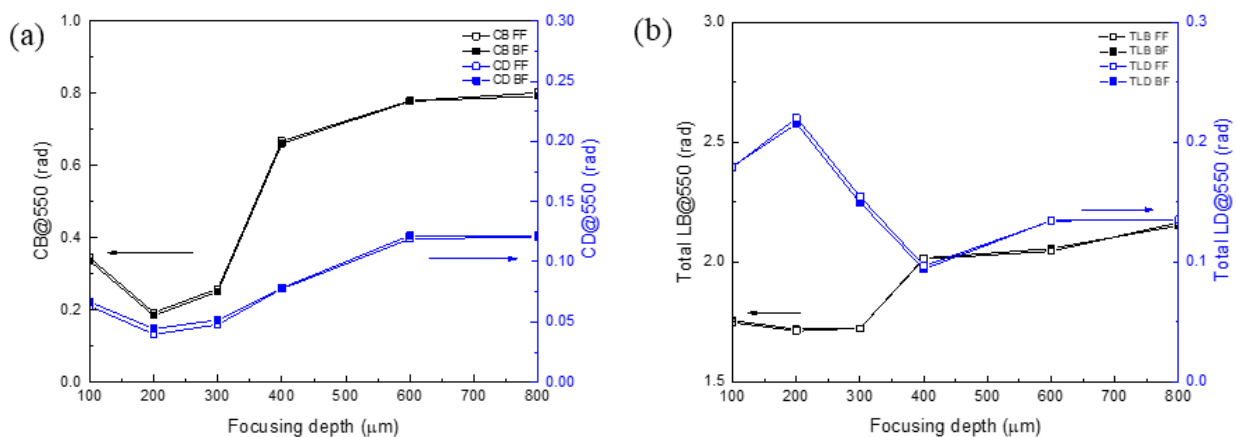


Figure 4.12: (a) Experimental values of effective circular birefringence, CB, and circular dichroism, CD, at 550 nm as a function of the focusing depth from 100 up to 800  $\mu\text{m}$  (for both, back and front faces). (b) TLB and TLD recorded at 550 nm in the same conditions. Laser parameters: 1030 nm, 250 fs, 0.6 NA, 100 kHz, 1 mm/s, 1,5  $\mu\text{J}/\text{pulse}$ ,  $X+45^\circ$  configuration, SuprasilCG.

Note that TLB follows ore or less the same trend according to the focusing depth whereas TLD exhibits an enhancement for shallow focusing. This reveals a strong influence of spherical aberration on the laser-induced circular optical properties at this relatively high numerical aperture. Indeed above 200  $\mu\text{m}$ , the deeper the geometrical focus is moved into the bulk of the sample, the stronger the beam is distorted and elongated due to the spatial aberration leading thus to longer laser tracks and a higher TLB (or retardance as reported in the literature [25, 32-34]). This is confirmed by the SEM images in Figure 4.13 revealing longer laser tracks when increasing the focusing depth from 100 to 600  $\mu\text{m}$ .

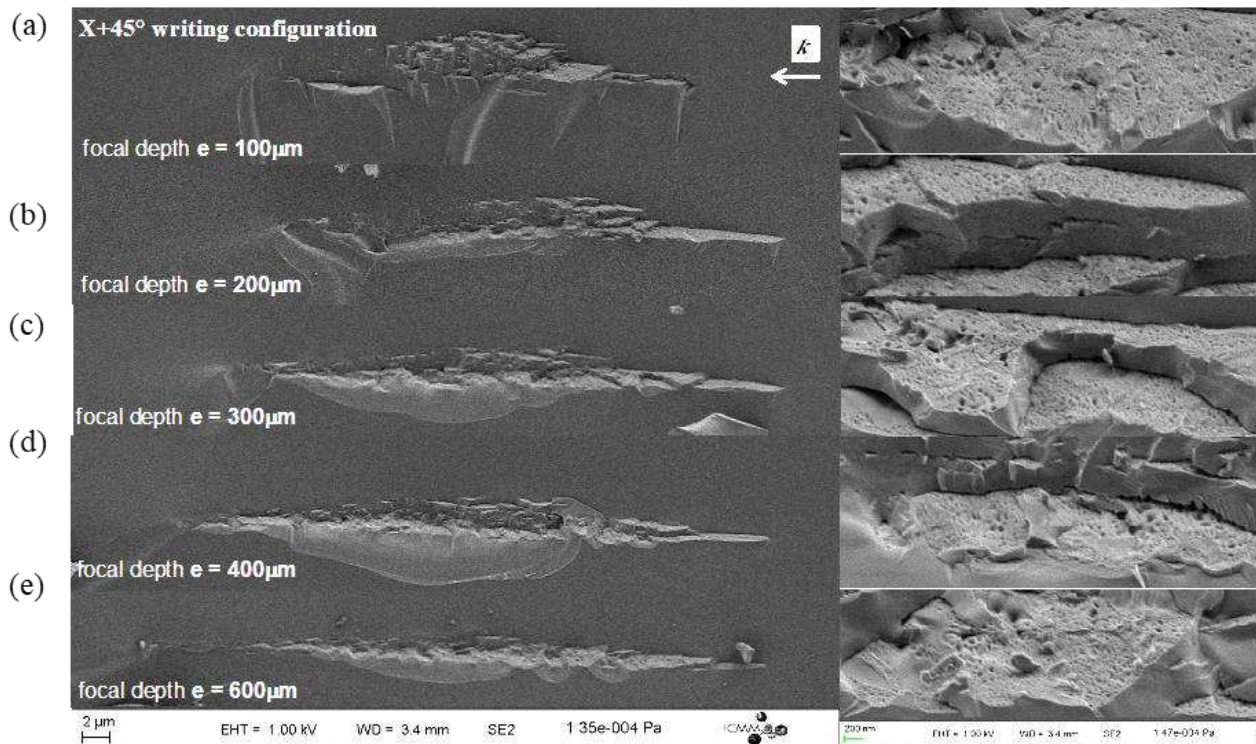


Figure 4.13: FEG-SEM, Secondary electrons images of laser tracks cross-section written with different focusing depths (100  $\mu\text{m}$  up to 600  $\mu\text{m}$ ). The laser parameters were: 1030 nm, 250 fs, 0.6 NA, 100 kHz, 1 mm/s, 1,5 J/pulse, X+45° configuration, SuprasilCG.

### *Partial conclusion*

At this step, we still don't know if the observed CB originates from internal arrangement of multiple LB components, which could be related to some sort of rotated lamellae along the beam path, or, from fs-induced molecular optical activity in the nanogratings. From the observed structural CB, we can now deduce an effective optical activity, i.e. CB per unit length to facilitate comparison with optically active materials. For example from Figure 4.7e we find that CB at  $\lambda = 550 \text{ nm}$  has an extreme value of around 0.25 rad (14.33°) produced by a laser track  $t = 50 \mu\text{m}$  thick. Therefore, the specific rotation power is:  $1/2 \text{ CB}/t \approx 143.3^\circ/\text{mm}$ . This should be compared with the intrinsic rotary power of natural materials, like quartz (25°/mm at 550 nm) or the structural rotary power of liquid crystals (thousands of °/mm) or that of the cuticle of some beetle species such as *C. Aurata* (180°/mm at 550 nm) [13].

## 4.5 Influence of the laser writing configuration

Two parameters of the linear birefringent modification, retardance and the azimuth of the slow axis, can be controlled during the laser direct writing process. In a simple view, the slow axis is defined by the polarization and the retardance can define as a function of the laser fluence. Retardance depends also on the laser wavelength, the pulse duration and the number of pulses transmitted through the modified region [25, 30]. However, the retardance also is affected by the orientation of the polarization plane with respect to the writing (also called scanning) direction. As the direction of the slow axis is varied during the writing

process, the angle between the laser polarization and the writing direction is changing accordingly, which couples the induced retardance with the polarization direction. The difference in modification for  $0^\circ$  and  $90^\circ$  angles of polarization with respect to the writing direction is known for metals [35]. Recently, a similar effect was reported for laser processing of dielectrics [36]. However, it is important to keep the retardance value independent on the light polarization for the fabrication of variant polarization optical elements, for applications such as polarization beam converters, polarization sensitive camera and 5D optical memory [37-39]. In the literature such polarization dependence has been tentatively explained by the boundary conditions i.e. the absorption is stronger for light polarized perpendicular to the interface, as described by the Fresnel coefficients. Thus the polarization parallel to the writing direction, which is absorbed more efficiently at the front kerf, is commonly used in metal cutting. For the perpendicular polarization, the light is absorbed more efficiently at the sidewalls. As an alternative, circularly or radially polarized light is used, which is equally absorbed at the front and sidewalls of the kerf [40].

But the polarization dependence also arises due to the spatio-temporal properties of the ultrashort pulse laser beam quantified by the spatial chirp (SC), the pulse front tilt (PFT) and also the angular dispersion (AD) [41, 42]. The PFT is usually produced by temporal and spatial chirps in femtosecond laser pulses [43] and it can lead to both the quill writing and the anisotropic photosensitivity phenomena [8, 9, 41]. When the laser pulse approaches the focal point, the beam diameter is shrinking and the pulse front tilt (but also the angular dispersion) is proportionally increasing. Thus even negligible pulse front tilt is strongly enhanced in the vicinity of the focus. Thus, by choosing the correct configuration of the beam (e.g. intensity gradient, pulse front tilt, polarization orientation, laser scanning direction and orientation) for controlling the ponderomotive force, we can imagine forcing the electrons to move to one specific side of the beam, creating inhomogeneous plasma. Therefore, the control of light intensity gradient and of the laser polarization according to the displacement should lead to the control of local symmetry and its orientation.

Following this view in chapter 3, we have thus reported circular di-attenuation and linear retardance variations for 16 different polarizations when the "lines structures" were written (scanned) at a fixed angle namely along x-axis. Based on these preliminary tests, it seems that the difference in the strength of CD is defined by the angle between the polarization and the writing direction. Throughout chapter 3, only the circular diattenuation was compared, as this parameter can be easily estimated with CD spectrometer. However, the difference in obtained structures could be also observed under a polarizing optical microscope e.g. areas with the stronger linear birefringence exhibited slightly stronger scattering, bubbles formation for one direction, stronger refractive index contrast as review in [9]. Recently, Raman spectroscopy revealed higher density of 3-tetrahedra rings for the longitudinal polarization compared to the transversal polarization [44].

In this *chapter now we are thus investigating* more deeply the overall anisotropic optical properties *and* to find the most suitable writing configuration to create some significant

circular anisotropic optical properties and to study the underlying mechanisms leading to their creation.

- In the first section we have analyzed a set of samples written with different azimuth of the linear polarization from 0 up to 360°, and with a fixed scanning direction along +X (i.e. along the laser compressor plane).
- In the second section we will fixed the linear polarization orientation along x-axis and we will varied the scanning direction from 0 up to 360°.

*Direct observations of the nanogratings by SEM*

In order to certify the existence of porous nanogratings, we have analyzed the laser tracks cross sections using SEM images for 16 configurations. For sake of clarity, we have chosen to show three different writing configurations noted Xx, Xy (namely parallel and perpendicular polarization to writing direction) and X+45° in the following. The FEG-SEM secondary electrons images shown in Figure 4.14 highlight the modifications morphology occurring within Type II regime. When the laser polarization was perpendicular to writing direction (Xy) we can reveal the nanogratings. For a deeper investigation of the nanoplane structure, we turned the laser polarization 90° into a parallel configuration Xx or X+45°. As shown in Figure 4.14, one can directly image the modified region inside the nanoplanes. The image is not uniform in term of nanoporosity and we observed what appears to be a “white” layer arising from surface topography variations that corresponds to silica material between the nanolayers. In all our samples (all investigated configurations), we observed that these pores always occur along with nanoplane formation for pulse energies higher than 0.5 J/pulse. Also the observed morphology remains quite similar in terms of laser track lengths and widths.

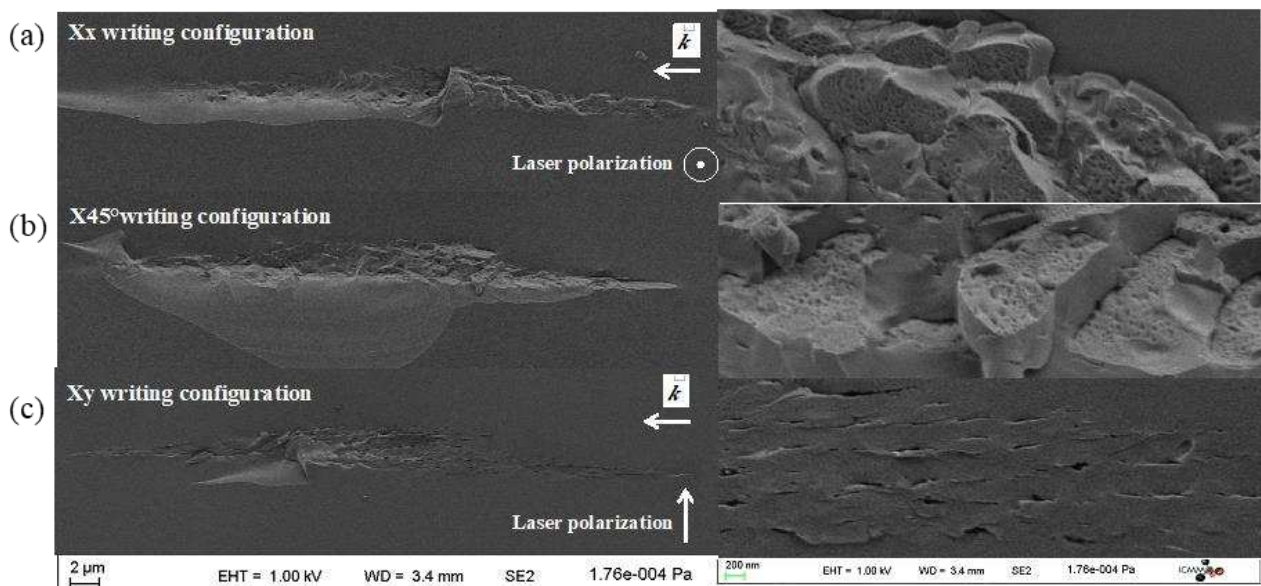


Figure 4.14: FEG-SEM, Secondary electrons images of laser tracks cross-section for three different writing configurations namely Xx, X+45° and Xy. The laser parameters were: 1030 nm, 250 fs, 1,5 J/pulse, 0.6 NA, 100 kHz, 1 mm/s.

#### 4.5.1 Influence of the writing polarization direction for a fixed scanning direction and orientation i.e. along +X

In this section we reported silica samples irradiated in the following conditions: 1030 nm, 250 fs, 100 kHz, 1 mm/s, 0.6 NA, 300 μm focusing depth. The pulse energy was fixed to 1,5 μJ/pulse ensuring we fall within Type II modifications regime. We have created 16 samples by setting the linearly polarized laser light to a specific orientation for each one. In overall, the polarization azimuth angle was varied from 0 to 360° by step of 22,5°. Once the polarization orientation was set, the laser was scanned along +X axis (X being the plane of the laser compressor). This allows the definition of a second angle, noted  $\theta$ , between the scanning direction and the plane of the laser compressor, so here  $\theta = 0$ . Then we create several squares (3x3 mm<sup>2</sup>) made of a set of lines with a line spacing of 1 μm to have a uniform scanned region and to avoid any diffraction effects. Spectral normalized Mueller matrices were recorded with a spectroscopic Mueller ellipsometer (Smart SE, JY HORIBA) in transmission at normal incidence in the wavelength range  $\lambda \in 450\text{--}1000$  nm. The Mueller matrices, measured experimentally are then decomposed using the logarithmic decomposition method to tentatively "disentangle" the anisotropic optical properties. In that way the effective values of the linear dichroism, LD, linear birefringence, LB, circular birefringence, CB, and circular dichroism, CD, can be treated independently. Apart from the multi-spectral behavior (not shown here), all anisotropic optical properties were then extracted at a fixed wavelength of 550nm.



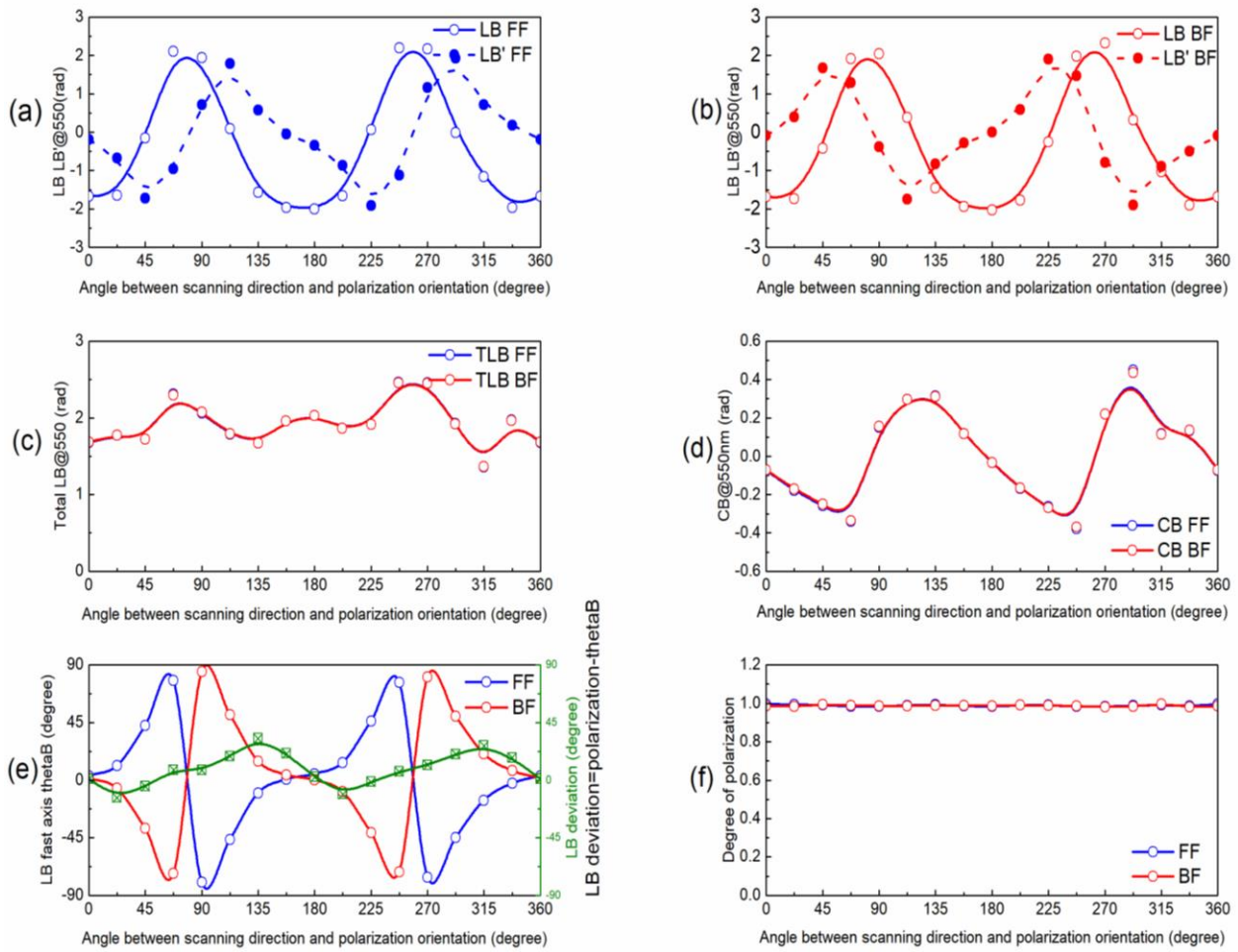


Figure 4.15: Experimental values of effective anisotropic optical properties at 550nm as a function of writing laser polarization azimuth  $\theta$ . (a) and (b) linear birefringence LB, LB' for FF and BF measurements respectively; (c) TLB; (d) circular birefringence CB; (e) slow axis orientation  $\theta_B$  and its deviation ( $\theta_B - \theta$ ); (f) degree of polarization DoP. Laser parameters: 1030 nm, 250 fs, 100kHz, 0.6 NA, 1 mm/s, 1.5 J/pulse. The writing direction is along X-axis i.e.

In Figure 4.15 and 4.16, we plot the effective anisotropic optical properties along the azimuth  $\theta$  from  $0^\circ$  to  $360^\circ$  for a fixed scanning direction (i.e.  $\theta_s = 0^\circ$ ) measured from both front face and back face (BF). Figure 4.15 presents the experimental polarimetric properties (LB, LB', TLB, CB, slow axis orientation, and DoP) in radians at the wavelength of 550 nm. Figure 4.15a illustrates that the linear properties (measured from the front face) show maximum values around every  $45^\circ$  of polarization angle of laser writing. Figure 4.15c indicates that the TLB ( $\theta_B - \theta$ ) is also slightly dependent on the polarization azimuth with a higher value for  $X+/-45^\circ$  or a higher value for  $\theta = 180^\circ$  than  $\theta = 0^\circ$  i.e. backward scanning rather than forward scanning. As it can be seen in Figure 4.15d, the maximum CB can be observed for  $X+45^\circ$  writing configuration and there is nearly no CB when  $\theta = 0, 90, 180$  and  $270^\circ$ .

Specifically for  $X+45^\circ$  configuration, it is seen that the couple of x-y linear effects (LB in Figure 4.13 but also LD shown in Figure 4.16) is small, while the couple of crossed linear

properties ( $LB'$ , and  $LD'$  drawn in Figure 4.16) is quite large. This is because the linear birefringence (and the linear dichroism) of the sample is oriented at  $\pm 45^\circ$  as revealed by Figure 4.15e (and Figure 4.16e for the dichroism) that represents the slow axis  $\theta_{LB} = 0.5 \tan(LB'/LB)$  and its deviation  $\theta_{LD}$  according to the laser polarization azimuth  $\theta$ . For comparison, when the writing laser polarization is parallel or perpendicular to the x-axis (e.g.  $X0^\circ$  or  $X+90^\circ$  configurations),  $LB$  and  $LD$  are maximal whereas  $LB'$  and  $LD'$  are minimized.

The spectral Mueller matrices were also measured in the reverse direction i.e. from the back face "BF". The extracted linear data are also shown on Figure 4.15a and Figure 4.15b for sake of comparison. As it can be seen,  $LB$  ( ) measurements are reversible whereas  $LB'$  ( ) are mirror reversed to each other from FF to BF. This is in agreement the geometry consideration discussed in section 4.2 i.e. component of the electric field have changed its sign due to the sample azimuthal rotation of  $180^\circ$  (case a in Figure 4.5). Finally both the total  $TLD$  ( ) and  $CB$  ( ) are identical for both FF and BF. Similar analysis and conclusions can be done on the dichroism results shown in Figure 4.16. In addition  $TLD$  ( ) and  $CD$  ( ) measurements are also identical for both faces.

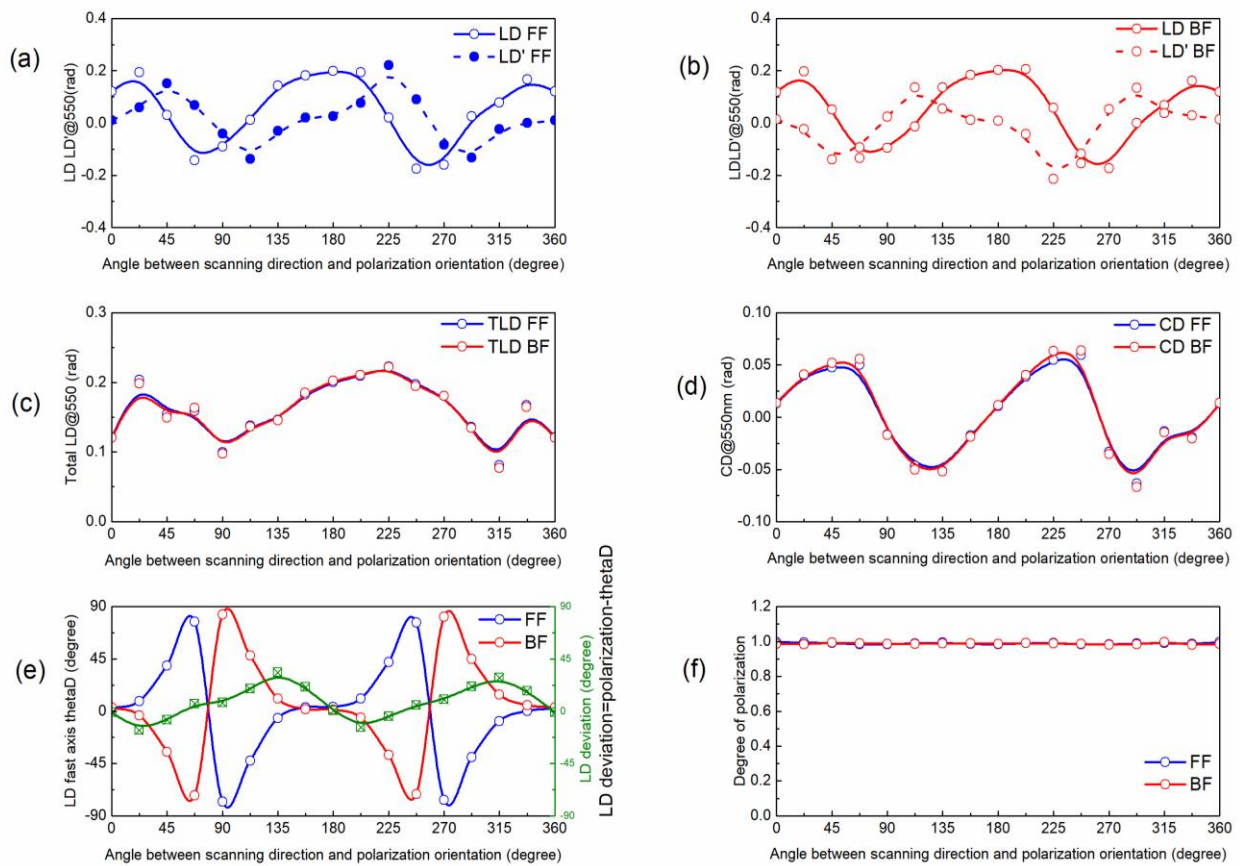


Figure 4.16: Experimental values of effective anisotropic optical properties at 550nm as a function of writing laser polarization azimuth  $\theta$ . (a) and (b) linear dichroism  $LD$ ,  $LD'$  for FF and BF measurements respectively; (c)  $TLD$ ; (d) circular dichroism  $CD$ ; (e) slow axis orientation  $\theta_{LD}$  and its deviation ( $\theta_{LD}$ ); (f) degree of polarization  $DoP$ . Laser parameters: 1030 nm, 250 fs, 100kHz, 0.6 NA, 1 mm/s, 1.5 J/pulse. The writing direction is along +X-axis i.e.

Note that if the samples were solely made of a single linear birefringent layer whose orientation will be linearly dependent of the laser polarization (i.e. “perfect nanogratings” with neither tilt nor stress), both LB and LB’ functions will be perfectly periodic with a 45° shift with respect to each other. In addition no circular properties will be observed as it is modeled later in the discussion section using Mathcad. However this is obviously not the case here since there are some deviations from this simple view:

- LB( ) exhibit a deviation for sinusoidal shape with a “flat” zone around 180°.
- LB’( ) is periodic modulo 180° but the angular response is not sinusoidal since it has a shoulder around 180° +/-22°.
- These in turn explain the observed deviation of the LB slow axis orientation  $\theta_{LB}$  that is not perfectly linearly dependent on the writing polarization direction as it can be seen on the deviation green curve  $\theta_{LB}$  in Figure 4.15e.
- TLB( amplitude depends on the polarization orientation, which is usually qualified or at least related to so-called anisotropy photosensitivity (or sometimes quill writing effect) in the literature. This can be seen on our results when looking at TLB or TLD, which both exhibit different amplitudes for X0° and X+90° or by comparing X+45° and X-45° configurations for example.
- And finally we have some significant CB and CD that exhibits a non-symmetric periodic dependence with the linear polarization azimuth (with respect to the scanning direction i.e. along x-axis).
- Note that DoP remains very close to 1 for all investigated configurations
- *Similar observations can be done on the linear dichroism LD, LD’, TLD and  $\theta_{LD}$ .*

*In the following these results will lead us to consider a second contribution to the linear birefringence that is non parallel, non orthogonal to the first one. We will then perform some numerical modeling using Mathcad software as described later in the discussion chapter of this PhD thesis to tentatively interpret the observations made in this section.*

#### 4.5.2 Influence of the laser scanning direction with respect to the writing laser polarization

As we mention earlier, another intriguing phenomenon about fs-laser direct writing in glass is the directional dependence of the writing structure (often called quill writing), which is often regarded as a consequence of asymmetry of the laser beam [41, 42, 45-47]. This can be seen in our results (previous section) when looking at TLB( or TLD( that both exhibit different amplitudes for X0 and X+90° or X+45° and X-45° configurations for example. In the past ten years, a lot of research has been focused in this area. Kazansky et al. proposed that the pulse front tilt (PFT), which usually originates from distortion of temporal and spatial chirp in fs pulse, is the main factor to cause material modification changing from nanogratings to bubbles formation when a reversed scan direction is applied close to the threshold [41]. Also, Vitek et al. utilized the simultaneous spatial and temporal focusing (SSTF) system to tune the PFT value at focus up to 16,000 fs/mm, resulting in relaxed depth-

dependence nonreciprocal structures for either dots or “Chevron shapes” related to stress field formation [42]. Salter et al. used a spatial liquid modulator (SLM) to adjust the PFT (and even remove it) or the asymmetry intensity distribution at the focus to achieve the control of directional dependent writing [45, 48]. Poumellec et al. [46, 47] have early shown that the induced stress in the laser-affected zone depends on laser parameters such as polarization and energy per pulse. Lately, this leads us to suggest that a space charge built from ponderomotive force ( $\vec{\nabla}E^2$ ) is associated with the PFT, which might be interpreted as the formation of an asymmetric stress field [2].

In this section we test the influence of the scanning direction with respect to the polarization that remains fixed. To some extent this experiment could allow to investigate the nanogratings orientation with respect to the stress-field (and related stress-induced birefringence) surrounding the laser-affected zones made of set of lines. Nanogratings are oriented perpendicular to the electric field of the light. Therefore, if the laser polarization is kept constant while writing squares with different scanning directions, the nanogratings will gradually “turn” with respect to the writing direction for consecutive lines.

To write these set of samples, fused silica substrates (SuprasilCG from Heraeus, 1mm thick) are exposed to a femtosecond laser emitting 1,5 J/pulse at 1030 nm, at a repetition rate of 100 kHz and a scanning speed of 1mm/s. The pulse duration is 250 fs. The numerical aperture of the aspheric lens for focusing the laser beam is 0.6. The azimuth of the laser polarization was fixed to  $=0^\circ$ .

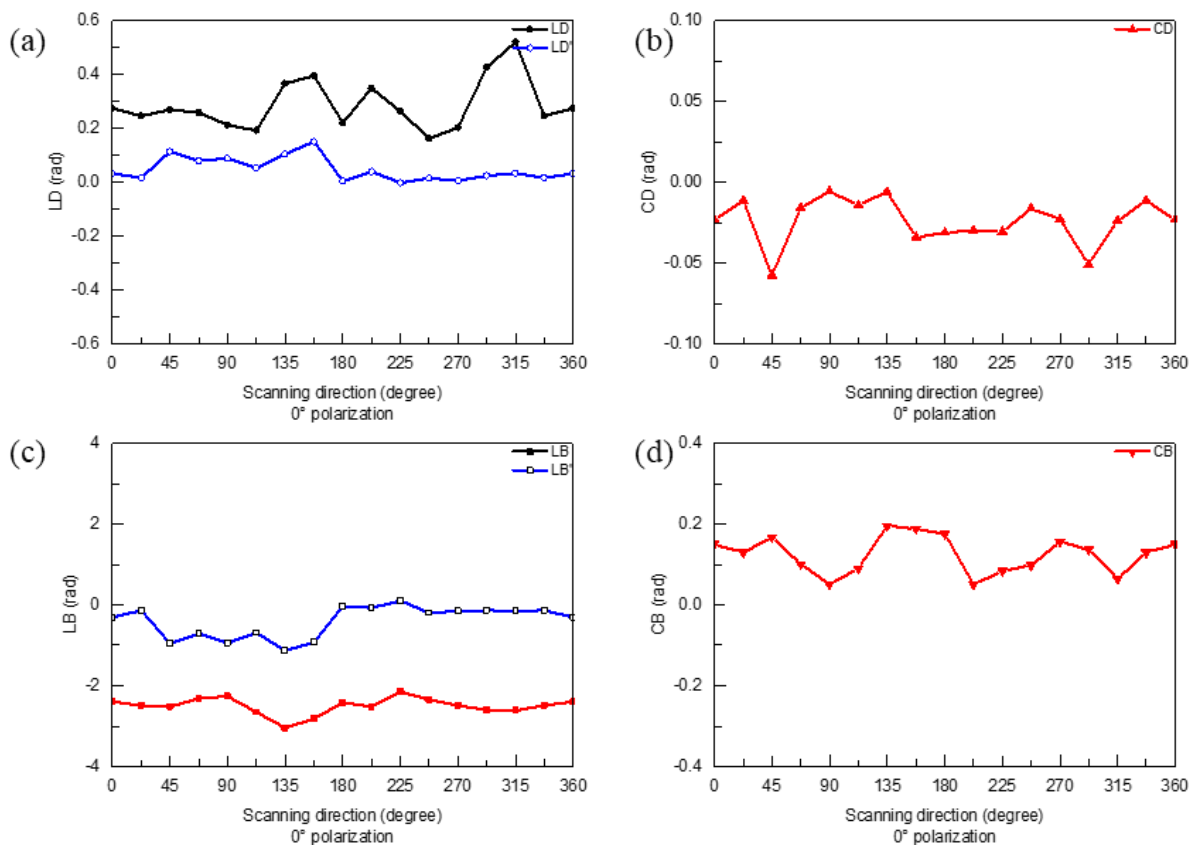


Figure 4.17: Experimental values of effective linear dichroism LD (a), linear birefringence LB (b), circular birefringence CB (c), and circular dichroism CD (d) at 550 nm as a function of the sample scanning direction. The laser writing polarization was set linear and oriented along x-axis (azimuth  $\phi = 0$ ). Laser parameters: 1030 nm, 250 fs, 100kHz, 0.6 NA, 1mm/s and 1,5 J/pulse.

Note that if the samples were solely made of a single linear birefringent layer whose orientation is determined by the laser polarization and not the scanning direction (i.e. “perfect nanogratings” associated with no quill writing effect), we will have a fixed amplitude for both LB( ) and LD( ), no LB’ and no LD’. In addition no circular properties will be observed. However this is obviously not the case in Figure 4.17 since there are some significant deviations from this simple view:

- The strength of both LB( ) and LD( ) exhibited variation with the angle of writing direction indicating some kind of quill writing effect or asymmetric orientational writing as we review these phenomena in [9].
- For scanning directions ranging from 180° up to 360°, we have nearly no LB’ and a quite constant LB amplitude. However LB’( ) and LD’( ) exhibit some significant deviations from zero for scanning direction between  $\phi = 22^\circ$  and 167°.
- This indicates a significant rotation of the neutral axis  $\theta_{LB}$  and  $\theta_{LD}$  of the total linear birefringence TLB and total linear dichroism TLD. This reveals either a tilt of the nanogratings orientation (with respect to the writing polarization azimuth) or the existence of the second contribution to anisotropic linear properties that is non-parallel non orthogonal to the first one.
- About the TLB( ), the amplitudes are quite similar when the scanning direction are  $\phi = 0^\circ$  and 180° but TLB( 90), is higher than TLB( 90). Also TLB( ) is higher than TLB( ), which is associated with a significant tilt of the slow axis  $\theta_{LB}$  azimuth when compared to .
- There is a small and negative CD( ) that is typically on the order of -0,05 rad at 550nm
- We have some significant positive CB( ) that exhibits some dependence with the scanning direction. The average CB is around 0,1 rad at 550nm. The CB amplitudes are more or less similar for  $\phi = 0^\circ$  and 180° but also for  $\phi = 45^\circ$  and 135°. In contrast CB is higher for 0° than 90°, and +45° higher than -45° (or 315°).

Going one-step further, it appears that if the scanning direction was aligned along the PFT (i.e. more or less along +X or -X), with the polarization always directed at about  $\phi = 0^\circ$  to the PFT, no difference in TLB or CB was observed (Figure 4.17). In contrast if the scanning direction was aligned at +/- 45° off the PFT or +/-90° off the PFT, a significant difference in both TLB and CB was observed (Figure 4.17).

## 4.6 Dependence of the stress-induced birefringence with the laser writing polarization

Several teams have highlighted the presence of an area of mechanical stress both within

Type I and Type II regimes, possibly associated with birefringence properties in the irradiated area, linked to the polarization of the incident laser beam. This is an additional indication in favor of densification/expansion (depending on regime and glass composition) at the origin of the refractive index changes, resulting from a fusion-resolidification process inside the glass. Simulations taking into account the stress fields in silica suggest that mechanical stress is induced by densification (within Type I regime) in the non-linear absorption zone of the optical field. In crystals, made amorphous by femtosecond irradiation, it is possible to observe a guiding zone in the region having undergone compressive mechanical stresses all around the irradiated zone exhibiting a volume expansion . Other experiments agree with this explanation, even showing similar results in silica glass within Type II regime where a non-guiding zone in the center due to the refractive index decrease .

As we said earlier, a big difference from ultrashort laser pulses is the formation of plasma of "free" electrons as an intermediate step between absorption of light and writing into the solid. In particular within Type II regime, the plasma is structured under the influence of light in relation to the solid. The structuring in space of the density of the plasma gives rise to a force field in the solid, which then leads, after extinction of the pulse, to the imprint of a stress field. This stress field is visible in polarized optical microscopy but also using a phase shift interferometer since it gives rise to surface topography during the cleavage of a glass plate in which laser traces have been "written". This is a frontier domain between plasma and laser-matter interaction which has not yet been explored much and which provides new results and questions. For example, our team has highlighted an astonishing effect within Type II regime: alternating shear along the path of the laser, which could result from an interaction of silica with interference between the fundamental optical wave and its third harmonic. We have established that there are three types of shear strain [47] : two types having long-range effects (at least 50  $\mu\text{m}$  away the irradiated zone) that are visible around the laser track. Another type of shear exists inside the track at the nanoscale [17].

So within Type II regime [46, 49-53], the formation of nanogratings is not solely creating form birefringence but also a stress-birefringence contribution, attributed to glass quenching and volume changes that participate to the total birefringence [46, 54, 55]. Indeed, irradiation of silica glass within Type II regime leads to a net volume expansion [44, 56], which correlates with the formation of porous nanolayers [16, 17] inside the nanogratings . The effective glass volume is expanded, and corresponds to the appearance of a [57] permanent strain. The later results into elastic strain as a direct response of the material, and therefore stress within and around the laser-modified region. By cleaving the laser-modified samples, part of the elastic strain relaxes, and a bump-like surface topography indicates the occurrence of glass expansion. Depending on the laser exposure conditions including polarization, the overall stress can be enhanced or minimized [52, 56] leading to tunable stress-induced birefringence values from  $10^{-5}$  up to  $\sim 10^{-3}$  [58-60]. Such stress-induced birefringence influences the inscribed object anisotropic optical properties but also likely the nanogratings themselves.

*In this section we have imprinted Type II modifications following a specific design in such a way we can create a confined stress-zone between laser-induced “stress bars”. In particular we will investigate stress-induced birefringence (its amplitude and its slow axis orientation) according to the orientation of the writing laser polarization.*

### *Femtosecond laser writing*

In the present case, a clear aperture was defined between two sets of lines creating 100x100  $\mu\text{m}$  squares made of 100 lines spaced by 1  $\mu\text{m}$ . The laser beam was produced by a femtosecond laser system operating at  $\lambda = 1030 \text{ nm}$  and delivering 250 fs pulses at a repetition rate of 100 kHz. The beam was focused to different depths below the front face of 1 mm thick silica glass plates (Heraeus SuprasilCG) using a 0.16 NA aspheric lens. Here the depths were fixed to 400-350-300-250 and 200  $\mu\text{m}$  resulting in a 5 layers structure for each square. Based on preliminary experiments the laser energy and the scanning speed were chosen so that the irradiated region falls within the Type II regime (typ. 2  $\text{J/pulse}$ , 0.5 mm/s speed in our conditions) corresponding to the formation of nanogratings in silica.

In Figure 4.18, the two microscope images taken between crossed polarizers reveal the formation of birefringence both within the irradiated areas, and also, in-between and around due to mechanical stress. The right image was made using a full order waveplate and highlights the slow axis orientation. According to the photos in Figure 4.18, there are yellow areas between the two squares and blue interferences inside the laser written squares. The yellow interference reveals a positive uniaxial birefringence within the clear aperture that is attributed to the stress-induced birefringence. In contrast the irradiated squares exhibit a negative uniaxial birefringence.

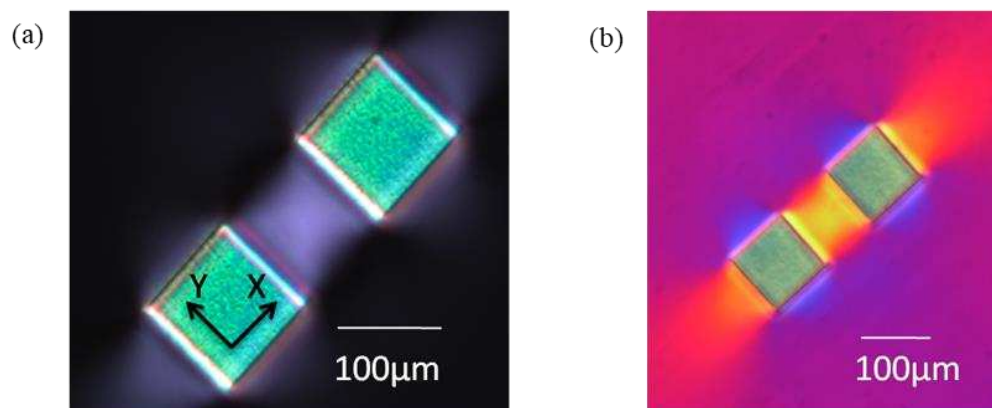


Figure 4.18: (a) Cross polarizers microscope image of a “stress study dedicated sample” written in Xx configuration and oriented at 45° off the polarizers; (b) Image of the sample taken using the full order waveplate technique that reveals the neutral axis orientation. Laser parameters: 1030 nm, 250 fs, 100kHz, 0.16 NA, 0,5mm/s and 2  $\text{J/pulse}$ .

We have reported in section 4.4 that the amplitudes of circular optical properties depend on the laser polarization orientation (as it controls the nanogratings orientation) [52]. In addition it has been reported by Bellouard’s group that the stress distribution around the

laser-exposed area depends on the laser polarization (as it controls the nanogratings orientation) [52] but it is clear about the neutral axis orientation of the stress-induced birefringence. Therefore, we chose to investigate here a wide range of writing configurations and to study the resulting stress-induced birefringence around the laser tracks. The glass sample was moved along an axis defined as the Y-axis (or scanning direction). The laser linear polarization was oriented from  $0^\circ$  (along the x-axis) up to  $360^\circ$  with a step of  $22,5^\circ$ . Optical images were measured using an Olympus BX51 polarizing optical microscope (Olympus, Tokyo, Japan). In addition we have performed quantitative linear birefringence imaging measurements at 550nm using "Open Polscope". So we can determine the cartography of the stress-induced birefringence amplitude together with its slow axis orientation: one example is reported in Figure 4.19.

*Dependence of the stress-induced birefringence with the writing laser polarization*

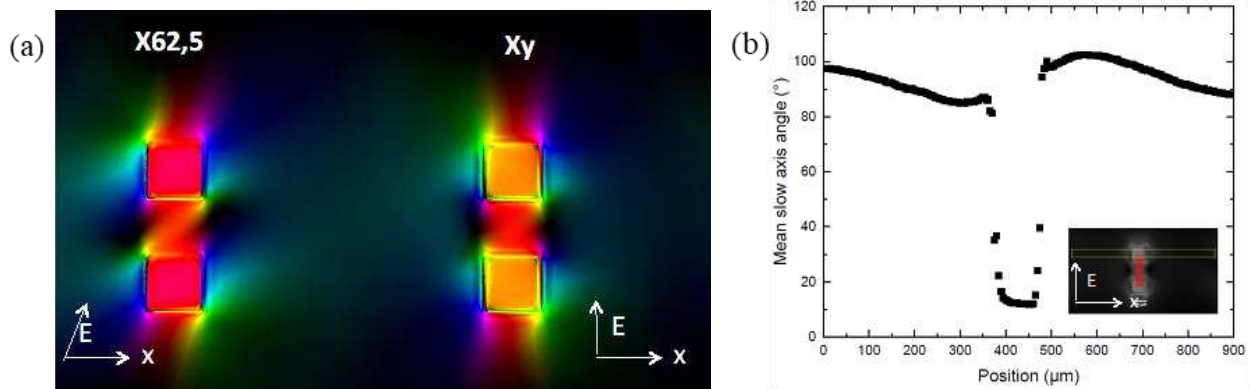


Figure 4.19: (a) Slow axis cartography of the linear birefringence for different writing configurations (Xy and X62,5°). (b) Example of slow axis profile across the clear aperture. The laser writing polarization was set linear and oriented along y-axis (azimuth =  $90^\circ$ ). Laser parameters: 1030 nm, 250 fs, 100 kHz, 0.16 NA, 0.5m m/s and 2 J/pulse.

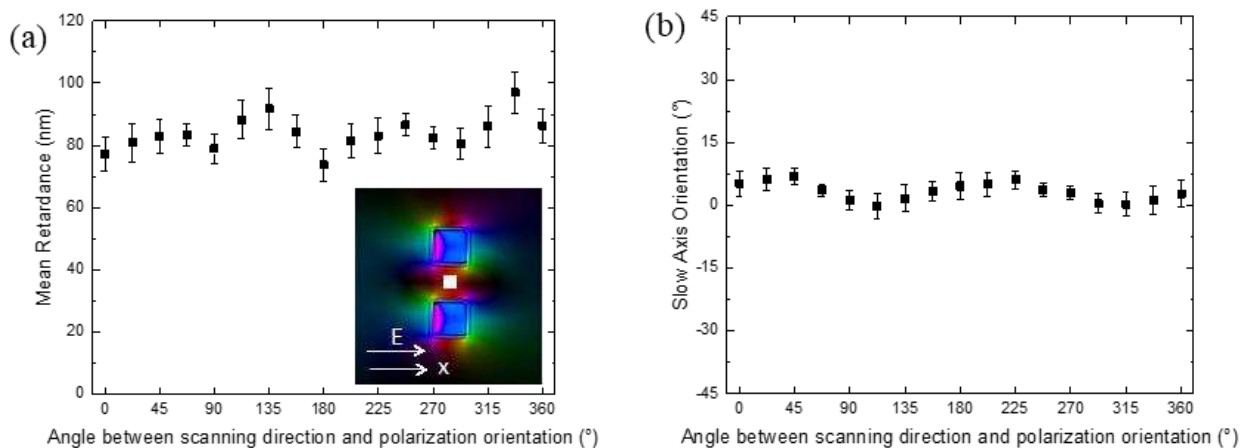


Figure 4.20: (a) Amplitude of the retardance R (proportional to the linear birefringence) in the center of the clear aperture (see the white square location in the inset) according to the laser writing polarization. (b) Slow axis orientation in the center of the clear aperture according to the laser writing polarization. Laser parameters: 1030 nm, 250 fs, 100 kHz, 0.16 NA, 0.5 mm/s and 2 J/pulse.

We have then extracted the retardance amplitude and its slow axis orientation within the clear aperture zone (see white square are in Figure 4.20a) that exhibits only stress-



induced birefringence. Figure 4.20b reveals that inside the clear aperture, the slow axis orientation does not depend on the laser writing polarization orientation as a first approximation (except at the edges of the written squares) i.e. whether the laser writing polarization is along x or y, the slow axis remains the same but the amplitude of the stress-induced birefringence changes a bit as shown in Figure 4.20a. It seems that neutral axes of the stress-induced birefringence are mostly determined by the long-range geometry of the written pattern, i.e. a line or set of lines, and therefore the slow (fast) axis appears to be parallel (perpendicular) to the laser writing direction. This will be discussed in the chapter 6.

## 4.7 Thermal stability of fs-induced anisotropic optical properties

Since their discovery in 2003 [61], these nanogratings have found numerous applications based on 2D or 3D space variant birefringence (such as waveplates [62], micro-patterned waveplates, polarization converters) but also because of the interest for high temperature applications like Fiber Bragg Gratings (FBG) [63] for Structural Health Monitoring (SHM) or 5D optical data storage [64] with virtually “unlimited lifetime” at room temperature. For most of these optical devices, the thermal stability is an important factor to be considered to ensure a reliable functionality during the component lifetime e.g. avoids any drift of the device optical response and thus the photo-induced birefringence. For example, securely storing large amount of information over even relatively short time scales of 100 years, comparable to the human memory span, is a challenging problem. So, the accelerated aging measurements are required to evaluate the stability of nanogratings at the working temperature with a view to forecast possible degradation. Therefore, the study on the thermal stability of the nanogratings is of great significance to understand the mechanism of erasure before to be able to perform a reliable lifetime prediction.

In particular the characteristic feature of Type II modifications is the formation of nanogratings that can easily be detected indirectly through linear birefringence measurements. However, the total birefringence of the nanogratings arises from the sum of several contributions, including form birefringence (related to the assembly of porous nanolayers), stress-induced birefringence (mostly due to glass expansion but there is also likely a contribution of Type I like densification present between the nanolayers), and potentially point defects contributing to the refractive index changes but that could be also anisotropic and oriented. In this section, a silica glass sample is first irradiated using fs laser. Then, accelerated aging experiments are performed to evaluate:

- The stability of the total birefringence but also the linear dichroism and the circular anisotropic optical properties using Mueller spectro-polarimetry,
- The stability of point defects using UV-Vis absorption spectroscopy,
- The stress relaxation by following the stress-induced birefringence in an irradiation-free zone,

- The nanogratings structure (period, nanopores size and filling factor) using SEM im-

*Of particular interest within this work, previous results reveal that the presence of nanogratings is correlated to the creation of circular anisotropic optical properties. In addition the polarization dependence study in section 4.4 indicates there is likely another contribution to the measured linear birefringence. In particular it is known that compaction and expansion processes affecting the surrounding medium and leading to the stress-induced birefringence accompany the formation of porous nanogratings. Further on in this chapter the thermal stability of the overall anisotropic optical properties (within Type II regime) by high temperature annealing is analyzed. Two cases are investigated: (1) samples with scanned squares, and (2) stack of multiple layers of lines to investigate stress-induced birefringence between two irradiated zones. The experimental results allow comparing the thermal stability of anisotropic linear optical properties and circular optical properties to tentatively bring additional insight on the origin of the imprinted chiral optical properties.*

aging.

#### *Femtosecond laser writing*

The laser radiation was produced by femtosecond laser system operating at 100kHz and delivering pulses of 250 fs in duration at a wavelength of 1030 nm. The beam was focused 300 μm below the front face using a 0.6 NA aspheric lens. The writing configuration was defined as X67.5°. Therefore, when the laser was moving along X and the polarization was linear and oriented at +67.5° off the horizontal axis. Next, moving the sample along the X-axis at a scanning speed of 1 μm/s, group of overlapping lines were photo-induced in 1mm thick silica plates with pulse energy of 1.5μJ. In summary, the samples were produced beyond the T2 threshold, where a strong birefringence appears due to presence of porous nanogratings.

#### *Accelerated ageing experiments*

Accelerated aging measurements are required to evaluate the stability of nanogratings and compare the stability of related anisotropic optical properties. The decay rate of these optical properties was evaluated using step isochronal annealing experiments in the range from 20°C to 1200°C with a fixed annealing duration  $t = 30$  min and annealing steps  $\Delta T = 50^\circ\text{C}$  or  $25^\circ\text{C}$ . After the step during which the sample was kept at  $T$  for a time  $t$ , the sample was quenched in air and then we record the retardance at room temperature. Thus, any temperature-induced reversible effects that may occur above room temperature did not spoil the measurements. Subsequently, these samples were measured in transmission using Mueller spectro-polarimetry. In the following all data were normalized to their initial value recorded at 20°C before any annealing treatment. As an example:  $TLB_{norm}(T) = TLB(t, T) / TLB(t=0, 20^\circ\text{C})$  with  $t = 30$  min in this study, but also for TLD, CB, CD etc...

It is worth pointing out that the obtained curves represent the "stability curve" provided that the criterion  $(\delta t \cdot k_0)^{-(\Delta T/T_{max})} \ll 1$  is fulfilled [65] where  $k_0$  is the constant rate of the erasure mechanism. For nanogratings written in silica,  $k_0$  has been estimated to be around  $5 \times 10^5$ -

$5 \times 10^7 \text{ s}^{-1}$  [66] depending on the laser writing parameters (energy, polarization). So, when this criterion is fulfilled, each point can be considered independent of each other. If the criterion is not fulfilled this means that measurements slightly under-estimate the real thermal stability.

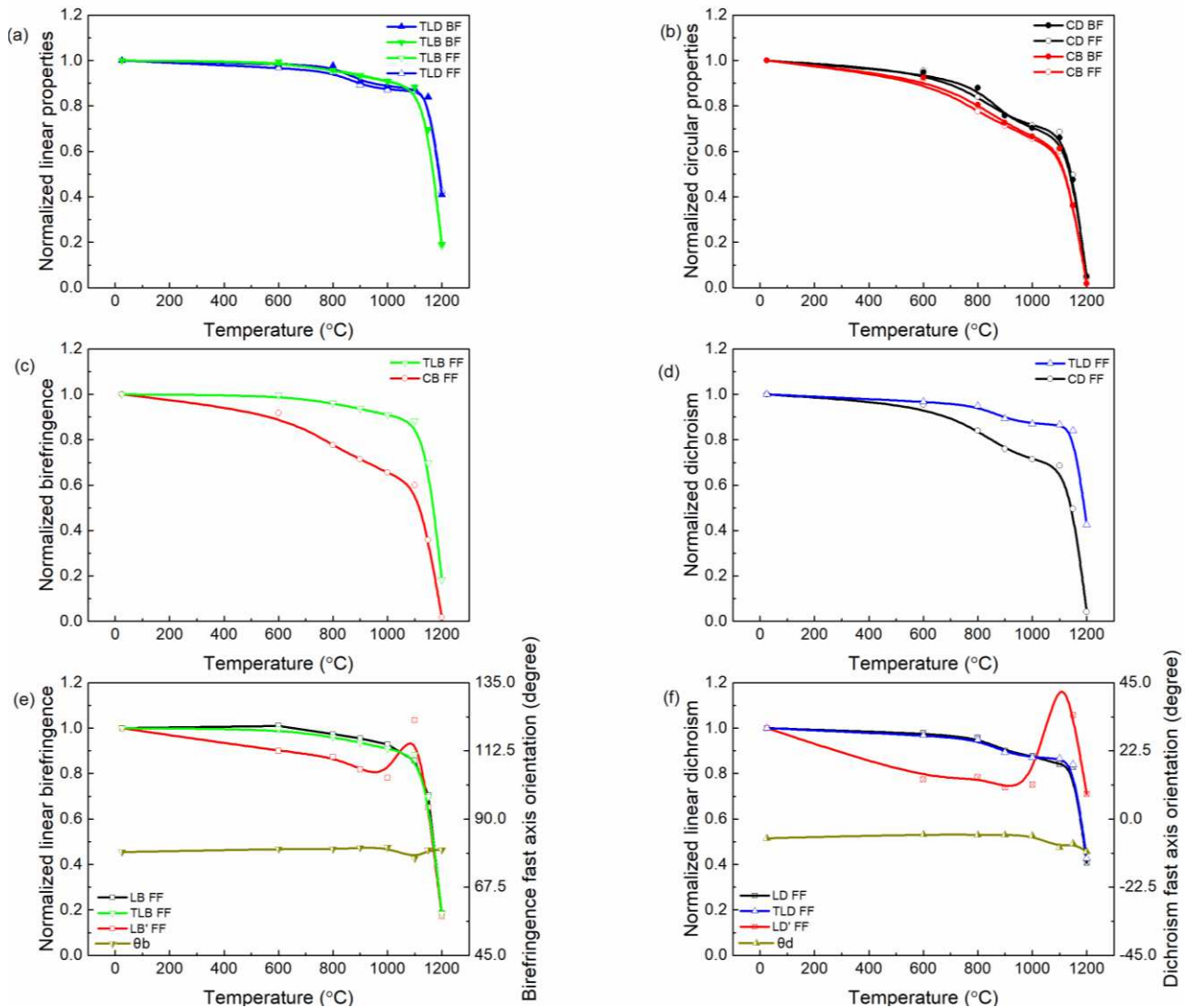


Figure 4.21: Experimental values of the normalized evolution of optical properties at 550nm according to annealing temperature: (a) TLB and TLD, (b) CB and CD, (c) TLB and CB, (d) TLD and CD, (e) LB, LB', TLB and fast axis orientation, (f) LD, LD', TLD and fast axis orientation of the linear dichroism. Laser parameters: 1030 nm, 250 fs, 100 kHz, 0.6 NA, 1 mm/s, X67.5° configuration.

Figure 4.21 shows the evolution of all normalized anisotropic optical properties as a function of the temperature  $T$  at which the sample was elevated. There is a number of key observations, which can be summarized as follows:

- Figure 4.21a:  $TLB_{norm}(T)$  and  $TLD_{norm}(T)$  exhibit also similar thermal stability. They are stable up to 800°C then there is a slow decay of 10% in the 800-1100°C range. Finally there is a steep decay at higher temperatures leading to full erasure around 1250°C. Note that measurements are similar for both front face (FF) and back face (BF).

- Figure 4.21b:  $CD_{norm}(T)$  and  $CB_{norm}(T)$  exhibit similar thermal stability. They start to be erased slowly in the 600°C-1100°C range until 0,6 and then there is a steep decay at 1100°C and a full erasure at 1200°C. Again front face and back face measurements lead to the same results on the extracted anisotropic optical properties.
- Figure 4.21c and Figure 4.21d: Anisotropic Linear optical properties have a higher thermal stability when compared to circular ones. As an illustration, after 30min at 1000°C, linear properties are at 0,9 whereas circular ones are around 0,7. However they follow similar trends i.e. also decay up to 1100°C and steep decay at higher temperatures.

For a more careful analysis we have decided to draw LB, LB' and the fast axis orientation of the linear birefringence according to the isochronal annealing temperature T. The same approach was also applied to LD, LD' and linear dichroism fast axis. Except the fast axis values all properties were again normalized to their initial values recorded at room temperature prior annealing treatments.

As it can be seen in Figure 4.21e, TLB and LB follow very similar trends whereas LB' has a more complex evolution. Note in this writing configuration X+67.5°, the amplitude of LB is one order magnitude higher than LB'. The minor contribution, LB', is slowly decreasing from 600°C and it follows an evolution that is quite close to  $CB_{norm}(T)$ . There is then a strong increase at 1100°C up to 1,1 and finally a steep decay at higher temperature like for other properties. Having a look on the neutral axis orientation, it can be seen a slight increase (typ +5°) of the fast axis up to 1000°C and then a decay at higher T but it remains more or less oriented around +79° in the whole T range. *Similar comments can be done for the linear dichroism properties, which follow the same trends reported above for the linear birefringence as shown in Figure 4.21d and Figure 4.21f.*

*Nanogratings observations using SEM after heat treatments*

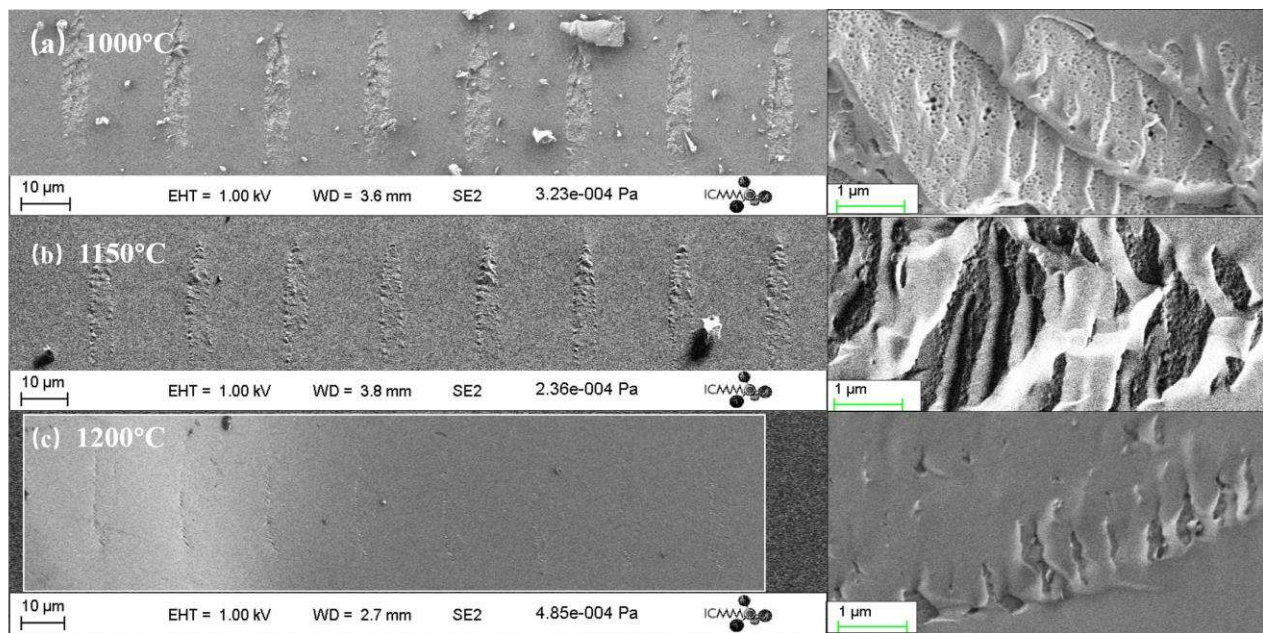


Figure 4.22: FEG-SEM, Secondary electrons images of laser tracks cross-section for a parallel writing configuration after annealing at different temperature for 3h. (a) 1000°C, (b) 1150°C, (c) 1200°C. The laser parameters were: 1030 nm, 250 fs, 0.6 NA, 100kHz, 0,1 mm/s, Xx writing configuration, SuprasilCG.

We have analyzed the laser tracks cross-sections using SEM images for three different annealing temperatures noted as (a) 1000°C; (b) 1150°C; (c) 1200°C shown in Figure 4.22. In the case of 1000°C, the SEM images show the nearly no damage in the nanolayers, and their morphology was well preserved. The latter corresponds to the linear birefringence trend shown in Figure 4.16c with  $TLB_{norm}(1000^{\circ}C) = 0,9$ . As the temperature rises, the edges become blurred, and nanolayers gradually dissolve then disappear, corresponding to the decline curve shown in Figure 4.21c where  $TLB_{norm}(1150^{\circ}C) = 0,7$  and  $TLB_{norm}(1200^{\circ}C) = 0,2$  whereas there is no more measurable circular anisotropic optical properties.

Next, in order to correlate the thermal stability of anisotropic optical properties to the porous nanogratings characteristics, SEM images were analyzed in order to deduce the nanoplanes and porosity changes according to the laser parameters. In perpendicular configuration Xy (not shown here), we can see that the average spacing between nanoplanes does not change with the annealing temperature. From the data gathered in parallel configuration Xx we can deduce that the average pore size and the number of nanopores (filling factor) for each laser track. These evolutions as a function of annealing temperature (for isochronal steps  $\Delta t$  of 30 minutes) are reported in Figure 4.23 and Figure 4.24. In this experiment, we observe that the pore size diameter decreases first as the temperature increases, but appears to plateau at the highest temperature. On the other hand, we observe a diminution of the filling factor that is that it is clearly correlated to the decrease of the value of the total birefringence (hence the measured retardance). We also observed that small size pores tends to disappear for thermal treatment above 1000°C and up to 1250°C whereas big ones (typ. diameter > 70nm) are able to resist to higher temperatures as shown in Figure 4.23(e-h). As a result, the fully erased small pores are not included in the counting

to determine the average pore size diameter. This has an effect of "shifting up" the average pore size diameter to larger values. However, the filling factor still decreases as pores are progressively erased, which are in agreement with the observation of a decrease in retardance.

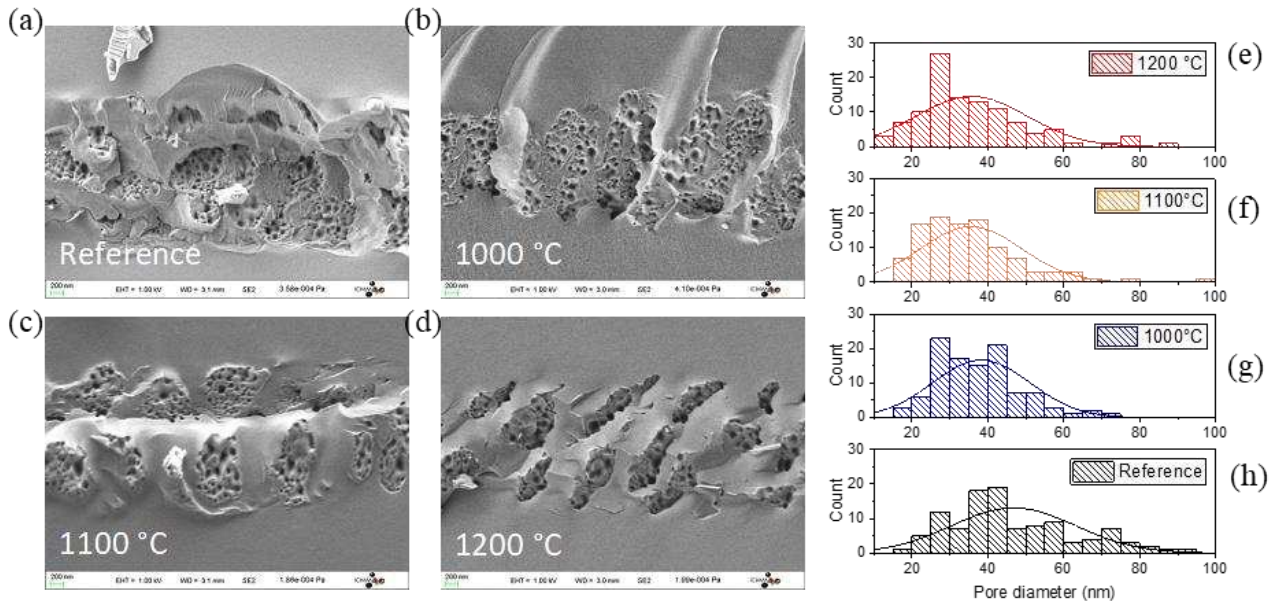


Figure 4.23: (a, b, c, d) Scanning electron micrograph of the nanoporous regions for different annealing temperature; (e, f, g, h) Pore size diameter distribution with respect to the annealing temperature. The laser parameters were: 1030 nm, 250 fs, 0.6 NA, 100kHz, 1 mm/s and Xx configuration.

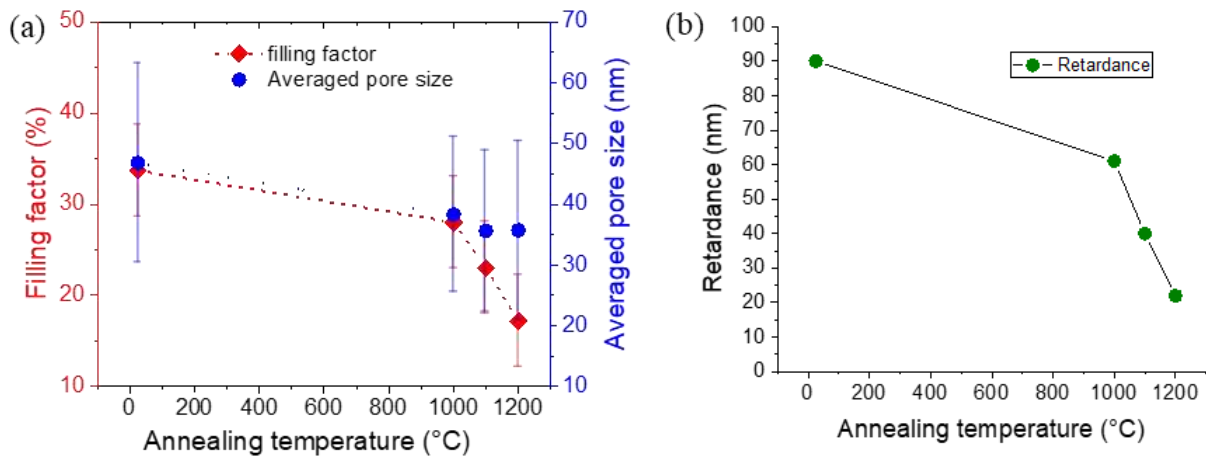


Figure 4.24: (a) Plot of the nanopores number and diameter according to the annealing temperature. (b) Calculated retardance based on the form birefringence model introducing the porous filling factor (T) and nanogratings spacing deduced from SEM data. The laser parameters were: 1030 nm, 250 fs, 0.6 NA, 100kHz, 1 mm/s and Xx writing configuration.

### *Optical absorption and point defects according to the annealing temperature*

In order to gain insight into the molecular structure of the nanogratings domains, we measured the spectral distribution of the absorbance introduced by nanogratings-type modifications. To this end, we determined the transmittance of continuous layers of

nanogratings (as for Mueller measurements) realized by inscribing parallel lines with a spacing of 1  $\mu\text{m}$ . During the isochronal annealing experiment, UV-absorption spectra were collected at room temperature after each annealing step (to monitor the absorbance of Type II modifications). The results are reported in Figure 4.25. Several contributions are aggregated in the absorbance spectra: 1) the intrinsic absorption losses 2) the Fresnel reflection losses at the glass/air interface, and, 3) the light scattering caused by the fs-laser structure [67]. As the reference curve shows in the graph, the non-irradiated fused silica glass exhibits a flat absorption curve with roughly no absorption from the visible to the near-infrared region. In contrast, the absorbance of Type II modifications significantly increases as one moves along the curve from the IR side to the UV side of the spectrum.

The signature of light scattering (with an increasing loss intensity at short wavelengths), and which attributed to the nanoporosity inside the nanoplanes, is well visible at  $T > 600\text{ }^\circ\text{C}$  in Fig. 3a. In addition, the polarization dependence of scattered light [68] reveals higher losses for a probe polarization oriented perpendicular to the nanolayers, which indicates that the scattering centers might be inside the nanogratings. This agrees with a model describing a layered medium made of alternating layers of two different isotropic materials with complex refractive indices, which exhibits linear dichroism [69] or let's say polarization dependent scattering losses (in our case) that are due to the intrinsic nanoporous nature of the nanogratings .

Additional features contributing to absorption losses, not attributed to Rayleigh scattering, are clearly annealed away as the temperature is progressively increased from room temperature up to  $600\text{ }^\circ\text{C}$ . The evolution of these features is attributed to the bleaching of defects. The first band peaking at 255 nm (5.08 eV) corresponds to SiODC(II) whereas the second one peaking at 215 nm (around 5,8 eV) has been attributed to SiE' centers. Upon annealing up to  $600\text{ }^\circ\text{C}$  we can observe a significant impact on both bands at 5 eV and 5.8 eV. This is in accordance with the temperature dependent decay of SiE' centers reported by Messina and Cannas [70]. After a thermal treatment at  $400\text{ }^\circ\text{C}$  most of these defects have been bleached. Then for annealing treatments in the  $600\text{-}1200\text{ }^\circ\text{C}$  range (Figure 4.25b) there is a slight continuous decrease of the UV tail. Finally, the last step at  $1200\text{ }^\circ\text{C}$  leads to a strong decrease of the remaining absorption tail, which is characteristic of a lesser nanoporosity in the porous nanolayers.

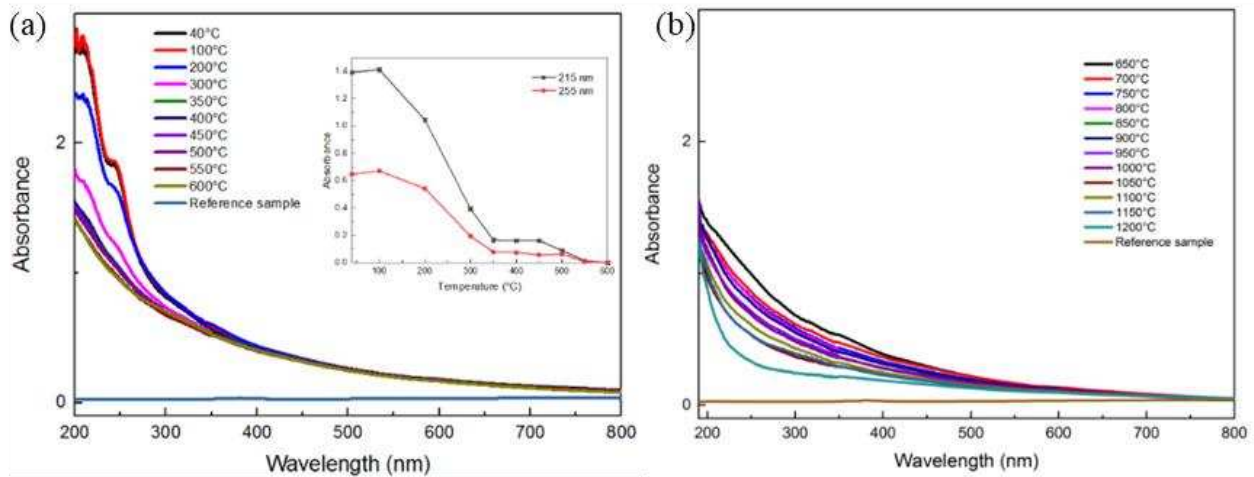


Figure 4.25: UV-Vis absorption spectra of Type II modification area, as a function of annealing temperature: (a) 40 °C – 600 °C range and (b) 650 °C – 1200 °C range, the spectrum for the non-irradiated region was inserted as the reference. Inset graph in (a): the absorbance as a function of temperature for the specific wavelengths (215 nm and 255 nm). The laser parameters were: 1030 nm, 250 fs, 0.6 NA, 100kHz, 0,1 mm/s and X+10° writing configuration.

### *Impact of the stress-induced birefringence*

The formation of nanogratings is not solely creating form birefringence but also a stress-birefringence contribution, attributed to a net volume expansion [44, 56], which correlates with the formation of porous structures inside the nanogratings. Here we chose to investigate a specific writing configuration that maximizes the stress amplitude around a laser track [71] as well as minimizes the imprinting of anisotropic circular optical properties (within the laser affected zone) such as CD and CB [72, 73]. The silica sample was moved along an axis defined as the Y-axis (or scanning direction). The laser linear polarization was oriented perpendicular to such axis (along the x-axis). This writing configuration is defined as “Yx” configuration of writing. The laser-induced nanogratings wave-vector is thus oriented perpendicularly to the laser scanning direction. In this simple arrangement, we did not use the “etched cuts” as initially proposed by Mc Millen et al. [71]. However, the stress-induced birefringence remains confined within the area of interest as visible in Figure 4.18 and Figure 4.19. More information’s can be found in the second section of chapter 5 about the related design.

In agreement with the literature, the nanogratings-based waveplates (both *Total LB* red curve in Fig. 4.26 but also *Total LD* shown in Figure 4.21) can survive for 10’s minutes to temperatures higher than 1100 °C in SiO<sub>2</sub> and typically erase for annealing treatments above the glass annealing temperature  $T_a$  (i.e. 1120 °C for SuprasilCG and with  $T_a$  defined as  $(T) = 10^{13}$  dPa.s). In contrast, we can observe the reduction of the stress-induced birefringence (black curve) by a factor of two after 30 minutes of annealing at 1050 °C as shown in Figure 4.26a. This agrees with the widely accepted idea that an annealing at around 0,8-0,9  $T_a$  (depending on the duration of the thermal treatment) should relax the stress-induced birefringence, as it is well known in glass manufacturing. Following this view, A. Čerkauskaitė [74] has demonstrated that annealing of nanogratings-based samples for 24 hours at 950 °C,



6 hours at 1000°C, 2 hours at 1050°C, and 1 hour at 1100-1150°C “totally” eliminates the stress-induced birefringence. In contrast, since the annealing of nanogratings is governed by the slow decay term, the form birefringence remains after these thermal treatments. Note in Figure 4.26b, we show the “decomposition” of TLB (within nanogratings area) into LB and LB’ that reveals a non monotonous evolution of LB’ with the annealing T whereas LB remains quite stable (up to 1100°C). So LB’ seems to follow the stress to some extent: LB’ decrease when stress increases (400-800°C) and then when stress sharply decrease we observed a correlated increase (typ. by 20%) of LB’ (900-110°C).

Under similar conditions this can be compared with the decrease of the circular optical properties as shown in Figure 4.26a. Indeed in the situation where the stress has been relaxed and thus stress-induced birefringence cannot be observed anymore around the laser track, circular optical properties also exhibit a steep decay and then disappear. Again this reveals somehow a link between the presence of stress-induced birefringence (within nanogratings regime) and the appearance of CB (and CD as well ice it exhibits a similar thermal stability).

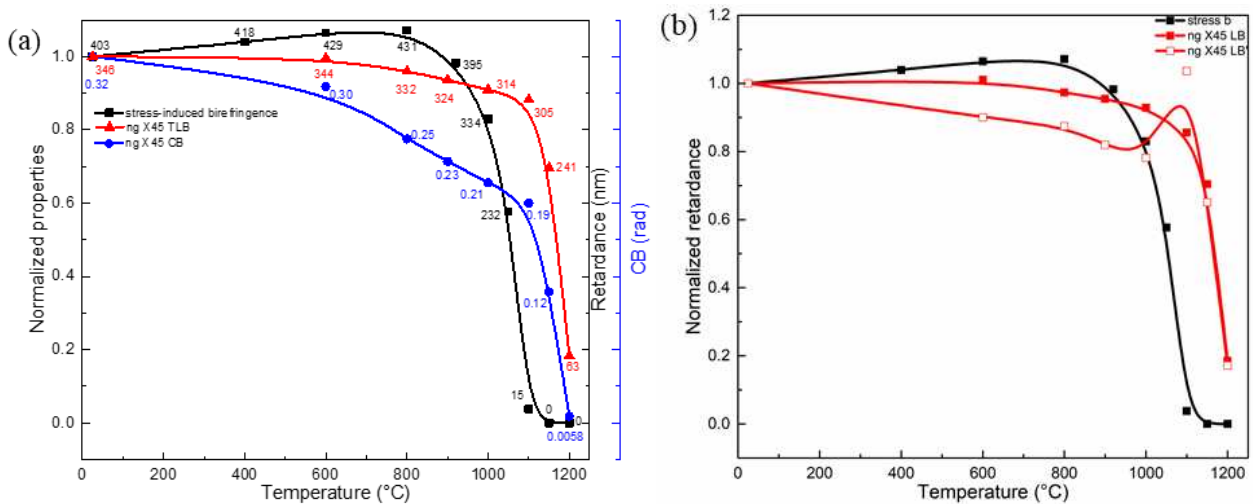


Figure 4.26: (a) Experimental values of the normalized evolution of optical retardance  $R$  (proportional to LB) and CB at 550nm with annealing temperature  $T$ . Note we add the retardance values for each point as a label. Black dots are for LB related to the stress-engineered waveplate whereas red and blue symbols are ascribed to LB and CB for a nanogratings-based waveplate written in X45° configuration. (b) Normalized evolutions of LB and LB’ according to annealing temperature. Lines are only guides for the eye.

### Conclusions on thermal stability within Type II regime

The characteristic feature of Type II modifications is the formation of nanogratings that can easily be detected through optical birefringence measurements. However, the total linear birefringence of the nanogratings arises from the sum of several contributions, including form birefringence, stress-induced birefringence associated to a permanent volume changes (typ. a volume expansion within Type II regime in SiO<sub>2</sub>), and point defects. In this section, we discussed shortly the different contributions of the total linear birefringence response in silica glass induced by femtosecond laser irradiation, as well as the corresponding effect on the circular optical properties during step isochronal annealing process.

The results of UV absorption spectra had revealed the effect of point defects on nanogratings refractive index modifications. However, it should be pointed out that they induce a minor effect to the nanogratings refractive index difference  $n_2-n_1$  (and thus on the measured birefringence or retardance). The point defects centers are bleached under a fairly low temperature thermal treatment ( $<500$  °C) and no significant or minor change in the retardance value can be found in this temperature range in agreement with previous work [68].

We have then investigated the thermal stability of the stress-induced birefringence. The unexpected rise of the stress-induced birefringence from 600 °C - 1000 °C might be attributed to the co-existence of Type I and Type II modifications, the erasure of the former occurred at this stage and eventually caused an unusual increase of the retardance  $R$  related to the stress. This would need a more detailed study together with modeling in the future. Beyond 1000 °C, stress-induced birefringence value drastically diminishes and reaches a null value at 1150 °C, which is associated to stress relaxation when approaching the glass transition temperature [75]. Then, by comparing and monitoring the circular optical properties (CB and CD) within the irradiated area and the surrounding stress-induced birefringence area during the annealing process, it is determined that stress relaxation is strongly related to the steep decay of the circular properties. However a significant part of the linear optical properties still remain whereas CB and CD have fully disappeared.

Finally the evolution of porosity parameters: filling factor and the pore size (determined by the SEM micrographs) seem to play an extremely important role in the erasure of nanogratings and their associated birefringence in a high temperature regime. This sheds light on the major role played by the temperature dependence of the glass viscosity on the thermal stability of fs-induced Type II modifications. The viscous behavior of the glass, at high temperature, is likely the major parameter that drives the nanogratings erasure and related form birefringence. The future research efforts are ongoing to better understand the role played by the nanopores on the overall thermal stability of the laser induced Type II modifications, which can be valuable for reliable nanogratings lifetime prediction to be investigated in future work.

## 4.8 Conclusions

The objective of this chapter was to investigate in depth circular optical properties, mostly in the visible range, using differential matrix formalism [7] on transmission Mueller matrices measured on femtosecond laser-induced modifications in silica within Type II regime. By using differential decomposition of the Mueller matrix, we quantified the effective or equivalent circular birefringence and dichroism in the presence of strong linear optical properties namely LB and LD. In particular, we have focused on optical activity (or circular birefringence) photo-induced in silica glass by laser irradiation.

*To summarize the main observations of this chapter:*

- By using differential decomposition of the Mueller matrix, we revealed and quantified the equivalent values of CB for the first time, to the best of our knowledge.
- Such a strong effective CB( ) (circular birefringence) accompanied by an apparent CD( ) (circular dichroism) are observed in the whole investigated spectral range and in many silica glass samples irradiated by femtosecond laser in various experimental conditions.
- In contrast to circular dichroism measurements reported in Chapter 3, we did not observe any significant asymmetric transmission of polarized light using Mueller spectro-polarimetry.
- Within Type I regime and below the energy threshold for the appearance of porous nanoplanes, there is no CD and CB. On the contrary, for higher pulse energies within Type II regime, a significant amount of CD and CB appear.
- Based on energy, pulse-to-pulse overlap and focusing depth dependence, we reveal that both CB and CD formation appears to be correlated with the formation of Type II modifications in silica (i.e. nanogratings formation). The formation of nanogratings and their nanoporous nature were directly confirmed using SEM measurements.
- The control of polarization orientation (with respect to the scanning direction) offers a way for creating strong circular optical properties. For all measurements we made in X+45° configuration, the apparent sign of the CD is positive (whereas CB is negative), but it can be reversed by rotating the polarization axis of the laser by 90°.
- In addition we have further investigated the polarimetric properties of femtosecond laser induced nanogratings in a wide spectral range extending from UV up to the NIR. The equivalent circular optical properties using Mueller-matrix spectroscopic ellipsometry in transmission mode were extracted. A high effective specific rotation of  $\alpha \sim -860^\circ/\text{mm}$  at  $\lambda = 290 \text{ nm}$  and  $143^\circ/\text{mm}$  at  $550 \text{ nm}$  are found, which are sufficient to think about devices. We also reveal the formation of a linear and circular dichroism band peaking around  $\lambda \sim 1240 \text{ nm}$ .

In particular, investigation of the optical properties related to the writing configuration (scanning direction vs linear polarization direction) reveals a number of key results:

- LB( ) and LB'( ) exhibit a deviation from the expected periodic shape and thus a deviation of the slow axis orientation  $\theta_{LB}$  when compared to
- TLB( ) amplitude depends on the polarization orientation which is usually qualified or at least related to so-called anisotropy photosensitivity in the literature.
- Similar observations can be done on the linear dichroism LD, LD', TLD and  $\theta_{LD}$ .
- Above 550nm the DoP remains very close to 1 for all investigated writing configurations.
- CB and CD exhibit a non-symmetric periodic dependence with the linear polarization azimuth with maximum amplitude for  $\pm 45^\circ$  (with respect to the scanning direction).

### *About stress investigations*

- Stress-induced birefringence has been investigated following an approach proposed by Y. Bellouard group based on stress bars engineering creating a “stress only zone” [71]. For the involved geometry (set of lines), we reveal that the slow axis orientation of the stress-induced birefringence does not depend on the laser writing polarization (except at the edges of the written line). But the polarization orientation impacts the amplitude of the stress-induced birefringence: higher for a perpendicular writing configuration.
- Stress-engineered half-waveplates in the UV-Vis range with no linear dichroism and minor optical losses (below  $1 \text{ cm}^{-1}$  from 200 nm to 1500 nm) were reported. In addition, these stress-induced birefringent waveplates were stable up to  $1000^\circ\text{C}$ , making them attractive candidates for UV-Vis birefringent and space variant birefringent devices.
- In contrast, nanogratings-based waveplates present strong losses accompanied with a significant linear dichroism and a significant depolarization increasing at short wavelengths. The positive *LD for Xx configuration* (and negative for Xy writing configuration) implies that higher losses were measured for polarization oriented perpendicular to the nanolayers in agreement with [68]. LD is likely due to anisotropic light scattering induced by the intrinsically porous nanolayers constituting the fabricated waveplate.

### *About isochronal step annealing results*

- The point defects centers are bleached under a fairly low temperature thermal treatment ( $<500^\circ\text{C}$ ) and no significant changes in the CB, CD properties nor the linear ones can be found in this temperature range in agreement with previous work.
- Thermal stability of CB, CD is strongly correlated with the one of the stress-induced birefringence measured in a non-irradiated area i.e. they all disappear after 30min at  $1100^\circ\text{C}$ . In contrast a significant part (80%) of the linear optical properties still remain whereas no CB, CD remain.
- Finally the porosity filling factor and the nanopores size (determined by SEM) play an extremely important role in the erasure of nanogratings and their associated birefringence in a high temperature regime.

About the observed circular optical properties in the UV-Vis range, we do not know yet if the observed circular birefringence originates from internal linear birefringence that could be related to a non-parallel non-orthogonal assembly of two (or more) linear contributions, or from a fs pulse induced molecular optical activity. This will be investigated in the next chapter that is dedicated to discuss and tentatively interpret some key results observed in this chapter.

## 4.9 References

1. Jones, R.C., *A new calculus for the treatment of optical systemsiii. the sohncke theory of optical activity*. Josa, 1941. **31**(7): p. 500-503.
2. Poumellec, B., et al., *Parity violation in chiral structure creation under femtosecond laser irradiation in silica glass&quest*. Light: Science & Applications, 2016. **5**(11): p. e16178.
3. Desmarchelier, R., et al., *Chiroptical properties photo-induced by femtosecond laser irradiation in silica glass*. Applied Physics Letters, 2017. **110**(2): p. 021112.
4. Le Roy-Brehonnet, F. and B. Le Jeune, *Utilization of Mueller matrix formalism to obtain optical targets depolarization and polarization properties*. Progress in Quantum Electronics, 1997. **21**(2): p. 109-151.
5. Yoo, S.H., R. Ossikovski, and E. Garcia-Caurel, *Experimental study of thickness dependence of polarization and depolarization properties of anisotropic turbid media using Mueller matrix polarimetry and differential decomposition*. Applied Surface Science, 2017. **421**: p. 870-877.
6. Shimotsuma, Y., K. Miura, and H. Kazuyuki, *Nanomodification of Glass Using fs Laser*. International Journal of Applied Glass Science, 2013. **4**(3): p. 182-191.
7. Ossikovski, R., et al., *Depolarizing Mueller matrices: how to decompose them?* physica status solidi (a), 2008. **205**(4): p. 720-727.
8. Kazansky, P.G., et al., *Photosensitivity control of an isotropic medium through polarization of light pulses with tilted intensity front*. Optics express, 2011. **19**(21): p. 20657-20664.
9. Poumellec, B., et al., *Asymmetric Orientational Writing in glass with femtosecond laser irradiation*. Optical Materials Express, 2013. **3**(10): p. 1586-1599.
10. Ossikovski, R., *Differential matrix formalism for depolarizing anisotropic media*. Optics letters, 2011. **36**(12): p. 2330-2332.
11. Ossikovski, R. and O. Arteaga, *Statistical meaning of the differential Mueller matrix of depolarizing homogeneous media*. Optics letters, 2014. **39**(15): p. 4470-4473.
12. Bricchi, E., B.G. Klappauf, and P.G. Kazansky, *Form birefringence and negative index change created by femtosecond direct writing in transparent materials*. Optics Letters, 2004. **29**(1): p. 119-121.
13. Arwin, H., et al., *Structural circular birefringence and dichroism quantified by differential decomposition of spectroscopic transmission Mueller matrices from *Cetonia aurata**. Optics letters, 2016. **41**(14): p. 3293-3296.
14. Desmarchelier, R., et al., *Achromatic polarization rotator imprinted by ultrafast laser nanostructuring in glass*. Applied Physics Letters, 2015. **107**(18): p. 181111.
15. Ghabbach, A., et al., *Depolarization and enpolarization DOP histograms measured for*

- surface and bulk speckle patterns*. Optics express, 2014. **22**(18): p. 21427-21440.
16. Canning, J., et al., *Anatomy of a femtosecond laser processed silica waveguide [Invited]*. Optical Materials Express, 2011. **1**(5): p. 998-1008.
  17. Lancry, M., et al., *Ultrafast nanoporous silica formation driven by femtosecond laser irradiation*. Laser and Photonics Reviews, 2013. **7**: p. 953-962.
  18. Desmarchelier, R., et al., *In the Heart of Femtosecond Laser Induced Nanogratings: From Porous Nanoplanes to Form Birefringence*. World Journal of Nano Science and Engineering, 2015. **5**(04): p. 115.
  19. Lancry, M., et al., *Nanoscale femtosecond laser milling and control of nanoporosity in the normal and anomalous regimes of GeO<sub>2</sub>-SiO<sub>2</sub> glasses*. Optical Materials Express, 2016. **6**(2): p. 321-330.
  20. Li, L., *Symmetries of cross-polarization diffraction coefficients of gratings*. JOSA A, 2000. **17**(5): p. 881-887.
  21. Arteaga, O. and A. Canillas, *Pseudopolar decomposition of the Jones and Mueller-Jones exponential polarization matrices*. JOSA A, 2009. **26**(4): p. 783-793.
  22. Arteaga, O., Z. El - Hachemi, and A. Canillas, *Application of transmission ellipsometry to the determination of CD spectra of porphyrin J - aggregates solid - state samples*. physica status solidi (a), 2008. **205**(4): p. 797-801.
  23. Schellman, J. and H.P. Jensen, *Optical spectroscopy of oriented molecules*. Chemical Reviews, 1987. **87**(6): p. 1359-1399.
  24. Poumellec, B., et al., *Parity violation in chiral structure creation under femtosecond laser irradiation in silica glass? Light: Science & Applications*, 2016. **5**(11): p. e16178.
  25. Poumellec, B., et al., *Modification thresholds in femtosecond laser processing of pure silica: review of dependencies on laser parameters [Invited]*. Optical Materials Express, 2011. **1**(4): p. 766-782.
  26. Song, H., et al., *Femtosecond laser-induced structural difference in fused silica with a non-reciprocal writing process*. Applied Physics A, 2017. **123**(4): p. 255.
  27. Burakov, I., et al., *Spatial distribution of refractive index variations induced in bulk fused silica by single ultrashort and short laser pulses*. Journal of Applied Physics, 2007. **101**: p. 043506.
  28. Song, J., et al., *Formation mechanism of self-organized voids in dielectrics induced by tightly focused femtosecond laser pulses*. Applied Physics Letters, 2008. **92**(9): p. 092904.
  29. Couairon, A., et al., *Filamentation and damage in fused silica induced by tightly focused femtosecond laser pulses*. Physical Review B, 2005. **71**(12): p. 125435.
  30. Richter, S., et al., *Nanogratings in fused silica: Formation, control, and applications*. Journal of Laser Applications, 2012. **24**: p. 042008(1)-042008(8).

31. Wei, S.-E., et al., *Thermal Stability of Type II Modifications by IR Femtosecond Laser in Silica-based Glasses*. *Sensors*, 2020. **20**(3): p. 762.
32. Lancry, M., et al., *Compact Birefringent Waveplates Photo-Induced in Silica by Femtosecond Laser*. *Micromachines*, 2014. **5**(4): p. 825-838.
33. Beresna, M., *Polarization engineering with ultrafast laser writing in transparent media*. 2012, Southampton.
34. Ashcom, J.B., et al., *Numerical aperture dependence of damage and supercontinuum generation from femtosecond laser pulses in bulk fused silica*. *Journal of Optical Society of America B*, 2006. **23**(11): p. 2317-2322.
35. Venkatakrisnan, K., et al., *The effect of polarization on ultrashort pulsed laser ablation of thin metal films*. *Journal of Applied Physics*, 2002. **92**(3): p. 1604-1607.
36. Corbari, C., et al., *Femtosecond versus picosecond laser machining of nano-gratings and micro-channels in silica glass*. *Optics Express*, 2013. **21**(4): p. 3946-3958.
37. Zhang, J., et al., *Seemingly unlimited lifetime data storage in nanostructured glass*. *Physical Review Letters*, 2014. **112**(3): p. 033901.
38. Gecevičius, M., M. Beresna, and P.G. Kazansky, *Polarization sensitive camera by femtosecond laser nanostructuring*. *Optics letters*, 2013. **38**(20): p. 4096-4099.
39. Beresna, M., et al., *Radially polarized optical vortex converter created by femtosecond laser nanostructuring of glass*. *Applied Physics Letters*, 2011. **98**(20): p. 201101.
40. Nesterov, A.V. and V.G. Niziev, *Influence of beam polarization on laser cutting efficiency*. *Journal of Physics D: Applied Physics*, 1999. **32**: p. 1455-1461.
41. Kazansky, P.G., et al., *"Quill" writing with ultrashort light pulses in transparent materials*. *Applied Physics Letters*, 2007. **90**(15): p. 151120.
42. Vitek, D.N., et al., *Spatio-temporally focused femtosecond laser pulses for nonreciprocal writing in optically transparent materials*. *Optics express*, 2010. **18**(24): p. 24673-24678.
43. Akturk, S., et al., *Pulse-front tilt caused by spatial and temporal chirp*. *Optics express*, 2004. **12**(19): p. 4399-4410.
44. Champion, A. and Y. Bellouard, *Direct volume variation measurements in fused silica specimens exposed to femtosecond laser*. *Optical Materials Express*, 2012. **2**(6): p. 789-798.
45. Salter, P. and M. Booth, *Dynamic control of directional asymmetry observed in ultrafast laser direct writing*. *Applied Physics Letters*, 2012. **101**(14): p. 141109.
46. Poumellec, B., et al., *Femtosecond laser irradiation stress induced in pure silica*. *Optics Express*, 2003. **11**(9): p. 1070-1079.
47. Poumellec, B., et al., *Non reciprocal writing and chirality in femtosecond laser irradiated silica*. *Optics Express*, 2008. **16**(22): p. 18354-18361.

48. Salter, P., R. Simmonds, and M. Booth. *Adaptive control of pulse front tilt, the quill effect, and directional ultrafast laser writing*. in *Frontiers in Ultrafast Optics: Biomedical, Scientific, and Industrial Applications XIII*. 2013. International Society for Optics and Photonics.
49. Sudrie, L., et al., *Writing of permanent birefringent microlayers in bulk fused silica with femtosecond laser pulses*. Optics Communications, 1999. **171**(4-6): p. 279-284.
50. Gorelik, T., et al., *Transmission electron microscopy studies of femtosecond laser induced modifications in quartz*. Applied Physics A, 2003. **76**(3): p. 309-311.
51. Sudrie, L., et al., *Study of damage in fused silica induced by ultra-short IR laser pulses*. Optics Communications, 2001. **191**(333-339).
52. Champion, A., et al., *Stress distribution around femtosecond laser affected zones: effect of nanogratings orientation*. Optics Express, 2013. **21**(21): p. 24942-24951.
53. Zhang, X.R., X. Xu, and A.M. Rubenchik, *Simulation of microscale densification during femtosecond laser processing of dielectric materials*. Applied Physics A, 2004. **79**(4-6): p. 945-948.
54. Bhardwaj, V., et al., *Stress in femtosecond-laser-written waveguides in fused silica*. Optics Letters, 2004. **29**(12): p. 1312-1314.
55. Dürr, F., et al., *Tomographic measurement of femtosecond-laser induced stress changes in optical fibers*. Applied Physics Letters, 2004. **84**(24): p. 4983-4985.
56. Thomson, R.R., et al., *Stress-state manipulation in fused silica via femtosecond laser irradiation*. Optica, 2016. **3**: p. 1285.
57. Canning, J., et al., *Anatomy of a femtosecond laser processed silica waveguide [Invited]*. Optical Materials Express, 2012. **1**(5): p. 998-1008.
58. Yuan, L., et al., *Stress-induced birefringence and fabrication of in-fiber polarization devices by controlled femtosecond laser irradiations*. Optics Express, 2016. **24**(2): p. 1062-1071.
59. Fernandes, L.A., et al., *Stress induced birefringence tuning in femtosecond laser fabricated waveguides in fused silica*. Optics Express, 2012. **20**(22): p. 24103-24114.
60. Fernandes, L.A., et al., *Strong birefringence tuning of optical waveguides with femtosecond laser irradiation of bulk fused silica and single mode fibers*. Journal of Lightwave Technology, 2013. **31**(22): p. 3563-3569.
61. Shimotsuma, Y., et al., *Self-organized nanogratings in glass irradiated by ultrashort light pulses*. Physical review letters, 2003. **91**(24): p. 247405.
62. Lancry, M., et al., *Dependence of the femtosecond laser refractive index change thresholds on the chemical composition of doped-silica glasses*. Optical Materials Express, 2011. **1**(4): p. 711-723.
63. Kahandawa, G.C., et al., *Use of FBG sensors for SHM in aerospace structures*. Photonic



Sensors, 2012. **2**(3): p. 203-214.

64. Beresna, M., M. Gecevičius, and P.G. Kazansky, *Ultrafast laser direct writing and nanostructuring in transparent materials*. Advances in Optics and Photonics, 2014. **6**(3): p. 293-339.

65. Poumellec, B. and M. Lancry, *Kinetics of Thermally Activated Physical Processes in Disordered Media*. Fibers, 2015. **3**: p. 206-252.

66. Gecevičius, M., *Polarization sensitive optical elements by ultrafast laser nanostructuring of glass*. 2015, University of Southampton.

67. Zhang, F., et al., *Wavelength response and thermal stability of embedded nanograting structure light attenuator fabricated by direct femtosecond laser writing*. Applied Physics B, 2014. **117**(1): p. 53-58.

68. Beresna, M., et al., *Broadband anisotropy of femtosecond laser induced nanogratings in fused silica*. Applied Physics Letters, 2013. **103**(13): p. 131903.

69. Yeh, P., *A new optical model for wire grid polarizers*. Optics Communications, 1978. **26**(3): p. 289-292.

70. Messina, F. and M. Cannas, *Stability of E' centers induced by 4.7 eV laser radiation in SiO<sub>2</sub>*. Journal of non-crystalline solids, 2007. **353**(5-7): p. 522-525.

71. McMillen, B., C. Athanasiou, and Y. Bellouard, *Femtosecond laser direct-write waveplates based on stress-induced birefringence*. Optics express, 2016. **24**(24): p. 27239-27252.

72. Tian, J., et al., *Study of femtosecond laser-induced circular optical properties in silica by Mueller matrix spectropolarimetry*. Optics letters, 2017. **42**(20): p. 4103-4106.

73. Tian, J., et al., *Femtosecond laser-induced circular dichroism in silica: Dependence on energy and focusing depth*. Nuclear Instruments and Methods in Physics Research Section B: Beam Interactions with Materials and Atoms, 2018. **435**: p. 258-262.

74. Čerkauskaitė, A., *Ultrafast laser nanostructuring for photonics and information technology*. 2018, UNIVERSITY OF SOUTHAMPTON. p. 206.

75. Musgraves, J.D., J. Hu, and L. Calvez, *Springer Handbook of Glass*. 2019: Springer Nature.



# Chapter5 Investigations of the UV-Vis-NIR spectral properties: comparison between nanogratings and stress-induced birefringence silica glass

---

---

## Content

5.1 Introduction.....	203
5.2 Spectral dependence of femtosecond laser induced circular optical properties in silica .....	204
5.3 A Comparison between Nanogratings-Based and Stress-Engineered Waveplates Written by Femtosecond Laser in Silica .....	205

## 5.1 Introduction

In chapter 4 Mueller-matrix spectroscopic ellipsometry was used in the visible range (typ. 450-1000nm) to investigate silica glass modified by femtosecond laser within nanogratings regime. This method is a powerful tool to examine structural and optical properties of surfaces, thin films, and multilayered materials that exhibit both linear and circular anisotropic optical properties from a single set of measurements in a few seconds. In the previous chapter we showed how values of the effective structural circular birefringence can be extracted in the presence of strong linear optical properties and found a maximum value of the effective specific rotation  $\sim -143^\circ/\text{mm}$  at 550 nm.

In the first part of this chapter, the spectral dependence of both linear and circular optical properties are investigated according to pulse energy and in a wide spectral range extending from  $\lambda = 250$  nm up to  $\lambda = 1800$  nm. In particular, we reveal a large effective optical rotation in the UV range and a specific dichroism band in the near-IR range around 11240 nm when the laser polarization is oriented at  $45^\circ$  off the scanning direction.

In the second part, we will compare the anisotropic linear optical properties of a waveplate made of nanogratings with the ones of a clear aperture waveplate based on stress-induced birefringence. Here again, Mueller-matrix spectroscopic ellipsometry is used as it provides the spectral dispersion of linear birefringence  $LB$ , linear dichroism  $LD$ ,  $LB$  neutral axis orientation and the depolarization rate from the UV to the Near-IR range. Moreover, a comparison of both optical losses and thermal stability between these two alternative designs will be provided, enabling engineering of uniform and space-selective birefringent optical components.

## **5.2 Spectral dependence of femtosecond laser induced circular optical properties in silica**



# Spectral dependence of femtosecond laser induced circular optical properties in silica

JING TIAN,<sup>1</sup> RUBING LI,<sup>2</sup> SANG HYUK YOO,<sup>3</sup> BERTRAND  
POUMELLE, <sup>1</sup>  ENRIC GARCIA-CAUREL,<sup>3</sup> RAZVIGOR  
OSSIKOVSKI,<sup>3</sup>  MICHEL STCHAKOVSKY,<sup>4</sup> CELINE EYPERT,<sup>4</sup> JOHN  
CANNING,<sup>5</sup>  AND MATTHIEU LANCRY<sup>1,\*</sup> 

<sup>1</sup>Institut de Chimie Moléculaire et des Matériaux d'Orsay, UMR CNRS-UPS 8182, Université Paris Sud, Orsay, France

<sup>2</sup>Institute of Circular Economy, Beijing University of Technology, Beijing, 100124, China

<sup>3</sup>LPICM, CNRS, Ecole Polytechnique, Palaiseau, France

<sup>4</sup>HORIBA Europe Research Center, Palaiseau, France

<sup>5</sup>interdisciplinary Photonic Laboratories (iPL), University of Technology Sydney (UTS), NSW 2007, Sydney, Australia

\*[matthieu.lancry@u-psud.fr](mailto:matthieu.lancry@u-psud.fr)

**Abstract:** Transmission Mueller-matrix spectroscopic ellipsometry is applied to study femtosecond laser induced nanogratings in silica glass in a wide spectral range 250–1800 nm. By using differential decomposition of the Mueller matrix, the circular birefringence and dichroism of femtosecond laser irradiated SiO<sub>2</sub> are quantified for the first time in the UV and near-IR range. A maximum value of the effective specific rotation of  $\alpha \sim -860^\circ/\text{mm}$  at 290 nm is found. In the near-IR range, we found a linear and circular dichroism band peaking around 1240 nm, which might be attributed to the formation of anisotropic species like the formation of oriented OH species and Si-O-Si bond.

© 2019 Optical Society of America under the terms of the [OSA Open Access Publishing Agreement](#)

## 1. Introduction

Femtosecond laser direct writing (FLDW) starts with multiphoton ionization [1,2], which induces various permanent modifications in silica glass depending on the laser parameters [3]. Such changes include refractive index changes [4], the formation of porous nanogratings and related linear birefringence [5–7], or even voids. The processing of glass with low-energy femtosecond laser pulses (sometimes combined with chemical etching) defines a flexible manufacturing platform suitable for technologies like optical data storage, optofluidics, optomechanics, marking, and photonics such as 3D optical waveguides and their combination [8,9], fiber Bragg gratings [10,11] and polarization devices [12,13]. Manufacturing monolithically integrated devices is attracting great interest because it is possible to induce strong refractive index increases ( $\Delta n$  from  $10^{-3}$  to more than  $10^{-2}$  in a large range of transparent glasses), which are localized in the bulk due to strong non-linear effect. Controlling these modifications could potentially allow exceeding current fs laser applications opening additional new possibilities in material science. In particular, the industrial demand for sophisticated all-optical integration is increasingly large as the volume of exchanged data and information increases demanding more complex devices and therefore greater nuance and complexity of laser treatment. Presently, one crucial optical property is still missing from the component library: the integration of circular optical properties (optical rotation and circular dichroism) in glass optical materials and devices.

In a previous study done in 2008, based on measurements done with a phase shift interferometer, we revealed that femtosecond laser interactions can shear matter like a scissor giving rise to a chiral strain if the light propagation axis is considered [14,15]. But shearing does not give rise to optical circular properties by itself like it is with torsion. Taylor *et al.* reported highly ordered «

chiral-like » nanostructures using circular polarized laser light but no circular optical properties [16]. In this direction, we have shown in 2016 that it is possible to produce circular diattenuation by inducing and controlling chirality within an achiral glass namely SiO<sub>2</sub> by controlling the laser writing polarization with respect to the scanning direction [17]. Last estimates of equivalent circular diattenuation using a circular dichroism spectrophotometer [18,19] show values up to  $-30^\circ/\text{mm}$  in the UV wavelength range and  $-20^\circ/\text{mm}$  at  $\lambda = 550 \text{ nm}$ . However it was difficult to extract the real spectral shape of the circular diattenuation due to the co-existence of strong linear properties [19].

Recently Mueller-matrix spectroscopic ellipsometry was used in the visible range to investigate silica glass modified by femtosecond laser within nanogratings regime [20,21]. This method is a powerful tool to examine structural and optical properties of surfaces, thin films, and multilayered materials that exhibit both linear and circular optical properties from a single measurement. We applied the differential matrix formalism [22,23] on transmission Mueller matrices measured for femtosecond laser-induced modifications in silica within the type II laser-processing regime. We showed how values of the effective structural circular birefringence can be extracted in the presence of strong linear optical properties and found a maximum value of the effective specific rotation  $\alpha \sim -143^\circ/\text{mm}$  at 550 nm.

In this letter, the spectral dependence of both linear and circular optical properties are investigated according to pulse energy and in a wide spectral range extending from  $\lambda = 250 \text{ nm}$  up to  $\lambda = 1800 \text{ nm}$ . In particular, we reveal a large effective optical rotation in the UV range and a specific dichroism band in the near-IR range when the laser polarization is oriented at  $45^\circ$  off the scanning direction.

## 2. Experimental details

The laser radiation was produced by a femtosecond laser system operating at  $\lambda = 1030 \text{ nm}$  and delivering 250 fs pulses at 100 kHz repetition rate. The beam was focused to a depth 300  $\mu\text{m}$  below the front face of 1 mm thick silica glass plates (Heraeus Suprasil1 containing [OH]  $\sim 830 \text{ ppm}$  and a solgel silica with [OH]  $\sim 100 \text{ ppm}$ ) using a 0.6 NA aspheric lens (estimated beam waist  $w \sim 1,5 \mu\text{m}$ ). The laser energy was varied from 0,15  $\mu\text{J}$  up to 4  $\mu\text{J}$  so we crossed the type II threshold (typ. 0,3  $\mu\text{J}$  in our experimental conditions) corresponding to the formation of nanogratings in SiO<sub>2</sub>. Based on preliminary results, we choose to investigate here a specific writing configuration in terms of polarization orientation that maximizes the imprinting of circular optical properties. When the laser was moving along x-axis (horizontal direction) and the laser linear polarization was oriented  $\theta = +45^\circ$  from the writing direction, we define it as "X + 45°" configuration of writing. Then, in this X + 45° configuration and using a scanning speed of  $v = 1 \text{ mm/s}$ , we created several squares  $3 \times 3 \text{ mm}^2$ , made up of a set of lines with a line spacing  $\Delta y = 1 \mu\text{m}$  to have a uniform anisotropic area and avoiding any diffraction effects. Scheme about the laser writing procedure is shown in Fig. 1 and more details can be found in Ref. [17].

Anisotropic optical properties are investigated using a phase modulated spectroscopic ellipsometer (UVISEL+, HORIBA Scientific) over  $\lambda = 250$  to 1800 nm spectral range. Since this equipment gives access to the three first columns of the Mueller matrix [24], we will explain in the results section how to estimate the values of the 4<sup>th</sup> column based on symmetry properties of Mueller matrices. In order to validate this approach, we compared the data obtained with the UVISEL+ with data obtained with a home-made Mueller ellipsometer [24,25] (Smart-SE, HORIBA Scientific), which provides a full Mueller matrix over a shorter spectral range between  $\lambda = 450$  and  $\lambda = 1000 \text{ nm}$ . All measurements were made using a collimated probe beam in normal incidence. The probe beam size of these two instruments was fixed to 1 mm for all measurements. The samples were oriented in such a way their writing/scanning axis was set horizontal  $\pm 2^\circ$  for the referential of the Mueller ellipsometers.

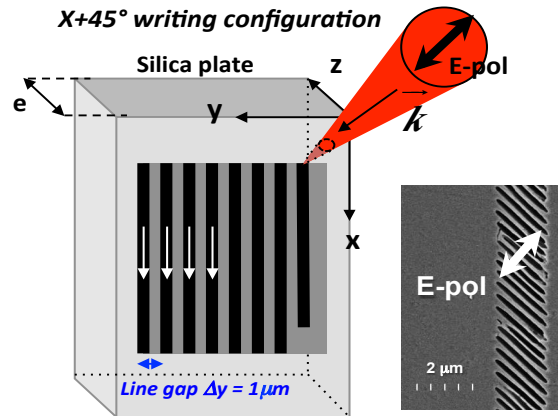


**Fig. 1.** Experimental setup scheme for X + 45° writing configuration and SEM image of sub-wavelength periodic structure formed in cross-section of the irradiated region. Original image is courtesy of Dr. Cyril Hnatovsky.

### 3. Results

We have seen in our preliminary experiments that our samples show asymmetric transmission when measuring ellipticity using a circular dichroism spectrometer [19]. In 2018 we investigated this observation by measuring both  $\mathbf{M}$  and  $\mathbf{M}_{\text{rev}}$ , i.e., the Mueller matrix in the reverse direction (from the backface) [21]. The differences were that  $m_{13}$ ,  $m_{31}$ ,  $m_{24}$ , and  $m_{42}$  change their respective signs whereas all other elements remain invariant. This symmetry implies that  $\mathbf{M}$  fulfills the principle of reciprocity. The difference between the elements of predicted  $\mathbf{M}_{\text{rev}}$  from a measured Mueller matrix,  $\mathbf{M}$ , and the elements of the measured  $\mathbf{M}_{\text{rev}}$  is typically  $< 0.01$  which corresponds to instruments accuracy. This indicates that both linear and circular anisotropic optical properties are quite similarly distributed in depth.

Figure 2 shows the normalized ( $m_{11}$  was normalized to 1) spectral Mueller matrices  $\mathbf{M}$  obtained with the two instruments. The Mueller matrix represented in this figure corresponds to a Suprasil1 sample written at pulse  $E = 1.5 \mu\text{J}/\text{pulse}$  with a X + 45° writing configuration. The sample exhibits low linear and circular dichroism because the elements  $m_{12}$ ,  $m_{21}$ ,  $m_{14}$  and  $m_{41}$  are very small. In contrast, the elements  $m_{24}$  and  $m_{42}$ , being close to +1 and -1 respectively highlight a significantly high linear birefringence [26]. The Mueller matrix of this “X + 45°” sample, can be firstly approximated by  $\mathbf{M} = \mathbf{R}(-45^\circ) \cdot \mathbf{M}_{\Psi\Delta} \cdot \mathbf{R}(45^\circ)$ , where  $\mathbf{R}(\alpha)$  is the rotation matrix and  $\mathbf{M}_{\Psi\Delta}$  is the Mueller matrix for a perfect linear dichroic retarder. This corresponds to the slow axis direction coinciding with the chosen writing polarization orientation; that is, rotated  $\alpha = 45^\circ$  from the direction of writing. The element  $m_{33}$  should ideally be equal to one. However, the measured values appear to be slightly smaller (0.95–0.99) indicating a slight depolarization, and down to 0.85 in the UV range at  $\lambda = 250 \text{ nm}$ . In summary, our samples for  $\lambda \in 450\text{--}1800 \text{ nm}$  are characterized by having high linear retardation, low dichroism, and a small depolarization. Note there is an interesting dichroic band around  $\lambda = 1300 \text{ nm}$ . In the UV range, there is an increase of the linear dichroism and a significant depolarization.

So as a first approximation if we consider that our sample is indeed a linear dichroic retarder at 45° (i.e. circular properties are very small compared to the linear ones), we can use symmetry properties of Mueller matrices to evaluate the values of the 4<sup>th</sup> column i.e.  $m_{14} = m_{41}$ ,  $m_{24} = -m_{42}$ ,  $m_{34} = m_{43}$ ,  $m_{44} = m_{22}$ . Note that both matrices coincide quite well in the common spectral range so this first approximation to deduce the values of the 4<sup>th</sup> column of the Mueller matrix from phase-modulated ellipsometry could provide some reliable information. Note that the differences



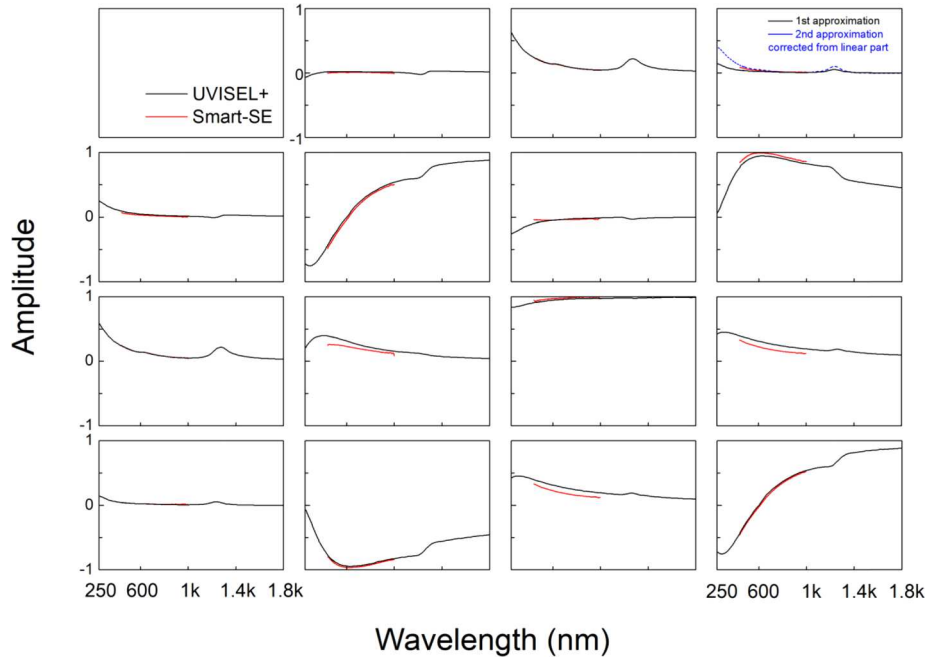


**Fig. 2.** Normalized Mueller matrix of Suprasil1 written using X + 45° configuration. Red lines are for the liquid crystals ellipsometer whereas the one obtained with photoelastic modulator ellipsometer correspond to the black lines. The dash blue line corresponds to the second order approximation taking into account the linear contribution

between the two ellipsometers (e.g. up to 0,1 in  $m_{32}$  and  $m_{34}$ ) are related to a slightly different azimuthal orientation ( $\pm 2^\circ$ ) of the samples during measurements. This leads to different “projections” of the linear properties in the xy plan but this has no impact on the intrinsic polarimetric properties that we extract after decomposition.

As a second order approximation we can take into account that elements  $m_{14}$  and  $m_{41}$  is formed by a superposition of effects due to both circular and linear parts, with the linear contribution intervening with opposite signs in  $m_{14}$  and  $m_{41}$  respectively as it has been extensively study in Refs. [27–29]. Therefore since linear properties are non-zero, one expects that before decomposition  $m_{14}$  be different than  $m_{41}$ . So the dash blue line in Fig. 2 corresponds to  $m_{14}$  taking into account the linear, which agree quite well with the full Mueller ellipsometer (Smart-SE). This enables further data treatment in order to determine the complete polarimetric properties of our fs-irradiated samples.

According to [23] the polarimetric optical response of a medium of length,  $l$ , with a complex refractive index  $\tilde{n} = n + i.\kappa$ , can be defined as a superposition of the following optical phase shift related to basic polarimetric properties: linear birefringence  $LB = \frac{2\pi}{\lambda} \cdot (n_X - n_Y) \cdot l$ , 45° linear birefringence  $LB' = \frac{2\pi}{\lambda} \cdot (n_{45} - n_{135}) \cdot l$ , linear dichroism  $LD = \frac{2\pi}{\lambda} \cdot (\kappa_X - \kappa_Y) \cdot l$ , 45° linear dichroism  $LD' = \frac{2\pi}{\lambda} \cdot (\kappa_{45} - \kappa_{135}) \cdot l$ , circular birefringence  $CB = \frac{2\pi}{\lambda} \cdot (n_L - n_R)$ , circular dichroism  $CD = \frac{2\pi}{\lambda} \cdot (\kappa_L - \kappa_R) \cdot l$  and the degree of polarization  $DoP$ . By using the differential decomposition described in [5–6], it is possible to extract all the above mentioned polarimetric properties from the Mueller matrix of a sample providing that the laser track is considered as homogeneous in the direction of light propagation. A differential decomposition of  $\mathbf{M}$  to find its differential matrix,  $\mathbf{m}$ , implies determining its logarithm  $\mathbf{L} = \ln(\mathbf{M})$ . Since  $d\mathbf{M}/dz = \mathbf{m}(z) \cdot \mathbf{M}(z)$ , if the differential matrix  $\mathbf{m}$ , does not depend on  $z$ , then the matrices  $\mathbf{m}$  and  $\mathbf{L}$  are related by  $\mathbf{L} = \mathbf{m} \cdot l$ . For a

non-depolarizing medium, the differential matrix  $\mathbf{L}$  is Minkowski antisymmetric and contains the six elementary optical properties fully characterizing the medium namely  $LD$ ,  $LB$ ,  $LD'$ ,  $LB'$ ,  $CD$ ,  $CB$  and the  $DoP$ . When the medium is depolarizing as it is the case here in the UV range ( $DoP$  decreases down to 0,7 at  $\lambda = 300$  nm as shown in the right inset of Fig. 3), the depolarization can be interpreted as resulting from the fluctuations of the optical properties  $n$  and  $\kappa$ , which influence the elementary polarization properties of the irradiated silica glass [22,23]. Result of the differential decomposition of the experimental Mueller matrix is shown in Fig. 3. Based on preliminary investigations [17,19] we know that fs-irradiation modifies inhomogeneously the physical structure of the material along the pulse path across the sample. Consequently, we think that the measured birefringence parameters do not correspond to intrinsic material properties but to effective or equivalent optical parameters induced by fs laser. For sake of comparison we add the  $CB$  and  $CD$  spectra obtained from the decomposition of the Mueller matrix using the two different approximations describe above: first one (full line) considers circular properties are very small when compared to the linear ones whereas the second one (dash line) introduce a linear term correction to calculate the elements of 4<sup>th</sup> column as described in [27–29].

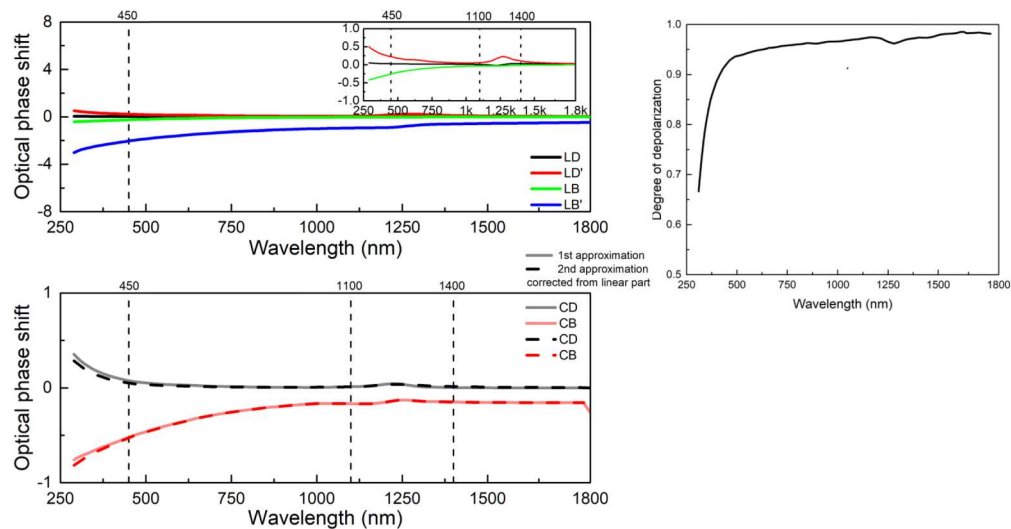


**Fig. 3.** Spectral dependence of the anisotropic linear and circular optical properties and extracted after Mueller matrix decomposition. (Suprasil1 silica, 1030 nm, 250 fs, 0.6 NA, 1 mm/s, 100kHz, 1,5 $\mu$ J/pulse, X + 45 $^\circ$  configuration). The dashed lines correspond to data decomposed using the second order approximation taking into account the linear contribution. The right inset corresponds to the Degree of Polarization (DoP) spectral dependence.

We can observe three spectral regions in Fig. 3: (I) below  $\lambda = 450$  nm, (II)  $\Delta\lambda = (450-1100)$  nm and above  $\lambda = 1400$  nm, and (III) between  $\lambda = 1100$  and  $\lambda = 1400$  nm. In region I, the absolute values of the off-diagonal elements in  $\mathbf{M}$  are quite high which have values above 0.3 rad. For example, at  $\lambda = 250$  nm, we reveal 0.5 for  $LD'$ ,  $-3$  rad for  $LB'$  and significant circular properties as well 0.3  $CD$  for and  $-0.75$  rad for  $CB$ . Note that the reliable presence of  $CD$  in the UV range has previously been confirmed using a spectro-polarimeter in [18]. In region II, all depolarization effects remain smaller than 10% and monotonically decrease with  $\lambda$  below 3% for  $\lambda > 1100$  nm. According to the data shown in Fig. 3, it is seen that the two  $xy$  linear effects ( $LB$  and  $LD$ ) are small, while the crossed linear properties ( $LB'$  and  $LD'$ ) are quite important. This is because the polarization of the sample (X + 45 $^\circ$ ) written by laser was oriented  $\pm 45^\circ$  to the reference axis. If the polarization had been oriented parallel or perpendicular to the x-direction (X0 $^\circ$  or X90 $^\circ$ ), the pair ( $LB$  and  $LD$ ) would have been maximal and the pair ( $LD'$  and  $LB'$ ) would have been

minimized. For the circular effects we notice a monotonous increase of  $CD$  towards shorter wavelengths.

In region III  $\Delta\lambda = (1100 - 1400)$  nm, the sample exhibits a strong linear dichroism at  $45^\circ$  ( $LD'$ ) band. In particular we notice that  $m_{13} \approx m_{31}$  with  $LD'$  values up to 0.25. For the chosen orientation we also observe that  $m_{14} \approx m_{41}$  and is nonzero with  $CD$  values up to 0.10, which reveals a slight circular dichroic band. The corresponding Kramers–Kronig consistent feature in  $LB'$  and  $CB$  also creates a related feature  $\sim \lambda = 1240$  nm.

The spectral dependence of both linear and circular anisotropic optical properties are shown respectively in Figs. 4 and 5 as a function of the pulse energy. In Fig. 4 we chose to draw the “Total  $LB$ ” and the “Total  $LD$ ” that correspond to the following equations  $Total\ LB = \sqrt{LB^2 + LB'^2}$  and  $Total\ LD = \sqrt{LD^2 + LD'^2}$ . Note that these two properties are thus independent of the samples azimuthal orientation during the ellipsometry measurements.

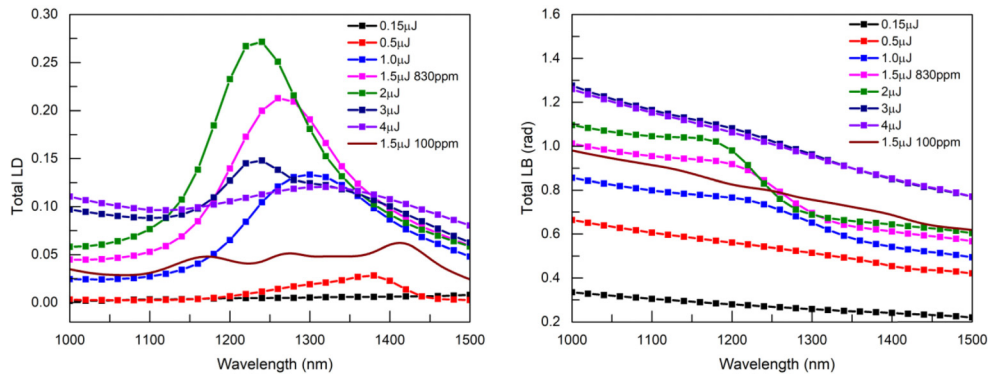


**Fig. 4.** Near-IR spectral dependence of the total linear birefringence, LB (Left), and the total linear dichroism, LD (Right), as a function of fs pulse energy. (1030 nm, 250 fs, 0.6 NA, 1 mm/s, 100kHz, X +  $45^\circ$  configuration). Dots are for Suprasil silica whereas full line is for 100 ppm OH sample.

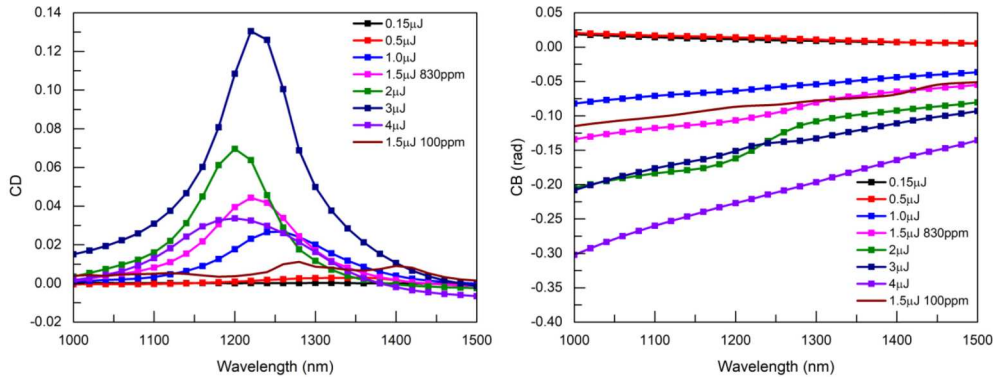


**Fig. 5.** Near-IR spectral dependence of circular birefringence, CB (Left), and circular dichroism, CD (Right), (expressed in radians) as a function of femtosecond laser pulse energy (1030 nm, 250 fs, 0.6 NA, 1 mm/s, 100kHz, X +  $45^\circ$  configuration). Dots are for Suprasil silica (830 ppm OH) whereas full brown line is for 100 ppm OH silica sample.

Below 1100 nm, the amplitudes of the anisotropic linear properties are increasing monotonously with increasing pulse energy,  $E$ , from 0.15  $\mu\text{J}$  up to 4  $\mu\text{J}$ . Above 0.5  $\mu\text{J}$ , we can observe a linear

dichroism band within  $\Delta\lambda = (1100\text{--}1400)$  nm as revealed in Fig. 4(Left). The amplitude of this *LD* band increases with the energy of the fs pulse and the sample shows a maximum *LD* of 0.27 rad at  $\Delta\lambda = 1240$  nm for  $E = 2$   $\mu\text{J}$ . The spectral position of the band also shifts from 1380 nm at  $E = 0.5$   $\mu\text{J}$  down to 1240 nm at 2  $\mu\text{J}$ . This agrees with the corresponding Kramers–Kronig-consistent feature in the *LB* spectra that creates an increasing spectral feature around  $\Delta\lambda \sim 1240$  nm up to 2  $\mu\text{J}$  as shown in Fig. 4(Right). However above 3  $\mu\text{J}$ , we observe a decrease of the *LD* amplitude and the band shifts back to longer wavelengths. Now comparing the two OH samples written with  $E = 1.5$   $\mu\text{J}$ , we can see that the « background *LB* » (away from the dichroic band e.g. around 1000 nm) did not almost change irrespectively of the OH species concentration in agreement with [30]. In contrast the amplitude of *LD* band(s) around 1100–1400 nm is much lower in the “low OH” sample (100 ppm, full brown line). It is worth noting that the dichroic band appears to be composed of 2 or even 3 unknown contributions that still remain to be identified.

The corresponding spectra related to the circular optical properties are shown in Fig. 5. Similar to the linear properties, we observed a *CD* band in the 1100–1400 nm spectral range, which evolves in the same way (increasing amplitude and blue shift) as the *LD* band according to the pulse energy up to 2  $\mu\text{J}$ . It is worth noting that the *CD* amplitude in the near IR is much lower (by a factor 5) in the “low OH” sample. In addition the *CB* spectra are consistent with Kramers–Kronig and a related feature that can be seen in Fig. 5(Right) around  $\lambda \sim 1250$  nm, especially up to  $E = 2\text{--}3$   $\mu\text{J}$ . Then from 3  $\mu\text{J}$ , the dependence is more complex since the *LD* amplitude is decreasing whereas *CD* band in Fig. 5(Left) is strongly increasing. This indicates that *CD* and *LD* amplitudes are not simply connected to each other. Following the same trend, *CD* and *CB* are no more Kramers–Kronig consistent for  $E = 3$   $\mu\text{J}$ . This suggests that the origin of the circular properties is likely not related to chiral molecular species but rather to a chiral arrangement of anisotropic linear layers along the probe beam pathway. In the later case, a non-parallel non-orthogonal assembly of two *LB* (or *LD*) contributions would create some effective *CB* (respectively *CD*) whose amplitude is proportional to the *LB* (or *LD*) and the misalignment angle between the two contributions [31].

#### 4. Discussion

Apart from the spectral feature around  $\lambda \sim 1250$  nm, the linear optical properties are mainly related to the formation of nanogratings resulting in a strong linear form birefringence. However, there is also a slight contribution of stress-induced birefringence, which has been investigated in the literature [32,33]. We reported earlier that the spectral dependence of the optical pathway difference expressed as  $(n_x - n_y) \cdot l$  is quite flat in the investigated spectral range, which results in an increase of  $LB = \frac{2\pi}{\lambda} \cdot (n_x - n_y) \cdot l$  at short wavelengths. An increasing apparent *LD* at short wavelength accompanies the linear birefringence, which is related to the nanogratings. The positive *LD'* (and nearly zero *LD*) observed in Fig. 3 implies that a higher losses were measured for polarization oriented perpendicular to the nanolayers in agreement with [34]. It is known that a layered medium made of alternating layers of two different isotropic materials with complex refractive indices, exhibits a linear dichroism [35]. However the linear dichroism observed in the UV-Vis range should be rather called linear diattenuation since it can be mostly attributed to polarization dependent scattering [34] due to the intrinsic nanoporous nature of the nanogratings.

About the observed circular optical properties in the UV-Vis range, we do not know yet if the observed circular birefringence originates from internal linear birefringence that could be related to a non-parallel non-orthogonal assembly of two (or more) linear contributions, or from a fs pulse induced molecular optical activity. However, we may, from the observed structural circular birefringence, estimate the value of an effective specific rotation; i.e. circular birefringence per unit length to facilitate comparison with naturally optically active materials. From Fig. 3, we find that *CB* at  $\lambda = 290$  nm has an extreme value of  $-0.75$  rad produced by the birefringent laser track

that exhibit a length of  $l = 50 \mu\text{m}$  (in the  $z$ -propagation direction). Therefore the specific rotation is  $\frac{CB_{180}}{2\pi l} \approx -860^\circ/\text{mm}$ .

Following the same view in the Near-IR range, we can deduce from Fig. 5 a maximum  $CB$  of  $-0.22$  rad at  $1240$  nm for  $4 \mu\text{J}/\text{pulse}$  corresponding to an equivalent specific rotation estimated to  $-126^\circ/\text{mm}$ . This could be compared with the specific rotation of natural materials, like quartz (less than  $5^\circ/\text{mm}$  at  $1240$  nm and  $49^\circ/\text{mm}$  at  $400$  nm) or the structural rotary power of liquid crystals (cholesteric monocrystalline layer can reach thousands of  $^\circ/\text{mm}$ ) [36]. Within this specific wavelength range, we can observe an intense dichroism band both linear and circular.

These bands might be related to vibrational absorption bands ascribed to the combination of  $2 \cdot \nu_{\text{stretching Si-OH}} + \nu_{\text{stretching Si-O-Si}}$ . Another possibility would be the combination  $2 \cdot \nu_{\text{stretching Si-OH}} + \nu_{\text{bending Si-OH}}$  [37]. Note there are some variants Si-OH silanol groups as described in [38], which could explain the occurrence of 2-3 bands as observed in the “low OH” sample. However there is no  $CD$  band at  $1400$  nm corresponding to the first harmonic of SiOH stretching,  $2 \cdot \nu_{\text{OH}}$ , which indicates that  $CD$  origin might be related to Si-O-Si bonds arrangement. This was tentatively interpreted through the breaking of symmetry arising from a volume torque  $\vec{P} \wedge \vec{E}_{DC}$  due to the combined action of the stress field and a DC electric field (defined by the pulse front tilt, the focusing conditions and the laser polarization). This volumetric torque may contribute to twist local matter and create chiral atomic arrangements [17]. However, it is unlikely that this could create a high enough population of Si-O-Si bonds with a chiral arrangement (such as tetrahedra in  $\alpha$ -quartz) to achieve the observed high  $CD$ . Another possibility would be that  $CD$  band originates from several internal linear dichroism and birefringence contributions with non-parallel neutral axes. Following this view, the amplitude of the observed  $CD$  band is not only related to the  $LD$  or  $LB$  optical phase shift of each contribution but also to the misalignment between their neutral axes. Note that the  $LB$  neutral axis is mainly related to the form birefringence of the nanogratings.

## 5. Conclusion

We have investigated the polarimetric properties of femtosecond laser induced nanogratings in a wide spectral range extending from UV up to the NIR. The equivalent circular optical properties using Mueller-matrix spectroscopic ellipsometry in transmission mode were extracted. A high effective specific rotation of  $\alpha \sim -860^\circ/\text{mm}$  at  $\lambda = 290$  nm is found. We also reveal the formation of a linear and circular dichroism band peaking around  $\lambda \sim 1240$  nm.

## Funding

Fondation de Coopération Scientifique Campus Paris-Saclay (FCS) (AAP Pré-maturation optoFLAG); Distinguished International Students Scholarship provided by the China Scholarship Council.

## References

1. P. B. Corkum, “Plasma perspective on strong field multiphoton ionization,” *Phys. Rev. Lett.* **71**(13), 1994–1997 (1993).
2. A. Couairon and A. Mysyrowicz, “Femtosecond filamentation in transparent media,” *Phys. Rep.* **441**(2-4), 47–189 (2007).
3. B. Poumellec, M. Lancry, A. Chahid-Erraji, and P. Kazansky, “Modification thresholds in femtosecond laser processing of pure silica: review of dependencies on laser parameters [Invited],” *Opt. Mater. Express* **1**(4), 766–782 (2011).
4. K. Davis, K. Miura, N. Sugimoto, and K. Hirao, “Writing waveguides in glass with a femtosecond laser,” *Opt. Lett.* **21**(21), 1729–1731 (1996).
5. M. Lancry, B. Poumellec, J. Canning, K. Cook, J. Ä. Poulin, and F. Brisset, “Ultrafast nanoporous silica formation driven by femtosecond laser irradiation,” *Laser Photon. Rev.* **7**(6), 953–962 (2013).
6. S. Richter, A. Plech, M. Steinert, M. Heinrich, S. Doering, F. Zimmermann, U. Peschel, E. B. Kley, A. Tunnermann, and S. Nolte, “On the fundamental structure of femtosecond laser-induced nanogratings,” *Laser Photon. Rev.* **6**(6), 787–792 (2012).

7. Y. Shimotsuma, P. Kazansky, J. Qiu, and K. Hirao, "Self-organized nanogratings in glass irradiated by ultrashort light pulses," *Phys. Rev. Lett.* **91**(24), 247405 (2003).
8. H. Zhang, S. Eaton, and P. Herman, "Low-loss Type II waveguide writing in fused silica with single picosecond laser pulses," *Opt. Express* **14**(11), 4826–4834 (2006).
9. S. M. Eaton, M. L. Ng, R. Osellame, and P. R. Herman, "High refractive index contrast in fused silica waveguides by tightly focused, high-repetition rate femtosecond laser," *J. Non-Cryst. Solids* **357**(11-13), 2387–2391 (2011).
10. G. Marshall and M. Withford, "Rapid Production of Arbitrary Fiber Bragg Gratings using Femtosecond Laser Radiation," Lasers and Electro-Optics Society, 2005. LEOS 2005. *The 18th Annual Meeting of the IEEE*, 935–936 (2005).
11. G. D. Marshall, R. J. Williams, N. Jovanovic, M. Steel, and M. J. Withford, "Point-by-point written fiber-Bragg gratings and their application in complex grating designs," *Opt. Express* **18**(19), 19844–19859 (2010).
12. M. Beresna, M. Gecevičius, and P. G. Kazansky, "Ultrafast laser direct writing and nanostructuring in transparent materials," *Adv. Opt. Photon.* **6**(3), 293–339 (2014).
13. M. Beresna, M. Gecevičius, and P. G. Kazansky, "Harnessing Ultrafast Laser Induced Nanostructures in Transparent Materials," in *Progress in Nonlinear Nano-Optics* (Springer, 2015), pp. 31–46.
14. B. Pommellec, M. Lancry, J. C. Poulin, and S. Ani-Joseph, "Non reciprocal writing and chirality in femtosecond laser irradiated silica," *Opt. Express* **16**(22), 18354–18361 (2008).
15. B. Pommellec, L. Sudrie, M. Franco, B. Prade, and A. Mysyrowicz, "Femtosecond laser irradiation stress induced in pure silica," *Opt. Express* **11**(9), 1070–1079 (2003).
16. R. Taylor, E. Simova, and C. Hnatovsky, "Creation of chiral structures inside fused silica glass," *Opt. Lett.* **33**(12), 1312–1314 (2008).
17. B. Pommellec, M. Lancry, R. Desmarchelier, E. Hervé, and B. Bourguignon, "Parity violation in chiral structure creation under femtosecond laser irradiation in silica glass?" *Light: Sci. Appl.* **5**(11), e16178 (2016).
18. J. Tian, R. Desmarchelier, B. Pommellec, and M. Lancry, "Femtosecond laser-induced circular dichroism in silica: Dependence on energy and focusing depth," *Nucl. Instrum. Methods Phys. Res., Sect. B* **435**, 258–262 (2018).
19. R. Desmarchelier, M. Lancry, J. Tian, and B. Pommellec, "Chiroptical properties photo-induced by femtosecond laser irradiation in silica glass," *Appl. Phys. Lett.* **110**(2), 021112 (2017).
20. Y. Shimotsuma, K. Miura, and H. Kazuyuki, "Nanomodification of Glass Using fs Laser," *Int. J. Appl. Glass Sci.* **4**(3), 182–191 (2013).
21. J. Tian, M. Lancry, S. H. Yoo, E. Garcia-Caurel, R. Ossikovski, and B. Pommellec, "Study of femtosecond laser-induced circular optical properties in silica by Mueller matrix spectropolarimetry," *Opt. Lett.* **42**(20), 4103–4106 (2017).
22. R. Ossikovski and O. Arteaga, "Statistical meaning of the differential Mueller matrix of depolarizing homogeneous media," *Opt. Lett.* **39**(15), 4470–4473 (2014).
23. R. Ossikovski, "Differential matrix formalism for depolarizing anisotropic media," *Opt. Lett.* **36**(12), 2330–2332 (2011).
24. E. Garcia-Caurel, A. De Martino, J.-P. Gaston, and L. Yan, "Application of spectroscopic ellipsometry and Mueller ellipsometry to optical characterization," *Appl. Spectrosc.* **67**(1), 1–21 (2013).
25. E. Garcia-Caurel, A. De Martino, and B. Drevillon, "Spectroscopic Mueller polarimeter based on liquid crystal devices," *Thin Solid Films* **455-456**, 120–123 (2004).
26. J. J. G. Perez and R. Ossikovski, *Polarized Light and the Mueller Matrix Approach* (CRC Press, 2016).
27. O. Arteaga and A. Canillas, "Pseudopolar decomposition of the Jones and Mueller-Jones exponential polarization matrices," *J. Opt. Soc. Am. A* **26**(4), 783–793 (2009).
28. O. Arteaga, Z. El-Hachemi, and A. Canillas, "Application of transmission ellipsometry to the determination of CD spectra of porphyrin J – aggregates solid – state samples," *Phys. Status Solidi A* **205**(4), 797–801 (2008).
29. J. Schellman and H. P. Jensen, "Optical spectroscopy of oriented molecules," *Chem. Rev.* **87**(6), 1359–1399 (1987).
30. Y. Shimotsuma, S. Kubota, A. Murata, T. Kurita, M. Sakakura, K. Miura, M. Lancry, and B. Pommellec, "Tunability of form birefringence induced by femtosecond laser irradiation in anion – doped silica glass," *J. Am. Ceram. Soc.* **100**(9), 3912–3919 (2017).
31. S. H. Yoo, R. Ossikovski, and E. Garcia-Caurel, "Experimental study of thickness dependence of polarization and depolarization properties of anisotropic turbid media using Mueller matrix polarimetry and differential decomposition," *Appl. Surf. Sci.* **421**, 870–877 (2017).
32. A. Champion, M. Beresna, P. Kazansky, and Y. Bellouard, "Stress distribution around femtosecond laser affected zones: effect of nanogratings orientation," *Opt. Express* **21**(21), 24942–24951 (2013).
33. A. Champion and Y. Bellouard, "Direct volume variation measurements in fused silica specimens exposed to femtosecond laser," *Opt. Mater. Express* **2**(6), 789–798 (2012).
34. M. Beresna, M. Gecevičius, M. Lancry, B. Pommellec, and P. Kazansky, "Broadband anisotropy of femtosecond laser induced nanogratings in fused silica," *Appl. Phys. Lett.* **103**(13), 131903 (2013).
35. P. Yeh, "A new optical model for wire grid polarizers," *Opt. Commun.* **26**(3), 289–292 (1978).
36. S. Ermakov, A. Beletskii, O. Eismont, and V. Nikolaev, "Brief review of liquid crystals," in *Liquid Crystals in Biotribology* (Springer, 2016), pp. 37–56.
37. A. Burneau and C. Carteret, "Near infrared and ab initio study of the vibrational modes of isolated silanol on silica," *Phys. Chem. Chem. Phys.* **2**(14), 3217–3226 (2000).

38. V. G. Plotnichenko, V. O. Sokolov, and E. M. Dianov, "Hydroxyl groups in high-purity silica glass," *J. Non-Cryst. Solids* **261**(1-3), 186–194 (2000).

### **5.3 A Comparison between Nanogratings-Based and Stress-Engineered Waveplates Written by Femtosecond Laser in Silica**



Article

# A Comparison between Nanogratings-Based and Stress-Engineered Waveplates Written by Femtosecond Laser in Silica

Jing Tian <sup>1</sup>, Heng Yao <sup>1,\*</sup>, Maxime Cavillon <sup>1</sup> , Enric Garcia-Caurel <sup>2</sup>, Razvigor Ossikovski <sup>2</sup>, Michel Stchakovsky <sup>3</sup>, Celine Eypert <sup>3</sup>, Bertrand Poumellec <sup>1</sup> and Matthieu Lancry <sup>1,\*</sup>

<sup>1</sup> Institut de Chimie Moléculaire et des Matériaux d'Orsay, Université Paris Saclay, 91405 Orsay CEDEX, France; jing.tian@u-psud.fr (J.T.); maxime.cavillon@u-psud.fr (M.C.); bertrand.poumellec@u-psud.fr (B.P.)

<sup>2</sup> LPICM, CNRS, Ecole Polytechnique, Institut Polytechnique de Paris, 91128 Palaiseau, France; enric.garcia-caurel@polytechnique.edu (E.G.-C.); razvigor.ossikovski@polytechnique.edu (R.O.)

<sup>3</sup> HORIBA Europe Research Center, 91120 Palaiseau, France; michel.stchakovsky@horiba.com (M.S.); celine.eypert@horiba.com (C.E.)

\* Correspondence: heng.yao22021992@gmail.com (H.Y.); matthieu.lancry@u-psud.fr (M.L.)

Received: 3 January 2020; Accepted: 21 January 2020; Published: 24 January 2020



**Abstract:** This paper compares anisotropic linear optical properties (linear birefringence, linear dichroism, degree of polarization) and performances (absorption coefficient, thermal stability) of two types of birefringent waveplates fabricated in silica glass by femtosecond laser direct writing. The first type of waveplate is based on birefringence induced by self-organized nanogratings imprinted in the glass. On the other hand, the second design is based on birefringence originating from the stress-field formed around the aforementioned nanogratings. In addition to the provided comparison, the manufacturing of stress-engineered half waveplates in the UV-Visible range, and with mm-size clear aperture and negligible excess losses, is reported. Such results contrast with waveplates made of nanogratings, as the latter exhibit significantly higher scattering losses and depolarization effects in the UV-Visible range.

**Keywords:** femtosecond laser processing; silica glass; birefringent devices; stress birefringence

## 1. Introduction

In 2003, a new type of self-organized structures was observed inside SiO<sub>2</sub> glass after irradiation with an ultrafast femtosecond laser [1]. Such structuration of the glass was found to be strongly anisotropic [2–4]. These highly ordered sub-wavelength structures with lamellae-like oxygen-deficient regions are oriented perpendicular to the incident beam polarization [1,5]. A decade ago, Bricchi et al. demonstrated that such thermally stable nanostructures [6], due to their sub-wavelength periodicity, behave as a negative uniaxial birefringent material where the fast axis (slow axis) is parallel (perpendicular) to the orientation of the laser polarization [7]. These induced birefringent modifications are ideal candidates to design numerous optical elements such as Fresnel zone plates, lens-based spin filters, polarization gratings, radial/azimuth polarization converters, Airy beam converter and high-order laser mode converters [8–11]. Additionally, multi-dimensional optical data storage with unprecedented thermal stability has been demonstrated [12,13], as well as micro-waveplates and their arrays [14,15], or achromatic polarization convertor [16] for polarimetry applications.

Although of considerable interest, birefringent optics made of nanogratings exhibit significant drawbacks. One of them is the particularly high photo-induced losses in both visible (Vis) and ultraviolet (UV) regions [17]. This is caused by the intrinsic nanoporous nature [18] of the nanogratings yielding a significant amount of Rayleigh scattering. This drawback also couples with significant

light depolarization [19], which is detrimental for most applications. Additionally, the effect of form birefringence, unlike intrinsic birefringence due to the anisotropy of oriented molecules, is induced by the alignment of submicroscopic rodlets or platelets. In our case nanogratings are made of isotropic objects (the nanopores) organized in an anisotropic way (in nanoplanes). This results into a strong birefringence response for wavelengths longer than the nanogratings periodicity ( $\lambda \gg \Lambda$ ). On the other hand, for  $\lambda \approx L$ , this response is strongly decreased to a level that is no more exploitable for most applications.

Moreover, formation of nanogratings is not solely creating form birefringence but also a stress-birefringence contribution, attributed to glass quenching and morphological changes that participate to the total birefringence [20–22]. Indeed, irradiation of silica glass by a femtosecond laser beam leads to a net volume expansion [23,24], which correlates with the formation of porous structures inside the nanogratings [18,25]. The effective glass volume is reduced, which correlates to the appearance of a permanent strain. The later results into elastic strain as a direct response of the material, and therefore into stress within and around the laser-modified region. By cleaving the laser-modified samples, part of the elastic strain relaxes, and a valley-like surface topography indicates the occurrence of glass densification. Several research groups have shown the presence of a zone of mechanical stresses, possibly associated with birefringence properties in the irradiated zone, related to the polarization of the incident laser beam [26]. Depending on the laser exposure conditions, the overall stress can be enhanced or minimized [24] leading to tunable birefringence values from  $10^{-5}$  up to  $\sim 10^{-3}$  [27–29]. Such stress-induced birefringence influences the inscribed object optical properties, and can lead to the formation of undesired cracks, especially in a multilayer structure made of subsequent irradiations at different depth levels. Therefore, it results in a complicated and unreliable writing procedure where the stress must either be considered or eliminated.

Alternative approaches are based on stress-induced birefringence resulting from different conditions such as process-induced temperature gradient, applied external pressure (from mounting hardware, etc.), or again primary manufacturing processes (thermal expansion coefficient mismatch in optical fibers manufacturing, etc.). For example, recent research has been conducted to use stress-induced birefringence in a glass plate to generate an optical vortex and full Poincaré beams (optical beams that have every possible polarization states across its cross-section) [30]. Within last years there are few examples of stress-engineered optical elements made by femtosecond laser direct writing (FLDW) for waveguides applications. For example, the Herman group has developed the fabrication of integrated optical components for polarization control, like guided wave retarders and polarization beam splitters [28,31,32]. In this work, the possibility of tuning the waveguide birefringence in fused silica was explored by inducing stressors with femtosecond written laser tracks formed parallel to the waveguides. By exploiting this stress, together with the form birefringence generated by the laser-formed nanogratings, the prospects of either increasing or decreasing the waveguide birefringence is allowed.

In addition, this opens the door towards the design of polarization-dependent devices not only in waveguides but also for free space optics as recently demonstrated by Y. Bellouard's group. Unlike fs-laser nanogratings or laser-oriented liquid crystal devices, this provides a "birefringent clear aperture" that is free from laser direct modifications. Within last years micro-lens formation was reported [33], along with the formation of 1 mm clear aperture waveplate with retardance up to 50 nm [34], i.e., a quarter waveplate at 200 nm. Very recently, optical components exploiting Pancharatnam-Berry phase were implemented by harnessing femtosecond laser based stress-induced birefringence. For example, beam converters to obtain beams with orbital angular momentum were demonstrated in glass and crystalline materials using circular polarized light to imprint "stressors" and resulting space variant birefringence [35].

In this context, the goal of this paper is to compare the anisotropic linear optical properties of a waveplate made of nanogratings with a clear aperture waveplate based on stress-induced birefringence. Therefore, Mueller-matrix spectroscopic ellipsometry is used as it provides the spectral dispersion of linear birefringence  $LB$ , linear dichroism  $LD$ ,  $LB$  neutral axis orientation and the depolarization rate from the UV to the Near-IR range. Moreover, a comparison of both optical losses and thermal stability between these two alternative ways will be provided as well, enabling engineering of uniform and space-selective birefringent optical components.

## 2. Materials and Methods

The initial principle of femtosecond (fs) laser imprinted stress-induced waveplates has been introduced and described in detail in reference [34]. In the present case, a square shaped clear aperture was defined by writing two sets of lines (each single line is called a stressor) in a multilayer approach called ‘stressor bars’ throughout the paper. The laser beam was produced by a femtosecond laser system operating at  $\lambda = 1030$  nm and delivering 250 fs pulses at a repetition rate of 100 kHz with a typical average power up to 10 W (Amplitude Systèmes, Pessac, France). The beam was focused to different depths below the front face of 3 mm thick silica glass plates (SuprasilCG, Heraeus, Hanau, Germany) using a 0.16 NA aspheric lens (estimated beam waist  $w \sim 3.5$   $\mu\text{m}$ ). Based on preliminary experiments the laser energy and the scanning speed were chosen so that the irradiated region falls within the type II regime (type 0.4  $\mu\text{J}/\text{pulse}$ , 1 mm/s speed in our conditions) corresponding to the formation of nanogratings in silica glass.

It has been reported by Bellouard’s group that the stress distribution around the laser-exposed area depends on the laser polarization (as it controls the nanogratings orientation) [26]. Therefore, here we chose to investigate a specific writing configuration that maximizes the stress amplitude around a laser track as well as minimizes the imprinting of anisotropic circular optical properties (within the laser affected zone) such as circular dichroism and circular birefringence [36,37]. The glass sample was moved along an axis defined as the Y-axis (or scanning direction). The laser linear polarization was oriented perpendicular to such axis (along the x-axis). This writing configuration is defined as “Yx” configuration of writing. The laser-induced nanogratings wave-vector is thus oriented perpendicularly to the laser scanning direction. In this simple arrangement, we did not use the “etched cuts” as initially proposed by McMillen et al. [34]. However, the stress-induced birefringence remains confined within the area of interest as visible in Figure 1a.

Optical retardance of the laser-induced modifications, defined as the product of linear birefringence ( $LB$ ) by the thickness of the birefringence object ( $l$ ), i.e.,  $R = LB \times l$ , is measured using an Olympus BX51 polarizing optical microscope (Olympus, Tokyo, Japan) equipped with a “de Sénarmont” compensator. The “de Sénarmont” compensator couples a high precision quarter wave birefringent plate with a 180-degree rotating analyzer to provide retardation measurements in the visible range i.e., at 550 nm in the present paper. Such setup has an accuracy that approaches a few nm when used in our conditions. Additionally, UV-Vis-NIR absorption spectra were performed using a Cary 5000 spectrophotometer (Agilent, Santa Clara, California, USA) with a data interval of 0.5 nm. Anisotropic optical properties were investigated using a phase modulated spectroscopic ellipsometer (UVISEL+, HORIBA Scientific, Kyoto, Japan) over  $\lambda = 200$  to 1500 nm spectral range. Since this equipment gives access only to the three first columns of the Mueller matrix [38], we used a recent approach [39,40] allowing for the completion of an experimental nondepolarizing Mueller matrix with a column or a row missing to a full, 16-element one. All measurements were made using a collimated probe beam in normal incidence. The probe beam size of these two instruments was fixed to 0.8 mm for all measurements. The samples were oriented in such a way that their writing/scanning axis was set horizontal  $\pm 1^\circ$  in the reference frame of the Mueller ellipsometer.

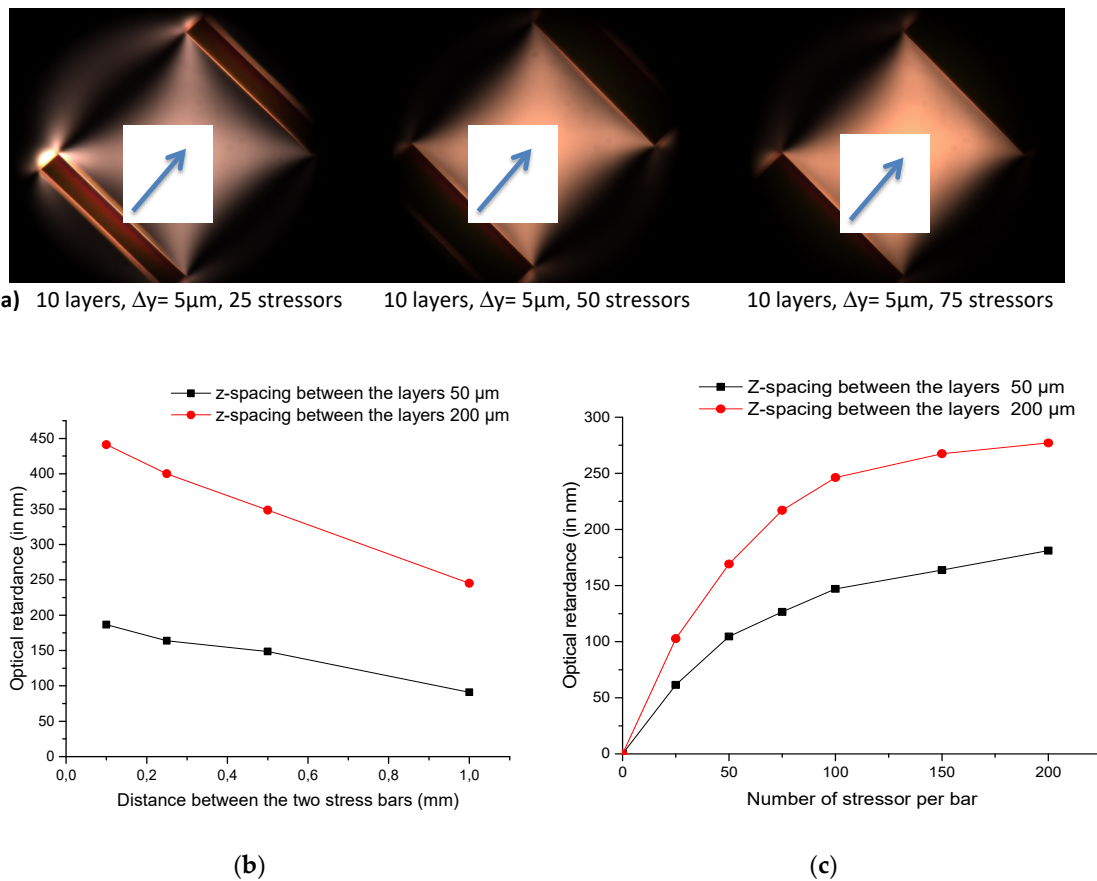


**Figure 1.** (a) Typical optical microscope images of stress-engineering waveplates taken between in crossed polarizers. Blue arrow indicates the center of the clear aperture. (b) Optical retardance  $R$  (in nm) as a function of the distance  $d$  (in mm) between the two stress bars (stressor gap 5  $\mu\text{m}$ , 100 stressors per bar, 10 layers). (c) Optical retardance  $R$  measured at 550 nm as a function of the number of stressors per bar. The clear aperture was fixed to 1 mm. Conditions: SuprasilCG glass,  $\lambda = 1030$  nm; 250 fs; 100 kHz; 1 mm/s scanning speed; numerical aperture 0.16 NA; 2  $\mu\text{J}/\text{pulse}$ .

### 3. Results

As a preliminary work, based on the results published by McMillen et al. [34], the design has been tailored so that we could reach a high optical retardance  $R$  of 200 nm (i.e., a half waveplate at 400 nm) or even more, with a 1 mm  $\times$  1 mm clear aperture, through careful control of the number, density, layers and laser exposure parameters of the stressors. So, in the following, we created several twin columns of lines (defined as “stress bar” above) with a typical spacing  $d$  ranging from 0.1 mm up to 1 mm, which defines the clear aperture. Each stress bar is made up of an assembly of 10 layers written with a spacing  $\Delta z$  of either 50  $\mu\text{m}$  or 200  $\mu\text{m}$ . The pulse energy was fixed to 2  $\mu\text{J}/\text{pulse}$  for the numerical aperture used in this study namely a 0.16 NA aspheric lens. Some typical polarized optical microscope images of three stress-engineered waveplates are shown in Figure 1a. These images were obtained in transmission mode with the sample oriented at 45° between crossed polarizers.

In the first set of results presented in Figure 1b, the parameter of the study is the distance,  $d$ , between the stress bars that defines the clear aperture of the stress-engineered waveplate. The fixed parameters were as follows: a stressor gap  $\Delta\gamma = 5$   $\mu\text{m}$ , 100 stressors per bar and 10 layers per stress bar with a  $\Delta z$  spacing of either 50 or 200  $\mu\text{m}$ . As it can be seen in Figure 1a, there is a significant decrease in the photo-induced retardance  $R$  when the clear aperture size  $d$  is increased. In addition, increasing the layer spacing  $\Delta z$  allows the writing of a much higher retardance, in agreement with the use of a low NA, which leads to the imprinting of quite thick laser tracks in the laser propagation direction.

In the second set of experiments, displayed in Figure 1c, we changed the number of lines for a relatively large clear aperture of 1 mm, which allows one to consider the development of birefringent optics from this design. In this figure, the retardance values measured at the center between the two stress bars increase when the number of stressors increases. There is also a tendency for the retardance value to saturate when the number of stressors is greater than 100. The amplitude of the retardance reaches almost 180 nm for  $\Delta z = 50 \mu\text{m}$  layer spacing and 280 nm for  $\Delta z = 200 \mu\text{m}$ , which makes possible envisioning the production of both half and quarter waveplates in this configuration.

As a first approximation, the Mueller matrix of the “stress-engineered waveplate” can be approximated by the Mueller matrix of a perfect linear retarder. In contrast, the waveplate made of nanogratings exhibits some significant linear dichroism especially in the UV-Vis range [17,19] but also some anisotropic circular properties depending on the writing configuration [36,37]. Then, by using the differential decomposition described in [41,42], it is possible to extract all the polarimetric properties from the Mueller matrix of a sample provided that the laser track is considered as homogeneous in the direction of light propagation. As described in Ref. [41] the polarimetric optical response of a medium of length  $l$ , with a complex refractive index  $\tilde{n} = n + i\kappa$ , can be defined as a superposition of the following basic polarimetric properties: linear birefringence  $LB = \frac{2\pi}{\lambda} \cdot (n_X - n_Y) \cdot l$ ,  $45^\circ$  linear birefringence  $LB' = \frac{2\pi}{\lambda} \cdot (n_{45} - n_{135}) \cdot l$ , linear dichroism  $LD = \frac{2\pi}{\lambda} \cdot (\kappa_X - \kappa_Y) \cdot l$ ,  $45^\circ$  linear dichroism  $LD' = \frac{2\pi}{\lambda} \cdot (\kappa_{45} - \kappa_{135}) \cdot l$ , circular birefringence  $CB = \frac{2\pi}{\lambda} \cdot (n_L - n_R) \cdot l$ , circular dichroism  $CD = \frac{2\pi}{\lambda} \cdot (\kappa_L - \kappa_R) \cdot l$ , together with the Degree of Polarization (termed  $DoP$ ).

According to the data shown in Figure 2a, we can observe a strong negative  $LB$  whose amplitude (in radians) is monotonously increasing at low wavelengths and reaches  $-\pi$  rad around 450 nm (i.e., a half waveplate at this wavelength). It can also be seen that the  $xy$  linear birefringence  $LB$  is one order of magnitude higher than the  $45^\circ$ -birefringence ( $LB'$ ). From these two curves, the azimuthal  $\theta_{LB}$  of the birefringence orientation ( $\theta_{LB} = 0.5 \cdot \text{atan}(LB'/LB)$ ) is calculated, and is displayed in the Figure 2b. Such calculations reveal that the stress-induced birefringence exhibits a slow axis orientation more or less parallel ( $\pm 1-2^\circ$ ) to the reference x-axis. This confirms that the arrangement of opposing stress bars has induced a quasi-uniaxial loading of the material in the center of the clear aperture, in addition to creating a strong optical retardance. This agrees with the design where nanogratings (wave-vector) are oriented perpendicularly to the laser scanning direction  $Y$ , such that the principal component of the stress tensor [26,43] is directed perpendicular to the lines/stressors orientation. As for the anisotropic circular optical properties, we did not observe any significant  $CD$  or  $CB$  in the investigated spectral range.

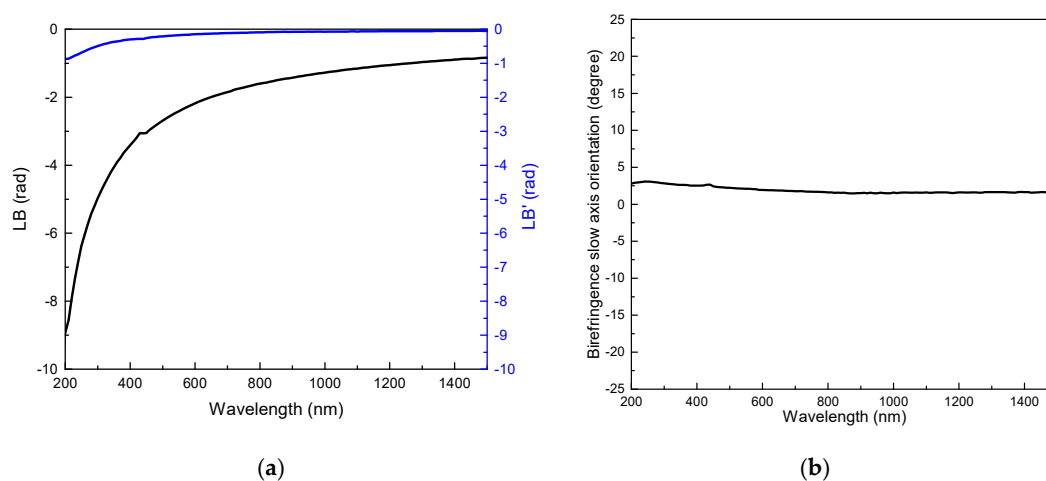


**Figure 2.** Experimental values of effective linear anisotropic optical properties for 1 mm clear aperture stress waveplate: (a) Linear birefringences  $LB$  and  $LB'$  (defined in text). (b) Slow axis orientation (in degree) of the linear birefringence as a function of the wavelength. Waveplate design: stressor gap  $\Delta y = 5 \mu\text{m}$ , 100 stressors per bar, 10 layers with  $\Delta z = 50 \mu\text{m}$ .

Figure 3a shows “Total LB” and the “Total LD” corresponding to the following equations:  $Total LB = \sqrt{LB^2 + LB'^2}$  and  $Total LD = \sqrt{LD^2 + LD'^2}$ . Note that these two properties are thus independent of the azimuthal orientation of the samples with respect to the polarimeter reference frame. Apart from the weak dichroic band around 1200–1400 nm which has been discussed in a previous publication [19], the anisotropic linear optical properties of the nanogratings waveplates (type a quarter waveplate at 500 nm) are mostly attributed to the formation of sub-wavelength nanolayers resulting in a strong form birefringence. However, there is also a contribution of stress-induced birefringence, which has been partly investigated in the literature [23,24,26,44]. We reported earlier that the spectral dependence of the optical path length difference expressed as  $(n_X - n_Y) \cdot l$  is quite flat in the Vis and Near-IR spectral range, which results in an increase of  $LB = \frac{2\pi}{\lambda} \cdot (n_X - n_Y) \cdot l$  with decreasing the probe wavelength, as it can be seen here. However, the measured LB dependence with the wavelength shows a steady decrease in the spectral region from 200 to 300 nm for Xx writing configuration and 200–400 nm for Xy writing configuration. This trend is expected by the effective medium theory as, at short wavelengths, the nanogratings period  $\Lambda$  approaches the probe light wavelength  $\lambda$ . In contrast, the TLB of the stress-engineered waveplate (a half waveplate at 450 nm) still follows a monotonous increase for decreasing wavelengths down to 200 nm, which allows, in principle, to imprint waveplates in the UV range.

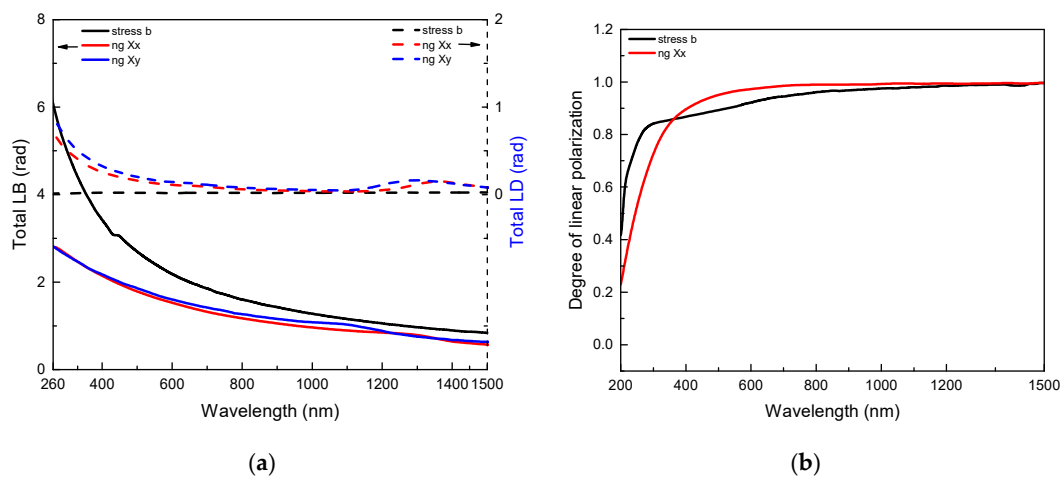


**Figure 3.** (a) Spectral dependence of the anisotropic linear optical properties  $Total LB$  (continuous lines) and  $Total LD$  (dashed lines) extracted from Mueller matrix decomposition. Black lines are for the stress-engineered waveplate (a half waveplate at 450 nm) whereas red and blue lines are for nanogratings-based waveplates written in Xx and Xy configurations. (b) Spectral dependence of the linear Degree of Polarization.

An increase of  $Total LD$  at short wavelengths accompanies the linear birefringence in the nanogratings regime as observed in Figure 3a. The positive  $LD$  (and nearly zero  $LD'$  not shown here) implies that higher losses were measured for polarization oriented perpendicular to the nanolayers in agreement with [17]. It is known that a layered medium, made of alternating layers of two different isotropic materials with complex refractive indices, exhibits a linear dichroism [45]. Note that the linear dichroism observed in the UV-Vis range should be rather called linear diattenuation since it can be mostly attributed to polarization dependent scattering [2,17] due to the intrinsic nanoporous nature of the nanogratings [18] rather than to polarization dependent absorption. In contrast, we did not observe any linear dichroism for the stress-engineered waveplates (type  $Total LD < 0.02$  rad).

Another interesting feature is the Degree of Polarization  $DoP$ , which is shown in Figure 3b. For  $\lambda > 600$  nm all depolarization effects remain smaller than 10% and monotonically decrease with  $\lambda$  reaching a level below 5% for  $\lambda > 800$  nm. However, the  $DoP$  strongly decreases in the UV range reaching less than 80% below 250 nm. In the case of the stress-engineered waveplate depolarization is likely due to the fact that the distribution of the polarimetric properties (birefringence and dichroism) is

not homogeneous within the area probed by the light beam i.e., the clear aperture (see Figure 1a). In consequence there is a non-coherent addition of contributions with different polarization states at the level of the detector, which creates the measured depolarization. However the in the case of the nanogratings-based waveplate, the observed depolarization effects are more likely due to presence of nanopores that generates some strong scattering effects in the UV-Vis range. The latter create a random distribution of polarization states which incoherently add at the level of the detector, and which can be properly described in the frame of the randomly fluctuating media approximation by Ossikovsky and Arteaga [42].

In terms of optical performance, the transmission spectra (200–1700 nm) of the laser written waveplates were measured using a spectrometer (Cary 5000). To this end, the nanogratings samples were first annealed at 600 °C for 2 hours to bleach absorption bands observed at the short wavelengths, which are attributed to SiE' centers at 210 nm (i.e.,  $\equiv\text{Si}$ , corresponding to an unpaired electron in a silicon atom bound to three oxygen atoms), and oxygen deficiency center (ODC)(II) at 245 nm, ( $-\text{O}-\text{Si}-\text{O}-$ , a divalent silicon atom) [46]. The erasure of these defects resulted in significantly lower losses from 200 to 500 nm, as published earlier [17,47,48] without significantly affecting the linear birefringence.

Following this, the transmission spectra were corrected by removing the multiple-reflection spectral losses that are independent of the sample thickness and we calculated the internal transmittance  $T_{int}(\lambda)$  as well as the absorption constant  $k_{abs}(\lambda)$  expressed in  $\text{cm}^{-1}$ . Figure 4a shows the absorption spectra of the stress-engineered waveplate compared both to the nanogratings-based waveplate and the pristine silica substrate. Figure 4b exhibits the dependence of spectra with the pulse energy within the nanogratings regime. The main contribution to the losses observed for the nanogratings-based waveplate originates from the Rayleigh scattering of the inhomogeneous structure, which has dependence in  $1/\lambda^4$  leading to strong losses in the UV-Vis range. In addition, there is a weak absorption band in the 1200–1400 nm spectral range, which was discussed in [19] in the form of a strong linear dichroism. However, the attribution of this band is still not clear. Comparison to the absorption coefficient for the stress-engineered waveplate reveals negligible absorption much below  $1 \text{ cm}^{-1}$  over the entire spectral range, i.e., of same order of magnitude as that of the pristine sample. This experience clearly shows that while the nanogratings create a strong scattering effect in the UV range, which is detrimental to the optical performance of the device, the stress-engineered sample does not show this drawback, which is an important point in favor of the latter technologies when it comes to use short wavelengths.

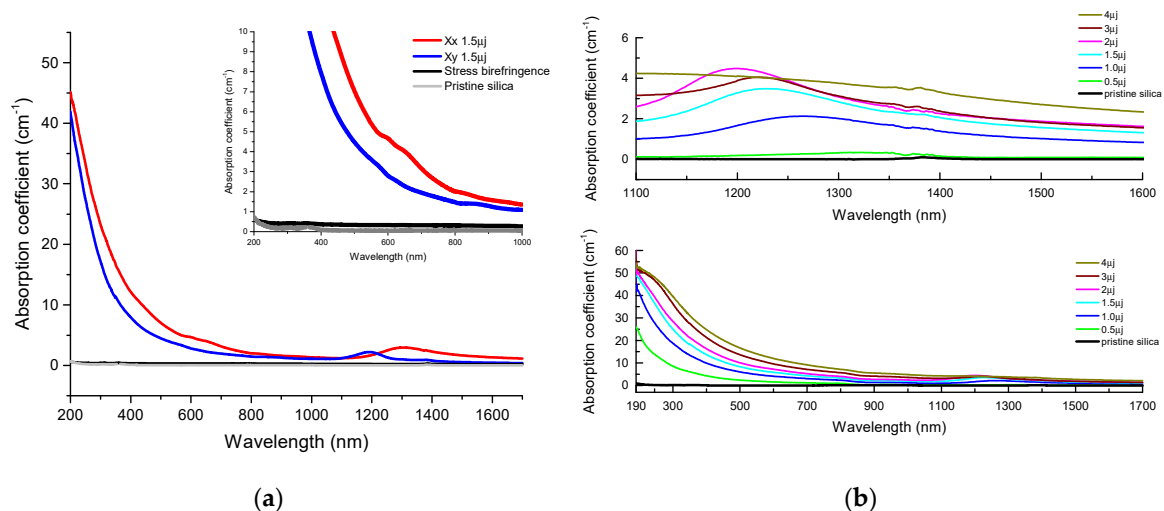


**Figure 4.** (a) Comparison of absorption coefficient  $k_{abs}(\lambda)$  spectra for different waveplates together with pristine silica. Black line is for the stress-engineered waveplate (a half waveplate at 450 nm) whereas red and blue lines are for nanogratings-based waveplates written in Xx and Xy configurations. (b) Absorption coefficient  $k_{abs}(\lambda)$  spectra of nanogratings-based waveplates for different pulse energies. Note that each waveplate was annealed for 2 hours at 600 °C prior to measurements.

An advantage giving rise to a significant interest in nanogratings and related birefringent optical components is the so-called “extraordinary” thermal stability reported in 2006 [6]. This has led to the development of 5D optical data storage with seemingly-unlimited lifetime by Kazansky’s group [13], as well as to the extensive studies of Fiber Bragg Gratings for structural health monitoring in high temperature environment, which has triggered the fabrication of commercial fiber sensors based on nanogratings (FemtoFiber Tech@, Berlin, Germany; FemtoSensing@, Atlanta, GA, USA). Consequently, in Figure 5a is displayed a comparison of the thermal stability of the waveplates, studied through an annealing experiment of isochronal ( $\Delta t = 30$  min) annealing steps ( $\Delta T = 50$  °C). It is worth pointing out that the curves in Figure 5 represents the “stability curve” provided that the criterion  $(\delta t k_0)^{-\Delta T/T_{\max}} \ll 1$  is fulfilled [49] and where  $k_0$  is the pre-exponential factor in the Arrhenius rate constant of the erasure reaction. For nanogratings written in silica,  $k_0$  has been estimated to be around  $de\ 5.10^5\text{--}5.10^7\ s^{-1}$  [50] depending on the laser writing parameters. Therefore, when this criterion is respected, each point can be considered independent to each other.

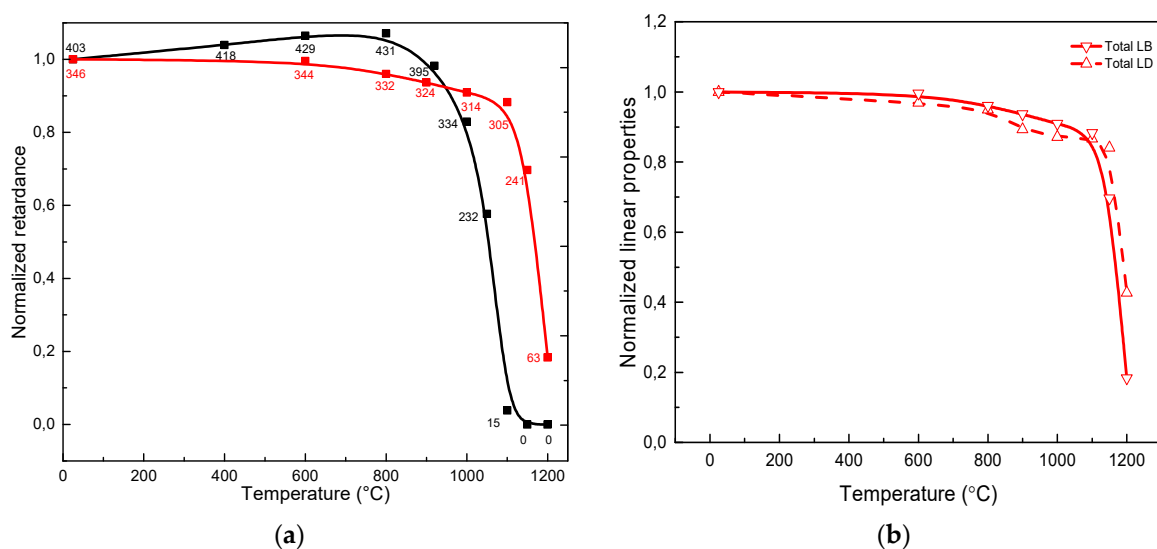


**Figure 5.** (a) Experimental values of the normalized evolution of optical retardance  $R$  (proportional to  $LB$ ) at 550 nm with annealing temperature. Note we add the retardance values for each point as a label. Black dots are for the stress-engineered waveplate whereas red squares are for a nanogratings-based waveplate written in  $Xy$  configuration. (b) Normalized evolutions of  $Total\ LB$  and  $Total\ LD$  according to annealing temperature. Lines are guides to the eye.

In agreement with the literature, the nanogratings-based waveplates (both  $Total\ LB$  and  $Total\ LD$  as shown in Figure 5b) can survive hours to temperatures higher than 1100 °C in  $SiO_2$  and typically erase for annealing treatments around the glass annealing temperature  $T_a$  (i.e., 1120 °C for SuprasilCG and with  $T_a$  defined as  $\eta(T) = 10^{13}\ dPa.s^{-1}$ ). In contrast, we can observe the reduction of the stress-induced birefringence by a factor of two after 30 min of annealing at 1050 °C. This agrees with the expanded idea that an annealing at around  $0.8\text{--}0.9.T_a$  (depending on the duration of the thermal treatment) should relax the stress-induced birefringence, as it is well known in glass manufacturing. Following this view, A. Čerkauskaitė [50] has demonstrated that annealing of nanogratings-based samples for 24 hours at 950 °C, 6 hours at 1000 °C, 2 hours at 1050 °C, and 1 hour at 1100–1150 °C “totally” eliminates the stress-induced birefringence. In contrast, since the annealing of nanogratings is governed by the slow decay term, the form birefringence remains after these thermal treatments.

#### 4. Conclusions

In conclusion, spectral properties of stress-engineered waveplates made by femtosecond laser direct writing were characterized for a wide range of wavelengths from 200 nm to 1500 nm. The transmission



spectra of stress-engineered waveplates show that such objects exhibit only minor increment of the absorption constant with respect to the silica substrate, and it remains below  $1 \text{ cm}^{-1}$  in the investigated spectral range. In contrast, nanogratings-based waveplates present strong losses accompanied with a significant linear dichroism, which are attributed to the scattering induced by the intrinsically-nanoporous layers constituting the fabricated waveplate.

The spectral dispersion of anisotropic optical properties was reported, demonstrating the possibility to imprint stress-engineered half-waveplates in the UV-Vis range with no linear dichroism and minor optical losses. In addition, these stress-induced birefringent waveplates were stable up to  $1000 \text{ }^\circ\text{C}$ , making them attractive candidates for UV-Vis birefringent and space variant birefringent devices.

**Author Contributions:** J.T., H.Y., M.C. and M.L. for experiments and formal analysis, E.G., M.S. and C.E. for methodology and resources; J.T. and M.L. for writing—original draft preparation; M.C., E.G.-C. and R.O. for review and editing; M.L. and B.P. for supervision and project administration. All authors have read and agreed to the published version of the manuscript.

**Funding:** This research was funded by Agence Nationale pour la Recherche, FLAG-IR project, grant number ANR-18-CE08-0004-01.

**Conflicts of Interest:** The authors declare no conflict of interest.

## References

1. Shimotsuma, Y.; Kazansky, P.; Qiu, J.; Hirao, K. Self-organized nanogratings in glass irradiated by ultrashort light pulses. *Phys. Rev. Lett.* **2003**, *91*. [[CrossRef](#)] [[PubMed](#)]
2. Kazansky, P.G.; Inouye, H.; Mitsuyu, T.; Miura, K.; Qiu, J.; Hirao, K.; Starrost, F. Anomalous anisotropic light scattering in Ge-doped silica glass. *Phys. Rev. Lett.* **1999**, *82*, 2199–2202. [[CrossRef](#)]
3. Bricchi, E.; Mills, J.; Kazansky, P.; Klappauf, B.; Baumberg, J. Birefringent Fresnel zone plates in silica fabricated by femtosecond laser machining. *Opt. Lett.* **2002**, *27*, 2200–2202. [[CrossRef](#)] [[PubMed](#)]
4. Sudrie, L.; Franco, M.; Prade, B.; Mysyrowicz, A. Writing of permanent birefringent microlayers in bulk fused silica with femtosecond laser pulses. *Opt. Commun.* **1999**, *171*, 279–284. [[CrossRef](#)]
5. Hnatovsky, C.; Taylor, R.; Simova, E.; Bhardwaj, V.; Rayner, D.; Corkum, P. Polarization-selective etching in femtosecond laser-assisted microfluidic channel fabrication in fused silica. *Opt. Lett.* **2005**, *30*, 1867–1869. [[CrossRef](#)] [[PubMed](#)]
6. Bricchi, E.; Kazansky, P.G. Extraordinary stability of anisotropic femtosecond direct-written structures embedded in silica glass. *Appl. Phys. Lett.* **2006**, *88*, 2–4. [[CrossRef](#)]
7. Bricchi, E.; Klappauf, B.G.; Kazansky, P.G. Form birefringence and negative index change created by femtosecond direct writing in transparent materials. *Opt. Lett.* **2004**, *29*, 119–121. [[CrossRef](#)]
8. Beresna, M. Polarization Engineering with Ultrafast Laser Writing in Transparent Media. Ph.D. Thesis, University of Southampton, Southampton, UK, 2012.
9. Beresna, M.; Gecevičius, M.; Kazansky, P.G. Ultrafast laser direct writing and nanostructuring in transparent materials. *Adv. Opt. Photonics* **2014**, *6*, 293–339. [[CrossRef](#)]
10. Beresna, M.; Gecevičius, M.; Kazansky, P.G. Harnessing Ultrafast Laser Induced Nanostructures in Transparent Materials. In *Progress in Nonlinear Nano-Optics*; Springer: Berlin/Heidelberg, Germany, 2015; pp. 31–46.
11. Drevinskas, R.; Beresna, M.; Zhang, J.; Kazanskii, A.G.; Kazansky, P.G. Ultrafast laser-induced metasurfaces for geometric phase manipulation. *Adv. Opt. Mater.* **2017**, *5*. [[CrossRef](#)]
12. Zhang, J.; Gecevičius, M.; Beresna, M.; Kazansky, P.G. 5D Data Storage by Ultrafast Laser Nanostructuring in Glass. In Proceedings of the CLEO: Science and Innovations, San Jose, CA, USA, 9–14 June 2013. CTh5D. 9.
13. Zhang, J.; Gecevičius, M.; Beresna, M.; Kazansky, P.G. Seemingly unlimited lifetime data storage in nanostructured glass. *Phys. Rev. Lett.* **2014**, *112*. [[CrossRef](#)]
14. Ohfuchi, T.; Sakakura, M.; Yamada, Y.; Fukuda, N.; Takiya, T.; Shimotsuma, Y.; Miura, K. Polarization imaging camera with a waveplate array fabricated with a femtosecond laser inside silica glass. *Opt. Express* **2017**, *25*, 23738–23754. [[CrossRef](#)] [[PubMed](#)]
15. Gecevičius, M.; Beresna, M.; Kazansky, P.G. Polarization sensitive camera by femtosecond laser nanostructuring. *Opt. Lett.* **2013**, *38*, 4096–4099. [[CrossRef](#)] [[PubMed](#)]

16. Desmarchelier, R.; Lancry, M.; Gecevicius, M.; Beresna, M.; Kazansky, P.; Poumellec, B. Achromatic polarization rotator imprinted by ultrafast laser nanostructuring in glass. *Appl. Phys. Lett.* **2015**, *107*, 181111. [[CrossRef](#)]
17. Beresna, M.; Gecevicius, M.; Lancry, M.; Poumellec, B.; Kazansky, P. Broadband anisotropy of femtosecond laser induced nanogratings in fused silica. *Appl. Phys. Lett.* **2013**, *103*, 131903. [[CrossRef](#)]
18. Lancry, M.; Poumellec, B.; Canning, J.; Cook, K.; Poulin, J.-C.; Brisset, F. Ultrafast nanoporous silica formation driven by femtosecond laser irradiation. *Laser Photonics Rev.* **2013**, *7*, 953–962. [[CrossRef](#)]
19. Tian, J.; Li, R.; Yoo, S.H.; Poumellec, B.; Garcia-Caurel, E.; Ossikovski, R.; Stchakovsky, M.; Eypert, C.; Canning, J.; Lancry, M. Spectral dependence of femtosecond laser induced circular optical properties in silica. *Osa Contin.* **2019**, *2*, 1233–1241. [[CrossRef](#)]
20. Bhardwaj, V.; Corkum, P.; Rayner, D.; Hnatovsky, C.; Simova, E.; Taylor, R. Stress in femtosecond-laser-written waveguides in fused silica. *Opt. Lett.* **2004**, *29*, 1312–1314. [[CrossRef](#)]
21. Dürr, F.; Limberger, H.; Salathe, R.; Hindle, F.; Douay, M.; Fertein, E.; Przygodzki, C. Tomographic measurement of femtosecond-laser induced stress changes in optical fibers. *Appl. Phys. Lett.* **2004**, *84*, 4983–4985. [[CrossRef](#)]
22. Poumellec, B.; Sudrie, L.; Franco, M.; Prade, B.; Mysyrowicz, A. Femtosecond laser irradiation stress induced in pure silica. *Opt. Express* **2003**, *11*, 1070–1079. [[CrossRef](#)]
23. Champion, A.; Bellouard, Y. Direct volume variation measurements in fused silica specimens exposed to femtosecond laser. *Opt. Mater. Express* **2012**, *2*, 789–798. [[CrossRef](#)]
24. Bellouard, Y.; Champion, A.; McMillen, B.; Mukherjee, S.; Thomson, R.R.; Pépin, C.; Gillet, P.; Cheng, Y. Stress-state manipulation in fused silica via femtosecond laser irradiation. *Optica* **2016**, *3*, 1285–1293. [[CrossRef](#)]
25. Canning, J.; Lancry, M.; Cook, K.; Weickman, A.; Brisset, F.; Poumellec, B. Anatomy of a femtosecond laser processed silica waveguide [Invited]. *Opt. Mater. Express* **2011**, *1*, 998–1008. [[CrossRef](#)]
26. Champion, A.; Beresna, M.; Kazansky, P.; Bellouard, Y. Stress distribution around femtosecond laser affected zones: Effect of nanogratings orientation. *Opt. Express* **2013**, *21*, 24942–24951. [[CrossRef](#)] [[PubMed](#)]
27. Yuan, L.; Cheng, B.; Huang, J.; Liu, J.; Wang, H.; Lan, X.; Xiao, H. Stress-induced birefringence and fabrication of in-fiber polarization devices by controlled femtosecond laser irradiations. *Opt. Express* **2016**, *24*, 1062–1071. [[CrossRef](#)]
28. Fernandes, L.A.; Grenier, J.R.; Herman, P.R.; Aitchison, J.S.; Marques, P.V. Stress induced birefringence tuning in femtosecond laser fabricated waveguides in fused silica. *Opt. Express* **2012**, *20*, 24103–24114. [[CrossRef](#)]
29. Fernandes, L.A.; Grenier, J.R.; Marques, P.V.; Aitchison, J.S.; Herman, P.R. Strong birefringence tuning of optical waveguides with femtosecond laser irradiation of bulk fused silica and single mode fibers. *J. Lightwave Technol.* **2013**, *31*, 3563–3569. [[CrossRef](#)]
30. Beckley, A.M.; Brown, T.G.; Alonso, M.A. Full poincaré beams. *Opt. Express* **2010**, *18*, 10777–10785. [[CrossRef](#)]
31. Fernandes, L.A.; Grenier, J.R.; Herman, P.R.; Aitchison, J.S.; Marques, P.V. Femtosecond laser writing of waveguide retarders in fused silica for polarization control in optical circuits. *Opt. Express* **2011**, *19*, 18294–18301. [[CrossRef](#)]
32. Fernandes, L.A.; Grenier, J.R.; Herman, P.R.; Aitchison, J.S.; Marques, P.V. Femtosecond laser fabrication of birefringent directional couplers as polarization beam splitters in fused silica. *Opt. Express* **2011**, *19*, 11992–11999. [[CrossRef](#)]
33. McMillen, B.; Bellouard, Y. Direct-write diffracting tubular optical components using femtosecond lasers. In Proceedings of the Frontiers in Ultrafast Optics: Biomedical, Scientific, and Industrial Applications XIV, San Francisco, CA, USA, 2–5 February 2014; p. 89720Z.
34. McMillen, B.; Athanasiou, C.; Bellouard, Y. Femtosecond laser direct-write waveplates based on stress-induced birefringence. *Opt. Express* **2016**, *24*, 27239–27252. [[CrossRef](#)]
35. Beresna, M.; Brambilla, G.; Juodkazis, S.; Wang, X.; Rumpf, R. Geometric phase via stress induced birefringence. In Proceedings of the CLEO-Pacific Rim, Singapore, 31 July–4 August 2017; p. 2.
36. Tian, J.; Lancry, M.; Yoo, S.H.; Garcia-Caurel, E.; Ossikovski, R.; Poumellec, B. Study of femtosecond laser-induced circular optical properties in silica by Mueller matrix spectropolarimetry. *Opt. Lett.* **2017**, *42*, 4103–4106. [[CrossRef](#)] [[PubMed](#)]

37. Tian, J.; Desmarchelier, R.; Poumellec, B.; Lancry, M. Femtosecond laser-induced circular dichroism in silica: Dependence on energy and focusing depth. *Nucl. Instrum. Methods Phys. Res. Sect. B Beam Interact. Mater. At.* **2018**, *435*, 258–262. [[CrossRef](#)]
38. Garcia-Caurel, E.; De Martino, A.; Gaston, J.-P.; Yan, L. Application of spectroscopic ellipsometry and Mueller ellipsometry to optical characterization. *Appl. Spectrosc.* **2013**, *67*, 1–21. [[CrossRef](#)]
39. Arteaga, O.; Ossikovski, R. Complete Mueller matrix from a partial polarimetry experiment: The 12-element case. *JOSA A* **2019**, *36*, 416–427. [[CrossRef](#)] [[PubMed](#)]
40. Ossikovski, R.; Arteaga, O. Completing an experimental nondepolarizing Mueller matrix whose column or row is missing. *J. Vac. Sci. Technol. B Nanotechnol. Microelectron. Mater. Process. Meas. Phenom.* **2019**, *37*. [[CrossRef](#)]
41. Ossikovski, R. Differential matrix formalism for depolarizing anisotropic media. *Opt. Lett.* **2011**, *36*, 2330–2332. [[CrossRef](#)] [[PubMed](#)]
42. Ossikovski, R.; Arteaga, O. Statistical meaning of the differential Mueller matrix of depolarizing homogeneous media. *Opt. Lett.* **2014**, *39*, 4470–4473. [[CrossRef](#)]
43. McMillen, B.; Bellouard, Y. On the anisotropy of stress-distribution induced in glasses and crystals by non-ablative femtosecond laser exposure. *Opt. Express* **2015**, *23*, 86–100. [[CrossRef](#)]
44. Streltsov, A.M.; Borrelli, N.F. Study of femtosecond-laser-written waveguides in glasses. *JOSA B* **2002**, *19*, 2496–2504. [[CrossRef](#)]
45. Yeh, P. A new optical model for wire grid polarizers. *Opt. Commun.* **1978**, *26*, 289–292. [[CrossRef](#)]
46. Skuja, L.; Hirano, M.; Hosono, H.; Kajihara, K. Defects in oxide glasses. *Phys. Status Solidi (C)* **2005**, *2*, 15–24. [[CrossRef](#)]
47. Lancry, M.; Desmarchelier, R.; Cook, K.; Poumellec, B.; Canning, J. Compact Birefringent Waveplates Photo-Induced in Silica by Femtosecond Laser. *Micromachines* **2014**, *5*, 825–838. [[CrossRef](#)]
48. Richter, S.; Heinrich, M.; Döring, S.; Tünnermann, A.; Nolte, S.; Peschel, U. Nanogratings in fused silica: Formation, control, and applications. *J. Laser Appl.* **2012**, *24*, 042008(042001)–042008(042008). [[CrossRef](#)]
49. Poumellec, B.; Lancry, M. Kinetics of Thermally Activated Physical Processes in Disordered Media. *Fibers* **2015**, *3*, 206–252. [[CrossRef](#)]
50. Čerkauskaitė, A. *Ultrafast Laser Nanostructuring for Photonics and Information Technology*; University Of Southampton: Southampton, UK, 2018.



© 2020 by the authors. Licensee MDPI, Basel, Switzerland. This article is an open access article distributed under the terms and conditions of the Creative Commons Attribution (CC BY) license (<http://creativecommons.org/licenses/by/4.0/>).



# Chapter 6 Discussion on the origin of the anisotropic linear and circular optical properties created within Type II regime

---

## Content

6.1 Introduction.....	208
6.2 On the origin of the anisotropic linear optical properties within Type II regime in fs-irradiated silica glass .....	209
6.2.1 Form birefringence within Type II regime.....	209
6.2.2 Stress-induced birefringence within Type II regime .....	215
6.2.3 Point defects formation and annealing within Type II regime.....	219
6.2.4 Conclusion on anisotropic linear properties thermal stability .....	222
6.3 Modeling anisotropic circular optical properties using Mueller matrix formalism using a two linear retarders model .....	223
6.3.1 Short description of the modeling procedure .....	224
6.3.2 Modelling a single linear retarder .....	226
6.3.3 Modelling the formation of CB only using two linear retarders.....	227
6.3.4 Modeling the formation of CD with two linear retarders .....	231
6.3.5 Modeling the formation of both CB and CD using two linear retarders.....	234
6.4 Polarization dependent anisotropic optical properties: a comparison between modeling and experimental measurements.....	236
6.5 Interpretation of the polarization dependent anisotropic optical properties and the creation of circular optical properties.....	239
6.6 Conclusions.....	244
6.7 References.....	246

## 6.1 Introduction

The use of Mueller matrix spectro-polarimetry in the experiments described in chapters 4 and 5 allowed a thorough investigation of the polarimetric properties of our samples, and we tentatively extracted all anisotropic optical properties, namely LB, LB', LD, LD', CB, CD and the depolarization rates, but also their spectral dependence from the UV to the near-IR range (see the two publications [1, 2] inserted in chapter 5).

Beside the imprinting of linear anisotropic optical properties (discuss in the first section of this chapter), due to nanogratings formation but also to stress-induced birefringence as a result of permanent volume expansion, analyses from the previous chapters confirmed that a linearly polarized femtosecond laser beam entering an isotropic sample—a glass—under an axially symmetric geometry is able to break the chiral symmetry of the pristine glass. Additionally, we confirmed that laser–matter interaction can imprint circular optical properties beside linear ones with such efficiency that the reciprocity of light propagation is broken and asymmetric transmission is revealed.

In chapter 3 we discussed a qualitative model introduced by Poumellec et al. [3] to explain the imprinting of circular optical properties, based on the breaking of symmetry that may arise from a volume torque due to the combined action of the stress field and a DC electric field ( $\vec{E}_{DC}$ , which is a function of by the pulse front tilt, the focusing conditions and the laser polarization). Accordingly, the misalignment between  $\vec{E}_{DC}$  and the material polarization  $\vec{P}$  generates a volumetric torque  $\vec{P} \wedge \vec{E}_{DC}$ . Its orientation and sign depend on the laser pulse characteristics and can therefore be controlled. The torque may be responsible of matter twisting, with the subsequent creation of chiral atomic arrangements or maybe some kind of “twisted nanogratings arrangement” as further discuss in the last section of this chapter.

However, we decided to investigate an alternative hypothesis to explain the presence of circular properties arising from the fs-written laser track. This quantitative model is feed by the results presented in chapters 4 and 5, to take into account several observations, especially the polarization dependence, the spectral dispersion of CB and CD (and the link between the two) and the presence of stress-induced birefringence. The main hypothesis is built on the basis of the propagation of light in inhomogeneous media composed of superimposed anisotropic layers. As a direct consequence, the CB would originate from several (at least 2) internal linear birefringence contributions with both non-parallel and non-perpendicular neutral axes [4]. Similarly, CD band would result from the cumulative action of LD and LB present in the different layers of the inhomogeneous media, having non-parallel and non-perpendicular neutral axes. Furthermore, the amplitude of the observed CD and CB will not only be related to the LD or LB optical phase shift of each contribution, but also to the misalignment between their respective neutral axes.

## 6.2 On the origin of the anisotropic linear optical properties within Type II regime in fs-irradiated silica glass

The key characteristic feature of Type II modifications in SiO<sub>2</sub> is the formation of porous nanogratings that can easily be detected through linear birefringence measurements (polarization dependent) associated with a significant linear dichroism (or diattenuation). These nanogratings can also be directly imaged using SEM and TEM techniques. However, the measured linear birefringence arises from the aggregate contribution of several factors, including form birefringence, stress-induced birefringence, as well as the formation of point defects and Type I-densified area (e.g. in between the porous nanolayers). In this section, we will shortly review these different linear contributions in pure silica and we will also discuss their respective thermal stability since it provides a way to estimate the contribution of each mechanism and their potential link with the original chiral-optical properties we observed in this thesis.

### 6.2.1 Form birefringence within Type II regime

Briefly, in 2003, a new type of self-organized structures was observed inside SiO<sub>2</sub> glass after irradiation with an ultrafast femtosecond laser [5]. Such structuration of the glass was found to be strongly anisotropic [6-8]. These highly ordered sub-wavelength structures with lamellae-like oxygen-deficient regions were oriented perpendicular to the incident beam polarization [5, 9]. A decade ago, Bricchi et al. demonstrated that such thermally stable nanostructures [10], due to their sub-wavelength periodicity, behave as a negative uniaxial birefringent material where the fast axis (slow axis) is parallel (perpendicular) to the orientation of the writing laser polarization [11]. Unlike intrinsic birefringence, which is due to the anisotropy of oriented molecules or atomic arrangements in uniaxial or biaxial crystals, the effect of form birefringence manifests itself due to the alignment of submicroscopic rodlets or platelets [12, 13]. The light polarized parallel to the interfaces experiences a larger refractive index and as a result, a phase difference for two perpendicular polarizations is acquired. The strength of the form birefringence can be controlled by the filling factor and the materials refractive indices (and thus the chemical composition) of the microstructure.

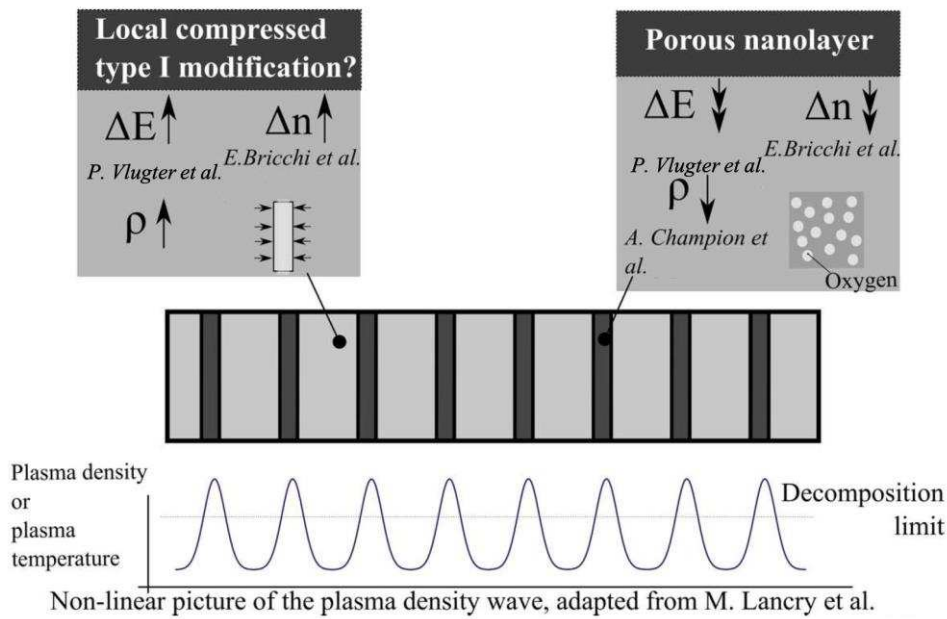


Figure 6.1 Middle: an illustrative summary of the nanogratings structure. Top-right: an illustration of the predicted material properties and chemical composition signature of a porous layer - the refractive index change estimated by [13], the oxygen filled pores [14] and elastic modulus [15]. In the top-left, a refractive index increase [13] and the elastic modulus increase [15]. Below the spatial distribution of plasma density, with peaks exceeding the decomposition limit. Schemes are adapted from Ref. [14].

Recently our group has demonstrated that the form birefringence is related to the formation of nanoporous silica [16] and is quantitatively correlated to the porosity-filling factor  $ff_{porous}$  of the nanolayers [17]. Control of the porosity was achieved by adjusting the pulse energy and the number of pulses/ m i.e. the overlapping rate [17] but also through the chemical composition [18-21]. In strongly Ge-doped  $\text{SiO}_2$  (a "normal" glass [20]), we found that the matter surrounding the nanopores exhibited significant  $n$  decrease that is likely due to a fictive temperature increase (corresponding to a  $n$  increase in  $\text{SiO}_2$ ). A second possibility may be that this matter in-between nanopores could be composed of silica with a significant amount of Frenkel oxygen defects  $O_0^x \rightarrow V_0^{\cdot\cdot} + O_I$  (an interstitial oxygen and a vacancy) resulting in a  $n$  decrease as suggested in Ref. [17]. Furthermore, a densification in between these porous nanolayers has been indirectly suggested in [10], where the authors estimated a  $n$  increase by measuring the form-birefringence.

The increase of the Young's modulus [15], refractive index, and possible densification, is like a Type I modifications [22-24], which exhibit similar characteristics. Previous works [14, 25] made similar observations. Lancry et al. [14] proposed a plasma density profile where, in the non-porous layers, the glass met the thermo-mechanical conditions for a modification of Type I, while in the position of the porous nanolayers, a decomposition threshold for  $\text{SiO}_2$  molecules would be exceeded. Therefore, the local Young's modulus increases [15] and its corresponding  $n$  response also increases as measured in [13] and going from  $2 \times 10^{-2}$  to  $5 \times 10^{-2}$ . This value is significantly higher than the one found for regime I modifications, where a  $n$  increase up to a few  $10^{-3}$  is expected [26-28]. For completeness, the formation of color centers is expected to decrease the glass Young's modulus, as it will lower the connectivity of the 3D glass network. Therefore it is more likely that a mechanism based on the occurrence of fast compressive stress combined with thermal quenching is responsible for the noticeable  $n$  increase observed in [15]. The aforementioned mechanisms and their



contributions to properties (density, Young's modulus, refractive index) within the porous nanogratings are schematically summarized in Figure 6.1.

### Form birefringence

The birefringent properties of materials are usually explained in terms of the anisotropic electrical properties of molecules they are made of. We start the discussion from a classical wave propagation approach; the medium being in two dimensions, there are two modes of propagation according to whether the field oscillates in the plane or perpendicular to the plane of the medium. If the electric field is parallel to the nanolayers, the mode is TE (ordinary index). If the field is perpendicular to the nanolayers, the mode is TM (extraordinary index). The proper modes of propagation are:

$\vec{E} = \vec{E}_k(z) * \exp(i(\omega t - \beta x - Kz))$ , with nanolayers along  $x$ ,  $y$ , and perpendicular to  $z$ . So the  $x$  here represents any component in the  $x$ ,  $y$  plane. In the case of nanogratings, they are used in such a way that there is always a component  $\beta$ , but  $K = 0$ . There are two branches in the dispersion relationships, one for TE and the other for TM. They are given by the solutions of Maxwell's equations and boundary conditions. Note here  $\frac{\omega}{c} = \frac{2\pi}{\lambda}$ . We have:

$$\cos(K \Lambda) = \cos(k_{1z}a) \cos(k_{2z}b) - \frac{1}{2} \left( \frac{k_{2z}}{k_{1z}} + \frac{k_{1z}}{k_{2z}} \right) \times \sin(k_{1z}a) \sin(k_{2z}b) \quad (TE) \quad \text{Equation 6.1}$$

$$\begin{aligned} \cos(K \Lambda) = \cos(k_{1z}a) \cos(k_{2z}b) \\ - \frac{1}{2} \left( \frac{n_2^2 k_{1z}}{n_1^2 k_{2z}} + \frac{n_1^2 k_{2z}}{n_2^2 k_{1z}} \right) \times \sin(k_{1z}a) \sin(k_{2z}b) \quad (TM) \end{aligned} \quad \text{Equation 6.2}$$

$$\text{With: } k_{1z}^2 = \left( \frac{n_1 \omega}{c} \right)^2 - \beta^2 \text{ and } k_{2z}^2 = \left( \frac{n_2 \omega}{c} \right)^2 - \beta^2$$

As shown in Figure 6.2,  $\Lambda = t_1 + t_2$ , the grating period with  $t_1$  and  $t_2$  the two thicknesses,  $n_1$  and  $n_2$  the refractive indices of the two materials which are assumed to be isotropic. If the linear dimensions of the faces of the plates are assumed to be large but the thickness  $t_1$  and  $t_2$  are small compared to the wavelength, we can get  $\Lambda \ll \lambda$  and developed until  $\left(\frac{\Lambda}{\lambda}\right)^2$ , the field in the plates and in the spaces may be considered uniform so that we can drive to the equation [29]:

$$\frac{K^2}{n_0^2} + \frac{\beta^2}{n_0^2} = \left( \frac{\omega}{c} \right)^2 \quad (TE) \quad \text{Equation 6.3}$$

$$\frac{K^2}{n_0^2} + \frac{\beta^2}{n_e^2} = \left( \frac{\omega}{c} \right)^2 \quad (TM) \quad \text{Equation 6.4}$$

$$\text{With: } n_0^2 = \frac{t_1}{\Lambda} n_1^2 + \frac{t_2}{\Lambda} n_2^2 \text{ and } \frac{1}{n_e^2} = \frac{t_1}{\Lambda} \frac{1}{n_1^2} + \frac{t_2}{\Lambda} \frac{1}{n_2^2}$$

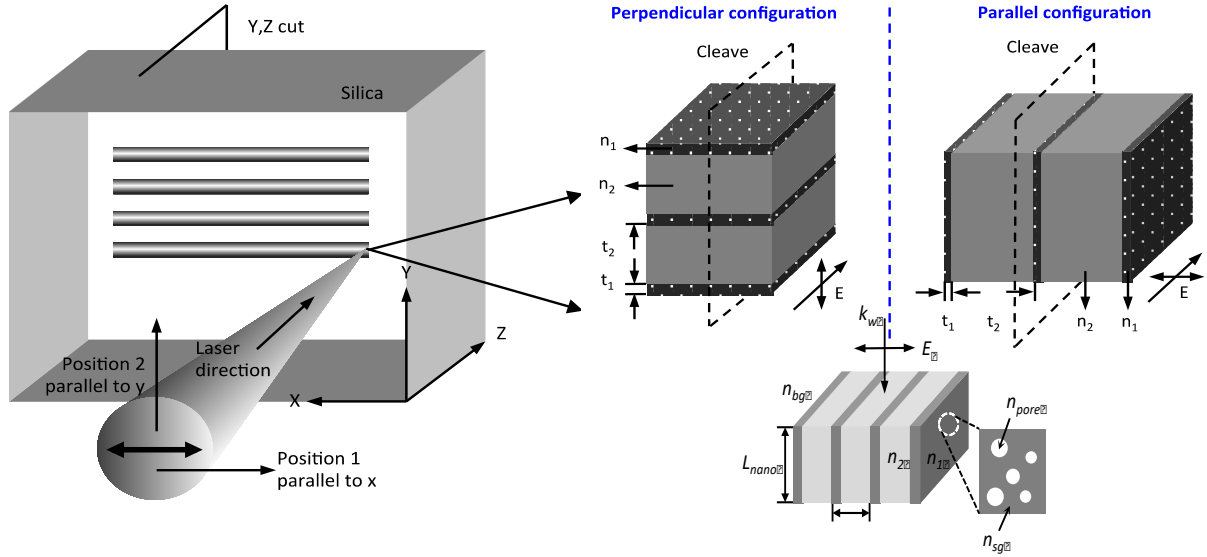


Figure 6.2 Experimental setup scheme for configuration for writing and schematic of sub-wavelength periodic structure formed in cross-section of the irradiated region.  $n_1$  et  $n_2$ : local refractive indices of the nanolayers;  $t_1$  and  $t_2$ , are their respective thicknesses. Right bottom: Schematic of sub-wavelength periodic structure formed in cross-section of the irradiated region.  $n_{\text{pore}} (=1)$  and  $n_{\text{sg}}$ : local refractive index for nanopores and for surrounding oxygen defect regions, respectively;  $\Lambda = t_1 + t_2$ : period of nanogratings and  $n_{\text{bg}}$ : refractive index of the surrounding material,  $L_{\text{nano}}$ : thickness of nanogratings. Schemes are adapted from Ref. [17].

As a result, we see that a layered material with a period much less than the wavelength is uniaxial. Birefringence is also negative with  $n_e < n_o$ . Note that the indices depend on the ratio  $\frac{t_1}{t_2}$ , and the dispersion in  $\lambda$  is only in the dispersion of  $n_1$  and  $n_2$ . As we would have  $K = 0$  in our case, in TE polarization (field parallel to the layers), the dispersion relation expressed in wavelength is:

$$\beta_{TE}^2(\lambda) = n_o^2(\lambda) \left(\frac{\omega}{c}\right)^2 = n_o^2(\lambda) \left(\frac{2\pi}{\lambda}\right)^2 \quad \text{Equation 6.5}$$

and in TM polarization (field perpendicular to the layers), the relation is:

$$\beta_{TM}^2(\lambda) = n_e^2(\lambda) \left(\frac{\omega}{c}\right)^2 = n_e^2(\lambda) \left(\frac{2\pi}{\lambda}\right)^2 \quad \text{Equation 6.6}$$

For an irradiated area larger than the probe beam, it is well known that the strength of form birefringence depends on the thickness of the nanolayers ( $t_1$  and  $t_2$ ) and their respective refractive indices ( $n_1$  and  $n_2$ ). If the materials are not isotropic (a textured microstructure, aligned ellipsoid nanopores for example), and when  $\Lambda \ll \lambda$ , the uniaxial birefringence  $\Delta n$  due to the nanogratings can be written as a refractive index difference between ordinary ( $n_o$ ) and extraordinary ( $n_e$ ) wave:

$$\Delta n = n_e - n_o = \frac{n_1 n_2}{\sqrt{f_{\perp} n_2^2 + (1 - f_{\perp}) n_1^2}} - \underbrace{\sqrt{f_{\perp} n_1^2 + (1 - f_{\perp}) n_2^2}}_{n_o} \quad \text{Equation 6.7}$$

where  $f_{\perp} = t_1 / (t_1 + t_2) = t_1 / \Lambda$  is the 1D nanogratings filling factor  $f_{\perp}$  and  $\Lambda$  is the nanoplanes spacing,  $n_1$ ,  $n_2$ ,  $t_1$  and  $t_2$  are defined in Figure 6.2. This relation, valid for

nanogratings, can be generalized for any anisotropic structures like series of nanoplanes, in the case where the probe beam diameter  $w$  is larger than nanoplanes area:

$$\Delta n = \frac{\Lambda - \sqrt{(t_1 n_1^2 + t_2 n_2^2) \left( \frac{t_1}{n_1^2} + \frac{t_2}{n_2^2} \right)}}{\Lambda \left( \frac{t_1}{n_1^2} + \frac{t_2}{n_2^2} \right)} \quad \text{Equation 6.8}$$

and, in the case where  $w$  is smaller than nanoplane area:

$$\frac{w - \sqrt{[l_t n_2^2 + N_p (t_1 n_1^2 + t_2 n_2^2)] \left[ \frac{l_t}{n_2^2} + N_p \left( \frac{t_1}{n_1^2} + \frac{t_2}{n_2^2} \right) \right]}}{\sqrt{w \left[ \frac{l_t}{n_2^2} + N_p \left( \frac{t_1}{n_1^2} + \frac{t_2}{n_2^2} \right) \right]}} \quad \text{Equation 6.9}$$

where  $N_p$  is the number of period  $\Lambda$  and  $w$  is probe beam diameter and  $l_t$  is defined by  $l_t = w - N_p \Lambda$ .

This results into a strong birefringence response for wavelengths longer than the nanogratings periodicity ( $\lambda \gg \Lambda$ ). On the other hand, for  $\lambda \approx \Lambda$ , this response is strongly decreased to a level that is no more exploitable for most optical applications [29].

**Let's go back to the general case.** The next consideration is therefore the value of  $n_1(\lambda)$  and  $n_2(\lambda)$ . The material should be unchanged between the nanolayers as a first approximation (whereas a densification up to  $10^{-2}$  has been reported [13]), so we know its dispersion. For the other, it consists of nanopores, possibly ellipsoidal, more or less aligned, immersed in a material whose index has decreased compared to that of silica. If we know the refractive index of nanopores  $n_{pore}$  considering that it is a gas, it could be assigned a constant dispersion and a value equal to 1, whereas the index of the surrounding  $n_{sg}$  reduced silica [17] will have to be hypothesized for a complete description of the problem. To obtain the index of the composite material of the nanoplanes, it is necessary to apply the theory of the effective medium whose application to the permittivity is due to Maxwell-Garnett [30, 31].

For spheres distributed randomly, we have:

$$\frac{\varepsilon_{eff} - \varepsilon_m}{\varepsilon_{eff} + 2\varepsilon_m} = f f_{porous} \left( \frac{\varepsilon_i - \varepsilon_m}{\varepsilon_i + 2\varepsilon_m} \right) \quad \text{Equation 6.10}$$

With  $\varepsilon_{eff}$  for the composite,  $\varepsilon_i$  for the inclusion,  $\varepsilon_m$  for the medium, and  $f f_{porous}$  for volume fraction taken by the nanopores. For a material made up of ellipsoid inclusions randomly oriented to each other, there is no birefringence, but a correction in the following formulas [32, 33].

$$(1 - f_{fporous}) \frac{\epsilon_{eff} - \epsilon_m}{\epsilon_{eff} + 2\epsilon_m} = f_{fporous} \left( \frac{\epsilon_i - \epsilon_m}{\epsilon_i + 2\epsilon_m} \right) \quad \text{Equation 6.11}$$

On the other hand, for a textured and therefore anisotropic material, with two axes such as collectively aligned ellipsoid nanopores, there would be two values of permittivity  $\epsilon_{\parallel}$  and  $\epsilon_{\perp}$  according to the polarization plane aligned parallel or perpendicular to the direction of the ellipses. However, we will not further consider this case in this PhD thesis.

### Note on absorption and apparent linear dichroism

The theory of the effective medium approximations applies to complex permittivity; therefore the above formulas must ideally take into account the imaginary parts of the quantities of the medium and of the inclusions as well. Up to now these two contributions are set to zero so the permittivity do contain neither absorption nor scattering effects. So it has been shown that a medium, which consists of alternating layers of different isotropic substances with complex refractive indices, exhibits both linear birefringence and linear dichroism [34]. The linear dichroism is related to the difference in attenuation between two perpendicularly linearly polarized beams. The polarization dependent losses of laser-induced nanogratings were characterized in Refs. [35-37]. The measurements made on annealed samples, so all defect centers were bleached before the analysis. The difference in losses was measured for two orthogonal probe polarizations: perpendicular and parallel to nanolayers. The results clearly indicate the increase of the differential losses at short wavelengths (Figure 6.3a). For instance, at 550 nm the absorption difference was about 0.1 in optical density [35]. To elucidate whether scattering or absorption exhibits polarization dependence, the scattering was selectively characterized at 515 nm using a 1 mm pinhole. By rotating the polarization of an incident laser beam we observed that the scattering increased, while the transmitted signal decreased. In chapters 3 and 4, we discuss a series of results that shows the presence of a positive LD for  $X0^\circ$  (or  $X_x$ ) configuration (and negative for  $X90^\circ$  (or  $X_y$ ) writing configuration) as published in Ref. [37]. This implies that higher losses were measured for polarization oriented perpendicular to the nanolayers. Therefore, the linear dichroism observed in the UV-Vis range should be rather called linear diattenuation since it can be mostly attributed to polarization dependent scattering [35] due to the intrinsic nanoporosity of the nanogratings.

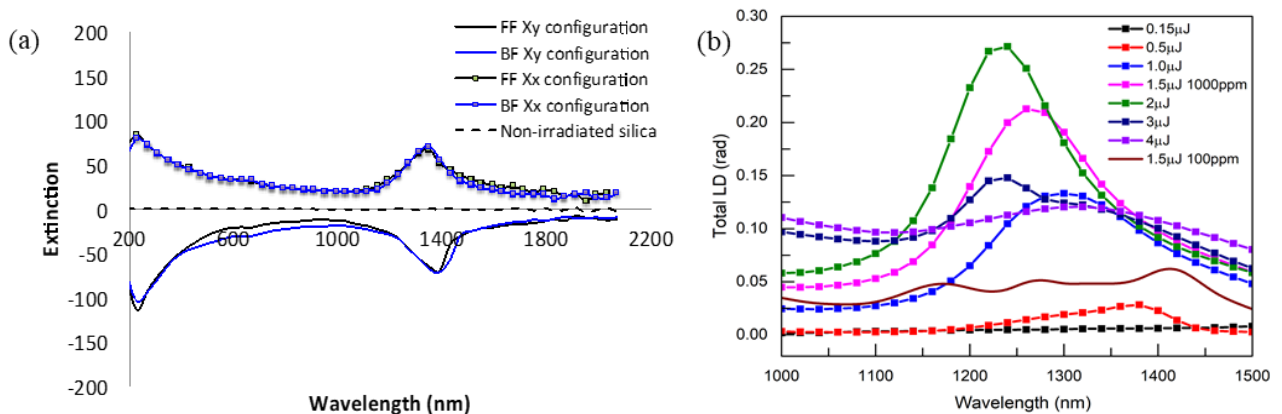


Figure 6.3 Dichroism (scattering and absorption if any) exhibited by femtosecond laser (1030 nm) induced nanogratings. (a) Extinction difference  $\Delta\kappa = \kappa_x - \kappa_y$  for two irradiated samples with  $X_x$  and  $X_y$

configurations written at 1.5μJ/pulse [37]. (b) Total linear dichroism, LD, as a function of fs pulse energy (X+ 45° configuration) [36]. Laser writing conditions: 1030nm, 250fs, 100kHz, 0.6-NA, 1mm/s. Samples were previously annealed for 30min at 600°C to bleach most of the defect centers.

The above-described results suggest that the observed differential losses may be mainly related to light scattering in the UV-Vis range whereas a linear dichroic band appears around 1,3-1,4 μm depending on OH-content and pulse energy [36]. The polarization dependence of scattered light indicates that the scattering centers are likely inside of the nanogratings. We speculate that the losses are introduced by nanoporous glass inside the nanogratings with characteristic dimensions of few tens of nanometers [14, 16], which is usually assumed to be a Rayleigh signature in the literature. In order to go beyond in the characterization of the scattered light, it could be possible to apply the more general Mie theory to the distribution of small spheres (note that Rayleigh theory is a limit case of Mie theory when the spherical “particles” are much smaller than the wavelength), or the Rayleigh-Gans-Debye approximation if the size of the sphere is larger. The latter procedure would allow for the modeling (and the interpretation) of the polarization-sensitive contribution of the porous nanolayers to the scattered light. The latter model could be used to model the intensity losses according to the refractive index ratio between that of the medium and that of the inclusions, and also the size of the inclusions.

## 6.2.2 Stress-induced birefringence within Type II regime

### Generalities

Stress-induced birefringence can result from different conditions such as applied external pressure, process-induced temperature gradients, manufacturing processes (thermal expansion coefficient mismatch in optical fibers manufacturing, etc...) but also laser writing (due to permanent volume changes  $\rho$  leading to elastic strain  $\epsilon$  and thus stress  $\sigma$ ). Therefore, the glass refractive index also becomes locally anisotropic through photoelastic effects. The plane-polarized wave will propagate through the stressed part of the glass at different speeds according to its polarization direction. For electromagnetic radiation with a polarization parallel and/or perpendicular to the direction of the mechanical stress the refractive indices can be rewritten as  $n_{\parallel} = n_0 + \Delta n_{\parallel}$  and  $n_{\perp} = n_0 + \Delta n_{\perp}$ . Whereby  $n_0$  is the refractive index of the isotropic medium. For the small mechanical stress  $\sigma$ , the refractive index changes  $\Delta n_{\parallel}$  and  $\Delta n_{\perp}$  are proportional to the mechanical stress  $\sigma$  where  $\Delta n_{\parallel}$  ( $\Delta n_{\perp}$ ) is the refractive index change for oscillating light parallel (perpendicular) to the stress direction. The appropriate differential quotients are called the stress optical coefficients:  $K_{\parallel} = \frac{dn_{\parallel}}{d\sigma}$ ,  $K_{\perp} = \frac{dn_{\perp}}{d\sigma}$  with  $K = (K_{\parallel} - K_{\perp})$  ( $3.55 \times 10^{-12} \text{ Pa}^{-1}$  for fused silica at 546 nm). The difference in the optical path length, also called the retardance  $R$ , can be easily measured and is proportional to the stress-induced birefringence  $n_{\parallel} - n_{\perp}$  and the birefringent layer thickness  $d$ . As a simple view, for a single axis stress state,  $R$  can be directly related to the principal stress components and the stress optic coefficient  $K$  by the following equation:  $R = (n_{\parallel} - n_{\perp}) \cdot d = (K_{\parallel} - K_{\perp}) \cdot d \cdot \sigma = K \cdot d \cdot \sigma$ . The orientation and the amount of birefringence is thus related to the amount of stress applied in a given point via the photoelastic tensor.

### Femtosecond laser direct writing and stress field

As mentioned earlier, femtosecond laser exposure of SiO<sub>2</sub> leads to various structural modifications including the appearance of stress-fields for different reasons. As the laser pulse energy increases, there are two types of structural modifications of interest here. First, the Type I modifications where homogeneous optical changes occur, it leads to an increase of refractive index in SiO<sub>2</sub> (albeit negative in most other glasses) mostly attributed to a permanent glass densification. Moreover a tensile stress field and a minor contribution of point defects centers (typ. 25%, see chapter 1) are also contributing to the observed  $n$ . In contrast Type II modifications correspond to the formation of porous nanogratings [14, 16]. During the decomposition of SiO<sub>2</sub>, many nanopores or nanocavities are created within these hot plasma nanolayers leading to a net glass volume expansion [38, 39], which correlates with the formation of nanogratings. The specific glass volume is expanded inside the Type II irradiated zone, and corresponds to the appearance of a permanent strain  $\epsilon^p > 0$  (whereas it is negative for a densification e.g. Type I in SiO<sub>2</sub>). The latter results into elastic strain  $\epsilon^e < 0$  as a direct response of the material, and therefore a compressive stress  $\sigma$  within and around the laser-modified region. According to the photoelastic effect, when a stress is applied to a material, the latter develops a form of linear birefringence. In addition, dealing with the stress profile measurements, Champion et al. have used a laser-written pattern, which enlarges the span of the stressed region, and derived an equation to model the stress field accordingly [38]. Their results indicate that the stress surrounding the irradiated area should depend on the nanolayers orientation with respect to the writing direction. Thus depending on the laser exposure conditions including polarization, the overall stress can be enhanced or minimized [39] leading to tunable birefringence values from  $10^{-5}$  up to  $\sim 10^{-3}$  [40-42] but what about the neutral axis orientation ?

### **Neutral axis orientation of the stress-induced birefringence around a laser written line**

In the following we provide a simple qualitative model to illustrate the properties of the stress-induced birefringence in the proximity of a line written with series of femtosecond laser pulses. Here we discussed the following writing conditions: a single line with a length of around several hundreds of microns along x-axis, a width of a few microns (typ. 1-5  $\mu\text{m}$ ) along y-axis and a thickness of around 50-100  $\mu\text{m}$  in the z-direction (the typical length of a laser track), which induces a field of displacement  $u_z$  mainly perpendicular to the widest face of the sample namely (x,y) plane.

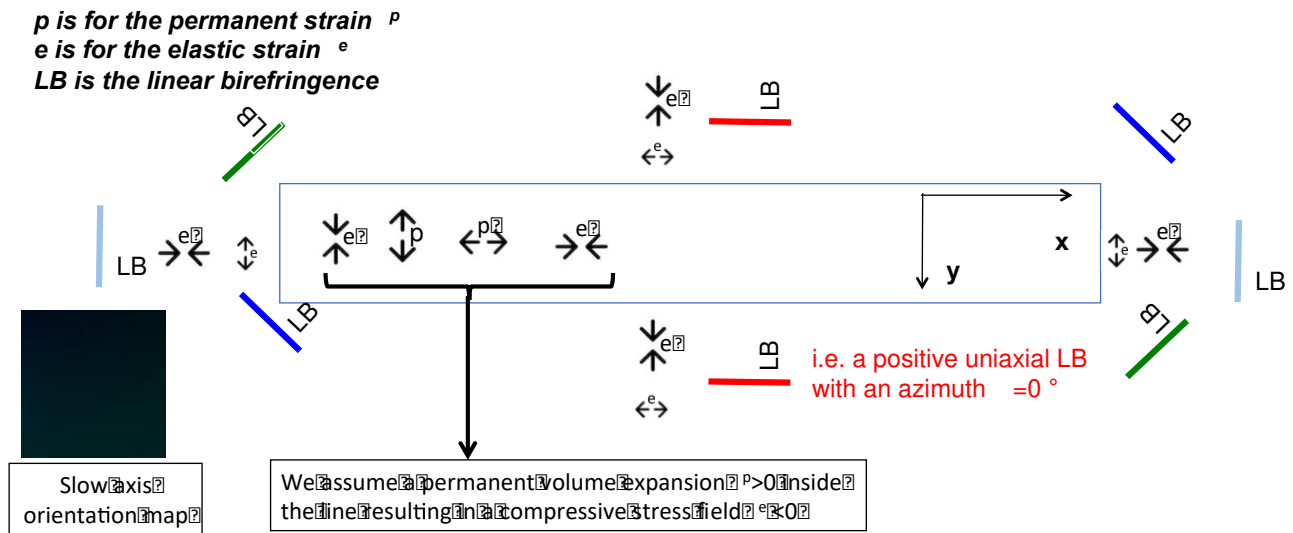


Figure 6.4 Scheme of laser line represents together with permanent strain (volume expansion) and related elastic strain within Type II regime. The slow axis orientation of the resulting stress-induced birefringence (notes LB) is shown out of the laser line and is code in colour following the orientation map shown in the bottom left.

Within the line, nanogratings consist of planar structures i.e. lamellas made of nanoporous  $\text{SiO}_2$  that are in expansion. Thus nanogratings formation implies a net volume expansion within the line: it is a positive permanent strain  $\epsilon^p_{\text{Type II}} > 0$  (inside the laser irradiated zone), therefore the response of the material leads to a negative elastic strain  $\epsilon^e_{\text{Type II}} < 0$  and the related stress field being in compression. Consequently, the  $n$  decreases (within porous nanolayers but also in the overall Type II affected volume in agreement with the observed net volume expansion) and *the slow axis direction of the stress-induced birefringence is parallel to the written line* (the red line in the Figure 6.4). Here the slow axis orientation is only determined by the geometry and does not depend on the laser writing polarization as a first approximation (except at the two extremities of the written line where the slow axis is azimuthally distributed). In other words, whether the laser writing polarization is aligned along  $x$  or  $y$ , the slow axis orientation remains unchanged. However, stress-induced birefringence amplitude will be different [43]. Next, if we consider an irradiated area like a rectangular or a square with the dimensions around  $100 \times 100 \text{ m}^2$ , such as a stressor, it can be considered as the superposition of lines (as a first approximation) and therefore the slow axis of the stress-induced birefringence results to be parallel to the lines. *Finally, if we stack the areas, we make the same approximation and the slow axis appears to be always parallel to the lines as we observed experimentally in chapter 4, section 4.5. Note this is a key point that will be useful to interpret the dependence of CB and CD with the writing polarization.*

### Form birefringence vs Stress-induced birefringence

In the framework of this work, stress-induced birefringence can be induced by the presence of Type I or Type II modifications but also by their co-existence. On the one hand, if we consider a "pure Type II" modification (so associated Type I), the combination the form birefringence and stress-induced birefringence will have either an additive or subtractive superposition of the two components. For Xx writing configuration we will have a subtractive

superposition, whereas it is an additive superposition for Xy writing configuration. Moreover, under thermal treatment (annealing) a part of the stress is expected to relax when approaching a temperature around  $0.8T_g$  ( $T_g$  = glass transition temperature) for a few hours or  $0.9T_g$  for a few tens of minutes as we effectively observed in the last section of chapter 4. On the other hand, the formation of Type I modifications can happen along the laser track like in its tail but also likely occur inside Type II regions as suggested initially by Bricchi [13] and later by Bellouard [44] and Poumellec [45]:

- In the first case, the measured retardance corresponds to two “additive” contributions  $R_{\text{Type I}} + R_{\text{Type II}}$  but one needs to consider different problems including overlapping and the respective neutral axis orientation of these contributions (which can lead to additive or subtractive effects).
- In the second case, Type I modifications might be present either between the nanolayers (refractive index  $n_2$ ) as suggested in the literature[13] but also in the material (refractive index  $n_{sg}$ ) surrounding the nanopores inside the nanolayers (refractive index  $n_1$ ).

### **Stress-induced birefringence and annealing treatments**

For going a step further we can exploit the thermal annealing treatments. Indeed in the literature it has been demonstrated that Type I modifications (and its stress-induced birefringence) will be erased at a lower temperature than the nanogratings themselves (i.e. porous nanolayers) during the thermal treatments [46-48]. Thus depending on the location of Type I modifications and on the laser writing configuration, the relaxation of the permanent densification (and also point defects but to less extent) under annealing will impact the overall retardance measurements in different ways:

- Optically: by affecting the refractive index difference  $|n_2 - n_1|$ .
- Mechanically: by increasing the average volume expansion  $\varepsilon^p_{\text{Type II}}$  in the affected volume.

So if we erase some Type I (typ. up to  $+5 \cdot 10^{-3}$  according to [13]) being present in the material surrounding the nanopores during the heat treatment, the refractive index  $n_1$  of the nanolayers will decrease, then the index difference  $|n_2 - n_1|$  of the nanolayers increases and therefore the retardance will increase also. In contrast if we are dealing with Type I densified zone in-between the nanolayers, thermal treatment will lead to a decrease of  $n_2$ , thus  $|n_2 - n_1|$  and retardance will decrease.

However, the erasure of Type I densified zones has another collateral mechanical effect that appears to be dominating. The relaxation of the glass densification ( $\varepsilon^p_{\text{Type I}} < 0$ ) is thus accompanied by an increase of the net volume expansion ( $\varepsilon^p_{\text{Type II}} > 0$ ) within Type II regions since there are two contributions to the total permanent strain that exhibit opposite signs i.e.  $\varepsilon^p_{\text{Type II}} = \varepsilon^p_{\text{Type I}} + \varepsilon^p_{\text{porous}}$ , where  $\varepsilon^p_{\text{porous}} > 0$  is related to the porous nanolayers. This could explain the unexpected increase of the retardance or index modulation in FBG (Fiber Bragg Gratings) observed in the literature [48-50] but also our observation in chapter 4 (section 4.6) where the stress-induced birefringence (measured



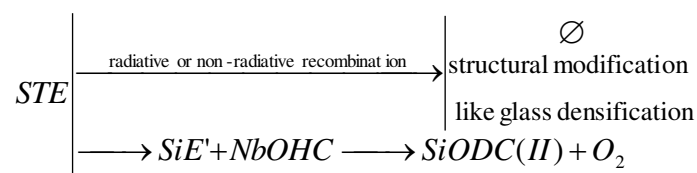
between two stress bars) is first increasing (600-1000°C) before to relax at higher temperature (typ. above 1000°C).

### 6.2.3 Point defects formation and annealing within Type II regime

In addition to the form birefringence and stress-induced birefringence we mentioned above, the nanogratings also contains a variety of point defects. Through their optical absorption bands, mostly located in the UV range, they are contributing to the observed refractive index changes through the Kramer-Kronig (KK) relationship. Generally, most defects are absorbing in the UV-VUV range and they are contributing positively to the refractive index changes measured in the Vis, near IR range. Once these defects are bleached under thermal treatment, the refractive index is therefore found to decrease. Consequently, the existence of such point defects could affect the measured birefringence (more accurately the measured retardance) that is usually too simply attributed to the nanogratings form birefringence. *However and according to most of the literature, the contribution of point defects to the nanogratings refractive index difference  $n_2-n_1$  (and thus birefringence) remains minor as described below in a short review.*

#### Point defects generate within Type II regime

In the literature the main part of the losses observed for Type II modifications has been attributed to the Rayleigh scattering due to the inhomogeneous nanostructure, which has a  $1/\lambda^4$  dependence for spherical inclusions much smaller than the probing wavelength. Additionally, two absorption bands can be distinguished at short wavelengths that are attributed to SiE' centers at 210 nm, ( $\equiv\text{Si}$ , an unpaired electron in a silicon atom bound to three oxygen atoms), and ODC(II) at 245 nm, ( $\equiv\text{Si-Si}\equiv$ , a divalent silicon atom) [51]. For comparison, structures exhibiting isotropic refractive index increase showed negligible scattering and only absorption band related to E' centers could be observed at short wavelengths. The E' centers, together with NBOHC (non-bridging oxygen hole centers), are produced as a result of self-trapped exciton decay [52, 53]. Indeed, recently an absorption peak at 244 nm was attributed to the NBOHC [53]. However, the absorption of NBOHC normally peaks at 260 nm and has much wider width of the peak, which extends to almost 300 nm [54]. The NBOHC can react with E' centers when some critical concentration is reached forming ODC(II) as it is sketched below [55-57].



#### Point defects and annealing treatments

The study on the thermal stability of the nanogratings is of great significance to understand not only the mechanisms of erasure but the writing ones as well and the contribution of each mechanism to the measured birefringence. Indeed, in 2006, Bricchi et al. [10] reported the first experiments related to the annealing of fs-laser written Type II modifications (Laser conditions:  $\lambda = 800$  nm, 100 kHz, 0.06 mm/s, pulse duration = 200 fs), which showed extraordinary thermal stability: such modifications can withstand at least 2 hours at 1000 °C without any degradation. The unexpected behaviour displayed by these structures, namely a slight growth of the absolute value of the ordinary and extraordinary refractive index difference as the temperature progressively increased in the 200-500 °C range, was suggested to come from the erasure of point defects centers like SiODC and SiE' defects generated in the irradiated volume.

This was followed by a few studies as summarized here. In 2012, Richter et al. [58] confirmed that nanogratings exhibit an extremely large temperature stability, i.e., up to 1150°C for 30 minutes (Laser conditions:  $\lambda=1030-515$  nm, 9.4 MHz, average power = 5 W, NA = 0.55, pulse duration = 450 fs). Investigations of the thermal stability of nanogratings showed that E' centers vanished upon annealing, whereas NBOHCs remained stable up to 900°C after initial hydrogen-recombination. In addition the signature of free O<sub>2</sub> is detected up to ~600 °C using Raman spectroscopy (see Figure 3.14 of Ref. [59]), and agrees well with the aforementioned defect bleaching. Thus, they proposed that nanogratings based components could be rendered truly thermally stable by a thermal annealing in order to erase the unstable part mostly related to point defects.

Krol et al. [60] have subsequently investigated the thermal stability of femtosecond laser modification inside fused silica (Laser conditions:  $\lambda=800$  nm, 1 kHz, NA = 0.25, 0.05 mm/s, pulse duration = 150 fs). Raman and photo-luminescence spectroscopy showed that fs-laser induced NBOHC defects completely disappeared at 300 °C (for a 10 hours annealing), whereas changes in Si-O ring structures only anneal out after heat treatment at 800-900 °C (for a 10 hours annealing). After annealing at 900 °C optical waveguides written inside the glass had completely disappeared whereas more significant damages induced in the glass remained.

In 2014, Qiu et al. [61] highlighted that the linear birefringence response of the nanogratings experiences a slight increase with increasing annealing temperature up to 900°C (Laser conditions:  $\lambda=800$  nm, 1 kHz, NA = 0.55, 0.01 mm/s, pulse energy = 2  $\mu$ J, pulse duration = 150 fs, laser polarization = 45°) in agreement with Bricchi et al. [10]. But after annealing at 1100 °C for 1 h, the birefringence sharply decreased by a factor of 4. They also monitored the so-called "defects" lines (labelled D1 and D2) using Raman spectroscopy as a function of temperature. These lines are related to 3 and 4-membered rings in the silica network.

In chapter 4, some silica samples were annealed for 30min at 600°C. The absorption bands attributed to E' and ODC(II) defects were annealed for Type II modifications as it can be seen in Figure 6.5a. Note that all point defects generated within Type I modifications were also completely erased in similar conditions (2hours at 450°C) [35]. As a result,

significantly lower losses were measured from 200 to 350 nm. In the visible range, however, no major improvement in optical quality was observed.

The retardance variation of Type II structures was also measured from 200 nm to 2100 nm in the same samples [35] as shown in Figure 6.5b. The retardance dependence with the wavelength shows a steady rise in the spectral region from 200 to 680 nm and when asymptotically decreases to a plateau extending to at least 2.1  $\mu\text{m}$ . A long plateau tail is expected as at longer wavelengths the retardance approaches asymptotically to the value predicted by the effective medium theory as mentioned in section 6.1. The annealing for 2 hours at 450°C decreased the overall retardance value only by than 5% whereas all defects were bleached. This indicates that defects centers exhibit only a minor contribution to the observed birefringence for the chosen writing conditions.

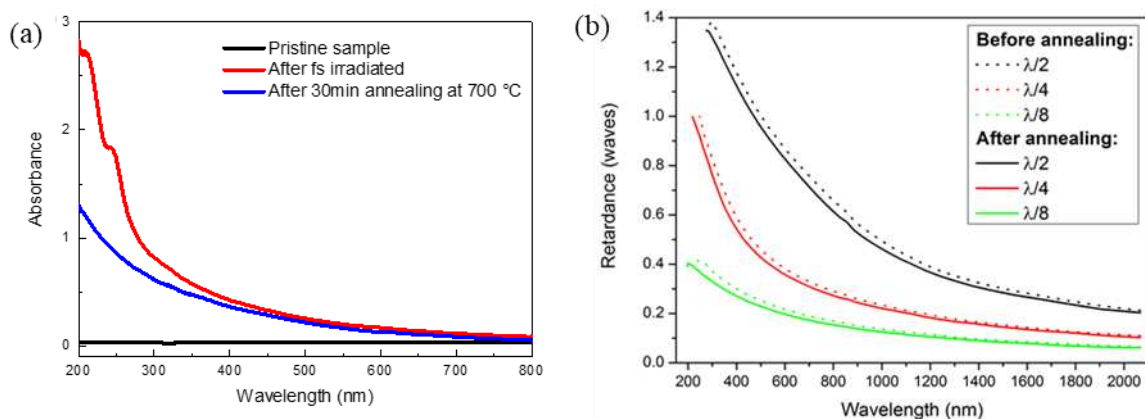


Figure 6.5 (a) Spectral absorbance of pristine, irradiated sample (at 1.5 J/pulse) and after 30min annealing at 600°C. (b) Spectral retardance dependence before and after annealing (2 hours at 450°C) measured with the ellipsometer. The target retardance values were half, quarter and eighth of 1030 nm. Graph extracted from Ref. [35]. The laser parameters were: 1030 nm, 250 fs, 0.6 NA, 100kHz, 0,1 mm/s.

To sum up on point defects, it is still not fully clear how the point defects are contributing to the observed birefringence but this appears quantitatively small. We can think about two main cases: 1) the anisotropic/oriented defects and 2) isotropic defects but spatially distributed in an anisotropic way, both of them can create small amount of birefringence.

- The first possibility would be the formation of anisotropic and oriented defects that would create a linear dichroism and thus a linear birefringence through KK relationship. However, we did not detect any LD band in the UV-Vis range (see chapter 5). LD bands were observed recently but only around 1.2-1.4  $\mu\text{m}$ . The apparent linear dichroism in the UV-Vis range has been attributed to polarization dependent light scattering. Indeed the arrangement of porous nanolayers creates anisotropic light scattering resulting in a linear diattenuation [29] (rather than linear dichroism) tail observed in the UV-Vis range. Because the impact of anisotropic/oriented defects appears no significant (no linear dichroic bands have been observed), we chose to ignore it in the following.

- The second possibility about distributed isotropic defects can separate itself into two branches. On the one hand, defects are present between the nanolayers (area of index  $n_2$  in Figure 6.2). When they are bleached under thermal treatment,  $n_2$  decreases and therefore the retardance  $R$  (proportional to  $n_2 - n_1$ ) decreases. On the other hand, we expect the formation of defects inside the nanolayers (area of index  $n_1$  in Figure 6.2) especially in the material surrounding the nanopores ( $n_{sg}$ ). When they disappear during the heat treatment, the refractive index  $n_{sg}$  (and  $n_1$ ) decreases and thus the refractive index difference  $|n_2 - n_1|$  increases resulting in an increase of the retardance deduced from the form birefringence model.

Compared with the form birefringence and the stress-induced birefringence, although the defects induce a minor effect to the nanogratings refractive index difference  $|n_2 - n_1|$  (and thus on the measured birefringence or retardance), they have still to be considered as a part that cannot be ignored. This is especially the case when considering their sensitivity to the thermal stability that will impact the response of photonic objects such as Fiber Bragg Gratings, or the measured retardance  $R$  when we study the erasure of nanogratings written in a bulk glass sample. Another example is their contribution to the reduction (typ. 40%) of the coefficient of thermal expansion (CTE) observed by Y. Bellouard's group within Type I regime [62], which was attributed to the presence of point defects. Note after an annealing of 10 hours at 300°C most defects were erased and CTE recovers its initial value like the pristine glass.

#### 6.2.4 Conclusion on anisotropic linear properties thermal stability

In this section, we summarized the different contributions of the total birefringence response in silica glasses induced by femtosecond laser irradiation, as well as their corresponding erasure mechanism during a high temperature annealing process as summarized in Figure 6.6. Those events are not necessarily characterized in our work but have been synthesized both from literature and from our observations.

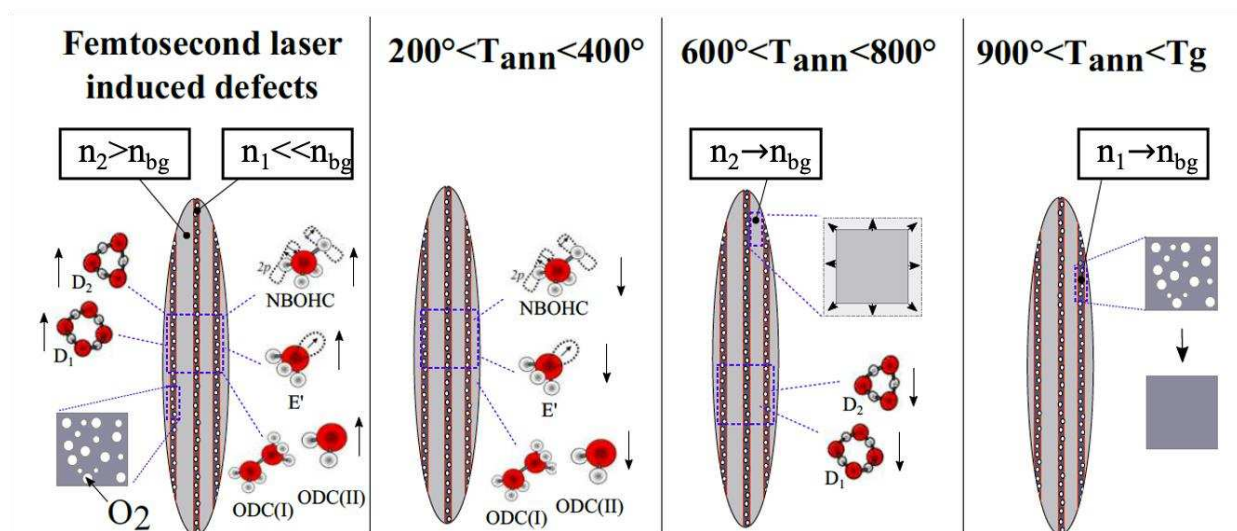


Figure 6.6. An illustrative summary of laser induced defects and changes for the nanogratings modifications under step isochronal thermal annealing at  $T_{ann}$ .  $n_2$ ,  $n_1$  and  $n_{bg}$  are the densities of the non-porous

layer, nanoporous layer and pristine substrate, respectively.  $T_g$  is the glass transition temperature of  $\text{SiO}_2$  (typ.  $T_g$  is around  $1120^\circ\text{C}$  for SuprasilCG).

The results of Raman and UV absorption spectroscopies had revealed the effect of defects on nanogratings structural modifications. However, it should be pointed out that they induce a minor effect to the nanogratings refractive index difference  $|n_2 - n_1|$  (and thus on the measured birefringence or retardance). The point defects centers are bleached under a fairly low temperature thermal treatment ( $< 600^\circ\text{C}$ ) and only minor changes (typ.  $< 5\%$ ) in the retardance value can be found in this temperature range. The subsequent unexpected rise from  $600^\circ\text{C} - 1000^\circ\text{C}$  is attributed to the co-existence of Type I (densification) and Type II modifications, the erasure of the former occurred at this stage and likely caused an unexpected increase of both the overall retardance  $R$  (seen in the literature) but also the stress-induced birefringence (as shown in chapter 4). Then, through monitoring the anisotropic optical properties of the irradiated area and the surrounding stress-induced birefringence area during the annealing process, it is determined that stress relaxation (typ. around 30 min at  $1100^\circ\text{C}$ ) is an important factor leading to full erasure of [CB, CD] associated with a slight decrease (typ. 20%) of the [LB, LD] properties. Finally, at high temperature the last contribution is related the nanopores size and their filling factor ( $ff_{\text{porous}}$ ), which have been determined by the SEM micrographs. In a recent work our group has revealed that the evolution of the pore size can be calculated by the Rayleigh-Plesset (R-P) equation under a viscoelastic regime revealing the key role of the glass viscosity behavior at high temperatures [63].

### **6.3 Modeling anisotropic circular optical properties using Mueller matrix formalism using a two linear retarders model**

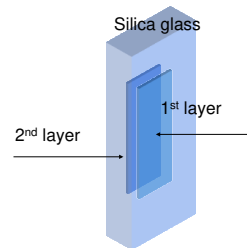
After discussing the various contributions on the observed linear birefringence, we turn into the understanding of the creation of circular optical properties. One possibility could be the presence of an additional force that imprints a given rotation to the nanogratings along the beam propagation. The latter will result in the formation of "twisted nanogratings" i.e. a 3D helical distribution of nanogratings along the propagation distribution like twisted nematic liquid crystals, thus creating both CB and CD. However another more likely mechanism for the creation of circular optical is the combination of the linear birefringence due to nanogratings, and to the stress-induced birefringence. The theory of light propagation in multilayered anisotropic media can be used as a framework to represent the optical effects and to model the experimental data. Accordingly, CB may originate when at least two linear birefringence contributions appear to have their axes oriented at angle other than  $0^\circ$  or  $90^\circ$  [4]. In our case, one of the mechanisms is the birefringence due to the nanogratings,  $LB_{\text{form}}$ , while the second is the stress-induced birefringence,  $LB_{\text{stress}}$ . The latter hypothesis is supported by the data discussed in chapter 4, which shows some correlation between the presence of a stress field and the existence of circular optical properties. These results lead us to consider such a second contribution to the linear birefringence and to perform some numerical modeling. We used Mathcad software to perform the latter.

## 6.3.1 Short description of the modeling procedure

### Jones matrices of the sample

To have a better understanding of our results, we decided to model the birefringence and dichroism measurements (linear and circular) in the Mueller formalism instead of Jones matrix, because the light is partially polarized after passing through our samples. It is therefore necessary to define the Mueller matrices to explain our sample and making it possible to define one or more phase shifters (and possibly a rotator) in order to translate the observed phenomena including the possible effects of depolarization.

In the following, we consider the case of a first homogeneous layer with linear anisotropic optical properties, and a second homogeneous layer also with linear anisotropic properties but this time whose neutral axis orientations may be different from that of the first layer. This model may seem very simplistic but as shown in the literature [64], retains the essential physics to represent our samples because it takes into account the two more likely sources of birefringence and because these two mechanisms appear in two different layers, which fulfill the minimum condition to create an object exhibiting both linear and circular properties (not entangled / entangled depending on the type of decomposition applied). It is recalled that the linear properties are associated with a potentially absorbing phase shifter (dichroic) and therefore contain both a linear birefringence term LB and a linear dichroism term LD. In the Mueller formalism that we have chosen here, the optical phase shifter **MDR** (a linear retarder) is written according to the following relation:

$$\text{MDR}(R, \text{Psi}) := \begin{pmatrix} 1 & -\cos(2\text{Psi}) & 0 & 0 \\ -\cos(2\text{Psi}) & 1 & 0 & 0 \\ 0 & 0 & \sin(2\text{Psi}) \cdot \cos(R) & \sin(2\text{Psi}) \cdot \sin(R) \\ 0 & 0 & -\sin(2\text{Psi}) \cdot \sin(R) & \sin(2\text{Psi}) \cdot \cos(R) \end{pmatrix}$$


where  $R$  is the linear phase shift (also called LB when expressed in radians) expressed in degree and  $\text{Psi}$  translates the absorbing property of the phase shifter (linear dichroism LD in radians), also expressed in degree. We note that a zero dichroism corresponds to a value of  $\text{Psi}$  equal to  $45^\circ$  or  $\frac{\pi}{4} \text{rad}$ . As a reminder, the complex phase shift  $\phi_1$  is composed of the properties of linear birefringence  $\delta = n_x - n_y$  and linear dichroism  $\varepsilon = \kappa_x - \kappa_y$  such that the total phase shift is written  $\phi_1 = 2 \left( \frac{\pi}{\lambda} \delta_{1,2} + i \frac{\pi}{\lambda} \varepsilon_{1,2} \right) \cdot l_{1,2}$  where the index 1 or 2 corresponds to the layer; and it would be the same for the circular phase shift  $\phi_c$  if there is any. We also define  $\alpha$  that is the angle between the slow axis and the x-axis of the benchmark of the laboratory, which leads to the introduction of the two angles  $\alpha_1$  and  $\alpha_2$ , which are attached to each of the two layers i.e. to each of the two phase shifters.

After having determined the Mueller matrix **M** corresponding to the assembly of these two respective orientation phase shifters  $\alpha_1$  and  $\alpha_2$ , we can formally decompose the resulting matrix using the logarithmic approach presented in chapter 2. The effective anisotropic optical properties then can be extracted from the medium thus modeled.

$$M = [M_R(\alpha_1) \cdot MDR(1^{st}layer) \cdot M_R(-\alpha_1)] \cdot [M_R(\alpha_2) \cdot MDR(2^{nd}layer) \cdot M_R(-\alpha_2)] \quad \text{Equation 6.12}$$

**Attribution of the phase shifters:** In the following, the optical parameters  $R_{1,2}$  and  $\Psi_{1,2}$  of the two phase shifters will be set. One of the two phase shifters will be representative of the form birefringence attributed to the nanogratings and thus exhibiting a strong uniaxial negative linear birefringence as reported by Bricchi et al. [13]. It will also be associated with a non-zero “apparent” linear dichroism (positive for Xx writing, negative for Xy writing) corresponding to experimental observations and which is mainly attributed to optical light scattering due to nanoporosity within the nanolayers. Firstly, the second phase shifter is not, in principle, associated with a particular physical origin. Secondly, it will be attributed to the presence of a stress-induced birefringence that will guide us in the definition of its properties, such as positive uniaxial, of lower amplitude (typ. an order of magnitude) than the first layer. Its orientation  $\alpha_2$  is fixed by the direction of the laser scanning and remains independent of the direction of polarization of the laser, in agreement with the experimental observations i.e.  $\alpha_2 = 0$  for a laser scanning fixed along the x-axis.

**Orders of magnitude:** To fix orders of magnitude for the different layers, we use as a reference the results from our experimental data. The first layer representing the nanogratings (form birefringence + anisotropic optical scattering) will be assigned for example  $\pi/2$  (i.e. a delay of 250 nm at  $\lambda = 500$  nm) for the parameter  $R_1$  related to the linear birefringence,  $\pi/5$  (i.e.  $36^\circ$  knowing that  $45^\circ$  corresponds to no dichroism) for the parameter  $\Psi_{1,1}$  related to the LD of the first layer. Concerning the second layer, a typical value of  $\pi/10$  will be assigned for the parameter  $R_2$  relating to the linear birefringence and 0 for the parameter  $\Psi_{2,2}$  relating to the LD. The parameters mentioned above are set as a starting point, but can be subjected to variations in order to represent different cases in a pedagogical way.

**Orientations:** The two phase shifters can be oriented in order to try to account for the values of the polarimetric properties in our different experimental data, and to represent the dependence of the linear and circular anisotropic properties as a function of the orientation of the writing polarization with regard to the direction of laser scanning. For example we will obtain the resulting matrix **M**:

$$M = [M_R(\alpha_1) \cdot MDR(1^{st}layer) \cdot M_R(-\alpha_1)] \cdot MDR(2^{nd}layer) \quad \text{Equation 6.13}$$

when  $\alpha_2 = 0$  i.e. the second layer is independent of the direction of laser polarization while the first layer will rotate linearly with the  $\theta$  orientation of the laser polarization when writing  $\alpha_1 = \theta$ .

**Protocol:** Letting free to vary these parameters, i.e. linear birefringence and linear dichroism, we intend to represent the influence of these on the resulting Mueller matrix and therefore on the effective anisotropic properties of the sample. The amplitudes  $R_{1,2}$  and  $\Psi_{1,2}$  as well as the two angles  $\alpha_1$  and  $\alpha_2$  between the slow axis of each phase shifter and the x axis of the laboratory, will be our six variables at the first order then only the two angles (or even only one) will need to be adjusted in order to represent our experimental observations.

Indeed, according to our operating mode, the 16 samples that we want to model were registered with a laser polarization initially positioned along the x axis (associated with an angle  $\alpha_{1,2} = 0$ ) and going up to  $360^\circ$  by steps of  $22.5^\circ$  thus passing through various classical cases such as a polarization along y (associated with an angle  $\alpha_{1,2} = \pi/2$ ). We will then observe the resulting properties that we can compare with our [LB, LD] measurements in the xy plane but also these same properties measured at  $\pm 45^\circ$ , noted LB' and LD', as well as for circular properties denoted CB and CD.

Before discussing the final "adjustments", we will first analyze a series of particular cases (case studies) to identify in a systematic and pedagogical way the configurations for which it is possible to create circular CD dichroism alone, circular birefringence CB alone or the two properties CB, CD combined from a simple stacking of two birefringent (non-zero LB) and potentially absorbing phase shifters (i.e. presence of a possible linear dichroism denoted LD). All of the cases studied are summarized at the end of this section in Table 6.1. We illustrate below some specific cases that we believe to be the most relevant and educational. *To some extent, we will try to associate these different cases with experimental observations from our work or from the literature and concerning the effects of femtosecond laser irradiation in silica.*

### 6.3.2 Modelling a single linear retarder

#### 1. Case description: a single layer of linear retarder with either LB only or both [LB, LD]

- $R_1 = -90^\circ$  and  $R_2 = 0$  i.e. a single birefringent layer with a negative uniaxial birefringence
- Subcase 1a:  $\Psi_{i1} = \Psi_{i2} = 45^\circ$  i.e. no linear dichroism
- Subcase 1b (not shown here):  $\Psi_{i1} = 40^\circ$  and  $\Psi_{i2} = 45^\circ$  i.e. both LB and LD
- $\alpha_1 = 0-360^\circ$ ,  $\alpha_2 = 0^\circ$  i.e. the slow/fast axis are rotated linearly with the laser writing polarization orientation i.e.  $\alpha_1 = \theta$ . and the slow axis of the linear retarder is perpendicular to the laser polarization.

#### *Relationship with laser imprinted effects*

This case corresponds to the modelling of ideal nanogratings, i.e. as a first approximation they exhibit negative uniaxial form birefringence (case a: no dichroism, case b: dichroism) with the slow axis oriented parallel to the nanolayers themselves and perpendicular to the orientation of the linear polarization of the writing laser. In addition, we consider neither tilt effect nor the introduction of stress-induced birefringence.

#### *Results*

Figure 6.7 shows the optical properties LB, LD and the crossed optical properties [LB' and LD'] planes for an ideal retarder as function of the orientation of the corresponding slow axis in the range from  $0^\circ$  up to  $360^\circ$ . Since the sample made of a single linear birefringent layer, both LB and LB' functions are perfectly periodic with a  $45^\circ$  shift respect to the orientation of the slow axis. In addition, no circular optical properties [CB or CD] are observed.



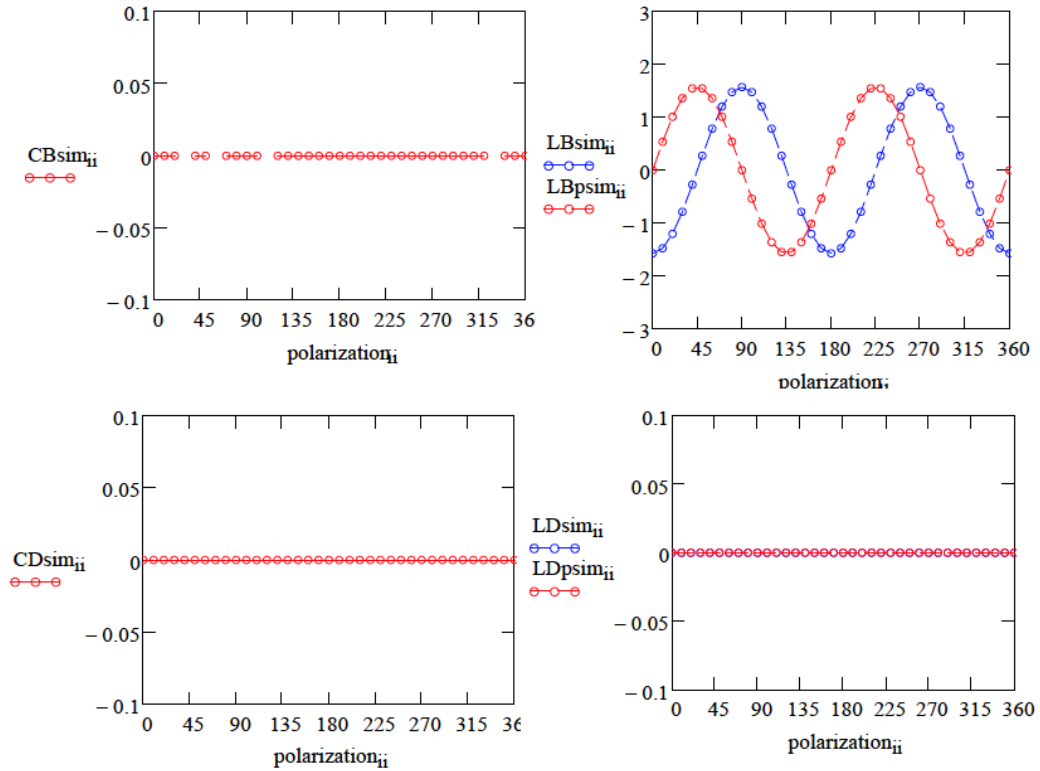


Figure 6.7 Modelling of effective anisotropic optical properties (in radians) at 550 nm as a function of writing laser polarization azimuthal angle (noted polarization<sub>ii</sub>): circular birefringence CB, linear birefringence LB, LB', circular dichroism CD and linear dichroism LD, LD'. Case1: a single layer of linear retarder with LB only. Parameters:  $R_1 = -90^\circ$ ,  $R_2 = 0^\circ$ ,  $\Psi_{i1} = 45^\circ$ ,  $\Psi_{i2} = 45^\circ$ ,  $\theta_1 = 0-360^\circ$  and  $\theta_2 = 0^\circ$ .

The data in Figure 6.7 shows that a single linearly birefringent layer cannot create circular properties by itself. Therefore, the next steps are to investigate the modelling using two linear retarders in such a way we could create CB only, CD only and finally both CB, CD with the observed periodicity according to the writing laser polarization orientation  $\theta$ .

### 6.3.3 Modelling the formation of CB only using two linear retarders

#### 2a. Case description: two linear LB layers that remain parallel or perpendicular to each other

- $R_1 = -90^\circ$  and  $R_2 = 25^\circ$  i.e. one birefringent layer with a negative uniaxial birefringence and a second one with a positive uniaxial birefringence
- $\Psi_{i1} = \Psi_{i2} = 45^\circ$  i.e. no linear dichroism
- $\theta_1 = \theta_2 = 0-360^\circ$  (slow axes are parallel to each others) or  $\theta_1 = 0-360^\circ$  and  $\theta_2 = \theta_1 + 90^\circ$  (slow axes are perpendicular to each others). In both cases, the slow/fast axis turn linearly with the laser writing polarization orientation  $\theta$  and the two layers maintain their respective neutral axis mutually parallel or perpendicular to each other.

#### *Results*

This situation corresponds to a set of samples made of two LB layers with respective slow axis that turn the same angle when the laser writing polarization changes from 0 up to  $360^\circ$ . Figure 6.8 shows the optical properties LB, LD and the crossed optical properties (LB' and LD') planes for an ideal retarder as function of the orientation of the corresponding

slow axis in the range from  $0^\circ$  up to  $360^\circ$ . Since the samples were made of two linear birefringent layers (with neutral axis that always remain parallel to each others) controlled by the laser polarization, both LB and LB' functions are perfectly periodic with a  $45^\circ$  shift. In addition no circular optical properties (CB or CD) are observed as it is modelled here.

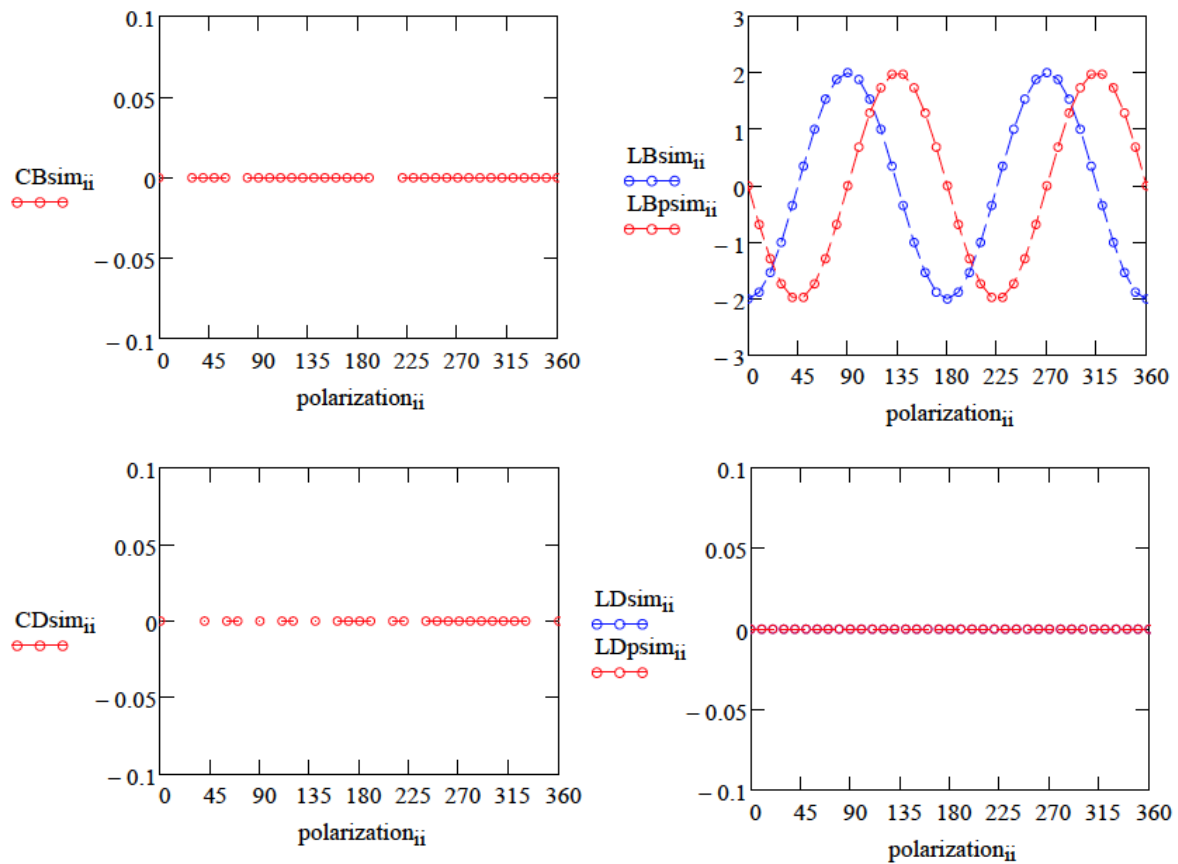


Figure 6.8 Modelling values of effective anisotropic optical properties (expressed in radians) at 550nm as a function of writing laser polarization azimuth  $\theta$ : circular birefringence CB, linear birefringence LB, LB', circular dichroism CD and linear dichroism LD, LD'. Case 2a: two linear LB layers that remain parallel or perpendicular to each other. Parameters:  $R_1 = -90^\circ$ ,  $R_2 = 25^\circ$ ,  $\Psi_{i1} = 45^\circ$ ,  $\Psi_{i2} = 45^\circ$ ,  $\theta_1 = 0-360^\circ$  and  $\theta_2 = \theta_1$  or  $\theta_1 + 90^\circ$ .

2b. Case description: two linear LB layers with a  $10^\circ$  offset between their respective neutral axis

- $R_1 = -90^\circ$  and  $R_2 = 25^\circ$  i.e. one birefringent layer with a negative uniaxial birefringence and a second one with a positive uniaxial birefringence
- $\Psi_{i1} = \Psi_{i2} = 45^\circ$  i.e. no linear dichroism
- $\theta_1 = 0-360^\circ$  and  $\theta_2 = \theta_1 + 10^\circ$  i.e. the slow/fast axis turn the same amount with the laser writing polarization orientation  $\theta$  and the two layers have a  $10^\circ$  offset between their respective neutral axis.

*Results*

Figure 6.9 shows the result of the model for a sample without linear dichroism. It is noted that the CB is not zero and remains constant with respect to the orientation of the polarization of the writing laser. Additionally, we make the observation that the CD is zero for these samples because none of them possess linear dichroism (LD and LD' are zero)

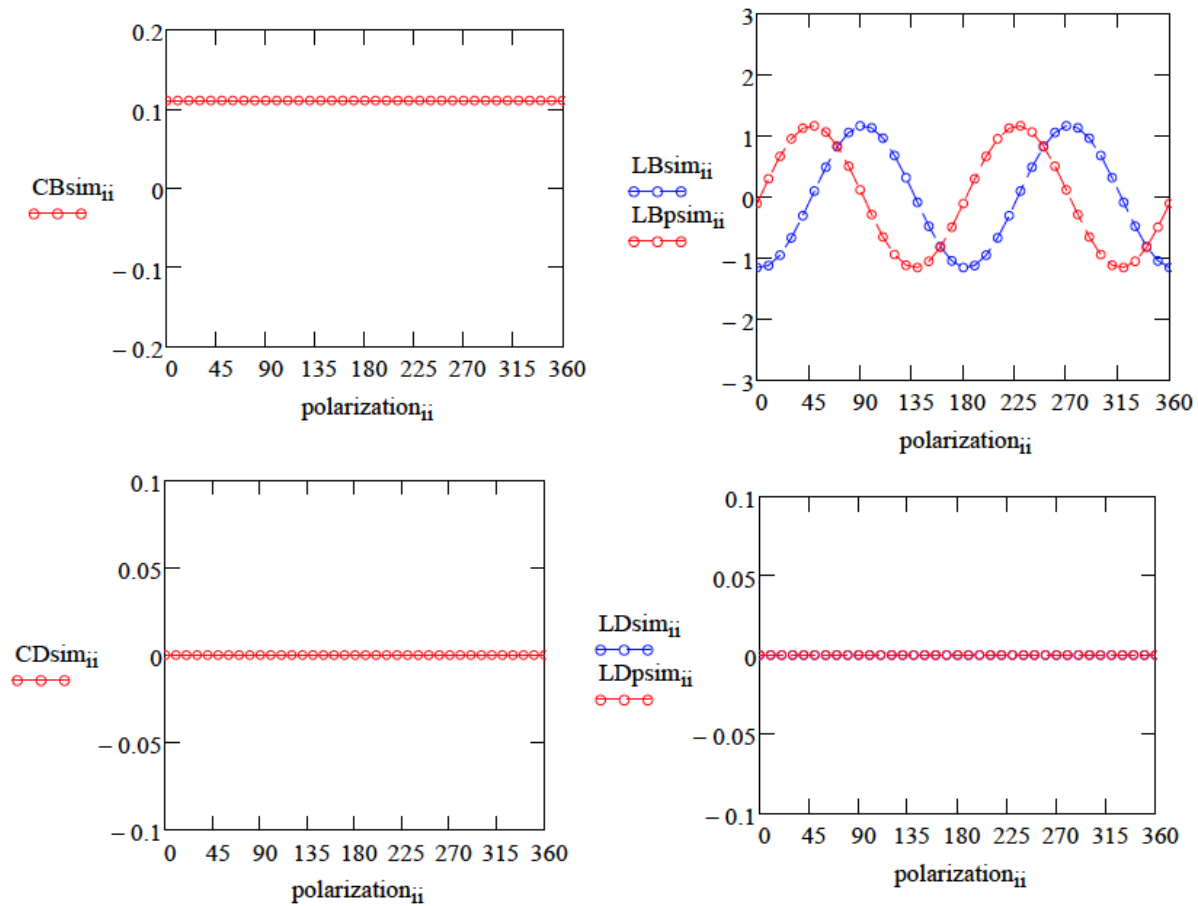


Figure 6.9 Modelling values of effective anisotropic optical properties (expressed in radians) at 550 nm as a function of writing laser polarization azimuth  $\alpha$ : circular birefringence CB, linear birefringence LB, LB', circular dichroism CD and linear dichroism LD, LD'. *Case 2b: two linear LB layers with a 10° offset between their neutral axis. Parameters:  $R_1 = -90^\circ$ ,  $R_2 = 25^\circ$ ,  $\Psi_{i1} = 45^\circ$ ,  $\Psi_{i2} = 45^\circ$ ,  $\alpha_1 = 0-360^\circ$  and  $\alpha_2 = \alpha_1 + 10^\circ$ .*

2c. Case description: two linear layers; one fixed, one rotating

- $R_1 = -90^\circ$  and  $R_2 = 25^\circ$  i.e. one birefringent layer with a negative uniaxial birefringence and a second one with a positive uniaxial birefringence
- $\Psi_{i1} = \Psi_{i2} = 45^\circ$  i.e. no linear dichroism
- $\alpha_1 = 0-360^\circ$  and  $\alpha_2 = 0^\circ$  i.e. the slow/fast of the first layer turns with the orientation of the writing laser polarization, whereas the second layer is fixed

*Results*

As in the case 2a shown in Figure 6.10, we can observe a non-zero CB provided the two layers are not parallel not orthogonal to each other. Then we can see that the CB amplitude is dependent on the angle between these two layers. In particular CB is maximum when the angular misalignment (offset) is  $\pm 45^\circ$  between the neutral axis of two linear retarders. It is possible to obtain a negative CB when the second layer is at  $+45^\circ$  of the first one and a positive CB for a  $135^\circ$  (or  $-45^\circ$ ) misalignment.

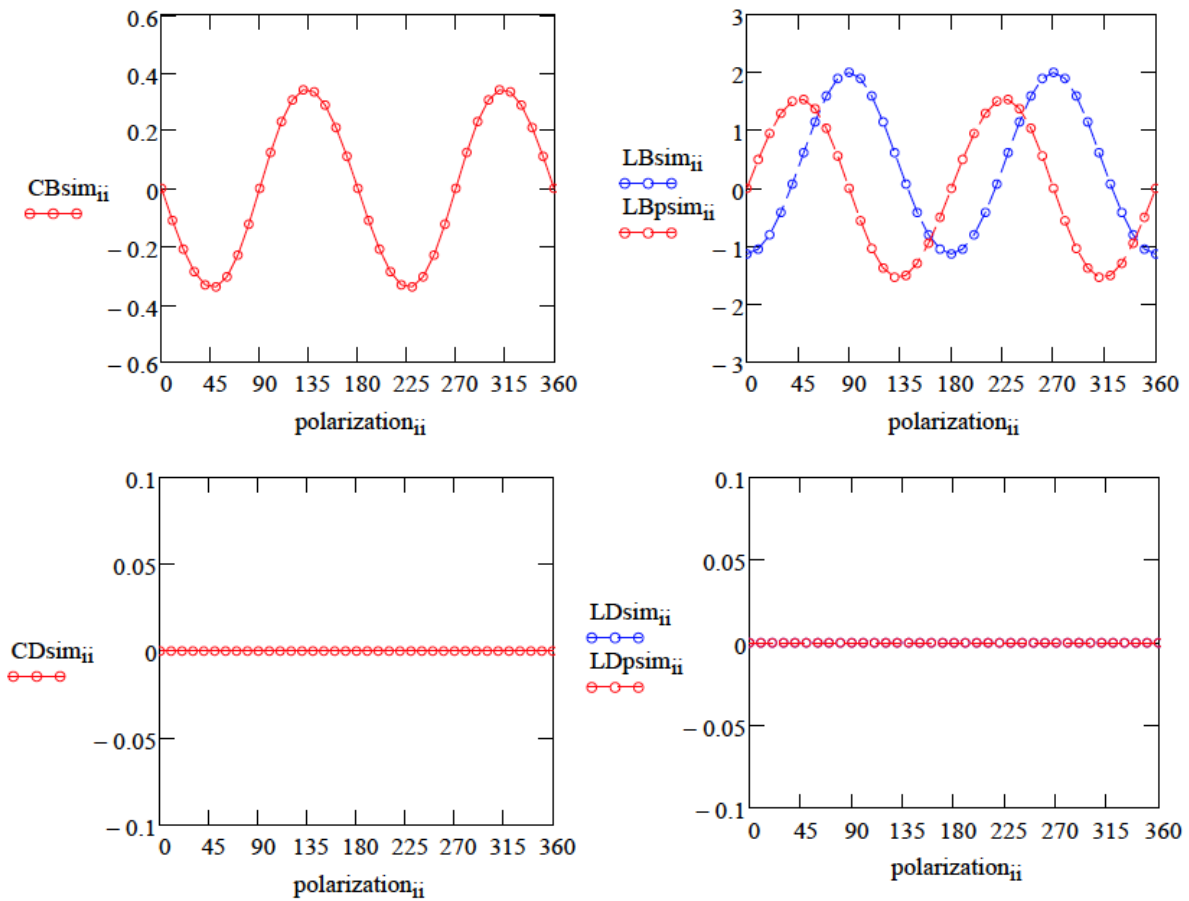


Figure 6.10 Modelling values of effective anisotropic optical properties (expressed in radians) at 550nm as a function of writing laser polarization azimuth  $\theta$ : circular birefringence CB, linear birefringence LB, LB', circular dichroism CD and linear dichroism LD, LD'. *Case 2c: two linear LB layers: one remains fixed and the second one is rotating linearly with the laser polarization.*

2d. Case description: two linear layers with a 45° offset between their respective neutral axis

- $R_1 = 0-360^\circ$  and  $R_2 = -25^\circ$  i.e. one birefringent layer with a negative uniaxial birefringence (variable amplitude noted  $R_1$ ) and a second one with a positive uniaxial birefringence (fixed amplitude  $R_2$ )
- $\Psi_1 = \Psi_2 = 45^\circ$  i.e. no linear dichroism
- $\theta_1 = 45^\circ$  and  $\theta_2 = 0^\circ$  i.e. the slow/fast axis are fixed.

*Results*

The orientation of the first layer is fixed at  $+45^\circ$  compared to the second layer, which is the angular configuration to create a maximum CB amplitude provided the amplitudes  $R_1$  and  $R_2$  exhibit non-zero values. As expected, the CB amplitude depends on the linear birefringence  $R_1$  amplitude, see Figure 6.11. We observe no CB when  $R_1 = 0$  or  $2\pi$  (i.e. 0 or 360°) and the CB is maximum when  $R_1 = \pi$  rad.

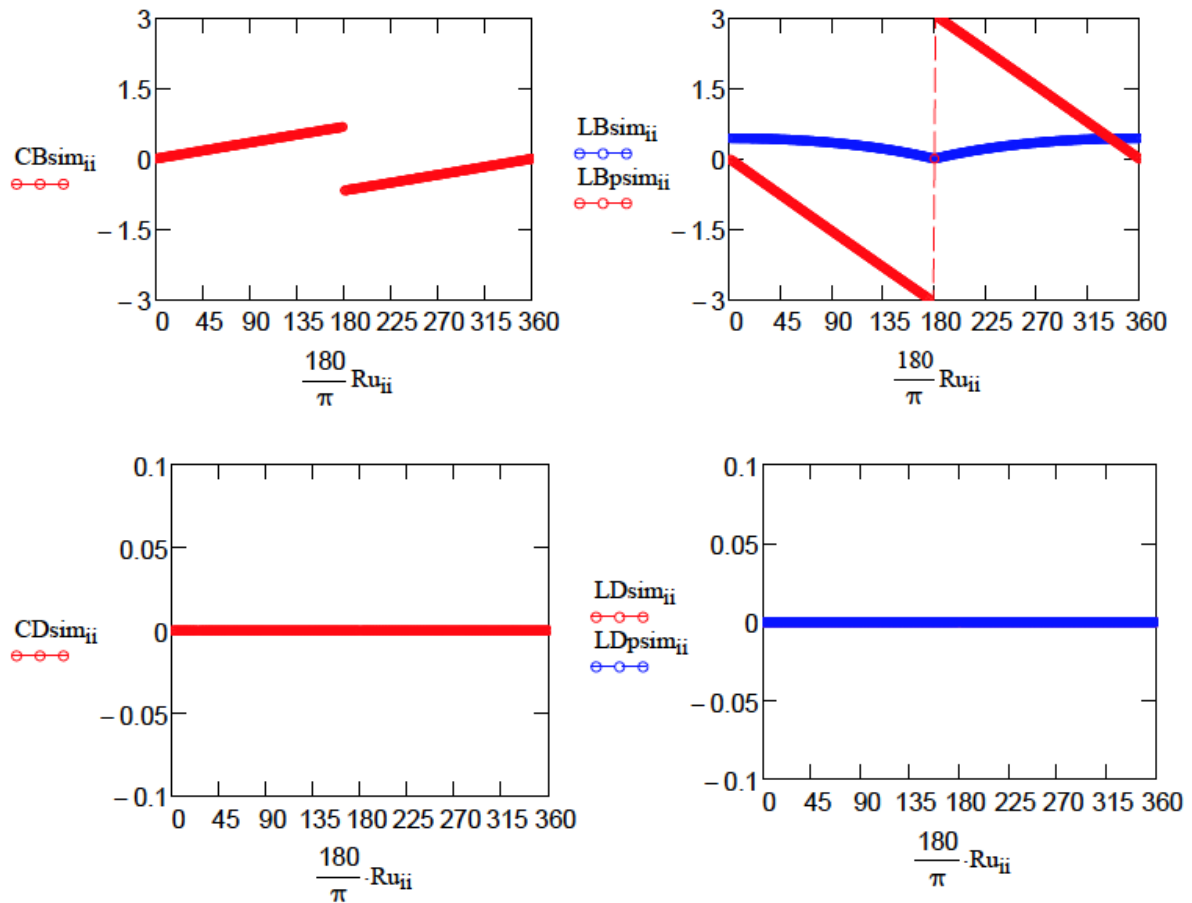


Figure 6.11 Modelling values of effective anisotropic optical properties (expressed in radians) at 550nm as a function of writing laser polarization azimuth  $\theta$ : circular birefringence CB, linear birefringence LB, LB', circular dichroism CD and linear dichroism LD, LD'. *Case 2d: two linear LB layers with a 45° offset between their neutral axis. The variable is the amplitude of the first layer noted Ru (in the graph) or R<sub>1</sub> in the text and changing from 0 up to 2π. Parameters: R<sub>1</sub> = 0-360°, R<sub>2</sub> = 25°, Psi<sub>1</sub> = 45°, Psi<sub>2</sub> = 45°,  $\theta_1$  = 45° and  $\theta_2$  = 0°.*

### 6.3.4 Modeling the formation of CD with two linear retarders

#### 3a. Case description: two linear LD layers; one LD fixed, one LD rotating

- R<sub>1</sub> = R<sub>2</sub> = 0° i.e. no linear birefringence
- Psi<sub>1</sub> = 24° and Psi<sub>2</sub> = 24° i.e. two linear dichroic layers
- $\theta_1$  = 0-360° and  $\theta_2$  = 0° i.e. the slow/fast axis turns linearly with the laser writing polarization orientation whereas the neutral axes of the second layer remain fixed whatever the orientation of the laser writing polarization.

#### *Results*

As shown in Figure 6.12, a sample with two linear dichroic layers leads to the creation of LD and LD' as expected (when LD is zero, LD' is maximum and vice versa) but no LB, LB'. In addition we did not observe any CD but surprisingly we observe the creation of CB with amplitude that depends on the angle between the two layers and a  $\pi$  period according to writing polarization orientation  $\theta$ . CB is maximum when the angular misalignment (offset) is 45° between the neutral axis of two linear dichroic layers.

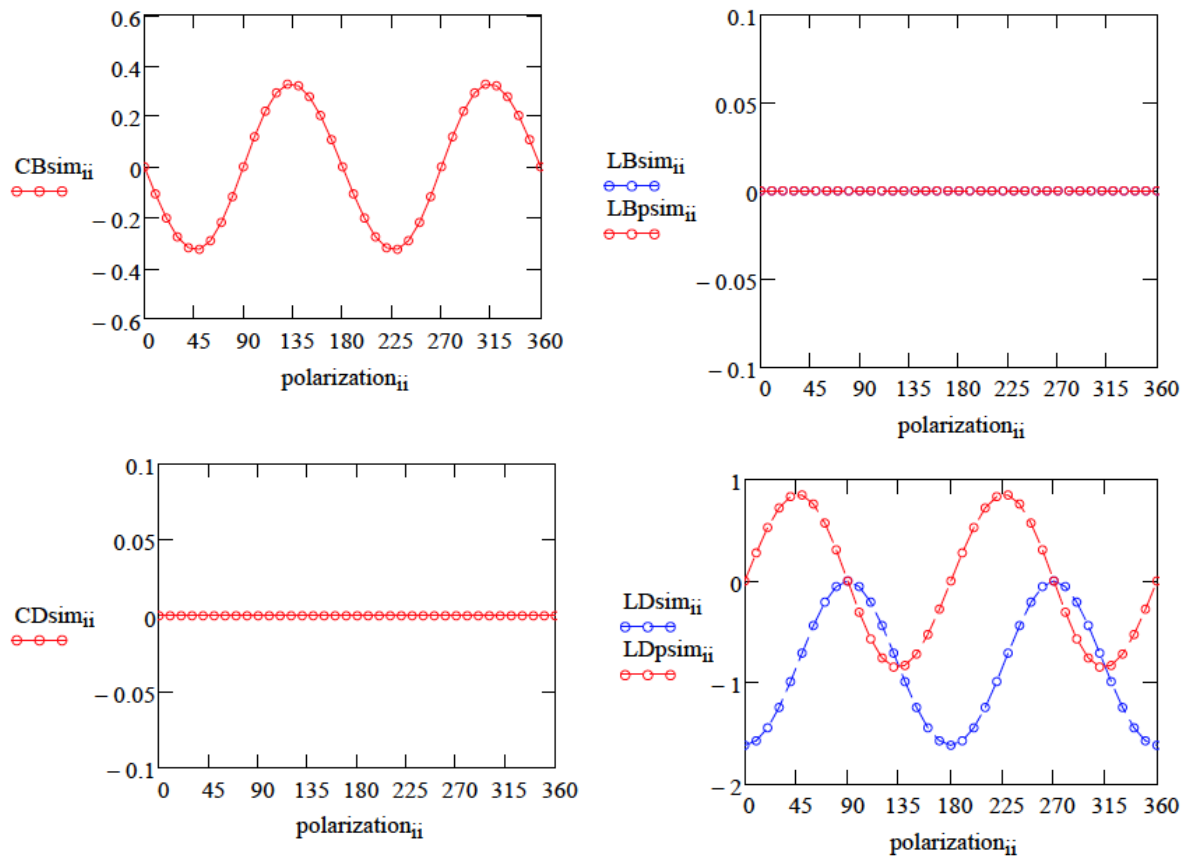


Figure 6.12 Modelling values of effective anisotropic optical properties (expressed in radians) at 550nm as a function of writing laser polarization azimuth  $\theta$ : circular birefringence CB, linear birefringence LB, LB', circular dichroism CD and linear dichroism LD, LD'. *Case 3a: two linear LD layers: one remains fixed and the second one is rotating linearly with the laser polarization. Parameters:  $R_1 = 0^\circ$ ,  $R_2 = 0^\circ$ ,  $\Psi_{i1} = 24^\circ$ ,  $\Psi_{i2} = 24^\circ$ ,  $\theta_1 = 0-360^\circ$  and  $\theta_2 = 0^\circ$ .*

3b. Case description: two linear layers: one LB rotating, one LD fixed (or the reverse case)

- $R_1 = -90^\circ$  and  $R_2 = 0^\circ$  i.e. only layer1 exhibits linear birefringence
- $\Psi_{i1} = 45^\circ$  and  $\Psi_{i2} = 47^\circ$  i.e. layer1 is not dichroic but layer 2 is slightly dichroic
- $\theta_1 = 0-360^\circ$  and  $\theta_2 = 0^\circ$  i.e. the orientation of the pure LD layer turns linearly with the orientation of the laser writing polarization, whereas the orientation  $\theta$  of the LB layer remains fixed.

*Results from Figure 6.13:*

- We observe both the creation of CB and CD.
- The amplitudes of CB, LD and LD' are really small so we have performed a second modeling shown below with  $\Psi_{i1} = 45^\circ$  and  $\Psi_{i2} = 24^\circ$ .
- CB has a  $\theta/2$  periodicity and max CB is observed at  $22.5^\circ$ . Its maximum amplitude remains very small i.e. 0,033 rad even for a strong LD ( $\Psi_{i2} = 24^\circ$ ).
- CD has a  $\theta$  period and max CD is observed at  $45^\circ$  which is in agreement with our experimental results by the way.

- The maximum CD amplitude is around 0.055 rad for  $\Psi_{i2}=47^\circ$  and one order magnitude higher (typ. 0,6 rad) for  $\Psi_{i2}=24^\circ$  as shown in Figure 6.14. The CD sign depends on  $\Psi_{i2}$  and  $\theta$  e.g. if  $\theta = 0$ , CD is negative for  $45^\circ < \Psi_{i2} < 90^\circ$  and positive for  $0 < \Psi_{i2} < 45^\circ$ .

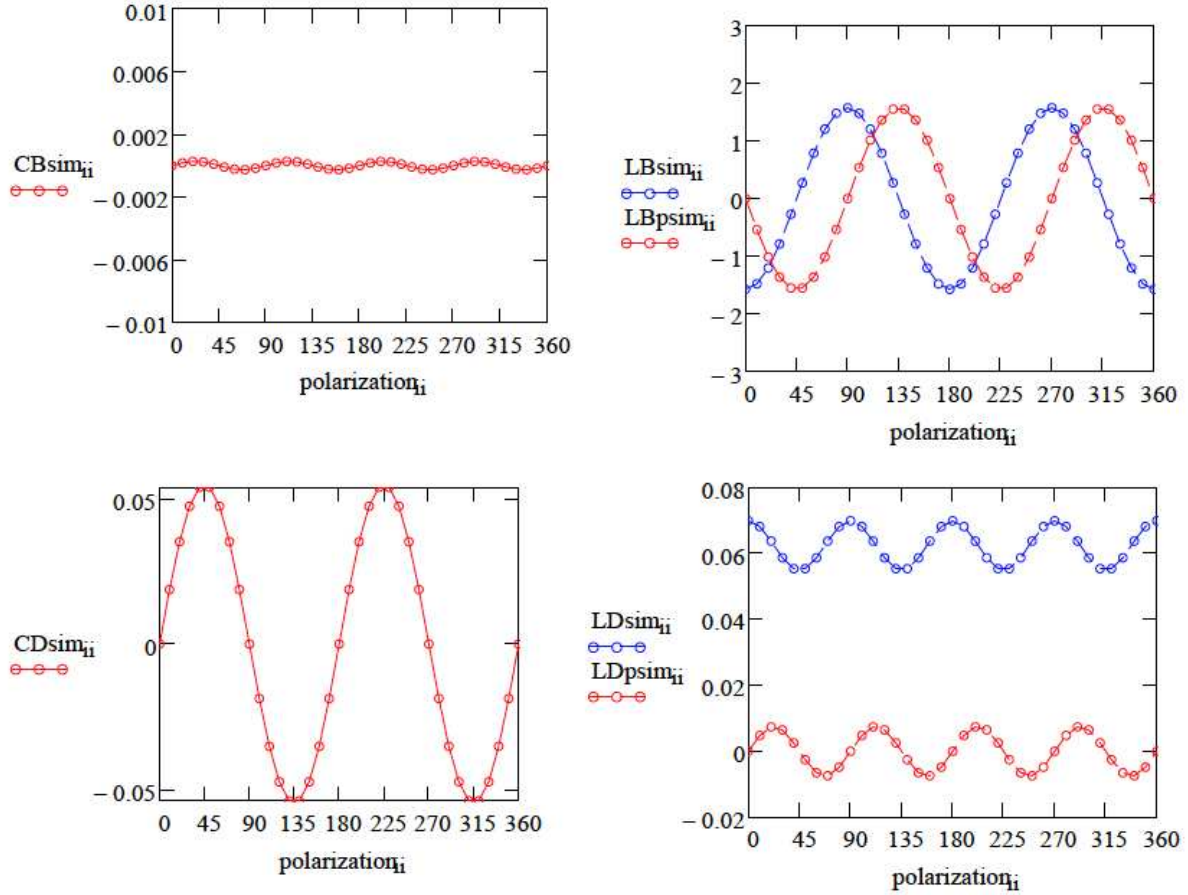


Figure 6.13 Modelling values of effective anisotropic optical properties (expressed in radians) at 550nm as a function of writing laser polarization azimuth  $\theta$ : (a) circular birefringence CB, (b) linear birefringence LB, LB', (c) circular dichroism CD and (d) linear dichroism LD, LD'. *Case 3b: two linear layers: the first one is a LB layer that rotates rotating linearly with the laser polarization and one the second one is a LD layer that remains fixed. Parameters:  $R_1 = -90^\circ$ ,  $R_2 = 0^\circ$ ,  $\Psi_{i1} = 45^\circ$ ,  $\Psi_{i2} = 47^\circ$ ,  $\theta_1=0-360^\circ$  and  $\theta_2=0^\circ$ .*

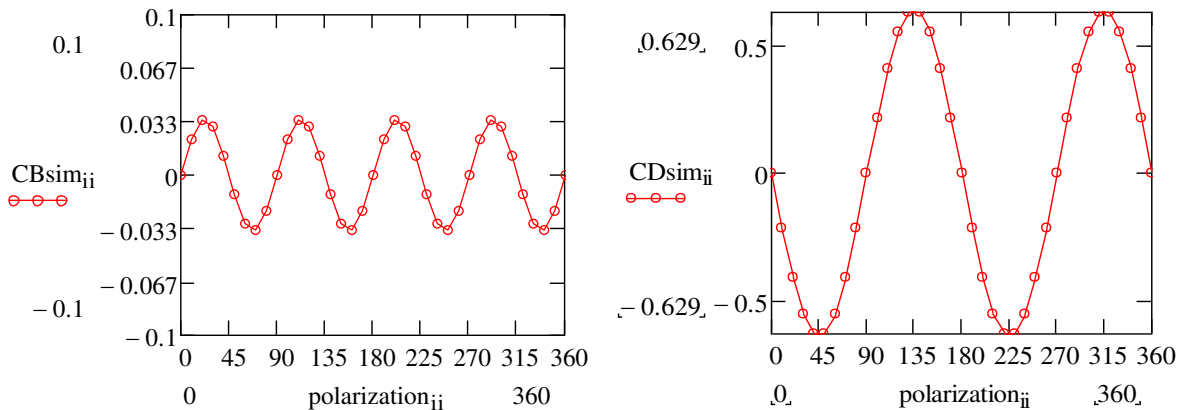


Figure 6.14 Modelling values of effective anisotropic optical properties (expressed in radians) at 550nm as a function of writing laser polarization azimuth  $\theta$ : circular birefringence CB, circular dichroism CD. *Case 3b: two linear layers: the first one is a LB layer that rotates rotating linearly with the laser polarization and one the second one is a LD layer that remains fixed. Parameters:  $R_1 = -90^\circ$ ,  $R_2 = 0^\circ$ ,  $\Psi_{i1} = 45^\circ$ ,  $\Psi_{i2} = 24^\circ$ ,  $\theta_1=0-360^\circ$  and  $\theta_2=0^\circ$ .*

### 6.3.5 Modeling the formation of both CB and CD using two linear retarders

Starting from the above results we will try to find a case with a minimum number of constraints to reproduce our experimental observations: The conditions are as follows:

- We need two LB layers, with non-parallel non-orthogonal neutral axis, in order to create CB but without CD.
- A maximum value of CB is observed when the offset between the layers neutral axes is  $45^\circ$  and when  $R_1$  amplitude is equal to  $\pm \pi$  rad.
- At least one of the two linear retarders should exhibit linear dichroism to create CD with the correct periodicity as a function of the laser polarization  $\theta$ .
- The easiest way to get the right periodicity of  $\theta$  on both CB and CD is to fix the orientation of one LB layer and to have the second layer whose neutral axes vary according to the direction of the laser writing polarization,  $\theta$ .

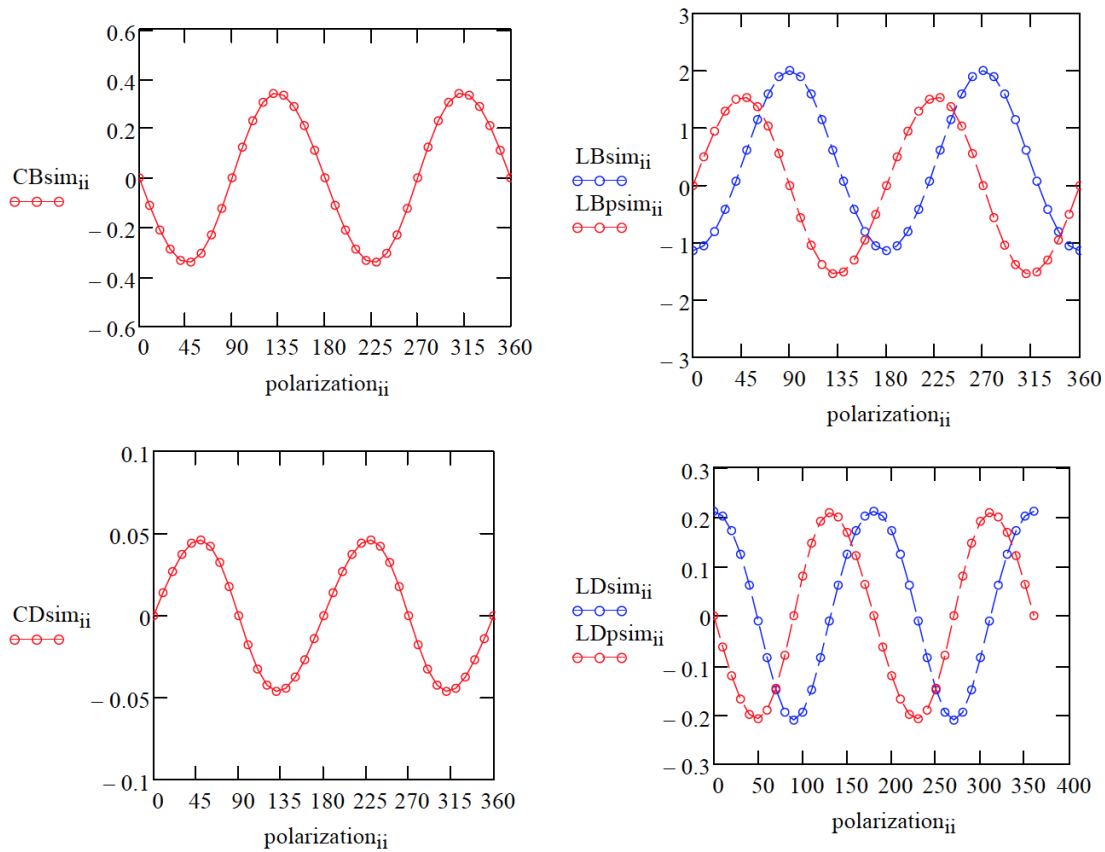


Figure 6.15 Modelling values of effective anisotropic optical properties (expressed in radians) at 550nm as a function of writing laser polarization azimuth  $\theta$ : circular birefringence CB, linear birefringence LB, LB', circular dichroism CD and linear dichroism LD, LD'. *Case 4: two linear layers: the first one is a LB,LD layer that rotates rotating linearly with the laser polarization and one the second one is a LB layer that remains fixed. Parameters:  $R_1 = -90^\circ$ ,  $R_2 = 25^\circ$ ,  $Psi_1 = 40^\circ$ ,  $Psi_2 = 45^\circ$ ,  $\theta_1=0-360^\circ$  and  $\theta_2=0^\circ$ .*

Thus in the following we have chosen to define two layers with the following conditions:



- a LB, LD layer with a high LB (uniaxial negative) and a small LD (positive for Xx writing) that corresponds to ideal nanogratings with  $R_1 = -90^\circ$ ,  $\Psi_1 = 40^\circ$  and a slow axis  $\alpha_1$  that remains perpendicular to the laser writing polarization  $\theta$  i.e.  $\alpha_1 = \theta + 90^\circ$ .
- a second retarder that exhibits LB only (e.g.  $R_2 = 25^\circ$ , positive uniaxial LB) that has a fixed orientation ( $\alpha_2 = 0^\circ$ ) independent of the orientation of the polarization of the writing laser.
- The amplitudes of the linear retardation  $R_1$ ,  $R_2$  have then been adjusted to fit our experimental data in terms of LB, LB', CB and CD whereas  $\Psi_1$  was adjusted to fit correctly LD, LD' data together with circular ones.

Results that can be deduced from Figure 6.15:

- We observe both the creation of CB and CD.
- The amplitudes of CB and CD have both a  $\pi$  periodicity according to the writing laser polarization  $\theta$  but they exhibit opposite signs as we observed experimentally in chapter 4.
- Maximum CB, CD amplitudes are observed at  $\theta = 45^\circ$  in close agreement with our experimental results. This corresponds to a maximum angular misalignment between the neutral axes of the two-modeled layers.
- CB maximum amplitude is quite high e.g. nearly -0,4 rad at  $\theta = 45^\circ$ .
- CD amplitude is one order magnitude smaller than CB: e.g. around +0,05 at  $\theta = 45^\circ$  (using  $\Psi_1=40^\circ$ ) in agreement with our experimental results. But its amplitude can be adjusted using the amplitude of  $\Psi_1$ .

Table 6.1 Summary of the main cases investigated to tentatively describe the creation of CB and CD and their dependence with the laser polarization azimuth angle.

<b>LB<sub>1</sub></b>	<b>LD<sub>1</sub></b>	<b>LB</b>	<b>LD<sub>2</sub></b>	<b>Observations about CB and CD</b>
<b>R1=-90°</b>	<b>Ψ1=24°</b>	<b>R2=25°</b>	<b>Ψ2=24° or 59°</b>	
X				CB = 0 ; CD = 0
	X			CB = 0 ; CD = 0
		X		CB = 0 ; CD = 0
			X	CB = 0 ; CD = 0
X	X			CB = 0 ; CD = 0
X		X		CB if non parallel, non orthogonal layers / max at 45° ; CD=0
X			X	CB $\pi/2$ periodicity; CD $\pi$ periodicity

	X	X		CB $\lambda/2$ periodicity; CD $\lambda$ periodicity
	X		X	CB if non parallel, non orthogonal layers; CD = 0
		X	X	CB = 0 ; CD = 0
	X	X	X	CB, CD if non-parallel, non-orthogonal layers, max at 45°, $\lambda$ periodicity. But cannot match both CB and CD amplitudes that we observed in our experiments.
X		X	X	CB, CD if non-parallel, non-orthogonal layers, max at 45°, $\lambda$ periodicity
X	X		X	CB, CD if non-parallel, non-orthogonal layers, max at 45°, $\lambda$ periodicity. But cannot match both CB and CD amplitudes that we observed in our experiments.
X	X	X		CB, CD if non-parallel, non-orthogonal layers, max at 45°, $\lambda$ periodicity
X	X	X	X	CB, CD if non-parallel, non-orthogonal layers, max at 45°, $\lambda$ periodicity

## 6.4 Polarization dependent anisotropic optical properties: a comparison between modeling and experimental measurements

In the following, the “two-layer” model previously described will be used and the properties of the parameters describing the two layers will be adjusted to try to “fit” the experimental data. In the following figures, the symbols, “o”, or, “x”, correspond to the experimental measurements while the continuous lines correspond to modeled data. In addition, we consider two cases:

- The case where the probe beam enters the side of the first layer (the retarder corresponding to the birefringence of the nanogratings associated with the presence of a non-zero LD) (case 1 or the so-called “FF” case for front face) then the second layer (positive uniaxial with null LD).
- The opposite case (case 2 or case called “BF” for back face, which actually corresponds to the experiment when we turn the sample, in which case the angle  $\alpha$  becomes  $-\alpha$ ).

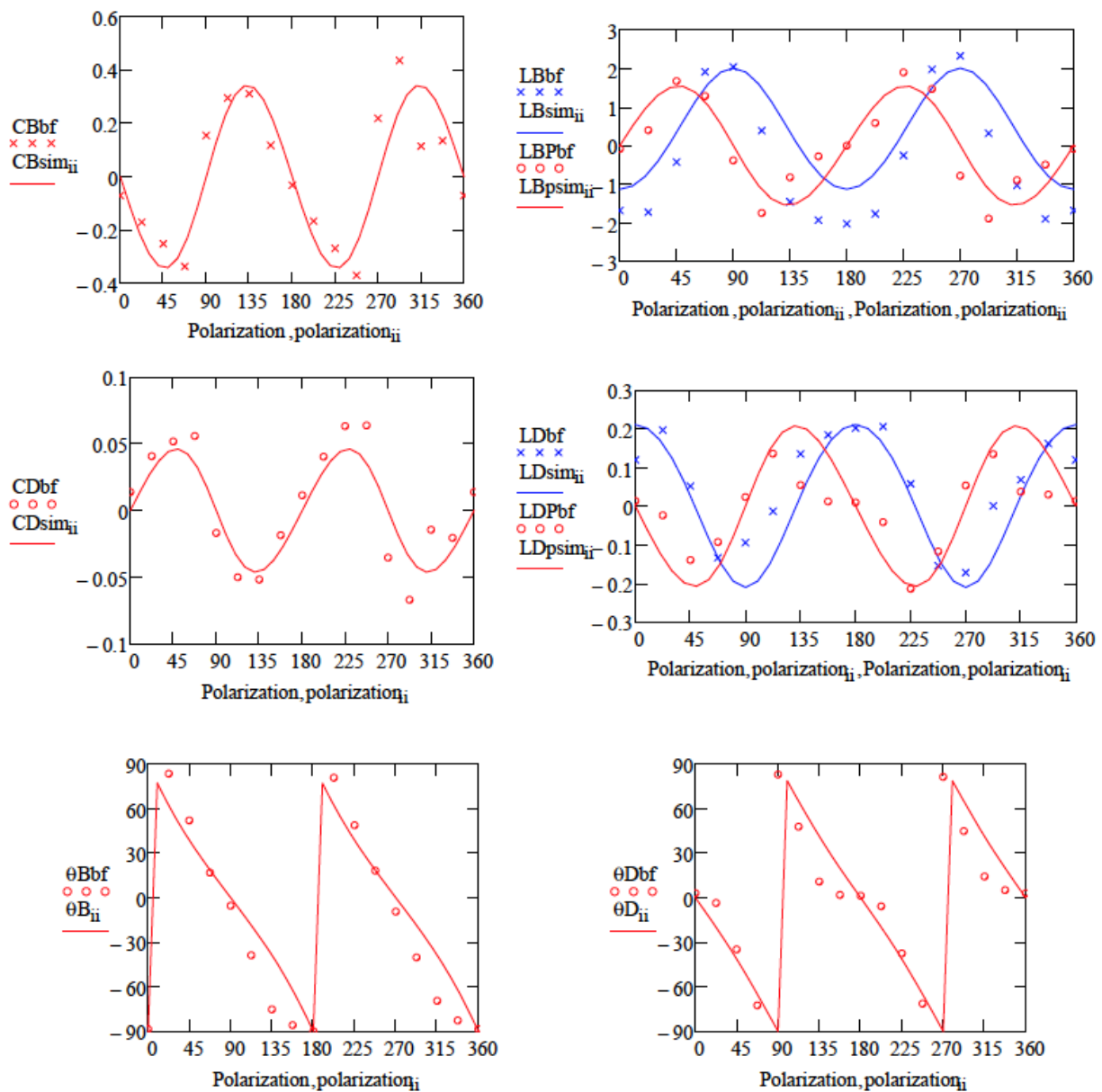


Figure 6.16 Comparison between modelled and experimental values of effective anisotropic optical properties (for Back Face, BF) at 550 nm as a function of writing laser polarization azimuth  $\theta$ . (a) circular birefringence CB, (b) linear birefringence LB, LB', (c) circular dichroism CD, (d) linear dichroism LD, LD'; (e) slow axis orientation of LB  $\theta_B$ ; (f) slow axis orientation of LD  $\theta_D$ .

*Modelling parameters:* Case 4 (two linear layers): the first one is a (LB, LD) layer that rotates rotating linearly with the laser polarization  $\theta$  and the second one is a LB layer that remains fixed.  $R_1 = -90^\circ$ ,  $R_2 = 25^\circ$ ,  $\Psi_{i1} = 40^\circ$ ,  $\Psi_{i2} = 45^\circ$ ,  $\alpha_1 = 0-360^\circ$  and  $\alpha_2 = 0^\circ$ .

*Laser parameters:* 1030 nm, 250 fs, 100 kHz, 0.6 NA, 1 mm/s, 1.5 J/pulse. The writing direction is along X-axis i.e.

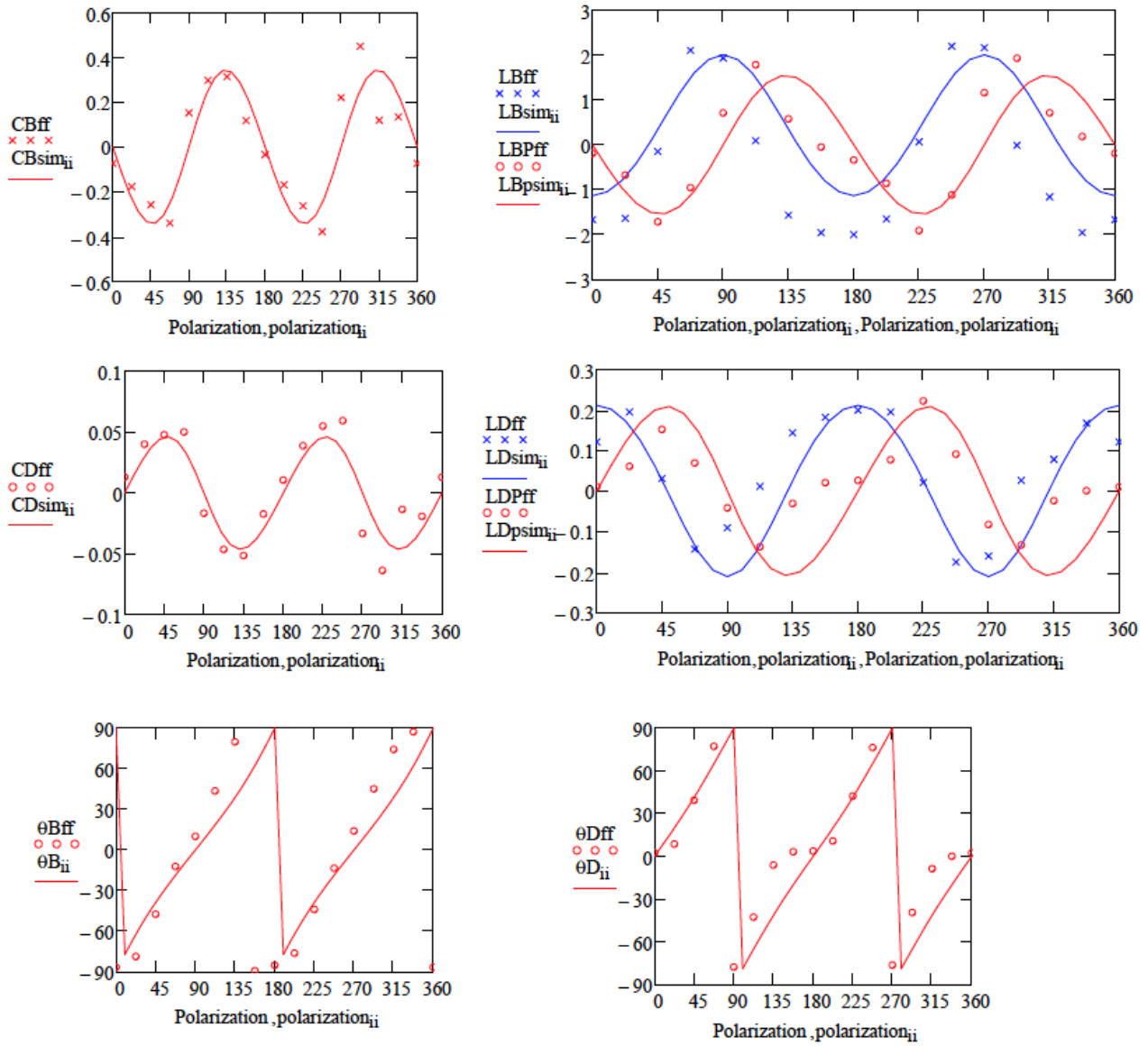


Figure 6.17 Comparison between modelled and experimental values of effective anisotropic optical properties (for Front Face, FF) at 550nm as a function of writing laser polarization azimuth  $\alpha$ . (a) circular birefringence CB, (b) linear birefringence LB, LB', (c) circular dichroism CD, (d) linear dichroism LD, LD'; (e) slow axis orientation of LB  $\theta_B$ ; (f) slow axis orientation of LD  $\theta_D$ .

*Modelling parameters:* Case 4 (two linear layers): the first one is a LB, LD layer that rotates rotating linearly with the laser polarization  $\alpha$  and the second one is a LB layer that remains fixed.  $R_1 = -90^\circ$ ,  $R_2 = 25^\circ$ ,  $\Psi_{i1} = 40^\circ$ ,  $\Psi_{i2} = 45^\circ$ ,  $\alpha_1=0-360^\circ$  and  $\alpha_2=0^\circ$ .

*Laser parameters:* 1030 nm, 250 fs, 100 kHz, 0.6 NA, 1 mm/s, 1,5 J/pulse. The writing direction is along X-axis i.e.

First, the effects reported herein can be discussed and tentatively linked to the formation of nanogratings: they exhibit negative uniaxial form birefringence with the slow axis oriented parallel to the nanolayers, the latter being perpendicular to the writing laser polarization orientation [13].

But, if the samples were solely composed of a single linear birefringent layer (e.g. perfect nanogratings) controlled by the laser polarization, both LB and LB' functions will be perfectly periodic with a  $45^\circ$  shift and no circular properties (CB nor CD) will be observed as it is modeled in Figure 6.17 (case1 or case FF) using Mathcad. However, this is obviously not the

case here since there are some deviations from this simple view:

- $LB(\theta)$  exhibit a deviation for sinusoidal shape with a “flat” zone around  $180^\circ$ .
- $LB'(\theta)$  is periodic modulo  $180^\circ$  but the angular response is not sinusoidal since it has a shoulder around  $180^\circ \pm 22^\circ$ .
- These are directly related to the observed deviation of the LB slow axis orientation  $\theta_B$  that is not perfectly linearly dependent on the laser writing polarization azimuth  $\theta$ .
- Total LB (TLB) and total LD (TLD) depend on the polarization orientation with respect to the scanning direction (here along X-axis), which is usually qualified or at least related to so called anisotropy photosensitivity or asymmetric orientational writing in the literature when this happens for LB that is different for  $0, 45$  or  $90^\circ$  writing polarization i.e. TLB is much higher for  $X90^\circ$  configuration than for  $X0^\circ$ .

On the other hand, we have reported some significant circular anisotropic optical properties namely CB and CD whose creation and control are the key points of this PhD work:

- CB and CD both exhibit a period and a significant non-symmetric periodic dependence with the linear polarization azimuth  $\theta$  (with respect to the scanning direction i.e. along x-axis). Their amplitudes are maximum for  $\theta = \pm 45^\circ$ .
- Note that CB and CD amplitudes depend on the polarization orientation with respect to the scanning direction (here along X-axis), which could be also related to some “kind of” anisotropy photosensitivity or asymmetric orientational writing.

## 6.5 Interpretation of the polarization dependent anisotropic optical properties and the creation of circular optical properties

In terms of linear anisotropic optical properties and orientation of the nanogratings, there are already some deviations reported in the literature or that can be deduced from the literature. At first, the difference in modifications written with  $0^\circ$  (parallel) and  $90^\circ$  (perpendicular) polarization plane angles, with respect to the scanning direction, cannot be explained by the effect of the polarization dependent Fresnel reflection at the boundaries of the photo-induced structure [65, 66]. This would cause polarization effects in metals and dielectrics as p-polarized light (due to Fresnel reflections) will be deposited into material more efficiently compared to s-polarized light. However, TLB varies from 1,5 up to 2,5 rad depending on the polarization orientation and does not follow this view, i.e. the induced TLB in perpendicular polarization ( $X+90^\circ$  configuration) conditions is higher than in parallel polarization conditions ( $X0^\circ$  configuration). In addition, this mechanism cannot explain nor the neutral axes deviations neither the creation of circular optical properties that we observed.

**A first plausible explanation is based on the nanogratings tilt with respect to the laser writing polarization.** While it was widely considered (sometimes for sake of simplicity) that nanogratings are occurring perfectly perpendicular to the incident laser polarization [5,

67, 68], however, a significant tilt is observed depending on the scanning direction relative to the laser polarization in the literature (often related to the quill writing effect). The tilt of the nanogratings orientation is a puzzling phenomenon, which is often regarded as a consequence of asymmetry of the laser beam [69-73]. In the past ten years, a lot of research has been focused in this area. Kazansky et al. [69] proposed that the pulse front tilt (PFT) is the key phenomenon creating nanogratings tilt. Salter et al. used a spatial liquid modulator to achieve the control of directional dependent writing [70, 74] but they did not perform any direct observation of nanogratings using SEM. In a recent work from S. Juodkasis group [75], for linearly polarized laser pulses, the strongest variations of the nanogratings width and period were observed for the scanning directions parallel and perpendicular to the electric field direction (i.e. smaller width and higher period for perpendicular configuration) while the maximum tilt of the nanogratings orientation was observed when the scanning direction was at  $45^\circ$  relative to the electric field direction. In the conditions used for the experiments presented here, the pulse duration was the shortest, and the pulse front tilt was negligible. Therefore, temporal and spatial chirps cannot be invoked to explain the nanogratings tilt dependence on the scanning direction. All these observations were consistently explained by an anisotropic heat-diffusion model that takes into account coupling of the hot electrons in the plasma with the pulse electric field, enhancing the heat diffusion in the direction of the latter. According to these authors, the anisotropic heating of the substrate is responsible for a modulated absorption of light along the different scan directions and explains all the observed features in the above-mentioned references. In short, when the heat affected zone is asymmetric with respect to the scanning direction, absorption will be different on the two sides of the focal volume (larger absorption for the pre-modified material), and this will induce a nanogratings period that is shorter (longer) in the pre-modified (unmodified) side. As a consequence, the overall nanogratings orientation will be affected, with a wave vector  $K$  rotated toward the pre-modified side. *This could qualitatively explain the observed experimental deviations from linearity of the slow axis orientation for both LB and LD with respect to the writing laser polarization orientation. However this cannot explain the significant higher total linear birefringence TLB that we measured for a perpendicular writing configuration.*

**But a 2D tilt of the nanogratings by itself cannot explain the creation of CB, we need an additional phenomenon to break the symmetry.** Thus one possibility would be the creation of "twisted nanogratings" i.e. a 3D helical distribution of nanogratings along the propagation distribution like twisted nematic liquid crystals. This possibility would relate to some recent work from Y. Dai group [76]. These authors observed the orientation of the written nanogratings in silica glass depends on the correlation between the polarization plane azimuth and the PFT [77]. Indeed femtosecond pulse laser with tilted intensity front demonstrates the capability of rotating nanogratings in glass in 3D space. Other than the light polarization, this phenomenon is also associated with the quill-writing effect, which depends on the correlation between the sample movement and the pulse front tilt orientation. This is likely because a ponderomotive force, perpendicular to the tilted intensity plane, can push the excited electron plasma in the direction of the pulse front. This behavior further tilts the electrical field plane and eventually result in a forced rotation of nanogratings in 3D space. This in turn results in the creation of circular optical properties namely CB and

CD. An alternative hypothesis involves the distribution of the laser polarization state and its orientation along the beam propagation direction in the presence of strong focusing and spatial aberrations. This could involve some rotation of the polarization Eigen-states imprinting some 3D rotation of the nanogratings orientation.

A more likely possibility that could explain such a deviation of the linear optical properties orientation is the presence of a second contribution to the LB that is non-parallel, non-orthogonal to the neutral axis of the nanogratings from birefringence. **Here, the most obvious mechanism to explain 1/ the observed deviations of anisotropic linear optical properties but also 2/ the creation of polarization-dependent circular optical properties is related to the formation a significant stress field in but also out of the laser tracks.** Indeed another source of writing polarization dependences and writing direction asymmetries, which is not directly connected with the boundary conditions, was demonstrated. This is related to the creation of a stress field and thus accompanied by a stress-induced birefringence. In 2003, Poumellec et al. [72] have early shown that the induced stress in the laser-affected zone depends on laser parameters such as polarization and energy per pulse. Furthermore, the polarization dependence on the optical retardance observed inside laser tracks depends also on stress and pulse front tilt [39]. For example stress measurement indicates that during laser writing the material is dragged by the thermal gradient and it causes chevron-shape stress distribution [39]. Stress-induced birefringence also causes "tilt" in the front of tracks. As a result, the light polarized at 45° to the writing direction induces the highest retardance when compared to 0° or 90°, which is not the case here as it can be seen on TLB measurements in chapter 4. Lately, Poumellec et al. suggest that a space charge built from a ponderomotive force ( $\vec{\nabla}E^2$ ) is associated with the PFT [78], which might be interpreted as the formation of an asymmetric stress field [73] that can explain the orientational writing dependence effects observed in the literature. In addition, the polarization dependence is strongly affected by the pulse density of laser written tracks. For overlapping tracks, this dependence is mainly defined by the stress-induced birefringence. In contrast it seems that the PFT is playing the major role mostly for separated tracks. As a result, the effect of spatio-temporal distortion can be minimized by overlapping adjacent tracks but at the expense of a higher impact of the stress-induced birefringence, which is likely the situation for our samples.

On the other hand, Y. Bellouard group demonstrated that nanogratings induce a localized permanent volume expansion and consequently, the build-up of compressive stress around laser affected zones [38]. From these experiments, a pressure ( $\sigma_0$ ) has been estimated as a function of the energy deposited in the material. A direct consequence of the "lamellae-expansion hypothesis" is that the amplitude of the stress surrounding laser-written lines should depend on the nanogratings orientation (i.e. the lamellas orientations with respect to the writing direction) as sketched in Figure 6.18. In contrast the orientation of the neutral axis of the stress-induced birefringence is mostly determined by the geometry of the problem, in this case the orientation of the lines as we explained at the beginning of this chapter. So the slow axis of the stress-induced birefringence is parallel to the lines (excluding around the two extremities) whatever the nanolayers orientation may be.

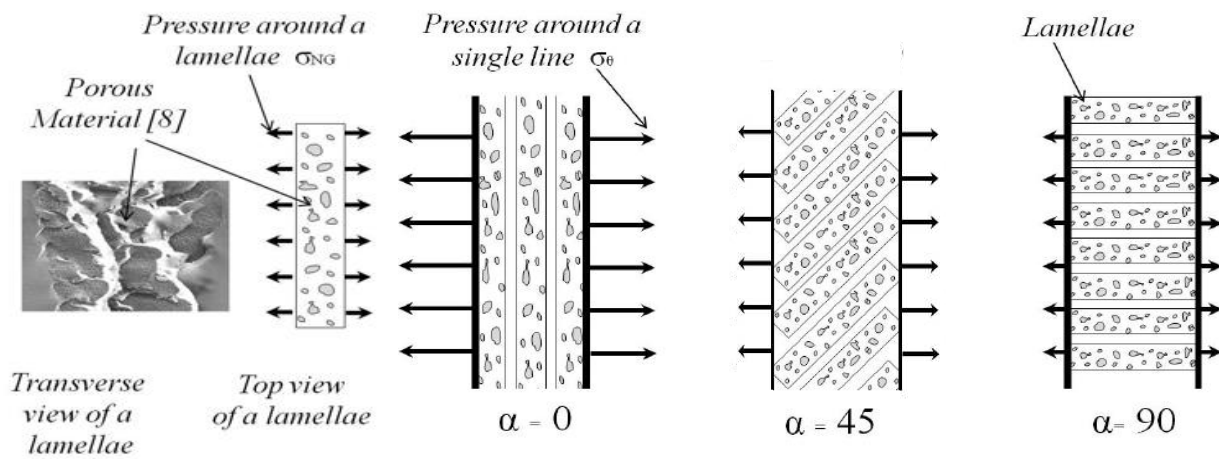


Figure 6.18 (Left) Transverse and top view of a single nanolayer made of porous material [14] (Right) Top view of three lines with different nanogratings orientation according to the writing direction and different  $\sigma_{\theta}$ . ( $\alpha$  is the angle between the writing direction and nanogratings orientation). These schemes are extracted from Ref. [38].

As a result, fs-laser light polarized at  $90^{\circ}$  to the writing direction (with nanolayers parallel to the line direction) would produce stronger stress-induced birefringence than for light polarized at  $0^{\circ}$  [43] i.e. parallel to the writing direction. While the light polarized at  $45^{\circ}$  should have identical conditions as the light polarized at  $-45^{\circ}$  and thus produce identical modifications. In addition the slow/fast axis axes of the total birefringence TLB depend on both the mutual angle between the ones of the form birefringence (dictate by the laser polarization) and the stress-induced birefringence (dictate by the writing direction as a first approximation when writing lines) but also their relative amplitudes. This situation could explain the observed TLB and  $\theta_B$  dependencies on polarization  $\theta$  (Figure 6.16 and Figure 6.17) but also the creation of both CB and CD as we modeled above:

- On the one hand, if we combine the form birefringence and the stress-induced birefringence, we will have either additive or subtractive superposition of the two components. For Xx (or X $0^{\circ}$ ) writing configuration we will have a subtractive superposition, whereas it is an additive superposition for Xy (or X $90^{\circ}$ ) writing configuration explaining the much higher TLB that we measured for such a perpendicular configuration.
- On the other hand, assuming perfect (no tilt) nanogratings and no additional birefringence contribution, the slow axis orientation should be fixed by the laser polarization azimuth  $\theta$ . Now considering the stress-birefringence contribution, the deviation  $\theta - \theta_B$  of the TLB slow axis orientation from linearity should be maximum when the misalignment between the two components is  $\pm 45^{\circ}$  whereas it should be 0 when they are parallel (X $90^{\circ}$ ) or perpendicular (X $0^{\circ}$ ). However it is more difficult to explain the deviation  $\theta - \theta_D$  of the linear dichroism orientation. This might indicate there is a slight tilt of the nanogratings especially when polarization is around  $\pm 45^{\circ}$  off the writing direction.

Finally as sketched in Figure 6.19, we highlighted in the modeling section that a realistic mechanism for the creation of circular anisotropic optical properties can be modeled using multiple linear retarders in a stack. We reveal that CB could originate from several (at least 2) internal linear birefringence contributions with non-parallel, non-perpendicular neutral



axes. **One is obvious since it is related to the nanogratings form birefringence  $LB_{form}$  whereas stress-induced birefringence  $LB_{stress}$  is a great candidate for the second contribution.** Using this model, we were able to explain both the creation of CD and CB but also their dependence with the laser polarization and their respective sign as well. Again here the (CB, CD) amplitudes should be maximum when the misalignment between the two components is  $\pm 45^\circ$  whereas it should be 0 when they are parallel ( $X90^\circ$ ) or perpendicular ( $X0^\circ$ ) in agreement with our observations.

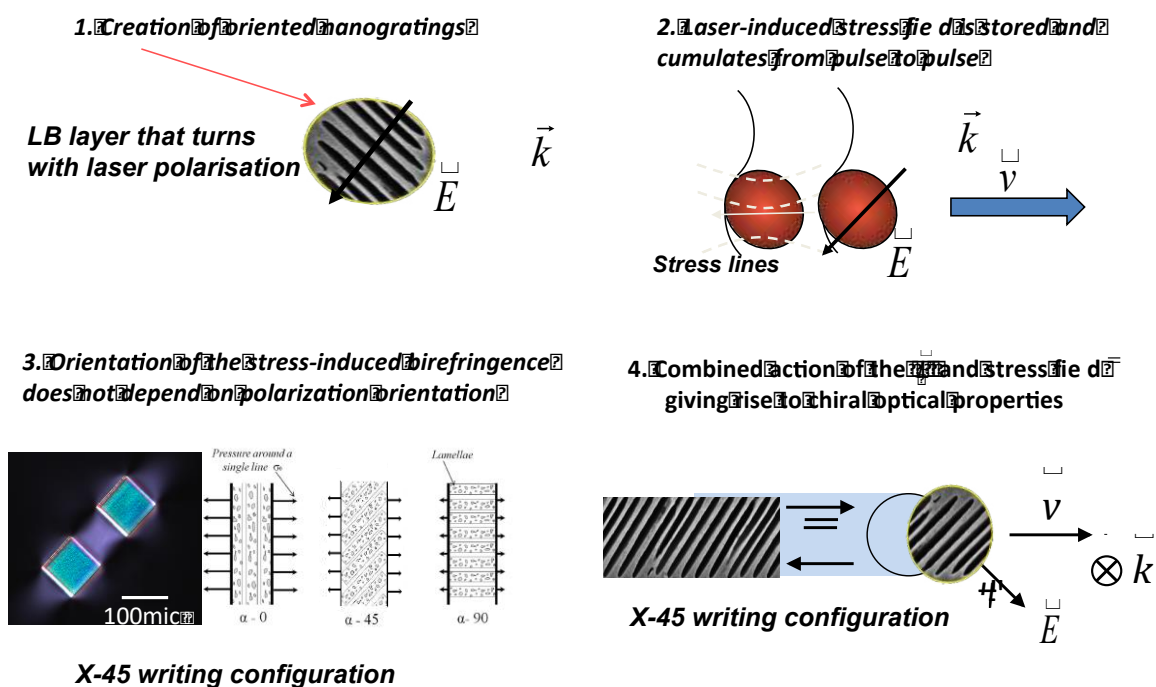


Figure 6.19 Illustrative scheme to qualitatively explain the creation of circular optical properties (1) creation of LB and LD due to nanogratings form birefringence (and dichroism) whose neutral axes are “attached” to the laser polarization, (2) formation of stress field due to permanent volume expansion related to nanoporous layers, (3) the stress-induced birefringence exhibits neutral axes mostly dictate by the scanning direction (for a line), (4) the creation of two LB contributions leads to CB formation when their respective neutral axes are non-parallel, non-orthogonal, the maximum is CB is created for a  $45^\circ$  “misalignment”.

## 6.6 Conclusions

In this last chapter we reveal that the main mechanism, which may be invoked to explain both the occurrence of linear optical properties and the creation of circular optical properties together with their polarization dependence, is the presence of a second contribution to the linear birefringence that is non-parallel, non-orthogonal to the neutral axis of the form birefringence due to nanogratings. All our results led us to consider such a second contribution to the linear birefringence and to perform simple, albeit quite realistic, numerical simulations. We revealed that the minimum conditions to explain qualitatively and quantitatively our overall measurements in terms of LB, LB', LD, LD', CD and CB is the presence of two linear retarders with the following properties:

- The first contribution consists of a negative uniaxial linear retarder that exhibit both LB and LD, which can be attributed to the form birefringence due to the nanogratings ( $LB_{form}$ ) and the related anisotropic light scattering ( $LD_{form}$ ). As a first approximation its orientation can be related to the laser polarization azimuth  $\theta$  i.e. the nanolayers and thus the slow axis orientation are perpendicular to the laser polarization.
- The second contribution is a positive uniaxial linear retarder (without any linear dichroism) with much lower amplitude than that of the first layer. The orientation of the anisotropy of the second layer is correlated to the laser writing direction. When writing lines or set of lines, whatever the orientation of the laser linear polarization may be, the slow axis orientation of this second contribution remains parallel to the writing direction.
- Based on these considerations and on the literature, the most obvious attribution is related to the formation a significant compressive stress field (resulting from the porous nanolayers volume expansion) and thus stress-induced birefringence  $LB_{stress}$ . This is also supported by our measurements with samples written with different directions of the polarization of the written laser. The second argument is the fact that after an annealing for 30 minutes at  $0.9T_g$  ( $T_g$  being around  $1120^\circ\text{C}$ ) all the stress-induced birefringence has been relaxed together accompanied by a reduction (or even an elimination) of the circular optical properties, whereas linear ones only exhibit a minor decay and survives up to  $T_{annealing} > 1200^\circ\text{C}$  for a short time.

In addition, we suggest that the observed deviation of the linear optical properties orientation, both LB and LD, could be attributed to the so-called "tilt" of the nanogratings i.e. a deviation of the nanolayers orientation with respect to the writing polarization orientation  $\theta$ , which needs further investigations to be verified and quantified.

Another possibility to explain the formation of CB and CD could be the presence of an additional force to imprint a rotation of the nanogratings along the beam propagation resulting in the formation of "twisted nanogratings". Some authors suggest a mechanism involving a polarization dependent ponderomotive force related to the PFT that could eventually result in a forced rotation of nanogratings in 3D space. However this could be also due to a "distorted" polarization distribution along the beam focus due to strong focusing conditions couple with a laser beam asymmetry. However, the vectorial nature of

light-matter interaction in the case of nanogratings formation has to be better investigated and understood to go further in this direction.

## 6.7 References

1. Maroufi, S., et al., *Dissolution of silica in slag in silicomanganese production*, in *The Fourteenth International Ferroalloys Congress*. 2015. p. 479-487.
2. Trávníček, P., et al., *Study of rheological behaviour of wines*. International Agrophysics, 2016. **30**: p. 509-518.
3. Poumellec, B., et al., *Parity violation in chiral structure creation under femtosecond laser irradiation in silica glass*. *Light: Science & Applications*, 2016. **5**(11): p. e16178.
4. Yoo, S.H., R. Ossikovski, and E. Garcia-Caurel, *Experimental study of thickness dependence of polarization and depolarization properties of anisotropic turbid media using Mueller matrix polarimetry and differential decomposition*. Applied Surface Science, 2017. **421**: p. 870-877.
5. Shimotsuma, Y., et al., *Self-organized nanogratings in glass irradiated by ultrashort light pulses*. Physical review letters, 2003. **91**(24): p. 247405.
6. Kazansky, P.G., et al., *Anomalous anisotropic light scattering in Ge-doped silica glass*. Physical Review Letters, 1999. **82**(10): p. 2199-2202.
7. Bricchi, E., et al., *Birefringent Fresnel zone plates in silica fabricated by femtosecond laser machining*. Optics Letters, 2002. **27**(24): p. 2200-2202.
8. Sudrie, L., et al., *Writing of permanent birefringent microlayers in bulk fused silica with femtosecond laser pulses*. Optics Communications, 1999. **171**(4-6): p. 279-284.
9. Hnatovsky, C., et al., *Polarization-selective etching in femtosecond laser-assisted microfluidic channel fabrication in fused silica*. Optics Letters, 2005. **30**(14): p. 1867-1869.
10. Bricchi, E. and P.G. Kazansky, *Extraordinary stability of anisotropic femtosecond direct-written structures embedded in silica glass*. Applied Physics Letters, 2006. **88**(11): p. 2-4.
11. Bricchi, E., B.G. Klappauf, and P.G. Kazansky, *Form birefringence and negative index change created by femtosecond direct writing in transparent materials*. Optics Letters, 2004. **29**: p. 119-121.
12. Yu, N., et al., *AIPO 4 in Silica Glass Optical Fibers : Deduction AIPO 4 in Silica Glass Optical Fibers* .: IEEE Photonics Journal, 2019. **11**: p. 1-13.
13. Bricchi, E., B.G. Klappauf, and P.G. Kazansky, *Form birefringence and negative index change created by femtosecond direct writing in transparent materials*. Optics Letters, 2004. **29**(1): p. 119-121.
14. Lancry, M., et al., *Ultrafast nanoporous silica formation driven by femtosecond laser irradiation*. Laser and Photonics Reviews, 2013. **7**: p. 953-962.
15. Vlugter, P. and Y. Bellouard, *Elastic properties of self-organized nanogratings produced by femtosecond laser exposure of fused silica*. Physical Review Materials, 2020. **4**(2): p. 023607.
16. Canning, J., et al., *Anatomy of a femtosecond laser processed silica waveguide [Invited]*.

Optical Materials Express, 2011. **1**(5): p. 998-1008.

17. Desmarchelier, R., et al., *In the Heart of Femtosecond Laser Induced Nanogratings: From Porous Nanoplanes to Form Birefringence*. World Journal of Nano Science and Engineering, 2015. **5**(04): p. 115.
18. Garapon, J., *Etude théorique des défauts déficients en oxygène dans la silice pure ou dopée*. 2001, Université de Paris Sud.
19. Zimmermann, F., et al., *Femtosecond laser written nanostructures in Ge-doped glasses*. Optics letters, 2016. **41**(6): p. 1161-1164.
20. Lancry, M., et al., *Nanoscale femtosecond laser milling and control of nanoporosity in the normal and anomalous regimes of GeO<sub>2</sub>-SiO<sub>2</sub> glasses*. Optical Materials Express, 2016. **6**(2): p. 321-330.
21. Stanczyk, T., et al., *Influence of high temperatures on optical fibers coated with multilayer protective coatings*, in *Proc. SPIE 9816, Optical Fibers and Their Applications 2015*. 2015. p. 98160F.
22. Davis, K.M., et al., *Writing waveguides in glass with a femtosecond laser*. Optics Letters, 1996. **21**(21): p. 1729-1731.
23. Bellouard, Y., et al., *Nanoindentation and birefringence measurements on fused silica specimen exposed to low-energy femtosecond pulses*. Optics express, 2006. **14**(18): p. 8360-8366.
24. Bellouard, Y., et al., *Stress-state manipulation in fused silica via femtosecond laser irradiation*. Optica, 2016. **3**(12): p. 1285-1293.
25. Mishchik, K., et al., *Ultrafast laser induced electronic and structural modifications in bulk fused silica*. Journal of Applied Physics, 2013. **114**(13): p. 133502.
26. Mishchik, K., et al., *Nanosize structural modifications with polarization functions in ultrafast laser irradiated bulk fused silica*. Optics express, 2010. **18**(24): p. 24809-24824.
27. Hernandez-Rueda, J., et al., *The influence of femtosecond laser wavelength on waveguide fabrication inside fused silica*. Applied Physics Letters, 2017. **110**(16): p. 161109.
28. Royon, M., et al., *X-ray preconditioning for enhancing refractive index contrast in femtosecond laser photoinscription of embedded waveguides in pure silica*. Optical Materials Express, 2019. **9**(1): p. 65-74.
29. Born, M. and E. Wolf, *Principles of optics: electromagnetic theory of propagation, interference and diffraction of light*. 2013: Elsevier.
30. Glezer, E.N., et al., *3-D Optical Storage Inside Transparent Materials*. Optics Letters, 1996. **21**: p. 2023-2026.
31. Holmberg, P., F. Laurell, and M. Fokine, *Influence of pre-annealing on the thermal regeneration of fiber Bragg gratings in standard optical fibers*. Optics Express, 2015. **23**: p. 27520.

32. Rosales-sosa, G.A., et al., *Crack-resistant Al<sub>2</sub>O<sub>3</sub> – SiO<sub>2</sub> glasses*. 2016: p. 1-7.
33. Zhang, B., X. Liu, and J. Qiu, *Single femtosecond laser beam induced nanogratings in transparent media - Mechanisms and applications*. Journal of Materiomics, 2019. **5**: p. 1-14.
34. Yeh, P., *A new optical model for wire grid polarizers*. Optics Communications, 1978. **26**(3): p. 289-292.
35. Beresna, M., et al., *Broadband anisotropy of femtosecond laser induced nanogratings in fused silica*. Applied Physics Letters, 2013. **103**(13): p. 131903.
36. Tian, J., et al., *Spectral dependence of femtosecond laser induced circular optical properties in silica*. OSA Continuum, 2019. **2**(4): p. 1233-1241.
37. Desmarchelier, R., et al., *Chiroptical properties photo-induced by femtosecond laser irradiation in silica glass*. Applied Physics Letters, 2017. **110**(2): p. 021112.
38. Champion, A. and Y. Bellouard, *Direct volume variation measurements in fused silica specimens exposed to femtosecond laser*. Optical Materials Express, 2012. **2**(6): p. 789-798.
39. Thomson, R.R., et al., *Stress-state manipulation in fused silica via femtosecond laser irradiation*. Optica, 2016. **3**: p. 1285.
40. Yuan, L., et al., *Stress-induced birefringence and fabrication of in-fiber polarization devices by controlled femtosecond laser irradiations*. Optics Express, 2016. **24**(2): p. 1062-1071.
41. Fernandes, L.A., et al., *Stress induced birefringence tuning in femtosecond laser fabricated waveguides in fused silica*. Optics Express, 2012. **20**(22): p. 24103-24114.
42. Fernandes, L.A., et al., *Strong birefringence tuning of optical waveguides with femtosecond laser irradiation of bulk fused silica and single mode fibers*. Journal of Lightwave Technology, 2013. **31**(22): p. 3563-3569.
43. Champion, A., et al., *Stress distribution around femtosecond laser affected zones: effect of nanogratings orientation*. Optics Express, 2013. **21**(21): p. 24942-24951.
44. Curien, L.H., et al., *X-ray preconditioning for enhancing refractive index contrast in femtosecond laser photoinscription of embedded waveguides in pure silica*. Optical Materials Express, 2019. **9**: p. 65-74.
45. Poumellec, B. and M. Lancry, *Damage Thresholds in Femtosecond Laser Processing of Silica: A Review*. Bragg Gratings, Photosensitivity, and Poling in Glass Waveguides, OSA Technical Digest (CD), 2010.
46. Mihailov, S.J., et al., *Extreme Environment Sensing Using Femtosecond Laser-Inscribed Fiber Bragg Gratings*. Sensors, 2017. **17**.
47. Smelser, C., S. Mihailov, and D. Grobnic, *Formation of Type I-IR and Type II-IR gratings with an ultrafast IR laser and a phase mask*. Optics Express, 2005. **13**(14): p. 5377-5386.
48. Grobnic, D., et al., *Long-term thermal stability tests at 1000°C of silica fibre Bragg*

- gratings made with ultrafast laser radiation*. Meas Science and Technology, 2006. **17**(5): p. 1009.
49. Bricchi, E. and P.G. Kazansky, *Extraordinary stability of anisotropic femtosecond direct-written structures embedded in silica glass*. Applied Physics Letters, 2006. **88**(11).
  50. Biriukov, A.S., et al., *Strength and Reliability of Metal-Coated Optical Fibers at High Temperatures*, in *MRS Proc.* 1998. p. 297-300.
  51. Zoubir, A., et al., *Laser-induced defects in fused silica by femtosecond IR irradiation*. Physical Review B, 2006. **73**(22): p. 224117.
  52. Saeta, P.N. and B.I. Greene, *Primary relaxation processes at the band edge of SiO<sub>2</sub>*. Physical review letters, 1993. **70**(23): p. 3588.
  53. Richter, S., et al., *The role of self-trapped excitons and defects in the formation of nanogratings in fused silica*. Optics letters, 2012. **37**(4): p. 482-484.
  54. Skuja, L.N., *Optically active oxygen-deficiency-related centers in amorphous silicon dioxide*. Journal of Non-Crystalline Solids, 1998. **239**(Section 1. Defect studies in vitreous silica and related materials): p. 16-48.
  55. Martinez, A., I.Y. Khrushchev, and I. Bennion, *Thermal properties of fibre Bragg gratings inscribed point-by-point by infrared femtosecond laser*. Elec. Letters, 2005. **41**: p. 176-178.
  56. Poumellec, B., et al., *Modification thresholds in femtosecond laser processing of pure silica: review of dependencies on laser parameters [Invited]*. Optical Materials Express, 2011. **1**(4): p. 766-782.
  57. Lancry, M., et al., *Dependence of the femtosecond laser refractive index change thresholds on the chemical composition of doped-silica glasses*. Optical Materials Express, 2011. **1**(4): p. 711-723.
  58. Richter, S., et al., *Nanogratings in fused silica: Formation, control, and applications*. Journal of Laser Applications, 2012. **24**(4): p. 042008.
  59. Zimmermann, F., *Ultrashort pulse induced nanostructures in transparent materials*. 2017.
  60. Witcher, J.J., et al., *Thermal annealing of femtosecond laser written structures in silica glass*. Optical Materials Express, 2013. **3**(4): p. 502-510.
  61. Zhang, F., et al., *Wavelength response and thermal stability of embedded nanograting structure light attenuator fabricated by direct femtosecond laser writing*. Applied Physics B, 2014. **117**(1): p. 53-58.
  62. Vlугter, P., E. Block, and Y. Bellouard, *Local tuning of fused silica thermal expansion coefficient using femtosecond laser*. Physical Review Materials, 2019. **3**(5): p. 053802.
  63. Cavillon, M., et al., *Erasure of nanopores in silicate glasses induced by femtosecond laser irradiation in the Type II regime*. Applied Physics A 2020.
  64. Huard, S., *Polarisation de la lumière*. 1994.
  65. Wang, T., et al., *Temperature and strain characterization of regenerated gratings*. Optics

Letters, 2013. **38**: p. 247-249.

66. Frazão, O., M.J.N. Lima, and J.L. Santos, *Simultaneous measurement of strain and temperature using type I and type IIA fibre Bragg gratings*. Journal of Optics A: Pure and Applied Optics, 2003. **5**: p. 183-185.
67. Hnatovsky, C., et al., *Pulse duration dependence of femtosecond-laser fabricated nanogratings in fused silica*. Applied Physics Letters, 2005. **87**: p. 14104-1/3.
68. Hnatovsky, C., et al., *Polarization-selective etching in femtosecond laser-assisted microfluidic channel fabrication in fused silica*. Optics Letters, 2005. **30**(14): p. 1867-1869.
69. Kazansky, P.G., et al., *"Quill" writing with ultrashort light pulses in transparent materials*. Applied Physics Letters, 2007. **90**(15): p. 151120.
70. Salter, P. and M. Booth, *Dynamic control of directional asymmetry observed in ultrafast laser direct writing*. Applied Physics Letters, 2012. **101**(14): p. 141109.
71. Vitek, D.N., et al., *Spatio-temporally focused femtosecond laser pulses for nonreciprocal writing in optically transparent materials*. Optics express, 2010. **18**(24): p. 24673-24678.
72. Poumellec, B., et al., *Femtosecond laser irradiation stress induced in pure silica*. Optics Express, 2003. **11**(9): p. 1070-1079.
73. Poumellec, B., et al., *Non reciprocal writing and chirality in femtosecond laser irradiated silica*. Optics Express, 2008. **16**(22): p. 18354-18361.
74. Salter, P., R. Simmonds, and M. Booth. *Adaptive control of pulse front tilt, the quill effect, and directional ultrafast laser writing*. in *Frontiers in Ultrafast Optics: Biomedical, Scientific, and Industrial Applications XIII*. 2013. International Society for Optics and Photonics.
75. Shao, L.Y., et al., *Viscosity of silica optical fibres characterized using regenerated gratings*. Acta Materialia, 2013. **61**: p. 6071-6081.
76. Dai, Y., et al., *Forced rotation of nanograting in glass by pulse-front tilted femtosecond laser direct writing*. Optics Express, 2014. **22**(23): p. 28500-28505.
77. Dai, Y., et al., *Femtosecond laser induced rotated 3D self-organized nanograting in fused silica*. Optics Express, 2012. **20**(16): p. 18072-18078.
78. Poumellec, B., et al., *Asymmetric Orientational Writing in glass with femtosecond laser irradiation*. Optical Materials Express, 2013. **3**(10): p. 1586-1599.





## Conclusions and perspectives

Femtosecond laser direct writing (FLDW) starts with multiphoton ionization, which induces various permanent modifications inside a solid, such as silica glass. These modifications, which are dependent of laser parameters, include refractive index variations, formation of porous nanogratings and related linear birefringence, or even voids. The processing of glass with low-energy femtosecond laser pulses (sometimes combined with chemical etching) defines a flexible manufacturing platform suitable for technologies like optical data storage, optofluidics, optomechanics, marking, and photonics such as 3D optical waveguides and their combination, fiber Bragg gratings and polarization devices. Manufacturing monolithically integrated devices is drawing great interest because it gives the possibility to induce strong refractive index changes ( $\Delta n$  from  $10^{-3}$  to more than  $10^{-2}$  in a large range of transparent glasses), in extremely well localized volumes in the bulk due to strong non-linear effects. Controlling these modifications could potentially exceed the domain of current fs laser applications. More specifically, the industrial demand for sophisticated all-optical integration is increasingly growing as the volume of exchanged data and information increases. This ultimately yields to a demand in devices with an ever increase of "smartness" with enhanced performance, and therefore greater nuance and complexity of laser treatment are required. Therefore, this stimulates the necessity of optical integration. In this realm, one needs to realize 3D optical circuits, through which the light can be treated. This context was the basis of my dissertation work.

Prior to this work, one critical optical property was still missing from the component library: the integration of circular optical properties (optical rotation and circular dichroism) in glass optical materials and devices. In a previous study performed in 2008, based on measurements done with a phase shift interferometer, the research group in which I did the present PhD revealed that femtosecond laser interactions can shear matter (much like a scissor would do) giving rise to a chiral strain if the light propagation axis is considered. But shearing does not give rise to optical circular properties by itself, as opposed to torsion for instance. Taylor et al. reported highly ordered « chiral-like » nanostructures using circular polarized laser light but no circular optical properties. However, the inscription of orientable circular properties has not made a breakthrough until this PhD thesis. This last point is a breakthrough because the creation of this circular property was done in an achiral glass (pure silica) with a beam that could be considered achiral under an orthogonal geometry. The community thoroughly debated the latter result, as well as the experimental conditions in which it can be obtained, before being accepted. The novelty related to the fact of being able to create and to control circular properties in an achiral medium resulted in a number of publications, which are related to the present PhD. The challenge of this work was thus to pave the way in the control the overall anisotropic optical properties (along with their signs, amplitudes, orientations) at the microscale level and within transparent solid materials, using a low cost, ideally environmentally friendly, and sustainable technology for optical applications.

### Key results

In this direction, the chapter 3 addresses the experimental conditions leading to the creation strong circular dichroism from fs laser irradiation with a linear polarization strongly focused in silica glass and having a perpendicular incidence. In principle, all aspects related to such experimental conditions are achiral, and should not give rise to chiral property creation if taken alone. We investigate the laser-induced circular dichroism according to orientation of the laser polarization, pulse energy, pulse-to-pulse overlap and focusing depth. We have shown that it is possible to produce circular diattenuation by inducing and controlling chirality within an achiral glass, namely SiO<sub>2</sub>, by controlling the laser writing polarization with respect to the scanning direction. The strongest circular dichroism can be imprinted when the laser light polarization is oriented at  $\pm 45^\circ$  with respect to the scanning direction (the latter being perpendicular to the laser beam propagation direction). In addition it appears that deep focusing under high numerical aperture conditions leads to higher ellipticity when compared to shallow focusing or low numerical aperture focusing. **Thus, the generation of circular dichroism appears to be closely related to the spatial aberration, spatial chirp and beam elongation under strong focusing conditions: the deeper the geometrical focus penetrates into the bulk of the sample, the stronger the beam is distorted and elongated and the stronger observed circular dichroism is observed.** Last estimates of equivalent circular diattenuation using a circular dichroism spectrophotometer show values up to  $-30^\circ/\text{mm}$  in the UV wavelength range and  $-20^\circ/\text{mm}$  at  $\lambda = 550 \text{ nm}$ . However it was difficult to extract the real spectral shape of the circular diattenuation due to the co-existence of linear properties with strong response.

In chapter 4 we discuss the use of Mueller matrix ellipsometry in the visible range to investigate silica glass modified by femtosecond laser within nanogratings regime. This method is a powerful tool to examine structural and optical properties of surfaces, thin films, and multilayered materials that exhibit both linear and circular optical properties from a single measurement. We applied the differential matrix formalism on transmission Mueller matrices measured for femtosecond laser-induced modifications in silica within the type II laser-processing regime. A systematic study of the main nanogratings features relative to the direction of the laser beam scanning was carried out on a broad range of the available parameter landscape. In particular, different pulse energies, scanning speeds, focusing, and polarization orientation have been investigated. In all these conditions, we have shown for the first time a reproducible dependence of the nanogratings anisotropic optical properties (namely LB, LB', TLB, LD, LD', TLD, CB, CD and DoP) on the polarization orientation with respect to the writing scanning direction. This can affect the performance of directly written photonic components based on the properties of the nanogratings, as for example the laser-written q-plates. **For linearly polarized laser pulses, the strongest circular optical properties were observed for the electric field direction at  $\pm 45^\circ$  to the scanning directions while the maximum TLB was observed when the scanning direction was at  $90^\circ$  relative to the electric field direction.** We showed how values of the effective structural circular birefringence can be extracted in the presence of strong linear optical properties, and found a maximum value of the effective specific rotation of  $\sim -143^\circ/\text{mm}$  at 550 nm. In contrast, the neutral axes of the stress-induced birefringence appear to be independent of the laser polarization orientation and seem to be mainly oriented according to the scanning (writing) direction of the laser (i.e. lines or set of lines).

In the last section of chapter 4, we report a preliminary study of the thermal stability related to the different contributions of the anisotropic optical properties response in silica. **UV absorption spectra reveal the minor (<5%) effect of point defects on nanogratings birefringence or dichroism. In contrast the stress-induced birefringence exhibits an unexpected rise from 600°C – 1000°C. This increase might be attributed to the existence of Type I-densified area (e.g., between nanoporous layers) within Type II modifications;** the erasure of the former (confirmed by Raman spectroscopy) would cause an increase of the net volume expansion and thus an increase of the compressive stress. This mechanism would need a more detailed study together with modeling, which is the dissertation work of Yitao Wang (PhD student in the period 2019-2022). **Beyond 1000°C, it is determined that stress relaxation is strongly related to the steep decay of the circular optical properties.** Finally above glass transition temperature, the porosity filling factor and the pore size play an extremely important role in the “ultimate” erasure of nanogratings and their associated linear properties (LB and LD) in a high temperature regime.

In chapter 5, we discuss the results of applying transmission Mueller-matrix spectroscopic ellipsometry to study femtosecond laser induced nanogratings in silica glass in a wide spectral range ranging from  $\lambda = 250$  nm up to  $\lambda = 1800$  nm. **By using differential decomposition of the Mueller matrix, the circular birefringence and dichroism of femtosecond laser irradiated SiO<sub>2</sub> are quantified for the first time in the UV and Near-IR range.** A maximum value of the effective specific rotation of  $\sim -860^\circ/\text{mm}$  at 290 nm is found when the laser polarization is oriented at  $45^\circ$  off the scanning direction. **In the near-IR range, we found a linear and circular dichroism band peaking around 1240 nm,** which might be attributed to the formation of anisotropic species like the formation of oriented OH species and Si-O-Si bond.

In the second section of chapter 5, the spectral dispersion of anisotropic optical properties was reported in the UV-Vis-NIR spectral range, **demonstrating the possibility to imprint stress-engineered half-waveplates in the UV-Vis range.** The transmission spectra of these stress-engineered waveplates show that such objects exhibit only minor increment of the absorption constant with respect to the silica substrate, and it remains below  $1 \text{ cm}^{-1}$  in the investigated spectral range. In contrast, nanogratings-based waveplates present strong losses accompanied with a significant linear dichroism and strong depolarization rate in the UV range, which are attributed to the scattering induced by the intrinsically-nanoporous layers constituting the fabricated waveplate. In addition, these stress-induced birefringent waveplates were stable up to  $1000^\circ\text{C}$  (for 30 minutes), making them attractive candidates for UV-Vis birefringent and space variant birefringent devices.

**The results establish that a linearly polarized femtosecond laser beam focused in a glass under an axially symmetric geometry is able to break the chiral symmetry. Here the material (silica glass) is achiral but femtosecond laser irradiation actually gives rise to a chiral property i.e. a significant optical rotation that is reported for the first time.** In chapter 3 we suggested a tentative interpretation that involves the action of a light-induced torque on the matter due to the combined action of the stress field and a DC electric field (defined by the pulse front tilt, the focusing conditions and the laser polarization). The process involves a non-homogeneous electron density due to the effect of the ponderomotive force and the pulse front tilt. At the end of the pulse, electrons relax and become trapped

resulting in static electric field because the counter-ions are much heavier than electrons and are not displaced. **As glass photosensitivity varies with stress field (that increases with pulse overlap), we consider a coupling between the static electric field  $\vec{E}_{DC}$  and the laser-induced stress field. Finally, the misalignment between  $\vec{E}_{DC}$  and the material polarization  $\vec{P}$  generates a volumetric torque  $\vec{P} \wedge \vec{E}_{DC}$ , which may twist the matter.** This could create chiral atomic arrangements or a chiral stress distribution but this can also result in the formation of “twisted nanogratings” like a 3D helical distribution of nanogratings along the propagation distribution. Following this model, the orientation of the laser polarization according to the pulse front tilt (mostly along x-axis in our experiments) and the displacement should lead to the control of sign and amplitude of the circular optical properties. In Chapter 6, we propose another (more likely?) interpretation supported by modeling using Mueller matrix formalism that could explain both the deviation of the linear optical properties orientation and the creation of circular optical properties according to the polarization orientation. **This alternative explanation is the presence of a second contribution to the linear birefringence (LB) that is non-parallel, non-orthogonal to the neutral axis of the nanogratings form birefringence. The most obvious additional linear birefringence mechanism is related to the formation a significant compressive stress field** (resulting from the porous nanolayers volume expansion) and thus stress-induced birefringence in, but also out, of the laser tracks. This is supported by stress-induced birefringence measurements according to the laser polarization and by the correlation between its thermal stability and the one of circular optical properties.

In conclusion we reveal that the control of the polarization orientation with respect to the laser scanning direction (and pulse front tilt) provides a writing strategy to control the sign and the amplitude of the circular optical properties. This allows imprinting circular optical properties in glasses and waveguides and open new possibilities in materials science. This new functionalization process could provide a platform for a versatile new class of photonic devices. In biomimetic fashion, we can imagine producing cholesteric liquid crystal analogous optical devices using tiny lengths of inorganic glass i.e. “twisted silica glass”. An example could be the production of chiral devices that can be harnessed for producing sensors, circular polarizers and potentially optical isolators. We can also imagine a switchable plasmonic material based on chiral plasmonic nanostructures on glass surfaces (e.g., DNA nanostructures decorated with metal nanoparticles) and a plethora of chiral photonic devices. The femtosecond laser offers thus here a new advantage, partly in a non-conventional way: it allows restructuring of our utmost important optical material (silica glass), to enable chiral optical properties More generally, this approach paves the way towards control of the orientation of the crystallization of the compound of interest, e.g., the materials for second harmonic generation or for piezo-electric or ferro-electric effects, i.e., second-order non-linear materials but also chiral arrangement of nanocrystals (whatever they are themselves chiral or not) or oriented nanocrystals that exhibit intrinsic structural chirality.

### **Perspectives**

Towards a new paradigm – To go beyond a simple energy deposition mechanism to develop forces and torques

Understanding of nanoscale response of a material under intense laser excitation is underpinning future laser processing technologies. Mechanical, optical, structural and compositional-related properties of materials could be tailored for novel alloy formation, catalytic and sensor applications. Light polarization is an effective parameter to control the energy delivery in laser structuring of surfaces and volumes. But our objective is to go far beyond a simple deposition of laser energy in the matter. A classical effect of a light beam is a thermal effect (laser cutting, melting) but we want to show that we can develop forces and torques, after non-linear energetic excitation of the transparent matter by intense laser light. What one can imagine with sub-picosecond laser nowadays can be also realized more clearly with a truly femtosecond one appearing on the market in the next years. The time for a half period in the IR at a wavelength of 1  $\mu\text{m}$  is 1.7fs! In that case, opposite charges can be more easily separated. At the end, we will pave the way to materials science by sub-cycle laser pulses. In the future we will use them to show that it is a general possibility in transparent materials. We intend 1) to challenge the proposed theory by simulation work i.e. to show that the forces and torques are large enough, to compute the electric field, and to compute the induced mechanical field, 2) to show we can imprint twisted nanogratings and to figure out the appropriate laser parameters to use, and 3) to show that precipitation and orientation of nanostructures (like nanocrystals) can be controlled using the laser beam only. These future works will increase our knowledge in non-linear action involving the interaction of intense and ultrashort laser light with matter. This new knowledge will be applicable to any structuration of optical functionalization of any dielectric materials in adjacent fields of integrated optics but also to solid state chemistry in general.

#### Exploring vectorial aspects of light matter interaction process

The experimental results reported herein clearly bring to evidence a polarization-affected light matter interaction process. The observed features are expected to be even richer in the case of vector beams and at the tight focusing, where vectorial nature of light has a strong impact. One very exciting prospect is to combine the time and spatial distribution of the polarization, intensity, and phase of the light, inside a dielectric material. By doing so, it will become possible to efficiently control the non-linear force distribution and orientation in the excited solid state (e.g., the induced plasma) and thus the final effect in the matter, like a remote hand can do, exerting mechanical actions in matter in addition to thermal effect. This is possible only for large intensity and short pulse durations when electrons can be excited in delocalized states independently to the ionic motion.

The proposed ideas boil down to the following sentence: match the processing tool (i.e. laser and its spatio-temporal shaping) to a given task. For instance, an interesting result would be the creation of complex nanogratings by combination of several laser beams. This is another promising direction as well as the use of laser beams, which carry an SAM & OAM angular momentum (circularly polarized laser beams or optical vortices). These experiments could help answering the stating question if SAM and OAM are equivalent with respect the light absorption. Another example is Bessel beams that allow fabrication of high aspect ratio structures. Indeed, nanogratings imprinting can be explored not only for generation of known laser beams such as Bessel, Hermite-Gaussian, Laguerre-Gaussian modes, but also enable engineering of both the intensity and the polarization distribution at the focus of the

beam. Among particular vector beams are a class of solutions to the vector wave equation that are defined by a spatially varying direction of polarization. Cylindrical vector beams obey axial symmetry, such as radial and azimuthal polarization. Vector beams are of interest because of their unique focusing properties, which allow a great amount of control over the electric field shape near the focus, including the potential for tighter focusing than with normal beams. We will develop novel birefringent optical elements and will expand knowledge on ultrafast laser beam focus control under tight focusing. For instance, radially polarized laser beam focused with high NA objective will exhibit a strong longitudinal electric field, which could even accelerate charged particles. These possibilities of focal spot polarization engineering can bring benefits to both anisotropic circular but also nonlinear effects imprinting in glasses.

#### Exploring other glass systems – oriented crystallization

We expect to point out that crystallographic structure is controllable by playing with the morphology of the electromagnetic field in the focal volume of the beam focused inside a transparent glass. For instance, concerning the precipitation of chiral crystals from suitable glasses, we expect to get racemic nanocrystal assemblies, when the beam is axy-symmetric, while getting enantiomeric excesses when the beam is not axy-symmetric. The latter may lead to the controlled generation of circular optical properties. In the same time, we expect the orientation of the induced optical properties to be controllable with the orientation of the vector properties of light (polarization, gradients of intensity and phase). Results in this direction will represent a step forward in the understanding of non-linear interaction of light with glasses. In that way we will abandon the classical view in elaboration chemistry that the laser is only an energy source, for a new paradigm in which light can shape the matter at the microscopic level in many ways.

#### Towards applications

Besides the fundamental interest in these nanogratings, which are the smallest structures that can be created by light in the volume of a transparent material, the ability to control the birefringence slow/fast axis and even to induce circular optical properties lead to the engineering of unique integrated optical devices with 3D spatially varying birefringence and refractive index changes.

However currently, intrinsic parameters (period, rotation in 3D, nanoporosity) of femto-second laser induced nanogratings are still not fully controlled. We are now convinced that those spatiotemporal beam distortions are new parameters involved in this process. To improve the device quality, an ongoing major problem is to quantitatively establish the role played by each one of the laser parameters. In addition, the light scattering losses and stress accumulation must be reduced. Again, in this thesis we have brought the understanding of the vectorial nature of light-matter interaction in the case of nanogratings formation understood step further. The ability to manipulate them would open possibilities for engineering optical properties of a given material. We will investigate the ability to induce high retardance of up  $\pi/2$  at 5  $\mu\text{m}$  but also writing nanogratings at high speeds (Typ.  $>10\text{cm/s}$ ) to unlock the industrial potential of this direct writing technique. This will be one major objective of upcoming studies starting in November 2020. As a result, we will be able to develop birefringent based devices operating in a broad spectral range including super-achromatic

components, which are very important for applications ranging from polarimetry, spectroscopy, attosecond pulse generation, THz, military and domotics applications. Furthermore, this will allow us to locally control the phase and polarization of the light, and effectively replace costly equipment such as spatial light modulators.

As one perspective, we propose to specifically apply this 3D manufacturing technique for the fabrication of compact and low cost optical components in Vis and near-IR transparent materials like SiO<sub>2</sub> glasses. Additionally, we plan to extend our results in the UV range and towards the IR i.e. mid-IR using heavy oxide glass materials and later in the far IR using non-oxide glasses like fluorides and chalcogenides. Nanogratings formation inside polymers is another interesting area, which has not been explored yet. Indeed, in mid and far-IR instrumentation, there is a need for miniaturized, low weight and low cost optical systems for civil (domotics, smartphone, automobile) but also security and military applications (vehicles steering, survey, weapons guidance, unmasking, countermeasure identification). The constraints on size and weight of optical systems are so demanding that traditional optical systems with a single optical axis are reaching their limits. Therefore, new breakthroughs in optical design have been proposed that consist in developing bio-inspired multichannel architectures and integrating optical functions using planar optical components. In addition, the possibility of making 3D direct shaping by use of femtosecond lasers enlarges the panel of optical functions we could encode into a small device.

#### From Industry perspective

From the very beginning, the industrial community working in FLDW has strongly been influenced by the development of ultrafast laser systems, which are, in fact, the key part of the ultrafast laser direct writing setup. For example, the initial demonstration of waveguide writing was implemented after introducing Ti:Sapphire laser systems with high operation stability. Thus, future trends in this field should also be determined by the evolution of femtosecond laser systems. We can already see that high average power femtosecond laser systems operating at more than 100 W reached industrial-scale applications, where requirements are raised not only for quality but also for the sake of increasing the process speed. Several commercial systems based on compact and reliable fiber lasers were introduced for two-photon polymerization and glass processing. The flexibility of this technique in terms of materials and its ability to implement 3D geometries with subwavelength precision turned it into an ideal low-cost platform for rapid prototyping, which was explored in the fields of microfluidics, quantum optics, etc. However and for industrial applications, the implementation of parallel processing or at least increasing the volumetric writing speed in ultrafast laser direct writing is of crucial importance. Commonly, even nanojoule laser pulses can modify the material; however, conventional focusing techniques do not allow exploration of the whole power capacity of a laser system. Adding adaptive optics elements into the laser direct writing system has already demonstrated the potential of process parallelization, increasing writing speed (lineic, surface and volumetric), and reducing production cost.





## Publications list

### Journal papers

1. M. Lancry, F. Zimmerman, R. Desmarchelier, J. Tian, F. Brisset, S. Nolte, B. Poumellec, "*Nanogratings formation in multicomponent silicate glasses,*" Appl. Phys. B 122, 66 (2016)
2. R. Desmarchelier, M. Lancry, J. Tian, and B. Poumellec, "*Chiroptical properties photo-induced by femtosecond laser irradiation in silica glass,*" Applied Physics Letters 110 (2), 021112 (2017)
3. Jing Tian, Matthieu Lancry, Sang Hyuk Yoo, Enric Garcia-Caurel, Razvigor Ossikovski, and Bertrand Poumellec, "*Study of femtosecond laser-induced circular optical properties in silica by Mueller matrix spectropolarimetry,*" Opt. Lett.42, 4103-4106 (2017)
4. J. Tian, R. Desmarchelier, B. Poumellec and M. Lancry, "*Femtosecond laser-induced circular dichroism in silica: dependence on energy and focusing depth,*" Nuclear Instruments and Methods in Physics Research Section B 435, 258-262 (2018)
5. Jing Tian, Rubing Li, Sang Hyuk Yoo, Bertrand Poumellec, Enric Garcia-Caurel, Razvigor Ossikovski, Michel Stchakovsky, Celine Eypert, John Canning, and Matthieu Lancry, "*Spectral dependence of femtosecond laser induced circular optical properties in silica,*" OSA Continuum 2, 1233-1241 (2019)
6. Tian J, Yao H, Cavillon M, et al. *A Comparison between Nanogratings-Based and Stress-Engineered Waveplates Written by Femtosecond Laser in Silica[J].* Micromachines, 2020, 11(2): 131.

### International conferences proceedings

1. Tian J, Lancry M, Yoo S H, et al. *Evidence by Mueller spectropolarimetry of optical rotation imprinted by femtosecond laser in silica[C]//Bragg Gratings, Photosensitivity and Poling in Glass Waveguides and Materials.* Optical Society of America, 2018: BW1A. 2. <https://doi.org/10.1364/BGPPM.2018.BW1A.2>
2. Desmarchelier R, Lancry M, Tian J, et al. *Anisotropic circular optical properties photo-induced by femtosecond laser irradiation in silica glass[C]//Bragg Gratings, Photosensitivity, and Poling in Glass Waveguides.* Optical Society of America, 2016: BT3B. 3. <https://doi.org/10.1364/BGPP.2016.BT3B.3>

### International conferences

1. 11th international symposium on SiO<sub>2</sub>, advanced dielectrics and related devices, <https://sio2-2016.sciencesconf.org/> 13-15 June 2016, present poster «Anisotropic circular optical properties photo-induced by femtosecond laser irradiation in silica glass»

2. R. Desmarchelier, M. Lancry, J. Tian, and B. Poumellec, "Anisotropic circular optical properties photo-induced by femtosecond laser irradiation in silica glass," in Photonics and Fiber Technology 2016 (ACOFT, BGPP, NP), OSA Technical Digest (online) (Optical Society of America, 2016), paper BT3B.3.
3. 19th International Conference on Radiation Effects in Insulators (REI-19) <https://rei2017.sciencesconf.org/resource/news> 2-7 July 2017, oral presentation «Study of writing laser polarization dependence on femtosecond laser induced circular properties in silica glass»
4. Bragg Gratings, Photosensitivity and Poling in Glass Waveguides & Materials(BGPP2018) [https://www.osa.org/en-us/meetings/osa\\_meeting\\_archives/2018/bragg\\_gratings\\_photosensitivity\\_and\\_poling\\_in\\_gla/](https://www.osa.org/en-us/meetings/osa_meeting_archives/2018/bragg_gratings_photosensitivity_and_poling_in_gla/) 02-05 July 2018, oral presentation «femtosecond laser induced circular properties in silica glass»
5. 15th Physics of Non-Crystalline Solids and 14th European Society of Glass (PNCS-ESG 2018) <https://pncs-esg-2018.sciencesconf.org/resource/accs> 09-13 July 2018, oral presentation «femtosecond laser induced circular properties in silica glass»

## Summer schools and workshops

1. 1<sup>st</sup> Workshop on Materials for Optics and Optoelectronics 2016 by Charmmmat, <http://www.charmmmat.fr/en/> 8-9 June 2016, present poster «Anisotropic circular optical properties photo-induced by femtosecond laser irradiation in silica glass»
2. Ecole Thématique du GDR CNRS OXYFUN, <http://www.im2np.fr/Ecole-themOxyfun2016/index.html> 25-30 Sept. 2016
3. 1<sup>st</sup> European workshop on Biophotonics and Optical Angular Momentum "BIOAM-2016" <https://bioam-2016.sciencesconf.org/> 14-15 Nov. 2016, present poster «Circular dichroism photo-induced by femtosecond laser in silica glass»
4. Ecole thématique du GDR-Verres à l'Institut d'études scientifiques de Cargèse « STRUCTURAL ROLE OF ELEMENTS IN GLASSES, FROM CLASSICAL CONCEPTS TO A REFLEXION OVER BROAD COMPOSITION RANGE » <http://gdrverres.univ-lille1.fr/> 27-31 Mar. 2017
5. 4<sup>th</sup> ICG School-The Workshop for New Researchers in Glass Science and Application Glass Formation, Structure, and Properties & Glass for Nuclear Waste Immobilization [http://www.icglass.org/news\\_article/?id=2018&news=winter\\_school\\_in\\_wuhan](http://www.icglass.org/news_article/?id=2018&news=winter_school_in_wuhan) 4-10 Nov. 2018.

## Résumé substantiel en Français

La photosensibilité de certains verres à des rayonnements laser continus ou impulsions en régime nanoseconde, a été perçue dans les années 1990 comme un outil de fonctionnalisation des matériaux transparents et en particulier des verres. La chimie prenait alors sa place puisque cette photosensibilité dépendait fortement de la composition chimique du verre et de son environnement physico-chimique dépendant de son histoire thermique. De plus, les propriétés physiques finales étaient issues d'une photochimie du solide. Les lasers utilisés à l'époque, bien que relativement puissants (jusqu'à  $100\text{MW}/\text{cm}^2$  au point focal) pour produire des modifications substantielles, demeuraient encore dans l'optique linéaire ou dans celle non-linéaire à deux photons et devaient utiliser les défauts ponctuels (STE, pièges à électrons etc.) absorbant dans la « gap optique » comme étape initiale. Le faisceau laser était de structure homogène, axisymétrique et déposait son énergie lumineuse principalement par absorption linéaire. L'arrivée du laser femtoseconde (typ. 30 fs à quelques ps), dont les impulsions sont très puissantes, a complètement transformé cette vision. La densité de puissance crête est telle que l'on est d'emblée dans le domaine de l'optique non-linéaire avec la possibilité de « traverser » la bande interdite de la silice avec six photons à 800nm ou encore huit photons à 1030nm. De ce fait, un faisceau focalisé agit naturellement de manière très localisée autour du point focal. C'est donc la porte ouverte vers la microstructuration 3D des propriétés optiques des matériaux transparents (verres, cristaux, polymères). Cependant, on notera que leur distribution spatiale n'est pas toujours évidente comme le laisserait penser un simple dépôt ponctuel de l'énergie contenue dans l'impulsion lumineuse. De plus avec l'accession aisée à l'optique non-linéaire, une porte gigantesque s'ouvrait, celle permettant d'utiliser les propriétés vectorielles de la lumière (polarisation, gradient d'intensité ou de phase).

Ainsi certains aspects de l'interaction lumière-matière sont fondamentalement nouveaux. Ici, la matière et la lumière sont en interaction produisant une auto-organisation structurée du plasma en cohérence le faisceau laser et ses propriétés vectorielles. Après l'impulsion, cette distribution de densité électronique est "imprimée" en piégeant des électrons dans le solide et un champ de contraintes local peut même être stocké. Celle-ci peut être utilisée comme source par l'impulsion suivante assurant ainsi un « effet mémoire ». Dans cette opération, le solide est restructuré par le champ de force créé par le laser. On peut donc imaginer l'orientation des modifications structurales telles que la décomposition d'oxydes solidifiés directionnellement, la formation de nanocristaux orientés ou encore la création de structures chirales. C'est une nouvelle physique. Mais pour la chimie aussi, il y a de nouveaux aspects car les processus passent par des états fortement excités, largement hors équilibres. Il est donc nécessaire de remettre en question certaines idées précédentes pour comprendre l'excitation et la relaxation de la matière puis de contrôler la structure du produit.

**L'idée a été, et est, de les utiliser en science des matériaux pour contrôler les phases formées dans les verres et pour orienter les nano/microstructures (e.g. eutectiques orientés ou d'autres nanostructures qui s'auto-organisent en présence de l'impulsion laser telles que des structures chirales) ou les textures cristallines formées à volonté et en volume.**

Comme notre groupe l'a montré ces dernières années, l'irradiation des verres silicates par

un laser femtoseconde conduit à des modifications structurales de différentes sortes : des changements d'ordre (changement de température fictive), des changements de phase (cristallisation, décomposition, séparation de phase), des migrations chimiques... Ces modifications induisent des changements permanents dans les propriétés physiques (indice de réfraction scalaire ou tensoriel mais aussi les propriétés optiques non-linéaires). Au-delà du simple dépôt d'énergie (lasers d'impulsions longues, >10ps), le laser femtoseconde conduit à la création de forces agissant sur la matière qui conjuguées aux effets déjà connus, « impriment » des structures orientées dans les verres jusqu'alors inconnues. La maîtrise de ces forces peut permettre de dépasser les applications actuelles basées sur l'utilisation de lasers et ouvrir de nouvelles possibilités en sciences des matériaux. La détermination de ces effets est bien sûr utile pour la compréhension fondamentale du problème, mais elle est aussi déterminante dans la maîtrise des futures applications. Ainsi, les plus importantes sont actuellement dans le domaine de l'optique avec l'élaboration de lentilles quelconques adaptées à tout type de correction y compris d'implants oculaires modifiables in situ. Au-delà de l'écriture de lentilles plates ou de guides d'ondes 3D par simple modification de la structure du verre et donc de l'indice de réfraction, on peut maîtriser l'amplitude et l'orientation de la biréfringence optique mais on peut aussi penser maîtriser au niveau tensoriel des susceptibilités d'ordre 3 et surtout d'ordre 2 ou encore à la production d'une chiralité optique (pouvoir rotatoire, dichroïsme circulaire). Notons que la demande pour une intégration optique est très importante car le volume d'informations échangées augmente rapidement et la complexité du traitement en même temps. Son développement est cependant empêché par plusieurs verrous technologiques cruciaux tels que des modificateurs de fréquence et des isolateurs optiques qui requièrent de créer des propriétés non-linéaires du second ordre et des pouvoirs rotatoires, les deux avec des **orientations maîtrisées** mais aussi de maîtriser l'état de polarisation de lumière. Nous avons montré récemment que l'utilisation du laser femtoseconde permet de le faire. Dans ce domaine, nous avons ainsi obtenus les **résultats exceptionnels** suivants :

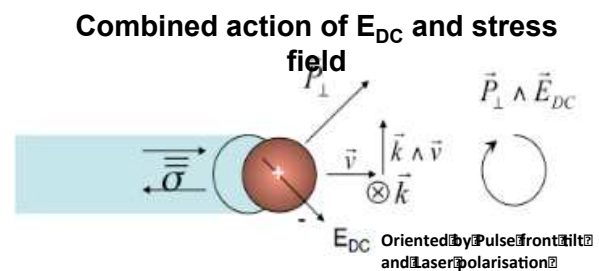
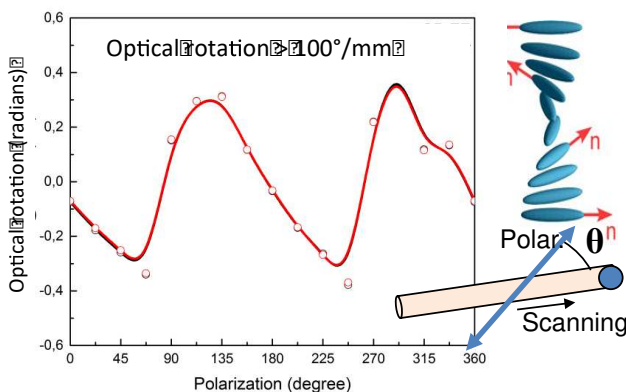
1) **Une décomposition ultra-rapide de la silice (en 160 fs !) à l'origine de la biréfringence.** Les dommages créés dans la silice dans le « régime 2 » sont tels qu'une forte biréfringence est observée. Elle serait principalement due à une biréfringence de forme due à un réseau de nanoplans espacés de l'ordre de 300 nm et de 30 nm d'épaisseur. Cette découverte a été faite par un de nos collaborateurs (P. Kazansky de l'ORC Southampton) avec qui nous collaborons au travers d'un PHC (Partenariat Hubert Curien) et d'un contrat Européen (FP7-PEOPLE-IRSES) dont j'étais le coordinateur. Il restait à déterminer la nature de ces nanoplans. Certains y voyaient des fractures, d'autres des déplétions d'oxygène. Nous avons élucidé cette question en analysant la structure intime de ces nanoplans avec le FEG-MEB de l'ICMMO. Ces nanoplans sont donc formés par une décomposition de la silice. Ce résultat important a été publié en 2013 dans la revue « Laser and Photonics Review » (IF-8, papier joint à cette notice dans le dossier en ligne)

2) Il existe un domaine de paramètres laser où le contrôle de la nucléation-croissance est possible. Dans cet espace, l'action de **la polarisation du laser permet d'orienter les nanocristaux**. Ainsi les axes polaires des cristaux se placent perpendiculaires à la direction de polarisation conduisant au contrôle de la réponse angulaire des propriétés optiques NL d'ordre deux (comme la génération de seconde harmonique). Nous avons proposé des

interprétations de ce phénomène ainsi qu'une rationalisation de la nucléation/croissance cristalline par irradiation laser femtoseconde en fonction de tous les paramètres laser (énergie de l'impulsion, fréquence de répétition des impulsions, vitesse de balayage du laser, état de polarisation du laser et son orientation). *Le caractère exceptionnel de ce résultat réside dans le fait que l'on dépasse l'effet thermique qui était jusqu'à présent seulement utilisé en science des matériaux par laser. Avec ce résultat, on prouve que l'on peut utiliser des propriétés vectorielles de la lumière, ici la polarisation de la lumière.*

3) Les présents travaux ouvrent la voie **vers l'impression 3D de propriétés optiques chirales dans les verres**. Outre l'impression bien connue d'une forte biréfringence linéaire et d'un dichroïsme linéaire principalement dus à la formation de nanoréseaux, nous sommes arrivés conclure sur l'existence de la production de propriétés optiques circulaires dans les échantillons de silice pure après quatre années d'étude. Les résultats de ces travaux de thèse établissent qu'un faisceau laser femtoseconde polarisé linéairement et focalisé dans un verre sous une géométrie axialement symétrique est capable de briser la symétrie chirale, même sous une géométrie d'expérience achiral (l'incidence normale). Ici, le matériau (un verre de silice, SiO<sub>2</sub>) est achiral, mais l'irradiation laser femtoseconde donne en fait lieu à une propriété optique chirale, c'est-à-dire qu'un pouvoir rotatoire important est signalé pour la première fois. Ce résultat important est exposé à la figure ci-dessous montrant des pouvoirs rotatoires très élevés. Un dichroïsme circulaire significatif apparaît également proche de la valeur trouvée pour les molécules organiques. Ce travail de thèse représente une nouvelle percée vers une structuration fonctionnalisante des verres massifs.

Nous avons, depuis quelques années accumuler des présomptions en mesurant des pouvoirs rotatoires, des excès apparents énantiomériques en luminescence au synchrotron, et des dichroïsmes circulaires. Cependant leur analyse a été difficile à mener car la forte biréfringence linéaire du solide irradié produit des artefacts qui « parasitent » les résultats et rendent difficile leur interprétation. Le résultat probant est la création de pouvoirs rotatoires très nets pour une énergie par impulsion dépassant un seuil. On vient de montrer que ce pouvoir rotatoire peut dépendre, et c'était là une des difficultés, dépend de la face de l'échantillon par lequel on fait la mesure. En effet, la présence simultanée de propriétés linéaires et circulaires donne lieu à un échantillon qui n'est plus réversible si ces propriétés ne sont pas homogènes en profondeur. De plus, nous produisons une rotation optique avec un contrôle du signe de la chiralité en contrôlant l'angle entre la polarisation linéaire et la direction de balayage du laser.



Nous avons suggéré une tentative d'interprétation qui implique l'action d'un couple induit par la lumière sur la matière portant un moment diélectrique induit par la lumière, qui pourrait induire une chiralité moléculaire. Dans la théorie que nous avons proposée, la clef de voûte est la formation d'une charge d'espace à partir de *l'exercice de la force lumineuse sur le plasma d'électrons excités*. Ceci développe un champ électrostatique enregistré dans le verre après l'extinction de l'impulsion lumineuse et permet la transmission de l'anisotropie. L'écart d'orientation entre le champ et la réponse du matériau génère alors un couple de torsion  $\vec{P} \wedge \vec{E}_{DC}$  qui peut être à l'origine de l'apparition des propriétés circulaires que nous avons mis en évidence. Il est maintenant nécessaire d'éprouver cette théorie par de nouvelles expériences et simulations.

Une autre explication est basée sur la biréfringence linéaire interne qui pourrait créer un pouvoir rotatoire au travers d'un assemblage non orthogonal non parallèle de deux (ou plus) contributions linéaires. Ici, il existerait une chiralité dans le faisceau pour certaines positions de la polarisation et du déplacement du laser. Le signe de chiralité peut-être contrôlé par les directions relatives des vecteurs de polarisation et déplacement.

L'écriture directe par laser femtoseconde offre donc ici un nouvel avantage, en partie de manière non conventionnelle: il permet de restructurer notre matériau optique, pour permettre non seulement l'impression de propriétés anisotropes linéaires mais aussi de propriétés optiques chirales. De façon biomimétique, on peut imaginer produire des dispositifs optiques analogues à cristaux liquides cholestériques en utilisant de minuscules longueurs de verre inorganique c'est-à-dire du verre de silice « twisté ou torsadé ». Ces propriétés optiques circulaires pourraient jouer un rôle crucial dans les dispositifs optoélectroniques, la détection biologique et la chimie analytique.

**Title :** Femtosecond laser direct writing of circular optical properties in silica glass

**Keywords :** glasses, femtosecond laser processing, photonic, chirality, circular dichroism, Mueller spectroscopy

**Abstract :** Femtosecond Laser Direct Writing (FLDW) allows 3D highly localized permanent modifications of transparent materials with minimal collateral damages. To date, no other manufacturing process has the potential to integrate 3D multifunctional devices made in a single monolithic chip and within a variety of transparent materials. Some aspects of the light-matter interaction are fundamentally new. Solid and plasma coexist for a fraction of picoseconds. In addition, both matter and light interact, resulting to the structuration and shaping of the induced plasma. Here the solid intervenes as a source of electrons. Its microstructure organizes the plasma in coherence with that of the light beam and its vectorial properties (e.g., polarization and its distribution). Then, following the light pulse energy deposition inside the matter, this electron density distribution is "imprinted" by trapping electrons in the solid. A localized stress field can also be stored. The latter can serve as a "source" for the next pulse, thus ensuring a memory effect. In this operation, the solid is restructured by the force field created during the laser irradiation. We can therefore imagine the orientation of the structural modifications like oriented nanostructures (so-called nanogratings), directionally solidified oxide decomposition, oriented nanocrystals or even chiral structures. This is a new physics. But from a chemistry standpoint, there are new aspects to explore as well, since the processes involved are performed in highly excited states, and largely off equilibrium. It is therefore necessary to question some previous ideas for understanding matter excitation and relaxation, and then to control the laser-induced structure and properties. Recently, these properties were successfully harnessed for multiple practical applications, including polarization optics, microfluidics, polarization selective holography and ultra-stable optical data storage opening the door towards all-integrated photonics circuits. However, several technological critical limitations prevent further developments among

which 1) the creation of second order non-linear optical properties and 2) imprinting some optical rotation, both with tunable orientation in 3D. Apart the well-known imprinting of linear birefringence and dichroism mostly due to the formation of nanogratings, the results establish that a linearly polarized femtosecond laser beam focused inside a glass, and under an axially symmetric geometry, is able to break the chiral symmetry of the material. Here, the material is a silica glass and therefore achiral, but femtosecond laser irradiation actually gives rise to a chiral optical property, i.e., a significant optical rotation. This is reported for the first time. Additionally, we were able to induce optical rotation and to control the chiral sign by tuning the angle between the linear polarization direction and the scanning direction. A significant circular di-attenuation also appears that is close to the value found for organic molecules. We suggested a tentative interpretation that involves the action of a light-induced torque on the matter carrying a light-induced dielectric moment that could induce molecular optical activity. Another suggested explanation is based on internal linear birefringence that could be related to a non-parallel and non-orthogonal assembly of two (or more) linear contributions.

Thus, in this context FLDW offers a new advantage, partly in a non-conventional way: it allows restructuring of our most important optical materials, to enable the imprinting of anisotropic linear optical properties but also chiral optical properties. In a biomimetic way, we can envision the fabrication of cholesteric liquid crystal analogous optical devices using tiny lengths of inorganic glass i.e. "twisted silica glass". Such circular optical properties could play a determining role in optoelectronic devices, biological sensing, and analytical chemistry.





**Titre :** Ecriture directe de propriétés optiques circulaires dans la silice par laser femtoseconde

**Mots clés :** verres, laser femtoseconde, photonique, chiralité, dichroïsme circulaire, Mueller spectroscopie

**Résumé :** L'écriture directe par laser femtoseconde (FLDW) permet de créer des modifications permanentes fortement localisées en 3D dans les matériaux transparents. Certains aspects de l'interaction lumière-matière sont fondamentalement nouveaux. Ici, la matière et la lumière sont en interaction produisant une auto-organisation structurée du plasma en cohérence le faisceau laser et ses propriétés vectorielles. Après l'impulsion, cette distribution de densité électronique est "imprimée" en piégeant des électrons dans le solide et un champ de contraintes local peut même être stocké. Celle-ci peut être utilisée comme source par l'impulsion suivante assurant ainsi un « effet mémoire ». Dans cette opération, le solide est restructuré par le champ de force créé par le laser. On peut donc imaginer l'orientation des modifications structurales telles que la décomposition d'oxydes solidifiés directionnellement, la formation de nanocristaux orientés ou encore la création de structures chirales. C'est une nouvelle physique. Mais pour la chimie aussi, il y a de nouveaux aspects car les processus passent par des états fortement excités, largement hors équilibres. Il est donc nécessaire de remettre en question certaines idées précédentes pour comprendre l'excitation et la relaxation de la matière puis de contrôler la structure du produit. Récemment, ces propriétés ont été exploitées avec succès pour de multiples applications pratiques, notamment des optiques biréfringentes, la microfluidique, l'holographie sélective de polarisation et le stockage de données optique ultrastable ouvrant la porte à l'impression laser de circuits photoniques entièrement intégrés. Cependant, plusieurs verrous technologiques cruciaux empêchent son développement : la création de propriétés optiques non linéaires du second ordre et l'impression d'un pouvoir rotatoire toutes deux avec une orientation correcte en 3D. Outre l'impression bien connue d'une forte biréfringence linéaire et d'un dichroïsme linéaire principalement

dues à la formation de nanoréseaux, les résultats de ces travaux de thèse établissent qu'un faisceau laser femtoseconde polarisé linéairement et focalisé dans un verre sous une géométrie axialement symétrique est capable de briser la symétrie chirale. Ici, le matériau (un verre de silice,  $\text{SiO}_2$ ) est achiral, mais l'irradiation laser femtoseconde donne en fait lieu à une propriété optique chirale, c'est-à-dire qu'un pouvoir rotatoire important est signalé pour la première fois. De plus, nous produisons une rotation optique avec un contrôle du signe de la chiralité en contrôlant l'angle entre la polarisation linéaire et la direction de balayage du laser. Un dichroïsme circulaire significatif apparaît également proche de la valeur trouvée pour les molécules organiques. Nous avons suggéré une tentative d'interprétation qui implique l'action d'un couple induit par la lumière sur la matière portant un moment diélectrique induit par la lumière, qui pourrait induire une chiralité moléculaire. Une autre explication est basée sur la biréfringence linéaire interne qui pourrait créer un pouvoir rotatoire au travers d'un assemblage non orthogonal non parallèle de deux (ou plus) contributions linéaires.

L'écriture directe par laser femtoseconde offre donc ici un nouvel avantage, en partie de manière non conventionnelle : il permet de restructurer notre matériau optique, pour permettre non seulement l'impression de propriétés anisotropes linéaires mais aussi de propriétés optiques chirales. De façon biomimétique, on peut imaginer produire des dispositifs optiques analogues à cristaux liquides cholestériques en utilisant de minuscules longueurs de verre inorganique c'est-à-dire du verre de silice « twisté ou torsadé ». Ces propriétés optiques circulaires pourraient jouer un rôle crucial dans les dispositifs optoélectroniques, la détection biologique et la chimie analytique.

